

Slovak University of Technology in Bratislava

Faculty of Electrical Engineering
and Information Technology



CS'99

ECSS'99

ECSS'c

Conference Proceedings

2nd Electronic Circuits and Systems Conference



DISTRIBUTION STATEMENT A
Approved for Public Release
Distribution Unlimited

September 6-8, 1999
Bratislava, Slovakia

19991105 098

REPORT DOCUMENTATION PAGE

Form Approved OMB No. 0704-0188

Public reporting burden for this collection of information is estimated to average 1 hour per response, including the time for reviewing instructions, searching existing data sources, gathering and maintaining the data needed, and completing and reviewing the collection of information. Send comments regarding this burden estimate or any other aspect of this collection of information, including suggestions for reducing this burden to Washington Headquarters Services, Directorate for Information Operations and Reports, 1215 Jefferson Davis Highway, Suite 1204, Arlington, VA 22202-4302, and to the Office of Management and Budget, Paperwork Reduction Project (0704-0188), Washington, DC 20503.

1. AGENCY USE ONLY (Leave blank)		2. REPORT DATE 6 October 1999	3. REPORT TYPE AND DATES COVERED Conference Proceedings	
4. TITLE AND SUBTITLE 2nd Electronic Circuits and Systems Conference			5. FUNDING NUMBERS F61775-99-WF024	
6. AUTHOR(S) Conference Committee				
7. PERFORMING ORGANIZATION NAME(S) AND ADDRESS(ES) Slovak University of Technology Ilkovicova 3 Bratislava 812 19 Slovakia			8. PERFORMING ORGANIZATION REPORT NUMBER N/A	
9. SPONSORING/MONITORING AGENCY NAME(S) AND ADDRESS(ES) EOARD PSC 802 BOX 14 FPO 09499-0200			10. SPONSORING/MONITORING AGENCY REPORT NUMBER CSP 99-5024	
11. SUPPLEMENTARY NOTES				
12a. DISTRIBUTION/AVAILABILITY STATEMENT Approved for public release; distribution is unlimited.			12b. DISTRIBUTION CODE A	
13. ABSTRACT (Maximum 200 words) The Final Proceedings for 2nd Electronic Circuits and Systems Conference, 5 September 1999 - 8 September 1999 This is an interdisciplinary conference. Topics include Analog and Mixed Circuits, Digital Signal Processing, Low-Voltage, Low-Power Design, Neural Networks, Microsystems, and Optical Communication Systems.				
14. SUBJECT TERMS EOARD, Signal Processing, Neural Networks, Microelectronics, Nanotechnology, Optical communications			15. NUMBER OF PAGES 323	
			16. PRICE CODE N/A	
17. SECURITY CLASSIFICATION OF REPORT UNCLASSIFIED	18. SECURITY CLASSIFICATION OF THIS PAGE UNCLASSIFIED	19. SECURITY CLASSIFICATION OF ABSTRACT UNCLASSIFIED	20. LIMITATION OF ABSTRACT UL	

NSN 7540-01-280-5500

Standard Form 298 (Rev. 2-89)
Prescribed by ANSI Std. Z39-18
298-102

AQF00-02-0428

ECS'99

Proceedings of the

2nd Electronic Circuits and Systems Conference

September 6-8, 1999
Bratislava, Slovakia

Edited by
Viera Stopjaková

FOREWORD

The organisers and hosts receive great pleasure presenting you the Proceedings of the Second International Conference on Electronic Circuits and Systems, ECS'99, and giving you the warmest welcome to the conference and the joint "Experts Session". The ECS'99 follows the successful and memorable conference which was held on this spot in September 1997. The event is primarily devoted to a wide spectrum of activities and latest results in the rapidly evolving information society where the electronic, particularly microelectronic and communication technologies play an important role, which also brings about a swift expansion in the field of microsystems and a wide variety of their applications. Another aspiration of the conference and of the joint Experts Session is to enhance the transfer of high-tech towards our industrial partners, particularly to SMEs.

We have received up to 100 submissions from 25 countries of the world. After a thorough reviewing process, the members of the International Program Committee have selected 46 submitted papers for oral presentation and 10 papers as posters. The invited globally renowned speakers will cover the main conference topics. The invited talks, expert session, contributed oral presentations and poster sessions along with many interesting personal meetings during coffee breaks, lunches and common evenings in Bratislava will give all of us excellent chances for fruitful discussions and dissemination of recent achievements. It is our pleasure to thank all authors and participants for the effort they made to prepare their contributions. We would like to express our gratitude also to the members of the International Program Committee for their effort and contribution to the quality of the conference.

The contributed and invited papers are resented in the Proceedings by extended abstracts which were not subject to further reviewing, except for non-technical editorial aspects. Thus, the contents of the papers are the sole responsibility of the authors.

We believe that ECS'99 will continue the aspiration of ECS'97 to establish a forum for regular European meetings bringing together the leading experts from the world, particularly from the countries of Europe. Frequent and intense international collaboration, globalisation of the world, and contacts of the Department of Microelectronics of the Slovak University of Technology in Bratislava, and the geographical location of Bratislava on the border of three countries, very close to the International Airport of Vienna, support this idea as well. The importance of the conference has been underlined by participation and support of the Ministry of Education of the Slovak Republic.

Technical co-sponsorship of the IEEE Computer Society, Test Technology Technical Council, as well as the support of IEE through its Slovak Centre are appreciated. The support of the cosponsoring organisations contributes to the quality of the event as well.

We wish to thank the European Office of Aerospace Research and Development, Air Force Office of Scientific Research, United States Air Force Research Laboratory for their contribution to the success of this conference.

The editors are very grateful to everybody who helped to bring this conference to fruition, especially the conference secretariat, the members of the program and organising committees, and all those who accepted invitations to present talks or who submitted papers for consideration.

On behalf of the Organising Committee we would like to wish all of you a great deal of success in your scientific discussions and a pleasant and memorable stay in Bratislava, the capital of the Slovak Republic.

Viera Stopjaková
Organising Committee Chairman

Daniel Donoval
General Chairman

General Chairman

Daniel Donoval, STU Bratislava, Slovakia

Program Committee

Hamed Al-Raweshidy, University of Kent, United Kingdom
 Karol Blunár, University of Žilina, Slovakia
 Ivo Bolsens, IMEC, Leuven, Belgium
 Anthony Boucouvalas, University of Bournemouth, United Kingdom
 Erik Bruun, Technical University of Denmark, Lyngby, Denmark
 Alfonso Carlosena, Public University of Navarra, Spain
 Eduard Cerny, Universite de Montreal, Canada
 Branka Zovko-Cihlar, University of Zagreb, Croatia
 Luc Claesen, IMEC, Leuven, Belgium
 Bernard Courtois, INPG, Grenoble, France
 Daniela Ďuračková, Slovak University of Technology, Bratislava, Slovakia
 Dan Dascalu, IMT Bucharest, Romania
 Kalman Fazekas, Technical University of Budapest, Hungary
 Norbert Frištacký, Slovak University of Technology, Bratislava, Slovakia
 Nobuo Fujii, Tokyo Institute of Technology, Japan
 Walter Geisselhardt, Gerhard-Mercator-University, Duisburg, Germany
 Manfred Glesner, Darmstadt University of Technology, Germany
 Elena Gramatová, Slovak Academy of Sciences, Bratislava, Slovakia
 Herbert Grünbacher, Technical University of Vienna, Austria
 Andrzej Kobus, Institut of Electron Technology, Warsaw, Poland
 Vello Kukk, Technical University of Tallinn, Estonia
 Vladimir Lantsov, Vladimir State Technical University, Vladimir, Russia
 Dušan Levický, Technical University of Košice, Slovakia
 Hans Manhaeve, KHBO, Oostende, Belgium
 Daniel Mlynek, Swiss Federal Institute of Technology, Lausanne, Switzerland
 Igor Mucha, Microtronic, Roskilde, Denmark
 Andrzej Napieralski, Technical University of Lodz, Poland
 Eros Pasero, Politecnico di Torino, Italy
 Adam Pawlak, University of Nantes, France
 Zebo Peng, Linköping University, Sweden
 Pavol Podhradský, Slovak University of Technology, Bratislava, Slovakia
 Jiří Pospíšil, Technical University of Brno, Czech Republic
 Marta Rencz, Technical University of Budapest, Hungary
 Antonio Rubio, CPU Barcelona, Spain
 Rimantas Seinauskas, Kaunas University of Technology, Lithuania
 Dieter Seitzer, Fraunhofer Institut für Integrierte Schaltkreise, Erlangen, Germany
 Leslie Smith, University of Stirling, United Kingdom
 Viera Stopjaková, Slovak University of Technology, Bratislava, Slovakia
 Gaynor Taylor, Leeds Metropolitan University, United Kingdom
 Raimund Ubar, Technical University of Tallinn, Estonia
 František Uherek, Slovak University of Technology, Bratislava, Slovakia
 Baldomir Zajc, Technical University of Ljubljana, Slovenia
 Yervant Zorian, Logic Vision, Princeton, USA

Cosponsorship

Ministry of Education of the Slovak Republic

FEI STU Bratislava

IEEE Computer Society TTTC

IEE Slovak Centre

EOARD

SIEMENS Slovakia

MOTOROLA

Euro Comp Bratislava

PROMOS Foundation

Table of Contents

<i>FOREWORD</i>	<i>ii</i>
<i>Program Committee</i>	<i>iii</i>
<i>Cosponsorship</i>	<i>iv</i>
<i>Table of Contents</i>	<i>v</i>

Invited Talk 1

System-on-Chip: Test and Diagnosis	1
Y. Zorian	

Session 1A: Testing and ATPG

Easily Testable Carry - Save Multipliers with Respect to Path Delay Faults	13
Th. Haniotakis, H. T. Vergos, Y. Tsiatouhas, D. Nikolos and M. Nicolaidis	
Fast and Efficient Static Compaction of Test Sequences Using Bipartite Graph Representation	17
A. Markus, J. Raik and R. Ubar	
A Hierarchical Test Generation Technique for Embedded Systems	21
G. Jervan, P. Eles and Z. Peng	
An Estimation-based Technique for Test Scheduling	25
E. Larsson and Z. Peng	
TPG for Combined I_{DDQ}-Voltage Testing of Combinational Circuits	29
E. Gramatová, J. Bečková and J. Gašpar	

Session 1B: Digital Circuits Design

Optimisation and Implementation of the Arctan Function for the Power Domain	33
A. Th. Schwarzbacher, A. Brasching, Th. H. Wahl, P. A. Comiskey and J. B. Foley	
Gallium Arsenide Implementation of the Building Blocks for a Direct Digital Frequency Synthesiser	37
S. Lachowicz, K. Eshraghian, M. Hollreiser and H-J. Pfeleiderer	
Introducing Delay Probability Graphs with the Design of a 32-bit Asynchr. ALU	41
F. Pessolano	
Efficient Controller Design for Data Stream Processing Applications in a FPGA Based Prototyping Environment	45
K. Feske, A. Krebs and M. Langer	
A Configurable 8051 Microcontroller Core	49
I. Janiszewski, R. Baraniecki and K. Siekierska	

Invited Talk 2

Design Technology for Future Embedded Telecom Systemsx	53
I. Bolsens	

Invited Talk 3

A product life-cycle view of the value of Boundary Scan	55
R. G. Ben Bennetts	

Session 2A: Current Testing & Microsystems

Implementation of On-Chip Supply Current Monitoring Unit in an Experimental CMOS Digital Design	65
V. Stopjaková, B. Straka, H. Manhaeve and B. Weber	
IOCIMU-2: An Integrated Off-Chip I_{DDQ} Measurement Unit	69
M. Sidiropoulos, B. Straka, M. Švajda, H. Manhaeve and J. Vanneuville	
Integrated Circuit Temperature Estimation Using QR-RLS Adaptive Algorithm	73
M. Janicki and A. Napieralski	
Use of Absorption Resonance Frequency Meter in Measure Sensor System	77
M. Husák and B. Palán	

Session 2B: H/S Co-design & Design Methodology

Properties Coverification for HW/SW Systems	81
M. Azizi, E. Aboulhamid and S. Tahar	
A New Approach for Parallelising and Optimising Hardware Compilation and Partitioning in Hardware/Software Co-Design	85
M. Theisen, T. Hollstein, J. Becker and M. Glesner	
A Design Methodology to Secure Memories in Space Environment	89
F. M. Roche and T. Monnier	
A Methodology for System-Level Functional Verification of Multi-Media Applications	93
M. Čupák, F. Cathoor and H. De Man	

Invited Talk 4

Analog (S)witchcraft, or How to Perform Accurate and Linear Data Conversion Using Inaccurate Nonlinear Elements	97
G. C. Temes, U-K. Moon and J. Steensgaard	

Invited Talk 5

100 Gbit/s Computer Optical Interconnect	103
I. Glesk, R. J. Runsen, K-L. Deng and P. R. Prucnal	

Session 3A: Analog Circuits Design

A 20-dB 200-MHz CMOS Single-to-Differential Amplifier	109
S. Pennisi, P. Tommasino and A. Trifiletti	
CMOS 7th-Order Equiripple-Phase Filter for PRML Read Channel Applications	113
A. Ryan, M. Neag and O. McCarthy	
An Ultra-Low-Power Switched-Current 2-Quadrant Multiplier	117
A. Graupner and R. Schüffny	
Sixth-Order Switched-Capacitor Bandpass Filter with Reduced Capacitor Spread	121
N. A. Radev, K. P. Ivanov and S. S. Vladov	

Session 3B: Optical Communication Systems

A Technique For Improving The Gain/Phase Error Cancellation in LINC Transmitters	125
H. S. Al-Raweshidy and S. O. Ampem-Darko	
Asymmetric Throughput in Optical Wireless Links	129
A.C. Boucouvalas and P. Barker	
Dispersion Measurement of Optical Code Division Multiple Access Coder	135
I. Srdić, I. Perić and B. Zovko-Cihlar	

Optical Networks with Code-Division Multiple-Access	139
M. Poľaško	

Session 4A: Analog Signal Processing

Analog Fuzzy Controller in SC Technique	143
G. Giustolisi, G. Palmisano and G. Palumbo	
Implementation of Harmonic Linearization Using Monotonic Phase Function	145
V. Kukk	
Principles of Interactive Analog Circuit Synthesis	149
M. Koort	
Noise Properties of High-Order BP OTA-C Filter Structures	153
N. Stojković and N. Mijat	

Session 4B: Optical & Microwave Systems
--

D-Fibre Antenna Networks for Microcellular Systems	157
H.S. Al-Raweshidy, A. Bhatti and G. Murtaza	
Properties of Optical Encoders for CDMA Systems	161
F. Uherek, P. Hábovčík, J. Chovan and B. Issa	
Monolithic Microwave Integrated Circuits Simulation and Optimisation Using HSPICE	165
M. Tomáška	
Investigation of Non-linear Behavior of Optical Receiver for Multi-Channel High-Speed Communications	169
M. Krnáč and M. Tomáška	

Poster Session

Computer-aided Design of Application Microcontrollers	173
D. Cherniakovski, K. Kazakevich, I. Kazimirovski, V. Stepanets and S. Trofimov	
Design and Implementation of Error-Control Coding: Cyclic Code Architectures	177
K. Vlček	
Electrodynamics Analysis of Shielded Microstrip Lines by Partial Domain Method	181
S. Cantaragiu	
The Possibilities to Prepare Chemosensors by Thick Film Technology – The Market Implementation for the Future	185
M. Přádka and I. Szendiuch	
Synthesis and Simulation of HW/SW Systems with Performance Estimation	189
G. Polanšek, A. Žemva, A. Trost and B. Zajc	
Single-Input Rail-to-Rail Voltage-to-Current Converter Consisting of Three Complementary MOS Transistor Pairs	193
R. Ižák	
A Low-pass 1-Hz 2V-Supply Current Conveyor-based Amplifier	199
P. De Laurentiis, G. Ferri, G. Palumbo and S. Pennisi	
Neural Network Control Using Sliding Mode Technique	203
V. Mkrttchian and A. Lazaryan	
Pattern Classification with the BCM Neural Network	207
S. Poljovka and L. Beňušková	
Use of Information Technology Implementation Methods in Microelectronic Systems Design	211
P. Áč and V. Áč	

Validation of Behavioral VHDL Descriptions Using Software Engineering Concepts Ch. Paoli and J. F. Santucci	215
Invited Talk 6	
Real Implementation of Artificial Neural Networks Joan Cabestany	219
Session 5A: Neural Networks	
Mixed-Signal VLSI for Skeletonization by Grassfire Transformation – Design and Evaluation M. Oláh, S. Török, A. Poppe, P. Masa and A. Lőrincz	227
A New Refresh Circuit for Analogue Artificial Neural Networks J.V. Molnár and D. Ďuračková	231
Performance of the RBF Neural Network Models for Estimating Human Signal Detection Performance M. Roháčová and M. Koska	235
Switched Capacitor-Based Learning Synapse for Integrate-And-Fire Neural Networks D. Hajtáš, D. Ďuračková and F. Míka	239
Session 5B: Digital Signal Processing	
A 32-bit RISC Microprocessor with DSP Functionality B-I. Moon, D-R. Ryu, J-W. Hong, S. Moon, Y-H. Lee and Y-S. Lee	243
A Better Hearing for Cochlear Implant Subject with an Improved CIS-like Speech-Coding Strategy M. Polák and O. Ondráček	247
A Signal Processing Algorithm of the Digital Filter for the Improvement of the Signal to Noise Ratio Magnetic Anomaly Detection System W-H. Kim, K-H. Song and J-S. Park	251
Modified 4-IF Downconversion Technique with Flexible IF Settings R. Paško, S. Vernalde and D. Ďuračková	255
Session 6: Telecommunication Applications	
Feasibility of a Fully Digital Radio-Frequency Stage for a DAVIC Compliant Modem Application J. Ph. Lambert, A. Dandache, F. Monteiro and B. Lepley	259
A Novel ATM System over PON Access Network Using Fuzzy Logic Sets M. M. Jahromi and H. S. Al-Raweshidy	263
Empirical Formula of Diffracted Field from Corners for Urban Micro-cellular Communications K-H. Song, W-H. Kim, C-Y. Kim	267
Simulated Annealing for Optimisation Multipoint Routing in Broadband Telecommunication Networks R. Vrba, V. Olej and K. Blunár	271
Experts Session I	
Radio Over Fibre for the Third Generation Microcellular Networks H.S. Al-Raweshidy	275
Analog V-Series Modems for Embedded Internet Products A. Miller and A. Moskowitz	285

Implementation of Telecommunications Department of FEI STU into the ATM Network in the Slovak Republic - The Pilot Project	293
I. Baroňák	

Experts Session II

Design and Test of Next Generation Integrated Systems Embedding MEMSs	301
S. Mir	
An Object Oriented Methodology for Hardware Design	311
S. Vernalde, P. Schaumont and I. Bolsens	

<i>Author Index</i>	<i>319</i>
---------------------	------------

System-on-Chip: Test and Diagnosis

Yervant Zorian, Ph.D,
Chief Technology Advisor,
LogicVision, Inc.
101 Metro Dr., Third Floor
San Jose, CA 95110, USA
zorian@logicvision.com

Abstract: As system-on-chip (SOC) complexity and the move to very deep submicron (VDSM) technology pushes the threshold of semiconductor technology, conventional test methods become inadequate and costly. This new level of complexity demands that designers alter the way they approach chip development in order to keep up with diminishing time-to-market requirements and stay within budgets. Embedded test enables customers to produce higher-quality products in less time. The use of embedded test raises margins and significantly reduces the time required for system verification, test and debug. The speaker will address chip- and board- level signal integrity issues, system architecture design, business (time to market), embedded systems (design considerations for embedded systems, testing real-time systems, systems integration), test (high-density design issues, mixed-signal testing, digital testing issues, test technologies – IDDQ, SCAN, design for testability), SOC integration /test issues – making SOC a reality, and the importance of embedded test and front-end (time to money, quality and cost).

1. Introduction:

The electronics revolution we are witnessing today is driven by market demands to provide better, cheaper, smaller and faster products while meeting users' quality requirements. Meeting these quality requirements necessitates performing adequate test and diagnosis procedures. This article concentrates on the dynamic changes in the electronics industry and its impact on test and diagnosis.

The market driven electronics industry keeps introducing products with greater functionality, higher reliability, lower costs and shorter product realization intervals. These are realized by the unprecedented advancements in semiconductor IC technology. Semiconductor ICs are considered the foundation of modern products, even traditionally the non-electronic ones. Semiconductor transistors are becoming so cheap and commonly available that whole industries now live on continuously integrating more and more functions into smaller and smaller packages, hence creating system-on-chips. Being able to rapidly develop, manufacture, test, diagnose and verify complex new chips and products using such chips is crucial for the continued success of our economy at-large. This growth is expected to continue full force at least for the next decade, while making possible the production of 100 million transistor chips. However, to make its production practical and cost effective, the National Technology Roadmap for Semiconductors identified in 1997 a number of major hurdles to be overcome. Some of these hurdles are related to test technology. This article analyzes these hurdles, relates them to the advancements in semiconductor technology and presents potential solutions to address them. These solutions are meant to ensure that test contributes to the overall growth of the semiconductor industry and does not slow it down.

Test is a critical technology in the semiconductor production process. On the one hand, IC test is performed multiple times during volume production to screen the ICs upon their manufacturing. IC test starts with wafer probing even before patterned wafers are diced and goes into individually packaged chips. On the other hand, IC test also plays a key role in analyzing defects in the semiconductor manufacturing process. The feedback derived from the test is the only way to analyze and isolate many of the defects in today's processes. Time-to-yield, time-to-market, time-to-quality are all gated by test. Moreover, ICs are tested at each additional manufacturing step beyond IC production because each step can introduce new defects. With the increasing needs for high quality electronic products, at each new physical assembly level, such as board and system assembly, IC test is used for debugging, diagnosing and repairing the sub-assemblies in their new environment. Similarly with the increasing reliability, availability and serviceability requirements, most users of high-end product perform periodic tests in the field throughout the full life cycle. As the semiconductor technology keeps moving towards the creation of monster chips, we will continue to confront the key scaling trends: *greater complexities, increased performance, and higher densities*.

To allow advancements in each one of the above four scaling trends, fundamental changes are expected to emerge in different IC realization disciplines such as IC design, packaging and silicon process. These changes have a direct impact on the test methods, tool and equipment adopted. Test must keep up with the pace of such changes to ensure that 100 million transistor monster chips adequately tested, diagnosed, measured, debugged and even sometimes repaired.

In the following, we will take the three key scaling trends one at a time, observe their implications on test, identify the key hurdles/challenges and discuss the potential solutions. Each of the three challenges our ability to efficiently create new products. It is not sufficient to address just one of the challenges; all must be met at the same time.

2. Implications of Increased Complexity:

Moore's law predicts how the achievable transistor count per chip grows over time. The Semiconductor Industry Association's (SIA's) National Technology Roadmap of Semiconductors lay out the consequences of that prediction. The growth rate in IC transistor count is far higher than the rate for IC pins. The drastic increase in the ratio of transistor per pin continuously reduces the accessibility to the transistors from chip pins. The limited accessibility to internal transistors is a big problem for IC test.

The problem associated with limited Input/Outputs (I/O's) that have to be overcome do not end with access difficulties. There is a growing disparity between internal clock frequencies and the output capability of I/Os. This I/O limitation makes at-speed performance testing of an IC very difficult if not impossible. Combining the roadmap numbers for transistor count, chip I/O count, cost, chip internal frequency and I/O switching speeds reveals that, the rate of growth for how much information can be generated and consumed inside a chip (internal bandwidth, defined as number of transistors per IC times internal switching frequency) outpaces by far the rate at which the available I/O bandwidth grows (number of I/Os times I/O switching speed), see Fig (1). At the same time the cost of package pins declines much more slowly than the cost of a transistor. The physical characteristics of I/Os must remain in macroscopic level dictated by chip attachment and board manufacturing constraints; whereas the silicon feature sizes are rapidly moving down from a micrometer to nanometer. In other words, the chip I/Os and board-

level interfaces don't scale physically at nearly the rate of the internal circuits, contributing to a growing number of transistors behind each chip I/O and a widening performance gap between the chip internals and the I/O interface.

The data from SIA Roadmaps reveals that the gap between external bandwidth and internal bandwidth will grow in a fast pace, see Fig (1). This bandwidth gap is the main reason why we are starting to see processors and DRAMs being integrated into the same chip, rather than interacting with each other through the limited bandwidth of chip I/Os, as it was done traditionally when the bandwidth gap was negligible.

The I/O bandwidth had a major impact on chip test methods. In the very early days of IC technology (100 transistors per chip), the bandwidth gap was negligible. The test data was applied onto the chip I/Os directly from an external test data Source, and the response data received from the chip I/Os and evaluated for its correctness by an external Sink, see Fig (3-a). The combination of external Source and Sink, the test control software embedded in it, and the external test access mechanism (connecting the IC pins to the Source/Sink) represent the external test equipment.

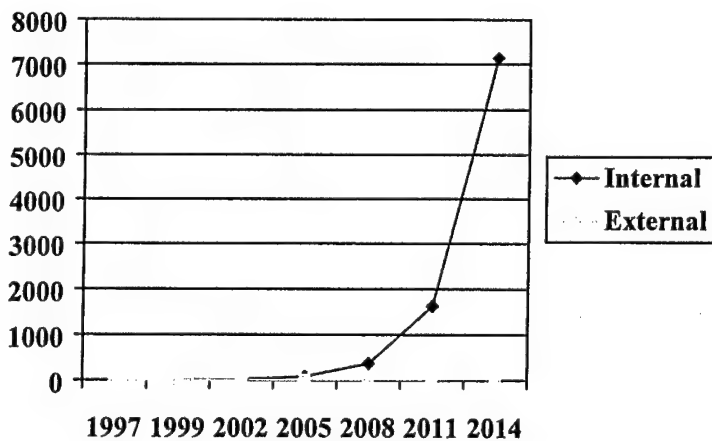


Figure (1) External vs. Internal Input / Output Bandwidth

With the next generation of IC technology, the transistor per pin ratio reached a level where the resulting IC complexity (10,000 transistors per IC) made the sole dependence on external test equipment insufficient. Hence, the concept of embedded test was introduced. This meant embedding test capabilities beyond the primary I/Os and into the internal transistors of the chip. One of the early embedded test techniques was scan path, which reduced the test complexity by extending the test access mechanism into the internal transistors, see Fig. (3-b). The process of incorporating embedded test circuits into the design of a chip became known as design-for-testability. Embedded test hardware, namely scan paths in this case, facilitated the transport of test data from the chip I/Os and applied it into a large number of internal transistors.

The amount of test data needed for testing an IC with a certain level of fault coverage grows with the transistor count of the IC under test. For the embedded test based on scan paths, the growth rate is proportional to the growth in transistor count. When the external Source and Sink is providing all stimulus and response data through the chip I/Os, the pin buffer depth to apply the test need to grow with the number of transistors per pin. With complexities beyond a million transistors per IC, the pin buffer depth started to become a major concern. Moreover, with this same IC generation the external test equipment has started to confront another key hurdle, the drastic increase in silicon speed. In order to test an IC at its system speed, a semiconductor producer either had to stay with the existing approach of having external Source and Sink, but this necessitates high-bandwidth test interaction between the IC and its external Source and Sink, as in Fig. (3-c). Often external test equipment were unable of performing this capability; or introduce a low-bandwidth communication with the IC by shifting certain feature from the external Source and Sink to embedded Source and Sink. These shifted features were the test speed and data volume oriented ones Fig (3-d). The Source and Sink features that required low-bandwidth interaction remained in the external test equipment. This drastically reduced the complexity of external tester.

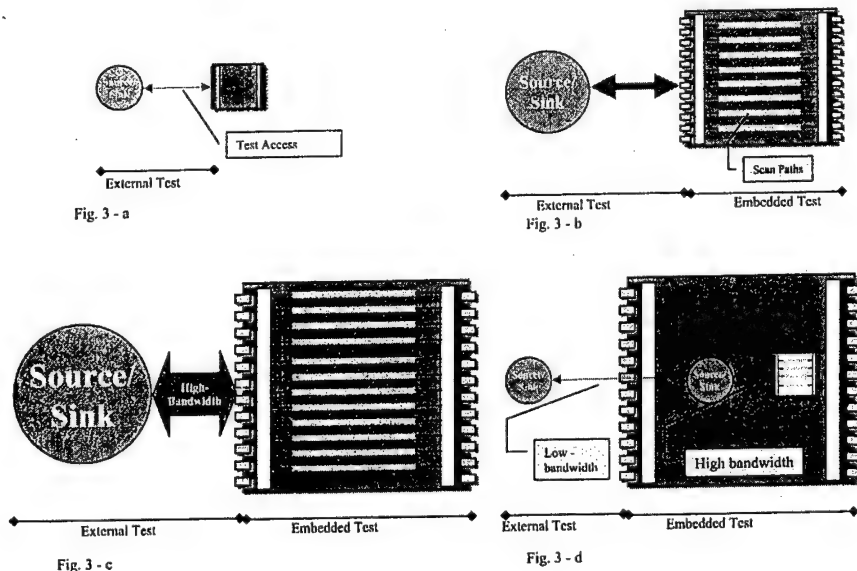


Figure (3) External and Embedded Test

As in Fig (3-d), the embedded Source performs an expansion function generating an at-speed and large test data volume applies it on the circuit under test; whereas, the embedded Sink collects the response data and performs an at-speed compaction function. This results in reducing the complexity of the external Source and Sink and allowing at-speed performance test. Without such a scheme it may have been impossible, since external test equipment is often built using yesterday's technology and would result in slow test throughput with long scan paths. While embedded Source and Sink help avoid the bandwidth limitation of the external test

equipment, but they do not perform total Built-In Self-Test (BIST), since they still depend on the external test equipment.

As the semiconductor technology moves to chips with over 100 million transistors, naturally the bandwidth gap between external test and embedded test will grow to levels, where more high-bandwidth test functions will need to migrate on-chip. This natural evolution of embedded test will result in a new partitioning of functions between external and embedded test. This partitioning will be an ongoing process of shifts from the functions of external test to the embedded one maintaining the two components as complementary test segments.

Mixing Technologies

Another implication of high complexity is mixing circuit types on a single IC. Monster chips are expected to comprise of non-homogeneous types of circuits. Today's complex chips have already started to mix diverse circuits, such as digital logic, embedded DRAM and analog blocks into a single IC. As chip integration technologies continue, more advanced circuits will be added to this list, such as embedded FPGA, Flash, RF/Microwave, and may even move beyond the electronics domain to contain micro-electromechanical (MEMS) and optical elements.

Different types of circuits exhibit distinct defect behavior and require different test solutions. Each type require different test Sources to generate the test data and Sinks to compare the responses. Typically, distinct external test equipment is used for each type of circuit. For example one tester for logic testing, one for embedded memory test and another for analog. The use of three external testers to test a single chip is termed as triple insertion, See Fig. (4-a) and is considered an expensive proposition. An alternate solution offered by test equipment vendors is to use a "Super" tester, which combines the test capabilities of all three above testers. The super testers do not assume embedded test capabilities in the chip under test, hence they tend to contain all test features and therefore turn this solution to an extremely expensive one.

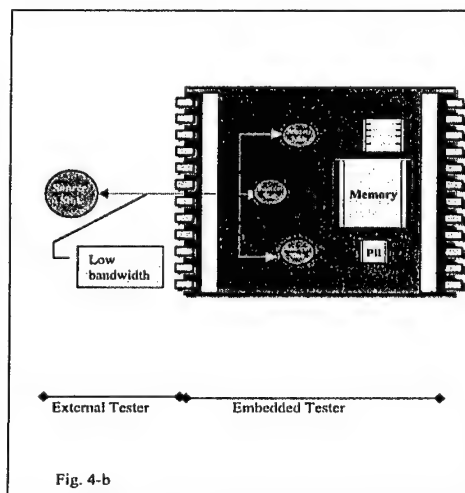
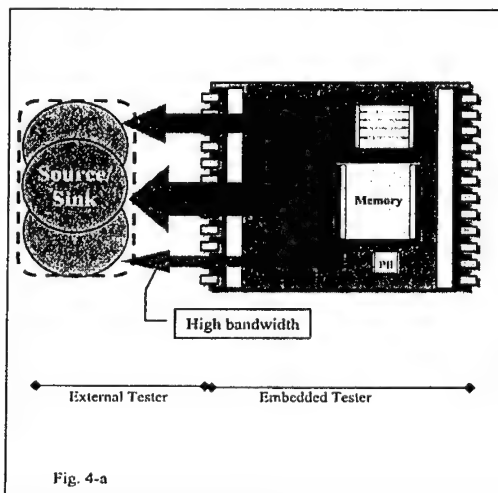


Figure 4 Mixing Technologies in a Single Chip

An easier and more cost effective way to handle these mixed circuit chips is by inserting embedded hardware Sources and Sinks corresponding to each circuit type, for example an embedded Source/Sink for digital logic, another for memories and a third for the FPGA circuit. Such an IC will not require more than a single, existing and lower-cost external tester, See Fig. (4-b).

System-on-Chip Test

Embedded core-based system-on-chip (SOC) design implies the reuse of pre-designed complex functional blocks, also called Virtual Components, Intellectual Property (IP). These embedded cores can come with different degrees of readiness for reuse in SOC design, from different sources, and are designed for use in a multiplicity of different SOC's. Being pre-designed, an embedded core may not only originate in a different organization, but it is also developed at a different time than the SOC that will use it. The embedded core design must be able to anticipate the desired SOC-level test constraints for all target SOC designs. Further, it must be possible to package the results of any enabled core-test in a form that is compatible with the test methodology contexts, and with the test-development tools available to the SOC designers who wish to reuse the core.

Core designs need to be more test-friendly to simplify the SOC integration task, while giving SOC designers more flexibility in choosing the best overall test methodologies for their chips. To ensure the test-friendliness and interoperability of cores from diverse sources, a standard for embedded core test is under development, namely IEEE P1500. The standard does not standardize a core's internal test methods or chip-level test access configuration. The standardization effort concentrates on:

- a standardized core test language (CTL), capable of expressing all test-related information to be transferred from core provider to core user; and
- a standardized - but configurable and scalable - core test wrapper, which allows easy test access of the core in a system chip design. The standard core test wrapper interfaces with an on-chip test access mechanism and may operate under several test modes (such as, internal, external, diagnosis, etc).

While it is possible to route the test access mechanism to the I/Os of the chips in order to receive/transmit the test patterns from/to external test equipment, but it is more practical and cost effective to use on chip test Sources and Sinks. They may be realized in two scenarios, either the embedded core would have a dedicated Source and Sink to perform its self-test; the test access mechanism connected to this core may obtain connect to a Source and Sink at the SOC or any other intermediate level. This is mainly meant for reusing the Source and Sink for more than one embedded core.

The most used cores today are the embedded memories. These cores have widely accepted the embedded Source and Sink approach. Most chip manufacturers have adopted memory BIST generation tools. As the monster chips incorporate more complex and larger numbers of embedded cores, such as microprocessors, analog blocks, and DSPs, the embedded Source and Sink approach need to be extended as the test solution of the other cores in an SOC.

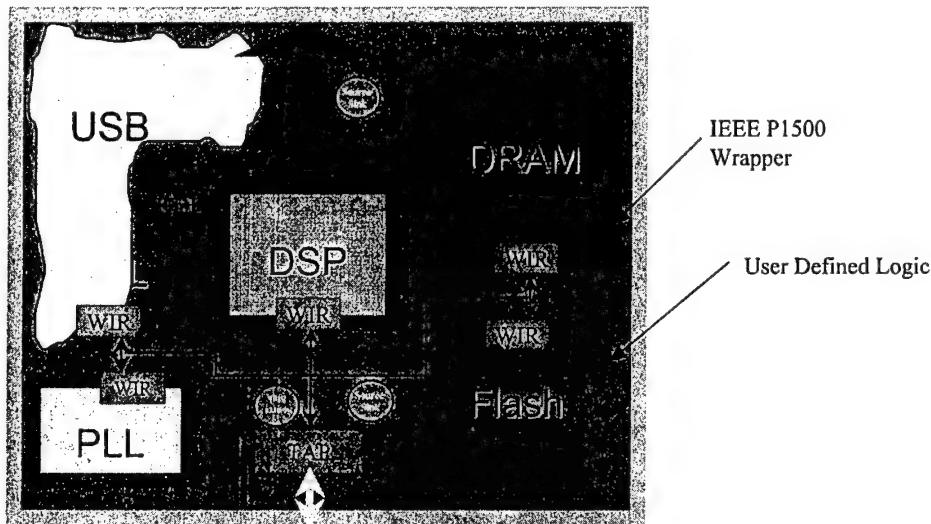


Figure (5) System-on-Chip Test

The monster chips are expected to embed very dense memories of large sizes (256K - 64M bits). These dense memories may include: SRAMs, DRAMs and/or Flash memories. For more than a decade, the smaller scale memories have been embedded in mostly logic chips and became an integral part of the ASIC libraries. These memories were among the first to use on-chip Sources and Sinks. This is utilized during the manufacturing test to avoid using a dedicated external memory tester, in addition to the external logic tester used for the rest of ASIC. Beyond a certain size such as 256K bits, memories necessitate redundancy and repair during manufacturing test. This has been performed regularly for large stand-alone memory. This is typically a fuse blow process using external laser repair equipment.

Due to the large sizes of the its embedded memories, the monster chip needs to have redundant rows and columns to help reconfigure it, if there were faulty cells detected. For the same reasons as for the smaller memories, these will rely on embedded Sources and Sinks to generate and evaluate the test data. Moreover, since the memory response data is evaluated by the embedded Sink, the role of this Sink could be slightly expanded in order to perform diagnosis of the failed bits. Furthermore, to avoid sending a large failed bit map to the external test equipment via limited I/O bandwidth, the embedded Sink can be expanded further to perform built-in redundancy analysis in order to identify the actual rows and columns needed for reconfiguration. In this case, only the repair list can be communicated to the external tester and hence the laser repair equipment can perform a hard repair.

The final augmentation of the embedded Source and Sink is to make the memory self-repairable. This is motivated by the fact that laser repair is often very expensive and some times continuous periodic field repair is desired. This will be achieved by expanding the embedded test resources even further to include a storage repair data and a soft reconfiguration mechanism. In summary, embedded test for very large memories may by required to move beyond fault detection to include failed bit diagnosis, redundancy analysis and self-repair.

3. Implications of Increased Performance:

With the continuous increase in IC internal speed, performance-related defect coverage has become increasingly important. The recent Sematech experiments have confirmed the criticality of performance-related tests. The 100 million transistor monster chip will necessitate a comprehensive performance test. Moreover, it has been predicted that Iddq test will lose its effectiveness for such chips due to higher sub-threshold currents. Most Iddq failures will probably be observed also as timing/performance anomalies.

A performance test that is applied from an external test equipment can not adequately and cost effectively test the high clock speeds and provide the necessary performance-related defect coverage. Because these equipment are typically made of older technology compared to the chips they test, and the higher speed test equipment are substantially more expensive. The SIA roadmap indicates that major yield losses and cost increases are related to the slower growth of external test equipment speeds versus the ever improving internal chip speed. While the external tester accuracy has improved at a rate of 12% per year, internal chip speeds have improved at 30% per year. Typical headroom of external testers five times faster than internal chip speeds have all but disappeared. With the current trend, cycle time of manufactured chips will approach external tester timing accuracy, see Fig. (6), in less than ten years. A crossover may occur near 2010, but by 2001, yield losses due to external test inaccuracy will be unacceptable.

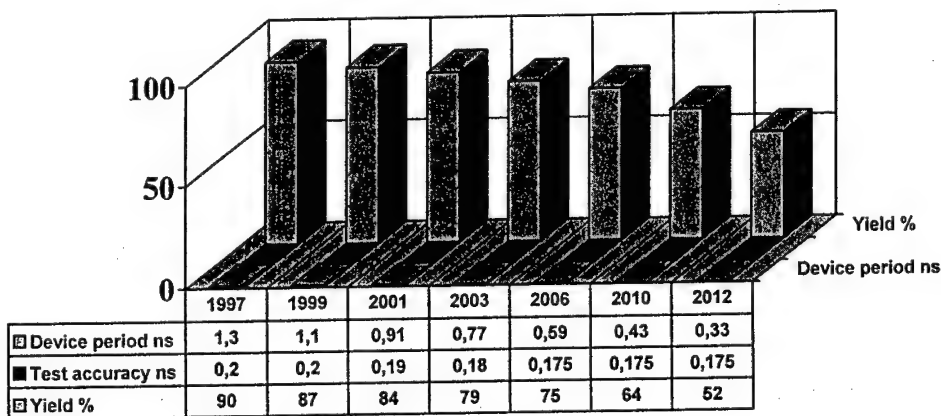


Figure (6) Test Accuracy and Yield

If external test accuracy cannot keep up with the internal chip speed, our monster chip need to leverage the internal speed of its silicon and utilize dedicated embedded test resource for the tests that require timing precision. Because it is built on the same piece of silicon as the monster chip, an embedded test resource will have a cycle time comparable to the chip internal speed. Therefore, it will allow accurate performance-related tests and precision measurements, and eliminate the potential yield losses predicated by the SIA roadmaps.

4. Implications of Higher Density:

The continuous advancement in semiconductor technology will keep increasing the silicon density. The number of millions of transistors per sq. cm. will increase by a factor of three in the next five years. The density level resulted in a monster chip will have a number of test-related implications.

According to the SIA roadmaps, the increase in semiconductor density causes reduction in defect sizes. The complexity of monster chips on the one hand, and the reduction in their defect sizes on the other, cause a drastic increase in the difficulty in fault localization. The difficulty in localizing faults increases one order of magnitude every six years.

The best tool to perform fault localization and defect analysis in semiconductor manufacturing is the test process. The feedback loop derived from the test process is the only way to analyze and isolate many of the defects in manufacturing. Understanding failure mechanisms and providing corrective actions cannot occur without the ability to localize faults to an area that can be inspected in a practical and cost-effective manner.

The increased density in monster chips will severely challenge the physical fault localization processes. The hardware for embedded test scales with the chip itself. The existing embedded test resources whether in embedded memories, cores, user defined logic or analog blocks can act as the infrastructure to collect the faulty data from the block under test. This helps to quickly isolate faults. Leveraging the embedded test hardware resources can aid in defect isolation. The failure pattern must map to a physical location on a circuit. Software-based test tools compatible with major embedded test methodologies (such as, scan or BIST) are needed to save failure pattern information so that it can be analyzed based on predetermined failure mode information. This allows yield engineers to more quickly and precisely determine the location and causes for circuit failures.

Collecting more parametric data as measured on external test equipment will aid in sourcing unmodeled defect types. The continuous increase in density and in multi-level metal layers result in new fault models, which make the traditional stuck-at fault less effective. Recent studies show that few large-area spot defects are causing single defects, which affect multiple transistors and gates simultaneously. In general, to reduce the test escapes due to such unmodeled faults, pseudo-random test patterns are used. A number of experimental studies showed the effectiveness of such pseudo-random patterns in reducing test escapes.

Signal integrity and electromagnetic phenomena will become an increasingly important test issue with the appearance of monster chips. New fault models including soft error models that incorporate the effects of electromagnetic fields need to be developed. The increase in soft errors is due to the reduction in device size and voltage supply, which cause an increase in noise sensitivity and an increase in susceptibility to cosmic variations, such as alpha particle radiation. The resulting soft errors, while not new for space oriented applications, will start to cause considerable risks on sea level altitude. Due to their transient nature, soft errors need to be continuously monitored during the field operation of a chip. Hence, this will require dedicated hardware for embedded test, which performs on-line testing technique.

New embedded sensors to monitor different on-chip parameters should be developed to identify race conditions and other failure modes that are functions of parametric variations. These sensors will be an integral part of the embedded test infrastructure and leverage the existing chip level test data and control mechanisms. Handling the test data through signature analysis techniques would significantly reduce the need for hardware failure analysis. In fact, the more embedded test monitoring and on-chip data acquisition resources are used the less hardware diagnostics is required for silicon debug and failure analysis. Especially with the high density packages, such as flip-chips, hardware diagnosis will become more and more constrained. Because the conventional electron beam or thermal imaging technique will not apply to flip-chip attach technologies due to the fact that there is no front side accessibility. Very limited back side accessibility hardware diagnosis techniques can be used, such as photon emission and scanned lasers, if defects are sensitive to them. New back side accessibility tools and solutions are needed.

In addition to fault localization and failure analysis, producing the monster chip requires integrated yield analysis capabilities that make use of the defect and failure analysis data. These capabilities need to be in software tools to automatically access multiple databases and establish correlation between data of different types. Some data sources are time-based, others are chip-based or wafer-based. Automated data reduction algorithms to source defects from multiple data sources must be developed to reduce defect sourcing time. The SIA roadmap identified this as one of the key requirements for yield learning and improvement.

5. Implications of Reduced Cost:

Increasing cost of capital for external test equipment is one of three major test-related problems the SIA roadmaps had predicted. While the cost per pin for external test has remained essentially flat for the past 20 years at around \$10K/pin. The demands for higher speed, greater accuracy, more time sets and increased data volume offset all the goals in cost reduction seen for improving external test equipment cost. In its 1997 roadmaps, SIA indicates that tester cost will reach \$20M in year 2010, unless there is change in IC design incorporating more embedded test. It also predicts that by the same year, it may cost more to test a transistor than it costs to manufacture the transistor.

The cost of embedded test is in terms of additional silicon needed to incorporate the test functions and a limited impact on yield. A set of embedded Sources and Sinks for a state-of-the-art mixed circuit IC is about 10,000 logic gate equivalent, assuming that a scan infrastructure is already in place. For designs of about 400,000 to 500,000 gates, the relative silicon cost of embedded test is equals the cost of external test. For chips above this size, the silicon investment constitutes less than 1 percent of the silicon manufacturing costs, See Fig. (7). As for the yield impact, the Embedded Sources and Sinks increase the silicon area and hence can reduce manufacturing yield. Because, the bigger the chip area, the more chance of a particle falling on that chip and causing a defect. However, with the addition of 10,000 gates on a monster chip of tens of Million of gates causes a negligible impact.

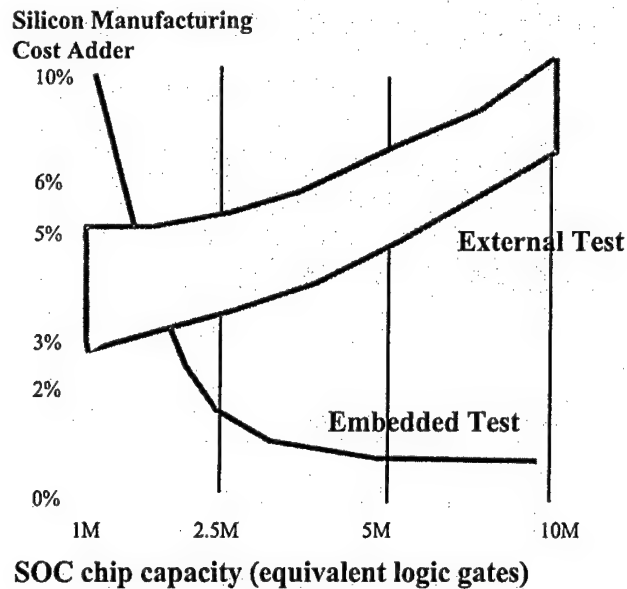


Figure (7) External vs. Embedded Test Cost

After it is successfully produced, a monster chip is deemed to become an integral part of a larger electronic system. The cost of test and diagnosis for such electronic systems, typically, reaches 40-50% of total product realization cost. If embedded test resources were incorporated into the chip, these resources can be reused hierarchically during board and system manufacturing. This reduces the time and cost required to develop diagnostic firmware and interfaces for board and system test and maintenance features. The concept of embedded test can be applied to every electronic assembly level, for instance, using chip level embedded test during board test; using board level embedded test during system/box test; and hardware/software use of the total embedded solution in the field test.

6. Conclusions:

The semiconductor scaling trends such as complexity, performance and density have major implications on testing the 100 million transistor chips. The industry has identified a number of hurdles as a result of such implications. Solving these hurdles require a new approach to testing, where the test functions are partitioned to two main components: embedded test and external test. The two complementary test components are needed, but the balance of functions in each component depends on numerous technological and economical factors.

The usage of embedded test hardware, which is invested on-chip, goes beyond plain chip test. This hardware provides a number of crucial test-related functions, such diagnosis, measurement,

debug, failure analysis, and even repair. Also, the embedded test hardware is reused from cores test level, to chip, to board and system test levels.

External test and embedded test will be used simultaneously on most chip designs. As chips become more complex new functions will be transfer from the external test component to the embedded one.

Easily Testable Carry – Save Multipliers with respect to Path Delay Faults

Th. Haniotakis¹, H. T. Vergos², Y. Tsiatouhas¹, D. Nikolos² & M. Nicolaidis³

¹ISD S.A, 22, K. Varnali Str, 152 33 Maroussi, Athens, Greece

e-mail : {haniotak, tsiatouhas}@isd.gr

²Dept. of Computer Engineering and Informatics, Patras Univ., 26 500, Greece

e-mail : {vergos, nikolosd}@cti.gr

³TIMA, 46, Avenue, Felix Viallet, 38031, Grenoble, France

e-mail : michael.nicolaidis@imag.fr

Abstract. In this paper we propose the design of an easily testable, with respect to path delay faults, $n \times m$ carry - save multiplier (CSM) and give a path selection method such that all the selected paths for testing are Single Path Propagating Hazard Free Robustly Testable (SPP-HFRT). Only three additional test inputs are required while the hardware overhead is very small and the delay overhead negligible.

I. Introduction

Increasing performance requirements makes difficult to design VLSI circuits with large timing margins. Hence, due to imprecise delay modeling, the statistical variations of the parameters during the manufacturing process as well as the occurrence of physical defects in the integrated circuits the performance of the manufactured circuits may be less than the expected one, while its logic function is correct. The path delay fault model is the most general delay fault model used to model changes in the timing behavior of a circuit. Under its use a path is declared faulty if it fails to propagate a transition from the path input to the path output within a specified time interval [1]. There are two major problems associated with path delay fault testing : a) the large number of physical paths and b) their robustness. Selection of paths for testing is especially difficult in performance optimized designs because they often have a large number of paths with long propagation delays. Moreover, a physical defect may increase the delay along a non-critical path so that it eventually becomes a critical path.

It has been shown in [2] that by measuring the delays along a suitable very small set R of physical paths the propagation delays along any other path can be calculated. However, to be able to measure the propagation delay along the R paths they must be SPP-HFRT [2]. Unfortunately for most circuits, among them the CSM as well, a suitable set of SPP-HFRT paths does not exist. In this paper modifications of the CSM are proposed leading to a suitable set R' of SPP-HFRT paths. We give a method to derive the set R' of SPP-HFRT paths and we show that it is an impressively small percentage of all physical paths. By measuring the delay along the paths of R' , the delay along any other path can be calculated. The delay overhead due to the modifications is negligible while the hardware overhead for practical size CSMs is very small.

II. CSM Modifications

An $n \times m$ CSM is a circuit with inputs (A_1, A_2, \dots, A_n) and (B_1, B_2, \dots, B_m) and outputs $(O_1, O_2, \dots, O_{n+m})$. Figure 1. presents the 4×4 carry save multiplier. We consider that the multiplier consists of two blocks. The first block D_0 consists of the network of carry save adders and the associated logic. The second block D_1 is an $(n-1)$ -bit adder, which can be implemented as a ripple carry or group carry look ahead adder.

In [3] we have shown that using multiplexers for making the inputs and outputs of the embedded blocks accessible by the primary ports of the circuit, the path delay fault testing of the circuit is reduced to the path delay fault testing of the blocks that constitute it. By adding multiplexers in the original CSM design (Figure 2), we can manipulate the two blocks, D_0 and D_1 , individually. We will hereafter deal only with the path delay fault testing of D_0 , since efficient path delay fault testing techniques of both ripple-carry and carry look ahead implementations of D_1 have been presented in [4]. A suitable set R'' of SPP-HFRT paths of D_0 such that measuring the propagation delays along them the delay along any other path can be calculated, does not exist. Hence some additional modifications of D_0 are required. Specifically, the half adders of D_0 , that is, the adders of the first row, are substituted by full adders. The extra input of the leftmost adder, of the first row, is driven by a test input t_1 . The extra inputs of the rest adders of the first row are driven alternately by the t_2 and t_3 test inputs. During normal circuit operation all three test inputs t_1, t_2 and t_3 are driven to 0.

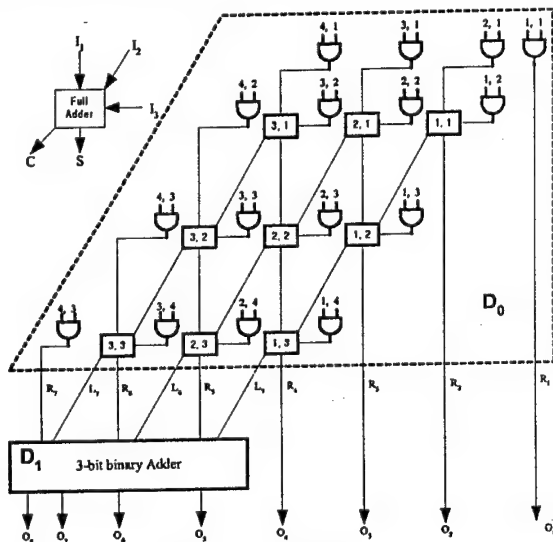


Figure 1. A 4×4 CSM.

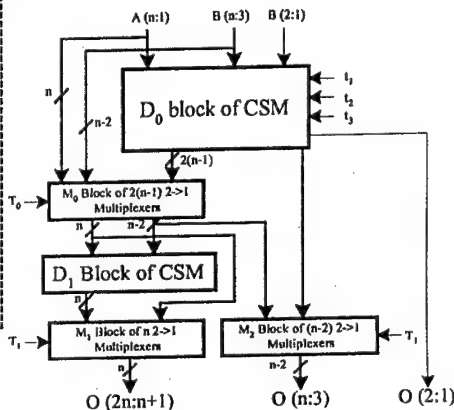


Figure 2. Modified $n \times n$ CSM.

III. Path selection procedure

We will denote an AND gate of D_0 as $\text{AND}(x, y)$ when its inputs are A_x and B_y . Since each AND gate has two inputs, there are two sub-paths starting from the inputs and ending to the output of every AND gate of the multiplier. Each such sub-path will be denoted by a triplet of the form (s, x, y) or (t, x, y) . The first element denotes the start of the sub-path, that is s or t defines the sub-path starting from the input $A_x, 1 \leq x \leq n$ or $B_y, 1 \leq y \leq m$ respectively,

and ending at the output of AND (x, y). The two latter elements of the triplet indicate the specific AND gate of the design that we refer to.

We consider that each full adder has been implemented in a robustly testable way, as for example in [4]. Each full adder has three inputs I_1, I_2, I_3 and two outputs, S (sum) and C (carry), as shown in Figure 1. Table 1 lists the possible sub-paths of any full adder. Each full adder of D_0 will be described as ADDER (x, y) in a similar to the AND gates notation introduced earlier. We again denote the sub-paths along full adders by triplets of the form (u, x, y), where $u \in \{a, b, c, d, e, f, g, h, i, j, k, l, m, n, o, p, q, r\}$ is used to specify one of the possible sub-paths along the full adder and x, y indicate the specific full adder of the design we refer to. From Table 1 we can easily see that for the same values of I_1, I_2, I_3 we may have two sub-paths, one starting from an input and ending at the S output and the other starting from the same input and ending to the C output.

Table 1. Sub-paths along any full – adder of D_0 .

From	To	Other Input Signal Values	Notation	From	To	Other Input Signal Values	Notation
I_1	S	$I_2 = 0, I_3 = 0$	a	I_3	S	$I_1 = 0, I_2 = 1$	j
I_1	S	$I_2 = 0, I_3 = 1$	b	I_3	S	$I_1 = 1, I_2 = 0$	k
I_1	S	$I_2 = 1, I_3 = 0$	c	I_3	S	$I_1 = 1, I_2 = 1$	l
I_1	S	$I_2 = 1, I_3 = 1$	d	I_1	C	$I_2 = 0, I_3 = 1$	m
I_2	S	$I_1 = 0, I_3 = 0$	e	I_1	C	$I_2 = 1, I_3 = 0$	n
I_2	S	$I_1 = 0, I_3 = 1$	f	I_2	C	$I_1 = 0, I_3 = 1$	o
I_2	S	$I_1 = 1, I_3 = 0$	g	I_2	C	$I_1 = 1, I_3 = 0$	p
I_2	S	$I_1 = 1, I_3 = 1$	h	I_3	C	$I_1 = 0, I_2 = 1$	q
I_3	S	$I_1 = 0, I_2 = 0$	i	I_3	C	$I_1 = 1, I_2 = 0$	r

Using the above notations, a physical path of D_0 can be described as an ordered set of sub-paths. Given that each sub-path is denoted as a triplet we conclude that a path can be described as an ordered set of triplets.

In the following, we will give a very small subset of the paths of D_0 , that if we measure the delay along them we can calculate the delays along every path of D_0 (the proof is given in [5]). In [5] we have also proven that all selected paths are SPP-HFRT.

- P_{A1} is the set of paths $\{(s, x, y), L\}$ where all sub-paths of L have the form (a, x', y') . Obviously $|P_{A1}| = m + n - 1$, where $|X|$ denotes the cardinality of set X .
- P_{A2} is the set of paths $\{(t, x, y), L\}$. $|P_{A2}| = m + n - 1$.
- P_{A3} is the set of paths $\{(s, x, y), O\}$, where O are all possible sub-paths with only one sub-path of the form (w, x', y') for $w = b, c, d$ and all other sub-paths of the form (a, x'', y'') . $|P_{A3}| = 3(m-1)(n-1)$.
- P_{B1} is the set of paths $\{(s, x, y), (w, x, y-1), L\}$, where $w \in \{i, j, k, l\}$. $|P_{B1}| = 4(n-1)(m-1)$.
- P_{B2} is the set of paths $\{(t, x, y), (i, x, y-1), L\}$. $|P_{B2}| = (n-1)(m-1)$.
- P_{C1} is the set of paths $\{N, (m, x, y), (w_2, x, y+1), M\}$, $w_2 \in \{e, f, g, h\}$, and N, M include only s or a type sub-paths. $|P_{C1}| = 4(n-1)(m-1) + (n-1)$.
- P_{C2} is the set of paths $\{N, (n, x, y), (e, x, y+1), M\}$. $|P_{C2}| = n(m-1)$.
- P_{D1} is the set of paths $\{(s, x, y), (w_1, x, y-1), (e, x, y), M\}$, $w_1 \in \{q, r\}$. $|P_{D1}| = 2(n-1)(m-1)$.
- P_{E1} is the set of paths $\{N, (m, x, y-1), (p, x, y), (e, x, y+1), M\}$. $|P_{E1}| = 2(n-1)(m-2)$.
- P_{E2} is the set of paths $\{N, (n, x, y-1), (o, x, y), (e, x, y+1), M\}$. $|P_{E2}| = 2(n-1)(m-2)$.

IV. Conclusions

Path delay fault testing of a CSM is a difficult task due to the excessively large number of its physical paths. In this paper by introducing minor modifications to the original multipliers design (Table 3 presents the hardware overhead of the proposed easily testable design) we present a method for selecting a very small subset of physical paths that the propagation delay along them should be measured. The cardinality of this subset is orders of magnitude smaller than the number of all physical paths of the original design as listed in Table 2 for multipliers with their last stage implemented as a ripple carry adder. The delay along any other path of the multiplier can be calculated by the delays along the selected paths [5]. The selected paths have been proven to be SPP-HFRT [5].

Table 2. Reduction in number of paths that need to be tested

CSM size n×m	Total number of physical paths	Number of paths to be tested	Reduction %
8×8	5.825×10^8	1032	99.9998
16×16	3.189×10^{17}	4392	≈100
32×32	6.245×10^{34}	18408	≈100
64×64	2.142×10^{69}	75624	≈100

Table 3. Hardware overhead of the proposed Easily Testable Multipliers

CSM size n×m	Number of Gates				Overhead %	
	M _{RC}	M _{CLA}	ETM _{RC}	ETM _{CLA}	(ETM _{RC} ·M _{RC})/M _{RC}	(ETM _{CLA} ·M _{CLA})/M _{CLA}
8×8	792	818	934	960	17.93	17.36
16×16	3496	3534	3798	3836	8.64	8.54
32×32	14664	14726	15286	15348	4.24	4.22
64×64	60040	60150	61302	61412	2.10	2.1

M_{RC} : original CSM with the last stage implemented as a ripple carry adder.

M_{CLA} : original CSM with the last stage implemented as a group carry look ahead adder.

ETM_{RC} : proposed CSM with the last stage implemented as a ripple carry adder.

ETM_{CLA} : proposed CSM with the last stage implemented as a group carry look ahead adder.

References

- [1] G. L. Smith, "Model for delay faults based upon paths", Proc. of ITC - 85, pp. 342 - 349.
- [2] J. D. Lesser and J. J. Shedletsky, "An Experimental Delay Test Generator for LSI Logic", IEEE Trans. on Computers, C-29 (3), March 1980, pp. 235 - 248.
- [3] D. Nikolos et al., "Path Delay Fault Testing of ICs with Embedded Intellectual Property Blocks", Proc. of DATE '99, March 1999, pp. 112 - 116.
- [4] T. Haniotakis, Y. Tsiatouhas and D. Nikolos, "C-Testable One-Dimensional ILAs with Respect to Path Delay Faults : Theory and Applications", Proc. of IEEE Int. Symp. on Defect and Fault Tolerance in VLSI Systems, November 1998, pp. 155 - 163.
- [5] T. Haniotakis et al., "Easily Testable Carry - Save Multipliers with Respect to Path Delay Faults", Computer Technology Institute Technical Report 1999.

Fast and Efficient Static Compaction of Test Sequences Using Bipartite Graph Representations

A. Markus, J. Raik, R. Ubar

*Dept. of Comp. Eng., Tallinn Technical University, Raja 15, Tallinn, Estonia
{antti/jaan/raiub}@pld.ttu.ee*

Abstract. Current paper presents a novel idea of test set minimization, which is based on representing fault matrices of test sets by *bipartite graphs*. We show that bipartite graphs provide for a remarkable speed-up of the compaction of test sequences in comparison with matrix representations. Results show that, in a number of realistic cases, the proposed algorithm is capable of proving that global minimum of the static test set compaction problem has been reached.

I. Introduction

Minimization of the number of patterns in a test set is an essential problem for the chip manufacturer, who faces the test of millions of units per annum [1]. The time required to test a chip by the ATE is directly proportional with the length of the test sequence. Therefore, the number of patterns in a test set is an important parameter when speaking of test pattern generation. There exist two types of test compaction techniques: *static* and *dynamic*. With static compaction a test set is generated and subsequently attempts are made to minimize it without reducing its fault coverage. Dynamic test set minimization, on the other hand, is performed at the time when tests are being generated. This often implies modification of the test generation algorithm. Current paper considers the static technique only, where test sets are created by any test pattern generator (ATPG) and compacted by a standalone compaction tool.

The problem of static test set minimization is NP-complete. In order to try all possible solutions, $n!$ sequences of the test patterns have to be considered. However, this is impractical even for a moderate value of n . Thus, more sophisticated methods have to be applied to solve the problem. Some of the advanced ATPG algorithms include test set compaction. For example, in [2] and [3] test sets are compacted by fault simulating the patterns in a reverse order. However, this method is too simple to guarantee satisfactory results. Many authors [4, 5, 6] have successfully applied genetic algorithms for test set compaction. Current paper presents a deterministic approach, which has the following advantages over the above mentioned methods: 1) In some cases, it is capable of proving that global minimum is reached; 2) It is considerably faster than genetic methods.

II. Bipartite Graph Representations

An example of abstract fault matrix is given in Fig. 1a. Each row in the matrix corresponds to a test pattern and each column represents a fault. A '1' in a row denotes that the pattern covers corresponding fault, while '0' denotes that it does not. Our aim is to minimize the number of rows in the matrix so that there would be as many columns with at

least one '1' as in the initial matrix. It is easy to see that the minimal solution for current example is to select patterns p2 and p4 while discarding p1 and p3.

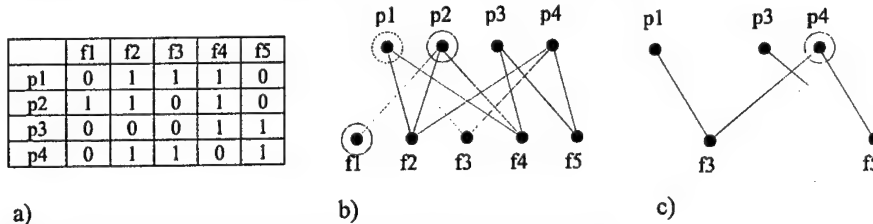


Figure 1. Fault Matrix and Its Bipartite Graph Representation

The matrix can be represented by a bipartite graph $G=(V, E)$ with two disjoint subsets of vertices P and F ($P \cap F = \emptyset$, $P \cup F = V$). Each vertex p_i ($p_i \in P$) corresponds to a vector and each vertex f_i ($f_i \in F$) corresponds to a fault. There exists a connection between p_i ($p_i \in P$) and f_i ($f_i \in F$) if vector p_i covers fault f_i . Graph derived from the fault matrix in Figure 1a is presented in Figure 1b. Bipartite graphs provide for a more compact data structure for the problem. In the classical approach we have to traverse $n \times m$ matrix, while in the graphs $n + m$ vertices with all the edges have to be considered. In other words, the room to be traversed in bipartite graphs is, in the worst case, equal to the number of ones in the matrix multiplied by two. (Each edge has two ending points). Section 4 presents the experimental results that show the speed-up provided by bipartite graph representations in comparison with fault matrices.

III. Compaction Algorithm

There have been numerous arguments whether to implement genetic or greedy approaches in order to solve the test set compaction problem. Supporters of genetic approaches claim that greedy algorithms are often stuck to local minima [8]. In order to investigate the possibilities of the greedy approach we propose a simple algorithm, which uses a number of previously undetected faults detected by a vector as heuristics. Let us consider the simple method described in procedure 1.

procedure 1

1. Initial test set $T = \emptyset$.
2. Select a vertex p ($p \in P$) which has the highest degree
3. Remove p and all the vertices f_i ($f_i \in F$), which have an edge between them and p .
4. Add the pattern corresponding to p to the test set T .
5. If $F \neq \emptyset$ go to point 2, otherwise T forms the minimized test set.

On the fault matrix this procedure would be equivalent to recursively choosing these patterns that detect more new faults in respect to the faults already covered by the previously chosen patterns. In practice procedure 1 works fairly well. However, in many cases it does not guarantee minimal results. For example, if we apply it to the graph presented in Figure 1b, we will see that vertex p_1 could be chosen first, since it is one of the patterns with the highest degree. This choice would not lead to the minimal test set, which is p_2, p_4 . In order to minimize such kind of incorrect decisions we introduce the following preprocessing step to our algorithm.

preprocess

1. If a vertex f ($f \in F$) exists, whose degree is 1 then go to point 2, else end preprocessing.
2. Remove p_k ($p_k \in P$) that is connected to f and f_i ($f_i \in F$), which are connected to p_k .
3. Include pattern corresponding to vertex p_k to the test set T and go to point 1.

The presented preprocessing step is equivalent to choosing *unique patterns*. We say that a pattern is unique when it covers some faults that are not covered by any other pattern. It is obvious that these patterns have to be included to the minimal test set. On the right in Fig. 2 is the graph after application of the preprocessing step. As our experiments show, majority of patterns in the generated test sets are unique. Therefore, by choosing these patterns as a first step, the search space can be significantly reduced. In order to further compact the test sets obtained by the above described algorithm, we tried to detect any *dispensable* patterns in our test sets, i.e. patterns when removed would not lower the fault coverage. We did not find any such patterns in our test sets. This means that all the test sets that we generated are *reducts* [9]. However, it does not imply that they are the global *minima* for the static compaction problem. The next section explains the conditions that allow to determine whether a test set is a global minimum.

In the following we present the criterion for global minimum detection by the above described algorithm. The criterion is more general and can be applied to any other compaction algorithm: *A static test set compaction algorithm has reached global minimum if the number of patterns in the minimized test set is less than three patterns larger than the number of unique patterns.* If the minimized test set contains three patterns more than the set of unique patterns, we can not any more prove the 'globalness' of the solution, although probability is very high. In these cases, more sophisticated techniques have to be applied. Experimental results show that many of the minimized test sets are proved to be global minima since they comply with the above-mentioned criterion.

IV. Experimental Results

Experiments were carried out with three types of test pattern generators: deterministic, genetic and random. For deterministic test pattern generation, the PODEM algorithm [11] was implemented. All of the test generation tools were taken from the Turbo Tester package [7]. Table I shows the test set compaction times for ISCAS85 benchmarks [10]. As the results show, the proposed algorithm performs very fast. The longest compaction time is required for the test set of c7552 that is generated by the random ATPG. Here, time spent by the algorithm on the bipartite graph model was 4 hundredths of second while it was 3 tenths of second for the matrix representation. The time required to construct the graph was not included. All the experiments were run on a 233 MHz Pentium II PC computer under Windows 95 operating system. In order to understand the experimental data in Tables II-IV some additional definitions must be added. A pattern that does not detect any additional faults in respect to the set of unique vectors is called a *noncontributing* pattern. The number of patterns in the test set that are neither noncontributing nor unique is referred to as the *search space*. Search space represents the size of the problem for the pattern selection algorithm.

Experiments show that selection of unique vectors as a preprocessing step considerably reduces the search space for the compaction algorithm. For the deterministic test sets 51-83 % of the patterns were unique and the search space included only up to 38 % from the initial test set, while the ratio of unique patterns was 71-100 % for genetic and 57-100 % for random tests. Search space was up to 21 % for genetic and 26 % for random generator sets.

circuit	PODEM, s		Genetic, s		Random, s	
	graph	matrix	graph	matrix	graph	matrix
c432	0.00	0.02	0.00	0.02	0.00	0.02
c499	0.00	0.02	0.00	0.02	0.00	0.02
c880	0.01	0.03	0.01	0.03	0.01	0.03
c1908	0.01	0.03	0.01	0.03	0.01	0.03
c2670	0.01	0.05	0.01	0.04	0.01	0.03
c3540	0.01	0.06	0.01	0.05	0.01	0.05
c5315	0.02	0.18	0.01	0.06	0.01	0.06
c6288	0.01	0.05	0.01	0.04	0.01	0.04
c7552	0.02	0.16	0.01	0.11	0.04	0.29

Table I. Compaction Times for the Test Sets

circuit	tests	unique	noncontrib	search	result
c432	89	52 (58%)	31	6	55
c499	140	94 (67%)	31	15	100
c880	70	50 (71%)	15	5	52*
c1908	144	120 (83%)	20	4	122*
c2670	160	111 (69%)	28	21	119
c3540	201	137 (68%)	37	27	145
c5315	178	91 (51%)	20	67	108
c6288	41	30 (73%)	3	8	33
c7552	276	190 (69%)	62	24	198

Table II. Results for Deterministic ATPG

circuit	tests	unique	non-contrib	search	result
c432	51	44 (86 %)	1	6	46*
c499	86	84 (98 %)	0	2	85*
c880	46	35 (76 %)	5	6	38
c1908	121	109 (90 %)	10	2	110*
c2670	112	80 (71 %)	9	23	87
c3540	155	133 (86 %)	11	11	138
c5315	115	93 (81 %)	9	13	99
c6288	21	21 (100 %)	0	0	21*
c7552	192**	149 (78 %)	27	16	156

circuit	tests	unique	non-contrib	search	result
c432	51	45 (88 %)	3	3	46*
c499	86	86 (100 %)	0	0	86*
c880	63	43 (68 %)	15	5	45*
c1908	132	109 (83 %)	16	7	112
c2670	107**	72 (67 %)	27	8	75
c3540	167	137 (82 %)	16	14	143
c5315	132	100 (76 %)	19	13	106
c6288	24	21 (88 %)	1	2	22*
c7552	249**	143 (57 %)	41	65	164

Table III. Results for Genetic ATPG Tests

Table IV. Results for Random ATPG Tests

* - global minimum was detected and proved

** - initial test set did not cover all the testable faults

The proposed algorithm achieved very effective compaction results on ISCAS85 benchmarks, where in few hundredths of seconds for 10 of the 27 test sets global minima were detected and proved. For the rest of the minimized test sets we can not claim with certainty that they are the global minima for the static compaction problem. However, by a simple postprocessing step we detected that the obtained test sets did not contain any indispensable patterns [9]. Thus, all of the test sets are reducts [9].

References

- [1] K. M. Thomson, "Intel and the Myths of Test", *Design & Test of Comp.*, Spring 1996.
- [2] J. A. Waicukauski et al., "ATPG for Ultra-Large Structured Designs", *ITC*, 1990.
- [3] M. H. Schulz, E. Auth, "Improved ...", *IEEE Trans. on CAD*, Vol. 8, No. 7, 1989.
- [4] E. M. Rudnick, J. H. Patel, "Putting the Squeeze on Test Sequences", *ITC*, 1997.
- [5] I. Pomeranz et al., "On the Compaction ...", *Proc. of the Asian Test Symposium*, 1997.
- [6] J. S. Takhar, et al., "The Derivation of Minimal Test Sets for Combinational Logic Circuits using GAs", *Midwest Symposium on Circuits and Systems*, Sacramento, 1997.
- [7] R. Ubar, et al., "Low-Cost ...", *Microelectronics Education*, Grenoble, Feb. 1996.
- [8] P. Sapiecha, "An Approximation Algorithm for Minimal Reduct Problem", *Proc. of the First Workshop on Rough Set Theory*, Poland, 1992.
- [9] Z. Pawlak, "Rough Sets, Theoretical Aspects of Reasoning about Data", *Kluwer*, 1991.
- [10] F. Brglez, H. Fujiwara, "A Neutral Netlist ...", *ISCAS*, pp. 662-698, 1985.
- [11] P. Goel, "An Implicit Enumeration ...", *IEEE Trans. Comput.*, vol. C-30, March 1981.

A Hierarchical Test Generation Technique for Embedded Systems

Gert Jervan, Petru Eles, Zebo Peng

Dept. of Comp. and Information Science, Linköping University, Sweden

e-mail: {gerje, petel, zebpe}@ida.liu.se

Abstract¹ This paper presents a hierarchical test generation technique for embedded systems containing hardware and software. The technique is applied to the system-level specification of such systems. Different from the traditional approaches, hardware and software parts of an embedded system are handled in a uniform way. We will in particular show how the proposed technique can be applied at high levels of abstraction and how the software domain of the specification can also be successfully covered.

1. Introduction

The development of hardware/software codesign techniques has made it possible to design hardware and software of an embedded system at the high levels of abstraction in a uniform way. However the testing of the hardware and software parts of the system are still considered as totally unrelated problems and solved with very different methods.

In the early phases of the design cycle, system synthesis is performed starting from an implementation independent specification. Reasoning about testability at this level can be facilitated by an uniform test generation technique, which is both applicable to the hardware and software domains. In [1], [4-5], [13] test generation and testability analysis for this particular problem has been studied, but not many efficient techniques have been developed yet.

In our approach, testability evaluation and test generation at the system level are based on hierarchical test generation (HTG) [9]. We apply HTG, using a decision diagram (DD) [12] based representation, and show that it can be used for both the hardware and software domains as well as for different levels of abstraction.

2. Hierarchical Test Generation for Hardware/Software Systems

Test generation has been proven to be an NP-complete problem [6]. There has been a lot of research devoted to solve the test generation problem for gate-level circuits. Working at this level provides very high quality of the tests but is computationally very expensive in the case of large circuits and therefore practically not usable. Several approaches have been developed to handle test generation for relatively large combinational circuits in a reasonable time. Test generation for large sequential circuits remains, however, an unsolved problem, despite rapid increase of computational power. Hierarchical test generation has been proposed as one possible solution [2, 8, 10].

To give the designer an opportunity to perform design for testability already in the

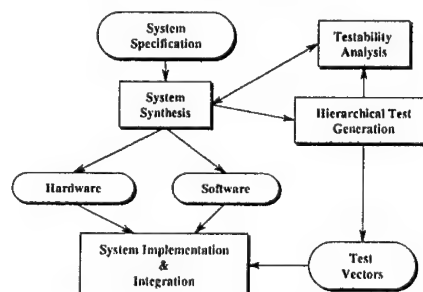


Figure 1. Test generation and testability analysis in a hardware/software co-design environment

¹ This work was partially supported by the Swedish National Board for Industrial and Technical Development (NUTEK).

early design stages, testability evaluation should be applied directly to the system specification. And a testability metric should be part of the cost function considered during system level synthesis, and in particular for hardware/software partitioning.

Figure 1 shows how testability evaluation and test generation fit into such a system synthesis concept. As discussed in section 1, testability evaluation and test generation are performed on a high level implementation-independent representation and they provide results to be interpreted and used in a coherent way for both the hardware and software partitions.

3. HTG for Specifications to be Implemented in Software

In our approach, decision diagrams are used for design modeling at the high abstraction levels. The main advantage of modelling with DDs lies in the fact that a uniform concept can be applied on different abstraction levels. An extended overview of DDs is presented in [12].

Our main objectives are to show how DDs can be used for test generation at the behavioural level and how HTG can be used for testing the part of the system which finally will be implemented as software. Hierarchical test generation technique for hardware has been reported at [8].

At this level, for every internal variable and primary output of the design a data-flow DD will be generated. Terminal nodes of the data-flow DD represent arithmetic expressions. Further, an additional DD which describes the control-flow has to be generated. The control-flow DD describes the succession of statements and branch activation conditions. Figure 2 depicts an example of DD, describing the behavior of a simple function. For example, variable A

will be equal to $IN1+2$, if the system is in the state $q=2$ (Figure 2c). If this state is to be activated, condition $IN1 \geq 0$ should be true (Figure 2b). The DDs extracted from a specification will be used as a computational model in HTG for symbolic path activation.

3.1. Test Generation Algorithm

There are two types of tests which we consider in the current approach. One set targets nonterminal nodes of the control-flow DD (conditions for branch activation) and the second set aims at testing operators, depicted in terminal nodes of the data-flow DD.

The whole test generation task is performed in the following way. Tests are generated sequentially for each nonterminal node of the control-flow DD. Symbolic path activation is performed and functional constraints are extracted. Solving the constraints gives us the path activation conditions to reach a particular segment of the specification. In order to test the operations, presented in the terminal nodes of the data-flow DD, different approaches can be

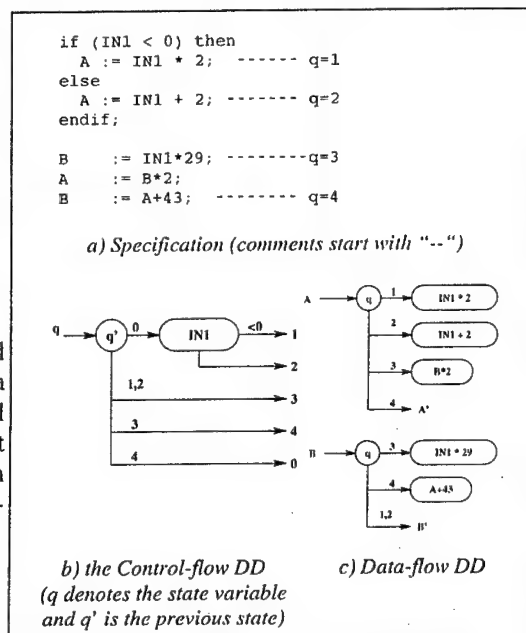


Figure 2. A DD example

used. In this paper, we use mutation testing [4] for test generation for the operations at the terminal nodes. For path activation, a slightly modified version of the algorithm described in [8] is used.

3.2. Conformity Test

For the nonterminal nodes of the control-flow DD, conformity tests will be applied. The conformity tests target errors in branch activation. In order to test nonterminal node *INI* (Figure 3), one of the output branches of this node should be activated. Activation of the output branch means activation of a certain set of program statements. In our example, activation of the branch $INI < 0$ will activate the branches in the data-flow DD where $q=1$ ($A:=X$). For observability the values of the variables calculated in all the other branches of *INI* have to be distinguished from the value of the variables calculated by the activated branch. In our example, node *INI* is tested, in the case of $INI < 0$, if $X \neq Y$. The path from the root node of the control-flow DD to the node *INI* has to be activated to ensure the execution of this particular specification segment. The conditions, generated here, should be justified to the primary inputs of the module. This process will be repeated for each output branch of the node. In the general case there will be $n(n-1)$ tests, for every node, where n is the number of output branches.

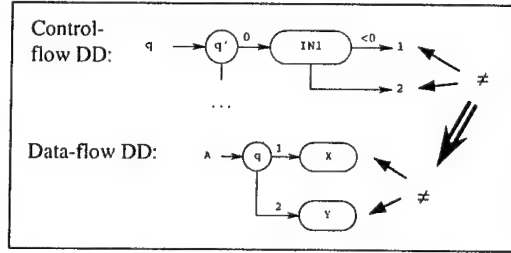


Figure 3. Conformity test

3.3. Testing Arithmetic Operators

As mentioned earlier, test vectors for the terminal nodes can be generated based on different approaches, and our HTG technique does not impose a specific one. Currently we use a mutation based fault model [4] for testing terminal nodes of the data-flow DD. We are using a library of operator mutations, which describes for each operator a set of corresponding mutants and conditions, which can distinguish between the mutant and the original operator. Suppose we have the expression: $x := (a+b) - c$. To rule out the fault that the first "+" is changed to "-", b must not be 0 (because $a+0=a-0$). Additionally, to rule out the fault that instead of "+" there is "*", we have to assure that $a+b \neq a*b$. For more details about operator mutants, we refer the reader to [7].

4. Experimental Results

Experiments were conducted in the environment consisting of our hierarchical test generator, the library of mutants for different arithmetic operators, and the Generic Coverage Tool (GCT) [11] which measures the quality of the generated test cases. Conversion between different representations (VHDL, C, Fortran and DD) is performed by corresponding translation tools. In order to evaluate our results we compare them with those produced by the software test generation tool Mothra [3]. Experiments were carried out on three embedded software examples. Table 1 presents the experimental results of our approach in comparison with the results achieved by Mothra. The Achieved fault coverage reflects synthetically several different coverage criteria (statement coverage, branch coverage, loop coverage etc.). As observed, the mutation based testing tool Mothra generates a much larger set of test vectors, which, at the same time, produces a weaker coverage.

Design module	Number of lines in the specification	Number of branches	Number of mutants	Mothra			Our approach	
				Number of generated test cases	Number of optimized test cases	Fault coverage	Number of generated test cases	Fault coverage
Square	38	12	813	707	5	77.65%	10	94.12%
Mult	20	6	478	449	3	84.00%	6	90.00%
FFT	31	4	1682	1639	4	83.91%	6	86.21%

Table 1. Experimental results

5. Conclusions

This paper describes a novel hierarchical framework for test generation in hardware/software systems. Hardware and software parts of an embedded system can be handled in a uniform way. The same DD representation can be used for describing systems at different abstraction levels, including the system level. Based on this representation, reasoning about testability in the early design phases and test generation for both the hardware and the software domain is possible. We have shown how HTG can be applied at the high levels of abstraction and how the software domain of the specification can be successfully covered. Experimental results have shown that the quality of the generated test vectors is even better than those produced by specific software test generation tools. Our future research is to integrate the testability metrics based on HTG into a hardware/software codesign environment.

6. Acknowledgements

The authors would like to thank Prof. Raimund Ubar from Tallinn Technical University for his helpful discussions concerning the Decision Diagrams.

7. References

- [1] G. Al-Hayek, C. Robach, "An Enhancement Process for High-Level Hardware Testing Using Software Methods," *IEEE European Test Workshop (ETW98)*, Barcelona, Spain, 1998, pp. 215-219
- [2] J. D. Calhoun, F. Brglez, "A Framework and Method for Hierarchical Test Generation," *IEEE Transactions on Computer-Aided Design*, Vol. 11, No. 1, January 1992
- [3] R. DeMillo, D. Guindi, K. King, M. M. McCracken, J. Offutt, "An Extended Overview of the Mothra Software Testing Environment," *Second Workshop on Software Testing, Verification, and Analysis*, Banff, Canada, July 1988, pp. 142-151
- [4] R. A. DeMillo, R. J. Lipton, F. G. Sayward, "Hints on Test Data Selection: Help for the Practical Programmer," *IEEE Computer*, Vol. 11, No. 4, Apr. 1978
- [5] O. P. Diaz, I. C. Teixeira, J. P. Teixeira, "Metrics for Quality Assessment of Testable Hw/Sw Systems Architectures," *IEEE European Test Workshop (ETW98)*, Barcelona, Spain, 1998, pp. 205-209
- [6] H. Fujiwara, "Logic Testing and Design for Testability," *MIT Press Series in Computer Systems*, MIT Press, Cambridge, Massachusetts, London, England, 1985
- [7] W. E. Howden, "Weak Mutation Testing and Completeness of Test Sets," *IEEE Transactions on Software Engineering*, Vol. SE-8, No. 4, July 1982
- [8] G. Jervan, A. Markus, J. Raik, R. Ubar, "Hierarchical Test Generation with Multi-Level Decision Diagram Models," *7th IEEE North Atlantic Test Workshop*, West Greenwich, RI, USA, 1998, pp. 26-33.
- [9] G. Jervan, P. Eles, Z. Peng, "A Uniform Test Generation Technique for Hardware/Software Systems," *IEEE European Test Workshop (ETW99)*, Constance, Germany, 1999
- [10] J. Lee, J. H. Patel, "ARTEST: An Architectural Level Test Generator for Data Path Faults and Control Faults," *IEEE International Test Conference (ITC'91)*, 1991, pp. 729-738
- [11] B. Marick, "Using Weak Mutation Coverage with GCT," *Testing Foundations*, 1992
- [12] R. Ubar, "Test Synthesis with Alternative Graphs," *IEEE Design and Test of Computers*, Vol. 13, No. 1, pp. 48-57, Spring 1996
- [13] H. P. E. Vranken, M. F. Witteman, R. C. Van Wuijtswinkel, "Design for testability in hardware software systems" *IEEE Design & Test of Computers* Vol. 13, No. 3, pp. 79-86, Fall 1996

An Estimation-based Technique for Test Scheduling

Erik Larsson and Zebo Peng

Dep. of Computer and Information Science Linköping University, Sweden

Email: {erila, zpc}@ida.liu.se

Abstract¹

A technique to schedule tests for complex digital systems is proposed where the test application time is minimized while the power dissipation is kept under control. The technique is based on estimations of the test application time and the power consumption. By experiments we show the efficiency of our approach.

1. Introduction

Development of microelectronic technology has lead to the implementation of system on chip (SOC), where a complete system, consisting of several ASICs, microprocessors, memories and intellectual properties (IP) blocks, is placed on a single chip. Such a system is usually made testable by the introduction of some design-for-testability (DFT) mechanism. Several DFT techniques such as test point insertion, scan and different types of built-in self-test (BIST) have been developed[1]. For a complex SOC design it is not unusual to combine several test techniques since they all have their respective advantages and disadvantages. Furthermore, when IP blocks are used, they may already contain a test methodology which is different from the rest of the design and it has to be incorporated in the overall test strategy of the whole system.

There are many similarities in testing PCB (printed circuit boards) and SOC. The major difference is however two-fold. In PCB, testing of each individual component can often be carried out before mounting and the components can be accessed for test via probing. Neither of these is possible when testing SOC. This means that testing the completed system becomes even more crucial and difficult. In order to keep test application time at a minimum, it is desirable to apply as many tests as possible concurrently. However, the power consumption must be kept under control. Otherwise, the chip could be damaged. Furthermore, due to resource conflicts, it is usually not possible to apply all tests concurrently.

Much research has focused on the scheduling problem in digital system design [6]. The main question has been to find a schedule that fulfills a set of constraints and minimizes a given cost function. In high-level synthesis the cost function has traditionally been an area performance function. Today, new approaches have been proposed where issues such as testability and power consumption are considered. In scheduling for low power, the scheduling is performed to find a design which minimizes the power consumption. These techniques focus on the normal mode and not at the test mode. The power consumption at the test mode can be much higher than during normal operation due to the high switching activity [2]. Therefore, it is very important to consider power consumption in the test mode. A major problem in synthesis for low power is that the switching activity depends on the input data. Several techniques have been proposed to estimate the input data.

A schedule has to be developed to determine the order of the tests. A dedicated test controller for a BIST based system is proposed by Zorian [5]. A general test scheduling algorithm is proposed by Chou *et al.* [4] and another test scheduling approach is proposed by Stroele *et al.* [3].

In this paper we assume a design with added DFT features. We propose a technique to estimate the test application time and the power consumption. Our approach is based on estimating the needed test vectors for the design. We propose a test scheduling technique which is based on these estimations. Our scheduling technique minimizes the test application time while the power dissipation is kept under control.

The rest of the paper is organized as follows. First we present the technique to determine which test will be used to test a resource in Section 2. In Section 3 the estimation of test application time is presented and the technique to estimate the test power consumption is given in Section 4. Our scheduling technique is presented in Section 5. Experimental results are in Section 6 and finally we conclude the paper in Section 7.

2. System Model and Test Strategy

A digital system can be seen as a set of interconnected blocks. To test it, a set of tests is applied and to minimize the test application time all tests should be applied as concurrently as possible. However, it might not be possible to apply

1. This work has partially been supported by the Swedish National Board for Industrial and Technical Development (NUTEK).

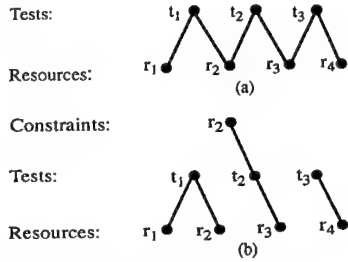


Figure 1: Tests, resources, and constraints.

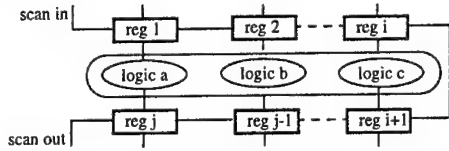


Figure 2: A Scan example.

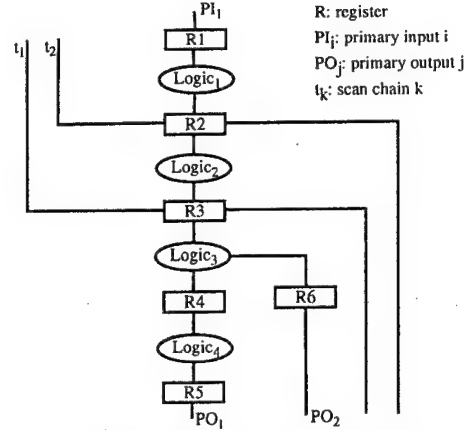


Figure 3: An example to illustrate shortest controllable and observable paths.

the test concurrently due to high power dissipation which might damage the circuit under test. Furthermore, there might exist different types of conflicts among tests and resources that restrict the ability for concurrent testing.

A resource graph can be used to describe the relationship between the tests and the IP blocks [4]. An example of resource graph is in Figure 1(a) where an edge from test t_1 to resource r_1 indicates that t_1 tests r_1 . In Figure 1(a) test t_1 and test t_2 can not be executed at the same time since both tests resource r_2 . In practice, we note that an edge, connecting t_i and r_j , in a resource graph could actually mean one or both of the following situations:

- A test t_i tests a resource r_j .
- When a test t_i is applied, resource r_j is required for test isolation and/or test access.

We introduce the *constrained resource graph* where a *constraint* level is added in order to distinguish between the two cases. If a resource is needed for other reasons but testing it is placed on the constraint level. For instance if resource r_2 in Figure 1(a) is needed in order to apply test t_2 , we place it on the constraint level, see Figure 1(b).

Our second observation is that a resource has to be tested only once. We introduce a technique to determine which test should be used to test a resource. For instance resource r_3 in Figure 1(a) can be tested by either t_2 or t_3 . In Figure 3 $logic_3$ can be tested using the primary input PI_1 , scan chain t_1 , or scan chain t_2 . If PI_1 is used for the test, the test vectors have to pass all the logic from PI_1 to $logic_3$. Furthermore, if PI_1 is used for the test of $logic_3$ neither scan chain t_1 or scan chain t_2 can be used concurrently. On the other hand, if scan chain t_1 is used to test $logic_3$ the test vectors have to pass through less logic and PI_1 and t_2 can be used to test other units at the same time. We use the *Shortest Controllable Path* and *Shortest Observable Path* to determine which test t_i should be used to test a resource r_j [8]. Let $G(V, E)$ be a directed graph where a vertex, $v \in V$, corresponds to a functional unit (operation). A *start vertex* is a vertex which gets its value directly from a primary input or a test access port. An *end vertex* is a vertex connected to a primary output or a test access port. A path, P_p , is a sequence of edges $\{(v_0, v_1), (v_1, v_2), \dots, (v_{n-1}, v_n)\}$ between v_0 and v_n . The *Shortest Controllable Path*, $SCP(op)$, for an operation op is the shortest path from a start vertex to op , and the *Shortest Observable Path*, $SOP(op)$ is the shortest path from an operation op to an end vertex.

For instance, in Figure 3, $SCP(logic_3) = \{(t_1, R_3), (R_3, Logic_3)\}$ and $SOP(logic_3) = \{(Logic_3, R_6), (R_6, PO_2)\}$. The first element on the SCP is where the test vectors are applied. The constraints in the constrained resource graph are the vertices on the SCP and SOP . According to our approach, $logic_3$ is tested via t_1 and R_3 , R_6 and PO_2 are in the set of constraints.

3. Estimation of Test Application Time for the Scan Technique

An operator is tested by applying a set of test vectors on the inputs and observe the response on the outputs of the operator. The test application time depends mainly on the number of test vectors and the clock frequency. The total test application time $T(t_i)$ for a test t_i is given by:

$$T(t_i) = T_c(t_i) + T_a(t_i) + T_o(t_i) \quad (1)$$

where T_c is the time to set up the test (*control*), T_a is the time to *apply* the test and T_o is the time needed to *observe* the test response. For the scan technique we use the following definition:

f_t : clock frequency at test mode, f_n : clock frequency at normal mode, n : number of clock cycles in normal mode.

$t_v(op)$: number of test vectors needed to test operation op .

$l_{in}(t_i, op)$: length of scan chain t_i (number of flip-flops) from the input to operation op .

$l_{out}(t_i, op)$: length of scan chain t_i (number of flip-flops) from operation op to the output.

$Op(t_i)$: the set of operators tested by test t_i .

$\max(t_i, tv(op))$: the maximal number of test vectors needed of any operator op tested by t_i where $op \in Op(t_i)$.

The test setup (control) time T_c , the application time T_a and the observation time T_o for a test t_i is estimated to:

$$T_c(t_i) = \frac{l_{in}(t_i, op)}{f_i} \times \max(t_i, tv(op)) \quad T_a(t_i) = \frac{n}{f_n} \times \max(t_i, tv(op)) \quad T_o(t_i) = \frac{l_{out}(t_i, op)}{f_i} \times \max(t_i, tv(op))$$

where $op \in Op(t_i)$.

An example of a scan-based system is given in Figure 2. Assume that $j=8$, the bit width of all registers to be 16 bits, $n=1$ and $f_n=f_i=10$ MHz, and logic a requires 100 test vectors, logic b 50 and logic c 10. Using the above formulae the estimated test application time is: $100 \times (32+32+1) \times 10^{-6} = 0.65$ ms.

In the above formulae we assume that we know in which position of the scan chain we have the operator to be tested by the vectors. If that is not known we have to scan in the whole vector for the scan chain before a test can be performed¹. In this case, instead of using $l_{in}(t_i)$ and $l_{out}(t_i)$ we use: $l(t_i)$: length of scan chain t_i (number of flip-flops).

The total estimated test application time becomes:

$$T(t_i) = \left(\frac{n}{f_n} + \frac{l(t_i)}{f_i} \right) \times \max(tv(op))$$

where $op \in Op(t_i)$.

Taking the example in Figure 2 with the assumptions above, we estimate test application time to: 1.29 ms.

4. Estimation of Test Power Consumption

The power dissipation in a CMOS circuit consists of a static and a dynamic part. The static power dissipation due to leakage current or other current drawn continuously from the power supply, and the dynamic power dissipation is due to switching transient current and charging and discharging of load capacitances [7].

The static power dissipation and the dissipation due to switching transient current are negligible compared to the dissipation due to load and unload of capacitances. The power dissipation due to charging and discharging capacitances is given by [7]:

$$P_{dyn} = \frac{1}{2} \times V^2 \times C \times f \times a \quad (2)$$

where V is the voltage, C is the capacitance, f is the frequency and a is the switching activity.

All parts but the switching activity in the formula 2 are given or can be extracted from a design library. The switching activity depends on the input data and there exists mainly two approaches to estimate it, based on simulation or probability. During testing the input to the design is known. It is the test vectors. We can for each component in a design use the test vectors generated by an ATPG tool as the input to a power simulation tool and then build a library with test power consumption for each unit in the design.

5. Test Scheduling Algorithm

In this section we propose a test scheduling algorithm which minimize the test application time while keeping power dissipation under control. It assumes that the test application time and the test power dissipation have been estimated for all units.

If two blocks are scheduled for test starting at the same time it is likely that one of the tests is completed before the other because the tests are of unequal length. This releases resources and a new test can be scheduled. However, if all tests in a test session are fully executed before tests from the next session is scheduled, the complexity of the test controller is minimized [4]. We present a test scheduling algorithm in Figure 4. The variable *time* in the algorithm refers to test session number.

At steps 1 and 2 in the algorithm we sort the tests according to estimated power consumption, see Figure 4. At step 4 we have a loop which terminates when all tests are scheduled and at step 7 we have an embedded loop where we try to schedule as many tests as possible at a specific test session. At step 8, we check if we can schedule the current test at this test session. We make sure that the power consumption is kept under the limit and we check the constrained resource graph in order to avoid conflicts between tests at the present test session.

In order to handle unequal test length the following step is modified:

15: *time* = *time* + min(scheduled units);

At step 15 we set *time* for next schedule to be the *time* when the shortest scheduled test is completed.

1. It is obvious that scan in and scan out can be performed simultaneously. However, here we are interested in the relative test application time for different blocks in the design. Therefore, we use an approach with low computation complexity.

```

(1) Sort the tests according to (estimated)
    power consumption;
(2) Place the tests in a list where the test
    consuming most power first;
(3) time=0;
(4) while not empty list
(5)   pwr(time)=0;
(6)   cur=first_test;
(7)   while not at end of list do begin
(8)     if pwr(time)+pwr(cur)<Max_pwr
        and no constraint(cur, scheduled)
        then
(9)       schedule(cur, time)
(10)      remove_from_list(cur);
(11)      pwr(time)=pwr(time)+pwr(cur);
(12)    end;
(13)    cur=next_test;
(14)  end;
(15)  time=time+1;
(16) end;

```

Figure 4: Test scheduling algorithm.

Block	Size	PB/active (mW)	PB/idle (mW)	Test Length
RL1	13400 gates	295	-	134
RL2	16000 gates	352	-	160
RF	64*17 bits	95	19	10
RAM1	768*9 bits	282	20	69
RAM2	768*8 bits	241	17	61
RAM3	768*5 bits	213	11	38
RAM4	768*3 bits	96	7	23
ROM1	1024*10 bits	279	23	102
ROM2	1024*10 bits	279	23	102

Table 1: Power dissipation and estimated test length for ASIC Z.

Test session	Zorian		Chou et al.		Our approach	
	Time	Blocks	Time	Blocks	Time	Blocks
1	69	RAM1, RAM4, RF	69	RAM1, RAM3, RAM4, RF	160	RL2, RL1, RAM2
2	160	RL1, RL2	160	RL1, RL2	102	RAM1, ROM1, ROM2
3	61	RAM2, RAM3	102	ROM1, ROM2, RAM2	38	RAM3, RAM4, RF
4	102	ROM1, ROM2	-	-	-	-
Tot. Time:	392		331		300	

Table 2: A comparison of different test scheduling approaches.

6. Experimental Results

We have used the ASIC Z [5] example to compare the scheduling algorithm presented in this paper with other approaches. The example consists of 9 blocks, see Table 1, where the estimation of the test length is made by Chou *et al.* based on the size of the blocks [4]. We use the same assumptions as Chou *et al.*, which is maximal power dissipation limited at 900 mW, all tests can be applied concurrently, the power consumption for idle blocks are excluded, and no tests can be started until all tests in the previous session is completed. In Table 2 we compare our test scheduling technique with Zorian's solution [5] and the approach proposed by Chou *et al.* [4]. Using our approach the total test length (application time) is 300 while the approach proposed by Zorian's has 392 and the Chou *et al.*'s approach has 331.

7. Conclusions

The high complexity in digital design has increased the need for design for testability techniques and the need to combine several DFT techniques. In order to minimize the test application time while keeping the test power consumption under control, efficient test scheduling is required. In this paper, we have discussed how to estimate the test application time and the test power consumption. We propose a test scheduling technique and experimental results show the efficiency of our approach.

References

- [1] M. Abramovici, M. Breuer, A. Friedman, Digital Systems Testing and Testable Design, IEEE Press, ISBN 0-7803-1062-4, 1990.
- [2] A. Hertwig, H-J Wunderlich, "Low Power Serial Built-In Self-Test", *Proc. of ETW*, pp 49-53, Sitges, May, 1998.
- [3] A. Stroele, H-J Wunderlich, "A Unified Method for Assembling Global Test Schedules", *Proc. of the Third Asian Test Symposium*, pp 268-273, Nov. 1994.
- [4] R. Chou, K. Saluja, V. Agrawal, "Scheduling Tests for VLSI Systems Under Power Constraints", *IEEE Trans. on VLSI Systems*, Vol. 5, No. 2, page 175-185, June 1997.
- [5] Y. Zorian, "A distributed BIST control scheme for complex VLSI devices", *VLSI Test Symposium*, April 1993.
- [6] D. Gajski, N. Dutt, A. Wu, S. Lin, High-Level Synthesis, Introduction to Chip and System Design, Kluwer Academic Pub., ISBN 0-7923-9194-2, 1992.
- [7] C. Svensson, D. Liu, Low Power Circuit Techniques, in Low Power Design Methodologies, Kluwer Academic Publisher, ISBN 0-7923-9630-8, 1996.
- [8] E. Larsson, Z. Peng, "Early Prediction of Testability by Analyzing Behavioral VHDL Specifications", *Proc. of NORCHIP*, pp 259-266, Tallinn, November, 1997.

Test Pattern Generation for Combined I_{DDQ} - Voltage Testing of Combinational Circuits

E. Gramatová, J. Bečková and J. Gašpar

Institute of Informatics, SAS, Bratislava, Slovakia
e-mail: gramatova.ui@savba.sk

Abstract. This paper deals with test pattern generation based on a deterministic algorithm and a fault simulation technique for combined I_{DDQ} and voltage testing. A deterministic test set is generated covering stuck-at, stuck-on, stuck-off faults and some inside gate shorts. The test set consists of combined current-voltage and pure voltage test patterns. The TPG system is running in two phases: the first one is test generation for covering the optimal test patterns for every primitive cell in a tested circuit and the second one is real defects detection and localisation over one selected defect library. Experiments using ISCAS'85 benchmark circuits have been done for the first phase of the ATPG system.

I. Introduction

Many defects causing bridges, breaks, and transistor stuck-on faults in CMOS circuits are not detected by a test set generated using the traditional single stuck-at fault model. Each physical defect should be covered by the test method that leads to the lowest overall testing costs, taking into account e.g. the complexity of the test generation, and the test application time. The length of the test sequence and the fault coverage of the test set which can be achieved contribute to the quality of the tested circuit. Certain types of CMOS defects are detected by current test patterns or by voltage test patterns only, and others by both [1]. Therefore the idea to use a combined test set for I_{DDQ} and voltage testing occurred. It could be one of the goals towards improving the test quality of complex CMOS circuits testing. Combination of functional and I_{DDQ} test patterns can create an effective test set. Up to now various Test Pattern Generation (TPG) techniques for I_{DDQ} testing have been presented [e.g. 2,3,4,5]. They are the TPG techniques only for I_{DDQ} testing or the classical TPG algorithms for stuck-at faults extended by current test patterns generation for those defects which are not detected by the voltage test patterns.

In the paper, an in-house experimental ATPG system is presented based on deterministic and random test generation techniques running with a fault simulator where the test set is generated currently for I_{DDQ} and voltage testing. Then the test set consists of combined current and voltage test patterns and of pure voltage test patterns. The system can also be used for different experiments for test pattern generation for combinational circuits testing. Some parts of the presented TPG system (random and deterministic TPG based on the critical path tracing technique) were published in [7-9]. A general description of the ATPG system is introduced in the next part together with some results using ISCAS'85 circuits. Algorithms for real defect coverage computation and real defect localisation are based on an analysis of a list of undetected fault conditions and a list of detected fault

conditions for the tested circuit over the selected defect library. The basic idea of the algorithms is presented in the second part of the paper. The algorithms are under implementation now.

II. TPG System for I_{DDQ} and Voltage Testing

The ATPG system allows to generate test patterns for a chosen fault list from the fault conditions cell library using two TPG approaches: random and deterministic TPG which run together with the fault simulator. Generally, the system can generate the optimum test set, in function of the constraints given for a cell library, which contains data regarding the detection of the possible faults/defects in a cell. The evaluation of a test set is based on its defect coverage. The following types of faults are considered in this system at the structural level using six different defect libraries based on electrical simulation results:

- stuck-at, stuck-open, stuck-on
- transistor shorts (intra -gate shorts) – the transistor short model considers shorts between four terminals of a transistor: source (s), drain (d), gate (g), bulk (b). There are six such shorts for every transistor.

The implicit fault model is used in the TPG system. The fault model is defined as a set of fault conditions - logical values for every primitive logic gate which has to be applied to it to cover the mentioned faults. Real defect coverage is computed from the undetected fault conditions and the specified defect library. The TPG system runs in two phases: in the first one, test pattern generation for covering an optimal test patterns for every primitive cell is done and in the second one, real defect coverage computation and defect localisation are applied over the selected defect library. The first phase of the test generation process is split into the following parts:

- The pre-process which consists of compilation of the circuit description into an internal form, selection of a design style, a testing mode and of a fault conditions list from the fault conditions cell library. Description of the tested circuit uses the language from the ISCAS'85 circuits. The testability measures (used in the deterministic TPG) are computed before test pattern generation.
- The main part consists of the random TPG, the deterministic TPG (based on FAN strategies) and the fault simulator.
- The post-process consists of the fault condition coverage and the statistics computation, the creation of output files (a test set, a list of undetectable fault conditions and/or a list of detectable fault conditions).

The critical path tracing technique has been implemented for current and voltage test patterns generation in the first ATPG prototype [7,8]. The new deterministic test generation algorithm based on FAN strategies has been implemented in the presented ATPG system because of a lot of test patterns for voltage testing which cannot be covered during the critical path tracing. The number of backtracks can be specified at the beginning of the test generation process and it can also be increased during the test generation according to the received fault conditions coverage.

The following table introduces results using both random and deterministic approaches for test pattern generation using ISCAS'85 benchmark circuits. The number of non-active test patterns was 5 000 test vectors during random test generation.

	Random + fault simulation						Deterministic + fault simulation					
	%	test	C/V	V	C	time	%	test	C/V	V	C	time
c432	95,82	80	42	38	0	00:09	95,82	84	35	47	2	00:07
c499	99,43	103	76	27	0	00:20	99,44	137	83	48	6	00:26
c880	100	120	56	64	0	00:58	100	81	14	66	1	00:06
c1355	99,74	121	103	18	0	01:01	99,75	133	82	47	4	01:25
c1908	99,68	186	143	43	0	02:13	99,78	171	115	51	5	01:03
c2670	89,07	123	77	46	0	02:23	96,79	158	123	28	7	04:41
c3540	96,85	264	184	80	0	06:19	97,08	151	41	107	3	18:01
c5315	99,47	238	90	148	0	06:13	99,45	229	32	196	1	07:50
c6288	99,40	48	44	4	0	03:42	99,21	62	16	45	1	14:30
c7552	97,07	314	115	199	0	08:26	98,56	216	38	177	1	19:21

Table 1: ISCAS experiments (C/V – current and voltage patterns)

III. An Algorithm for Defect Localisation

The second phase of the ATPG system consists of the defect diagnosis with real defect coverage computation and defect localisation algorithms. Fault coverage received from the first phase of the TPG process illustrates only coverage of fault conditions for all gates in the tested circuit for which the TPG is applied. It means a test set generated by the system is only the detection test set. Therefore two other algorithms have been proposed and implemented for defect coverage computation and defects localisation. The algorithms work on one selected defects library from six types and one user's defect library. The user's library concerning types of defects and test patterns for every gate can be specified by the user. The second phase of the ATPG system requires the following files:

- the list of undetected fault conditions
- circuit statistics
- the test set or the list of covered fault conditions.

These files are outputs of the first phase of the TPG system. The first input file consists of some statistical data about the tested circuit:

- type of used technology (it is important for selection of convenient defects library for every type of gates)
- numbers for each type of gates (for defects number calculation).
- number of lines and fan-out points.

The second input file is the list of undetected (voltage and/or current) fault conditions related to the gate specified by its type and name. Defects libraries for basic cells with two inputs – NAND, AND, OR, NOR, EXOR and NOT, BUFF for six technologies were received from electrical simulation.

This algorithm for defect localisation is being implemented in the same way as the defects coverage computation based on the huge files with defects dictionaries using fault conditions and fault conditions libraries created by the ATPG system. The type of defects libraries depends on the used technology and on the individual basic logical gates. The defects covered by voltage or current test patterns are deleted from the list of defects for the tested circuit. Both, current and voltage libraries are analysed but the voltage defects library is analysed first, because testing time for voltage pattern application is lower than for current pattern application. Results from the second phase using the ISCAS'85 benchmark circuits can be presented after its implementation and connection to the ATPG prototype.

IV. Conclusion

In this paper the TPG system for combined current and voltage test generation together with defect localisation has been presented. The system has been implemented in C language under WINDOWS and LINUX. The ATPG system can be used for different experiments using random, deterministic and fault simulation algorithms for combinational circuits testing. It's planned to extend the proposed and implemented ATPG prototype is by a conversion program from the EDIF format to the ISCAS input format used in the ATPG system. This work has been supported by the CP94: 0391 UBISTA project - A Unified Built in Self Test Approach for Full Defect Testing in Mixed Signals, and by the VEGA 2/6091/99 - Behavioural and Real Defects Oriented Test Generation for Digital Circuits and Systems.

References

- [1] B.Bennets: "IDDQ Test - Issues Facing EDA Vendors", Proc. of EDAC'95 User Forum, pp. 65-68.
- [2] U.Mahlsted, J.Alt, M.Heinitz: Current: "A Test Generation System for IDDQ Testing", Proc. of 13th IEEE VLSI Test Symposium, 1995, pp. 317-323.
- [3] U.Mahlsted, M.Heinitz, J.Alt: "Test Generation for IDDQ Testing and Leakage Fault Detection", Proc. of DAC'92, pp. 486-491.
- [4] J.F.Ferguson, T.Larrabee: "Test Pattern Generation for Realistic Bridge Faults in CMOS Ics", Proc. of ITC'91, pp 492-499.
- [5] S.W.Bollinger, S.F.Midkiff: Test Generation for IDDQ Testing of Bridging Faults in CMOS Circuits, IEEE Trans. On Computer Aided Design of Integrated Circuits and Systems, Vol. 13, No.11, November 1994, pp. 1413-1418.
- [7] E.Gramatová, A.Somorovská, J.Gášpar, H.Manhaeve: "Test Pattern Generation System for IDDQ-Voltage Test Experiments", Proc. of ETW'98, 1998 pp.193-194.
- [8] E.Gramatová, A.Somorovská, J.Gášpar, H.Manhaeve: "Random and Deterministic Test Pattern Generation for IDDQ-Voltage Testing", Proc. of EDC'98, pp.205-208.
- [9] E.Gramatová, A.Somorovská, J.Gášpar, H.Manhaeve: "Test Pattern Generation for IDDQ - Voltage Testing Based on Fault Simulation", Proc. of DDECS'98, pp.265-268.

Optimisation and Implementation of the Arctan Function for the Power Domain

A.Th. Schwarzbacher^{2,3}, A. Brasching^{1,2}, Th.H. Wahl^{1,2}, P.A. Comiskey² and J.B. Foley³

¹Fachhochschule der Deutschen Telekom AG, Dieburg, Germany

²Dublin Institute of Technology, Dublin, Ireland

³Trinity College, Dublin, Ireland

Abstract: Trigonometric functions are used in many applications including real time digital signal processing (DSP), navigation and astronomy. Today's demand for fast, small and portable equipment in those areas has resulted in the need for optimised structures for real-time processing of complex mathematical functions. Therefore, the multipurpose algorithms used traditionally for such implementations are investigated in this paper and new directions for future implementations are presented.

Keywords: CORDIC Algorithm, Low-Power Design, High-Level CMOS Design.

1 Introduction

The CORDIC Rotation Digital Computer (CORDIC) Algorithm [1] is traditionally used for the implementation of trigonometric functions. Volder first introduced the CORDIC Algorithm in 1959. Since then it has been the most popular algorithm for implementing mathematical functions. With this algorithm only shift steps and addition operations are required to calculate most mathematical functions. The basic idea of CORDIC is to take an angle and "rotate" a vector over this angle towards zero. The CORDIC Algorithm of Volder uses three input variables (x, y, z) and is based upon the algorithm shown in Figure 1.

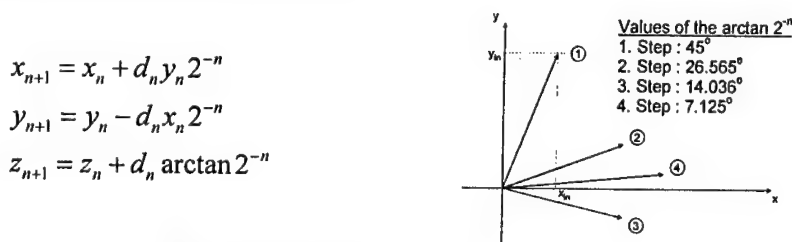


Figure 1: The Rotation Steps of the CORDIC Algorithm

The terms for $\arctan 2^{-n}$ are precomputed and stored, n is the index of the iteration (1, 2, 3, ..., n) and the value of d_n is either +1 or -1. The variables are initialised. Next, a set of iterative equations is repeatedly applied to these variables until the result converges to the required accuracy. The accuracy can be controlled using the number of computing steps. If accuracy necessary is not the main concern, the computation can be stopped after a few steps. The different functions are selected by the value of d_n . The term d_n is chosen in such a way, that with each step either y or z is driven toward zero. Figure 1 shows the rotation steps when, that y is driven toward zero.

2 Implementation of the Arctan

To show the performance of the CORDIC Algorithm, the trigonometric function arctan was implemented in hardware. Additionally, three further solutions were developed and compared with respect to error deviation, timing behaviour, power consumption and area requirements. One implementation for the arctan uses the CORDIC Algorithm. Two other implementations use a Lookup Table and the last one uses an approximation technique. The system input has a bitwidth of 7 bits and the output is 6 bits wide. In view to the fact that the arctan function is an odd function, the sign of the input value is cut off. The sign can be assigned directly from the input to the output, because of (1)

$$\arctan(x) = -\arctan(-x). \quad (1)$$

The input range from the arctan is from $-\infty$ to $+\infty$. The implementation of such a function is only possible by restricting the input range. The input range is restricted from 0 to 1.984375 with a bit step value of 0.015625. The output is defined such that 60° corresponds to an output 42 decimal. This results in a resolution of 1.4286° at the output. The input is normalised so that an input value of 1 corresponds to an output of 60° . Therefore, the input value is multiplied by the factor $\sqrt{3}$. All models are implemented as synchronous systems.

2.1 Using the CORDIC Algorithm

This model uses the CORDIC Algorithm as described in the previous section. Here, the value of y corresponds to the input value for the first stage and the value of z in the last stage corresponds to the output value. The design consists of 10 pipeline stages as shown in Figure 2. The required shift, addition and subtract operations are done in each stage, except the first one where no shift operation is needed. The fixed angle is stored separately in the calculation stage and will be added or subtracted from z depending on the value of y .

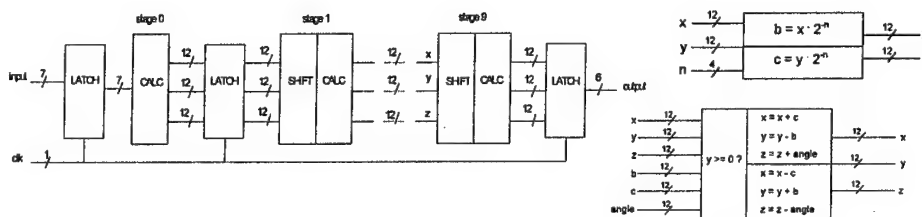


Figure 2: The Structure of the implemented CORDIC Algorithm

The result of y after several calculation steps results in $result = \arctan(y/x)$. Therefore, the value of x must be set to $1/\sqrt{3}$ to achieve the actual result of $\arctan(\sqrt{3} \cdot y)$.

2.2 Using a Lookup Table

A Lookup Table (LUT) is a simple storage device. All output values are precomputed and stored in the LUT. The input is an address in the LUT, which is used to access the output data. There are no calculations. Therefore, the design is very fast. All output values are so as to minimise the error. Thus, the error deviation can not exceed 0.7143° (half of the resolution). The LUT contains 128 values, because there are 7 bits at the input ($2^7=128$).

2.3 Modifying the LUT

The *modified* LUT uses the same precalculated and stored data as the LUT, except for the first 23 input values, which will be directly assigned to the output. The reason for this assignment is that for small x , the $\arctan(x)$ is approximately x . This direct assignment of output to input is implemented by changing the resolution of both input and the output. The change in resolution at the output with the definition, that 60° responds to 42 decimal results in a factor of 1.59. By multiplying the now adjusted and normalised input value by $\sqrt{3}$, the approximation of $\arctan(x) = x$ is valid again. Therefore, the value of the input will be assigned direct to the output for input values from 0000000 to 0010110.

2.4 Approximating the Arctan

The four implementation is based on an linear approximation of the arctan, which is optimised for hardware implementations. The characteristic of the arctan is divided in four sections as shown in Figure 3. Part I is based on the principle of direct assignment as used in the modified LUT before. Parts II to IV are use simple equations, which represent the desired values. All equations use a multiplier, which is a multiple of 2^n and one constant, which will be added. Therefore, it is easy to implement this equation into hardware by using shift and an adding operations. The equations shown in Figure 3 are only optimised for this particular input width and the function $\arctan(\sqrt{3} \cdot x)$ with the condition that 42 decimal is responding to 60° .

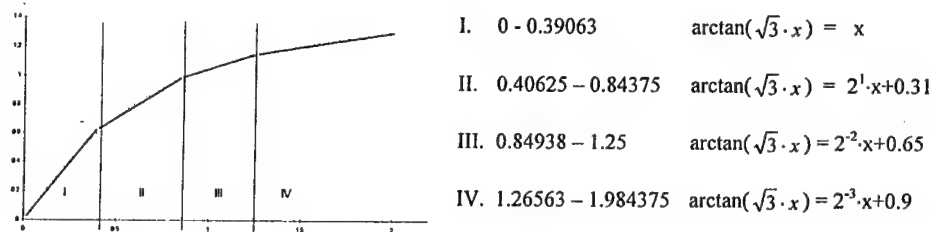


Figure 3: The four Sections for the Approximations of the Arctan

3 Results

In this section the four different implementations of the arctan algorithm are compared. The designs were written in VHDL, synthesised using Synopsys Design Compiler without any constraints using an ES2 0.7 μ m technology. All implementations were designed to have a deviation of less than one bit from the theoretical value. All designs have a propagation delay of less than 10ns. In respect of the timing behaviour there is nearly no difference between the version using the Approximations and both Lookup Table versions. However, the Approximations technique uses 80% less time for the calculation than the CORDIC Algorithm.

Figure 4 shows the power consumption of the different implementations. The power consumption was established using PowerCount [2] for an operating frequency of 10MHz and a supply voltage of 5V. As can be seen in Figure 4, the Approximation technique uses only 0.6mW at 10Mhz, compared to the CORDIC Algorithm which uses 17mW a reduction in power consumption by a factor of 25. The modified Lookup Table requires 78.5% of the power, that is consumed by the normal Lookup Table. The reason for this is that the first 23 of the 128 input values (from 0000000 to 0010110) are directly assigned to the output. The version using the

Approximation technique needs only 66.7% of the power of the Lookup Table and therefore, this version is the best with respect to power consumption.

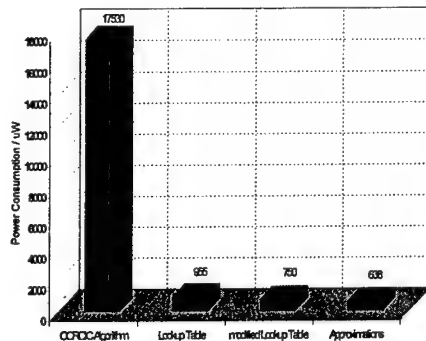


Figure 4: Power Consumption

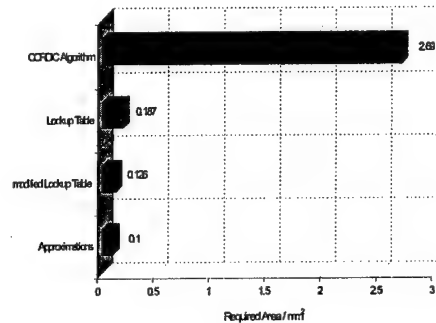


Figure 5: Area Requirements

Figure 5 presents the area requirements of the different implementations. Like the power consumption, the best result with respect to the required area is produced by the approximation technique. This version uses 53.5% of the area required by the Lookup Table, 79.4% of the area required by the modified Lookup Table and 24 times less area when compared to the original CORDIC algorithm.

4 Conclusion

The aim of this paper was to show that the investigation of traditional algorithms can reduce power consumption significantly. For this purpose the arctan function was investigated and three alternative implementations to the traditional CORDIC algorithm were implemented.

It was possible to reduce the power consumption of the traditional implementation by a factor of 25. This reduced power consumption was achieved without compromising any other performance feature such as accuracy or throughput. In fact, most other performance parameters also improved. For example the required silicon area was also reduced by a factor of 24. Therefore, the authors have shown, that traditional multi-purpose algorithms may not be optimised towards power consumption. In addition, there are many possibilities of performing the same operations with significantly reduced power consumption, without compromising the overall performance of any aspect of the implementation. Therefore it was shown that it is worth while to invest time and resources to investigate alternative implementations of traditional algorithms.

References

- [1] J.E. Volder, "The CORDIC trigonometric computing technique," *IRE Trans. Electron. Comput.*, vol. EC-8, no. 3, pp. 330-334, Sept. 1959
- [2] A.Th. Schwarzbacher, P.A. Comiskey and J.B. Foley, "Powercount: measuring the power at the VHDL netlist level," *Electronic Devices and Systems Conference*, Bruno, Czech Republic, pp. 70-73, June 1998.

Contact: schwarzbacher@gmx.net

Gallium Arsenide Implementation of the Building Blocks for a Direct Digital Frequency Synthesiser

S. Lachowicz¹, K. Eshraghian¹, M. Hollreiser², H.-J. Pflaederer³

¹ Centre for Very High Speed Microelectronic Systems, Edith Cowan University, 100 Joondalup Drive, Joondalup WA 6027, Australia, S.Lachowicz@cowan.edu.au, K.Eshraghian@cowan.edu.au

² European Space Research and Technology Centre, Electrical Engineering Department, Microelectronics Section, Postbus 299, NL-2200 AG Noordwijk, The Netherlands, mhollrei@estec.esa.nl

³ Microelectronics Department, University of Ulm, Albert Einstein-Allee 43, D-89069 Ulm, Germany, Hans-Joerg.Pflaederer@e-technik.uni-ulm.de

Abstract. Frequency Synthesisers are the key to precise time, frequency and phase in communications transmitters and receivers as well as in radar pulse compression. Digital implementations such as direct digital synthesis (DDS) are frequently selected because of their inherent advantages. Limiting factors are the spurious frequencies, which are generated due to quantisation effects and an output frequency limited to less than half of the sampling frequency according to the sampling theorem and taking into account a realisable anti-image filter. The fundamental part of any DDS architecture is a periodically overflowing phase-accumulator which generates linearly increasing phase values. In this paper we review an efficient self-timed highly-pipelined accumulator architecture implemented in MESFET Gallium Arsenide.

I. Introduction

Frequency Synthesisers [1] [2] are the key to precise time, frequency and phase in communications transmitters and receivers as well as in radar pulse compression. Digital implementations such as DDS are frequently selected because of their inherent advantages. These are as follows: any desired frequency resolution can be obtained merely by increasing the number of bits; fast switching and settling times and a very wide tuning range are available; the phase of the synthesised signal remains continuous whilst frequency switching; different modulation schemes (FM, PM and AM) are easily implemented; ideal I/Q decomposition is obtained; cost is reduced due to the absence of alignment requirements; improved temperature and aging stability; remote control capability; small size, mass and low power consumption. Limiting factors are the spurious frequencies, which are generated due to quantisation effects and an output frequency limited to less than half of the sampling frequency according to the sampling theorem and taking into account a realisable anti-image filter. A periodically overflowing phase-accumulator generates linearly increasing phase values. Using these values to address a ROM, which contains samples of the desired waveform, time discrete and quantised samples are produced. A digital to analogue converter

(DAC) in combination with a low-pass filter converts these samples into an analogue signal. Fig. 1 shows the basic principle of the Direct Digital Frequency Synthesis.

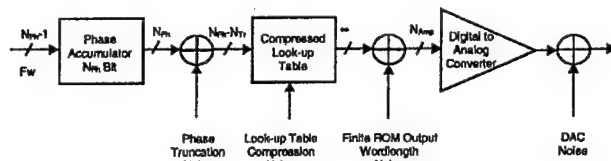


Fig. 1. DDS principle

The following sections demonstrate an efficient, high-speed, low-power implementation of an accumulator in MESFET GaAs using a self-timed approach.

II. Self-Timed MESFET GaAs Systems

Recently introduced, Pseudo Dynamic Latched Logic (PDLL) [3] and Latch Coupled FET Logic (LCFL) [4] GaAs logic families have shown to be a good compromise for high speed and low power dissipation for both synchronous, and asynchronous systems. They compare well with other design styles in terms of speed/area and speed/(area-power) based figures of merit and are especially efficient for highly pipelined systems. The main advantage of the latched structure is provided by the feedback which ensures that the noise margin is higher than for a simple Direct Coupled FET Logic (DCFL) gate. This enables to use serial connections of the E-type transistors in the pull-down section. Therefore, in GaAs latched logic it is possible to implement logic gates based on the AND function which gives more freedom in the design and leads to more area efficient circuits.

Self-timed approach has been chosen for the accumulator in order to eliminate the need for global distribution of extremely high frequency clock signals with the expected benefits of reduced power dissipation and inherent delay insensitivity. As in the frequency synthesiser the timing is of utmost importance, the synchroniser needs to be used prior to the D/A conversion.

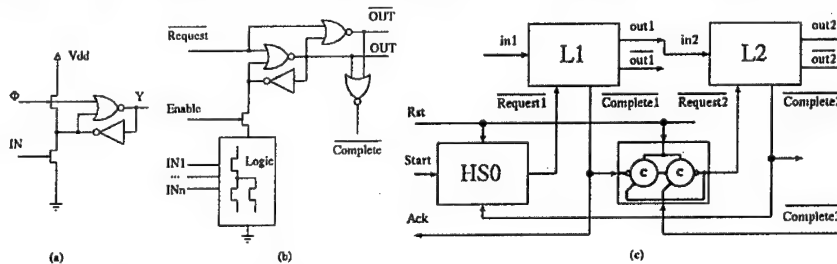


Fig. 2. (a) PDLL cell, (b) LCFL cell, (c) A self-timed pipeline

Fig. 2(a) shows a basic PDLL cell while the LCFL cell for self-timed applications is depicted in Figure 2(b). The self-timed pipeline is depicted in Fig. 2(c). The Muller-C element, as can be seen in Fig. 2, is the fundamental component of the handshake path of the self-timed pipeline. In terms of logic operation, it implements the AND function for events, such that if a specific transition takes place at one input and it is coincident with, or followed

by, a similar transition of the other input(s), then that transition will be presented at the output. In conventional logic terms its function can be described as:

$$Y(i+1) = Y(i)(A+B) + AB$$

Using an LCFL GaAs gate this equation can be implemented in the structure presented in Fig. 3.

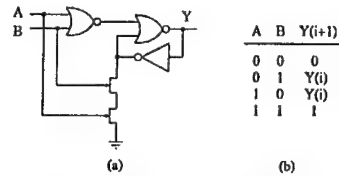


Fig. 3. LCFL implementation of the Muller-C gate.

III. The MESFET GaAs Accumulator

The accumulator has been designed using the self-timed approach and the basic LCFL cells. A one-bit adder cell consists of the sum cell shown in Fig. 4(a) and the carry cell presented in Fig. 4(b). Both cells use the AND connections in the pull-down section as this is allowed in the latched-logic design style. The sum cell uses the complements of the input data as these are readily available as shown in Fig. 2(b).

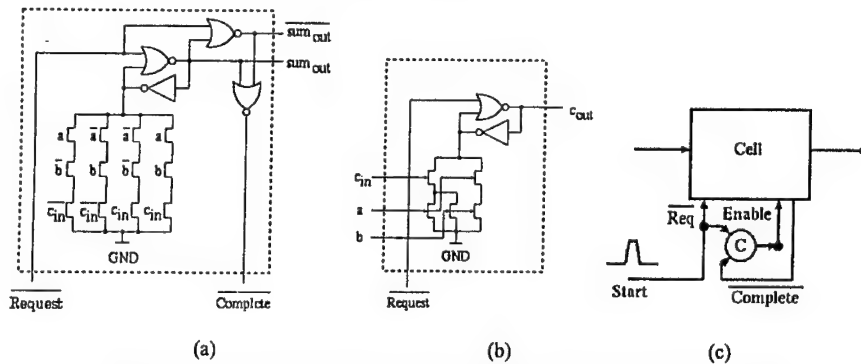


Fig. 4. (a) The sum cell, (b) The carry cell, (c) A special memory cell

The accumulator structure for 4 bits is shown in Fig. 5(a). It can be observed that the handshaking hardware overhead is not significant, especially for higher numbers of bits, although because of the limited fan-out of the GaAs gates some buffering might be required. The accumulator contains one-bit adder cells, and pre-skew and de-skew sections consisting of simple delay cells. However, because of the feedback present in the accumulator, special memory cells have to be employed. The memory cells ensure that regardless of the delay in the input data (which can be asynchronous) the accumulator adds correctly the new set of data to the current contents. The memory cell, shown in Fig. 4(c), uses the basic cell from Fig. 2(b) and one Muller-C cell to read the output of the adder and is triggered by the *Complete* signal from the adder cell.

IV. Simulation

The accumulator performance has been assessed using Hspice. Figure 5(b) shows the waveforms at the output of the accumulator for a 4-bit data word 0011, and Figure 5(c) shows the relationship between the spread of 0.6 μ m GaAs MESFET process parameters and the power dissipation of the circuit. The circuit throughput is 0.5 Gbps and does not depend on the data word width. It is expected that this value will further increase for the 0.4 μ m process.

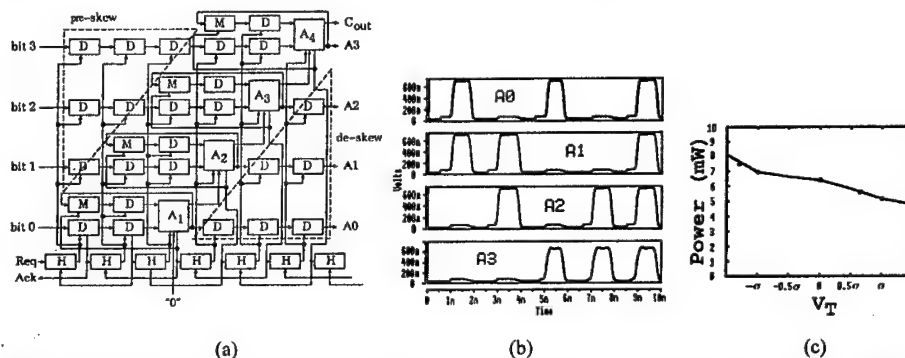


Fig. 5. A 4-bit version of the accumulator: (a) structure, (b) output waveforms for 0011 data word, (c) power dissipation as a function of V_T spread

V. Conclusions

The architecture of a self-timed GaAs MESFET accumulator has been presented. The problem of feedback in the high-speed pipeline has been resolved. The circuit is characterised by high speed, low power dissipation and inherent delay-insensitivity. It is specifically designed for the application as phase accumulator for the Direct Digital Frequency Synthesiser.

Acknowledgment

The support of the Australian Research Council and the Centre for Very High Speed Microelectronic Systems at Edith Cowan University is gratefully acknowledged.

References

- [1] M. Hollreiser, H-J. Pfeleiderer, S. W. Lachowicz, and K. Eshraghian, "Optimization of a DDFS Architecture with Respect to its Spurious and Bandwidth Performance and Considerations for Implementation", *to be published*.
- [2] M. Hollreiser, L. Fanucci, "Techniques for Spurious Reduction in Direct Digital Synthesis" *ESA Preparing for the Future*, Vol.6, No.2, June 1996.
- [3] J. F. López, K. Eshraghian, R. Sarmiento, A. Núñez and D. Abbott, "Gallium Arsenide pseudo-dynamic latched logic for high performance processor cores", *IEEE Journal of Solid State Circuits*, Vol. 32(8), pp. 1297-1303, August 1997.
- [4] S. W. Lachowicz, K. Eshraghian, J. F. López, and H-J. Pfeleiderer, "Design of Self-Timed Gallium Arsenide Integrated Systems for Multimedia Computing", *Proceedings of the MIXDES'98 Conference*, June 1998, Lodz (Poland), pp 93-98.

Introducing Delay Probability Graphs with the Design of a 32-bit Asynchronous ALU

F. Pessolano¹

¹*CCSV-SCISM, South Bank University, 103 Borough Rd.,
London SE1 0AA UK, francesco.pessolano@sbu.ac.uk*

Abstract: The need for low-power embedded processing cores and reduced EM noise is a pressing force towards changes in system design. This has suggested the adoption of self-timed systems, which consume energy and produce noise depending on data. In this paper, we analyze this data-dependency feature of self-timed system introducing Delay Probability Graphs. Delay Probability Graphs prove to efficiently help the designer and be also useful when applied to synchronous design.

I. INTRODUCTION

As suggested by the 1997 ISA roadmap, in a decade time CMOS technology will reach a point where switching delays will be less important than interconnection ones. In such a scenario, designers will face the daunting task of designing complex and extremely wide clock routing networks. Thus, the clock signal will no longer be able to travel from one side to the other of the chip in one cycle. This will affect complexity of the design process from architectural to layout level and limits performance improvements. A natural solution to this problem is to adopt local communication avoiding global clocks (i.e. self-timed computing [1]). This approach may be also effective in reducing power demand, electromagnetic noise, timing faults and so on. Asynchronous circuit design has been recently used and tested in few processing core designs: these cores are somehow simple, concentrating their attention on small ISA subsets or on the ARM embedded core.

In this paper, we focus our attention on the data-dependent behavior of such asynchronous systems: the delay of a unit depends on both the input data and the specified operation. This property allows variable delays for complex units like ALUs and FPUs, with possible reduction of overall execution time respect the synchronous discipline. The data-dependent behavior is analyzed through *Delay Probability Graph* and applied to the design of an asynchronous 32-bit ALU core as part of a larger processor design [5]. The paper is organized as follows: section 2 formally describes the Delay Probability Graphs. In section 3, DPGs are applied to the design of the asynchronous ALU and different circuits are analyzed. The final design is described in section 4. Some conclusions are drawn in section 5.

II. DELAY PROBABILITY GRAPHS

In order to formally describe *Delay Probability Graphs* some definitions are needed. Given a general unit S with n inputs X and m outputs Y , we define *input pattern* a generic input X , *input set* I all the possible input patterns and *output pattern* a generic output $Y=S(X)$. We indicate with $\Delta(X)$ the delay needed to fully produce the output pattern Y corresponding to an input pattern X . We define *delay set insisting on a interval* $[t_1, t_2]$ the set DS such that:

$$x \in DS \Leftrightarrow x \in I \wedge \Delta(x) \in [t_1, t_2] \quad (1)$$

We call *dimension* a function $\dim(DS)$ which returns the number of elements of DS . Given a group of n delay sets DS_i , it is a *uniform covering* of the input set if and only if the following statements are true:

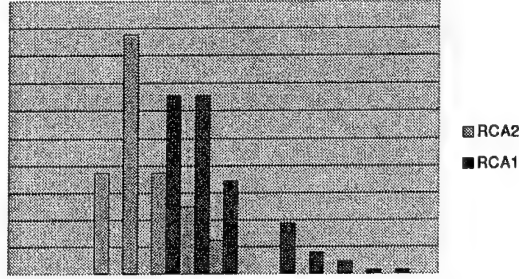


Fig.1: Comparative Delay Probability Graph for 8-bit integer Ripple Carry Adders.

$$\begin{aligned} \forall i, j \quad t_{2i} - t_{1i} &= t_{2j} - t_{1j} \\ \forall i, j \quad i \neq j &\Leftrightarrow DS_i \cap DS_j = 0 \\ I &= \bigcup_j DS_j \end{aligned} \quad (2)$$

A *Delay Probability Graph (DPG)* for a unit S is defined as a bar representation of one of its possible uniform coverings. Each bar i has dimension $\dim(DS_i)$ and x-axis relative to the interval DS_i insists on. An example of DPG for two 8-bit ripple carry adders is presented in Fig.1. It is evident that a DPG is a graphical representation of the input patterns percentage generating output in a given delay interval, and its shape depends on the chosen intervals as well. Each $\dim(DS_i)$ value is proportional to the probability of ready output within such delay. DPG can be generated only with complete knowledge of the unit S behavior. It allows comparison of different modules on the basis of their delay distribution and data dependent behavior.

III. ALU BASIC BLOCKS DPGs AND DESIGN

Delay Probability Graphs can be generated only through exhaustive simulation of the module under investigation. Moreover, different algorithms and architectures for the same module generate different DPGs; even different solutions for completion detection influence the DPG. For this reason, a proper DPG extraction environment has been studied, which can produce the required data in reasonable time and reasonable precision.

We have generated DPG using the C/C++ language, which allows timed execution of C/C++ scripts describing the module under investigation. The program and the scripts use delays extracted from circuit simulation of the basic blocks. It also generates information about statistics of the probability graph and test patterns to verify precision of those statistics. The adoption of a programming language has proved more efficient and faster respect to HDL languages or exhaustive circuit simulation. It also resulted more flexible and easily customizable to different needed statistics.

For our design, we have modeled different schemes for addition, multiplication, shifting, floating-point rounding, etc.. Basic cells have been designed following the standard cell

library convention in 0.5 μ m MOSIS technology with 3.3v supply voltage. As example, in Fig.1 we report the DPG for 8-bit ripple carry adders, where *RCA1* is based on a 1-bit DCVL FA cell and *RCA2* on a 2-bit one. *RCA2* is easily recognized as a better choice, since the distribution is less wide and delays smaller. Most of the input patterns can generate output faster then the faster *RCA1* input pattern.

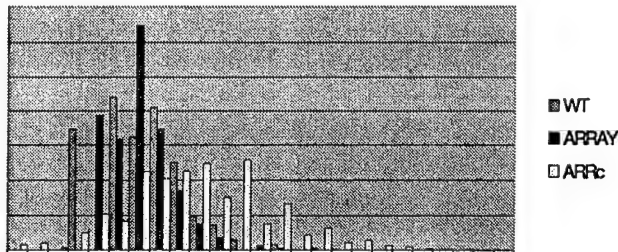


Fig.2: Comparative Delay Probability Graph for 8-bit unsigned integer multipliers producing 16-bit result.

In Fig.2 we report the DPG for three configurations of 8-bit multipliers all based on a 1-bit DCVL FA cell and generating a 16-bit result. The schemes being investigated are a 3:2 Wallace tree (WT), an array multiplier (ARRAY) and a conditional array multiplier (ARRc). The ARRc configuration has been recently proposed as valid way to improve data dependent behavior [2]. The DPG in Fig.2, confirms this argument, but at the same time it proves that this configuration is a poor design choice because of its wider DPG (i.e. greater standard deviation). As regards the WT and the ARRAY schemes, their DPG is similar with WT having a slightly wider graph. The ARRAY configuration has a smaller standard deviation, which corresponds to less data dependent behavior. For the ALU design we have chosen the ARRAY scheme because of better behavior at slow speed and possible optimizations that reduce both area and latency.

The DPGs in Fig.1/2 have been generated for asynchronous logic, so they are influenced by the completion detection logic. The C/C++ scripts allow evaluation of DPG even when the completion logic is not used (synchronous case). A comparative DPG analysis shows that the completion logic has two main effects: the best-case delay is increased: for example, in an RCA the best case with completion logic must be greater than the delay of the completion logic, while it is equal to two 1-bit FA delays without. Data-dependent behavior is introduced or amplified in schemes that are regular (e.g. WT), while it is reduced with intrinsically data-dependent modules (e.g. ripple carry adders). These results suggest that the synchronous design could exploit more data-dependent delays if properly exploited [3].

IV. THE ASYNCHRONOUS ALU

The block view of the 32-bit asynchronous ALU is presented in Fig.3. The ALU is composed of a ROM for opcode decoding, an asynchronous locking register file with dedicated locking port [4], and the Functional Unit. Handshake follows the zero-overhead PS0 configuration for all stages, except the FU one. For this unit, a slightly different choice has been made so to allow the preceding unit to independently restore its status. This proves to be extremely efficient with units, like the FU, whose delay is not predictable a priori.

The FU module has been designed at circuit level in order to execute the unsigned integer subset of the HCP instruction set. The basic blocks are a 32-bit ripple carry adder using the organization of RCA2, and an array multiplier generating a complete 64-bit result. The multiplier follows the same algorithm of the ARRAY configurations, but it is implemented with a non-pipelined self-timed ring and a 32-bit RCA2 adder for the upper double-word (ORM in Fig.6). The ALU has a minimum latency of about 6.5ns and a maximum one of about 16.2ns; cycle time varies from the best case of 3ns to the worst case of 11.6ns. Energy dissipation strongly depends on both data and operation.

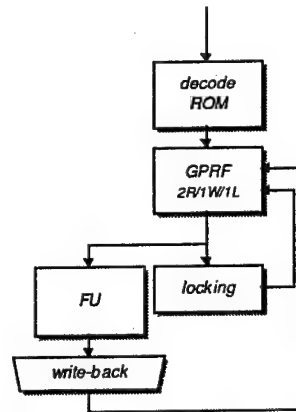


Fig.3: High-level view of the ALU core structure.

V. CONCLUSIONS

Improving system performance pushes designers to look for every possible design path and property. In this paper, we have introduced the *Delay Probability Graphs* or *DPGs* to analyze the data-dependent behavior of circuits. DPGs have been here applied to the design of basic cells for an asynchronous 32-bit ALU. Its application to synchronous design is also feasible and sensible, and it represents the next step of the current work.

Acknowledgments: This work has been supported by the Working Group on Asynchronous Circuit Design (ACiD-WG), Esprit Nr 21949, as part of the Fourth Framework. The author wishes to thank Prof. MB Josephs for his continuous support.

VI. REFERENCES

- [1] CH van Berkel, MB Josephs, SM Nowick, "Applications of asynchronous circuits", *Proc. of IEEE*, vol.87, No.2, pp.223-233, Feb, 1999
- [2] D Kearney, NW Bergmann, "Bundled data asynchronous multipliers with data dependent computation time" *Proc. of the 3rd Advanced Research in Asynchronous Circuits and Systems ASYNC'97*, pp.186-197, April 1997
- [3] F Pessolano, D Protheroe, ME Bush, "Data-Dependent Clocked Logic", to appear in *Proc. of the 14th European Conference on Circuit Theory and Design ECCTD'99*, Sept. 1999
- [4] F Pessolano, "An enhanced locking register file for asynchronous processors", *Proc. of the 1st PREP Conference*, Manchester, UK, Jan. 1999
- [5] F Pessolano, "Heterogeneous Clustered Processors: Organization and Design", to appear in *Springer-Verlag Lecture Notes in Computer Science*, Sept. 1999

Efficient Controller Design for Data Stream Processing Applications in a FPGA Based Prototyping Environment

Klaus Feske, Alexander Krebs, Mark Langer

FhG IIS Erlangen - Department EAS Dresden

Zeunerstr. 38, D-01069 Dresden, Germany, e-mail: feske@eas.iis.fhg.de

Abstract. To enhance efficiency in FPGA based rapid prototyping of digital telecommunication applications we insert the Protocol Compiler into a proved design flow. This paper focuses on domain specific modeling styles and synthesis strategies aiming design improvement, changeability, and reuse. We discuss two design case studies: a DAB (Digital Audio Broadcasting) Test Data Generator and a Digital Audio SPDIF Receiver. The achieved results are summarized concerning design quality and efficiency.

1 Introduction

The requirements rising from controller design for telecommunication applications are the starting point of our work. Using a proved rapid prototyping environment, we were faced with a bottleneck in the design process as visualized in Fig. 1: while the control part might occupy only 15% of the chip area, it often takes up to 75% of the design and debug effort [SHM-96]. Therefore, we studied high-level modeling styles and synthesis strategies to enhance efficiency in controller design for structured data stream processing.

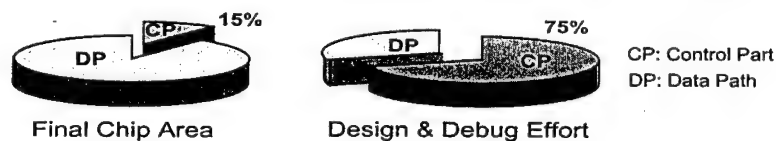


Fig. 1. Control Part: final chip area versus design and debug effort

The paper is organized as follows. First we discuss related work. Section 3 describes our experimental rapid prototyping design flow using the Protocol Compiler and outlines domain specific high-level modeling principles. In section 4 two case studies are explained: the design of a DAB (Digital Audio Broadcasting) Test Data Generator and the implementation of a Digital Audio SPDIF Receiver. Results concerning design quality and efficiency are presented. We finish with a summary and conclusions.

2 Related Work

A high-level approach for compiling and debugging structured data processing controllers, first published in [SHM-96], is based on previous work by Seawright and Brewer concerning logic synthesis from *grammatical productions* [Sea-94]. These results influenced the development of the Dali-approach and its integration into the Protocol Compiler [Syn98]. Various application reports [HoB-98, Bau-99, SDF-99] indicate an improved design productivity exploiting the capabilities of this high-level synthesis approach.

To enhance the efficiency in FPGA based rapid prototyping, in the paper [FRK-98] a finite state machine (FSM) partitioning technique, which takes technology specific features

into consideration, is inserted into the design flow. Based on this previous work and first experiences in utilizing Protocol Compiler in a DAB project [SDF-99] this paper outlines high level modeling principles and related synthesis solutions according to the discussion of two case studies.

3 Design Environment and Modeling Principles

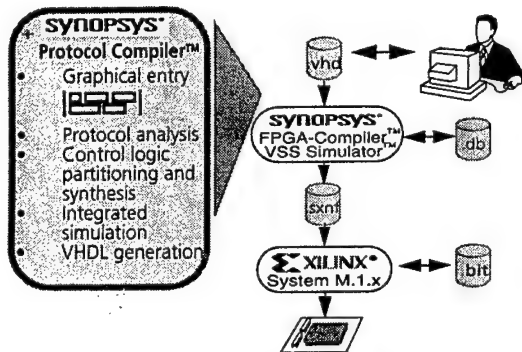


Fig. 2. Protocol Compiler in an experimental rapid prototyping design flow

Our conventionally used design flow starts at RT-Level with a VHDL description of the design specification. As a new element in the chain of this flow, the Protocol Compiler is set on top of the whole process (Fig. 2), by means of which the high-level specification is graphically composed. The Protocol Compiler provides the following features: graphical protocol level entry, formal protocol analysis, back annotation simulation, controller logic partitioning and synthesis, and VHDL code generation. The graphical symbolic format (Fig. 3a) is similar to the Backus-Naur-notation. It closely

matches the high level protocol specification. Using this specification facilities Fig. 3b shows the embedding of DAB audio test data into the DAB frame structure and a way to expand the subchannels: To add another module for inserting additional data services into the data stream a sequence is created by surrounding the existing block with a sequential frame operator. Afterwards, the appearing unspecified frame is replaced by a copy of the first module. Finally, a few parameters need to be adjusted.

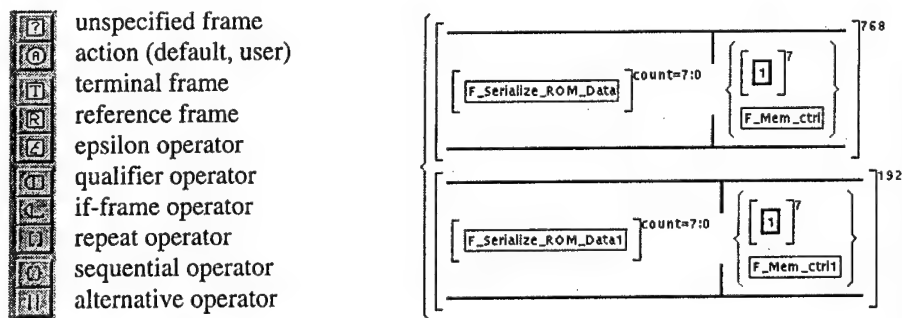


Fig. 3. a) Types of frames and frame operators, b) Modeling example

4 Case Study TDG: Design of a DAB Test Data Generator

The digital radio system DAB is a broadband system, which transmits multiple programs in a common program block: the ensemble transport interface ETI. Digitized and preprocessed audio signals and data services are put together using a multiplexer (DAB-MUX, Fig. 4).

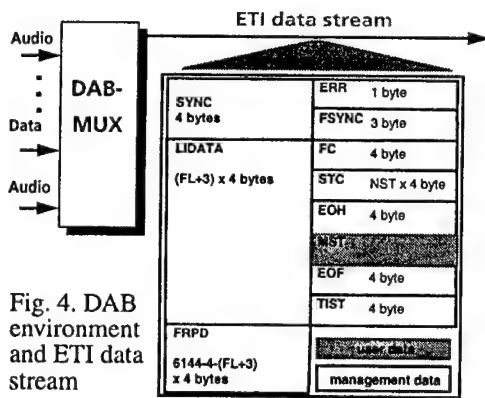


Fig. 4. DAB environment and ETI data stream

This multiplexer generates a complete ETI data stream out of the supplied input streams. The stream is fed to a modulator and finally the modulated HF carrier is sent out via antenna. The ETI data stream is a structured compilation consisting of three hierarchically subdivided parts: the synchronization block, the LIDATA, and the FRPD field. In a DAB project our institute is responsible for the DAB multiplexer design. Consequently, a suitable TDG is a useful facility to support design validation. The TDG can be used either as an MUX input signal source or to emulate the MUX output.

Now we discuss the ways to generate the hierarchical frame structure as visualized in Fig. 5. There are three basic approaches to obtain the needed clock cycle shift. The first one starts all branches in parallel and delays the actions by placing counters right before them. To obtain the desired timing, it is necessary to work in parallel because some variables need to be prepared even in the clock cycle before they will be serialized. The next possibility employs RunIdle frames [Syn-98]. The third way is the sequential processing. It consequently sequentializes the design as shown in Fig. 5. The successive action will be started not before its predecessor ends. The timing is guaranteed by the serializers.

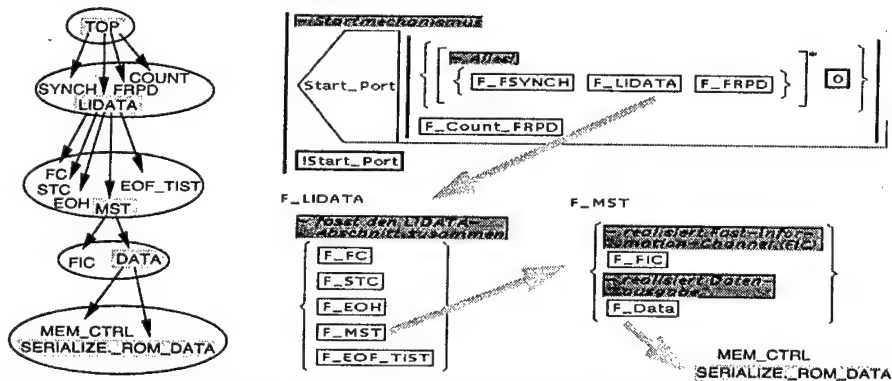


Fig. 5. Hierarchical ETI frame structure and corresponding high-level model

The results produced by the three particular modeling styles are shown in the bar charts in Fig. 6. Comparisons were made concerning the number of generated VHDL statements, the number of CLBs, the circuit delay, and the total CPU time needed for the whole synthesis process. We implemented the test data generator using sequential processing. It fits into a Xilinx FPGA XC4013E using 421 out of 576 CLBs and provides two independent data channels for audio data and for digital data services.

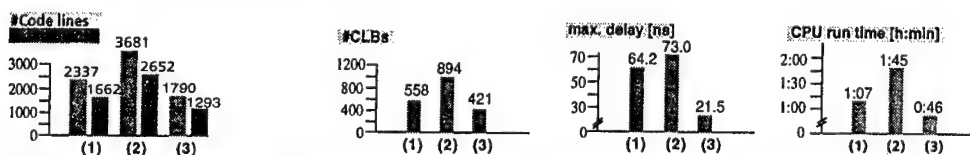


Fig. 6. Synthesis results: using (1) counters, (2) RunIdle frames, (3) sequential processing

5 Case Study DAR: Design of a Digital Audio SPDIF Receiver

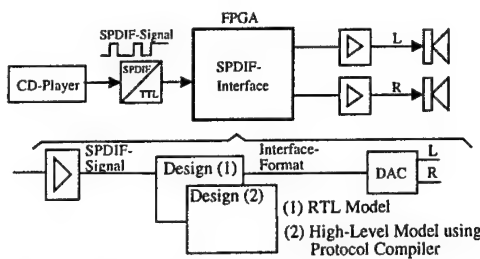


Fig. 7. Hardware Environment

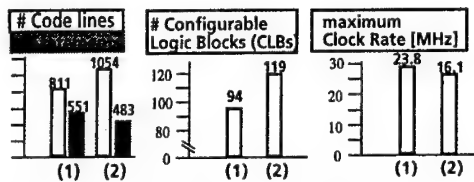


Fig. 8. High Level- versus RTL-Modeling

To estimate the efficiency of our extended rapid prototyping design flow we redesigned the Digital Audio Receiver - a project published by Blinzer [HoB-98]. This decoder receives SPDIF audio streams [IEC985] and transmits audio data to a digital analog converter (DAC) over a serial interface (Fig. 7). The SPDIF receiver design requires the separation of the SPDIF protocol layers: bit level, block level, and frame level. The output data stream needs to be reassembled according to the DAC input protocol.

To compare the two styles (1) high-level synthesis using Protocol Compiler and (2) design by means of a graphical RTL entry we performed the steps: design entry, validation, code generation, and synthesis using FPGA Compiler and Xilinx M1. Fig. 8 shows the RTL design methodology to be less efficient in terms of the number of CLBs as well as of the

maximum clock rate. Furthermore, the overall design and debug effort is reduced by approximately the factor two in case of the high-level approach.

6 Conclusions

We have presented high-level modeling principles and related synthesis results achieved for two design projects. We utilized a FPGA rapid prototyping design flow which we extended by a graphical high level design entry. This approach supports an application-oriented modeling style at the level of specification and enhances design efficiency and quality for structured data stream processing controllers. Additionally, it results in a quick design exploration, easy changes, and design cycle reduction. A further controller design improvement can be expected by utilizing reuse methodologies. Consequently, our future work aims at extending our rapid prototyping design flow by inserting a library of reusable protocol templates and components and aims at applying it to other projects in telecommunications and networking area.

References

- [Bau-99] Baumgart, A.: „Experiences made in using Protocol Compiler in a ATM ASIC project.“, SNUG'99, Munich, Germany, March 8-9, 1999.
- [FRK-98] Feske, K.; Rülke, St.; Koegst, M.: „FPGA Based Prototyping Using a Target Driven FSM Partitioning Strategy“, ICECS'98, Lisboa, Portugal, September 7-10, 1998.
- [IEC958] „Digital Audio Interface“, International Standard IEC958, First edition, 1989-03.
- [HoB-98] Holtmann, U.; Blinzer, P.: „Design of a SPDIF Receiver using Protocol Compiler“, 35th Design Automation Conference DAC98, 06/98, San Francisco, CA, USA.
- [SDF-99] Scholz, M.; Döring, M.; Feske, K.: „Design of a Digital Audio Broadcasting (DAB) Test Data Generator using the Synopsys Protocol Compiler“, SNUG'99, Munich, Germany, March 8-9, 1999.
- [SHM-96] Seawright, A. et al.: „A System for Compiling and Debugging Structured Data Processing Controllers“, EURO-DAC'96, Geneva, Switzerland, Sept. 16-20, 1996.
- [Sea-94] Seawright, A.: „Grammar-Based Specification and Synthesis for Synchronous Digital Hardware Design“, Ph.D. Thesis, Univ. of California at Santa Barbara, June 1994.
- [Syn-98] SYNOPSIS: „V1998.08 Protocol Compiler User's Guide“, Synopsys Inc., 1998.

A Configurable 8051 Microcontroller Core

I. Janiszewski, R. Baraniecki, K. Siekierska

*Institute of Electron Technology, Al. Lotników 32/46, Warszawa
{janiszew, rbar, k.siek}@ite.waw.pl*

Abstract: A configurable core of the 8051 μ C is presented. The core is fully consistent with industrial standards 80C51 and 80C52 regarding the instruction set and timing. Nevertheless the core's structure is flexible and can be configured according to user requirements. Such features as instruction set, interrupts, memory sizes etc., are easily modifiable. The core design has been checked in real applications and is offered now as an IP block.

I. Introduction

Nowadays a significant trend towards developing core-based (IP-based) designs can be observed in the area of complex application specific systems [1]. Rapidly growing market of soft, firm and hard macros offered by many IP providers sustain, and even strengthen this tendency. IPs are integrated at different levels of abstraction (from system- to transistors-level) in the design flow. This lead certainly to reducing of the time-to-market and global design cost.

HDLs allows creating of soft macros, which can be mapped onto various technologies e.g. standard cells, FPGA etc. HDLs are being the most efficiently applied on the RTL now. The reason for that lies in the synthesis tools, which have not been yet well adapted to higher level of abstraction. Very popular are soft macros of microprocessors and microcontrollers. Among them the 8051 μ C [2] and its mutations are still used, particularly in control systems.

At ITE an 8051-like μ C's core has been developed on the RTL with the VHDL synthesizable subset. The core is compatible with industrial standards 80C51 and 80C52 regarding the instruction set and timing. It is generic as well, which means it can be configured according particular design requirements (e.g. customized instruction set, interrupt priorities, execution cycle etc.).

II. A core architecture concept

The core can be roughly divided into two parts: an 8051 CPU and optional peripheral modules. During the CPU architecture developing the strong emphasis was put to make it independent of the peripheral modules connected to. Optional peripheral modules are not necessary for correct functioning of the CPU and its software compatibility (instruction execution times are consistent with the industrial standard). However they are indispensable if a fully compatible (in meaning of timing) 8051 μ C is being built. Peripheral modules are attached to the CPU by the use of a SFR (special function registers) bus, which consists of an address and data buses and some control signals (RD, WR and SFR_EN). Peripherals are accessed by the use of special function registers (SFRs). In our approach they are included in the peripherals. Upper half of available addresses (from 80H to FFH) of internal RAM is just reserved for SFRs. Hence the communication between the CPU and SFR is carried out in the same way as in case of any memory cell. Therefore each of the peripherals must include a piece of logic (e.g. an address decoder) for handling the SFR bus. This allows the CPU to

have the uniform access to each SFR. It is worth to note that two buses make the communication in the CPU. First one is for internal and external ROM, the second one for internal and external RAM and SFRs. Thus the SFR bus is only a subset of the common bus.

The CPU architecture is shown in Fig. 1. Four crucial functional blocks can be distinguished in the core: an arithmetic logical unit, an interrupt unit, an instruction decoder, and an execution controller. Two first modules have been implemented as peripheral modules. They contain own internal SFRs and are connected to the interperipheral bus according to the general concept of the core access to peripheral modules. There is also a block of registers used directly in the CPU that contains as follows: an instruction register (IR), a program counter (PC), a stack pointer (SP), a data pointer (DPTR), and a control power word (PCON).

The CPU interface has been designed to enable to build a μC that conforms industrial standards or to use it as a standalone software compatible CPU and to attach to it application specific peripheral required. Peripherals connected to the CPU can be either characteristic of 8051 μC (see Fig. 2) as: a serial port, a timer/counter module, parallel ports and external memories, or any others designed to satisfy the aim of a single project. All standard peripherals have been also designed and verified regarding compatibility. Moreover some other non-standard modules are available in frames of the core as: a matrix keyboard peripheral, and a 7-segment display driver.

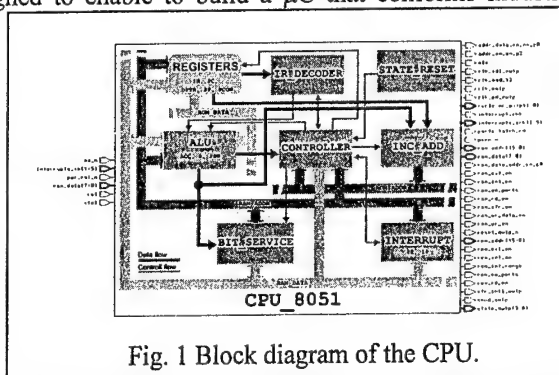


Fig. 1 Block diagram of the CPU.

III. Configuration properties of the core

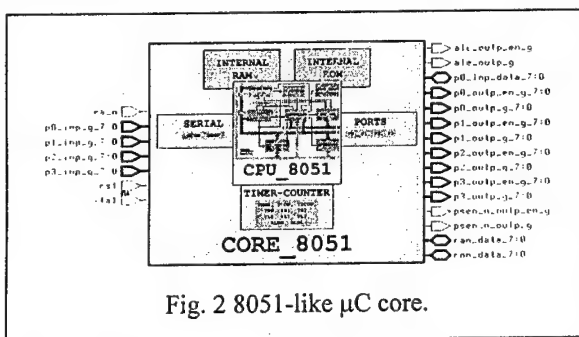


Fig. 2 8051-like μC core.

As it was already mentioned the core has been designed to be fully compatible with industrial standard. Nevertheless the core is very flexible as well. This is due to its generic structure. The core can be easily configured according special requirements. This leads to the more efficient use of the core in various applications and reducing design and fabrication costs.

All configuration capabilities of the core have been grouped in a configuration package. This allows for separation them from the indigenous part of the core, which remains untouched by a user and can be encoded to hide VHDL code. Inside the configuration package there are several constants. By assigning values to them, a user has opportunity to determine the core's structure, even the instruction set and execution cycle. How the instruction set is configured that is shown in Listing 1. Each instruction being needless can be eliminated by setting corresponding constant to zero.

```

constant INSTR_CODE_00_EN_CONST : Int_Bit := 1; -- NOP
constant INSTR_CODE_01_EN_CONST : Int_Bit := 1; -- AJMP addr11
...
constant INSTR_CODE_FF_EN_CONST : Int_Bit := 1; -- MOV R7,A

```

Listing 1. A cutting from the core's configuration package with settings of μ C instructions.

User's settings in the instruction set are propagated down through the core's hierarchy. They impact generics of instantiated components. Let's focus on the ALU now (look at Listing 2). Instructions performed by this module have been divided into several groups. These belonging to the same group have the same feature, which is a piece of common hardware needed by them to be executed. The instruction of multiplication (MUL AB) is switched on if the parameter MUL_EN is set up. MUL_EN depends directly and only on the core parameter INSTR_CODE_A4_EN and makes up one-element group – it is carried out only on operands stored in the accumulator and register B. Another situation occurs in the case of the addition with carry (ADDC). This instruction can be performed on operands located in different places (in accumulator, universal work register, and memory). All varieties of this instruction need the same piece of hardware thereby they must be gathered in the same group. A value of parameter ADDC_EN is dependent of several core parameters (INSTR_CODE_35_EN .. INSTR_CODE_3F_EN). If even only one of them is selected on in the configuration package, the common hardware for the group is inferred by a synthesis tool.

```

ALU_UNIT: ALU generic map(
...
  MUL_EN      =>  -- MUL A, B
  INSTR_CODE_A4_EN,
...
  ADDC_EN     =>  -- ADDC A, Rr; ADDC A, #n; ADDC A, ad; ADDC A @Ri
  (INSTR_CODE_38_EN or INSTR_CODE_39_EN or INSTR_CODE_3A_EN or INSTR_CODE_3B_EN or
   INSTR_CODE_3C_EN or INSTR_CODE_3D_EN or INSTR_CODE_3E_EN or INSTR_CODE_3F_EN) or
  INSTR_CODE_34_EN or INSTR_CODE_35_EN or (INSTR_CODE_36_EN or INSTR_CODE_37_EN),
...
)
port map
-- ( signals mapping )

```

Listing 2. Instantiation of ALU component.

The INTERRUPT is also an example of a parameterized module. It can service different number of interrupts depending on the core's application. The number of interrupts is modifiable and the hardware priority as well. All available interrupts are declared in the form of enumeration type INT_TYPE (see Listing 3). The position of the record is strictly tied to hardware priority. In case of adding or removing any interrupt service the INT_TYPE type and the INTERR_INFO constant are modified.

They are also other configurable features. In the standard a signal PSEN (program store enable) is active twice during each machine cycle and in case of a few instructions (e.g. 1-byte 2 cycle's instructions) some fetches are redundant. In the core these needless fetches can be removed. Moreover, a user can influence on how multiplication and division are carried out. Setting a proper generic, a one-cycle or four-cycle (as in the standard) multiplication is enabled. In similar way, the division with remainder or fraction is set up. Another feature is possibility to attach internal pure logic states holders. They can be applied to enable the bus go to the high-impedance if any module does not drive it. A user can also define types of pad

cells (inverting or non-inverting) intended for port pins and ALE and PSEN signals. Thanks to that a designer needn't care about inverters when pads are attached.

```
--Interrupts available in the 8051 microcontroller
type Int_Type (NONE,INT0_T,T0_T,INT1_T,T1_T,UART_T,T2_T);
-- Interrupt setup record
type Int_Info is record
  name : Int_Type; -- interrupt type
  addr : Int_Addr; -- interrupt vector
  index : Int_SFR_Id; -- index in "IE" i "IP"
end record;
-- Array of interrupt setup records
-- Position in the array corresponds to the hardware priority level
constant INTERR_INFO : Int_Info_Vector :=
  ((INT0_T, 16#03#, 0), -- INT0 (03H) (IX.0) p t ^ the highest
   (T0_T, 16#0B#, 1), -- T0 (0BH) (IX.1) r y /\
   (INT1_T, 16#13#, 2), -- INT1 (13H) (IX.2) i |
   (T1_T, 16#1B#, 3), -- T1 (1BH) (IX.3) o |
   (UART_T, 16#23#, 4), -- UART (23H) (IX.4) r |
   (T2_T, 16#2B#, 5)); -- T2 (2BH) (IX.5) i | the lowest
```

Listing 3. Declaration of interrupts.

IV. Conclusion

A configurable soft core of the 8051 μ C designed with the VHDL synthesizable subset has been presented in the paper. The main goal of efforts undertaken while design of the core, was full compatibility with the industrial standards 80C51 and 80C52. This aim has been reached and its structure is very flexible. The core can be easily optimized regarding current design constraints by changing generic parameters placed in the VHDL configuration package.

Summarizing, basic features of the core presented are as follows:

- Possibility of attaching different peripherals either standard 8051 modules or developed by customer. They can be easily connected to the core by a common SFR bus
- Peripheral modules enclose the SFRs that makes the core independent of them
- Full compatibility with the 80C51 and 80C52.

The following properties of the core can be set up in the configuration package to match design requirements:

- Internal RAM and ROM sizes are from ranges 0..256 Kbytes and 0..64 Kbytes respectively
- Instruction set and number of interrupt sources
- Optional use of internal bus holders for tri-state buses
- Execution of ROM fetches (they can be executed only if needed)
- Number of cycles for division and multiplication instructions.

The core has been fully verified after implementation in standard cell technologies. It was used in the smart pressure sensor chip and in 8031-compatible μ C. The compatibility with the industrial standards has been checked and confirmed by the use of the logic verifier LV500.

Acknowledgements

This work was supported by grants 8T11 B001 12 and 8 T11 036 13 from the State Committee for Scientific Research, Poland.

References

- [1] R. Seepold, A. Kunzmann: "Reuse Techniques for VLSI Design", Kluwer Academic Publishers, 1999.
- [2] Intel, "Embedded Controller Handbook", Intel Corporation 1987, Volume 1, MCS-51Family.

Design Technology for Future Embedded Telecom Systems
I. Bolsens

The paper not available at printing time.

A product life-cycle view of the value of Boundary Scan

R G "Ben" Bennetts

*Bennetts Associates, Burridge Farm, Burridge, Southampton, SO31 1BY, UK
benb@burridge.demon.co.uk*

Abstract

In the past, Design-For-Test (DFT) solutions (such as internal scan, built-in self test, and boundary scan), have been seen to be point solutions to individual problems. We now know that boundary scan opens up a re-use capability of other DFT structures and this allows a wider view of DFT and how it fits into a product life-cycle view of test. In effect, boundary scan has become the "internet of test".

The presentation will review the life-cycle view of DFT and comment on how this affects future developments of DFT technologies.

1. Introduction

Since the publication of the ANSI/IEEE 1149.1 Boundary Scan Standard in 1990 [1], there has been a steady acceptance of boundary-scan technology by the electronics manufacturing industry. Initially, the attention was focused on the application to board manufacturing test, targeted at boards with reducing access for traditional in-circuit bed-of-nail testers, sometimes known as the *limited access* problem. The increasing use of ball-grid array device packaging and other "tough-to-access" device packaging styles such as thin-shrink small-outline has accelerated the adoption of boundary scan and the technology is now clearly in the mainstream phase of the adoption cycle.

More recently, In-System Programming (ISP) applications of boundary scan has further increased the interest in the Standard, with many of the main suppliers of CPLDs and FPGAs supporting the use of 1149.1 as a gateway to the programming and re-programming of their devices. The advantages of ISP are many and are discussed later in the paper.

It is now clear however that boundary scan does a lot more than just solve board test and ISP problems. A decision to use boundary scan for either of the above reasons usually opens up a discussion about the whole life-cycle test requirements and test strategy for a product. Effectively, boundary scan allows re-use access to other forms of test structures, such as internal scan and built-in self test, and *InScan* ("scan-through-TAP") and *RunBist* instructions are now commonly required in complex full-custom devices [2]. These types of instruction can be invoked at any time during the life of the product and it has been shown that they have tremendous diagnostic value during system integration and field-service operations. An early example of this is the use of boundary scan in the design of the electronic systems in the *Iridium*^{TM/SM} satellites [3]. A more-recent example can be found in *Stratus Computer's* fault-

tolerant computers [4], and in the proposal by NASA to build a 3-dimensional MCM stack space flight computer [5].

Additionally, we are now seeing the implosion of boundary-scan concepts, from board back down to System-on-Chip devices. The IEEE P1500 Embedded Core Test standards activity is veering very close to 1149.1 structures with their ideas of test-access mechanisms and core wrappers [6].

In effect, boundary scan technology has become the *internet of test* [7], allowing various forms of DFT structures to become connected for re-use purposes. The paper explores this aspect of boundary scan and shows how the technology has a role at prototype board debug, volume manufacturing of boards, system integration, and field service.

2. The growth of PC-based testers

To take full advantage of boundary scan through the life-cycle of a product requires supporting test technology that is both versatile and portable. During the latter days of JTAG, the organisation that created the Standard, several companies began to program PCs with the boundary-scan integrity and interconnect algorithms. Indeed, the parallel printer port was even considered to be a crude form of driver/sensor channels!

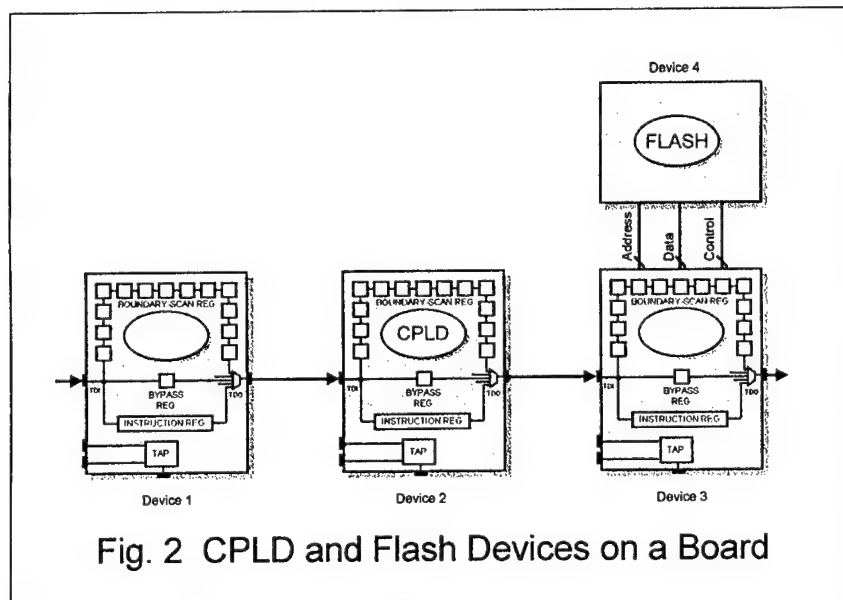
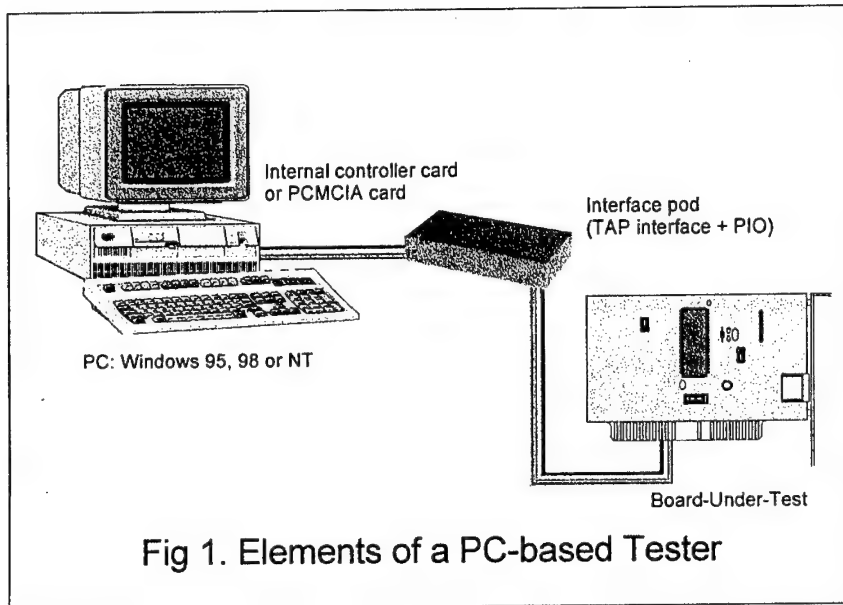
Nowadays, there is a variety of low-cost portable boundary-scan testers available, based on the PC as a hardware platform and equipped with a wide range of test capability. From a hardware perspective, the equipment usually consists of a PC, either a PC-Card or expansion-slot driver/sensor channel card, and a buffer interface to the board-under-test - Fig. 1. On the software side, these testers come equipped to handle both boundary scan and non-boundary-scan components on the board, where such components can be accessed via boundary-scan components.

3. In-System Programming via 1149.1 Boundary Scan

In-System Programming (ISP) of CPLDs, FPGAs and Flash memory devices through board-level 1149.1 boundary-scan interfaces has become an important new application of boundary scan [8, 9, 10]. This section reviews ISP basics and describes benefits and issues.

ISP is the loading of device-configuration data into a programmable device after the device has been assembled onto a board. ISP is also known as on-Board Programming or In-System Configuration (for FPGAs). The programming interface to the device is through the 1149.1 board-level boundary-scan structures. Fig. 2 shows an 1149.1-compliant CPLD (device 2) connected to other boundary-scan devices, along with a Flash memory device (device 4) accessible from a boundary-scan device (device 3).

The advantages of ISP, compared to off-line programming stations, are many:



- simplifies inventory management,
- reduces or removes the need for off-line programming stations,
- enables rapid prototype configuration and re-configuration, thereby increasing design flexibility,
- removes the need for on-board sockets which are often a cause of pin damage,
- reduces risk of damage caused by mechanical handling and Electro-Static Discharge, and
- allows program upgrades for System and Field-Service debug.

Fig. 3 shows the programming data flow for CPLDs. Essentially, ISP formatting data is passed from the PLD device-vendor's tools into a PC-based board-test-programming station where it is embedded in the 1149.1 access protocol for the board. The programmable device is targeted through the board boundary-scan path. Boundary-scan devices either side of the PLD are placed in *Bypass* mode i.e. devices 1 and 3 in Fig. 2. The programmable device is loaded with whatever instruction is necessary to commence the programming process. This instruction will first target the programming location and then enable programming data to be serially loaded into the addressed location.

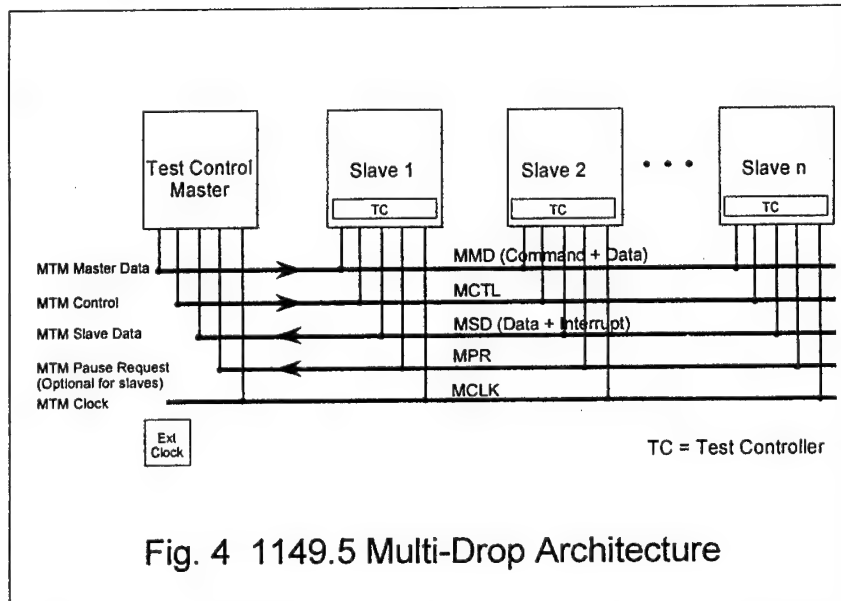
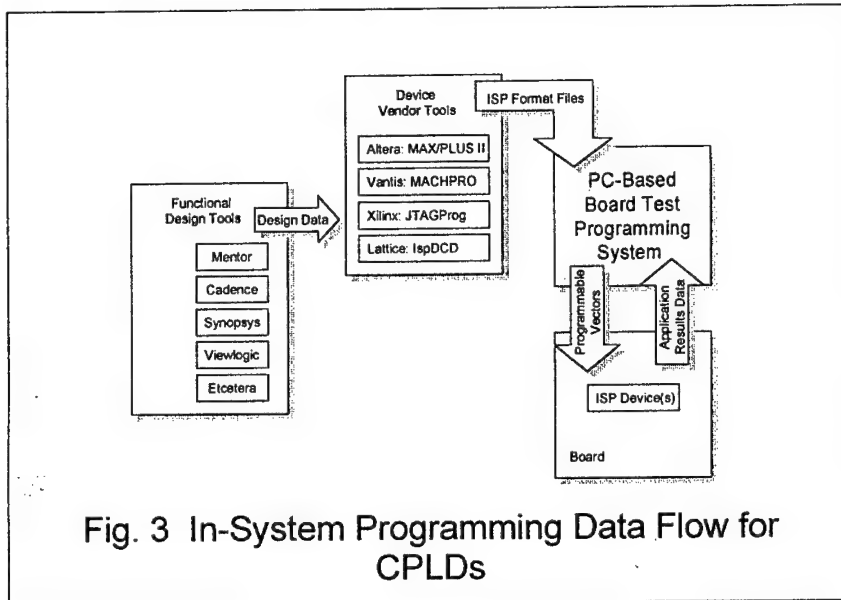
In the case of Flash memory devices, the initialise, erase, write and verify patterns are applied from the boundary-scan device, or devices, that has access to the Address, Data and Control pins of the Flash i.e. in Fig. 2, the boundary-scan register of device 3 is used to program the Flash device, device 4. In this case, devices 1 and 2 are placed in *Bypass* mode and device 3 is loaded with the *Extest* instruction.

4. Applications of boundary scan through the life cycle of a product

As acceptance of boundary scan techniques grew, designers began to question the re-use of DFT structures "above the board" i.e. during system integration and especially during field service [11, 12]. In the case where the product has multiple boards, system designers and field service engineers required a multi-drop architecture to allow drop-down access to individual boards, and hence individual devices, through a backplane bus - see Fig. 4. Eventually, the IEEE 1149.5 Module Test and Maintenance Bus was approved in 1996 [13], but Texas Instruments and National Semiconductors (now Fairchild) had already produced devices [14, 15] that allowed 1149.1 to be extended into the backplane domain. Although not as powerful as 1149.5, the use of 1149.1 as a backplane bus opened up the possibility of DFT structure re-use and allowed a life-cycle view of DFT.

Fig. 5 summarises this view. There are now four major DFT technologies: internal scan, BIST, I_{DDQ} and boundary scan. Each technique provides a point solution to a point problem. For example, internal scan solves several problems to do with the test and testability of devices e.g. it enables high levels of defect coverage of semiconductor manufacturing defects, plus the internal scan paths allow partitioning to support the difficult process of diagnostics.

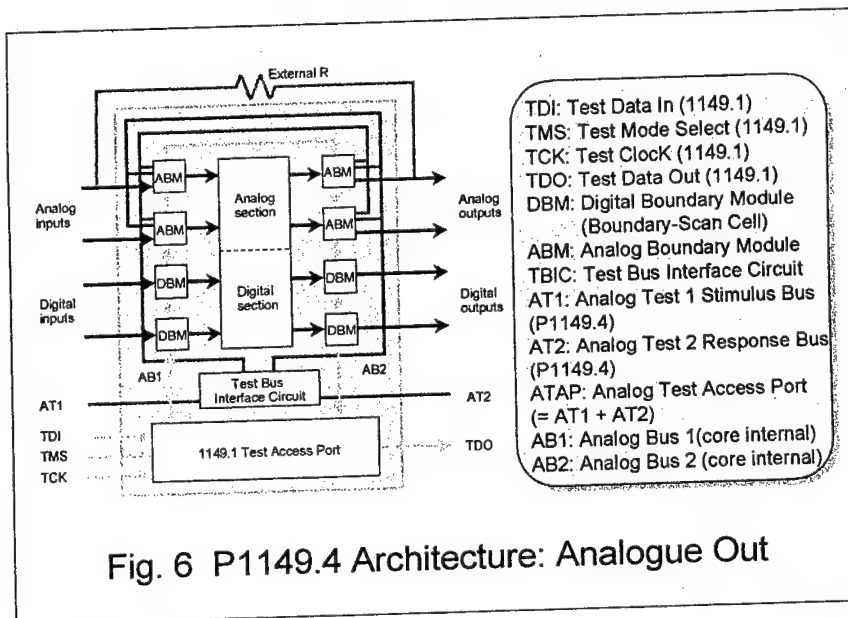
Similarly, BIST also solves many problems of testing devices: memory BIST algorithms can be targeted directly at known defect types allowing not only high defect coverage but also an at-



	Chip	Board	System	Field
Internal Scan	<ul style="list-style-type: none"> • Man^{ld} Defects • Diagnostics 	<ul style="list-style-type: none"> • Existence Test (Scan thru TAP) • Design & Manufacture Debug 	• Diagnostics	• Diagnostics (Direct or remote)
BIST	<ul style="list-style-type: none"> • Man^{ld} Defects • Diagnostics • Run Time • Access • Burn in 	<ul style="list-style-type: none"> • Existence test (RunBIST) • Design & Manufacture Debug 	• Diagnostics	• Diagnostics
Boundary Scan	• Pin Access	<ul style="list-style-type: none"> • Man^{ld} Defects • Design Debug 	• Diagnostics	• Diagnostics
I _{DDQ}	<ul style="list-style-type: none"> • Man^{ld} Defects • Diagnostics 	• Design & Manufacture debug (via BICMon)	• Diagnostics	• Diagnostics

Plus: Mixed-Signal BIST, P1149.4, 1149.5,

Fig. 5 Leveraging the DFT Investment



speed test to detect defects that affect the high-frequency performance. BIST also reduces problems of core access through the pins of a System-On-Chip device and provides protection of Intellectual Property for hard-core cores.

I_{DDQ} targets device defects which may not be detected through voltage measurement and recent work [16] has shown that I_{DDQ} signatures can be used to help locate defects.

Boundary scan is different to the other three DFT techniques. Boundary scan targets a board test problem but the structure has to be inserted into a device by a device designer. In other words, the person who sees the "pain" is different to the person who sees the "gain". But, boundary scan opens up re-use of the other techniques through instructions such as *InScan*, *RunBist* and providing access to the Pass/Fail result of internal Built-In Current monitors. This means that device DFT structures now have additional value at board level. They can be re-used to assist board diagnostics.

The further development of multi-drop architectures opens up yet more re-use, into systems integration and finally through to field service. The true value here is diagnostics. Once boards are assembled into racks and especially when the product is in use by a customer, determining the exact cause of a fault can become extremely difficult and eventually, very costly. So, the one word that dominates the right-hand-side of Fig. 5 is "diagnostics".

The more-recent development of ISP has reinforced the role boundary scan plays in life-cycle test. We can consider re-programming programmable devices during system integration and during field service either to fix a system design problem or to gracefully-degrade the behaviour of the product rather than take it off-line in the event of the occurrence of an environmental or wearout defect.

Finally, the new IEEE P1149.4 Mixed-Signal Test Bus Standard is nearly complete [17, 18]. When it arrives, it will specify additional boundary-scan cells on the analogue ports of mixed-signal devices. These cells will behave digitally in *ExTest* mode, thereby extending the application of boundary scan to the detection and location of interconnect defects. Additionally, P1149.4 will also allow the application of analogue stimulus and measurement of corresponding analogue response through an additional two test pins (AT1, AT2) and internal analogue test busses (AB1, AB2) - see Fig. 6. The publication of this new standard will provoke yet more interest in boundary scan as the "internet of test".

6. Conclusions

Boundary scan is here to stay. It has opened up the possibility of a life-cycle view of test through the ability to repeatedly re-use DFT structures. This paper has summarised these possibilities. For more in-depth discussion, see the forthcoming paper [19]

7. References

- [1] ANSI/IEEE Std 1149.1b-1994, "Standard test access port and boundary scan architecture." *IEEE Standards Board*, New York
- [2] IEEE Design & Test of Computers, Special Microprocessor Testing issue, July/Sept, 1998
- [3] C. Champlin, "Iridium satellite: a large system application of design for testability", *Proc. IEEE International Test Conference*, 1993, pp. 392 - 398
- [4] M. Boutin and P. Dziel, "Application of boundary scan in a fault-tolerant computer system", *Proc. IEEE International Test Conference*, 1996, pp. 809 - 817
- [5] K Sasidhar et al., "Testing NASA's 3D-stack MCM space flight computer", *IEEE Design & Test of Computers*, July-September, 1998, pp. 44 - 55
- [6] Y. Zorian and E-J Marinissen, "Testing embedded-core based system chips", *Proc. IEEE International Test Conference*, pp. 130-143. <http://grouper.ieee.org/groups/1500>
- [7] First attributed to Johan Renberg, ISS AB, Sweden
- [8] D. Bonnett, "Design for in-system programming", *Proc. IEEE International Test Conference*, 1999
- [9] K Wible (Hewlett Packard), "Careful PCB layout enhances on-board programming", *Test & Measurement World*, Jan., 1999, pp. 49-54
- [10] K Wible (Hewlett Packard), "Design a production and test strategy for PLD-based PCBs", *Test & Measurement World*, March, 1999, pp. 37-44
- [11] L. Whetsel, "A proposed method for accessing 1149.1 in a backplane environment," *Proc IEEE International Test Conference*, 1992, pp. 206-216
- [12] D. Bhavsar, "An architecture for extending the IEEE Standard 1149.1 Test Access Port to system backplanes," *Proc IEEE International Test Conference*, 1991, pp. 768-776
- [13] IEEE Standard 1149.5-1995, "Standard for module test and maintenance bus (MTM Bus) protocol." *IEEE Standards Board*
- [14] Texas Instruments, 10-bit Addressable Scan Port ('ABT8996) data sheet, SCBS489, <http://www.ti.com/sc/jtag>
- [15] Fairchild Semiconductor, SCAN Bridge Hierarchical and Multidrop Addressable JTAG Port (SCANPSC110) data sheet, DS011570, http://www.fairchildsemi.com/catalog/Digital_Boundary.html
- [16] A Gattiker & W Maly, "Toward understanding IDDQ-only fails", *Proc. IEEE International Test Conference*, 1998, pp. 174 - 181 (see also pp. 1168 - 1177)
- [17] IEEE P1149.4 Mixed-Signal Test Bus. <http://grouper.ieee.org/groups/1149/4>
- [18] M. Modi, "Mixed-signal test bus, embedded core test efforts advance", *IEEE Design & Test of Computers*, April-June, 1999, pp. 5 - 6, 93
- [19] M Wondolowski, B Bennetts, A Ley, "Boundary Scan: The Internet of Test", to appear in the July/September issue of *IEEE Design & Test of Computers*, 1999

Appendix: ISP programming issues and programming languages

There are several considerations regarding in-system programming:

- Given that on-board CPLDs are not configured prior to power-up, designers need to make sure that the board powers-up in a safe state. Boundary scan can help by allowing access to CPLD pin-locking pins (which determine the status of CPLD IO pins), output-enable control pins (to prevent bus contention) and master resets/clears.
- Some Flash devices require higher-than-usual power supplies to erase and re-load memory contents. Check that the power supply is adequate and that it is stable (use de-coupling capacitors alongside the devices to smooth out glitches).
- When a board is powered off, data in an FPGA's SRAM is lost. This data must be re-loaded when the board is re-powered. PC-based testers can be used to provide the re-configuration data.
- During PLD programming, care must be taken to ensure that on-board devices driven by programmable devices are not affected by random values present on the programmable device's outputs as programming proceeds. Some PLDs are designed such that their outputs are in a high-impedance state until programming is complete. If this is not the case, the boundary-scan instruction *HighZ* provides a way to hold PLD outputs to the high-impedance state during programming. PC-based boundary-scan management tools allow pre-programming macros to be executed to reduce the so-called "nearest neighbour disturb" problems.
- Some 1149.1 PLDs are not fully compliant with the 1149.1 Standard e.g. no boundary-scan register (*Extest* defaults to *Bypass*), or no path through from TDI to TDO (especially in some FPGAs where TDI is simply used to access the configuration registers). Non-compliance stretches the programming capability of PC-based testers and the simple solution is to make sure all PLDs are fully compliant with the 1149.1 Standard.
- Given that PLDs are programmed serially through a chain of boundary-scan devices, programming time might be an issue compared to, say, the time it would take to program in parallel through the nails of an in-circuit board tester. This increase in time is offset by two factors in favour of the PC-based board test programming system: the portability and lower cost of the PC-based system. Portability especially means that PLDs can be re-programmed even when the system is in operational use i.e. field upgrades.

There are two popular programming formats: Serial Vector Format (SVF) and JAM. SVF was originally developed as a format for specifying board tests to be applied through an 1149.1 infrastructure and is used by companies such as ASSET InterTech Inc., Texas Instruments and Teradyne Inc. It has also been widely used by PLD vendors such as Altera, Lattice Devices, Cypress, Xilinx and Vantis.

JAM was introduced by Altera and is more of a programming language than SVF. It is not widely supported by other PLD vendors, except Cypress, but it is now going through a JEDEC standardisation process (JEDEC Committee JC-42.1).

Implementation of On-Chip Supply Current Monitoring Unit in an Experimental CMOS Digital Circuit

V. Stopjaková*, B. Straka**, H. Manhaeve*** and B. Weber*

* *Department of Microelectronics, Slovak University of Technology,
Ilkovičova 3, 812 19 Bratislava, Slovakia, email:stopjak@elf.stuba.sk*

** *CEDO, s.r.o., Videňská 127, 619 00 Brno, Czech Republic*

*** *Department of Microelectronics, KHBO, Zeedijk 101, Oostende, Belgium*

Abstract

Two on-chip supply current monitors for I_{DDQ}/I_{DDT} testing of low-voltage CMOS circuits are considered. The proposed monitors were fabricated and their significant features are presented. Furthermore, an experiment on the built-in supply current monitoring unit, integrated into a digital design was carried out in order to evaluate the feasibility and the applicability of supply current testing as a complementary approach to conventional test methods. Thus, both the developed current monitors were implemented together with an experimental digital circuit on a single chip and prototyped in Alcatel-Mietec 0.7 μ m 3.3V CMOS technology. The experimental chip evaluation results are presented as well.

1 Introduction

It has been shown that some CMOS physical defects, due to process imperfections, usually escape logic testing because they do not affect the logic behaviour of a circuit. However, these 'hard-detectable' defects often significantly reduce the reliability of the circuit. Therefore, parametric test methods are used to augment logic test and to enhance the defect coverage. No doubt that testing is best performed using a set of test techniques, with each method dedicated to detect a class of defects. One of the parametric test techniques, widely used to detect mostly short defects (GOS), is quiescent power supply current monitoring (I_{DDQ} testing) [1]-[3]. Nevertheless, the efficiency of I_{DDQ} in detecting open class defects presents some limitations due to the fact that these failures may prevent changes of the quiescent power supply current. In these areas, the transient power supply current testing (I_{DDT} testing) [4]-[5] can be conveniently used. It was considered, that a combination of both the current test methods mentioned above might results in a unified and promising current-based parametric test approach, offering high defect coverage in CMOS circuits. However, the on-chip implementation of this approach is not easy task and a dedicated measurement hardware is needed to perform both I_{DDQ} and I_{DDT} current monitoring.

In this paper, the design and features of new on-chip current monitors for both quiescent as well as transient power supply current monitoring of CMOS circuits are presented. Furthermore, implementation of the built-in supply current monitoring unit, consisting of both the monitors, into an experimental CMOS digital circuit is considered. Such a current monitoring unit was placed in the VDD power supply line of the circuit under test (CUT). The experimental chip was fabricated through Alcatel-Mietec 0.7 μ m 3.3V CMOS technology.

2 Built-In Current Monitors

Quiescent BIC monitor

Firstly, a new quiescent current monitor based on a second-generation current conveyor CCII+ principle [6] was designed, fabricated and evaluated. Its general scheme is shown in Fig. 1. The CCII+ plays a main role in the monitor performance as it provides two important functions: it conveys the I_{DD} current to the output of the CCII+; and it holds approximately the same voltage on both its input terminals. Thus, the deviation of the *Virtual VDD* from the VDD power supply is very small. Due to the fact that the CUT obviously draws high transient

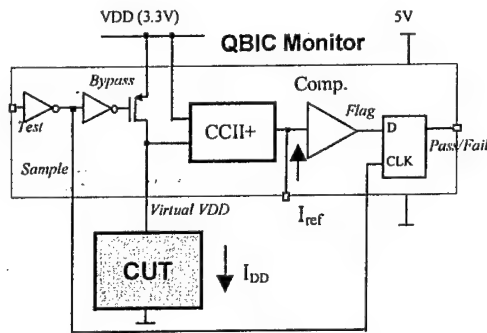


Figure 1 General scheme of QBIC monitor

After fabrication, the measurement of the prototype chips was performed and the obtained evaluation results overcame expectations in all essential parameters. The monitor offers sensitive current measurement in a range of I_{DDQ} currents from 50nA to 600 μ A. The best resolution of the monitor is 1nA at testing speed of 5kHz that is sufficient value to detect any CMOS defect that may occur. The maximum testing speed of 2MHz can be achieved if the loading capacitance is low. In the whole operation range, the BIC monitor keeps the supply voltage degradation below 50mV that should not affect the performance of the CUT.

Transient BIC monitor

Then, a novel transient current monitor that takes advantage of the metal layer's parasitic resistance was developed. It is known that the metal interconnections between the core of a design and its I/O pads always induce a small parasitic resistance. This small resistance (assumed around 1 Ω) can be used to sense the very high transient supply currents, typically drawn by the CUT during its switching actions. The transistor level scheme of the circuit providing this idea is depicted in Fig.2. The dynamic supply current I_{DD} flowing through the CUT always provides a small voltage drop across the parasitic resistance R_{MET} . This voltage difference makes the current mirror (MP1, MP2) unbalanced that implies a current I_{MIR} at its output. The whole transient monitor, using the current mirror principle, consists of two main parts: an unbalanced current mirror that mirrors the transient supply current, and circuitry providing the quantification of the charge involved in the supply current. This circuitry consists of a diode D, a switch M_S , a capacitor C_{charge} , and a differential amplifier A. The general scheme of the whole transient current monitor is shown in Fig. 3. The high transient peaks of the mirrored supply current I_{MIR} pass through the diode D and charge the capacitor C_{charge} .

Initially, in monitoring mode, the transistor M_s is switched off so that the capacitor C_{charge} is fully charged by the transient supply current and the resulting voltage is compared to the voltage reference V_{ref} by the amplifier. Then the switch is closed to discharge the capacitor C_{charge} and to ensure that before each transition the amplifier input is set to zero. The offset in the output current I_{MIR} requires the capacitor C_{charge} and the switch M_s to be connected to a voltage V_{offset} not to provide current flowing through the diode in the quiescent state of the CUT.

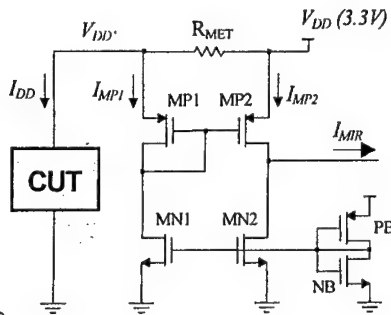


Figure 2 Current mirror principle of I_{DD} monitoring

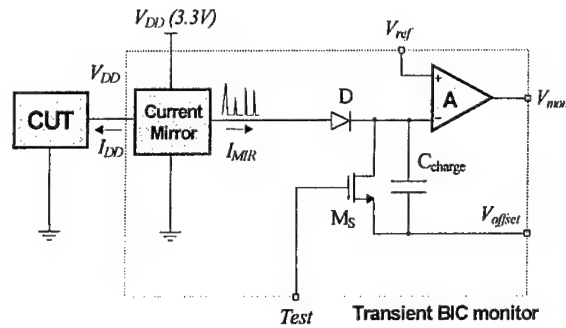


Figure 3 General scheme of TBIC monitor

The proposed transient monitor was also fabricated and evaluated. Due to the very small resistance of metal layer, the monitor is able to measure very high transient currents without affecting the CUT's performance. For the assumed R_{MET} value of 1Ω , the CUT supply voltage is lowered to 3.2V maximally for I_{DDT} currents up to 100mA. Linearity of current-to-voltage conversion of the monitor in a range of I_{DDT} currents from 1mA to 100mA, for $f=1\text{MHz}$ and the C_{charge} value of 0.5pF is shown in Fig. 4. Sensitivity of the monitor in frequency domain for different values of the I_{DDT} peak width is depicted in Fig. 5, where the minimum measurable values of transient current spikes versus testing rate for different transient current peak duration are illustrated.

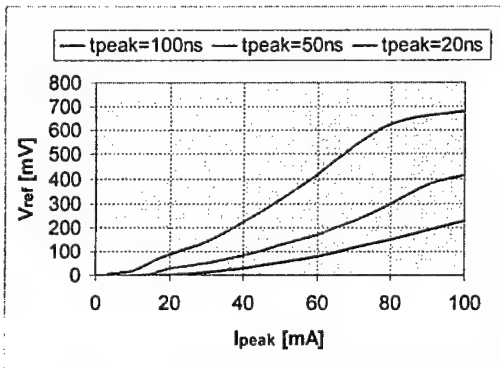


Figure 4 Linearity of current measurement

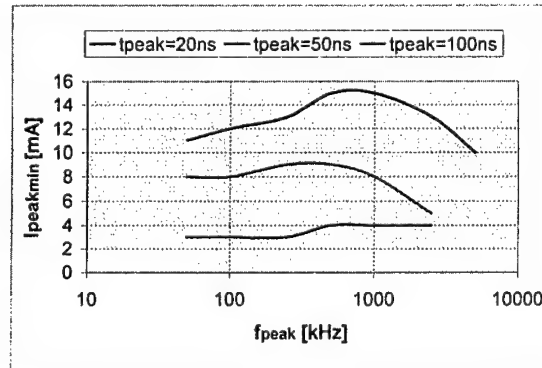


Figure 5 TBIC sensitivity versus testing speed

3 Implementation of the BIC Monitoring Unit (BIC-MU)

Finally, in order to verify feasibility and performance of I_{DDX} current monitoring in the real circuit testing, both the current monitors were integrated into a unified built-in supply current monitoring unit (BIC-MU) that was consequently implemented together with an experimental low-voltage digital circuit on a single chip and processed in Alcatel-Mietec 0.7 μ m CMOS technology. A digital two parallel 8-bit inputs multiplier was used as the digital CUT. The chip area of the digital circuit itself is 850 μ m \times 850 μ m. The BIC testing system is inserted in the VDD supply line and the parasitic resistance of the power supply routing is used to sense the transient supply current. The size of the whole I_{DDX} monitoring unit is 0.24mm² that takes around 24% of the total chip area.

Feasibility of the proposed I_{DDX} current monitoring unit were consequently proven by evaluation results obtained by measurement of the experimental circuit. Various static and dynamic measurements were performed to investigate the performance of the prototype chips. Evaluation results confirmed that both transient as well as quiescent BIC monitor performs well in conjunction with the CUT. Quiescent supply current of the CUT at room temperature monitored by QBIC monitor was 50nA. QBIC also clearly indicates that CUT supply current goes up as clock frequency of the CUT increases, which is natural for digital circuits. It was proven that the transient supply current peaks drawn by the experimental CUT depend on amount of the logic flipped by the system clock. Although the CUT is a relatively small digital circuit that generates transient supply current peaks a few tens of nanoseconds wide and several mA high; and the detection of such small peak variations is on the margin of TBIC sensitivity, the maximal detectable peak frequency of 5MHz was achieved.

4 Conclusion

A new on-chip I_{DDX} current monitoring system offering high-speed and accurate I_{DDQ}/I_{DDT} measurement was developed and implemented in an experimental digital circuit. The current monitoring unit is able to measure a wide range of supply currents without affecting the CUT performance. Evaluated parameters of the developed current monitors indicate the very promising possibility to use on-chip current monitoring in real test applications.

Acknowledgement

This work has been supported partially by the EC in the frame of the COPERNICUS Project UBISTA (COP94 : 0391) and by the Ministry of Education of the Slovak Republic under Grants No.: 1/6096/99 and No. 1/4294/97.

References

- [1] W. Mao, R. K. Gulati, D. K. Goel and M. D. Ciletti, "QUIETEST: A Quiescent Current Testing Methodology for Detecting Leakage Faults", Proc. of Inter. on CAD, 1990, pp. 280-283.
- [2] C.F. Hawkins and J.M. Soden, "Electrical characteristics and testing consideration for gate oxide shorts in CMOS ICs", Proc. of The 1985 Test Conf, Philadelphia, PA, 1985, pp. 544-555.
- [3] W. Maly and M. Patyra, "Built-in Current Testing", IEEE Journal of Solid State Circuits, Vol. 27, No. 3, March 1992, pp. 425-428.
- [4] S-T. Su and R.Z. Makki, "Testing of SRAMs by Monitoring Dynamic Power Supply Current", JETTA, Vol. 3, 1992, pp. 265-278.
- [5] S-T. Su, R.Z. Makki and T. Nagle, "Transient Power Supply Current Monitoring - A New Test Method for CMOS VLSI Circuits", JETTA, Vol. 6, February 1995, pp. 23-43.
- [6] V. Stopjaková and H. Manhaeve, "CCII+ Current Conveyor Based BIC Monitor for I_{DDQ} Testing of Complex CMOS Circuits", ED&TC'97, Paris, France, March 17-20, 1997, pp. 266-270.

IOCIMU-2: An Integrated Off-Chip I_{DDQ} Measurement Unit

M.Sidiropulos¹, B.Straka¹, M.Svajda², H.Manhaeve³, and J.Vanneuville¹

¹ CEDO, Brno

Czech Republic

Phone: +420-5-43 125 412

Fax: +420-5-43 125 307

sidiro@cedo.cz

² Technical University of Brno

Czech Republic

Phone: +420-5-43 167 103

Fax: +420-5-43 167 298

³ KHBO, Oostende

Belgium

Phone: +32 59 508 996

Fax: +32 59 704 215

manhaeve@micro.khbo.be

Abstract

The implementation of a second-generation integrated off-chip I_{DDQ} monitor is presented in this paper. The monitor can be incorporated into standard automated test equipment. The monitor can operate at the test rates up to 30kHz and offers a high resolution of 10nA. It is capable of driving a 2 μ F capacitive load and can perform measurements of the I_{DDQ} in the 0-1mA range, which enables to test complex ASIC's. The on-chip integrated bypass switch with the R_{ON} resistance of only 0.3 Ω is capable of handling DUT transient currents up to several amps. The IOCIMU-2 monitor was fabricated in the 2- μ m Mietec BiCMOS technology and has an active chip area of 10 mm².

1 Introduction

I_{DDQ} testing becomes common during last years and is widely used as a supplement to the functional tests to enhance the test quality. It is useful for detection of physical defects, such as gate-oxide shorts and bridging defects, which result in an increase of the quiescent current consumption of the affected circuit. The effectiveness of the I_{DDQ} test depends on the availability of a suitable measurement device, the test rate, the accuracy of the measurement and the quality of the test vector set used [1].

Basically two approaches to the I_{DDQ} measurement can be distinguished: on-chip and off-chip measurement. On-chip I_{DDQ} monitors are integrated with the circuit under test on the same silicon. On-chip monitors generally exhibit very high resolution and test rate [2]. On the other hand on-chip monitors occupy a valuable area on the

chip and require extra IO pins. On-chip monitors are often a part of built-in self-test applications [11].

In general, the use of off-chip I_{DDQ} monitors (OCM) offers more versatility and they can be easily combined with the automatic test equipment (ATE). The development of off-chip I_{DDQ} measurement hardware has been intensively treated by research groups during the last years, and it is now becoming either commercially available as add-on units, or as an ATE option [3-9]. Table 1 shows characteristic parameters of the discussed monitors. Most of the existing monitors are designed using discrete components. An OCM realisation based upon the use of well-selected discrete elements benefits from the possibility to exploit the availability of high performance components to realise each of its building blocks. A drawback of a discrete realisation is the space taken up by the board. This may cause difficulties to place the monitor on the load board close to the DUT and not to obstruct handlers.

A monolithic OCM can be placed easily on the loadboard, close to the DUT. Such a configuration is part of the QTAG standard proposal [10]. A first attempt to design a monolithic monitor was done in Philips. However, their IDUNA-2 monitor [7] was designed to test a specific class of circuits. It has featured a good performance but only for a small C_L .

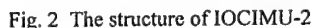
BOC	[5]	OCIMU [6]	DOCIMU [3]	[8]	IDUNA-2 [7]	IOCIMU [4]	IOCIMU-2
Technology	Discrete	discrete	discrete	CMOS 1.5 μ m	CMOS 0.8 μ m	BiCMOS 2 μ m	BiCMOS 2 μ m
Test rate	250kHz	10kHz	30kHz	20kHz	50kHz	30kHz	30kHz
I_{DDQ} range	25 μ A	1 μ A-1mA	1mA	500 μ A		1mA	1mA
Max. Resolution	100nA	800nA	50nA		10 μ A	60nA	10nA
Max. C_{DEC}	1-4nF	3 μ F	100n-2 μ F	Fixed	Fixed	20n-2 μ F	20n-2 μ F
T_s/C_{DEC}	1 μ s/1nF	100 μ s/1 μ F	100 μ s/1 μ F	50 μ s/1nF		100 μ s/1 μ F	100 μ s/1 μ F
Method	I-t	I-V	I-V	I-t	I-t	I-V	I-V
Bypass R_{ON}			0.05 Ω			0.6 Ω	0.3 Ω
Area				10mm ²	1mm ²	20mm ²	10mm ²

Table 1 Review of off-chip monitors

The architecture of the IOCIMU-2 has evolved from its discrete predecessor the OCIMU [6], and from a more recent monolithic prototype, the IOCIMU [4], fabricated and tested in 1997. The monitor is placed between the positive power supply and the DUT. The hierarchical structure and principal scheme of the IOCIMU-2 is shown in Figure 1 and 2, respectively.

[illegible]

The main part of the monitor, the current measuring unit (CMU), uses two matched-gain op-amps in a differential configuration. V_{DUT} pin provides the reference for the DUT power supply voltage, which is established and supplied at the DUT pin. The measured I_{DDQ} current is converted to a voltage and amplified. The resulting $V_{I_{DDQ}}$ voltage is compared with the reference pass/fail level, given at the $V_{P/F}$ pin, and the output pass/fail flag is generated at the P/F pin by the threshold unit (THU).



The use of S/H minimises the influence of interferences at the V_{DUT} pin, which significantly affects the measurement accuracy in other monitor designs. For the short moment of the measurement the DUT is supplied by the interference-free voltage stored in the $C_{S/H}$.



The typical measurement cycle of the I_{DDQ} monitor is shown in Figure 3. Bypass period is initialised by the MODE signal, during which the CBU is activated. The monitor comes to the measurement mode with the trailing edge of the MODE signal. The required measuring conditions can be set by the serial interface via the MODE and CLOCK pin at any time. The bypass NMOS is switched off and the OCU evaluates in less than $1\mu s$ whether I_{DDQ} exceeds the measured range $1mA$. If I_{DDQ} is higher, the monitor is returned to the bypass mode until the end of measurement cycle. Otherwise, the CMU is activated to perform the accurate I_{DDQ} measurement in the range under $1mA$. Outputs are valid at the end of this measurement cycle (60-100 μs), and the ATE can scan the Pass/Fail (P/F) output flag.

3 Implementation and Measurement Results

The IOCIMU-2 is implemented and fabricated in the 2- μm Mietec high voltage BiCMOS technology using the Europractice MPC services. The picture of the IOCIMU-2 chip die is shown in Figure 4. Better layout technique allowed to reduce the active area of the circuit to $10mm^2$, which is approximately a half of the original IOCIMU circuit.

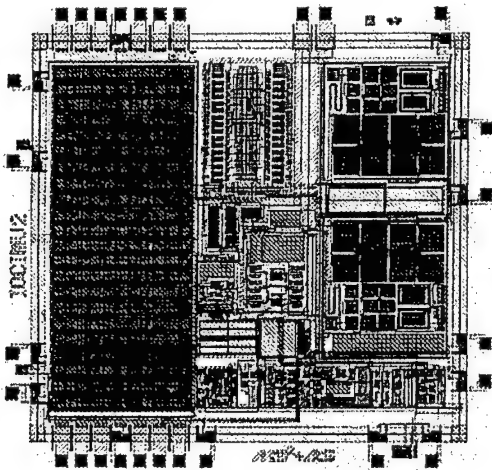


Figure 4 Picture of the IOCIMU-2.

The main problem of the integration of precision instruments in standard technologies is the high absolute tolerance of device parameters due to process variations (up to 20%). However, it gives an advantage of excellent matching properties of components placed on the same substrate. In the ideal case, the I-V conversion ratio of the monitor is $5.00mV/\mu A$. Due to the process tolerances the deviation of the on-chip sense resistors is about 5%. However, this deviation is compensated by means of a differential architecture with matched sensing resistors, which results in measurement error under 1%. If a voltage is applied as a reference, an additional error due to V-I conversion should be

considered. The comparator exhibits no significant DC errors.

The parameters and resolution of the IOCIMU-2 in function of the test rate and the loading capacitance C_L are shown in Table 2 and Figure 5, respectively.

Parameter	Min.	Typical	Max.
Die area		$10mm^2$	
Supply voltage	12V	15V	18V
DUT supply	0.5V	3-5V	7V
Power cons.		36mW	
I_{DDQ} range		1mA	1.5mA
Resolution	10nA	50nA	$3\mu A$
Test rate	2kHz	10kHz	30kHz
C_L	20nF	100nF	$2\mu F$
Bypass R_{ON}		0.3Ω	

Table 2 IOCIMU-2 parameters.

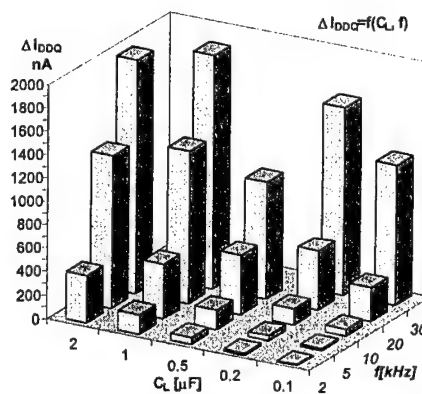


Figure 5 Measured IOCIMU-2 resolution.

4 Conclusion

IOCIMU-2 is a highly performing general purpose current monitor. It features an excellent performance for I_{DDQ} currents in the range from 0 to $1mA$, a loading capacitance between $20nF$ and $2\mu F$, and for DUT supply voltages V_{DUT} in the range of 0.5 to 7.5V. A maximum test rate of 30kHz, with a resolution $1.2\mu A$ was reached for the loading capacitance C_L of $0.1\mu F$. Maximum resolution of $10nA$ at $C_L=100nF$ and 2kHz test speed is an excellent value for the I_{DDQ} off-chip monitor. IOCIMU-2 proves a good piece of I_{DDQ} test hardware. Therefore it is expected to be used as a real industrial product, which enhances capabilities of testers with all the benefits.

Acknowledgment

The work was supported by the EC in the frame of the COPERNICUS project UBISTA (ref.: COP94-0391). We also acknowledge TU Brno microelectronics

design facilities and D. Becvar for his help with a part of the IOCIMU-2 layout.

References

- [1] W.Maly, P.Nigh, "Built-In Current Testing – Feasibility Study," IEEE ICCAD, pp. 340-343, Santa Clara, November 1988.
- [2] V.Stopjakova, H.Manhaeve, "CCII++ Current Conveyor Based BIC Monitor for I_{DDQ} Testing of Complex CMOS Circuits," European Design and Test Conference, pp. 266-270, Paris, March 1997.
- [3] B.Straka, H.Manhaeve, J.Vanneuville, M.Svajda, "A Fully Digital Off-Chip I_{DDQ} Measurement Unit," IEEE Design, Automation and Test in Europe Conference, pp. 495-500, Paris, February 1998.
- [4] M.Svajda, B.Straka, H.Manhaeve, "IOCIMU – An Integrated Off-Chip I_{DDQ} Measurement Unit," IEEE Design, Automation and Test in Europe Conference, pp. 959-960, Paris, February 1998.
- [5] K.M.Wallquist, A.V.Righter, and C.F.Hawkins, "A General Purpose I_{DDQ} Measurement Circuit," Int. Test Conference, pp. 642-651, October 1993.
- [6] H.Manhaeve, P.L.Wrighton, J.van Sas, and U.Swerts, "An Off-chip I_{DDQ} Current Measurement Unit for Telecommunication ASICs," Int. Test Conference, pp. 203-212, Washington, Oct. 1994.
- [7] K.Baker, A.Bratt, A.Richardson, and A.Welbers, "Development of A Class 1 QTAG Monitor," Int. Test Conference, pp. 213-222, Oct. 1994.
- [8] Pedros, A.Rubio, and J.Segura, "ISIS: An Integrated Standard Interfaced Sensor for I_{DDQ} Testing," Int. Test Conference, pp. 50-53, Washington, 1995.
- [9] G.H.Johnson, J.B.Wilstrup, "A General Purpose ATE Based I_{DDQ} Measurement Circuit," Int. Test Conference, pp. 97-105, 1995.
- [10] K.Baker, "Requirements Specification for the QTAG Monitor Description Format (MDF)," Philips Research, 1994.
- [11] M.Sidiropulos, V.Stopjakova, and H.Manhaeve, "Implementation of a BIC Monitor in Balanced Analog Self-Test," Electronic Letters, 1996.

Integrated Circuit Temperature Estimation Using QR-RLS Adaptive Algorithm

M. Janicki, A. Napieralski

*Division of Microelectronics and Computer Science,
Technical University of Lodz, Al. Politechniki 11, 93-590 Lodz, Poland
janicki@dmcs.p.lodz.pl*

Abstract. When monitoring circuit temperature, measurements taken from temperature sensors are usually corrupted with noise. Since inverse problems associated with temperature estimation are sensitive to errors, special techniques must be used to assure good quality of heat source temperature estimates. In this paper, the adaptive QR-RLS algorithm is employed to produce robust dissipated power density estimates. Numerical simulation results for the new approach are provided.

I. Introduction

Many modern applications require continuous on-line monitoring of circuit temperature. One of the most popular methods of such monitoring uses remote temperature sensors, e.g. p-n junctions, placed on the IC surface. The main drawback of this approach is that measurements from temperature sensors are corrupted with noise and, since the inverse heat conduction problem (IHCP) consisting in estimating source temperature is extremely sensitive to errors, it is necessary to filter noise out. More information on IHCPs can be found in [1].

The most common method used to improve the estimation quality consists in placing redundant temperature sensors, i.e. more sensors than heat sources, rendering the system overdetermined. In our simulations, we include an additional filtering stage implementing the inverse QR decomposition based recursive least squares (QR-RLS) adaptive algorithm to produce improved dissipated power density estimates. When the dissipated power is estimated, it is possible to determine temperature distribution in the whole circuit solving a direct heat conduction problem. The QR decomposition is performed using the Givens rotations.

II. QR-RLS Adaptive Algorithm

Adaptive filters are digital filters with adjustable coefficients. Their operation relies on an iterative algorithm used to modify digital filter coefficients. Filters of this kind are essential if the desired signal is corrupted with noise varying in time or occupying unknown spectral band. In stationary environments, algorithms converge to the optimal solution or, in non-stationary environment, they track the signal characteristic changes. Thus, an adaptive filter used to filter out noise from temperature sensor signal appears to be an appropriate tool for dissipated power estimation purposes.

There exists a wide variety of adaptive filter algorithms. The choice of a particular algorithm is based on its characteristics, such as misadjustment, steady-state fluctuation, numerical stability or rate of convergence. The QR-RLS algorithm employed in the conducted numerical simulations belongs to the group of square root adaptive algorithms, in which instead of processing the input data correlation matrix its square root is processed, hence their name.

As mentioned earlier, the QR-RLS algorithm is based on the QR matrix decomposition. One of many possible ways to perform the QR decomposition is to apply the Givens rotations. The Givens rotations, suggested for the first time by Jacobi, are used to rotate a vector by an arbitrary angle Θ without changing its Euclidean norm. When applied for the QR decomposition, the Givens rotations serve to annihilate selectively chosen elements in input data matrix changing only two columns or two rows of the matrix. Performing several successive Givens rotations all the required elements can be brought to 0 and the QR factorization of the input data matrix can be completed. For the full description of the decomposition technique, refer to [2].

The operation of the algorithm is summarized in equations 1-3. With each new arriving input data vector X_k successive simple Givens unitary rotations are performed on the left hand side pre-array to produce a zero block in the top right corner of the right hand side post-array matrix (see equation 1). The matrix Θ_k is the product of simple Givens rotation matrices. The main disadvantage of the simple form of QR-RLS adaptive algorithm is that the weight vector W_k is not given in an explicit way, which limits the number of possible applications, therefore the authors used the inverse QR-RLS algorithm. In this version of the algorithm, instead of operating on the input data correlation matrix Φ , the square root of its inverse $P^{1/2}$ is propagated. This solution requires in turn the pre-processing of input data vector (see [3] for details).

$$\begin{bmatrix} 1 & \lambda^{-1/2} X_k^T P_{k-1}^{1/2} \\ 0 & \lambda^{-1/2} P_{k-1}^{1/2} \end{bmatrix} \Theta_k = \begin{bmatrix} \gamma_k^{-1/2} & 0^T \\ K_k \gamma_k^{-1/2} & P_k^{1/2} \end{bmatrix} \quad (1)$$

$$K_k = (K_k \gamma_k^{-1/2}) (\gamma_k^{-1/2})^{-1} \quad (2)$$

$$W_k = W_{k-1} + K_k \xi_k^T \quad (3)$$

where:

K - filter gain

W - filter weight matrix

Φ - input signal correlation matrix

$k-1, k, k+1$ - sampling instants

γ - conversion factor

P - inverse of input signal correlation matrix

X - input data matrix

Θ -- unitary transformation

λ - memory parameter; $1 \geq \lambda > 0$

ξ - a priori estimation error

III. Simulation Results

In the computer experiments, an IC model containing 3 heat sources and 5 temperature sensors placed on its top surface was considered. The main objective of the simulations was to investigate the possibility of improving dissipated power estimates using adaptive filtering. Given the heat sources and temperature sensors configuration, all the coefficients relating sensor temperatures to the densities of power dissipated in the heat sources were computed from the analytical solution of the heat conduction equation. The detailed description of the solution method can be found in [4].

The assumed power pulses, which change independently in each of the heat sources, are considered to comprise combinations of linear and step-like functions. Based on the computed coefficients, thermal responses at the sensor positions were calculated. Then, a set of 600 test input temperature samples has been contaminated with noise of zero mean value and the standard deviation of 0.1 K. The generated data set was used to test the effectiveness of the QR-RLS adaptive algorithm. The number of filter taps was equal to the number of sensors. The algorithm memory parameter λ was experimentally set to 0.99. Due to the scarcity of space, only the results obtained for the hottest heat source are presented. The estimation quality improvement can be assessed from Fig. 1-2, which show the mean value and standard deviation of the difference between the estimate and the original uncorrupted power pulse. The dashed and dotted lines represent ordinary LMS space averaged estimate and QR-RLS adaptive filtered estimates respectively. The first ten sample values required for the algorithm to adapt have been omitted. The maximal value of the power signal for this particular heat source was 750 W/mm^2 .

As can be seen, the estimate mean values are very close to the actual signal value (3 % of the maximal signal value). The filtered estimate standard deviation value dropped to less than 20 % of the maximal signal value and was almost 40 % smaller than for the space averaged estimate. The estimate improvement attained for the other sources was even better (over 50 % reduction of standard deviation value).

IV. Conclusions

In the light of conducted computer experiments, the QR-RLS adaptive algorithm proved to be particularly useful for dissipated power estimation. The obtained estimate values were very close to the actual power signal values. Since the standard deviation of the adaptive filtered estimate was significantly smaller than the ordinary space averaged estimate, the adaptive estimates can be considered more accurate and more robust.

References

- [1] M. N. Ozisik, *Heat Conduction*, John Wiley & Sons Inc., 1993
- [2] H. Golub, C. F. van Loan, *Matrix Computations*, The John Hopkins University Press, 1996
- [3] S. Haykin, *Adaptive filter theory*, Prentice-Hall International, 1996
- [4] M. Janicki, M. Zubert, A. Napieralski, "Application of inverse heat conduction methods in temperature monitoring of integrated circuits", *Sensors & Actuators, A: Physical*, Vol. 71, pp. 51-57, Nov. 1998

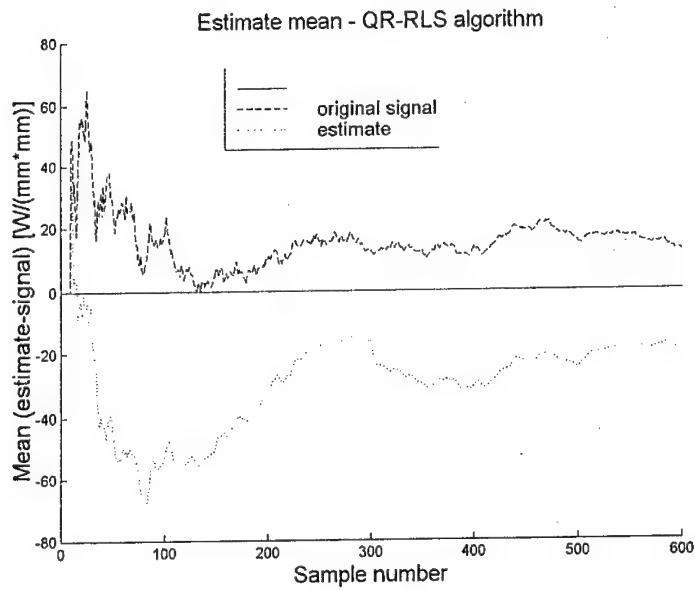


Fig. 1. Mean value of the difference between power signal and its estimate

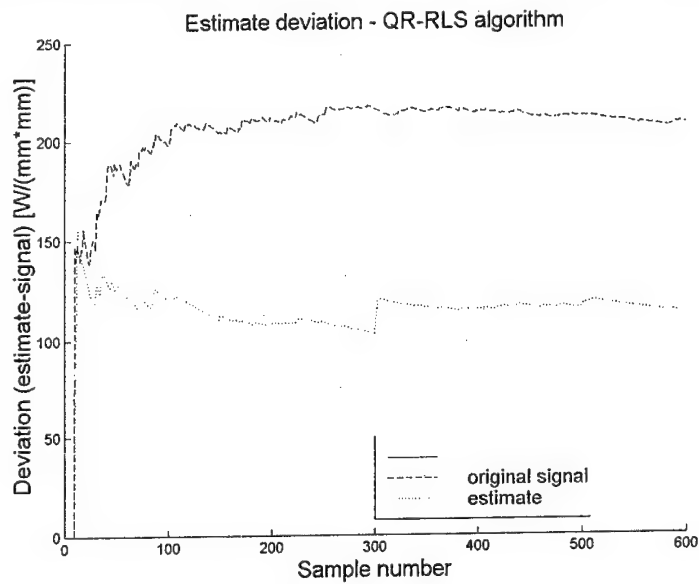


Fig. 2. Standard deviation of the difference between power signal and its estimate

Use of Absorption Resonance Frequency Meter in Measure Sensor System

M.Husák and B.Palán

*Department of Microelectronics, Czech Technical University in Prague,
Technická 2, 166 27 Prague 6, Czech republic
husak@feld.cvut.cz*

Abstract The paper describes design, construction and results obtained with a wireless information transmission measurement system. The system is intended for the measurement of small pressure variations and information transfer by a wireless process. The active part has the form of an absorption resonance frequency meter. The measurement control, approximations computation and results processing are performed on a PC. The passive one-chip resonant circuit has been realized as a monolith integrated sensor in CMOS technology.

1. Introduction

For the design of a wireless pressure measurement by a capacitive sensor it is possible to utilise, for example, the absorption principle. From the measurement principle it follows that a resonant circuit must be created whose part is the capacitive pressure sensor. The target was the design of an automatic wireless measurement system for evaluation of capacitance variations of a pressure sensor with sufficient accuracy. Due to the rather small Q-factor value it is very difficult to detect the rather flat top of the resonance response, or to discriminate between the resonance itself and the inherent oscillator amplitude. These difficulties can be suppressed by inclusion of a computer in the measurement system. It performs the seeking of an extreme by mathematical calculation (zero value of the derivative of a function). The measurement system consists of two parts - Fig.1. The first part is the passive resonant circuit whose capacitance is pressure-dependent. The second part consists of several blocks. The absorption meter proper has its output connected to the computer PC through AD and DA converters. The communication with the computer flows through an interfacing device (measurement card) to the respective converters.

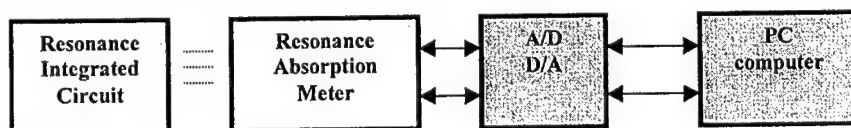


Fig. 1. Measure system

The construction and design of the absorption meter is governed by the required frequency variation of the resonant circuit, the adjustable step of frequency variation and the Q-factor of the resonant circuit. The Q-factor is rather low in single-chip integrated resonant circuits, generally of the order of units. Development of an integrated resonant circuit with a capacitive pressure sensor became the subject of our interest. Structures of capacitor pressure sensor differ in the pressure value either absolute or relative, in the shape of the diaphragm

(circular, square, donut) and in technology (monolithic, glued). From the point of view of precision and reproducibility, the exact dimensions of the diaphragm manufacturing plays the main role. Sensitivity and the pressure range are determined above all by its geometry and diaphragm properties. Several techniques can be used to realised precision diaphragms.

II. The design and realization of the wireless sensor system

A. The absorption frequency meter

In the design of the absorption meter parameters we have used the parameters of the integrated resonant circuit and the required measurement conditions as basic. These produced a requirement for a maximum capacitance variation for the maximum 5% measured phase variations of the sensor. It follows from the elementary equations of the resonant circuit that this variation corresponds to a resonant frequency variation of 2.4% maximum. With a resonant frequency 100 MHz this means a maximum full-range frequency variation 2.4 MHz. Further it follows from the required parameters that a minimum required number of steps is 100. Thus the minimum resolution of 24 kHz is given.

The data from [3] were used in the circuit design. A circuit with parameters satisfying the requirements was designed according to Fig.2. The basic circuit is a Colpitts oscillator. In the design it was necessary to adhere to the general principles of high frequency design rules. In order to minimise the sensitivity to external electromagnetic interference, the output signal was taken off from the transistor collector.

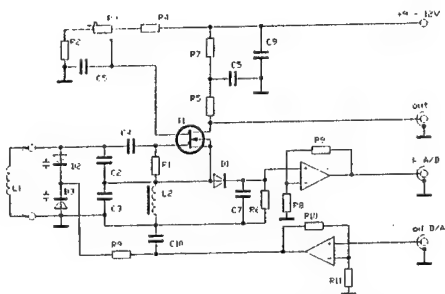


Fig. 2. The circuit connection of the absorption meter

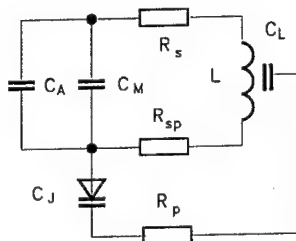


Fig. 3 The equivalent scheme of the sensor with parasitic elements

B. Integrated passive resonance circuit

The structure design was created by the intended application. The maximum dimensions of the whole integrated circuit was limited up to 3x3 mm. Maximum resonant frequency required is 100 MHz. The capacitor area of 1x1 mm was chosen. The assumed active capacitance was about 5 pF. A planar inductor, such as in [2], was chosen for the design with the wire width/gap ratio 2:1, the empirical rule can be used to calculate its inductance L. Parasitic circuit parameters of the resonance circuits play very difficult task in the design. It is necessary take that ones into the calculations. The dominant part of the parasitic capacitance is located on areas where the aluminium diaphragm is attached to the silicon dioxide layer. The parasitic resistor is located between the two capacitors. The equivalent scheme of the sensor with parasitic elements is shown in Fig.3. C_A designates the active capacitance, C_M is the parasitic inductor winding-substrate capacitance, L is inductance of the inductor and R_s its parasitic series

resistance, R_p is the parasitic resistance of the substrate between the p-n junction and the inductor, R_{sp} is the parasitic series contact resistance. MOS technology steps were available, for the development of the sensor structure. The standard technological process was modified on the samples realised. The polysilicon layer was omitted, the diaphragm was made of aluminium. Various modifications of the sensor structure were realised on the wafer. The first structure was divided into units of 1 mm length lumped into small capacitors in parallel of 90x90, 130x130 and 160x160 μm geometry. The second were a finger structures, the third were spiral structures and the last was a inverted structure. Inductors were modified with 5, 7, 9 windings in aluminium layer of 1.2 μm thickness and 3.6 μm in case of the planar inductor.

C. The PC interface

The suggested interface provides a communication through a converter and I/O circuits of the computer. It takes care of the A/D conversion for the evaluation of the oscillator amplitude variation, the D/A conversion for the oscillator tuning control signal, sufficient A/D and D/A speed with a minimum sampling frequency 80 kHz, sufficient A/D converter levels resolution (minimum 100). These requirements can be fulfilled by the PCA-1208 multifunction measurement card. The card makes possible a simple parameter configuration. When installing

it into the PC the only hardware setting necessary is to set up the base card address, to choose the voltage range of the D/A converter (unipolar or bipolar logic), determine the digital ports transfer direction or the mode of its software control. All other functions are software-controlled. Its physical dimensions permit its installation even in a notebook PC.

III. The results achieved

A. Absorption meter and measuring system

Frequency stability of the absorption meter oscillator was in the range from 10^{-5} to 10^{-4} in dependence on the coil used. Measurement of the transfer characteristic of the absorption meter is important for nonlinearity determination. The transfer characteristics for different coils are presented in Fig.4.

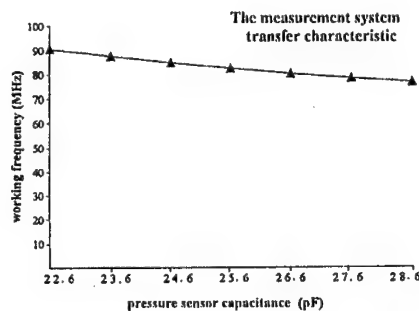
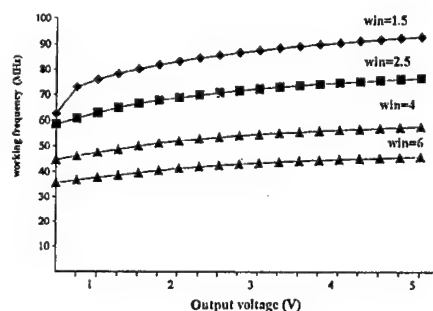


Fig.4 The transfer characteristics for different coils Fig. 5. The transfer characteristic of the complete system

The transfer characteristic of the complete system is presented in Fig.5. For good accuracy and reproducibility of the measurement the correct position of the measuring and measured coil must be set, as well as a proper coupling between the coils.

B. One-chip integrated resonant circuits

Properties of the samples realised were measured directly on the chip, some measurements were performed on encapsulated structures. For chip measurements needle probes, a microscope and a RLC-meter HP 4217B were used. The inductance of needle probes and external wires of the measurement instruments was about 370 nH. Elimination of the additional parasitic back electrode-substrate and inductor wire-substrate capacitance was necessary for measurement of the active capacitance C_A . The dependence of the capacitance on illumination has to be also taken into consideration. Measurement of the capacitance was performed after cutting off mechanically the connection lines to the inductor.

An impedance meter HP 4194A was used to measure the frequency response of the resonant LC circuits. These measurements were performed up to 40 MHz on samples encapsulated in DIL 16 package. Parameters of a simple equivalent circuit consisting of a series combination of inductance L , capacitance C and lossy resistor R_s were calculated. Example of the measured resonant curve with its parameters is shown in Fig.6. Some photographs of the realised structures are in Fig.7.

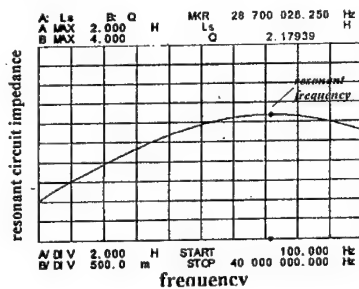


Fig. 6. The example of measured resonant curve of normal structure 9 win/130 μm

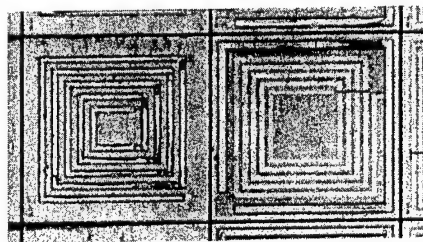


Fig. 7. Some photographs of the realised structures

IV. Conclusion

The absorption meter and structures of integrated resonant circuit with a capacitive pressure sensor were designed and realised. The structures were made in various modifications of the shape, i.e. inductor outside the capacitor, inductor inside the capacitor, spiral structures, finger structures. Parasitics were considered during the measurement. Resonant frequencies were measured. The resonant curves show very low Q (units). The absorption meter is connected to the PC through interface. The interface operation is controlled by PCA-1208 circuit.

The system makes possible contactless measurement of the capacity variation {through the resonant frequency variations}. The peak of the resonant curve is calculated from the measured values using PC. The transfer characteristics of the complete system were measured. Frequency stability of the absorption meter oscillator is 10^{-5} to 10^{-4} at operational frequency 100 MHz in dependence of the coils used. PC is used for the data storing and processing

References

- [1] Ko, W.H.- Bao, M.H.-Hong, Y.D., A High-Sensitivity Integrated Circuit Capacitive Pressure Transducer. IEEE Trans. on Electron Devices, 1982, ED-29, 1, pp.48-55.
- [2] Klabal, J., We construct a simple receivers VHF. Svazarm, Prague 1988.
- [3] Dip-Gate Meter. Amatérské rádio A4/1994, p..24.

Properties Coverification for HW/SW Systems

Mostafa Azizi¹, El Mostapha Aboulhamid¹ and Sofiène Tahar²

¹ *Département d'Informatique et de Recherche Opérationnelle, Université de Montréal*

² *Department of Computer and Electrical Engineering, Concordia University*
{azizi, aboulham}@iro.umontreal.ca, tahar@ece.concordia.ca
Montreal, Canada

Abstract. The coverification of a given HW/SW system consists of checking whether the implementation of the software and hardware parts and their integration fulfill or not some or all the specification requirements of this system. In the case of a distributed model, the SW and HW system blocks are described respectively by HLL (High Level Language) and HDL (Hardware Description Language) codes. When dealing with a unified model, both SW and HW components are implemented in the same language such as Java. In this paper, we propose a tool that allows designers to specify the properties of their systems in CPL (Coverification Properties description Language), and performs the coverification by simulation. The engine of this tool is implemented using the Java programming language and is mainly based on the management of threads.

I. Introduction

To avoid an eventual lengthy iterative codesign process of a given HW/SW system (that is often a result of an unsuccessful integration of hardware and software parts), performing an early coverification of the HW/SW integration before prototyping is strongly required. Coverification techniques currently used in the microelectronics industry are based on cosimulation environments, where SW and HW elements are respectively described in HLL (High Level Language) and HDL (Hardware Description Language), and simulated with specific simulators. The properties of a HW/SW system are included in its implementation codes, and are not separately expressed. The management of these properties (such as properties review, editing, description, checking, etc.) is hence time-consuming and inefficient.

We present in this paper a tool for the coverification of HW/SW systems. This tool is thread-oriented and currently assumes a unified description model of HW/SW systems. The software part of the HW/SW system and its interaction with the hardware part are described as a set of communicating threads. The system properties first are described in a CPL code (Coverification Properties description language), and then converted to Java threads in the objective of performing the coverification process.

The rest of this paper is organized as follows: Section II briefly reviews previous work related to coverification. Section III presents our proposed thread-oriented tool of coverification. Section IV illustrates the description of HW/SW system properties using CPL and their coverification. Finally, Section V concludes the paper.

II. Related work

The coverification process is tightly coupled with the cosimulation. Known coverification tools such as CVE-Seamless [1], Eaglei [2] and Ptolemy [3] are mainly based on cosimulation techniques.

The cosimulation approach simulates software and hardware parts and their interactions, known as virtual integration in the sense that this latter is made long before the prototyping process. In the case of a unified model [4, 5], only one simulator is used to perform cosimulation but when dealing with a distributed model [6, 7, 8, 9, 10], two or several simulators are required depending on how many languages are used to describe the software and hardware parts of the HW/SW systems. Other related work presents application cases such as the coverification of DPLL (Digital Phase Locked Loop) at NORTEL [11], and the HW/SW coverification performance estimation of a 24 embedded RISC core design at SIEMENS [12]. On the other hand, there are few papers in the literature that deal with the coverification using formal verification methods such as model checking [13, 14].

III. Multithreading-based coverification

When the design of a given HW/SW system is approximately achieved, designers integrate them to obtain the implementation of the whole system. The software part contains the original SW-code of the system and some data. The original SW-code encompasses memory addressing, hardware interfacing, and eventual functions decided after partitioning to be implemented by software. The hardware part is a set of circuit modules, registers, memories, IP blocks (blocks with Intellectual Properties), etc. The interface between hardware and software parts is built around a processor that runs software codes and manages the hardware signals. The problem of coverification is to verify if this global implementation satisfies the specification requirements of the system? This leads to check concurrently if software and hardware implementations satisfy their corresponding software and hardware specifications, and if the HW/SW integration respects the requirements of the global specification. Due to their complexity and heterogeneity, real HW/SW systems challenge current methods of verification and simulation.

The basic idea of our coverification technique consists of mixing the cosimulation process with a set of properties to be checked in concurrence [5]. This technique is summarized into four steps. The first one consists of organizing the software part, as a set of threads. The second step stores in observable registers the hardware signals, which are parameters of the HW/SW properties. The third step puts the system properties in threads and manages them. The fourth one finally starts cosimulating the system augmented by its properties. The execution flow of these steps is depicted on Figure 1. Details of the implementation and the description of the system properties are given in the following sections.

IV. Description and coverification of HW/SW properties

A. Specification of properties in CPL

The specification requirements of a HW/SW system are expressed as a set of properties described in CPL. CPL is a simple language that we have developed specially for the description of HW/SW properties. These latter will be validated by the coverification process. The parameters of coproperties (HW/SW properties) might belong to the HW part, to the SW part, or to both of them. In CPL, we specify which properties are concurrent and which can be executed together sequentially. For instance, in the example of Figure 2, $p1$ and $p2$ are concurrent between each other but $p2$ and $p3$ are not. $p2$ and $p3$ are independent in terms of concurrence and they are treated as a single property. The rest of the properties are considered by default as sequential and they are managed as a composed property. We note that CPL is strongly suitable for the description of properties at the behavioral level, and it could be used at the RTL-level as well.

Figure 1:
Execution flow of the steps
of our coverification
approach

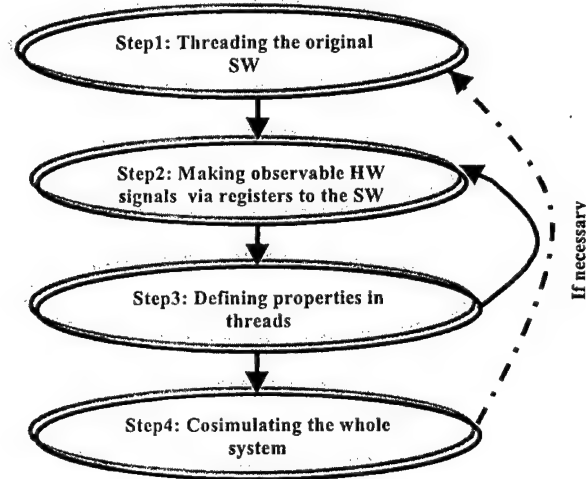


Figure 2:
Example of properties
described in CPL

```

p1 property ( flow_input - flow_output * sqrt(2) <= 0.5 ) end
p2 property if ( temperature == 199 ) ( current <= 0.2 ) end
p3 property if ( signal_1 == 199 ) not( signal_2 == 134 ) end
p4 property switch ( state )
{
case S1 : not(signal_ack & signal_start);
case S2 : (red_light & ~(green_light & orange_light));
default : (reg_R = 1);
}
end

concurrent ( p1, p2);

sequential (p2, p3);
  
```

B. Coverification of properties

The CPL code describing the properties is translated to a subset of Java code strongly thread-oriented. The properties declared as concurrent in the CPL code are manipulated each one as a thread; those identified as sequential are translated and treated as one thread. The rest of the properties that are neither parameters of “concurrent (...)” instruction nor of “sequential (...)” instruction are put in one thread and validated as a composed property. The threads obtained after translation are added to the system implementation in order to perform functional simulation of the whole code. For the

implementation of the HW/SW system, we use a Java unified model in which the HW part is seen as a set of registers with read/write accesses. The draft tool of this coverification process is depicted on Figure 3.

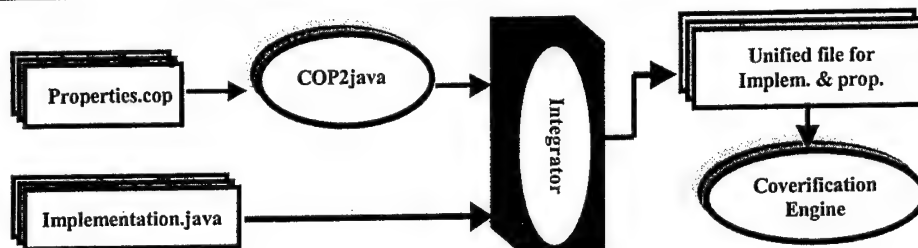


Figure 3: Global view of the semi-automatic coverification tool

V. Conclusions

In this paper, we have presented a tool for the coverification of HW/SW systems. This tool is based on the multithreading concept and cosimulation technology. The properties of a given HW/SW system are described in CPL, a simple language developed specially for the description of coverification properties. The whole implementation of the HW/SW system and its properties appears as a set of communicating threads. As perspective, we plan to complete this tool and make it fully automatic in the sense of managing properties and generating efficient test vectors for each property.

References

- [1] Mentor Graphics Corporation, "CVE-Seamless", <http://www.meng.com/>, 1998
- [2] View Logic, "EagleI", <http://www.Viewlogic.com/>, 1998
- [3] University of California at Berkeley, "Ptolemy project", <http://ptolcm.cecs.berkeley.edu/index.htm>, 1999
- [4] R. K. Gupta, C.N. Coelho Jr. and G. De Mecheli, "Synthesis and simulation of digital systems containing interacting hardware and software components", 29th Design Automation Conference (DAC'92), June 1992
- [5] M. Azizi, E.-M. Aboulhamid and S. Tahar, "Multithreading-based coverification of HW/SW systems", proceedings of the international conference of Parallel and Distributed Processing Techniques and Applications (PDPTA'99), Las Vegas, Nevada, USA, June 1999
- [6] D. Becker, R. K. Singh and S. G. Tell, "An engineering environment for HW/SW cosimulation", proceedings of the 29th Design Automation Conference (DAC'92), June 1992
- [7] D.E. Thomas, J.K. Adams and H. Schmit, "A model and methodology for HW/SW codesign", IEEE Design and Test of Computers, September 1993
- [8] J. Rowson, "HW/SW cosimulation", proceedings of the 31st Design Automation Conference (DAC'94), San Diego, June 1994
- [9] H. De Man, I. Bolsens, B. Lin, K. Van Rompaey, S. Vercouteren and D. Verkest, "Codesign of DSP systems", Kluwer Academic Publishers, 1997
- [10] C. A. Valderrama, F. Nacabal, P. Paulain and A. A. Jerraya, "Automatic generation of interface for distributed C-VHDL cosimulation of embedded systems: an industrial experience", proceedings of the 7th IEEE International Workshop on Rapid systems prototyping, June 1996
- [11] E. Hunnell and M. Lyons, "Coverification goes from cutting edge to mainstream: DPLL design demonstrates the viability of today's tools", Electronic Design, June 22, 1998
- [12] T. W. Albrecht, J. Notbauer and S. Rohringer, "HW/SW coverification performance estimation & benchmark for a 24 embedded RISC core design", Proceedings of 35th Design Automation Conference (DAC'98), pp. 808-811, San Francisco (California), June 1998
- [13] L. Lavagno, A. Sangiovanni-Vincentelli and H. Hsieh, "Embedded systems co-design: synthesis and verification", Kluwer Academic Publishers, 1997
- [14] R. Kurshan, V. Levin, M. Minea, D. Peled and H. Yenigun, "Verifying HW in its SW context", proceedings of the IEEE/ACM International Conference on Computer Aided Design (ICCAD'97), San Jose, November 1997

A New Approach for Parallelising and Optimising Hardware Compilation and Partitioning in Hardware / Software Co-Design

M. Theisen, T. Hollstein, J. Becker, M. Glesner¹

¹ Darmstadt University of Technology, Institute of Microelectronic Systems, Karlstraße 15,
64283 Darmstadt, Germany

theisen|hollstein|becker|glesner@mes.tu-darmstadt.de

Abstract. In this paper we present new features for an improved partitioning and a parallelising and optimising hardware compilation integrated in the hardware/software co-design environment DICE (Darmstadt Interactive Codeesign of Embedded Systems).

I. Introduction

The new methods introduced in this contribution are a part of the DICE-framework [6] for hardware / software co-design (Figure 1). The system to be designed with DICE is specified by concurrent VHDL and C processes. In the first step this description is converted to a concurrent control data flow graph (CCDFG). Based on this graph a semi-interactive approach for the hierarchical HW/SW partitioning with heterogeneous granularity is performed by the designer using the HiPART [6] graphical user interface. After an initial partitioning step the system can be repartitioned and the hardware and software parts can be migrated from C to VHDL and vice versa. In the next step the communication structure between the hardware and the software modules is synthesised, i.e. abstract communication operators are replaced by connections using busses, busses with shared memory or FIFO buffers [5]. After communication synthesis all constraints are checked. If some are hurt, the system has to be repartitioned. Otherwise it is synthesised and compiled to the final architecture (ASIC's, DSP's and microcontrollers) or to the DICE rapid prototyping platform (REPLICA) [7].

In the first part of this paper the integration of an optimisation algorithm based on tabu search [1], [2], [3] into the HiPART system is presented. First the simulated annealing algorithm has been implemented for partitioning, but this was very time consuming. In comparison the tabu search algorithm has the advantage that it is deterministic and that it is more appropriate for the class partitioning problems [2] within DICE, i.e. that the achieved solutions are nearly of the same quality, but the computation time is much shorter.

The second part focuses on a new hardware compilation method based on high-level loop transformations. These code optimisations are transferred and adapted from parallelising compilers into the synthesis process of systems with a generic hardware architecture. Since many algorithms spend about three quarters of the total execution time in loops, an optimal trade-off between the execution time and the area for the hardware has to be found. Finally, the optimised loop nest is mapped onto a generic hardware architecture.

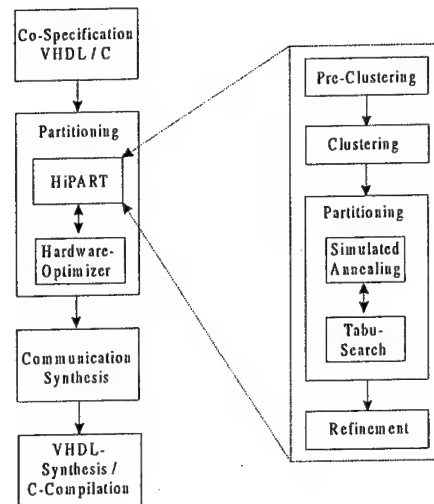


Fig. 1. Design Flow in the DICE Environment

II. HiPART: Fast Hardware / Software Partitioning

HiPART is a new hierarchical hardware / software partitioning approach. First of all the initial system (co-) specification (VHDL/C) is converted to a CCDFG [6]. In the pre-clustering step the granularity of the partitioning is fixed. Since the complexity of single operations or basic blocks may vary in a wide range, a heterogeneous granularity concept has been realised. In order to reduce the complexity of the optimisation problem, the number of clusters is reduced to an user specified number in a subsequent automated clustering step. During partitioning, the graph and resulting partitions can be visualised with a graphical user interface, which enables the designer to control the design process interactively. In the main partitioning step the assignment of the tasks to the partitions is improved in such a way, that a defined parametrised cost function is minimised. Because of the solution space reduction in the clustering step it is not guaranteed that the optimisation algorithm will find the global optimum. Therefore the clusters are resolved and post-partitioned during the iterative refinement.

III. Adapted Tabu Search Algorithm for fast Partitioning with HiPART

The task of the HiPART module is to find a partitioning such that a given user-parametrisable cost function is minimised and specified constraints are met. In order to save computation time the cost difference resulting from a movement of operations between two partitions is computed only. In this context the application of genetic algorithms would be very inefficient, since they contain operations (e.g. the crossover operation) which require a complete recomputation of the cost function. Since simulated annealing is able to find a global optimum if the cooling schedule is handled properly, this algorithm is an appropriate approach for solving the partitioning problem. Furthermore it may be used to evaluate the quality of the results of other partitioning heuristics. Because of the slow temperature decrease and a required minimum length of Markov chains, the optimisation process is very time consuming. Therefore additionally, a tabu search algorithm [1], [2] has been implemented to solve the partitioning problem. In order to avoid the tabu search algorithm getting stuck at a local

optimum, a deterministic diversification method has been integrated. The number of iteration steps is counted. If there is no improvement in comparison to the best found solution, after an user-defined number of iteration steps a diversification mechanism is applied. During diversification operations which have not been touched for a long time are moved in order to enter a different area in the search space. The number of diversification steps is chosen such that each task is moved at least once. The algorithm terminates, if during a predefined amount of optimisation/diversification cycles no improvement of the best solution is achieved. Tabu search is well suited to replace the initially applied simulated annealing algorithm, since it also requires incremental cost updates only. If the tabu search algorithm is handled properly (tabu length, tabu exceptions, diversification), results with the same quality as by application of simulated annealing can be achieved. By this alternative approach it was possible to reduce the computation time for a problem with 887 partitioning nodes from an average time of 150 minutes with simulated annealing to about 10 minutes [3].

IV. Hardware Compilation Techniques and Mapping onto Hardware

This new module enables the designer to optimise the data flow intensive part of a hardware / software system. Since this part is very computation intensive it will be realised in hardware and it is assumed that the specification is given in VHDL. Loops are the most computation intensive parts of an algorithm. Therefore the task of this module consists of mapping a perfect loop nest to an optimised parallelised hardware architecture, i.e. in finding an optimal trade-off between time and area. Towards this, the index space and the index functions are extracted from the loop nest. From this basis the dependences between the array references, the dependence vectors and the dependence matrix are determined. In the next step the sequential loop nest is transformed to be executed in parallel. This can be done by an unimodular transformation which converts it first to the maximal degree of parallelism [4], [8] and then by a coordinate transformation of the index space to a loop of a smaller degree of parallelism. This method has the advantage that it is unimodular but the loop cannot be mapped to all degrees of parallelism. Therefore we propose to generalise the wavefront method [9], i.e. that not only all those index points are scheduled to one time step which are on one wavefront but which are in the interval between two wavefronts. The advantage of this method is that a mapping to all degrees of parallelism is possible. Now the relation between the number of time steps and the number of processing elements corresponding to the degree of parallelism can be fixed and the optimal trade-off has to be found in dependence of the application area of the circuit. In order to find this optimum the hardware architecture which the parallelised code is mapped onto has to be considered (Figure 2). Since the memory has to be accessed in parallel it is subdivided into subRAMs and the data items are dynamically assigned to the processing elements by an array of multiplexers. In the next step the data are processed and in the third step they are written back to the subRAMs. With the help of this approach it became possible to map a perfect loop nest to an optimised and parallelised hardware architecture.

V. Summary

In this paper we have presented a fast approach for hardware / software partitioning and a method which maps a perfect loop nest onto an optimised and parallelised hardware architecture.

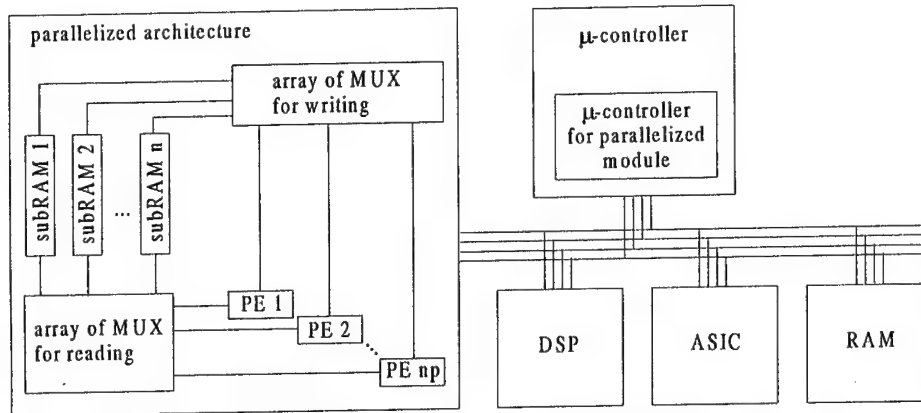


Fig. 2. Final System

References

- [1] Axelsson, Jakob, *Tree Search Strategies for Architecture Synthesis and Partitioning of Real-Time Systems*, Research Report, University of Linköping, 1996.
- [2] Eles, P., Peng, Z., Kuchcinsky, K., Doboli, A., *Hardware/Software Partitioning of VHDL System Specifications*, Proc. of EuroDAC, pp. 434 – 439, 1996.
- [3] Ballenberger, Dirk, *Implementierung und Vergleich von Optimierungsverfahren für Systempartitionierung*, Master's thesis, Darmstadt University of Technology, 1999.
- [4] Banerjee, Utpal, *Loop Transformations for Restructuring Compilers: The Foundations (Vol. 1), Loop Parallelization (Vol. 2)*, Kluwer Academic Publishers, 1993/94.
- [5] Gasteier, Michael, *Cosimulation und Kommunikationssynthese im Entwurf gemischter Hardware / Software – Systeme*, Shaker Verlag, ISBN 3-8265-3465-4, 1998.
- [6] Hollstein, Thomas, Becker, Jürgen, Kirschbaum, Andreas, Glesner, Manfred, "HiPART: A New Hierarchical Semi-Interactive HW- / SW Partitioning Approach with Fast Debugging for Real-Time Embedded Systems", *Proceedings of 6th International Workshop on Hardware/Software Codesign (CODES/CASHE'98)*, 1998.
- [7] Kirschbaum, Andreas, *Ein Rapid-Prototyping-Verfahren zum Entwurf von Kommunikationsarchitekturen in eingebetteten Systemen*, GCA-Verlag, ISBN 3-928973-47-9, 1998.
- [8] Schneider, Olaf, *Transformationen von Schleifenindizes zur Parallelisierung von VHDL-Verhaltenscode*, Master's thesis, Darmstadt University of Technology, 1999.
- [9] Theisen, Marc, Becker, Jürgen, Glesner, Manfred, Caohuu, Tri, "Parallel Hardware Compilation in Complex Hardware / Software Systems based on High-Level Code Transformations", *GI/ITG-Fachtagung für Architektur von Rechensystemen 1999, ARCS'99*, Jena, Germany.

A Design Methodology to Secure Memories in Space Environment

F.M. Roche and T. Monnier

*Laboratoire d'Informatique de Robotique et de Microelectronique de Montpellier
Université Montpellier II / CNRS
161 rue Ada, 34392 Montpellier Cedex 05, France
roche@lirmm.fr*

Abstract. The purpose of this paper is to present how to design the memory points of digital integrated circuits dedicated to operate in space. The proposed methodology relies on the use of an integrated Built-In Self Protection (BISP). This approach can prevent the loss of information due to heavy ions hits and save performances.

I. Introduction

The Integrated Circuits (IC) operating in space and high atmosphere are exposed to particles. Some of them like heavy ions are able to induce an electrical upset in CMOS digital circuits [1]. In combinational logic, this transient phenomenon can cause a false bit storage in sequential logic. Memory elements are responsible of this soft error [2-4]. The upset susceptibility of digital circuits increasing with the number of memory elements, memory hardening is the key for digital IC hardening.

Moreover, performances, size reduction, low power and *low cost* stay always essential for integrated circuits despite the perturbing phenomenon. Therefore, the hardening by acting at the design-level even on non-hardened commercial CMOS processes, received attention in the past, notably for memory elements [5-7]. But, no solution fulfills all requirements. The drawbacks are: high complexity or/and large area or/and writing time increase or/and static power consumption.

To overcome the impediments related to the high energy ion radiative environment, we propose and put in practice a hardening methodology based on design available for a standard technology (Bulk-CMOS).

II. Phenomenon description

When an heavy ion hits a reverse biased junction, charges are generated along the ion track and collected. A transient current pulse is then induced. Pointing out its random nature, this effect is called Single Event Upset (SEU) for discerning it of the total ionizing dose, another perturbing effect. In the digital circuits, the SEU appears as an uncontrolled logical level upset. If the phenomenon happens in a latch (Fig. 1) then the storage of an erroneous bit becomes possible due to the loop structure of the cell.

The sensitive MOS areas are sketched in Fig. 1 for $Q=N0=0$ and $Qb=1$. In these conditions, the upsets are possible uniquely at some junctions of the (m2,m4,mtg2,mtg4) transistors. In the alternate conditions, ($Q=N0=1$ and $Qb=0$), it is the turn to some junctions of (m1,m3,mtg1,mtg3) to become sensitive.

A HSPICE done using a current pulse generator [5,7] at the node N0, allows to observe the electrical response (Fig. 2) and illustrates how a change in the bit stored can happen.

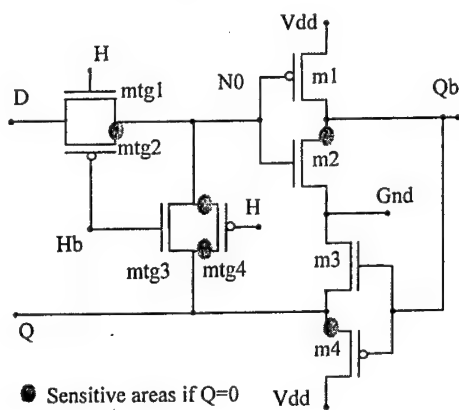


Fig. 1. Standard Latch and the sensitive areas pointed out for Q at the low level

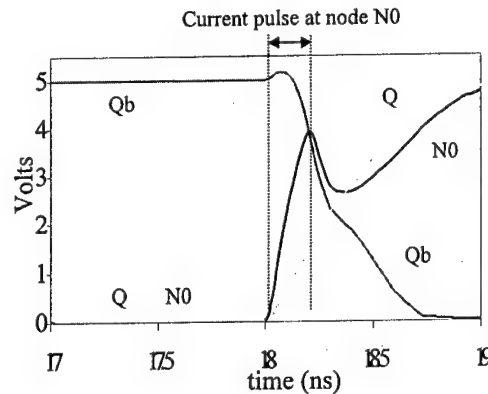


Fig. 2. Post-layout Spice simulation of a SEU effect at the node N0 showing the standard latch sensitivity (current pulse: 2 mA amplitude, 200 ps duration)

When an upset occurs at the node N0, its voltage turns from a low level onto a high level. Consequently, the upset propagates through the inverters (m1,m2) and (m4,m3) implying $Qb=0$, and $Q=1$. Then a false value is then memorized. We note that only a 0.4pC charge generated in the transistor mtg2 is sufficient to induce an error (Fig. 2).

Recently, another kind of perturbing event has been evidenced on latch structure [4]: it is an upset not generated in the cell itself but occurring at the D latch input. In this condition, the transient pulse is normally seen by the D latch as a change in the input logic value. If the upset arises as the clock is switching off, the writing operation can be jeopardized. During a time interval called the "window of vulnerability", the cell can store a false bit. This effect arising during a transition is specified as "dynamic SEU". On the contrary, the occurrence of Fig. 2 - for which the pulse surges in the D latch structure while the cell is working as an isolated memory point - will be referred as "static SEU".

III. Design methodology improving SEU hardening

Our design methodology is illustrated in the Fig. 3. The issue implies four criteria. (i) Only a reverse biased junction can be upset. As a consequence, nMOS storing a 0 and pMOS storing a 1 have their value preserved. (ii) The writing operation of the latch must be done with two signals, D and Db. This introduces a necessary redundancy. (iii) Resistors permit a RC filtering of upset. Therefore, upset cannot propagate. (iiii) Finally, inverters are replaced by tri-state inverters able to put in a high impedance state Q and Qb during upset.

To prevent possible upsets on the Q or Qb nodes, the RC filtering inhibit propagation in the loop (Fig. 3). For an upset generated at the nodes G or Gb, the lost of information is prevented by putting Qb or Q in a high impedance state during the disturbance.

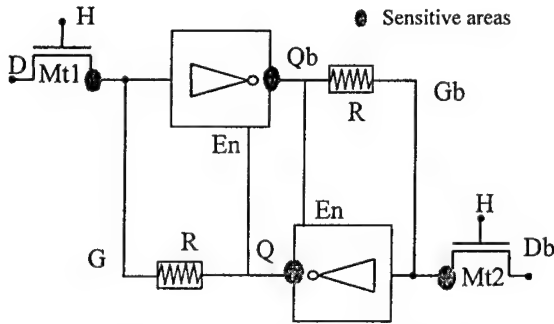


Fig. 3. Design methodology used to improve latch SEU hardening

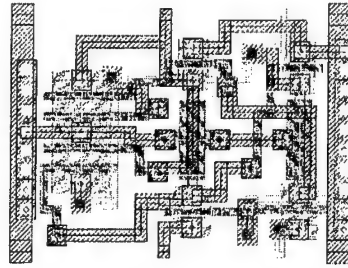


Fig. 4. Layout of a hardened latch

If one of the two latch inputs is upset during a clock transition, a dynamic SEU is transmitted. The erroneous value has to propagate through the inverter and the resistor of the latch. The delay necessary to this propagation combined to the presence of the dual input produces a very effective hardening.

IV. Results

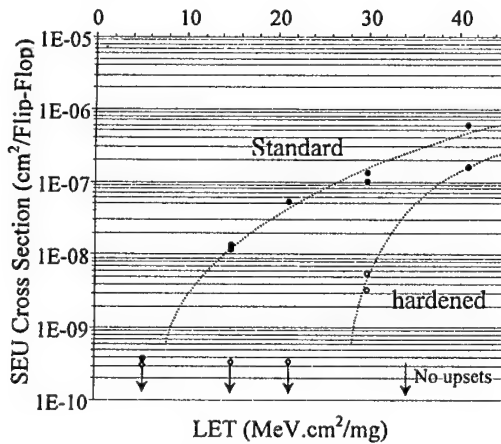


Fig. 5. Cross Sections of standard and hardened latches

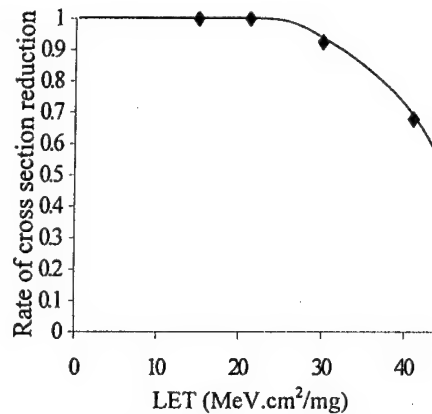


Fig. 6. Rate of reduction of the cross-section versus Linear Energy Transfer

A hardened latch based on the previous methodology [7] (Fig. 4) and a standard latch have been implemented in a test circuit (0.7 μm bulk-CMOS technology). The results of the irradiation performed at the Cyclotron of the Lawrence Berkeley Laboratory are given in Fig. 5 where the SEU cross sections are the errors number divided by the particles fluence (incident ions by cm^2). The rate of decrease in the cross section with respect to the standard latch is shown Fig. 6. The Linear Energy Transfer (LET) measures the particles energy efficiency.

These figures clearly show that up to a (LET) of 30 Mev.cm²/mg, only the standard latch makes errors. Above this LET threshold, the soft errors are still considerably reduced, but multiple event effects can appear.

	Standard Latch	Hardened Latch
area	600 μm^2	790 μm^2
writing time	600 ps	710 ps
sensitive junction area	106 μm^2	91 μm^2
Hardening	un-hardened	SEU hardened

Tab. I. Comparative characteristics

V. Conclusion

We have exposed a design methodology devoted to memory points, able to introduce a Built-in Self Protection (BISP) in SRAM, D-latches, registers... without any technology artefact. A circuit has been implemented to put in practice and validate these new concepts in bulk commercial technology. The irradiation results show a quite significant improvement of the SEU hardening capabilities. More, the electrical simulations performed prove that writing speed (18% decrease) and consumption of the tested cell are preserved. The cost in silicon area is only a 30% loss compared to the two to three hundred percents for a redundant system. The structure came with a surprising 14% reduction of the sensitive area, confirming the design feasibility of more safe devices.

References

- [1] Eugene Normand, Member IEEE, "Single event upset at ground Level", IEEE Transactions on nuclear science, Vol. 43, N° 6, December 1996, pp. 2742-2750.
- [2] P.M. O'Neil and G.D. Badhwar, "Single Event Upset for space shuttle flights of new general purpose computer memory devices", IEEE Transactions on nuclear science, Vol. 41, N° 5, October 1994, pp. 1755-1764.
- [3] B.R. Blaes, G.A. Soli, M.G. Buehler, "Bench-level characterization of a CMOS standard-cell D-latch using Alpha-particle sensitive test circuits", IEEE Transactions on nuclear science, Vol. 38, N° 6, December 1991, pp. 1486-1492.
- [4] S. Buchner, M. Baze, D. Brown, D. McMorrow, and J. Melinger "Comparison of error rates in Combinational and Sequential Logic", IEEE Transactions on nuclear science, Vol. 44, N° 6, 1997, pp. 2209-2216.
- [5] D. Wiseman, J.A. Canaris, S.R. Whitaker, J. Venbrux, K. Cameron, K. Arave, L. Arave, M.N. Liu and K. Liu, "Design and Testing of SEU/SEL Immune Memory and Logic Circuits in a Commercial CMOS Process", IEEE Radiations Effects Data Workshop, Record, 1993, pp. 51-55
- [6] R. Velazco, D. Bessot, S. Duzellier, R. Ecoffet, R. Koga, "Two CMOS memory cells suitable for the design of SEU tolerant VLSI circuits", IEEE Transactions nuclear science, Vol. 41, 6, 1994
- [7] T. Monnier, F.M. Roche, G. Cathébras, "Flip-flop Hardening for Space Applications", IEEE International Workshop on Memory Technology, Design, and Testing, San Jose, CA, USA, 1998, pp104-107

A methodology for system-level functional verification of multi-media applications

M. Čupák¹, F. Catthoor², H. De Man^{2,3}

¹*Dept. of Microelectronics, STU, Ilkovičova 3, Bratislava, Slovakia*

²*IMEC v.z.w., Kapeldreef 75, Leuven, Belgium*

³*Katholieke Universiteit Leuven, Belgium*

email: {cupac,catthoor,deman}@imec.be

Abstract. Today's multimedia applications represent complex systems implemented on a single piece of the silicon. Industrial experiments show that design of such applications has to start at system-level in order to fulfill increasing requirements for area and power reduction. Typically, reduction of area and power of the chip includes a number of sophisticated, but often manual optimisations applied on the initial specification. Those optimisations are very error-prone. In this paper, we propose a system-level methodology for functional verification of loop oriented transformations on multimedia applications. The methodology is based on the combination of two complementary existing techniques: formal verification of loop transformations and SFG-Tracing.

I. Introduction

One of the dominant requirements for current system-on-a-chip multimedia applications is the need for low power consumption and reduction of the area of the chip. Traditional methods solve this problem by optimisations at lower levels of design, usually exploiting a number of circuit techniques. Today's multimedia applications, however, represent typical data-dominated systems, where the dominant power contribution comes from the data transfers between the datapath and the hierarchical memories. The late low level optimisations do not bring any significant gain in terms of power, without first considering the reduction of wasted memory transfers. This fact has to be taken into account already at the early stages of the design process [10]. In practice this means that many important decisions have to be taken already at the system (algorithmic) level. The search space for looking for the promising algorithm descriptions at this level is very broad. In order to avoid the selection of good candidates on an ad-hoc basis with the expectation that their final implementation will satisfy the user requirements, novel methodologies are researched (see e.g. [2]) that allow the designer to meet the power and area constraints by exploring the initial algorithmic description. Code transformation techniques are a crucial part of such methodologies. They allow to manipulate the initial descriptions in order to reduce costly memory transfers [6].

Loop transformations applied on a code described on a number of pages can be very error-prone, however, especially when applied manually. In order to guarantee the correctness of the transformed code, the optimised descriptions should be always compared with the initial ones.

This paper propose complete functional verification methodology for multi-media applications at system-level based on combination of the two complementary verification techniques: verification of loop transformations and SFG-Tracing. We first review and compare both verification techniques in order to clarify their principles, advantages and shortcomings. Then, their combination will be explained in several steps. Concluding remarks are presented at the end of the paper.

II. Methodology for Verification of Loop Transformations

For a large class of system-level transformations in data-dominated signal processing applications, a technique for the behavioural equivalence of any two high-level descriptions has been developed at IMEC [9]. It is based on a geometrical domain modeling for each statement in the description.

A formal model [9] is proposed with aim to model the loop constructs and indexed signals in a very efficient way. Each statement in the description is defined by a *predicate (P.R)*, consisting of a *relation (R)* between the signals involved and *precondition (P)* under which the relation

holds. The relation [7, 8] is a unique representation of the statement, made independent from the original index names in the description. The precondition is derived from the manifest constraints on the indices of the loop bounds surrounding the statement. It defines the index domain for the relation (statement). The index domain is then represented in a geometrical way. The complete description is modelled by the conjunction of all the predicates representing the statements within description.

The basic loop verification technique consists of three steps [9]:

1. **Joining the relations.** In the first step, the corresponding statements are identified and their preconditions are merged in both initial and optimised description. Corresponding statements are the statements that have been distributed over the loops as a result of optimisations like loop unrolling or loop split. Their identification is based on simple syntactical pattern matching of the signal names in the statement. In case of equal names the relations of the statements are equal. In case of equal relations, the two constrained relations are joined to one new constrained relation by merging the preconditions of the two relations.
2. **Reduction of the domains.** In this step the merged preconditions are rewritten into canonic form, independent on original iterator names. Their domain representations are then reduced to a definition where only free variables remain.
3. **Computation of the difference of the domains.** In order to prove that the two descriptions have the same behaviour, the sets of predicates, one for the initial and other for optimised descriptions, have to be proven equal. The corresponding predicates between the two descriptions are found again by pattern matching of the signal names. The equivalence of their preconditions is done by computing the difference of the domains defined by them. The two related preconditions must define the same domain. If the result of the difference is an empty domain, the preconditions are same and the description is correct, otherwise an error was introduced during the transformation phase.

III. SFG Tracing Methodology

SFG-Tracing [3] is a formal verification methodology that enables to check the correctness between system-level behavioural specifications and low level implementations. The basic idea of this methodology is to divide the initial algorithmic specification represented in Signal Flow Graph (SFG) into a set of partial signal flow graphs (pSFG's). The partitioning to pSFG's enables then to overcome the complexity problem of overall verification. Each of these is traced in the implementation and checked for correctness. In order to make the verification feasible and efficient, a set of correspondence relations must be known between the high level specification and lower level implementation for the verification technique to work. These relations are called *reference signals* and *mapping functions*. *Reference signals* are corresponding to input and output signals of each pSFG and signals at a certain time and space in the implementation. *Mapping functions* describe the behavioural correspondence of the reference signals between implementation and specification in space and in time, under specific conditions.

The bit-true implemented behaviour of each of the pSFG's is compared with the expected one by symbolic simulation making use of Binary Decision Diagrams (BDD) [1]. The symbolic simulation is used to compare if the Boolean expression obtained by simulation of the implemented circuit represents the same BDD as the one that are derived from the specification.

IV. Comparison of Verification Methodologies

As mentioned above, SFG Tracing is the general verification methodology that allows to verify the behavioural correctness between specification and implementation at different abstraction levels. SFG Tracing has been mainly used for verification between the register transfer and transistor level verification and then extended towards algorithmic level [4]. At the algorithmic level also verification of loop constructs by means of mathematical induction have been proposed, but this approach is limited because the induction based proofs of loop constructs impose restrictions on the maximum number of nested loops. The number of proofs needed to prove the induction case grow exponentially with the nesting depth level of the loop. Moreover,

the technique was only suitable for same number of loops in two compared descriptions, having loops with regular structure and equal ordering of indexed signals. In case of loop transformations, loop unrolling was necessary. This is not acceptable for data-dominated applications we target here, in which a number of multidimensional signals are enclosed in differently nested loops.

On the other hand, the methodology for loop transformation verification has been used for verification of two algorithmic descriptions, but arithmetic and related control in the datapaths were not checked, because the formal model was not intended to express their behaviour. However, the shortcomings of both methods can be efficiently eliminated with their combination, thus allowing the complete verification of system level optimisations.

V. Combination of Sfg-Tracing and Loop Transformation Verification

The proposed overall methodology for system-level verification consists of several steps. Before the actual verification, specification has to be hierarchically partitioned into the part that will be affected by the code transformations, verified by the first technique, and the part which includes the scalar arithmetic and control operations, where SFG Tracing technique will be applied. This partitioning has to be preceded by careful code exploration. These steps, together with a short explanation of memory optimisation steps will be described in this section.

A. Code exploration

During the design of complex hardware and software (or mixed) systems, the designer has a number of possibilities to modify the initial design specification in order to obtain a better system implementation. For complex multimedia applications, exploration of all possibilities is not feasible. The designer has to concentrate only on the optimisations of the most relevant part of the code and suppress the parts that are not important. This can be achieved by pruning of the original specification where only the most promising parts for optimisation are selected [2]. From the point of view of memory optimisations, these parts represent code describing the communications between the data-path and memory, which are recognized after a high-level estimation of the number of main memory accesses (profiling), possibly making use of efficient access counting tools. The rest of the code which is not the object of the system-level loop optimisations represents the data-path and control.

B. Hierarchical specification modeling

As mentioned above, hierarchical partitioning of the specification is very important to model the separation of the optimisation related part and the data-path related part of the initial specification. In particular, the specification has to be split into three layers:

layer 1: a procedural process control flow top layer which is not of real interest for optimisations, except for the potential sequence/timing constraints which are imposed on the memory transfers.

layer 2: a middle layer which represents all the relevant information for the optimisation tasks. This layer contains multidimensional data flow to be stored/transferred in background memory.

layer 3: a bottom layer of local data-path/control functions which contains *scalar* data and local control flow. This layer hides all the foreground and arithmetic/control issues. Moreover, it is also used to hide some of the undesired constructs which are not of real interest to the system-level optimisation tasks.

Within this model, all arithmetic, scalars and code constructs that are not important from the point of view of optimisations at system-level are hidden in the lowest level functions. Those are called from higher levels in the middle layer where the M-D data flow is expressed by means of loops and indexed signals. Only this middle layer part of code is targeted to the optimisation considered here because only this contains the relevant information.

C. Optimisation Steps

After layering, the optimisation steps of the data transfer and storage exploration (DTSE) methodology [2] can be applied. These represent a hierarchical combination of procedures, each of them addressing a different task in the optimisation process. More of the steps involve global, complex loop manipulations. Also a parallelizing compiler approach could be applied.

D. Verification

Exploiting the leveling specification model as described in section B., the input specification can be divided into three different layers. This allows the separation of the code to the DTSE related and data-path related partitions. The descriptions covered at the different levels are then verified by the appropriate technique as described in the following procedure:

1. The first layer is inlined with the second layer leading to a single layer description. Such a joined layer is then verified fully by the method for verification of loop transformations as described in section II.. We exploit our novel extensions of the method [5] that can significantly reduce the computation time requirements in order to cope with initial complex multi-media specifications.
2. Functions in the third layer are matched in the two compared specifications and verified by SFG Tracing, because the problematic (nested) loop constructs are not present in there. Because both the specification and implementation lies at the same (algorithmic) abstraction level, the mapping functions can be found by signal matching on the signal names on the left and right sides of the statement.

If the functions in the layer-3 are equivalent, then the verification can concentrate on layer-2 and layer-1, otherwise the errors in these layer-3 functions have to be solved before proceeding to verification of layer-2.

VI. Conclusions

We propose methodology for the formal verification of data dominated multimedia applications at system-level. It is based on the combination of two complementary existing techniques: verification of system level loop transformations and the SFG Tracing technique for verification of correctness of arithmetic constructs and related control flow. This allows exploitation of benefits of both techniques to obtain complete formal verification technique at the level which has not been fully covered by other validation techniques. Although it is not illustrated in this paper, the verification technique has been successfully applied to real-life designs showing its ability to verify the complex transformations applied on multimedia applications.

References

- [1] Randal E. Bryant, "Graph-Based Algorithms for Boolean Function Manipulation", *IEEE Transactions on Computers*, Vol.C-35 No.8, pp. 667-691, August 1986.
- [2] F.Catthoor, S.Wuytack, E.De Greef, F.Balasa, L.Nachtergaele, A.Vandecappelle, "Custom Memory Management Methodology - Exploration of Memory Organisation for Embedded Multimedia System Design", Kluwer Academic Publishers, Boston, 1998.
- [3] L.Claesen, M.Genoe, E.Verlind, F.Proesmans, H.De Man, "SFG-Tracing: A Methodology of design for verifiability.", In P.Prinetto and P. Camurati, editors, *Correct Hardware Design Methodologies*, p. 187-202, North-Holland, 1992.
- [4] M.Cupak, M.Genoe, I.Bolsens, "Formal Verification of a Signal Flow Graph", *Proc. Workshop on Design Methodologies for Microelectronics*, Smolenice, pp.314-320 Slovakia, September 1995.
- [5] M.Cupak, F.Catthoor, H. De Man, "Efficient Functional Validation of System-level Loop Transformations for Multi-media Applications", *Proc. IEEE International High Level Design Validation and Test Workshop*, pp.72-79, La Jolla, CA, Nov. 1998.
- [6] F.Franssen, L.Nachtergaele, H.Samsom, F.Catthoor, H.De Man, "Control flow optimization for fast system simulation and storage minimization", *Proc. 5th ACM/IEEE Europ. Design and Test Conf.*, Paris, France, pp.20-24, Feb. 1994.
- [7] A.D.Gordon "The formal definition of a synchronous hardware-description language in higher order logic.", In *ICCD'92: 1992 IEEE International Conference on Computer Design: VLSI in Computers and Processors*, pages 531-534, Cambridge, Massachusetts, IEEE Computer Society Press, October 1992.
- [8] M.J.C.Gordon, "Why higher-order logic is a good formalism for specifying and verifying hardware.", In G.Milne and P.A.Subrahmanyam, editors, *Formal Aspects of VLSI Design.*, North Holland, 1986.
- [9] H.Samsom, F.Franssen, F.Catthoor, H.De Man, "Verification of loop transformations for real time signal processing applications", In *J.Rabaey, P.M.Chau and J.Eldon editors, VLSI Signal Processing VII IEEE*, New York, NY, USA; 1994; pp.208-217.
- [10] I.Verbaauwhede, F.Catthoor, J.Vandewalle, H.De Man, "Background memory management for the synthesis of algebraic algorithms on multi-processor DSP chips", *Proc. VLSI'89, Int. Conf. on VLSI*, Munich, Germany, pp.209-218, Aug. 1989.

Analog (S)witchcraft, or How to Perform Accurate and Linear Data Conversion Using Inaccurate Nonlinear Elements

Gabor C. Temes, Un-Ku Moon and Jesper Steensgaard
Oregon State University, Corvallis, OR 97331, USA

Abstract. This paper provides a tutorial overview of some recently developed methods for enhancing the accuracy and linearity of data converters (analog-to-digital as well as digital-to-analog) by introducing auxiliary digital circuitry which calibrates, cancels and/or corrects the errors introduced by the unavoidable inaccuracy of the analog components used in the conversion. Simple but practical examples are used to illustrate the various improvement techniques.

I. Introduction

Conventional high-accuracy data converters require extreme accuracy in the matching of analog components, which cannot be achieved in an integrated circuit. In this paper, three strategies: analog correction, error cancellation and spectral shaping are described for achieving accurate dynamic component matching. Switched-capacitor (SC) DACs will be used to illustrate the techniques.

II. Analog Correction Techniques

Fig. 1 shows the conceptual diagram of a DAC constructed using SC circuitry. The operation of the circuit is as follows. The input binary word is converted into a thermometer code with bits x_1, x_2, \dots, x_M such that if the integer value of the input word is m , the bits x_1, x_2, \dots, x_m are 1, and the rest are 0. During the reset phase ($\phi_1 = 1$), the feedback capacitor C_f is discharged and all input capacitors are charged to the reference voltage V_{ref} . Next, during the conversion phase ($\phi_2 = 1$), the first m input capacitors are discharged into C_f , resulting in an output voltage $V_{out} = (mC/C_f)V_{ref} = (m/M)V_{ref}$.

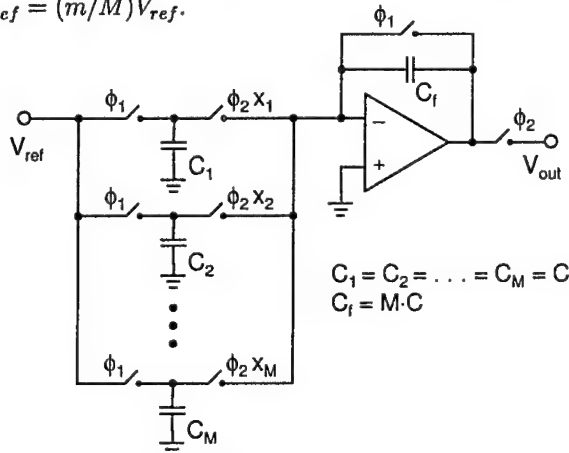


Figure 1: A switched-capacitor DAC

Analog correction of the matching error may be achieved by using the system shown in Fig. 2, where each capacitor C_i is split into a coarse and a fine part, C_{ci} and C_{fi} , respectively, and a separate buffered reference voltage V_{refi} is introduced for each the C_{fi} [1]. When ϕ_2 is high, capacitors C_{ci} and C_{fi} are discharged into C_f if $x_i = 1$, otherwise they hold their charges. A calibration stage, consisting of a transconductor and a reference capacitor C_{ref} , is used to

readjust the V_{refi} sequentially when the i -th calibration clock phase ϕ_{ci} is high, so as to make the combined charges stored in C_{ci} and C_{fi} equal to $C_{ref}V_{ref}$. To replace the capacitor being calibrated, an extra set of C_c and C_f is also needed. The resulting conversion accuracy can then be as high as 15 bits. The process is similar to that proposed earlier for current-mode DACs by Groenewald et al. [2].

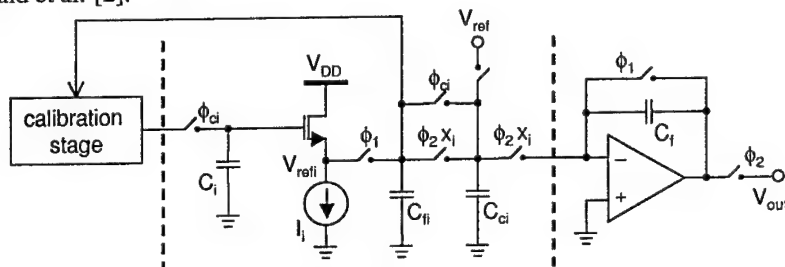


Figure 2: The DAC of Fig. 1 with analog mismatch correction

III. Error Cancellation Techniques

Error cancellation techniques are similar to analog correction in the sense that analog quantities (charge, voltage, etc.) are manipulated under digital control to achieve error cancellation.

Consider the DAC stage containing two equal-valued capacitors, shown in Fig. 3 [3]. Its operation under ideal conditions is as follows. The digital input words are entered serially, with the least significant bit (LSB) first. Before each word enters, both capacitors are discharged by the reset switches. Then, when $\phi_1 = 1$, C_1 is charged to a voltage V_{ref} or 0, depending on the LSB. Next, as $\phi_2 = 1$, C_1 and C_2 share charges. Afterwards, C_1 is disconnected from C_2 , and again is charged to V_{ref} or 0, depending on the value of the second LSB. This procedure is repeated for each bit, until the MSB has been processed. At this point the charge stored in both C_1 and in C_2 , and hence the voltage across them, represents the converted value of the input digital word.

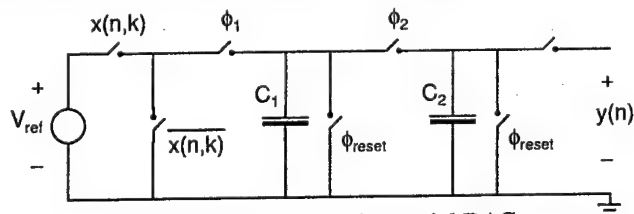


Figure 3: A two-capacitor serial DAC

In practice, the capacitors used cannot be made exactly equal, and hence the conversion becomes inaccurate. This introduces a deterministic nonlinearity into the process, which gives rise to harmonic distortion. We can quantify the imperfect capacitor matching property by defining the error coefficient $\delta = (C_1 - C_2)/(C_1 + C_2)$ for the nominally matched capacitors C_1 and C_2 . Analyzing in detail the charge transfers that occur for the N clock cycles, an explicit formula can be found for the error err of the final DAC output.

A simple way to perform capacitor mismatch error cancellation is to repeat the conversion for the same input word with the roles of capacitors C_1 and C_2 interchanged. This changes the sign of δ , while leaving the rest of the formula giving err unchanged. Hence, when the two outputs obtained in the two conversions for the same input word are added together, the effect of the capacitor mismatch error cancels. Thus, at the cost of doubling the conversion time, the accuracy is much enhanced. Capacitor mismatch error cancellation schemes using this property were suggested for a number of different architectures [4]-[5].

IV. Spectral Error Shaping

In spectral error shaping, the error signal generated by the mismatch of nominally equal-valued elements gets filtered so as to suppress its in-band spectral energy. Since the filtering is usually only first or second order, this technique will only be effective if the signal band occupies only a relatively small part of the 0 to $f_s/2$ range, where f_s is the sampling frequency, i.e., if the oversampling ratio $R = f_s/(2f_b)$ is much greater than 1. Here, f_b denotes the bandwidth of the signal being converted. The filtering action can be obtained by appropriately choosing the indices of the matched elements participating in the conversion of each signal sample. One option is to choose the capacitors used in converting each input sample randomly, rather than deterministically as described above [6]. Now the error will be in general different each time a fixed code is entered into the DAC, and hence the matching errors introduce random noise, rather than distortion. Thus, using this strategy, the mismatch error is converted into a wide-band noise, only a fraction of which falls in the signal band. This process can be regarded as zero-order spectral shaping.

First-order spectral shaping can be achieved based on the following considerations. Consider the input/output characteristics of an ideal SC DAC (Fig. 1). It is possible to choose the elements used during conversion such that the *average* value of the output for each code falls on a straight line. This suppresses harmonic distortion, and eliminates the dc error for any input. Specifically, if all input elements are used with equal frequency for each code, then the average outputs will fall on a straight line, and hence the element-value errors will result in a noise with a zero mean value. This indicates that the power spectral density (PSD) of the mismatch noise has a zero at dc, and the PSD is nonuniform. This process thus provides a first-order mismatch-noise shaping.

There exist numerous techniques for achieving the required equal average usage for the individual capacitors. In one (called barrel shifting [7]), the capacitors used for the first sample with value m_1 are C_1, C_2, \dots, C_{m_1} ; for the second sample with value m_2 , the set $C_2, C_3, \dots, C_{m_2+1}$ is used, etc., and the selection wraps around to C_1 once the last of the C_i has been used. Another averaging technique (called individual level averaging [8]) keeps track of the past usage of each element C_i for each input code, and assigns them so as to keep the average usage uniform. Yet another (named data-weighted averaging [9]) uses the set C_1, C_2, \dots, C_{m_1} for the first sample, $C_{m_1+1}, C_{m_1+2}, \dots, C_{m_1+m_2}$ for the second, etc., with wrap-around to C_1 after the last C_i (C_M) has been used. These techniques have various relative advantages and disadvantages; the barrel-shifting method is simple to perform, but it can generate undesirable tones in the pass-band for some input frequencies, while individual level averaging, which is not susceptible to tone generation, requires more elaborate digital circuitry, and takes longer to achieve the desired averaging. Data-weighted averaging is relatively simple, and achieves rapid averaging since no element will be used twice until all others are used. Other techniques have also been proposed for achieving first-order noise shaping [10]-[11].

To achieve higher-order noise shaping, the binary logic signal $x_i(n)$, which decides whether or not V_i will contribute to V_{out} in the n -th sampling period, can be forced to assume the form

$$x_i(n) = f(n) + h(n) * [e_i(n) - r(n)] \quad (1)$$

Here, the asterisk denotes the discrete-time convolution; also, $f(n)$ is a bounded function, independent of i , and $h(n)$ is the impulse response of the desired shaping filter. Finally, the $e_i(n)$ are pseudo-random bounded functions, in general different for each i . Then, the output error in the n -th period is

$$err(n) = \sum_i x_i(n) dV_i = [f(n) - h(n) * r(n)] \sum_i dV_i + h(n) * \sum_i e_i(n) dV_i \quad (2)$$

where dV_i is the output error introduced by the i -th mismatched capacitor. If the full-scale output is accepted as correct, the first term on the RHS is zero, and the second term contains the desired filter function. Hence, if we can generate a set of binary logic sequences x_i such that in each sampling period they satisfy eq.(1) and their sum equals the input value m , the error shaping is accomplished.

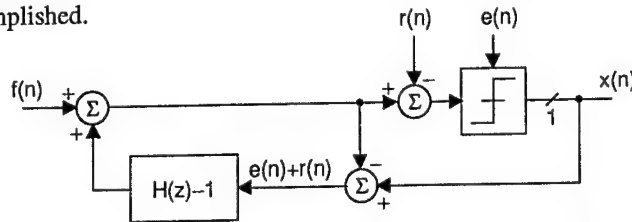


Figure 4: Digital delta-sigma loop for generating the $x_i(n)$ sequence of eq.(1)

Consider next the digital delta-sigma loop shown in Fig. 4 [12]. Analysis shows that its single-bit output sequence $x_i(n)$ is given exactly by eq.(1), if the truncation error of the comparator is denoted by $e_i(n)$, and if $H(z)$ is the z -transform of $h(n)$. Hence, M such structures (one for each capacitor C_i) can be used to generate the $x_i(n)$ sequences for the operation of the DAC.

For a positive integer system, the common input $f(n)$ of the loops can be chosen so that the input of the truncation block in one of the loops is zero, and in all others it is positive. This will minimize the signals in the loops, and hence helps to keep their operation stable. The sequence $r(n)$ is essentially a time-variable threshold for the comparators. It is chosen such that exactly $m(n)$ of the M loops have outputs $x_i(n) = 1$ during period n .

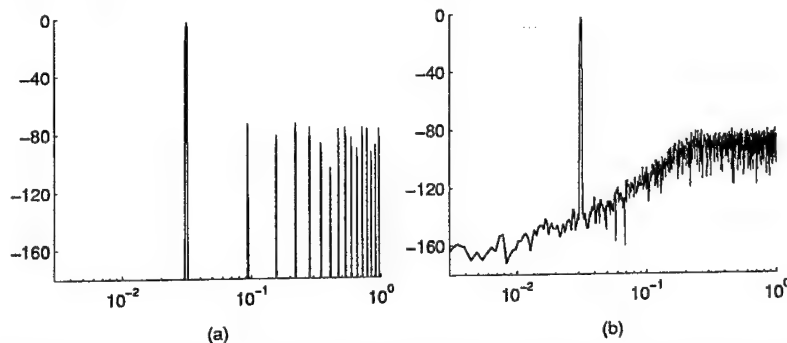


Figure 5: Unshaped (a) and shaped (b) output spectra of the two-capacitor DAC

The mismatch error shaping process can be applied to other structures, such as the two-capacitor serial DAC described above and shown in Fig. 3 [5],[13]. Whereas in the case of the M -element DAC of Fig. 1 the degree of freedom which allowed spectral error shaping without changing the signal processing function was the arbitrary choice of the C_i in generating the analog output, here there is the option of interchanging the roles of C_1 and C_2 in each clock cycle when $\phi_1 = 1$. By generating a binary sequence $t(n, k)$ which decides the role of the capacitors during the conversion of the k -th bit of the n -th input word with a digital delta-sigma loop, a filtered mismatch error can be obtained. Fig. 5 compares the unshaped and shaped output spectra of the DAC for a sinewave input with a peak-to-peak amplitude of $0.7V_{ref}$, an oversampling ratio of 10 and an assumed mismatch of $\delta = 0.1\%$. A third-order noise shaping and dithering was used in the loop generating $t(n, k)$. The unshaped error gives a S/THD ratio of only 70 dB; the S/(N+THD) for the mismatch-shaped spectrum is around 96 dB, a gain of

26 dB. Note that unlike the error-cancelling scheme discussed earlier for this structure, mismatch shaping does not double (or change in any way) the conversion time; the only cost is the added digital circuitry, which is insignificant.

VI. Conclusions

In this tutorial paper, it was shown that very high accuracy and linearity may be obtained in data conversion even when using inaccurate analog components, by introducing additional digital logic which takes advantage of the hidden degrees of freedom in the operation of the converter circuit to achieve cancellation, calibration or frequency shaping of the error introduced by the analog imperfections. This enables the designer of mixed-mode interface circuits to satisfy the increasing demands for ever faster and more accurate fully integrated data converters.

References

- [1] U. Moon, J. Steensgaard and G.C. Temes, "A simple SC DAC with mismatch correction and shaping," to appear.
- [2] D.W.J. Groeneveld, H.J. Schouwenaars, H.A.H. Termeer and C.A.A. Bastiaansen, "A self-calibration technique for monolithic high-resolution D/A converters," *IEEE J. of Solid-State Circuits*, vol. 24, pp. 1517-1522, Dec. 1989.
- [3] R. Suarez, P. Gray and D. Hodges, "ALL MOSFET charge-redistribution A/D conversion techniques—Part II," *IEEE J. of Solid-State Circuits*, vol. 10, pp.379-385, Dec. 1975.
- [4] P. Rombouts et al., "Capacitor mismatch compensation for quasi-passive switched-capacitor DAC," *IEEE Trans. on Circuits and Systems-I*, vol. 45, pp. 68-71, Jan. 1998.
- [5] J. Steensgaard, U. Moon and G.C. Temes, "Mismatch-shaped pseudo-passive two-capacitor DAC," *Proc. IEEE Alessandro Volta Memorial Workshop*, Como, Italy, March 1999.
- [6] L.R. Carley, "A noise-shaping coder topology for 15+ bit converters," *IEEE J. of Solid-State Circuits*, vol. 24, pp. 267-273, April 1989.
- [7] Y. Sakina, "Multi-Bit Sigma-Delta A/D Converters with Nonlinearity Correction Using Dynamic Barrel Shifting," M.S. Thesis, UC Berkeley, June 1990.
- [8] B.H. Leung and S. Sutarja, "Multi-bit sigma-delta A/D converter incorporating a novel class of dynamic element matching techniques," *IEEE Trans. on Circuits and Systems-II*, vol. 39, no.1, pp. 35-51, Jan. 1992.
- [9] R.T. Baird and T.S. Fiez, "Improved delta-sigma DAC linearity using data-weighted averaging," *Proc. IEEE Internat. Symp. on Circuits and Systems*, Seattle, WA, May 1995.
- [10] R.W. Adams and T.W. Kwan, "Data-Directed Scrambler for Multi-Bit Noise-Shaping D/A Converters," U.S. Patent No. 5,404,142, April 4, 1995.
- [11] I. Galton, "A hardware-efficient noise-shaping network," *Proc. Internat. Symp. on Circuits and Systems*, Atlanta, GA, May 1996.
- [12] R. Schreier and B. Zhang, "Noise-shaped multi-bit D/A converter employing unit elements," *El. Letters*, vol. 31, no. 20, pp.1712-1713, Sept. 28, 1995.
- [13] J. Steensgaard, U. Moon and G.C. Temes, "Mismatch-shaping serial digital-to-analog converter," *Proc. IEEE Internat. Symp. on Circuits and Systems*, vol. II, pp. 5-8, Orlando, FL, June 1999.

100 Gbit/s Computer Optical Interconnect

Ivan Glesk, Robert J. Runser, Kung-Li Deng, and Paul R. Prucnal

Department of Electrical Engineering, Princeton University, Princeton, NJ08544

glesk@ee.princeton.edu

Abstract. An experimental demonstration of an error free 100Gbit/s optical time division multiplexing (OTDM) broadcast star computer interconnect is presented. A highly scalable novel node design provides rapid inter-channel switching capability on the order of the single channel bit period (1.6 ns).

I. Introduction

Although lightwave technology is meeting the demand for point-to-point and long-haul transport of digital information, routing packets at the nodes of the network has typically been carried out using electronically switched backplane routers. The growing capacity on the Internet is placing an ever greater demand on electronic routing technologies. While WDM can support large aggregate traffic bandwidths, it is difficult to perform routing functions which may involve challenging techniques such as dense wavelength conversion. Additionally, present WDM laser and filter tuning techniques rely upon slow technologies which increase the channel access latency and reduce the effective network bandwidth.

Recent advances in optical time division multiplexing (OTDM) have proven this technology's capability to handle the switching and routing needs for future. Channel access in OTDM networks is achieved by using time slot tuners and all-optical demultiplexers. Timing precision of less than 1ps is required to tune, multiplex, and demultiplex individual channels within the OTDM frame.

The computer interconnect we are constructing is based upon an OTDM broadcast star architecture. The high-level architecture and node design is shown in Fig. 1. Nodes transmit information at a slow data rate, B , by modulating picosecond optical pulses. By using a scalable time slot tuner, the pulse is appropriately delayed to correspond to the desired destination time slot. Data pulses from all nodes are multiplexed into a time frame with an aggregate bandwidth of NB , where N is the number of nodes in the network. The pulse spacing between adjacent channels is $(NB)^{-1}$ or typically less than 10ps to achieve 100+ Gbit/s. Ultrafast all-optical demultiplexers like the TOAD are used to extract the desired channel from the high capacity OTDM frame at the node receivers. Nodes can select the received time slot by using a time slot tuner to align the clock with an incoming time slot within the frame for all-optical demultiplexing.

To perform the functionality of a router, addresses are mapped to specific time slots within the network. Routing is achieved by sending each bit of the packet in a unique time slot corresponding to its destination node. All nodes in the network are synchronized by splitting and amplifying the optical output of a single modelocked fiber laser. Packet routing is performed by rapidly changing the state of the time slot tuner to transmit into time slots corresponding to destination addresses on the network.

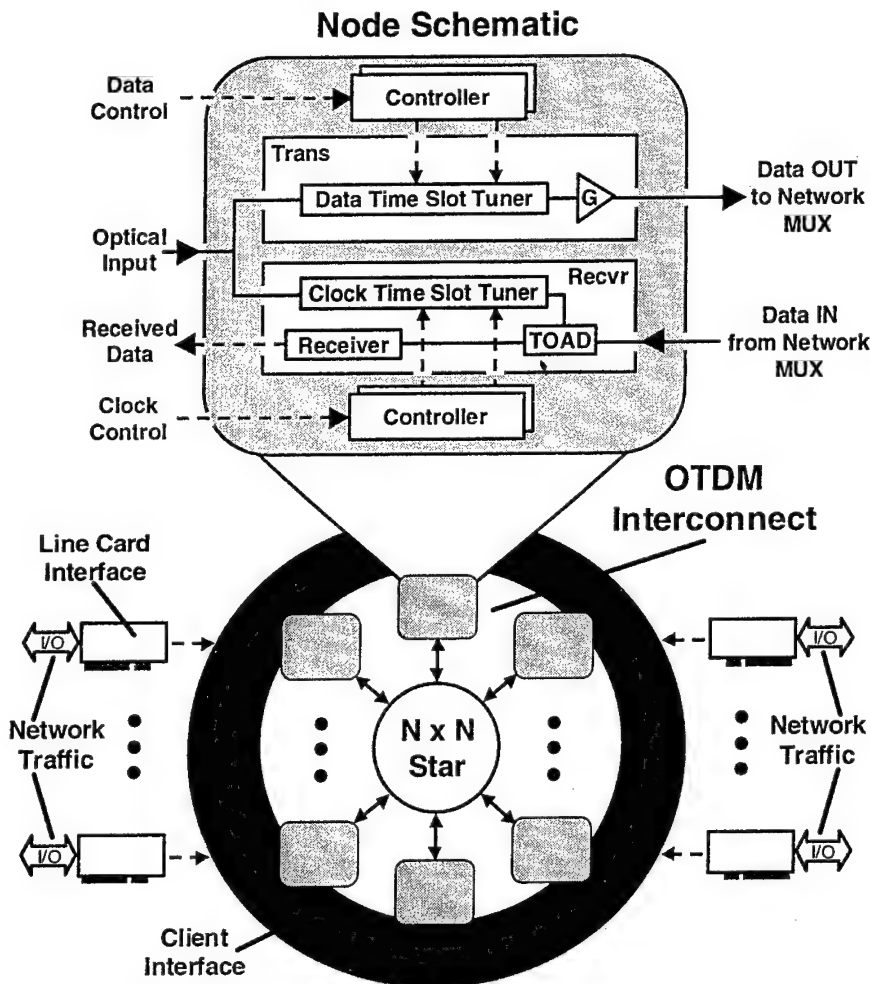


Fig. 1 OTDM router and node architecture

Recently, several experimental demonstrations [1-3] have shown that OTDM can meet many of the demanding needs of a router and a multiprocessor interconnect system which include full connectivity, low latency, and high aggregate throughput, reliability, and scalability. We report the demonstration of a testbed for a bit-interleaved 100-Gbit/s OTDM broadcast star architecture that was previously proposed [4]. Unique to our network is a highly scalable, novel node design that provides inter-channel switching within the single channel bit period (1.6 ns). By combining this hardware with a highly efficient arbitration protocol [4], near lossless channel allocation with low latency is achievable for high speed switching applications such as future all-optical routers.

II. Experimental Demonstration and Results

Fig. 2 shows the network and novel node architecture experimental setup. The two key optical components of the node are the recently developed fast tunable delay line (FTDL) [5] and the terahertz optical asymmetric demultiplexer (TOAD) [6]. A controller card residing in a workstation sends electronic NRZ data at the single channel bit rate, B , and control bits to the driver board specially designed to control the two FTDLs on the clock and data fibers. The FTDLs consist of cascaded feed-forward Mach-Zehnder fiber delay lattices designed to produce optical copies of the incoming pulse stream organized into 2^k -bit subcells spaced by T with inter-subcell bit spacing τ [5]. The two modulators controlled by the driver board select one of the $2^k \times 2^k (= N)$ time slots into which one of the copies is transmitted. The FTDLs in the node are used to transmit data into a selected time slot within the OTDM frame and align the clock with a given time slot for optical demultiplexing. Ultimately, the dimensionality of the network, N , is determined by k , the number of stages in the FTDL. The intermediate processing bandwidth, $B' (= 1/T)$, of the driver controller and the electro-optic modulators is designed to match the repetition rate of the picosecond pulsed fiber laser source and is related to the single channel bit rate as $B' = 2^k B$. Pulses are amplified by EDFAs and distributed to the individual nodes by $1 \times N$ splitters. After node data modulation and time slot selection, the data is multiplexed by precision fiber delays feeding an $N \times N$ star coupler. The high bandwidth OTDM frame is broadcast to all nodes in the network. Each node can demultiplex any single channel from the frame using an FTDL on the clock and a TOAD.

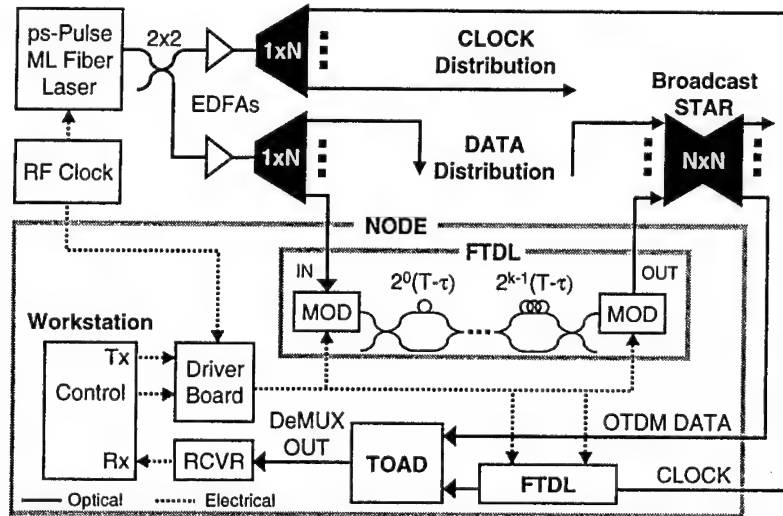


Fig. 2 Experimental OTDM computer interconnect and node architecture

In our experimental testbed, we populated 16 ($= N$) time slots in the OTDM frame by constructing 2 ($= k$) stage FTDLs. The single channel data rate was chosen to match the OC-12 rate ($B = 622.08 \text{ Mbit/s}$). The 2-ps pulsed 1550-nm fiber laser repetition rate and intermediate electronic processing bandwidth were set to the OC-48 rate ($B' = 1/T = 2.48832$

GHz). The simple electronic design of the driver board permits the rapid control of the FTDL and provides low latency, arbitrary channel selection. The driver board was constructed using 4-bit electronic multiplexers (Vitesse) and simple logic operating at the OC-48 rate. To produce an OTDM frame with an aggregate bit rate of 100 Gbit/s, $\tau = 10$ ps was chosen. Each TOAD was designed with a demultiplexing window width of about 10 ps at FWHM and a polarization splitter was used to separate data from clock at the output.

The 100-Gbit/s multiplexing and demultiplexing experimental results are shown in Fig. 3. According to the design of the FTDL, the 16 time slots in our OTDM frame are arranged in 4 subcells each containing 4 time slots spaced by 10 ps. Our network demonstration focused on one of the subcells within the frame. Fig. 3a shows the aggregate eye diagram for a subcell with multiplexed data from 4 nodes with a fixed pattern, $1 - \text{pseudorandom} - 1 - 0$, on a bandwidth limited detector (34-GHz photodetector, 50-GHz oscilloscope). Upon demultiplexing by TOADs tuned to the individual channels, each is resolved in Fig. 3b (the 4th time slot is omitted as it is 0).

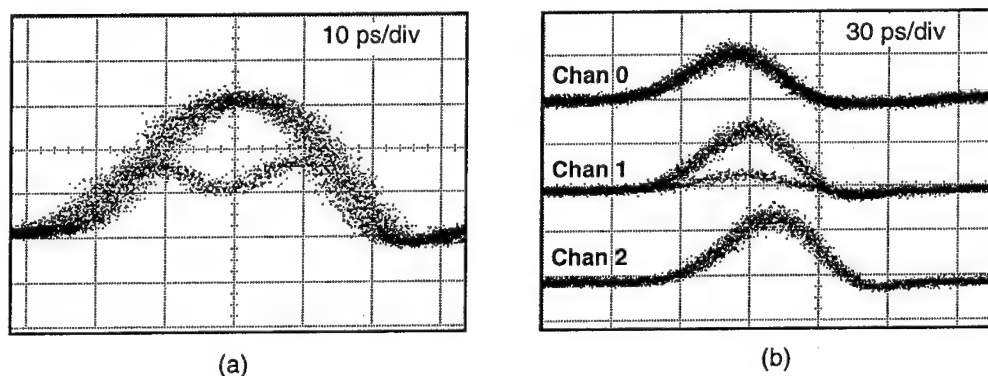


Fig. 3 100 Gbit/s multiplexed data OTDM subcell eye diagram on bandwidth limited detector, and demultiplexed TOAD output eye diagrams for three channels in subcell.

- a) 100 Gbit/s multiplexed data OTDM subcell eye diagram
- b) Demultiplexed TOAD output eye diagrams

We constructed two fully functional nodes to measure the bit error rate (BER) and demonstrate the rapid inter-channel switching capability of the network nodes using an arbitration protocol. These experiments were performed using adjacent channels in the same 100-Gbit/s subcell (Channels 0 and 1). Fig. 4a shows a plot of the BER versus the single channel average data input power at the TOAD when Chan 0 and Chan 1 were modulated with pseudorandom data. For average data and clock input powers greater than -21 dBm (13 fJ pulse energy) and -8 dBm (250 fJ pulse energy) respectively, several hours of error free operation have been achieved. Additionally, we have observed that the TOAD can provide gain to the demultiplexed signal. The inset to Fig. 4a shows the eye diagram of the data input (upper trace) and demultiplexed output (lower trace) of a TOAD demultiplexing a single channel of pseudorandom data with identical oscilloscope settings. The demultiplexed output is larger in amplitude than the input by approximately 6 dB.

The fast inter-channel switching capability of the network was also demonstrated by using a previously proposed, low latency arbitration protocol [4] and two nodes of the network. The receivers of both nodes are fixed to listen to their own time slots. Each node transmits its binary address at the single OC-12 channel rate into its own time slot. If successfully received, each node then transmits its address into the time slot of the other node. Fig. 4b shows a demonstration of the protocol using two nodes in the network whose time slots are adjacent in the 100-Gbit/s subcell. The addresses assigned to Node 0 and Node 1 were 0101 and 0111 respectively. The traces shown are the demultiplexed TOAD outputs directly from the analog output of the receivers for the two nodes. After each node successfully receives its own address, the FTDLs rapidly reconfigure within a single bit period to transmit into the time slot of the other node. Note that each node now successfully receives the address of the other in its own time slot. The FTDLs and driver board electronics are capable of tuning to any one of the 16 time slots in the network within 1.6 ns, greatly reducing the hardware latency of the protocol.

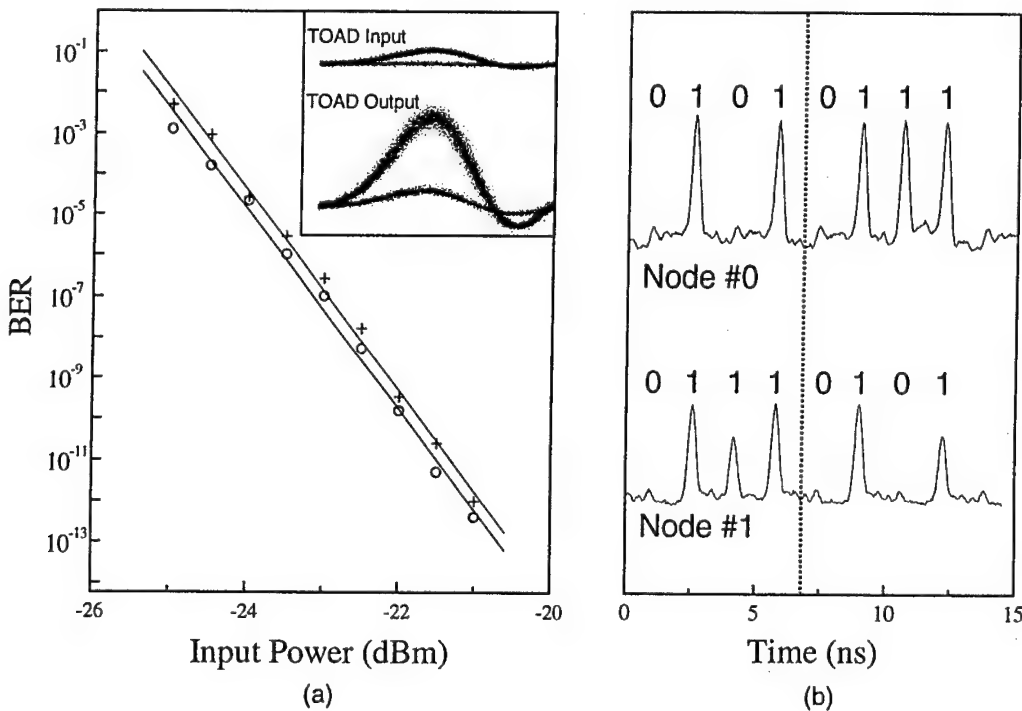


Fig. 4 BER of channels 0 and 1 against average single channel input power, and demonstration of rapid channel selection on bandwidth limited analogue detector

a) BER of channels 0 and 1 against average single channel input power

Inset: TOAD input and output eye diagrams demonstrating gain

○ -channel 0

+ -channel 1

b) Demonstration of rapid channel selection

III. Conclusion

We have demonstrated a fully connected 100-Gbit/s OTDM network architecture that offers fast switching among data channels with reliable, error free operation and low latency. Since the active components of the FTDLs do not scale with the number of nodes [5], simply adding another stage, $k = 3$, (3 dB additional loss per node), scales the interconnect up to 64 ($= N$) nodes without taxing the power budget significantly. If OC-24 ($B = 1.24416$ GHz) is chosen as the single channel data rate and 10-GHz ($= B'$) intermediate processing bandwidth electronics are used, an 80-Gbit/s interconnect with a rapid inter-channel switching speed of 800 ps is feasible. In such a 64-processor architecture, coherent crosstalk does not limit the BER performance significantly [7]. Since the demultiplexer [8] and other optical components in the node can be integrated, we believe this network is practical for future, high-speed multiprocessor interconnect systems.

Acknowledgement: This work has been supported by DARPA Contract No. F30602-97-2-0316.

References

- [1] Barry, R.A., Chan, V.W.S., Hall, K.L., Kintzer, E.S., and Moores, J.D.: 'All-optical network consortium - ultrafast TDM networks', *IEEE J. Sel. Areas Commun.*, Vol. 14, No. 5, pp. 999-1011, 1996.
- [2] Lucek, J.K., Gunning, P., Moodie, D.G., Smith, K., and Pitcher, D.: 'Synchrolan: a 40 Gbit/s optical-TDMA LAN', *Electron. Lett.*, Vol. 33, No. 5, pp. 887-888, 1997.
- [3] Tsukada, M., De Zhong, W., Matsunaga, T., Masaki, A., and Oohara, T.: 'An ultrafast photonic ATM switch based on bit-interleave multiplexing', *J. Lightwave Technol.*, Vol. 14, No. 9, pp. 1979-1985, 1996.
- [4] Nowatzky, A.G., and Prucnal, P.R.: 'Are crossbars really dead? The case for optical multiprocessor interconnect systems', *Proc. 22nd Int. Symp. On Computer Arch.*, June, 1995, Santa Margherita, Italy.
- [5] Deng, K.-L., Kang, K.I., Glesk, I., and Prucnal, P.R.: 'A 1024-channel fast tunable delay line for ultrafast all-optical TDM networks', *IEEE Photon. Technol. Lett.*, Vol. 9, No. 11, pp. 1496-1498, 1997.
- [6] Glesk, I., Sokoloff, J.P., and Prucnal, P.R.: 'Demonstration of all-optical demultiplexing of TDM data at 250 Gb/s', *Electron. Lett.*, Vol. 30, No. 4, pp. 339-340, 1994.
- [7] Deng, K.-L., Glesk, I., Kang, K.I., and Prucnal, P.R.: 'Influence of crosstalk on the scalability of large OTDM interconnects using a novel rapidly reconfigurable highly scalable time-slot tuner', *IEEE Photon. Technol. Lett.*, Vol. 10, No. 7, pp. 1039-1041, 1998.
- [8] Jahn, E., Agrawal, N., Arbert, M., Ehrke, H.-J., and Franke, D.: '40 Gbits all-optical demultiplexing using a monolithically integrated Mach-Zehnder interferometer with semiconductor laser amplifiers', *Electron. Lett.*, Vol. 31, No. 21, pp. 1857-1858, 1995.

A 20-dB 200-MHz CMOS SINGLE-TO-DIFFERENTIAL AMPLIFIER

S. Pennisi¹ - P. Tommasino² - A. Trifiletti²

¹ DEES (Dipartimento Elettrico Elettronico e Sistemistico)
UNIVERSITA' DI CATANIA
Viale Andrea Doria 6, I-95125 CATANIA - ITALY
Phone ++39.095.7382318; Fax ++39.095.330793
E-mail spennisi@dees.unict.it

² DIE (Dipartimento di Ingegneria Elettronica)
UNIVERSITA' "LA SAPIENZA" DI ROMA
Via Eudossiana 18, I-00184 ROMA - ITALY
Phone ++39.06 44585679; Fax ++39. 06 44585787
E-mail trifilo@csgb-hp2.ing.uniroma1.it

Abstract. In this communication a novel CMOS amplifier providing a differential gain higher than 20 dB and a cut-off frequency of 200 MHz is presented. The circuit includes a single-to-differential input converter that, unlike traditional approaches, avoids reducing the very high input resistance of the main differential amplifier. Moreover, thanks to an auxiliary section, an extra 6-dB gain is achieved. The whole amplifier has been designed with a 0.8- μ m *p*-well technology and uses a supply voltage of 3 V.

I. Introduction

Fully differential approach is usually required in high-frequency applications [1-5], due to its attractive and well-known properties of immunity to common-mode disturbances, rejection to parasitic couplings and increased dynamic range [6-7]. However, there are cases in which a single-ended source comes from an external filter although the differential approach must be preserved into the chip. Examples are the circuits, which are placed in cascade to RF image filters and IF filters. In addition, there are circuits, such as four-quadrant multipliers, that require pure differential signals to perform their function. In all these cases, a stage able to convert a single-ended signal into a differential one is needed.

A differential pair with one grounded input terminal can perform this basic function, if the symmetry of the output is not the main goal. At this purpose, to provide a proper bias condition to the differential pair, the most common solution is that of using the R-C network around the main amplifier as shown in Fig. 1. For sufficiently high frequencies (where capacitor C can be assumed short-circuited) the gain of the amplifier is therefore

$$A = \frac{V_{out}}{V_{in}} = -g_{m1,2} R_{1,2} \quad (1)$$

where g_{mi} is the transconductance of the *i*-th transistor. The main drawback of this approach is represented by the heavy reduction of the input resistance of the amplifier. This can represent a serious problem in many applications. Additionally, the use of high values of resistance *R* is area consuming

and worsens the noise performance of the amplifier. Moreover, as the frequency increases, the *CMRR* decreases causing in turn a reduction in the symmetry of the output.

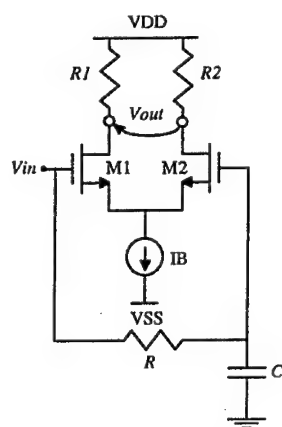


Fig. 1. Single-input differential-output amplifier with traditional input biasing

II. Proposed Solution

To overcome the previously mentioned limitations, the arrangement in Fig. 2 was developed.

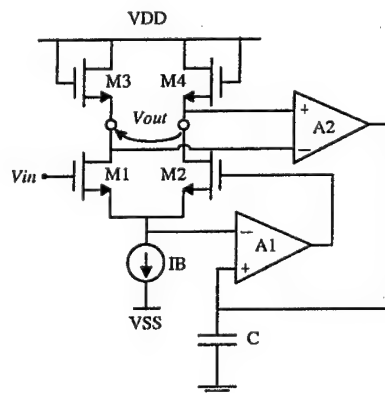


Fig. 2. Simplified schematic of the proposed amplifier

Observe that IF CMOS stages can profitably take advantage of active loads based on diode-connected transistors. Indeed, unlike bipolar transistors, amplifier gains which are set by the ratio of MOS transconductances of transistors with different dimensions can provide values higher than 20 dB at hundreds megahertz operating frequencies [8]. The DC condition of circuit in Fig. 2 is now accurately set by the auxiliary amplifier A2 which senses any deviation of the output voltage from zero, properly driving A1 and, in turn, the gate of M2. This feature reduces the output offset and compensate for any parameter mismatching in the differential stage. On the other hand, for frequencies where capacitor C can be assumed as short-circuited, the auxiliary amplifier A2 gives a virtual ground on the source of the coupled-pair M1-M2. More specifically, assuming a finite differential gain for A1 equal to A_1 and denoting with r_B the output resistance of current generator I_B , the voltage at the gate of M2 is

$$V_2 = \frac{g_{m1}A_1}{g_{m1} + \frac{1}{r_B} - g_{m2}(1+A_1)} V_{in} \approx -\frac{g_{m1}}{g_{m2}} \frac{A_1}{(1+A_1)} V_{in} \quad (2)$$

Thus, if $A_2 \gg 1$ and $g_{m1} = g_{m2} = g_{m1,2}$, a signal about equal to V_{in} but with a phase shift of 180° is provided to the gate of M2. This feature allows an extra 6-dB gain to be achieved. In fact the gain is now given by

$$A = -2 \frac{g_{m1,2}}{g_{m3,4}} \quad (3)$$

The detailed schematic of the amplifier is shown in Fig. 3, where the auxiliary amplifiers were implemented with simple differential stages with mirror active load, and where a common drain transistor, M5, with the associated bias current generator IB2 was introduced for level-shifting purposes.

A final observation concerns the stability of the loop made up of A1, the main amplifier and M5. Let r_{o1} and C_{o1} be the equivalent output resistance and capacitance at the output of A1, respectively, and C_s the total capacitance at the source of M1-M2. By breaking the loop at the gate of M5 and restoring the load conditions we find the expressions of the loop gain, $T_o = g_{m6,7}r_{o1}/2$, the dominant pole, $\omega_1 = 1/r_{o1}C_{o1}$, and the second pole $\omega_2 = 2g_{m1,2}/C_s$. Hence, to achieve a given phase margin, ϕ , we have to set $\omega_{GBW} = \omega_2/\tan \phi$, that is

$$C_{o1} = \tan \phi \frac{g_{m6,7}}{g_{m1,2}} C_s \quad (4)$$

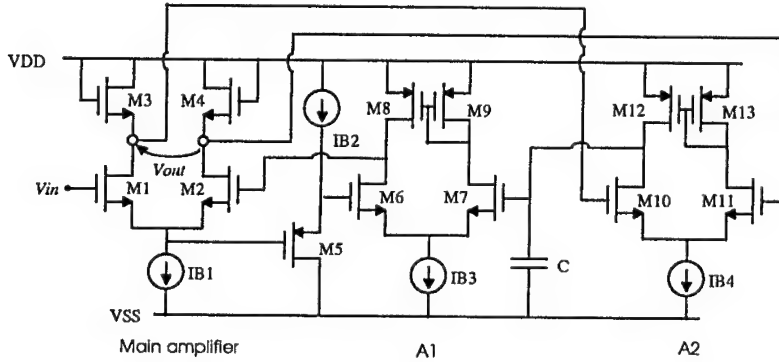


Fig. 3. Detailed schematic of the proposed amplifier

III. Simulations

The circuit in Fig. 3 was simulated with SPICE using the parameters of a $0.8\text{-}\mu\text{m}$ p -well technology. The supply voltage was set to 3 V. Transistor dimensions and bias currents are reported in Tab. I. The loop stability was ensured with these settings. Only an additional 1-pF capacitor was connected between the gate and source of transistor M5, to provide a feed-forward compensation.

Fig. 4 illustrates the frequency responses of the complete solution in Fig. 3 and that of the amplifier in Fig. 1. For the latter the same settings as in Tab. I were chosen. Moreover, $R = 10\text{ k}\Omega$ and

$C = 10$ pF was set. It can be observed that the proposed amplifier achieves a gain of 21.5 dB which is 6-dB higher than that in Fig. 1. The high cut-off frequency is higher than 200 MHz. The flat band with a gain variation of 0.5 dB ranges between 10 to 80 MHz (being the lower limit due to the chosen capacitor value of 10 pF). For the same two circuits, Fig. 5 illustrates the $CMRR'$ defined as $CMRR' = |V_{o,dm}/V_{o,cm}|$, where $V_{o,dm}$ and $V_{o,cm}$ is the differential- and common-mode output voltage, respectively. For almost all the frequency range of interest the circuit in Fig. 3 exhibits a better $CMRR'$ with a maximum difference of about 95 dB at 70 MHz.

Tab. I. Circuit Parameters

Parameter	Value
M1 M2	30/0.8
M3 M4	3/0.8
M5 M6 M7	20/0.8
M8 M9 M12 M13	6/0.8
M10 M11	2/0.8
IB1	80 μ A
IB2 IB4	20 μ A
IB3	160 μ A
C	10 pF

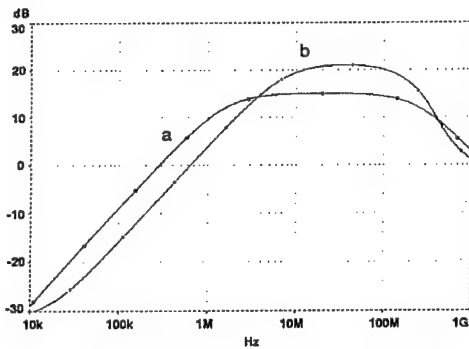


Fig. 4. Module of the frequency response for circuits in Fig. 1 (curve a) and Fig. 3 (curve b)

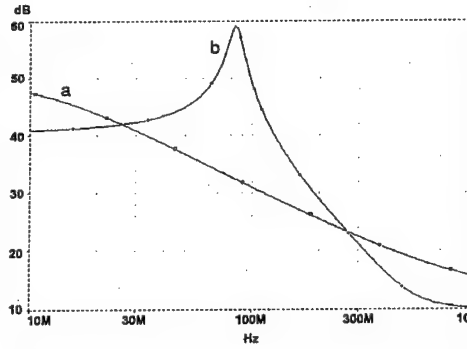


Fig. 5. $CMRR'$ for circuits in Fig. 1 (curve a) and Fig. 3 (curve b)

References

- [1] A. Rofougaran et al., "A 1 GHz CMOS RF front-end IC for a direct-conversion wireless receiver" *IEEE J. Solid State Circuits*, vol. 31, pp. 880-889, July 1996.
- [2] A. R. Shahani, D. K. Shaeffer, T. H. Lee, "A 12-mW wide dynamic range CMOS front-end for a portable GPS receiver" *IEEE J. Solid State Circuits*, vol. 32, pp. 2061-2070, Dec. 1997.
- [3] C. Toumazou, D. G. Haigh, "Level shifting differential to single ended converter circuits for GaAs MESFET implementation", *IEE Electronics Letters*, Vol. 23, No. 20, Sept. 1987, pp. 1053-1055.
- [4] N. Larciprete, F. Loriga, P. Marietti, A. Trifiletti, "A High $CMRR$ GaAs single-input to differential converter," *Proc. Eur. GaAs Symp. 96*, Paris 5-7 June 1996, paper 4C9.
- [5] S. Wu, B. Razavi, "A 900-MHz/1.8 GHz CMOS receiver for dual-band applications" *IEEE ISSCC Dig. Tech. Paper*, San Francisco, California, 1998.
- [6] R. Gregorian, G. C. Temes, *Analog MOS Integrated Circuits for signals processing*, John Wiley & Sons, 1986.
- [7] K. Laker, W. Sansen, *Design of Analog Integrated Circuits and Systems*, Mc Graw-Hill, 1994.
- [8] G. Palmisano, S. Pennisi, "High-frequency CMOS Amplifier with Improved Bandwidth Performance" in print on *IEE Electronics Letters*.

CMOS 7th-Order Equiripple-Phase Filter for PRML Read Channel Applications

Adrian Ryan, Marius Neag and Oliver McCarthy

*Circuits & Systems Research Centre (CSRC),
University of Limerick, Limerick, Ireland.
email: adrianryan@ieee.org*

Abstract. A CMOS 7th-order equiripple-phase filter for PRML read channel applications is presented. The key element of this design is a G_m cell in which the unbalanced differential pairs used to increase the linearity of the transconductor core also introduce a zero which cancels the parasitic pole of a high-impedance folded-cascode output stage. The filter was designed using a $0.35\mu\text{m}$ 3.3V process—all simulation results presented here use a supply voltage of 2.5V. The total power consumption is 110mW for a cut-off frequency of 100MHz without boost.

1. Introduction

Continuous-time filters are the only practical solution for signal frequencies above 100MHz. A prime application in this area as far as design challenges and market opportunities are concerned is the read channel for data storage systems. The combination of low-pass filter/equaliser limits the passband noise, increasing the signal-to-noise ratio, and adjusts the read-back signal to the target pulse shape. The common partial-response targets require the equaliser to provide amplification (or boost) at frequencies around 0.4 times the data rate, with programmable values up to 12dB. The cutoff frequency of the low-pass filter must be programmable with a typical tuning range of 8:1 to take advantage of the zone bit recording technique where the data rate is increased on a zone-by-zone basis as the head moves from the innermost to the outermost track.

2. Proposed Transconductor and Filter

The first and third differential pairs of the proposed transconductor of Figure 1 are deliberately unbalanced so that $(W/L)_1 = n(W/L)_2$ and $(W/L)_6 = n(W/L)_5$ while transistors M_2 , M_3 , M_4 and M_5 are identical. The mismatched differential pairs increase the linear input range [3] as illustrated in Figure 3(a). In addition, the mismatched differential pairs introduce a zero which can be used to cancel the parasitic pole created by the folded-cascode output stage [2]. Both the magnitude and phase response of the proposed transconductor is shown in Figure 3(b).

The complete results of a detailed AC analysis are not entered into here, but the general principle behind the pole-zero cancellation is outlined below. Unlike the classical case, the common-source node of a mismatched differential pair is not AC ground. It introduces a zero, z_1 , given by

$$z_1 = \frac{(g_{m16} + g_{m25})g_{m34} + 4g_{m16}g_{m25}}{(g_{m16} + g_{m25} + g_{m34})C_{ds}} + \frac{g_{ds}}{C_{ds}} \quad (1)$$

This work is supported by Silicon Systems Limited (SSL) and PEI Technologies, University of Limerick.

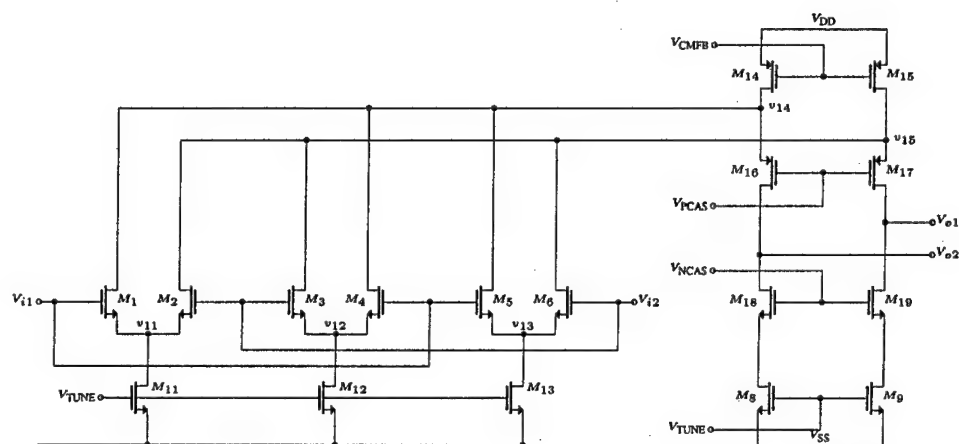


Figure 1: Transconductor consists of three differential pairs and a folded-cascode output stage.

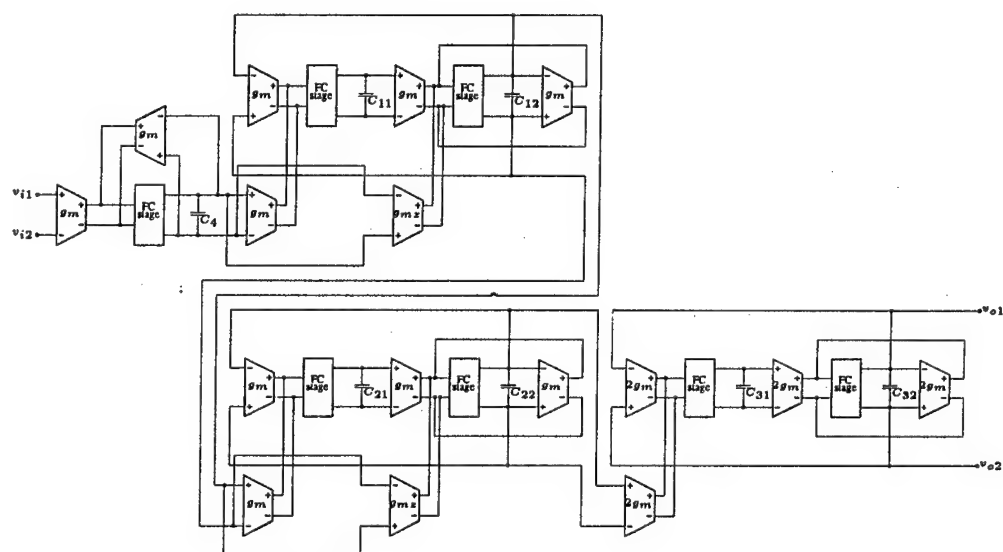


Figure 2: Filter structure consists of one single-pole stage followed by three biquadratic stages.

where g_{m16} , g_{m25} and g_{m34} represent the transconductance of transistors $M_{1,6}$, $M_{2,5}$ and $M_{3,4}$ respectively, and g_{ds} is the drain-source conductance and C_{ds} is the drain-source capacitance of transistors $M_{11,12,13}$. The location of the zero can be moved to cancel the parasitic pole created by the folded-cascode output stage through appropriate scaling of bias transistors M_{11} and M_{13} .

The filter boost is realised using two real zeros. The basic requirement is that the zeros are symmetrical with respect to the imaginary axis so as not to interfere with the group delay. However, by introducing a controlled asymmetry one can adjust the overall group delay to compensate for phase errors introduced by other blocks within the channel. The filter structure [1] shown in Figure 2 realises the zeros independently. Just one folded-cascode stage is required for each integrating node. The natural frequency of the last biquad is over twice the filter cutoff frequency which results in very low values for its integrating capacitances. To avoid this the transconductor cores of this biquad have been doubled. The complete filter transfer function is:

$$H(s) = \left(\frac{1}{1 + \frac{s}{\omega_p}} \right) \left(\frac{\omega_{o1}^2 (1 + \frac{s}{\omega_{z1}})}{s^2 + s \frac{\omega_{o1}}{Q_1} + \omega_{o1}^2} \right) \left(\frac{\omega_{o2}^2 (1 - \frac{s}{\omega_{z2}})}{s^2 + s \frac{\omega_{o2}}{Q_2} + \omega_{o2}^2} \right) \left(\frac{\omega_{o3}^2}{s^2 + s \frac{\omega_{o3}}{Q_3} + \omega_{o3}^2} \right) \quad (2)$$

3. Simulation Results

The filter was designed using a $0.35\mu\text{m}$ 3.3V process—all simulation results presented here use a supply voltage of 2.5V. The small-signal response is shown in Figure 4(a) with and without boost across the entire tuning range. The filter is tuned by varying the bias current of the G_m cells to give a tuning range of 2:1. Figure 4(b) shows the transient analysis for a 10MHz 200mV_{p-p} sine wave and the associated gain, phase and group delay. The filter THD is -44.5dB.

4. Conclusion

In this paper a CMOS 7th-order equiripple-phase low-pass filter for partial-response maximum-likelihood read channels was presented. The idea of increasing the linear input range of the transconductor using mismatched differential pairs was complemented by a novel pole-zero cancellation strategy, independent of tuning, allowing the use of a folded-cascode output stage.

5. References

- [1] Iuri Mehr and David R. Welland. A CMOS continuous-time $g_m - c$ filter for PRML read channel applications at 150 Mb/s and beyond. *IEEE Journal of Solid-State Circuits*, 32(4):499–513, April 1997.
- [2] Adrian Ryan, Marius Neag, and Oliver McCarthy. CMOS operational transconductance amplifier for PRML read channel applications. In *Proceedings of the International Symposium on Circuits and Systems*, May 1999.
- [3] Pan Wu, Rolf Schaumann, and W. Robert Daasch. A 20 MHz fully-balanced transconductance-C filter in $2\text{-}\mu\text{m}$ CMOS technology. In *Proceedings of the International Symposium on Circuits and Systems*, pages 1188–1191, May 1993.

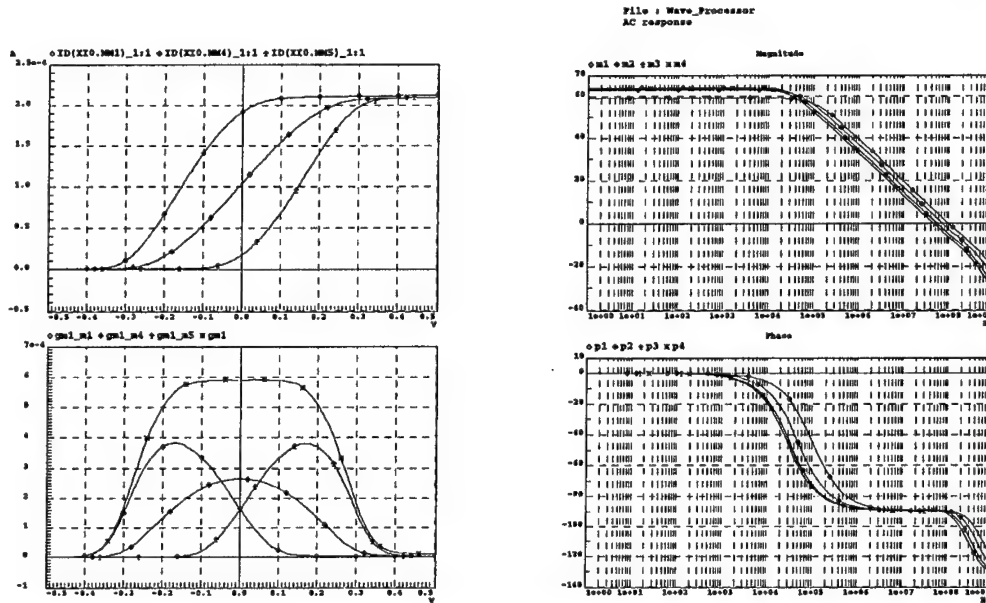


Figure 3: The plot on the left illustrates how combining three differential pairs (two of which are deliberately unbalanced) and adding their respective output currents increases the available linear input range. The small-signal plot on the right shows the magnitude and phase response of an integrator implemented with the proposed transconductor driving a 1pF load capacitance.

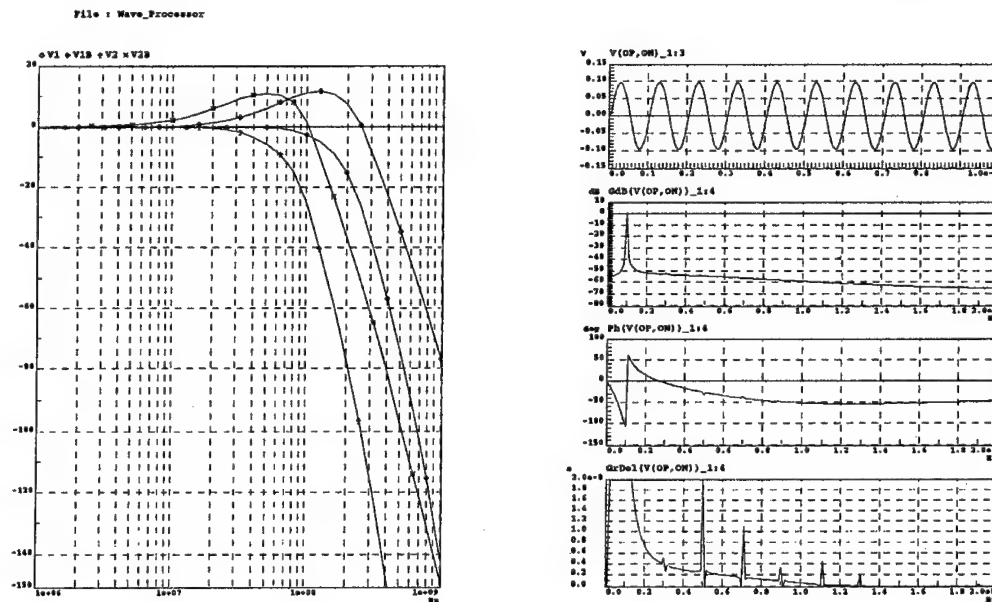


Figure 4: The plot on the left shows the magnitude response of the filter with and without boost across the entire tuning range. The plot on the right shows the filter gain, phase and group delay.

An Ultra-Low-Power Switched-Current 2-Quadrant Multiplier

A. Graupner and R. Schüffny

*University of Technology Dresden, Department of Electrical Engineering,
Mommstraße 13, 01062 Dresden, Germany,
graupner@iee.et.tu-dresden.de*

Abstract. This paper presents a switched current multiplier, dedicated for the use in highly parallel computation arrays or neural networks. It is designed for 3V supply voltage, performing 50k multiplications per second with a power dissipation of 100nW and an accuracy better than 1.5% considering the presence of possible device-mismatch.

I Introduction

Analog multipliers are fundamental functional blocks in many circuits and systems. A lot of different approaches to build analog multipliers has been investigated, one of them is the application of the translinear principle [1]. Originally formulated for bipolar devices, the translinear principle is based on the exponential voltage-to-current-transfer-characteristics of its comprising elements. Not only bipolar transistors show the required exponential behavior but MOS-transistors operating below threshold, too. Consequently, translinear circuits can be designed with a standard CMOS technology [2].

Unfortunately, translinear circuits comprising subthreshold MOS transistors are very vulnerable to device mismatch. This problem is often reported and analyzed [3] but simple solutions for this problem have not been reported yet. Alsam-Sidqui et al. [4] have proposed to use floating-gates to correct for errors caused by device mismatch. We suggest a dynamic principle to reduce the influence of device mismatch on the accuracy of a frequently used translinear multiplier circuit. Our analog multiplier cell is dedicated for the use in massive parallel computation arrays or in analog neural networks.

In section 2 a conventional translinear multiplier and the problems associated with it when implementing it in a standard CMOS-technology are reviewed. Furthermore, the general principle of our switched current multiplier is introduced. Section 3 deals with the actual implementation of the multiplier circuit and provides some simulation results.

II Translinear Multipliers

A typical translinear multiplier-circuit is depicted in Fig 1a. With the subthreshold transfer characteristics $I = I_{D0} \exp((V_{GS} - V_T)/nU_T)$ of a transistor in saturation, where I_{D0} is a current constant, V_{GS} the gate-source-voltage, V_T the threshold voltage, n the subthreshold slope factor and U_T the thermal voltage, the analysis of the translinear loop yields:

$$I_1 \cdot I_3 = I_2 \cdot I_4. \quad (1)$$

As one can see a multiplication or division of several unipolar currents can easily be performed using this circuit.

Employing differential signals this circuit is suitable for a two-quadrant operation as well. The first input signal then is the difference of the currents $I_1 - I_4$ and the output signal is represented by the current-difference $I_2 - I_3$. Using some basic algebra equation (1) can be

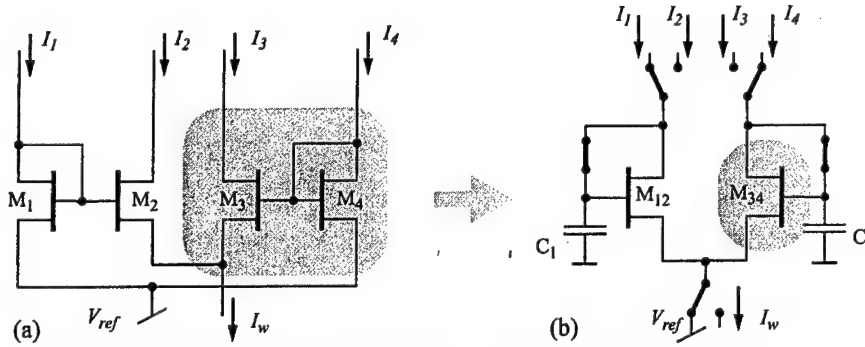


Fig. 1: (a) A translinear multiplier cell and (b) its switched-current counterpart transformed as follows:

$$I_2 - I_3 = \frac{I_1 - I_4}{I_1 + I_4} \cdot (I_2 + I_3). \quad (2)$$

As can be seen, the second input signal is the sum-current $I_w = I_2 + I_3$.

There are several drawbacks associated with this multiplier. As stated in the introduction this circuit-topology is very vulnerable to device-mismatch. Mismatch describes the effect that two identical designed devices have random differences in their behavior. In the subthreshold-operation device mismatch can be modeled by a variation of the current-constant I_{D0} from its nominal value [3]. As the mismatch decreases with increasing transistor area, the influence of mismatch can be reduced by employing large devices. However, to achieve a high accuracy the devices would have to be prohibitively large in area.

In order to analyze the influence of mismatch equation (1) is reformed again but the current constant I_{D0} is no longer assumed to be equal in all devices:

$$\frac{I_1}{I_{D0,1}} \cdot \frac{I_3}{I_{D0,3}} = \frac{I_2}{I_{D0,2}} \cdot \frac{I_4}{I_{D0,4}}. \quad (3)$$

Accordingly, the mismatch of the current constants yields a constant-gain error for the translinear loop. For the differential-signal case the device-mismatch entails a non-linearity error:

$$I_2 - I_3 = (I_2 + I_3) \cdot \frac{(I_1 - I_4)(\epsilon + 1) + (I_1 + I_4)(\epsilon - 1)}{(I_1 + I_4)(\epsilon + 1) + (I_1 - I_4)(\epsilon - 1)} \quad \text{with} \quad \epsilon = \frac{I_{D0,2} \cdot I_{D0,4}}{I_{D0,1} \cdot I_{D0,3}}. \quad (4)$$

Further limitations of this multiplier topology are due to the finite output resistance of the transistors, the body effect and the voltage-dependency of the slope-factor n . These limitations are common for all translinear subthreshold MOS circuits and discussed elsewhere, see [2], [5].

The idea for the dynamic approach is adapted from the current-copier-cell [6], where two devices are dynamically replaced by one device. The functional principle of the proposed multiplier is depicted in Fig. 1b. In the first clock cycle the transistors M12 and M34 perform the function of the outer transistors M1 and M4. When equilibrium is reached the input currents I_1 and I_4 equal the drain-currents of M12 and M34 respectively and the voltages across the capacitors C1 and C2 have an adequate value with respect to the common source voltage V_{ref} . In the

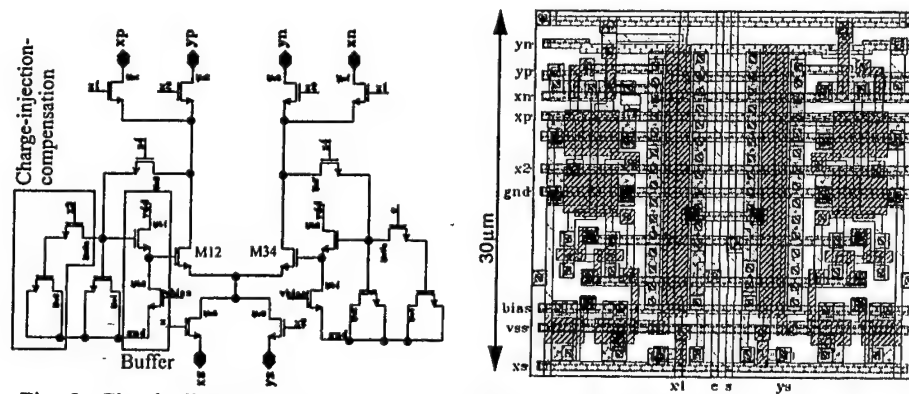


Fig. 2: Circuit diagram and layout of the proposed multiplier

second clock cycle all switches are toggled and the gate nodes are disconnected from the rest of the circuit. Thus, the voltages across the capacitors remain constant and store the input signal. The transistors M12 and M34 are connected to accomplish the function of the inner transistors M2 and M3. The second input signal is applied as current I_w into the common source node whereas the difference of the drain-currents of M12 and M34 represents the adequate output value.

This circuit operating in discrete time performs the same functionality as its time-continuous counterpart without being sensitive to device-mismatch: As the function of the transistors M1/M2 and M3/M4 are accomplished by the same devices M12 and M34 respectively there is no mismatch between the transistors M1-M2 and M3-M4. With $I_{D0,1} = I_{D0,2}$ and $I_{D0,3} = I_{D0,4}$ the error term ϵ of equation (3) becomes unity. Thus, this dynamic multiplier is inherently insensitive to device mismatch.

III Actual Circuit Implementation

The functional principle of the dynamic multiplier is shown in Fig. 1b. The main inaccuracies of an implementation are caused by the parasitic capacitances of MOS-transistors. From the first to the second clock cycle the drain and source voltages of M12 and M34 are changing. According to the capacitive divider formed by the transistor's overlap capacitances and the storing capacitors C1 and C2 the voltages across these capacitors change. As these voltages are storing the information the signal becomes corrupted. In our implementation the storing nodes are decoupled by means of source-followers.

A second problem is the clock-feedthrough of the switches connected with the storing capacitors. When these transistors switch off they release their channel charge. Thus, a part of the channel charge flows onto the storage-capacitors and corrupts the stored signal. To overcome this problem a compensation technique known from dynamic current mirrors is employed [7].

The complete circuit diagram is shown in Fig. 2. The translinear elements have a rather high W/L-ratio of $W/L=10$ because the subthreshold operation of the transistors for tail currents up to 20 nA has to be assured. The storage capacitors are implemented as gate-substrate capacitors. The source-follower and the transistors for the charge-injection compensation are marked in the circuit diagram. All switches are minimum-sized devices. This circuit was implemented using a 0.6 μm digital standard technology. As the layout in Fig. 2 illustrates, the

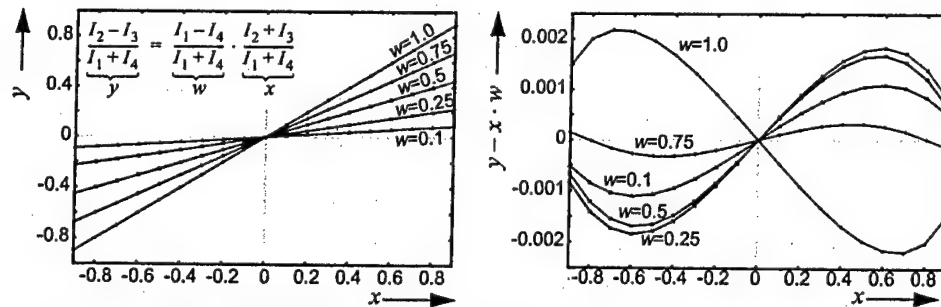


Fig. 3: Simulated multiplication result and multiplication error.

circuit is approximately as small as a basic digital standard cell ($30 \cdot 31 \mu\text{m}^2$).

A simulation result with no device-mismatch present is provided in Fig. 3. A small residual error of some 0.2% due to bulk-effect and finite output resistance of the transistors remains. By means of Monte-Carlo-simulations the maximum error was determined to be smaller than 1.5%. The main error is caused by the device mismatch of the switch-compensation transistor pair.

IV Conclusion

In this paper an accurate translinear two-quadrant-multiplier is presented. It can process up to 50.000 multiplications per second and dissipates less than 100nW of power. If the signal is stored up to 20ms the residual error is always less than 1.5% which equals an accuracy of 5 bit. For the derivation of this maximum error the possible mismatch of all devices was taken into account.

Acknowledgment

This work was supported by the Deutsche Forschungsgemeinschaft (DFG), Sonderforschungsbereich SFB358, project A7.

References

- [1] B. Gilbert, "Current-mode Circuits From A Translinear Viewpoint: A Tutorial", in C. Toumazou, F. I. Lidgley and D. G. Haigh (eds.), *Analogue IC Design: The Current Mode Approach*, Peter Pergrinus, London, 1990, Reprint 1993.
- [2] A. G. Andreou and K. A. Boahen, "Translinear Circuits in Subthreshold MOS", *Analog Integrated Circuits and Signal Processing*, Vol. 9, pp. 141-166, 1996.
- [3] A. Pavasovic, A. G. Andreou and C. R. Westgate, "Characterisation of Subthreshold MOS Mismatch in Transistors for VLSI Systems", *Analog Integrated Circuits and Signal Processing*, Vol. 6, pp. 75-85, 1994.
- [4] A. Aslam-Siddiqi, W. Brockherde, M. Schanz and B. J. Hosticka, "A 128-Pixel CMOS Image Sensor with Integrated Analog Nonvolatile Memory", *IEEE Journal of Solid-State Circuits*, Vol. 33, No. 10, 1998.
- [5] A. Graupner, *Entwurf und Modellierung von Subthreshold-Schaltungen für hochparallele VLSI-Systeme*, Diploma thesis, TU Dresden, 1998.
- [6] S. J. Daubert, D. Vallancourt and Y. P. Tsividis: "Current copier cell", *Electronics Letter*, vol. 24, pp. 1560-1562, 1988.
- [7] D. M. W. Leenaerts, G. R. M. Hamm, M. J. Rutten and G. G. Persoon, "High Performance Switched-Current Memory Cell", *Proc. ECCTD*, 1997, Budapest, pp. 234-239.

Sixth-Order Switched-Capacitor Bandpass Filter with Reduced Capacitor Spread

Nicolay A. Radev¹, Kantscho P. Ivanov¹, Simeon S. Vladov¹

¹ *Department of Theoretical Electrotechnics, Faculty of Automation,
Technical University of Sofia, 1756 Sofia, Bulgaria,
ivanovkp@vmei.acad.bg*

Abstract. A sixth-order SC bandpass filter based on conventional SC integrators is considered. The capacitor spread is reduced from 87.1 to 11.644 by replacing two of the conventional integrators by very-large-time constant (VLT) integrators. Subsequently the integrators of the last filter configuration are replaced by gain-and-offset-compensated SC integrators for reducing the influence of op amp imperfections. The effect of these consecutive replacements on the amplitude response and on the output offset voltage of the filter is investigated.

I. Introduction

In order to compare two different filter designs the capacitor spread is most often used as performance criterion. Large capacitor ratios (larger than 30) are difficult to achieve with any accuracy in integrated form [1]. To reduce the capacitor spread in SC circuits different techniques have been proposed [2-4]. Virtually all area-efficient implementations for VLT integrators generally suffer from higher sensitivity to finite amplifier gain and the offset voltages of the op amps.

II. Sixth-order bandpass SC filter with conventional integrators

Fig.1 shows a sixth-order bandpass SC filter [1], which is scaled for maximum

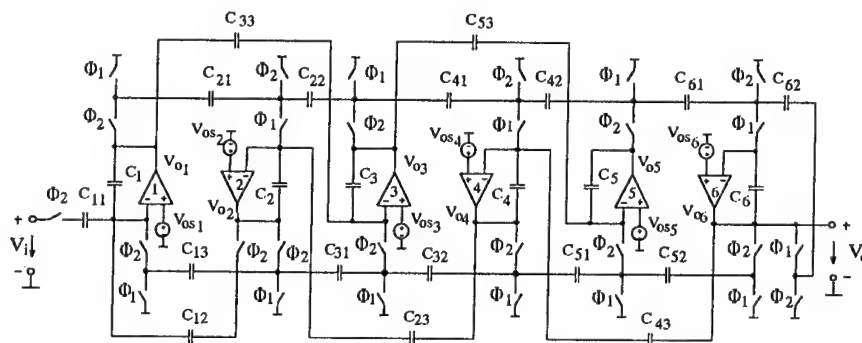


Fig 1 Sixth-order SC bandpass filter

dynamic range and output swing. The normalized capacitor values are :

$C_1=87.10$; $C_2=71.01$; $C_3=87.10$; $C_4=87.10$; $C_5=87.10$; $C_6=68.26$; $C_{11}=84.20$; $C_{21}=11.90$;
 $C_{31}=9.53$; $C_{41}=13.04$; $C_{51}=17.03$; $C_{61}=18.00$; $C_{12}=72.17$; $C_{22}=16.70$; $C_{32}=11.61$;

$C_{42}=7.82$; $C_{52}=8.73$; $C_{62}=9.75$; $C_{13}=1.00$; $C_{23}=22.26$; $C_{33}=7.48$; $C_{43}=3.67$; $C_{53}=25.39$. The capacitor spread is 87.10. The waveform of the two nonoverlapping clock signals Φ_1

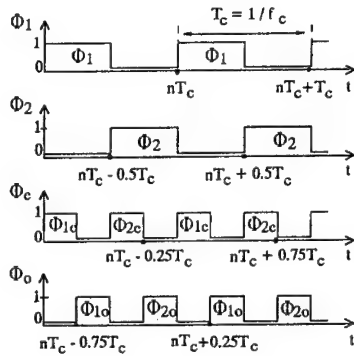


Fig 2 Waveform of the clock

and Φ_2 is sketched in Fig.2. For the sampling frequency $f_c = 100$ kHz the ideal filter passband characteristics are: lower passband edge 300 Hz, upper passband edge 3400 Hz, maximum passband ripple $|\Delta a| < 0.4$ dB.

Let us suppose that the capacitors and the switches are ideal. The op amps are assumed to be ideal except for a finite voltage gain described by the relation $A(j\omega) = -A_0$ and a nonzero input-referred dc offset voltage V_{os} .

The amplitude responses of the filter in the passband for two cases are shown in Fig.3:

- (i) $H_{id}(f)$ - ideal op amps with $A_0 \rightarrow \infty$;
- (ii) $H_c(f)$ - nonideal op amps with $A_0 = 1000$.

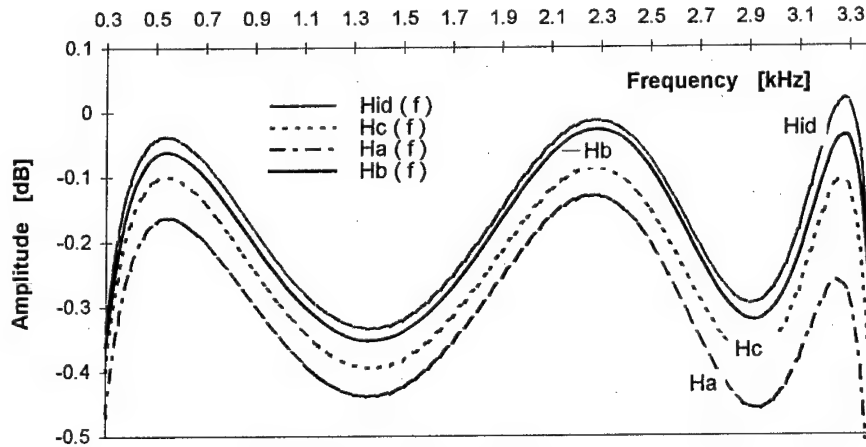


Fig 3 Amplitude responses of the filter

The output offset voltage $V_{oo, id}^1$ in steady state for $V_i = 0$ and $A_0 \rightarrow \infty$ is:

$$V_{oo, id}^1 = \frac{C_{31}C_{51}}{C_{32}C_{52}}V_{os1} - \frac{C_{51}}{C_{52}}\left(1 + \frac{C_{31}}{C_{32}}\right)V_{os3} + \left(1 + \frac{C_{51}}{C_{52}}\right)V_{os5} \quad (1)$$

This gives $V_{oo, id}^1 = 1.601 V_{os1} - 3.552 V_{os3} + 2.951 V_{os5}$. By computer simulation for $A_0 = 1000$ one obtains $V_{oo, A_0}^1 = 1.596 V_{os1} + 0.004 V_{os2} - 3.540 V_{os3} - 0.009 V_{os4} + 2.940 V_{os5} + 0.01 V_{os6}$.

III. Sixth-order bandpass SC filter with reduced capacitor spread

The capacitor spread can be reduced by replacing the first and the fourth conventional integrators in Fig.1 by two VLT integrators, proposed in [2,3]. The circuit diagram of the resulting filter is shown in Fig.4. The required clock signals are sketched in Fig.2.

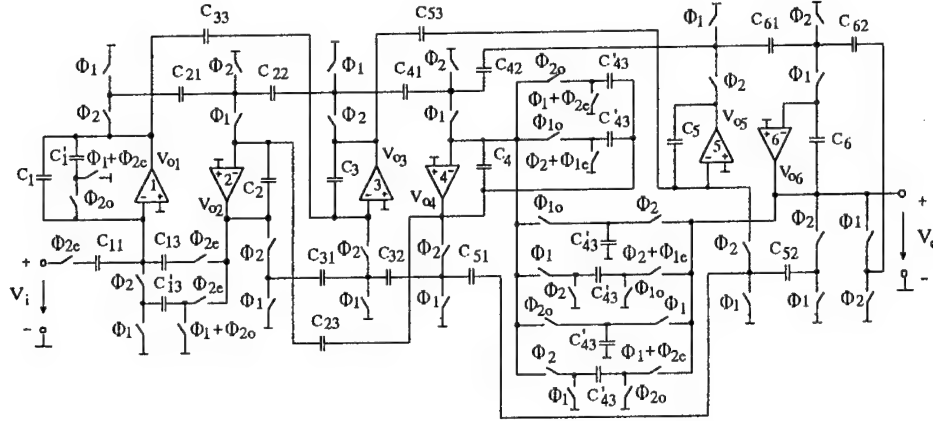


Fig 4 Sixth-order bandpass SC filter with reduced capacitor spread

The capacitance values C'_{13} and C'_{43} calculated from the design equations

$$\frac{C'_{13}{}^2}{C_1(C_1 + C'_{13})} = \frac{C'_{13}}{C_1} = \frac{1}{87.10}, \quad \frac{C'_{43}{}^2}{C_4(C_4 + C'_{43})} = \frac{C'_{43}}{C_4} = \frac{3.67}{87.10} \quad (2)$$

are: $C'_{13} = 9.846122$; $C'_{43} = 19.807875$. Hence, the capacitor spread is reduced to $C_3/C_{33} = 11.644$.

The maximum passband ripple of the magnitude response $H_a(f)$ (Fig.3) for $A_0 = 1000$ is $\Delta a = -0.652$ dB at frequency $f = 3.4$ kHz.

The output offset voltage V_{oo}^1 in steady state is :

$$(i) \quad V_{oo id}^1 = \frac{C_{31}C_{51}}{C_{32}C_{52}}(1 + \frac{2C_1}{C'_{13}})V_{OS1} - \frac{C_{51}}{C_{52}}(1 + \frac{C_{31}}{C_{32}})V_{OS3} - \frac{2C_{23}C_{31}C'_{43}C_{51}}{C_{32}C_{52}C_2(C_4 + C'_{43})}V_{OS4} + \\ + (1 + \frac{C_{51}}{C_{52}})V_{OS5} = 29.93V_{OS1} - 3.552V_{OS3} - 0.186V_{OS4} + 2.951V_{OS5}; \quad (3)$$

$$(ii) \quad V_{oo Ao}^1 = 29.467V_{OS1} + 0.0708V_{OS2} - 3.493V_{OS3} - 0.613V_{OS4} + 2.903V_{OS5} + 0.046V_{OS6}.$$

Compared to the original structure (Fig.1) the offset term, due to the first VLT integrator is $(1 + 2C_1/C'_{13})$ times larger. For reducing the effects of op amp imperfections (A_0 and V_{OS}) the first and the fourth VLT integrators in Fig. 4 are replaced by gain-and-offset-compensated VLT integrators, proposed by Nagaray and Lin [2,3]. All the others conventional integrators are replaced by FGI- integrators [5]. The circuit diagram of the resulting filter is shown in Fig. 5 (without the elements enclosed in broken line).

The values of the holding capacitances Ch_i ($i = 1 \div 6$) are $Ch_i = C_{33} = C_{min} = 7.48$.

The maximum passband ripple of the magnitude response $H_b(f)$ (Fig.3) for $A_0 = 1000$ is $\Delta a = -0.361$ dB at frequency $f = 300$ Hz. The output offset voltage V_{oo}^{10} in steady state is :

$$(i) \quad V_{oo id}^{10} = -\frac{C_{31}C_{51}}{C_{32}C_{52}} \left[(1 + \frac{C_{23}}{C_2})V_{OS2} - \frac{C_{23}}{C_2}V_{OS4} + \frac{C_{23}}{C_2} \frac{C'_{43}}{C_4 + C'_{43}}V_{OS6} \right] = \\ = -2.1032V_{OS2} + 0.502V_{OS4} - 0.093V_{OS6}; \quad (4)$$

$$(ii) \quad V_{oo Ao}^{10} = 0.03V_{OS1} - 2.101V_{OS2} - 0.0058V_{OS3} + 0.500V_{OS4} + 0.0047V_{OS5} - 0.0925V_{OS6}.$$

The influence of the offset voltage V_{OS2} can be reduced by the insertion of a gain-and-offset-compensated sample-and-hold-buffer, enclosed in broken line (Fig. 5).

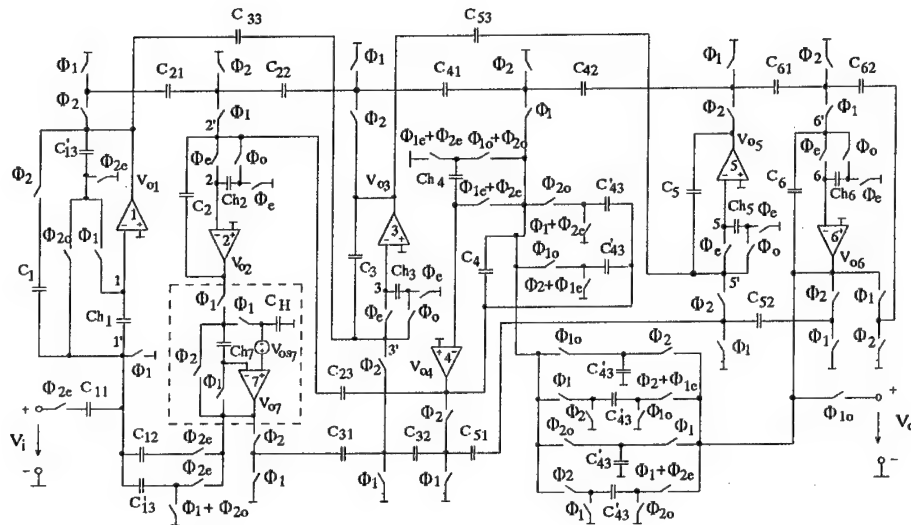


Fig 5 Gain-and-offset compensated bandpass SC filter with reduced capacitor spread

The magnitude response is computed for nonideal op amps with $A_0=1000$. The maximum passband ripple is $\Delta a = -0.369$ dB at frequency $f=300$ Hz. The corresponding curve practically converges on the scale chosen to the response $H_b(f)$.

The output offset voltage in steady state is :

- (i) $V_{oid}^1 = 0$;
- (ii) $V_{oAo}^1 = 0.03V_{OS1} - 0.0058V_{OS3} - 0.00015V_{OS4} + 0.0047V_{OS5} - 0.00006V_{OS6}$.

IV Conclusion

A 6th-order SC bandpass filter with reduced capacitance spread has been presented. Gain-and-offset-compensation technique was applied to achieve improvement in performance.

References

- [1] Murlat, A., G.S.Moschytz, "Computer Design and Optimization of Switched-Capacitor Ladder Filters Using Simple Performance Measures", *Proceedings of the ECCTD*, 1993, Davos, Switzerland, pp.1293-1298.
- [2] Nagaraj, K., "Parasitic-Insensitive Area-Efficient Approach to Realizing Very Large Time Constants in Switched-Capacitor Circuits", *IEEE Transactions on Circuits and Systems*, vol.36, No9, pp. 1210-1216, 1989.
- [3] Lin, J., W.-H. Ki, T. Edwards, S. Shamma, "Analog VLSI Implementations of Auditory Wavelet Transforms Using Switched-Capacitor Circuits", *IEEE Transactions on Circuits and Systems -I: Fundamental Theory and Applications*, vol.41, No9, pp. 572-583, 1994.
- [4] Enz, C.C., G.C.Temes, "Circuit Techniques for Reducing the Effects of Op-Amp Imperfections: Autozeroing, Correlated Double Sampling, and Chopper Stabilization", *Proceedings of the IEEE*, vol.84, No11, pp. 1582-1614, 1996.
- [5] Shafeeu, A., K.Betts, T.Taylor, "Novel amplifier gain insensitive SC integrator with same sample correction properties", *Electronics Letters*, vol.27, No24, pp. 2277-2279, 1991.

A Technique For Improving Gain/Phase Error Cancellation In LINC Transmitters

H.S. Al-Raweshidy and S. O. Ampem-Darko

Communication Systems Division
Electronic Engineering Laboratory
University of Kent at Canterbury
Canterbury, Kent CT2 7NT, UK
E-mail: H.Al-Raweshidy@ukc.ac.uk
Fax: (+44) 1227456084

Abstract: The application of spectral efficient modulation schemes, particularly in cellular radio systems requires linear but highly efficient power amplifiers. Linear amplification with non-linear components (LINC) is a promising linearisation technique for improving power amplifier efficiency. In this paper we present a novel technique for correction of gain/phase errors inherent in LINC transmitters. The technique employs a feedback signal to generate an error signal with the aid of a reference-modulated signal. A direct search algorithm is used to estimate the gain/phase imbalance between the two amplifying branches for correction. Computer simulation model is used to verify the validity of the technique. Simulation results indicate out-of-band radiation suppression by 10dB for a gain imbalance of 1dB.

I. INTRODUCTION

The linear amplification with non-linear components (LINC) design method is one of the promising techniques to achieve both power and spectral efficiency [1-4]. However, a major drawback in this technique is its inherent sensitivity to gain and phase imbalances between the two-amplifier branch [2]. The LINC transmitter linearity relies on the fact that the AM-AM and AM-PM characteristics and the operating point of the two-amplifiers are identical. This is not always the case in practise due to thermal drift, difference in electrical length and ageing. Most particularly quantisation error in the signal component separator (SCS) may cause changes in the amplitude of the input signals to the two amplifier branches, resulting in imbalance in amplifier gain [3]. Depending on the amplifier characteristics, any change in gain may introduce some degree of phase error between the two branches. In [4] a method for the correction of the phase error was proposed and in [2] a technique was proposed for correcting both gain and phase along the amplifier branches. The good idea in the latter technique is that it relies on the information of the out-of-band emission for the correction of the gain and phase imbalances. However, the drawback in this technique is the accuracy in optimisation of the complex gain and phase imbalances. Particularly, if the phase error in this system is a result of a combination of both gain imbalance and difference in electrical length. Caution must be taken in order not to compensate of out-of-band emission at the expense of less distorted in-band signal. In this paper, however, we propose a new technique for cancelling mainly the gain imbalance and automatically correcting the resulting phase error between the two-amplifier branches. In this technique we assumed there is no phase error due to difference in electrical length between the two amplifier branches.

The paper is organised as follows. In section II, we introduce the principles of the LINC transmitter design. In section III, we present a mathematical description of the proposed gain/phase error correction scheme. Then in section IV, the simulation

model of the LINC transmitter used to verify the validity of the proposed method is described. Finally, in section V, we present simulation results and discussion followed by conclusion in section VI.

II. PRINCIPLES OF LINC TRANSMITTER

The principle of LINC transmitter design is based on the fact that the complex envelope of the RF bandpass signal represented as

$$s(t) = r(t)e^{j\phi(t)}; 0 < r(t) \leq r_{\max} \quad (1)$$

can be split into two constant envelope signals

$$s_1(t) = s(t) + e(t) \quad \text{and}$$

$$s_2(t) = s(t) - e(t) \quad (2)$$

such that $|s_1(t)| = |s_2(t)| = r_{\max}$ and

$$s_1(t) + s_2(t) = 2s(t) \quad (3)$$

where $e(t)$ is a signal, quadrature to the source signal $s(t)$ [3] and is given as

$$e(t) = js(t)\sqrt{\frac{r_{\max}^2}{|s(t)|^2} - 1}; |e(t)| \leq r_{\max} \quad (4)$$

The two constant envelop signals in (2) are amplified separately in two amplifier branches and recombined to give the output signal as in (3).

If there is no gain or phase imbalance between the two amplifier branches then during recombination the source signals, $s(t)$ in (2) will add up in-phase whereas the quadrature signals $e(t)$ cancel out to give the output signal

$$S_o(t) = 2GS(t) \quad (5)$$

Where G is the small signal gain of each amplifier branch. If a gain imbalance of g and a corresponding phase error $\theta(g)$ exist between the amplifier branches, then the output signal, from (3) and (5) is given as

$$S_o(t) = G[S(t)(1 + (1 + g e^{j\theta(g)}) + e(t)(1 - (1 + g e^{j\theta(g)}))] \quad (6)$$

In the frequency domain the signal components in (2) consist of a narrowband source signal, $S(f)$ and a wideband signal, $E(f)$. In event of gain/phase imbalance, the latter spreads out into the adjacent band [2]. It is clear from (6) that the gain/phase imbalance introduces both in-band distortion and out of band radiation. Therefore, the transmitter output could be split with a 3dB-coupler attenuated by one of the amplifying branch linear gain (i.e. G) and lowpass filtered to recover the distorted source signal as

$$L(f) \approx S(f)(1 + \frac{g}{2} \cdot e^{j\theta(g)}) \quad (7)$$

The difference signal is obtained by subtracting (1) from (7). Here, we employed the criterion of uniform approximation. Thus, within the operation region of (1) the magnitude of difference signal is given as

$$|L(t) - S(t)| \leq \Delta \quad (8)$$

where Δ is a constant value, which in this particular case depends on g and r_{\max} and is given as

$$\Delta = \frac{g}{2} \cdot r_{\max} \quad (9)$$

Clearly, from (9) a simple search technique can be used to optimise the gain imbalance, g under the constrain that

$$|L(t) - s(t)|_{\max} \approx \frac{g}{2} \cdot r_{\max} \quad (10)$$

This technique is based on a similar method used in [5] for Cartesian loop lineariser. The main difference between this technique and that in [5] is that we combined what looks like the Cartesian loop lineariser with the LINC transmitter design with the aim of controlling the gain/phase difference between the two amplifier branches. Furthermore, in this method, the error signal generation and correction will be carried out at the RF stage without down conversion.

IV. SIMULATION MODEL

The baseband simulation model used is as shown Fig.1. The source signal is QPSK modulated and filtered with a square-root raised cosine filter with a roll-off factor 0.35. The sampling rate was 16 times the symbol rate (24.3kHz). The source signal is split into two constant envelope signals by the signal component separator (SCS), the principle of operation of which is in accordance with (4) and (2) for amplification in

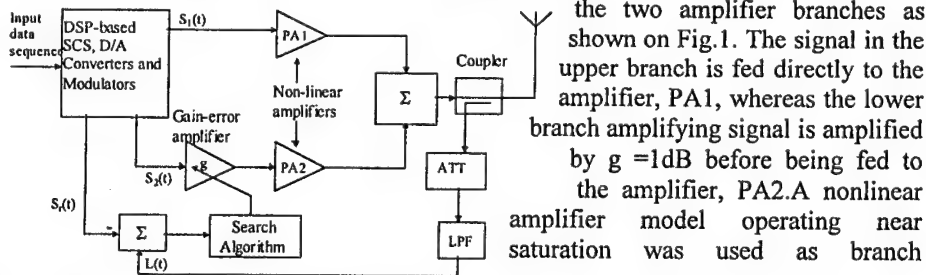


Fig.1. The baseband simulation model of the LINC transmitter with the linearisation technique.

the two amplifier branches as shown on Fig.1. The signal in the upper branch is fed directly to the amplifier, PA1, whereas the lower branch amplifying signal is amplified by $g = 1\text{dB}$ before being fed to the amplifier, PA2. A nonlinear amplifier model operating near saturation was used as branch

amplifiers in the simulation. The amplifiers output are combined and coupled into a variable attenuator

(ATT), which attenuates the signal by approximately the amplifier linear gain (G) and then fed to a fifth order IIR Butterworth lowpass filter (LPF) to suppress the wideband signal. The filter bandpass edge attenuation is 3dB with sampling frequency set at twice the symbol rate. A reference-modulated source signal is then subtracted from

the filtered signal to generate an error signal as shown in Fig.1. A direct search algorithm is used to estimate the gain/phase imbalance for correction in the lower amplifier branch. The search algorithm used here consist of programming codes based on (10), directly estimates the gain error g by determining the maximum magnitude reached by dropping previous values. The algorithm rapidly converges to the value g .

V. SIMULATION RESULTS AND DISCUSSION

The simulation results assume negligible distortion due to other RF components (i.e. mixers, filters). The results are depicted in Fig.2a and Fig.2b. Figure 2a shows the power spectral density (PSD) of the transmitter output when a gain imbalance of 1dB was introduced in the lower amplifier branch without the correction circuit. Figure 2b shows the PSD when the correction technique was used. As we can see a suppression

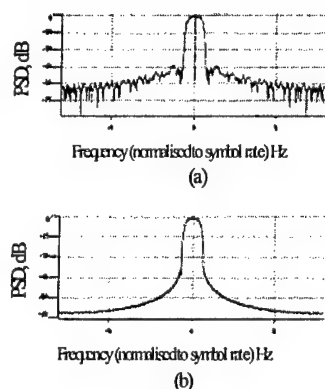


Fig.2. *a and b are power spectral density of the LINC transmitter output without and with the*

amplifier branches. The accuracy of this method suggests that separate circuitry for correction of gain imbalance and phase error, due to difference in electrical length can be used where necessary, depending on the application, design complexity and cost.

of the spectral re-growth by approximately 10dB was achieved using the technique. Obviously, this method reduces the out-of-band radiation and in-band distortion as well as the noise level at the transmitter output. The technique will consequently improve the performance in terms of adjacent channel radiation and the signal to noise ratio in communication systems employing LINC transmitters.

VI. CONCLUSION

A technique for improving the gain/phase imbalance correction in LINC transmitters has been presented. A 10dB suppression of out-of-band emission was achieved with a gain imbalance up to 1dB between the

References

- 1 Cox, D.C, "Linear amplification with nonlinear components", IEEE Trans., COM-22, pp., 1942-1945, 1974.
- 2 Sundström, L., "Automatic adjustment of gain and phase imbalances in LINC transmitters", Electron. Lett., 31, (3), pp. 155-156, 1995.
- 3 Sundström, L., "The effect of Quantization in a Digital Signal Component Separator for LINC Transmitters", IEE Trans., VT-45, (2), pp. 346-352, 1996.
- 4 Tomisato, S., CHIBA, K., and MUROTA, K., "Phase error free LINC modulator", Electron. Lett., 25, (9), pp. 576-577, 1989.
- 5 Mansell, A.R., and Bateman, A., "Transmitter linearisation using composite modulation feedback", Electron. Lett. 32, (23), pp. 2120-2121, 1996.

Asymmetric Throughput In Optical Wireless Links

A.C. Boucouvalas and P. Barker

*Bournemouth University,
Design Engineering and Computing,
Fern Barrow, Poole, Dorset, BH12 5BB
tboucouv@bournemouth.ac.uk*

Abstract: In this work we study optical wireless asymmetric communication. Specifically the work is focused on IrDA wireless links and third party interference to an already established optical link. We derive bit error rates at the physical layer, and furthermore, we calculate the average throughput of IrDA link access protocol (IrLAP) under the influence of third party interference. Results of the BER and IrLAP throughput degradation are presented.

Introduction

Wired communication links are mostly designed to be symmetric. By symmetry here we mean that bi-directional communications over the same link are of the same quality. Quality here is measured by low bit error rate (BER) and in this work we also determine the link access protocol throughput as the ultimate measure. In wired communications symmetric communication is possible because noise in a wired medium is much more controlled than in wireless media. In wireless communications and specifically in optical wireless links, bi-directional link asymmetry has been observed, [1], [3].

The ambient light noise, which directly influences the performance of IR links, is not always the same for both communicating users. For example, a user working on a PC/laptop and exchanging bi-directional information with another user may have a table lamp switched on in close proximity to the receiving circuits, with result to cause excess noise in his own receiver compared to the other communicating user. Since it is possible and likely that users are under the influence of differing quantity and sometimes type of ambient noise, it should not be expected that the links be symmetric.

Furthermore, component specification and manufacturing tolerances are present even in products from the same manufacturer. Within IrDA, the standard specifies components within bounds and it is likely that IrDA devices from various manufacturers would differ. Provided that transceiver parity [1], is not maintained, then asymmetries would be observed.

Another scenario which would cause asymmetric bi-directional communication when two identical users are linked and communicating under the same ambient noise conditions but a third user unaware of the already established link, is attempting to transmit. 'Third user' or 'interferer user' transmission in the proximity may detriment one of the existing link directions. This effect is accentuated by the fact that due to manufacturing tolerances on mass produced devices by the same or different manufacturer, no two transceivers are identical. It is possible therefore to have an interferer device with higher transmitted power and lower sensitivity receiver than the other two devices. This implies that the interferer may be unaware of the presence of the active link, and as a result continues to transmit, degrading one of the established link directions. This causes asymmetric throughput. The effect is often called the 'deaf-man-shouting' problem.

In this paper we describe an analysis of the degradation of the bit error rate (BER) of the affected link direction, as a function of the interferer parameters such as transmit power, receiver threshold, and spatial position. We present results of the BER as a function of the 2D position of the interfering device. Characteristics of asymmetries of this type are presented. We also present results of the IrDA link access protocol (IrLAP) throughput degradation due to the asymmetry of link BER. The results presented are for a specific IR link protocol, the IrDA IrLAP protocol, using a calculation of average packet end-to-end transmission times, and incorporating re-transmissions due to link errors, [2],[4]. We show that the affected link throughput in the case of 'deaf man shouting' interferer can be seriously affected. This work

focuses on the understanding the various types of asymmetries, and is important towards the design of robust future optical wireless links.

Basic system, two IR device model

The IR users A and B are linked and exchange data. Figure 1 illustrates the model. User 1 has transmitter Tx1 and receiver Rx1 and user 2 has Tx2 and Rx2. When A is transmitting to B, the link distance 'd' is related to the other system parameters, for NRZ data, by:

$$d = \sqrt{\frac{(m+1) \cdot P_{Tx1} A_r \cos^m \theta_A \cdot \cos^n \theta_B}{4\pi \sqrt{2e(P_{B_amb} + P_{Rx2}) \rho \cdot BW \cdot SNR}}} \quad (1)$$

where m and n are the Tx1 and Rx2 radiation pattern lobe index, BW is the receiver bandwidth and A_r is the receiver area. We assume here a normalised radiation pattern following shape as $\cos^m \theta_A$ and $\cos^n \theta_B$ respectively.

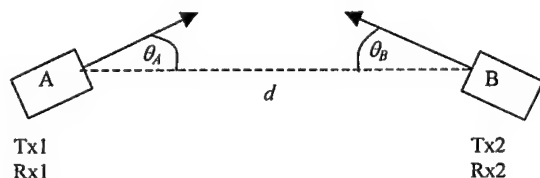


Figure 1: Two user IR link model Tx1 and Rx2 are at distance d apart, subtended by angles θ_A , and θ_B to d.

P_{Tx1} , P_{B_amb} and P_{Rx2} are the transmitted, received and ambient optical powers, SNR is the signal to noise ratio, ρ is the detector responsivity, (in A/W), and 'e' is the electronic charge. Equation 1, clearly describes the relation between the IR link distance and SNR which in turn is related to link Bit Error Rate, (BER), for fixed ambient light noise and the other parameters. The established link between users A and B is symmetric about the connecting line AB. Assuming the transmitting and receiving devices of A and B are the same, or the transceivers have the same parity, then the throughput is the same in both directions AB and BA, resulting in symmetric bi-directional throughput, provided the ambient light noise is not asymmetric.

Modelling third user interference

In this work, we assume that the ambient background noise (lamps, lighting of various types, cause ambient noise in all devices present. We consider, in the same way as that shown in Figure 1, two users A and B connected and exchanging data. For the sake of clarity we assume users A and B are identical and perfectly aligned. That implies that the angles θ_A , and θ_B are zero. This assumption implies that a maximum link distance between A and B is possible. The link A and B is symmetrical. Extending the model, we assume here the presence of a third user C, located further from user B, and invisible to user B, as illustrated in Figure 2. The receiver of user A however, will be affected by transmissions from C. The effect of transmissions from user C therefore is expected to cause degradation of link BA, due to interference from C to A. We assume C is located anywhere on the plane of AB, pointing towards A. We further assume for simplicity that $\theta_C = 0$. This means that C is aligned and pointing towards A. This maybe a situation when C attempts to connect to A being unaware however of the existing link between BA. The link AB is however unaffected by C. Asymmetry in link throughput between AB and BA would therefore occur due to transmissions from C towards A.

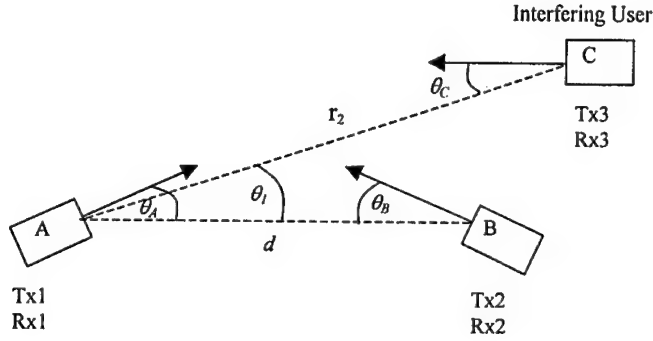


Figure 2: Interference by user C: User A is linked to B. User C interferes with user A.

Bit Error Rate of IrDA links

We assume that the transmissions from C degrade the eye diagram of the link BA as shown in Figure 3. The magnitude of the interference from C is shown by a vector in the opposite direction to the signal.

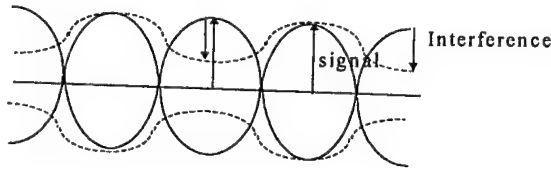


Figure 3: Eye diagram at receiver of user A. The interference from user C causes eye closure.

For user A, the probability of error P_e for the received data from user B, under the influence of interference from C is given by $P_e = Q(\sqrt{SNR})$. It follows that:

$$P_e = Q\left[\frac{\text{signal} - \text{interference}}{\sigma}\right] \quad (2)$$

as illustrated in Figure 3, with Q being the complementary error function, and σ is the rms noise amplitude at the receiver. Using the geometry of Figure 3, we can determine the signal and interference strengths in equation (2).

$$\text{signal} = \frac{P_B \cdot R \cdot A_r \cdot (m+1) [\cos^n \theta_A \cos^m \theta_B]}{2\pi d^2} \quad (3)$$

$$\text{and} \quad \text{interference} = \frac{P_C \cdot R \cdot A_r \cdot (m+1) [\cos^n (\theta_A - \theta_I) \cos^m \theta_C]}{2\pi r_2^2} \quad (4)$$

and P_C is the transmitted power from the interfering user C, P_B is the user B transmit power, R is the receiver responsivity in A/W, m and n are the transmitter and receiver lobe cosine values, and A_r is the receiver area in m^2 .

When $\frac{\text{signal - interference}}{\sigma} = 6$, this results in a BER = 10^{-9} .

Equation (2) for an IrDA link specified at $d=1\text{m}$, with error rate at this distance $P_e = 10^{-9}$ without interference. With interference from user C, (Figure 2), it becomes:

$$P_e = Q\left[\frac{6T_B \cos^n \theta_A \cos^m \theta_B}{R_A d^2} - \frac{6T_B T_C \cos^m \theta_C \cos^n (\theta_A - \theta_1)}{r_2^2 R_A^2}\right] \quad (5)$$

Where R_A is user A receiver threshold in W/m^2 , T_B , T_C are the transmit intensity of user B and interferer user C respectively in W/Sr .

Results

In order to demonstrate the effect of the interfering user C on the link BA error rate quality, we use the above principles on IrDA optical links. We combine the derived probability of errors using the model described here, with a model of the IrLAP (link layer protocol) to produce normalised throughput results. We have modeled here both the physical and link layer of IrDA. As outlined earlier, user C degrades the quality of link BA. As C approaches A, the degradation worsens, until C senses that A is actively linked with B. This happens at a distance called 'carrier sense' (CS). Carrier sense distance is the minimum distance from A necessary for C to sense transmissions from A. If CS is long enough, it stops C early from degrading significantly BA. However, we show here that if user C transmits with intensity more than 80 mW/Sr which is within the lower of the specified transmit intensity limits of the IrDA standard, it is possible for C to destroy the quality of link BA before it senses the presence of activity. The carrier sense distance [3] for a typical IrDA link is taken here to be 2.3 meters.

The results of Figure 4 were derived with the assumptions that Users A and B are aligned and the interfering user C is on the same line as AB and also aligned and aimed at user A. This translates to $\theta_A = \theta_B = \theta_C = \theta_1 = 0$. We can observe that as the interfering user's transmitted power increases the throughput of BA link deteriorates. This is understood from the fact that the interference level increases and the bit error rate of link BA increases. The results of Figure 4 have been derived for the IrLAP protocol of IrDA, [4]. User A is transmitting to user B with 40 mW/Sr intensity. When the intensity of the transmission from C has reached 80 mW/Sr , the throughput is less than 0.2 before CS can detect activity by user A. As the power increases even more, then the link throughput will be zero. This indicates that carrier sense is not sufficient in protecting an existing link. IrDA versions 1.x do not have a carrier sense provision. We can determine from Figure 4 that a user C identical to user A and B, (40 mW/Sr), if it approaches user A to less than 2 m, will noticeably reduce its throughput unless carrier sense is active. At 1.5 m distance it would deteriorate the throughput to zero. Manufacturing component tolerances and the standard transmitter band limits are wide enough to allow an interfering user to deteriorate or even destroy the quality and throughput of an IR link.

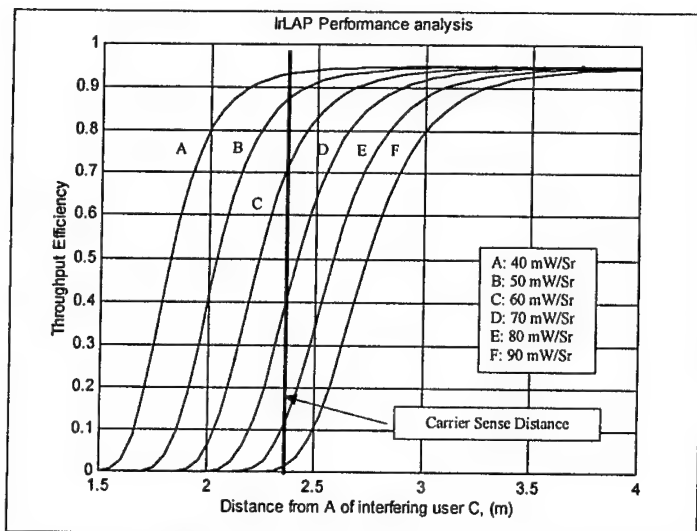


Figure 4: IrLAP throughput of link BA when an interfering user C is along the axis AB.

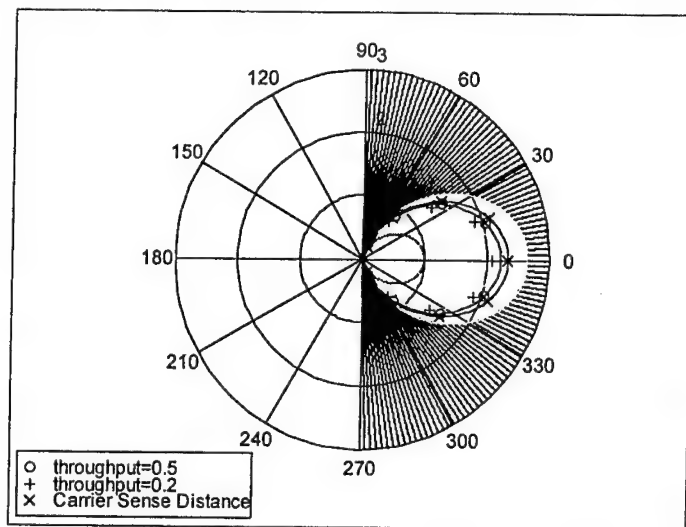


Figure 5: Darkened area represents the location of interferer C relative to user A. user A is located at the center of the polar plot, and user B is 1 m away. The darkened area represents the BA link throughput of better than 0.9. The inner contours represent throughput=0.5, and 0.2. The carrier sense distance is the contour at 2.3 m along the zero degree axis. $T_C = 60 \text{ mW/Sr}$ and $T_B = 40 \text{ mW/Sr}$.

In deriving the results of Figure 5 and 6, user C was allowed to move freely on a 2D plane containing A and B. If there is a carrier sense operation active, as shown in Figure 5, (first contour inside from the outer) it is sufficient to prevent throughput loss, since it is active just as the throughput of BA is about to drop. Finally, when the interfering user, C, transmit intensity is increased to 70 mW/Sr , still well within the IrDA limits, Figure 6 shows that the throughput of link BA is zero at a distance approximately 2 m along $\theta = 0$, without carrier sense. The chosen carrier sense distance of 2.3 m is not adequate to protect the link BA when the intensity of C is increased to 90 mW/Sr .

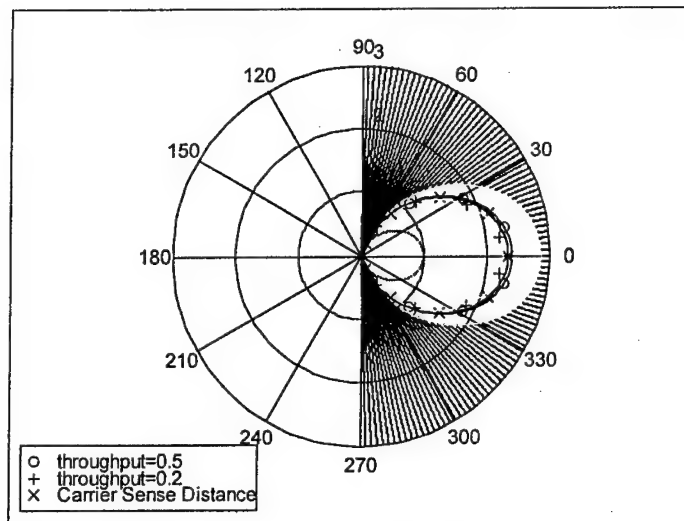


Figure 6: $T_C = 90\text{mW/Sr}$, $T_B = 40\text{mW/Sr}$: Carrier sense distance at 2.3 m along $\theta = 0$, is not adequate to prevent the throughput of link BA to be zero.

Conclusion

A model has been developed to describe the effect of third user interference on an active IR link. The model allows the position of the third user interferer to vary in 2D space. The results of the analysis for an IrDA link, indicate that it is possible for the interferer to shadow the existing link. The throughput can be degraded to zero, provided the intensity of the third user transmitter is as low as 80 mW/Sr , which is within the lower limit of an IrDA transmitter. This demonstrates the importance of carrier sense as a means of deterring third users transmitting within the range of an existing IrDA link. There is no provision in the IrDA 1.x standard for this kind of interference. However, for the AIR standard this is being recognized and carrier sense is part of the operation of the link.

References

- [1]: Asymmetry of Free Space Optical Links: Anthony Boucouvalas, SPIE Proceedings on All Optical Communication Systems: Architecture, Control and Network Issues: 25-26 Oct. 1995 Philadelphia, USA.
- [2]: IRDA: For information contact IrDA administrator, PO Box 495, Brookdale, California 95007-0495, USA
- [3]: Interference Induced IR Link Spatial Asymmetries, A.C. Boucouvalas, Jennifer Jerrams-Smith, and David Heathcote Third Communication Networks Symposium, Manchester Metropolitan University, 8-9th July 1996.
- [4]: IrLAP protocol performance analysis of IrDA wireless communications, A.C. Boucouvalas, P.Barker, IEE, Electronics letters, Vol.34, no.25, pp.2380-2381, 1998.

Acknowledgements: We would like to thank British Telecom Laboratories UK, for their financial support in carrying out this work.

Dispersion Measurement of Optical Code Division Multiple Access Coder

Ida Srdić, Ivan Perić and Branka Zovko-Cihlar¹

Croatian Telecom, Folnegovičeva 5, HR-10 000 Zagreb, Croatia

Phone +385 1 61 888 22, Fax +385 1 660 53 41, e-mail isrdic@svk.tel.hr

*¹Faculty of Electrical Engineering and Computing, Unska 3, HR-10 000 Zagreb,
e-mail bzovko@zea.cc.fer.hr*

Abstract. The code division multiple access (CDMA) is under consideration for broadband video delivery over fiber-optic local area networks (LANs). The basic principles of CDMA will be presented, as well as platform for dispersion measurement of Optical CDMA coder and measurement results.

I. Introduction

Broadband video has been carried out basically using microwave subcarrier multiplexing employing analog modulation schemes (VSB-AM, FM) due to early technical implementations producing a single analog lightwave containing the multiplexed video channels [1]. A digital transmission system promises progress due to developed high-speed fiber optics digital transmission technology and digital transmission is a better match to the fiber because of the fact that above the power level of 10 mW fiber becomes nonlinear in its transmission characteristics. The result is that fiber systems have up to 10 000 times (40 dB) less dynamic range than wireline and microwave systems. This is compensated by a 100 time lower loss in fiber and by using binary digital signaling rather than multilevel or analog modulation. Multilevel modulation can achieve greater spectrum efficiency ($> 1\text{b/s/Hz}$) which is necessary for video transmission in narrowband systems [2] and offers a possibility of better handling a number of parallel signals, but requirements for the linearity of optical sources are greater and specific distributed feedback (DFB) lasers must be employed.

A promising alternative is code division multiple access (CDMA), in which data of a video source are coded into uniquely addressed lightwave pulse sequences that can be recognized and separated at the receivers [3]. Recent developments in fiber optics communications such as in fiber amplifiers have removed the traditional limits for system performance which were based on attenuation, as a result pulse dispersion has been left as a primary limiting factor and major concern in very high bit rate optical systems [6]. Dispersion is found to be particularly destructive in optical CDMA systems which require narrow pulses on the order of picoseconds codes [4].

II. Optical CDMA

CDMA is a method that allows several users to share the entire bandwidth of the channel. Optical CDMA is accomplished by assigning each user a unique code usually

consisting of a series of "chips" or narrow pulses. The codes are designed so that there is minimal cross correlation between any two codes as well as minimal correlation between each code and any shifted or delayed version of itself so they produce high periodic crosscorrelations when properly matched and low crosscorrelation with all other sequences. Let $(X) = (x_0, x_1, \dots, x_n)$ and $(Y) = (y_0, y_1, \dots, y_n)$ be two (0,1) sequences, the crosscorrelation is:

$$\Theta_{XY}(k) = \sum_{i=0}^{N-1} x_i y_{i+k} \quad (1)$$

and with complement of sequence (X) define by (\bar{X}) whose elements are $1-x_i$ we look for sequences for which:

$$\Theta_{\bar{X}Y}(k) = \sum_{i=0}^{N-1} \bar{x}_i y_{i+k} = \Theta_{XY}(k) \quad (2)$$

A receiver that computes $\Theta_{XY}(k) - \Theta_{\bar{X}Y}(k)$ will reject the interference coming from user having sequence (Y) .

The CDMA system has the advantage of relatively simple laser sources (without need of wavelength control), standard photodetectors (without narrow optical filters), and improved power levels due to the laser pulsing. Matching of the code address to correlation, which can be achieved both optically and passively, provides the major advantage of this system.

III. Dispersion Measurement of CDMA Coder

Dispersion is the broadening of pulses as they propagate through a given medium. If the transmitted pulse spreads too much, then it may be virtually undetectable as well as interfere with neighbouring pulses, thereby making it inseparable (closes the "eye") and the overall signal unrecoverable. In a fiber-optics system there are three types of dispersion: modal, material, and waveguide. SMFs eliminate modal dispersion yet propagating pulses still suffer from material and waveguide dispersion jointly called chromatic dispersion.

For chromatic dispersion measurement we use a unique variant of the so-called "differential phase" method [5]. In a single mode optical fiber the light travels with a propagation delay $t(\lambda)$ which is proportional to the fiber length L and is a function of wavelength. Chromatic dispersion $D(\lambda)$ is derivative of the delay $t(\lambda)$ with respect to wavelength λ , and is a measure of the light pulse spreading observed in a fiber of given length and for a given light spectral width. This derivative is very closely approximated by the differential delay Δt between two wavelength points separated by $\Delta\lambda$ if λ is not too large:

$$D(\lambda) \approx dt(\lambda)/d\lambda \approx \Delta t/\Delta\lambda \quad (3)$$

This approximation is valid for all fibers and makes no assumption about the spectral shape of the delay curve, other than that the dispersion is slowly varying and has no discontinuities. The principle of the differential phase method is therefore to measure the differential fiber group delay Δt for two wavelengths separated by $\Delta\lambda$ and to obtain a direct dispersion measurement without data processing.

Measurement of delay $t(\lambda)$ is accomplished by measuring the phase shift ϕ imparted by the fiber delay upon the sinusoidal intensity modulation of a light source of a specific wavelength λ injected into the fiber:

$$t(\lambda) = \phi / 2\pi f \quad (4)$$

where f is the frequency of modulation.

Differential delay Δt between wavelengths can thus be measured by detecting the differential phase shift $\Delta\phi$. With method called double demodulation $\Delta\phi$ is detected. In this method a wavelength modulation is superimposed on the sinusoidal intensity modulation. The wavelength switches from λ_1 to λ_2 at several hundred Hz. High frequency phase detection system demodulates the intensity modulation using a reference signal derived from the master oscillator and detects in turn the phases ϕ_1 and ϕ_2 . The wavelength modulation signal gives rise to a synchronous square wave from the phase meter whose a.c. amplitude represents the differential phase, and the d.c. level absolute group delay at the mean wavelength.

In experiment we used a code set of four sequences, weight $w=4$, and length $L=25$ bits. All fibers including the delay lines was 9/125 standard single mode fibers, passive hard-wired fiber-optic parallel delay line combiners requiring delays of 1-10 ns (integrated circuit packages in future). In one encoder laser pulse is split into four separate delay lines as shown in Fig. 1. (a) and we have the OTDR readout from coder Fig. 1. (b).

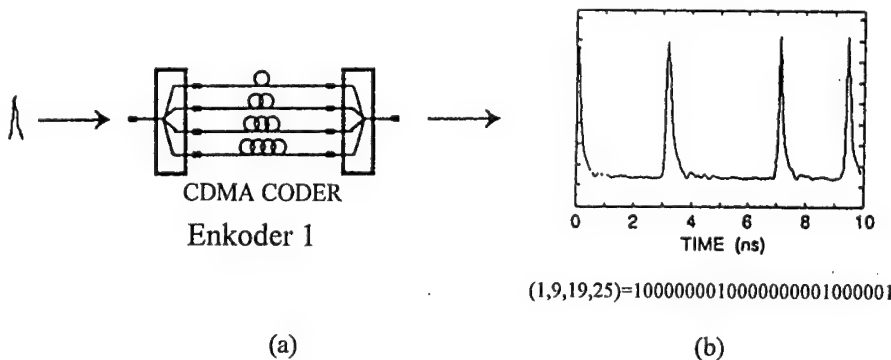


Fig. 1 (a) CDMA coder (b) OTDR readout from coder

In double detection method of dispersion measurement we used wide input signal from LED diode because the width of optical source has no impact on measurement. The results given in Tab I. show that CDMA coder has very little impact on overall dispersion in SMF, but there is more noticeable impact at zero-dispersion wavelength (1300 nm) than at 1550 nm wavelength.

Tab I. CDMA coder dispersion measurement

Fiber length	1550 nm		1300 nm	
	D [ps/ nm/km] without coder	D [ps/ nm/km] with coder	D [ps/ nm/km] without coder	D [ps/ nm/km] with coder
1 km	15.181	15.686	-1.705	4.236
5 km	17.004	16.970	-0.98	0.935
15 km	16.678	17.008	-1.113	-1.096
25 km	16.747	17.214	-1.095	-1.673

IV. Conclusion

This paper presents dispersion impact on an optical code division multiple-access (CDMA) coder using a single-mode fiber. A great deal of work has focused on reducing dispersion in general single-user optical communications systems. Both electronical and optical processing techniques have been explored. Electronical processing is, in general, too slow for the very small pulse widths involved in CDMA systems. Optical processing is powerful for single user communications but implementation on fiber that has already been installed is difficult, and it lacks flexibility in multi user situations when fiber lengths for different users may be different. Dispersion can lead to significant intersymbol and interchip interference, leading to unacceptable levels of multiuser interference. We can derive from dispersion measurement of one CDMA coder that it doesn't noticeably extend chromatic dispersion which will impact on CDMA system performance. Measurement values are still in range of ITU-T G. 652 recommendation which defines single mode fiber characteristics. Although in double detection method for chromatic dispersion measurement we cannot change the signal rate and thus measure dispersion impact on BER characteristic which together with changing the CDMA codes will give the complete dispersion influence results.

References

- [1] T. E. Darcie, "Subcarrier Multiplexing for Lightwave Networks and Video Distribution Systems", *IEEE Journal on Selected Areas in Communications*, 8, pp. 1240-1248, 1990.
- [2] N. Kanno, K. Ito, "Fiber Optic Subcarrier Multiplexing Video Transport Employing Multilevel QAM", *IEEE Transactions on Communications*, 8, pp.1313-1319, 1990.
- [3] R. Gagliardi, M. Dale, "Video Multiplexing Using Pulsed Coded Fiberoptics", *Proc. of the IEEE Conference on Communications*, 1994, New Orleans, pp. 111-115.
- [4] F. B. Mezger, M. Brandt-Pearce, "Dispersion limited fiber-optics CDMA systems", *Proc. of the NOC International Symposium*, 1996, Amsterdam, pp. 348-354
- [5] Operating principles of the EG&G 300 Series instrument
- [6] I. Srdić, I. Perić, B. Zovko-Cihlar, "Optical CATV", *Proc. of the 1st International Symposium ECS*, 1997, Bratislava, pp. 239 - 243
- [7] I. Srdić, I. Perić, B. Zovko-Cihlar, Modelling Platform for Study of Optical CDMA, *Proc. of the 5th International Symposium EDS*, 1998, Brno, pp. 313 - 316

Optical Networks with Code-Division Multiple-Access

Michal Poľaško

*Dept. of Telecommunications, Slovak University of Technology,
Ilkovičova 3, Bratislava. polasko@ktl.elf.stuba.sk*

Abstract—This paper presents the analysis of the potential of an code-division multiple-access technique for optical communication systems. The main system characteristics are discussed and comparison to existing technology is given.

I. Introduction

Spread spectrum communication technique is subject of the intensive research in the context of mobile and satellite communication and it offers many advantages for optical systems as well. Code division multiple access scheme (CDMA) uses the principles of spread spectrum systems to combine channels of individual users with high efficiency. CDMA is based on the assigning orthogonal codes to users what results in a substantial increase of the signal bandwidth. Therefore CDMA requires broadband communication channel as a optic fiber. Moreover, CDMA requires broadband signal processing in the receiver. Currently developed optical components will offer much higher bandwidth than their electronic equivalents and we might expect that future optical networks will perform most of the signal processing in the optical domain what allows to fully exploit advantages of CDMA.

II. System components

Optical CDMA [1] exploits wide bandwidth of monomode fiber. It converts electrical signal of a lower rate to the high-rate sequence of the optical pulses providing an asynchronous access to shared communication channel without additional control. Data signal from information source is usually represented by on-off signaling format, where the optical pulse symbolizes data bit 1. Output of the laser is then encoded in the CDMA encoder, which converts every pulse to the sequence of pulses. This sequence can be represented by the unipolar code, consisting of L chips. At the receiving end a correlation process is used to extract the desired data from the received signal. The encoder as well as the correlation receiver can be implemented in optically what allows to achieve high transmission rates. Since the matched filter is used in the receiver, the local synchronized generation of the spreading code is

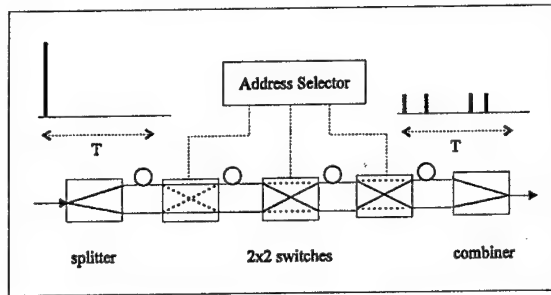


Figure 1: All-serial architecture of 2^n optical encoder.

not needed for the correlation. Optical CDMA networks then consist of N pairs transmitter-receiver, where assigned codes become network addresses. Receiver must be able to recognize the desired signal in the composite received signal containing information of all active network users. Therefore the design of the unipolar codes with good and cross-correlation properties is necessary. Another requirement posed on optical CDMA codes is the good autocorrelation function with the low sidelobes. This allows to easily distinguish the autocorrelation peak corresponding to the end of a bit interval. Therefore optical CDMA with the tapped lines matched filter and threshold detector does not require any synchronization.

There are proposed several classes of the codes for incoherent CDMA system. 2^n codes [2],[3] are suitable candidates since their encoder and decoder architecture provides substantially lower power loss and lower cost in comparison to the conventional parallel architecture. With 2^n codes an all-serial architecture (Figure 1) is used for code sequence generation, selection and correlation. In general, the encoder is constructed from a number of switching stages, each with a 2×2 switch and delay line. Each 2×2 switch is configured into two possible (mix-split or straight-through) states according to its DC bias voltage, controlled by the electronic address selector. Mix-split state allows optical pulses to mix and split inside a 2×2 switch, while the straight-through state allows optical pulses to pass through without changes. The decoder consists of 2×2 passive couplers with suitable optical delays, similar to the coder in Figure 1.

III. Networking

Optical CDMA offers a cost-effective method to transport, provision and protection of standard protocols as ATM or Ethernet. CDMA meets all basic requirements for an all-optical network. Due to its coding technique and the all-optical signal processing CDMA ensures an effective access and utilization of a large portion of the fiber spectrum. Because of the broadcast nature of CDMA, all information signals are available anywhere in the network. Placing the receiver with decoder matched to the desired code in any location within the network we are able to extract needed

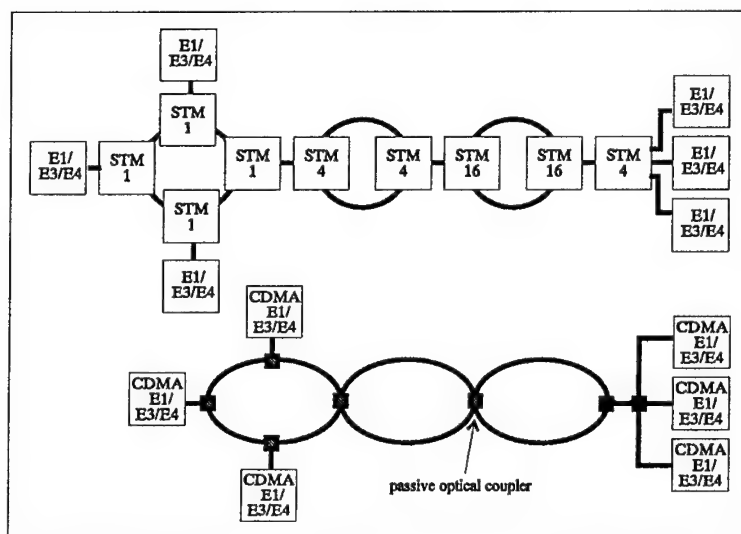


Figure 2: SDH and CDMA optical network infrastructure [4].

data and all other information will be rejected. It should be noted that CDMA as a spread spectrum technology provides secure communication. Programmable transmitter encoder (or receiver decoder) allows to direct the information to any destination within the network. This feature allows to reduce the size of the network cross-connect equipment and eliminate manual configuration hassle for network operator. The network protection can be achieved by the transmitting information using two code sequences around the ring in opposite directions. This provides 1+1 protection, where receiver can select one of two received signals.

Figure 2 compares the network infrastructure of the typical SDH network and its CDMA equivalent. It can be seen that CDMA requires fewer pieces of equipment, saving on total cost and decreasing the network complexity [4].

IV. System performance

The use of unipolar $\{0, +1\}$ pseudo-orthogonal codes with non-zero cross-correlation function in incoherent optical systems brings the problem of the multiple-access interference cancellation, since a simple correlation receiver (matched filter) ignores the cross-correlation between the modulating signals of different users and therefore it has poor performance in the system composed of many users. Optimum multiuser detection achieves important performance gains over the conventional single-user detection at the expenses of computational complexity that grows exponentially with the number of users [5]. There were analyzed also the linear and nonlinear multiuser detectors, which approach the performance of the optimum multiuser

detector [6], [7]. These detectors can unfortunately not be implemented optically. Another possible way of multiple-access interference cancellation is the use of an passive optical hard-limiter in the optical correlation decoder [8]. Optical hard-limiter allows to apply all-optical signal processing and therefore does not limit the transmission rate.

With ultra-short optical pulses of 1-3ps and code sequences length of thousands chips CDMA can support user data rates of hundreds Mbit/sec. However, the multiple access interference degrades the system performance and therefore it limits the total number of users accommodated by CDMA network.

References

- [1] J. Salehi, "Code division multiple access techniques in optical fiber networks—part I: Fundamental principles," *IEEE Trans. Commun.*, vol. 37, no. 8, pp. 824-833, August 1989.
- [2] W.C. Kwong, P.R. Prucnal, "All-serial coding architecture for ultrafast optical code-division multiple-access," *ICC'93 conf.*, Oct. 1993, Geneve.
- [3] W. C. Kwong, J. G. Zhang, G. C. Yang, "2ⁿ prime-sequence codes and its optical CDMA coding architecture," *Electronic Letters*, vol. 30, pp. 509-510, Mar. 1994.
- [4] B. R. Dutt, B. Johnon, "Optical CDMA offers all-optical network alternative," *Lightwave*, no. 9, pp. 54-58, Sept. 1998.
- [5] S. Verdú, "Multiple access channels with point-process observations: Optimum demodulation," *IEEE Trans. Inform. Theory*, vol. 32, pp. 642-651, Sept. 1986.
- [6] L. Nelson a H. Poor, "Performance of multiuser detection for optical CDMA—Part I: Error probabilities," *IEEE Trans. Commun.*, vol. 43, no. 11, pp. 2803-2810, Nov. 1995.
- [7] L. Nelson a H. Poor, "Performance of multiuser detection for optical CDMA—Part II: Asymptotic analysis," *IEEE Trans. Commun.*, vol. 43, no. 12, pp. 3015-3024, Dec. 1995.
- [8] M. Polaško, F. Uherek : Optical code division multiple access system with hard-limiters. *International Journal of Electronics and Communications (AEÜ)*, vol. 52 (1998), no. 1, pp. 43-48.

Analog Fuzzy Controller in SC Technique
G. Giustolisi, G. Palmisano and G. Palumbo

The paper not available at printing time.

Implementation of Harmonic Linearization Using Monotonic Phase Functions

Vello Kukk

*Tallinn Technical University, Ehitajate tee 5, 19086 Tallinn, Estonia,
vello.kukk@dcc.ttu.ee
Analog Design Ltd, Akadeemia tee 21, Tallinn Estonia*

Abstract. Harmonic linearization is standard method for modeling of narrow-band systems. In case of very high-Q resonators using of only one harmonic as input signal of nonlinear element(s) may be sufficient. To discover higher order effects, more complicated models must be applied. This paper deals with the method that uses large signal models based on virtual pure sine wave. This allows to split the model into two parts, one is specific for non-linearity and another is universal waveform transformation

I. Introduction

Oscillator circuits exhibit behavior that can be characterized as "near harmonic". That means the possibility to represent signals roughly as

$$u(t) = A(t) \cos(\omega_0 t + \varphi(t)) \quad (1)$$

where $A(t)$ and $\varphi(t)$ are slow if compared with phase change caused by the term $\omega_0 t$. The term "slow" is fuzzy and during transients, those "slow changes" may be comparable with "fast" ones. Separation of those two components is easy for long period samples of the signal and in steady state. Practical oscillator design needs very accurate models for correct determination of oscillation frequency, phase noise, and reactions to external excitations and control. Transient times become important for example in mobile communications. In short time processes, strict distinguishing of spectral bands may appear difficult, at the same time direct time-domain simulation is too time consumable and not enough accurate.

It is known that even simple oscillator structures (as Colpitts oscillator) may exhibit chaotic behavior that may appear through period-doubling process [1,5]. At the same time, oscillator circuits are usually simple, consisting of only several components. It follows that modeling of such circuits could be implemented using large equivalent circuits or systems of equations.

It has been demonstrated that simple equivalent circuits can be built for large-signal models that are based on harmonic linearization using fundamental frequency only [2] and modeling of transients can sometimes be accelerated more than 1000 times. However, frequency control mechanism, implemented as a simple feedback system trying to minimize one of quadratic components [2,3], causes sometimes fast time step decreasing or locking to double frequency, both slowing down simulation process. Not all reasons of that behavior are clear but one of them is obviously non-deterministic signal representation (1), and probably, too rough model based on fundamental frequency only. The consequence is that we have to extend such models including higher harmonics.

II. Basic ideas

Large signal models are based on the following construction: defining suitable signal space (e.g. narrow-band signals). We build the models, which operate with signal parameters, not their instant values. Assume the signal

$$u(t) = a_0 + a_1 \cos t + a_2 \cos 2t + a_3 \cos 3t + a_4 \cos 4t + \dots \quad (2)$$

to be represented as

$$u(t) = A_0 + A_1 \cos(p(t)) \quad (3)$$

in some finite interval of t . Considering p as a new independent variable (monotonic phase), we can compute the result of static non-linear transformation $y = f(u)$ in the p -domain. So, the signal space is defined by two parameters A_0 and A_1 . Applying $A_0 + A_1 \cos p$ to the input, we obtain output

$$y(p) = B_0 + B_1 \cos p + B_2 \cos 2p + B_3 \cos 3p + \dots \quad (4)$$

using pre-calculated formulas for $f(u)$. Now the how to return to t -domain. This procedure is universal, not depending on the $f(u)$, and so we can avoid building of very complicated multi-tone models. From (3) we obtain

$$\cos p = (u(t) - A_0) / A_1. \quad (5)$$

From this, we calculate $\cos p, \cos 2p, \cos 3p, \dots$ to substitute into (4). The problem is that function $p(t)$ may be complicated. Fortunately, we do not need this function directly as $\cos np$ can be expressed in the following form:

$$\cos np = \cos(n \arccos(w)) \quad (6)$$

where

$$w(t) = A_1^{-1}(a_0 - A_0 + a_1 \cos t + a_2 \cos 2t + a_3 \cos 3t + \dots) \quad (7)$$

Expression (6) is Chebyshev polynomial

$$\cos np = T_n(w), \quad (8)$$

and for truncated series (7), $\cos np$ can be computed by finite number of operations:

$$T_{n+1}(w) = 2wT_n(w) - T_{n-1}(w) \quad (9)$$

This together with (7) defines universal waveform transformation.

Notes: 1) as seen from (9), $|\cos p|$ needs not be limited by 1.0;

2) described model can be applied to any time domain segment - it may be exactly one period of the signal, part of it, or several periods.

III. Implementation

A. Choice of A_0 and A_1

We are quite free in this choice, for example, we can set $A_0 = a_0$ that simplifies implementation. Also we can set A_1 to any positive value. The only criterion for those choices is minimizing the components that are to be considered as non-zeroes. Optimal solution is obviously

$$A_0 = \frac{\max u(t) + \min u(t)}{2}, \quad A_1 = \frac{\max u(t) - \min u(t)}{2}. \quad (10)$$

However, detection of extreme values may be inconvenient and therefore, we can use evaluations based on *rms* values. The best practical solution tested is the following. Having from

previous step a waveform w and its Chebyshev transformation, we solve equations to find A_0 and A_1 using first components of waveform only. This appeared to be fast and productive.

B. Waveform representation and Chebyshev transformation

For analysis of transients, we cannot use standard Fourier series, as this would create equal values at both ends of period. In general, they may be different as seen from integration of constant signal:

$$v(t) = v(0) + C^{-1} \int_0^t i_0 d\tau = v(0) + C^{-1} i_0 t. \quad (11)$$

However, this function can be represented using half-frequency component $\cos t/2$. Finally, we obtain general form of signals to be used as

$$u(t) = a_0 + a_{1/2}^R \cos \frac{t}{2} - a_{1/2}^I \sin \frac{t}{2} + \sum_{k=1}^N (a_k^R \cos t - a_k^I \sin t). \quad (12)$$

This form consists of harmonic components only and therefore, processing is rather simple both in linear and non-linear operations. Description of integration formulas is partly given in [4]. Those and details of Chebyshev transformation will be omitted here.

C. Frequency control

Described method is usable for any time step. However, as the target is narrow-band system, we try to determine fundamental period T (or integer multiple of it) during simulation. Considering T as a variable, we add one equation, eg demanding that values of some variable $x(t)$ at the ends of period should be equal: $x(0) = x(T)$. This is equivalent to forcing $a_{1/2}^R = 0$ for that variable. If initial value of $x(t)$ was zero, we shall follow zero crossings of that variable.

IV. Examples.

D. Example 1.

Consider simple circuit shown on Figure 1 [4]. Iterations were implemented in two sections as described above: first section to determine A_0 and A_1 , and the second one to fix waveform. Period was multiplied when half-frequency components became very small, and so fast progress in simulation was achieved when reaching steady state. When modeling uses 1st harmonic only, steady state period is equal to resonance frequency of LC-tank, ie 2π . Using our model the value $T=6.29941436$ was obtained that makes difference of 0.26% or 2600ppm. This value of period was confirmed by special independent checking procedure.

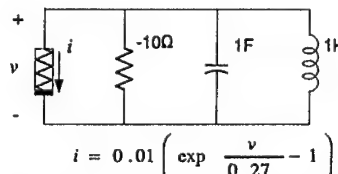


Figure 1. Simple oscillator circuit

E. Example 2

In this example, we consider Colpitts oscillator described in [5] that is able to exhibit chaos. The purpose was to test the method in case of the circuit that probably does not have fixed period. This oscillator with simplified BJT model (piecewise-linear approximation as in [5]) was modeled by Spice and our method using constant time step. We chose integration period

$1\mu\text{s}$ and used up to 9 harmonics and 9 terms in Chebyshev series. The result was compared with that obtained from PSpice using two sets of control parameters: 1) $\text{reltol}=1e-5$ and time step limit $0.1\mu\text{s}$ (10 steps per our step), and 2) $\text{reltol}=1e-6$ and step limit 20ns . All three cases gave almost the same result in time segment $[0...120\mu\text{s}]$. After that, the results became different (Figure 2): "Spice" simulation shows very different behavior. Higher accuracy "SpiceHA" is much closer to our result, however starts also to decline after $150\mu\text{s}$. We do not know which is the exact solution but this example demonstrates that our method can be used to implement numerical integration in general case using large time steps.

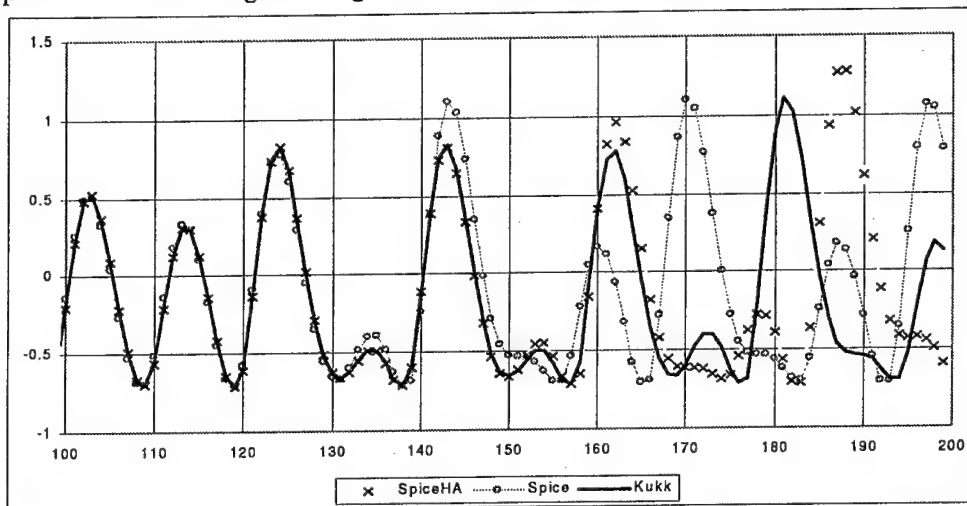


Figure 2. Colpitts chaotic oscillator: comparison of three simulations

V. Conclusion

Harmonic linearization model can be built using only two-dimensional signal space based on the use of monotonic phase signal representation. The method also allows performing numerical integration with large time step.

References

- [1] G.M.Maggio, M.P.Kennedy, M.Gilli, "An Approximate Analytical Approach for Predicting Period-Doubling in the Colpitts Oscillator," in *Proc ISCAS'98*, Monterey, May 31-June 3, 1998.
- [2] V.Kukk, "Large Signal Models for Oscillator Design," in *Proc ISCAS'98*, Monterey, May 31-June 3, 1998.
- [3] H.G.Brachtendorf, G.Welsch, R.Laur, "A time-frequency algorithm for the simulation of the initial transient response of oscillators," in *Proc ISCAS'98*, Monterey, May 31-June 3, 1998.
- [4] V.Kukk, "Large Signal Models and Monotonic Phase Signals for Modeling of Oscillators," in *Proc NDES'99*, Bornholm, Denmark, July 1999 (to appear).
- [5] M.P.Kennedy, "Chaos in the Colpitts Oscillator," *IEEE Trans. Circuits Syst.*, vol. 41, pp.771-774, Nov. 1994.

Principles of Interactive Analog Circuit Synthesis

Marko Koort¹

¹*Analog Design Ltd, Akadeemia tee 21, 12618 Tallinn, Estonia, e-mail:
koomar@adl.ee*

Abstract. An alternative approach to analog circuit design and analysis problems is presented. The proposed technique bases on a small-signal rational circuit function of complex variable with real numerical coefficients. The main idea is to build equivalent circuits for a given circuit function under control of the human designer. The architecture of Synthesis Calculator is presented along with data structures specially developed accounting for the needs of the interactive synthesis.

Keywords: *analog circuits, interactive computing, circuit functions, circuit synthesis, object recognition, object oriented programming.*

I. Introduction

A quite common problem in engineering practice is that despite all efforts the circuit fails to behave as expected. Then one may turn to symbolic analysis [6], [8], which is very error-prone and produces huge expressions. There exist however several methods for symbolic expression simplification [7].

The work with small-signal numerical circuit function(s) of complex frequency is much easier. The objective here is to synthesise equivalent circuits for the circuit under investigation. This calls for an interactive system for handling circuit functions, specially adapted for performing the classical synthesis steps on the circuit functions. The system must also be able to collect, interpret and present the circuit data obtained from the synthesis actions.

In Section II, a motivation example for the Interactive Synthesis is presented. In Section III, principles of interactive synthesis are proposed. In Section IV, Synthesis Object is identified along with its internal structure. Next, in Vth Section, the Synthesis Graph and its components are defined. In Section VI, the Synthesis Calculator is introduced, and the conclusions are drawn in Section VII.

II. Motivation example

A motivation example from [5] is adapted. The emulation of immittance using immittance converters is very widespread in the filter design. Most problems arise when emulating an inductor – the bandwidth is narrower than that of an emulated capacitor. The principle of immittance emulation is shown in Figure 1.

The idea is to state, that the admittance Y_{IN} , seen from the input, is the admittance of an ideal inductor. The problem is then to synthesise the Y_{LOAD} so that this condition would be satisfied. However, one is interested of monitoring the behaviour of Y_{IN} instead of Y_{LOAD} , for example for determining whether the Y_{IN} is already acceptable and the synthesis of Y_{LOAD} would be terminated prematurely. This monitoring will call for a circuit analysis program, so that the IS tool would be integrated with an analysis tool.

III. Interactive Synthesis

The Interactive Synthesis (IS) has also been under investigation in earlier papers [2], [3], [8] and a Master Thesis [1]. In this paper, the basics for development of the interactive

synthesis tool are given. The interactivity implies a decision from the designer's side at each IS step.

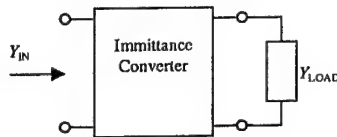


Figure 1. Immittance emulation example

The parameters, results and other related data is saved to a Synthesis Object (SO) at each IS step and the SO's are linked together to form an Synthesis Graph (SG). The IS data can be extracted from the vertices of the SG and presented in various forms – graphical plots, circuit diagrams, circuit netlists etc.

The principles of analog circuit IS are as follows:

1. Every calculation or synthesis step is automated and initiated by the designer;
2. The initial data and results of every IS step are collected automatically to a SG;
3. The designer may traverse the Synthesis Graph in arbitrary manner;
4. The designer may grow or reduce the SG from every vertex;
5. The complete set of data representation methods is included in the IS tool.

IV. Synthesis objects

A Synthesis Object (SO) has quite complicated internal structure (see Figure 2). The "input side" and "output side" distinguished in Figure 2 represent data after performing a synthesis step (i. e., the input of the next step), and the results of the performed IS step, respectively.

V. Synthesis Graph

The SO in Figure 2 has no information on the applied synthesis method nor what was the original circuit function (or a set of functions) on which the method was applied. This information will be made available via linking the SO to a lattice, consisting of other SO's and also of some special additional data structures for managing the lattice. This lattice of SO's is called Synthesis Graph (SG).

The reason why the SG is not necessarily a tree is the manifold of the solution of the synthesis problem, when the different sets of synthesis steps may yield the same result. The VSGs in the SG are interconnected with Arcs of SG (ASGs).

A. Vertex of the SG

The structure of the Vertex of SG (VSG) is presented in Figure 3, a. The VSG holds information on the SO it is encapsulating and the information on the placement of the VSG in the SG. References to the nearest neighboring VSGs are incorporated. The information on synthesis step performed on the circuit function is not in the VSG, but in the Arc of the SG. In Figure 3, a, the references to the arcs of the SG are gathered into one group, although the arcs may be either starting from the particular VSG or ending at the VSG.

There is one special VSG in the structure of SG, which is called the Start Vertex. This VSG does not have anything but the names of input nodes of the circuit to be synthesised on the output side, because no synthesis step has performed yet. The VSG is holding information on circuit function(s) *after* performing a particular synthesis step so that it could be deleted without affecting data in other VSGs. All connecting arcs are deleted when a VSG is deleted.

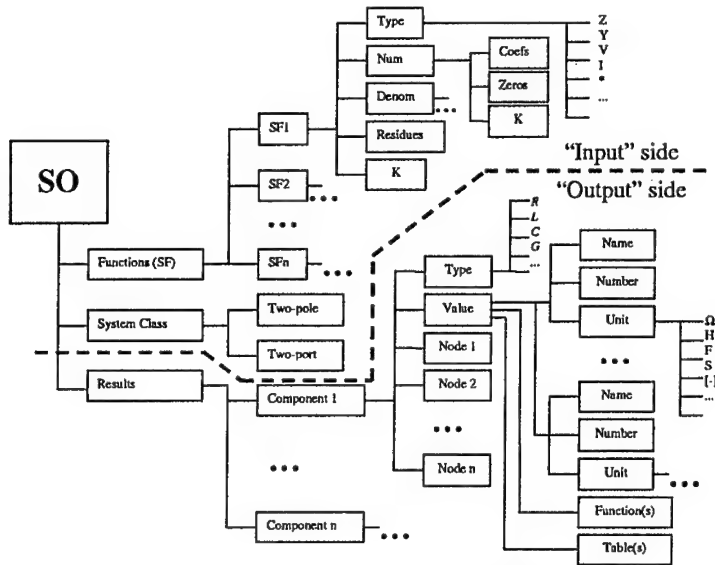


Figure 2. Structure of Synthesis Object

B. Arc of the SG

The structure of the Arc of SG (ASG) is presented in Figure 3, b. The ASG always connects to exactly two vertices of the SG, and carries information on the synthesis step, which was used to get from the start VSG of the particular arc to the end VSG (See Figure 3, b). Thus, the ASG has a direction, and the SG is a directed graph.

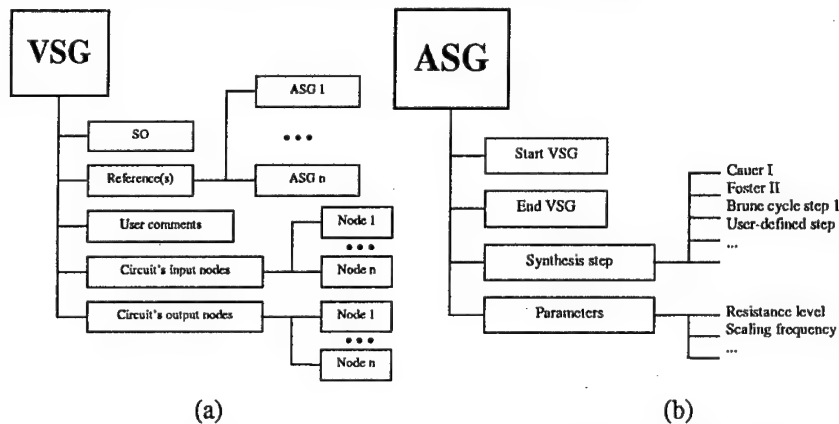


Figure 3. Structures of the Synthesis Graph Vertex (a) and Arc of Synthesis Graph (b).

VI. Synthesis Calculator

The tool performing IS steps on given circuit function(s) is called Synthesis Calculator. Its structure and relationships to the SG are shown in Figure 4. The SC Core is built up of two modules – the CommandSet (CS) arithmetics library and the CommandInterpreter (CI). The CS implements basic mathematical operations on polynomials and rational functions, and the CI, using the base functions from CS implements synthesis methods (see e. g., [1], [4]). The CI also extends the possibilities of IS by implementing a dedicated macro language, using

primitive methods and functions from both CS library and the CI itself. This will make adding new synthesis methods to the SC easier.

The SC also includes a UserInterface (UI) module, which organises all data exchange between the user and the SC. In Figure 4, the UI module is named Graphical User Interface (GUI) and taps its information from both input and output of the SC core. The UI might be implemented using some standard application program interface (API). The implementation of the data structures and the basic modules (CS and CI) of the SC is object-oriented. The object-oriented approach for implementation of the SC data items like polynomials and rational functions is briefly presented in [1].

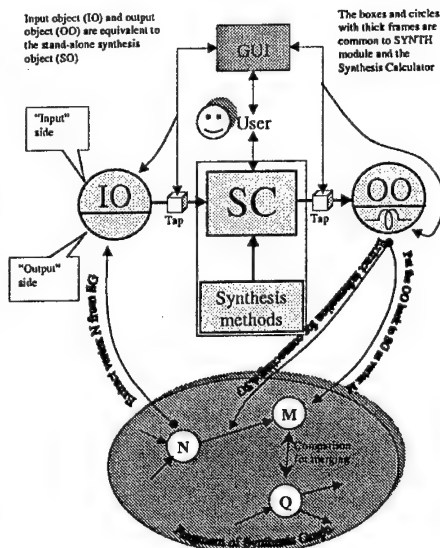


Figure 4. Structure of the Synthesis Calculator

VII. Conclusions and Outlook

The interactive synthesis principles and one way of implementation was proposed. The type of the function which can be synthesised is restricted to rational functions with real coefficients. It is possible, that some sequences of synthesis steps will become more used than others. This will raise a demand for module, which simply fulfils these steps for designer, like a macro, thus simplifying the interactive synthesis process. Moreover, planning modules may appear, which are capable of planning the actions which must be done by the synthesiser. This will turn the interactive synthesiser to just a synthesiser.

References

- [1] M. Koort, *Principles of Interactive Synthesis*. Master Thesis in Tallinn Technical University, Tallinn, Estonia, 1999.
- [2] M. Koort, V. Kukk, "Interactive Circuit Synthesiser", *Proc. of Baltic Electronics Conference, Tallinn, Estonia, October 7–11, 1996*, pp.245–248.
- [3] M. Koort, V. Kukk, "Interactive Synthesiser Development", *Proc. of First Electronic Circuits and Systems Conference, Bratislava, Slovakia, September 4–5, 1997*, pp. 67–70.
- [4] N. Balabanian, *Network Synthesis*, Prentice-Hall, 1958.
- [5] R. Saame, *Synthesis of Active Filters based on Real Converters*. (in Estonian), Diploma Thesis in Tallinn Technical University, Tallinn, Estonia, 1998.
- [6] G. Gielen, "Symbolic Analysis Methods and Applications – An Overview", *IEEE International Symposium on Circuits and Systems, San Diego, CA, USA, May 1992*, pp. 1141–1144.
- [7] F. V. Fernández et al., "On Simplification Techniques for Symbolic Analog Circuit Analysis", *IEEE International Symposium on Circuits and Systems, San Diego, CA, USA, May 1992*, pp. 1149–1152.
- [8] A. Konczykowska et al., "Symbolic Synthesis as a Tool for Circuit Optimization", *IEEE International Symposium on Circuits and Systems, San Diego, CA, USA, May 1992*, pp. 1161–1164.

Noise Properties of High-Order BP OTA-C Filter Structures

Nino Stojković and Neven Mijat

*Faculty of Electrical Engineering and Computing, University of Zagreb,
Unska 3, Zagreb, Croatia, nino.stojkovic@fer.hr, neven.mijat@fer.hr*

Abstract. Different realizations of 8th order band-pass filters using bipolar OTA-C structures are analyzed from the noise and dynamic range point. Noise voltage spectral density, RMS noise voltage and dynamic range are calculated for Cascade, Cascade of Biquarts, Follow-the-Leader-Feedback and Leap-Frog filter structures. The analyses results are compared to the results obtained from the filter structures using operational amplifiers. They are also confirmed by PSPICE simulation. The best noise properties for small signal level gives the Leap-frog 8th order OTA-C filter structure.

I. Introduction

Significant limitation in the realization of quality low voltage signal processing circuits can be noise level produced by used circuits. Particularly in high-order filter circuits, it is important to have the noise level as low as possible. In the recent paper [1] various second-order OTA-C filter sections are analysed and the contribution of each section element to the overall noise figure is analysed. In this paper the high-order structures such as: Cascade (CAS), Cascade of Biquarts (CBQ), Follow-the-Leader-Feedback (FLF) and Leap-Frog (LF) are analysed. Some of these structures are developed in order to minimize sensitivities to the filter element values mismatching. The question was whether the noise figures of low sensitive filter structures are good as well. The filters are designed using the OTA-C filter section (GFS) [2] as a building block. They are compared to the filters with the single amplifier biquad sections (SAB). Noise effects are calculated using the transfer functions with respect to each noise source [3]. The ratio of maximum undistorted voltage level and the RMS noise within a specified frequency range is used as a dynamic range (D_R) measure [4].

II. Noise and Dynamic Range

The noise models for resistors, operational amplifiers (OA), and operational transconductance amplifiers (OTA) used throughout the analysis are shown in the fig.1. Resistors are represented by a Nyquist current noise model shown in fig.1.a), while the OAs and OTAs are represented by models shown in fig.1.b), and fig.1.c), respectively, where $E_n=20\text{nV}/\sqrt{\text{Hz}}$ for OA, $E_n=8\text{nV}/\sqrt{\text{Hz}}$ for OTA and $I_n=0.01\text{pA}/\sqrt{\text{Hz}}$ for both amplifiers.

OTA-C filter structures are designed using the general OTA-C filter section (GFS) shown in the fig.2.a). The transfer function of this section is

$$T(s) = \frac{V_{OUT}}{V_{IN}} = \frac{s \frac{g_4}{C_2}}{s^2 + s \frac{g_3}{C_2} + \frac{g_1 g_2}{C_1 C_2}} \quad (1)$$

Second-order SAB filter section, used in the design of the filter structures with operational amplifiers, is shown in the fig.2.b) and its transfer function is

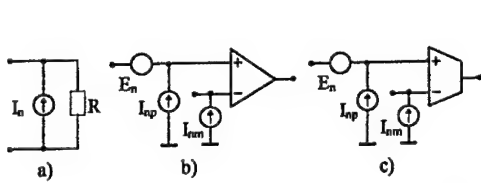
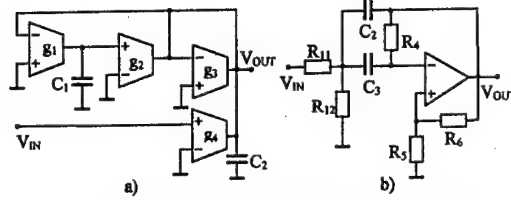


Fig. 1. Noise model for: a) resistor, b) OA, c) OTA

Fig. 2. 2nd order filter sections: a) GFS, b) SAB

$$T(s) = \frac{V_{OUT}}{V_{IN}} = \frac{-s \frac{1}{R_{11}C_1} \left(1 + \frac{R_5}{R_6}\right)}{s^2 + s \left(\frac{1}{R_4C_2} + \frac{1}{R_4C_3} - \frac{R_5}{R_1R_6C_2} \right) + \frac{1}{R_1R_4C_2C_3}} \quad (2)$$

Using the above exposed filter blocks, eight-order BP filter is realized using four different types of 8th order structures: CAS (fig.3.a), CBQ (fig.3.b), FLF (fig.3.c) and LF (fig.3.d). Substituting the elements in these structures by corresponding noise model, transfer functions

$$T_x(s) = \frac{V_{OUT}}{N_x} \quad (3)$$

are calculated, where N_x is in either voltage or current noise source. As a D_R measure is used

$$D_R = 20 \log \frac{(V_{OUT})_{ef}^{\max}}{(E_n)_{ef}} \text{ dB} \quad (4)$$

The numerator represents maximal undistorted RMS output voltage, and the denominator is RMS noise voltage within a specified frequency range given by

$$(E_n^2)_{ef} = \int_{\omega_1}^{\omega_2} V_n^2(\omega) d\omega \quad (5)$$

$V_n^2(\omega)$ is the square of the voltage noise spectral density derived from all noise sources and belonging transfer functions i.e.

$$V_n^2(\omega) = \sum_{k=1}^m |T_{i,k}(j\omega)|^2 (I_n)_k^2 + \sum_{l=1}^n |T_{v,l}(j\omega)|^2 (V_n)_l^2 \quad (6)$$

The transfer function $T_{i,k}(j\omega)$ is actually a transfer impedance i.e. a ratio of output voltage and input current of k -th current noise source $(I_n)_k$, while $T_{v,l}(j\omega)$ is a voltage transfer function i.e. a ratio of the output voltage and input voltage of l -th voltage noise source $(V_n)_l$. These transfer functions are too complex to be presented here. Using the above expressions noise voltage spectral density and dynamic range defined previously are analysed.

III. Example

Based on the above expressions voltage noise spectral density using (6), and correspondent dynamic range defined by (4) and (5) are calculated for the following example. The 8th order Chebyshev magnitude response filter is designed with 4kHz central frequency, 1.8kHz pass-band width, and 0.1dB pass-band ripple. Filter parameters are given in table I. Noise and dynamic range is calculated over the frequency range 10Hz-100kHz. The voltage noise spectral density of the structures using OTA-C 2nd order sections are presented in fig.4 and for the structures using SAB sections are given in fig.5. Comparing these results to the results obtained from the simulation program PSPICE, an excellent agreement was found. Particular attention in the design procedure of an OTA-C filter must be paid to the dynamic range. For D_R calculation upper limit of the output signal has to be known as well. It is for

OTA-C based filters approximately 50mV [6], and for the SAB based filters approximately 5V [5]. Additional problem is the existence of more than one section output. During the design procedure dynamic range optimization has to be performed. This was done for all filters in our case, and maximum of magnitudes at the outputs of 2nd order section are equal.

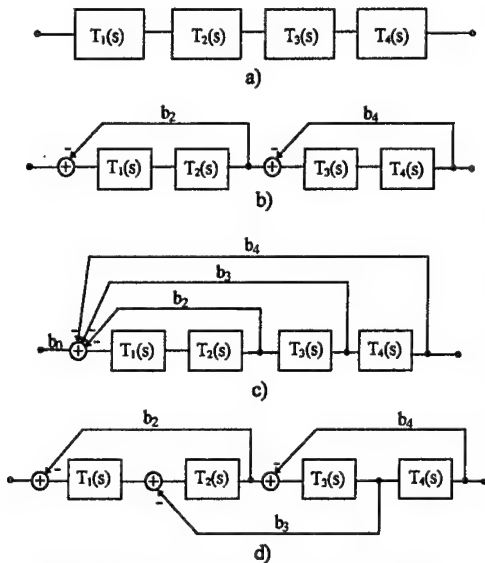


Fig. 3. Eight order filter structures: a)CAS, b)CBQ, c)FLF, d)LF

Tab. I. Parameters of 8 th order filter structures				
	1. section	2. section	3. section	4. section
CAS				
k	1.000713	1.547669	2.363918	8.481441
ω	22616.067	27929.462	19565.899	32283.458
Q	3.503996	3.503996	8.677604	8.677604
CBQ				
k	1.429154	1.071724	4.786445	3.936790
ω	25132.741	25132.741	25132.741	25132.741
Q	3.484582	3.484582	8.412524	8.412524
b		0.347111		0.958478
FLF				
k	2.970806	2.701294	2.597349	2.428101
ω	25132.741	25132.741	25132.741	25132.741
Q	4.927943	4.927943	4.927943	4.927943
b		0.862011	0.204056	0.155407
b ₀	0.391365			
LF				
k	1.243207			1.469175
k ω /Q		8145.5264	8658.0155	
ω	25132.741	25132.741	25132.741	25132.741
Q	2.488001	∞	∞	2.440403
b		0.863514	0.784205	0.674232

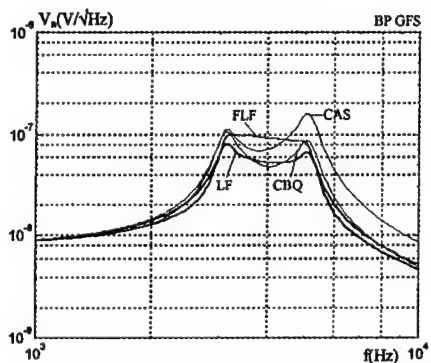


Fig.4. Spectral density for OTA-C structures

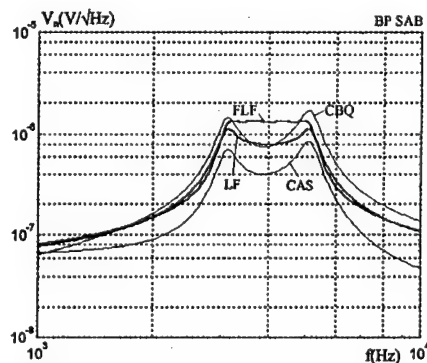


Fig.5. Spectral density for SAB structures

Numerical results of noise voltage spectral density, RMS noise voltage and dynamic range according to (4), (5), and (6) for each described structure are given in tables II and III. From the table II it can be seen that the highest D_R has the LF structure. This is very convenient because LF structure is superior from the sensitivity point as well. Using the presented GFS section the infinite pole Q-factors can be easily achieved. On the contrary, for filters using SAB sections, cascade structure has minimal RMS noise voltage but it also has maximal sensitivities. Which structure should be preferred depends primarily on particular application.

Generally, data from tables II and III shows that filter structures using OTA-C 2nd order building blocks have lower RMS noise voltage. On the other hand limitation on input voltage level gives lower D_R in comparison to the filters with operational amplifiers.

Tab. II. Noise voltage spectral density maximum, RMS voltage and D_R for GFS generated structures

	$(V_n)_{\max}(\mu V/\sqrt{Hz})$	$(E_n)_{\text{eff}}(\mu V)$	$D_R(\text{dB})$
CAS	0.1557	9.048	71.84
CBQ	0.1046	6.556	74.64
FLF	0.1003	7.662	73.28
LF	0.0794	5.707	75.84

Tab. III. Noise voltage spectral density maximum, RMS voltage and D_R for SAB generated structures

	$(V_n)_{\max}(\mu V/\sqrt{Hz})$	$(E_n)_{\text{eff}}(\mu V)$	$D_R(\text{dB})$
CAS	0.8209	52.296	96.60
CBQ	1.6734	102.48	90.76
FLF	1.3546	109.07	90.21
LF	1.1005	81.982	92.69

If the price of filter is important, advantage have SAB filters. Table IV presents number of amplifiers and D_R for the corresponding structures. Commercially available OAs have lower price than OTAs. Number of OA for the same configured 8th order filter is about four times lower then numbers of OTAs what make the price of SAB generated filter lower.

Tab. IV. Number of amplifiers and D_R for presented filters

	CASSAB	CBQSAB	FLFSAB	LFSAB	CASGFS	CBQGFS	FLFGFS	LFGFS
No. OA	4	6	6	7	16	22	21	25
$D_R(\text{dB})$	96.60	90.76	90.21	92.69	71.84	74.64	73.28	75.84

IV. Final Remarks

Noise and dynamic range properties of different filter structures have been analysed. The best noise figure gives the OTA-C Leap-frog structure. Since it is the best structure from the sensitivity point as well, there is no need for making the compromise during the design procedure. Possible limitation can be a filter price because of the need for relatively high number of used OTAs. In application where quality of a processed signal with respect to noise influence is important, LF structure is most suitable. CBQ follows the LF structure having a good noise figure, relatively low sensitivities and more simple design procedure.

From the obtained results it is obvious that the Leap-frog OTA-C filter structure has the smallest RMS noise and the best D_R . However, compared to any of SAB structures it has less dynamic range. Thanking to the better noise figure it is suitable for application in the low voltage signal processing.

References

- [1] Stojković N., Mijat N., "Noise and Dynamic Range of Second Order OTA-C BP Filter Sections", *Proceedings of ECCTD'99 Int. Conf.*, 1999., Stresa, Italy, (to be published)
- [2] Geiger R.L., Sanchez-Sinencio E., "Active Filter Design Using Operational Transconduc. Amplifiers: A Tutorial", *IEEE Circuits and Devices Magazine*, March 1985, pp.20-32
- [3] Zurada J., Bialko M., "Noise and Dynamic Range of Active Filters with Operational Amplifiers", *IEEE Transactions on Circuits and Systems*, October 1975, pp.805-809
- [4] Schaumann R., Ghausi M.S., Laker K.R., *Design of Analog Filters - Passive, Active RC and Switched Capacitor*, Prentice Hall, Englewood Cliffs, New Jersey 07632, 1990.
- [5] Bowron P., Mezher K.A., Muhieddine A.A., "The Dynamic Range of Second-Order Continuous-Time Active Filters", *IEEE Trans. on Circ. and Syst.*, May 1996, pp.370-373
- [6] Malvar H.S., "Electronically Controlled Active-C Filters and Equalizers with Operational Transconductance Amplifiers", *IEEE Trans. on Circuits and Syst.*, July 1984, pp.645-649

D-Fibre Antenna Networks for Microcellular Systems

H.S. Al-Raweshidy¹, A. Bhatti² and G. Murtaza²

¹ *Electronic Engineering Laboratory, University of Kent, UK*

H.Al-Raweshidy@ukc.ac.uk

² *Dept. of Electrical & Electronic Eng., Manchester Metropolitan University, UK*

Abstract. An all-fibre antenna using piezoelectric polymer coated circular core D-fibre has been characterised using finite element analysis. The response of the D-fibre antenna was determined over a wide frequency range from 1MHz to 700MHz. The modelling predicts an electric field induced phase shift of 2.43×10^{-5} rad/(V/m) per metre at 5MHz. At frequencies higher than 8MHz the optical response is dominated by radial resonances of the D-fibre/coating composite.

I. Introduction

Optical fibre microcellular networks have been the subject of extensive research over recent years mainly due to the low loss and large bandwidth of optical fibre. With the increasing requirement for high capacity mobile multimedia services, transmission systems incorporating both radio and optical fibre elements, known as radio-over-fibre (RoF) systems, are expected to find an increasing role in telecommunication networks over the coming years [1]. RoF systems rely on the RF subcarrier to modulate the optical signal, which is then distributed by optical fibre. A recent novel approach in generating an externally modulated optical signal for transmission through an RoF network has been to employ an optical fibre based antenna using piezoelectric polymer coated D-fibre [2]. The D-fibre antenna is used to phase modulate the lightwave with a received RF electrical signal.

The D-fibre as shown in Figure 1 has a D-shaped cross-section, with a flat surface parallel to the longitudinal axis of the fibre. The unique property of D-fibre which makes it more attractive than conventional circular fibre for sensing purposes originates from the greater interaction of the propagating optical field with the external space on the planar side of the fibre geometry. In conventional circular fibre the optical field remains within the fibre structure due to the glass cladding layer, in the case of D-fibre the guiding region is now closer to the outer surface of the fibre. Moreover, removing a small amount of the cladding layer from the flat surface will bring the optical field (known as the evanescent field) to the surface. In this way, the evanescent field allows a much greater interaction between the optical lightwave and any outside perturbation, thus allowing construction of a far more sensitive device.

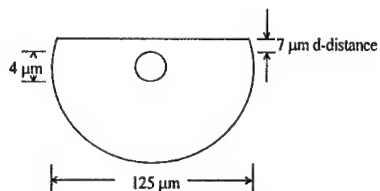


Figure 1. Cross-sectional view of an optical D-fibre

Using FEA this work presents, for the first time, a wide frequency response investigation of an optical antenna based on piezoelectric coated D-fibre. Results showing the frequency response from 1MHz to 700MHz of the phase shift induced in a circular core D-shaped optical fibre jacketed with a transversely polarised piezoelectric material are presented.

II. FEA Simulation

The commercial software package, Abaqus[®] was used to carry out the finite element modelling of the D-fibre antenna. A D-shaped optical fibre with a d-distance (flat surface/core distance) of 7 μ m, cladding diameter of 125 μ m and carrying 20 μ m thick piezoelectric coating was modelled by using three-dimensional finite element analysis. The mesh in Figure 2 represents a symmetrical cross-section of the D-fibre/jacket composite. Each region representing the D-fibre core, cladding and piezo-jacket was meshed separately by using linear brick elements.

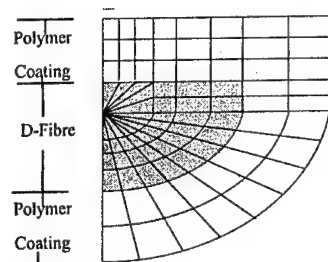


Figure 2. Finite element mesh representing symmetrical cross-section of the D-fibre with its PVDF coating

Steady-state dynamic response analysis was employed to compute the axial and radial strain distribution within the glass D-fibre resulting from the converse piezoelectric effect. This procedure is used when the steady-state response of a system is required as it undergoes excitation by harmonic loading at a given frequency. Such analysis is usually done as a frequency sweep by applying the loading (ac voltage) at a series of different frequencies and recording the response. The solution provides the peak amplitudes and phase relationships of the solution variables (strain, displacements, etc.) as a function of frequency. Once the strain coefficients are known, the optical phase shift resulting from both the change in fibre length and refractive index can be calculated [3].

III. D-Fibre Antenna Response

To obtain the response of the D-fibre antenna to an ac electric field, a frequency sweep was carried out over the range of values from 1MHz to 700MHz as shown in Figure 3. In this high frequency region the net axial strain tends to zero as the wavelength of the acoustic waves propagating in the D-fibre becomes smaller than the longitudinal dimensions of the device, hence the D-fibre response can be considered as being axially constrained [4]. Thus at high frequencies the dominant contribution to the overall phase shift is only from the radial strains induced by the electric field.

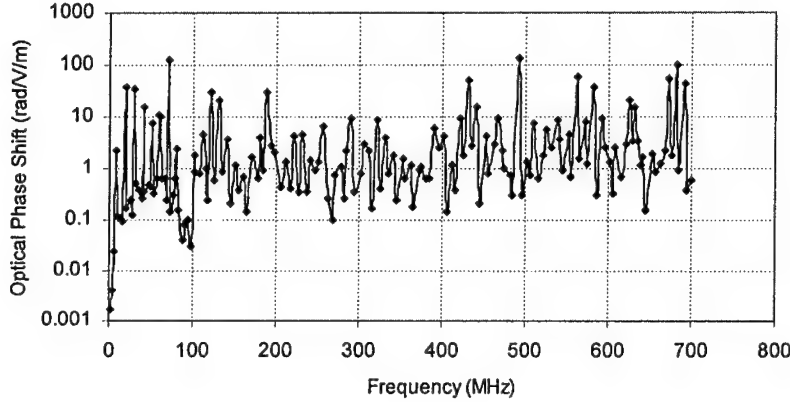


Figure 3. Finite element results showing optical phase shift as a function of the applied ac electric field frequency for a 10cm length D-fibre coated with PVDF polymer

An optical phase shift of 0.00173 rad/V/m was calculated at 1MHz. At frequencies higher than 8MHz, the response is dominated by radial resonances of the D-fibre/jacket composite as the acoustic wavelength becomes comparable to the radial dimensions of the device. A large number of radial resonance peaks are observed in the region from 8-700MHz. The first resonance peak is at ~8MHz and the last at ~694MHz.

IV. D-Fibre Antenna Network

A convenient detection scheme for the D-fibre antenna would be to mix the light beam at the output of the polymer coated D-fibre with that of a second reference fibre, which is not sensitive to the electric field, in a standard interferometric system. Using such a scheme it is assumed that in a mobile microcellular network each microcellular station will include one interferometric D-fibre antenna. Furthermore, in the proposed antenna network it is assumed that a group of microcellular antennae are connected together, and fed by a single laser diode as shown in Figure 4. The minimum detectable phase shift for the network is defined as that for which the total signal current equals the total noise current (i.e. when the SNR equals 1) thus [2]:

$$\Delta\phi_i = \left[\frac{4h\nu\Delta f N_a^3}{\eta P_o} \right]^{\frac{1}{2}} \quad (1)$$

where η is the quantum efficiency of the detector, P_o is the average laser power, $\Delta\phi_i$ is the minimum detectable phase shift for the i th D-fibre antenna, h is Planck's constant, ν is the frequency of light, Δf is the bandwidth of the detector and N_a is the number of D-fibre antennae within the network. Using the values $h = 6.626 \times 10^{-34}$ Js, $\eta = 0.5$, $\nu = 5 \times 10^{14}$ Hz and $P_o = 10^{-3}$ W then for a network comprising two interferometric D-fibre antennae and assuming shot noise limited detection, the minimum detectable phase shift using eqn.(1) can be shown to be 0.146 μ rad/ $\sqrt{\text{Hz}}$.

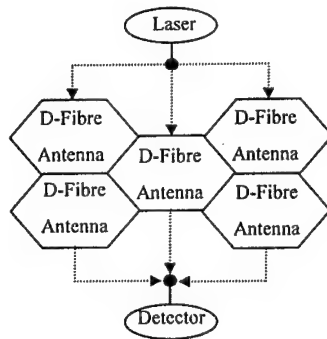


Figure 4. Microcellular D-fibre antenna network

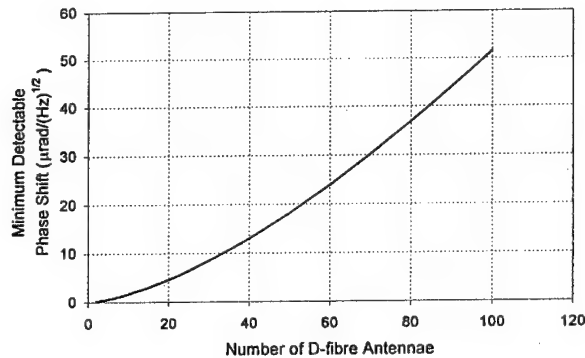


Figure 5. D-Fibre Network Sensitivity

The variation between the number of D-fibre antennae and the shot noise limited minimum detectable phase shift of the proposed network is shown in Figure 5. As can be seen from Figure 5, by increasing the number of D-fibre antennae the level of minimum detectable phase shift increases resulting in an overall decrease in network sensitivity.

V. Conclusions

The wide frequency response of an all-fibre optical antenna comprising a circular core D-fibre coated with a transversely poled piezoelectric material has been demonstrated. Finite element modelling was employed to compute the strain induced phase shift over the frequency range from 1MHz to 700MHz. The FEA simulations predict a phase shift value of 0.00173 rad/V/m in the high frequency (axially constrained) region. At frequencies higher than 8MHz the optical response is dominated by radial resonances of the D-fibre/coating composite. An antenna network has been analysed using shot noise limited detection, which compares the relationship between number of D-fibre antennae and network sensitivity. Since the D-fibre antenna is constructed from totally dielectric materials it can be used to receive radio frequency transmissions without distorting or disturbing the field lines since there are no metallic components to reflect or transmit radio frequency energy.

References

- [1] WU, J.S., WU, J. and TSAO, H.W.: 'A radio-over-fiber network for microcellular system application,' *IEEE Transactions on Vehicular Technology*, Vol. 47, No.1, pp. 84-94, (1998).
- [2] AL-RAWESHIDY, H.S., MUHAMMAD, F.A. and SENIOR, J.M.: 'D-fibre antenna for microcellular mobile communication systems,' *IEE Proceedings-Optoelectronics*, Vol. 143, No. 6, pp. 370-374, (1996).
- [3] DEPAULA, R.P. and MOORE, E.L.: 'Review of all-fiber phase and polarization modulators', *Proc. SPIE, Fiber Optic and Laser Sensors II*, 1984, Massachusetts, Vol. 478, pp. 3-16, (1984).
- [4] BHATTI, A., AL-RAWESHIDY, H.S. and MURTAZA, G.: 'Numerical modelling of a fibre-optic phase modulator using piezoelectric polymer coating,' *IEEE Photonics Technology Letters*, Vol. 11, No. 7, pp. 812-815, (1999).

Properties of Optical Encoders for CDMA Systems

Uherek F.^{1,2}, Hábovčík P.¹, Chovan J.² and Issa B.³

¹*International laser center, Ilkovičova 3, 812 19 Bratislava, Slovakia
uherek@laser.sanet.sk*

²*Department of Microelectronics, Faculty of Electrical Engineering and
Information Technology, Slovak University of Technology, Ilkovičova 3,
812 19 Bratislava, Slovakia*

³*Al-Asad Academy for Military Engineering, Aleppo, Syria*

Abstract. In this paper we report on the analysis of two different topologies of all-optical encoders for O-CDMA systems. The encoders consist of Y and X fibre splitters and single mode fibre delay lines. The measured insert losses of the realised encoders are 11 dB and 14.6 dB. The properties of realised O-CDMA systems with two-stage ladder encoder and decoder are analysed.

I. Introduction

Among the different means of achieving high capacity networks, time-division multiple access (TDMA), wavelength-division multiple access (WDMA) and code-division multiple access (CDMA) have received significant attention in recent years [1].

Optical code-division multiple access (O-CDMA) is a bandwidth utilisation scheme in which many users access a common channel simultaneously through the use of encoding. Each user employs a unique code to distinguish the user's signal from other users. Due to its advantages, CDMA has been the topic of research in the last years, primarily in the radio frequency domain, but also in the optical domain.

Security and privacy are increasingly important issues for many communication applications. While various algorithms can be applied to electronically encrypt data, implementation may lead to an electronic bottleneck for high-speed data transmission. In contrast, the optical coding schemes such as O-CDMA potentially provide high levels of security but are effectively transparent, since the encryption is performed optically and hence are suitable for high bit-rate applications.

In this paper, we examine two different topologies of optical encoders for O-CDMA systems, a two-stage ladder and single-stage star configuration, respectively. Both encoders are realised using Y and X fibre splitters. Generally, the first topology offers lower insert losses and the second more possibilities in independent coding of the signal. Finally the properties of the realised O-CDMA system with two-stage ladder encoder and decoder have been analysed.

II. All-optical encoders for O-CDMA systems

Two types of all-optical encoders for O-CDMA systems have been studied. Encoders were realised using singlemode Y and X fibre splitters from AMP and FOCI, optical fibres produced by SIECOR and optical connectors and couplers from SII. The two-stage ladder encoder shown in Fig. 1 consists of two Y-splitters and one X-splitter. The lengths of optical delay lines in the first and second stage of the encoder were 30 m and 60 m, respectively.

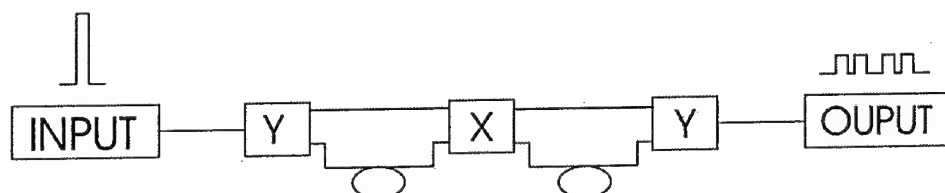


Fig.1 Two-stage ladder type of the encoder

The second, single-stage star encoder consists of six Y-splitters (three in every 1×4 splitter) and four optical fibres with different length as it is seen from Fig. 2. The first fibre delay line was 6 m, second 12 m, third 18 m and fourth 25 m long.

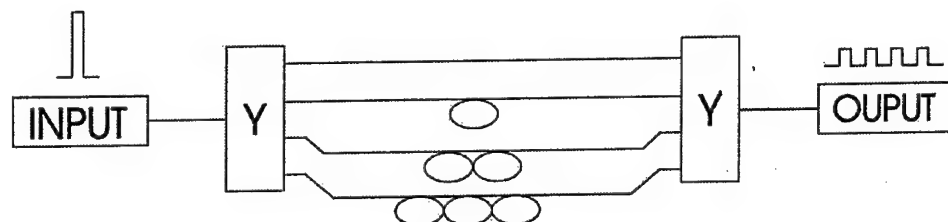


Fig.2 Single-stage star type of the encoder

III. Measurement and results

Properties of constructed encoders have been analysed using the experimental set-up on the Fig. 3. During the measuring of the properties of encoder the decoder has not been connected in the circuit. The pulse generator type TR 307, EMG Hungary, high speed digital laser transmitter BCP, model 51T- 231 (1310 nm, 1 mW, 1.5 Gbps), high speed O/E converter BCP, model 310B (InGaAs APD, 20 dB linear amplifier) and oscilloscope Le Croy 9362 (1.5 GHz, 10 Gs/s) were used for measuring of the properties of the encoders and realised O-CDMA system.

The insert losses of the encoders were measured using 5 ns input optical pulse with a period 750 ns. Measured input pulse amplitude was 24.5 mV (1 mW of optical power).

In the two-stage ladder type of the encoder the average amplitude of four output optical pulses was 1.94 mV. The delay between the first and the second optical pulse of output coded signal was 150 ns, between the first and third pulse 300 ns and between the first and forth pulse was 450 ns. The difference in amplitude of the output pulses was lower than 0.3 mV. It was caused by asymmetric splitting ratio in optical splitters. Measured total insert losses of the encoder are 11 dB, what is in a good agreement with expected value (10.8 dB).

In the single-stage star encoder the average amplitude of four output optical pulses was 0.85 mV. Measured total insert losses of the encoder are 14.6 dB, what correspond with expected value (14.4 dB). The higher total insert losses are the result of higher number of the

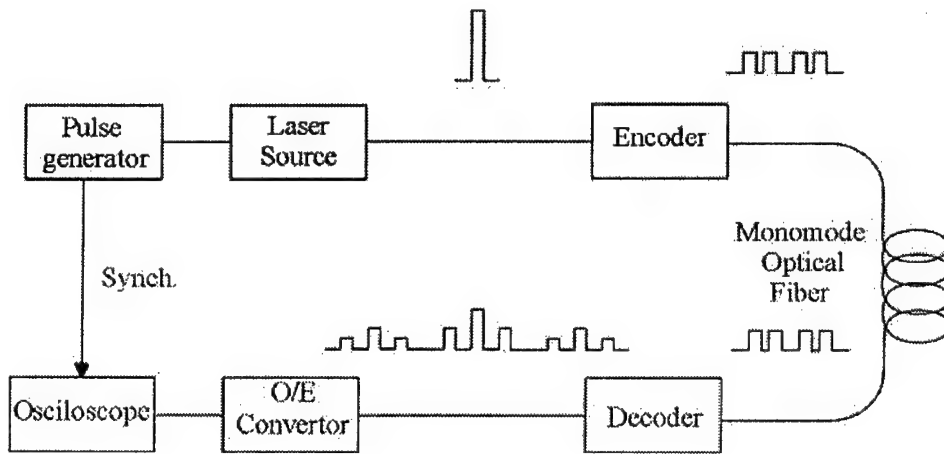


Fig.3 The block diagram of set-up for measurement

fibre splitters and optical connectors needed for realisation of this encoder topology. The delay between the first pulse of output coded signal and the second, third and a fourth pulse was 29, 60 and 117.6 ns, respectively.

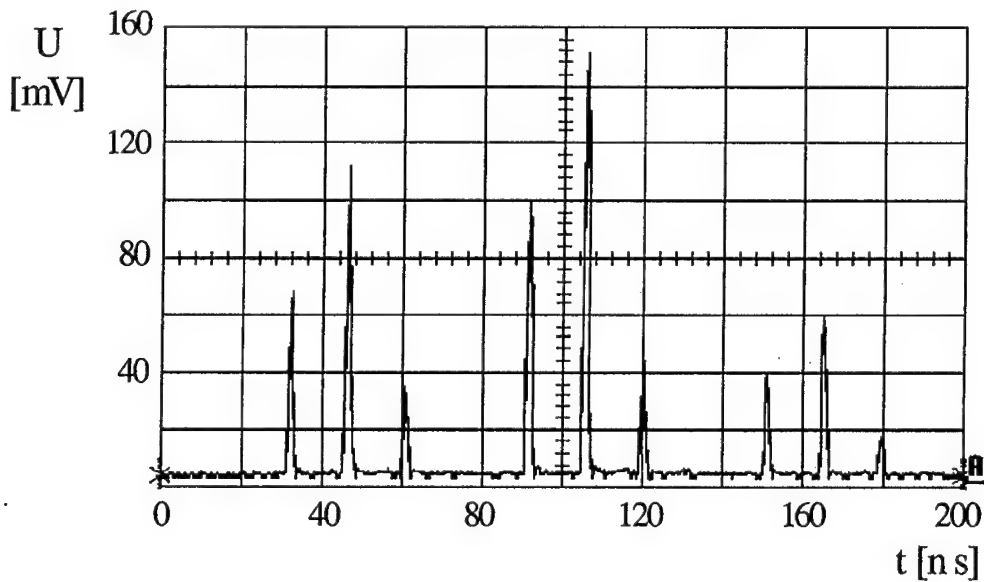


Fig 4 The output signal of the decoder with the autocorrelation peak in the center

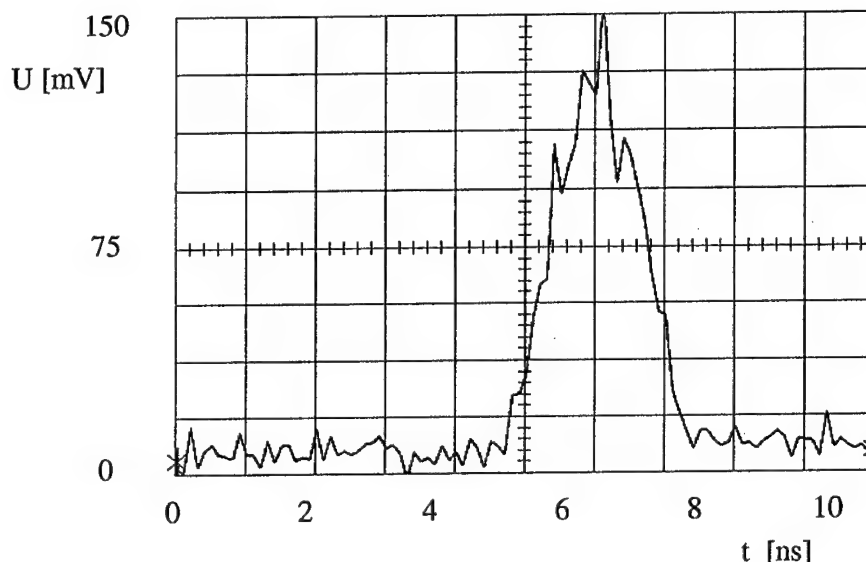


Fig 5 Detail view on the autocorrelation peak of the output signal

Finally, the simple O-CDMA system consisting of two-stage ladder type of the encoder and identical decoder (Fig. 3), was realised and its properties have been analysed.

The output signal with the autocorrelation peak in the centre of the output pulse sequence is in the Fig 4. Asymmetry in the amplitudes of the pulses of the output signal is caused by asymmetry in the fibre splitters. The detail analysis of output pulses shows, that the small differences in the length of the fibres in the delay lines cause the time shift between the subpulses, which create the autocorrelated peak, as it can be seen in Fig 5.

IV. Conclusion

The properties of the two types of all-optical encoders for O-CDMA systems have been analysed. The measured insert losses of the two-stage ladder type encoder and single stage star encoder were 11dB and 14.6dB, respectively. The one-stage star type of encoder offers higher variability and possibility for different coding methods, for example coding using optical switches [2].

Analysis of the realised O-CDMA system shows, that higher stability, quality and reliability O-CDMA system needs the construction of integrated all-optical encoders and decoders and the application of very short optical pulses. This allows using shorter length of delay lines and results in higher stability and accuracy of encoding and decoding signals.

References

- [1] S.W.Seo, K. Bergman, P.R. Prucnal, "Transparent Optical Networks with Time-Division Multiplexing", *IEEE J. Sel. Areas in Comm.* Vol. 14, No. 5, pp. 1039-1051, 1996
- [2] D.J.G. Mestdagh, "Fundamentals of Multiaccess Optical Fiber Networks", Artech House Publishers, 1995

Monolithic Microwave Integrated Circuits Simulation and Optimisation Using HSPICE

Martin TOMÁŠKA

*Microelectronics Department of the Slovak University of Technology
Ilkovičova 3, 812 19 Bratislava, Slovakia
e-mail: tomaska@elf.stuba.sk*

Abstract. The use of HSPICE for GaAs MMIC design and optimisation is described. HSPICE and MDS designs are compared. The use of the HSPICE F20 Standard Elements Library is shown.

Introduction

Usual way how to solve problems concerning the monolithic microwave integrated circuits (MMIC) design, analysis and optimisation is to use the specialised software packages for each particular task. However, there are some possibilities to use some existing wide spread SPICE-based software, i.e. HSPICE, which can be successfully used for AC analysis in frequency domain as well. The building elements of MMIC could be partly different from the usual elements in classical integrated circuits. In practical design, however, the designer's choice of building elements is constrained to devices produced by the foundry. For authentic circuit design the well-defined and verified models of used elements are necessary. They are usually given by foundry as an element library for specified microwave design tools, but not for HSPICE.

Device Modelling

In this work, the HSPICE library of basic MMIC building elements was implemented, based on the GEC-Plessey-Marconi "GaAs IC Foundry Design Manual" [1] for process F20. Since the F20 process is available in the EUROPRACTICE project, there are some perspectives to use this HSPICE F20 Standard Element Library [2] for the design of real MMIC, especially for educational purposes.

Devices are parametrically modelled using HSPICE *.subckt* and *.param* commands with the input of geometrical and/or electrical parameters. Following building element models are created in the library: spiral inductors (5 kinds), line inductors (2 kinds), capacitors (3 kinds), mesa resistor, lossless and lossy non-symmetric microstrip transmission lines (8 kinds), microstrip to MMIC transition (2 kinds), via, bondpad. Two-, four- and six-gate F20 MESFETs with and/or without vias in the source electrode are used as the active elements. Most of the models are driven by electrical or geometrical (layout) parameters, which all are optimisable. The parasitic properties are tracking optimisation or any change of the input parameters or frequency. The transistor models are scaleable, linear and non-linear as well. There are no noise properties modelled.

For the illustration of simple library element description, an example of mesa resistor subcircuit netlist is shown in Tab. I, where $le=100$ $lu=12$ $w=69$ $dw=0$ are resistor default layout parameters, which are optimisable. Equivalent circuit element values as shown in Fig.1 are dependent not only on resistor layout dimensions, but frequency as well.

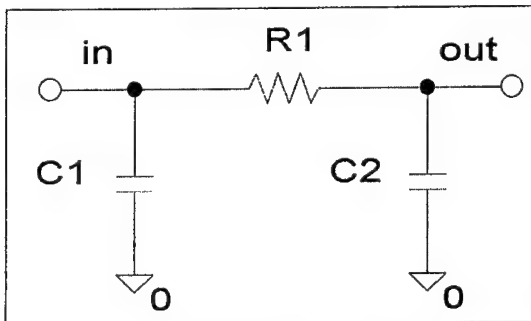


Fig. 1.:
Mesa resistor equivalent circuit

```
.subckt mesa_r in out le=100 lu=12 w=69 dw=0
.param Rdc='(300*Le+180*Lu+1080)/(W-dW)'
.param Z='A_Z+B_Z*W+C_Z*W*W-D_Z*W*W*W'
.param p1='(A_E*W+B_E)'
.param p2='C_E*exp(log(W)*log(D_E))+E_E'
.param p3='10f*(Le+Lu)/(18*Z)'
c1 in 0 '(sqrt(p1*hertz*ln+p2)*p3)'
r in out Rdc ac='Rdc*(1+0.007*hertz*ln)'
c2 out 0 '(sqrt(p1*hertz*ln+p2)*p3)'
.ends mesa_r
```

Tab. I:
Example of mesa
resistor description

The device call is then very simple as usual subcircuit call from library:

```
x_mesa_r_name node1 node2 mesa_r le=100 lu=12 w=69 dw=0
```

All available devices in the F20 HSPICE library [2] are described in similar manner.

Library Elements Verification

To approve the validity of the library elements and the idea of using HSPICE for MMIC simulation a system approach was used. Three-stage low noise amplifier (LNA) from Fig.5.49 in [3] was chosen as an exercise example for a comparison, because of the same foundry used. The circuit diagram of the LNA used for this comparison is shown in Fig. 2. The originally measured and simulated properties from [3] are drawn in Fig. 3.

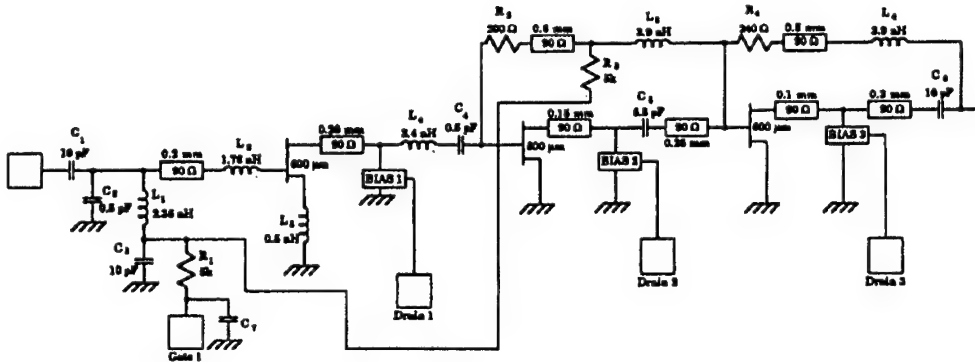


Fig. 2.: Circuit diagram of the three-stage LNA (Fig.5.49 in [3])

The same LNA from the circuit diagram in Fig. 2 was simulated using the HP Microwave Design System [4] with the EUROCHIP GEC F20 library from ENSEA [5] and HSPICE with our F20 HSPICE Library. Both simulated results are shown in the Fig. 4.

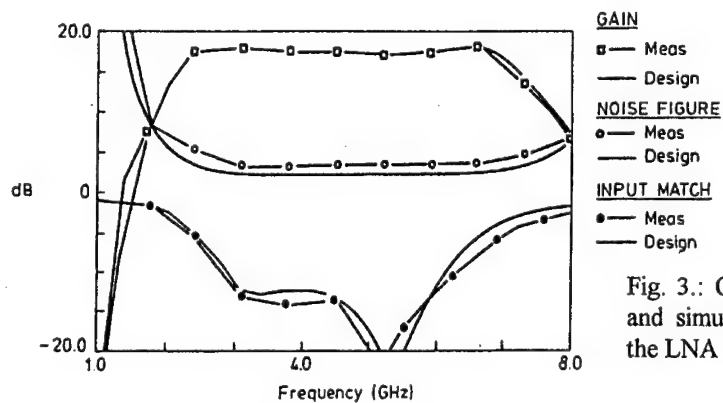


Fig. 3.: Originally measured and simulated properties of the LNA [3]

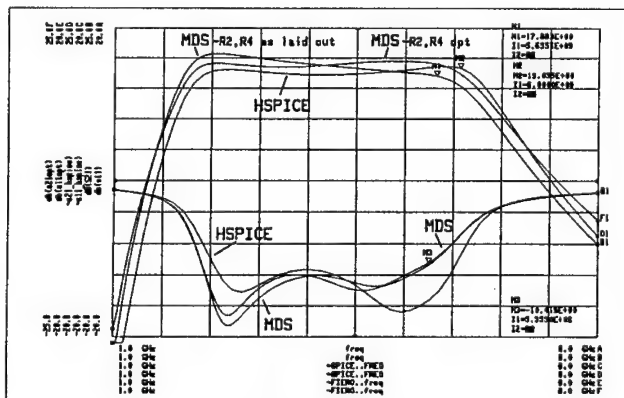


Fig. 4.: Simulated properties of the LNA - HSPICE and HP MDS comparison

There is a difference between MDS and HSPICE simulation, more meaningful in S21 parameter (gain), which is mainly influenced by the feedback resistors R2, R4. To find their differences, they were optimised, so that both HSPICE and MDS S21-responses were most close. Their new values were found (MDS) to be R2=147 ohm, R4=195 ohm, which differs from their original values (-26.5%, -18.75%). Then we found, that the different way to input resistors into MDS is responsible for such a variance. When the responses are compared, with the Fig. 3, a slight difference in S21 and more significant in S11 parameter (input match), can be recognised. However, the HSPICE simulation is more close to original one. The cause can be found in taking into account the discontinuities in MDS (neglecting them in HSPICE), moreover in small differences between the libraries (there are prescribed inductance values in HSPICE used, which results in non-integer quarter-turn number, but MDS library cannot accept them).

When both our results are compared with the original one in Fig. 3, more similar shape for HSPICE simulation results can be seen, S21 peak value is quite equal, S11 as discussed above, however, the bandwidths differ significantly. The gain rising edge is quite the same, but the falling one is shifted down by nearly 1GHz. The main reason responsible for this narrowing can be found in using different MESFETs geometry. Their total width is the same, however, in [3] they use 8x75µm, but in our work 6x100µm is used. Taking this different geometry into account, we can conclude that the HSPICE with our F20 library can be used for MMIC design and optimisation.

Conclusion

The use of HSPICE for GaAs MMIC design and optimisation is described. HSPICE F20 library was verified using system approach and foundry data as well. There was shown that HSPICE F20 Library can be used for MMIC design, especially for educational purposes.

This work was accomplished in the frame of the TEMPUS program, JEP 1565 and the project No. 1/4219/97 of the SGA.

References

- [1] *GaAs IC Foundry Design Manual, Process F20/F14*, The GEC-Marconi Company plc.
- [2] Tomáška, M. *Monolithic Microwave Integrated Circuits Simulation and Optimisation Using Hspice*; internal report, FEI STU Bratislava, 1999
- [3] Goyal, R. *Monolithic Microwave Integrated Circuits: Technology & Design*, Ravender Goyal, editor; Artech House Inc. 1989
- [4] *HP 85150B Microwave and RF Design System*; Hewlett-Packard Company 1992
- [5] *GEC F20 LIBRARY For Microwave Design System*; E.N.S.E.A Equipe Micro-Ondes, Septembre 91, Revised for Eurochip by R.A.L. August 93

Investigation of Non-linear Behavior of Optical Receiver for Multi-channel High-speed Communications

Martin Krnáč, Martin Tomáška

*Department of Microelectronics, Slovak University of Technology,
Ilkovičova 3, 812 19 Bratislava
krmacm@elf.stuba.sk*

Abstract

This work deals with intermodulation distortion (IMD) simulation and investigation of a multi-channel high-speed optical receiver including travelling wave amplifier (TWA) and metal-semiconductor-metal (MSM) photodetector. The final simulated parameters of optical receiver were following: Frequency bandwidth 19 GHz/1.3 dB, Transimpedance 41 dB Ω , Large-signal gain 9.7dB and Suppression of spurious products is near 40 dB.

Introduction

In the age of information technology, huge information transfer capacity is required. For effective communication a multi-channel, high-speed optical communication system could be used with advantage. For this purpose, optical receiver with travelling wave amplifier (TWA) [1] is suitable, because of its extreme wide bandwidth. This type of optical receiver has been designed and optimized using HSPICE [2], [3]. Metal-semiconductor-metal (MSM) photodetector [4] and microwave MESFET's [5] were used as active devices. Components employed in this design except MSM photodetector are from the GEC - Marconi Foundry, Process F20 technology [5]. For multi-channel transmission system with wideband optical receiver an investigation of intermodulation distortion and rejection of harmonics is needed, especially for the 2nd and 3rd order IMD products. It could be accomplished by fast Fourier transformation from time domain simulation using HSPICE.

Optical receiver design and simulation

For multi-channel high-speed optical receiver wide bandwidth amplifier is necessary. The travelling wave amplifier (TWA) for its extreme bandwidth was designed. Circuit diagram of TWA in our design is shown in Fig.1.

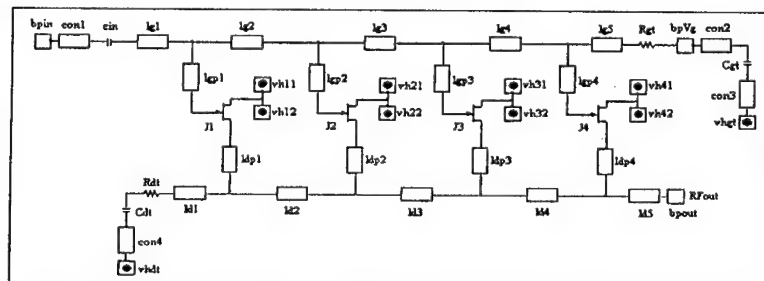


Fig. 1
Circuit diagram
of travelling wave
amplifier for optical
receiver

In construction type and bias point of MESFET's constrains the bandwidth of optical receiver. Simulated transimpedance Z_T frequency response of designed optical receiver with TWA and MSM photodetector is shown in Fig. 2. In our case we have achieved 19 GHz bandwidth. Linearity of the amplifier at 5.045 GHz is visible from Fig. 3.

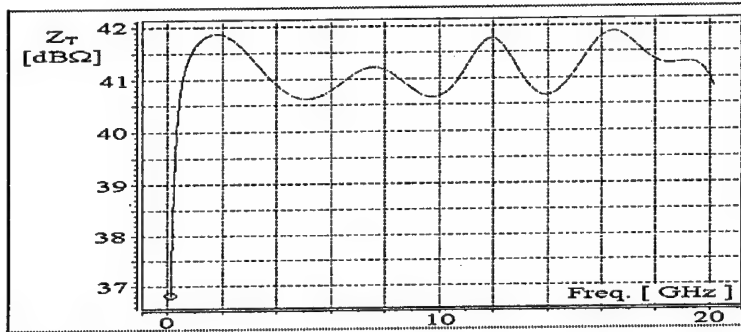


Fig. 2
Transimpedance Z_T
frequency response

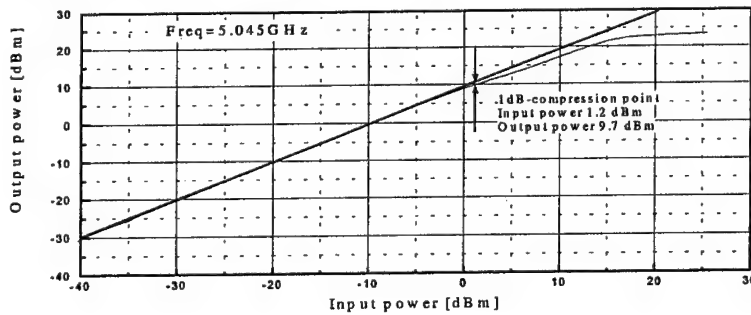


Fig. 3
Power transfer
function

The final simulated parameters of our optical receiver design are following: Bandwidth 19 GHz/1.3 dB, Transimpedance 41 dBΩ, Large signal gain 9.7 dB, and 1 dB gain compression point 9.7 dBm at 5.045 GHz.

Investigation of intermodulation distortion

Each of the non-linear devices can generate intermodulation distortion (IMD). This is defined as production of new spurious output signals, created from non-linear combination of two or more input signals mixing together. An intermodulation product depends on the number of input signals mixed together and which harmonics of those input signals have been mixed together [6].

For two input signal frequencies spurious signals are defined as follows

$$f_s = \pm Mf_1 \pm Nf_2 \quad (1)$$

Where

f_s - frequency of spurious signal

$M, N \geq 1$ - coefficients

f_1 - frequency of 1st signal

f_2 - frequency of 2nd signal

When $M = N = 1$, the spurious responses are called second-order intermodulation distortion products and f_3 and f_4 (Fig. 4) are defined as follows

$$\begin{aligned} f_3 &= f_2 - f_1 \\ f_4 &= f_2 + f_1 \end{aligned} \quad (2)$$

When $M + N = 3$, the spurious responses are called third-order intermodulation distortion products and example f_5 and f_6 (Fig. 4) are defined similarly

$$\begin{aligned} f_5 &= 2f_1 - f_2 \\ f_6 &= 2f_2 - f_1 \end{aligned} \quad (3)$$

The case of two input signals (two-tone test) is seen in Fig. 4.

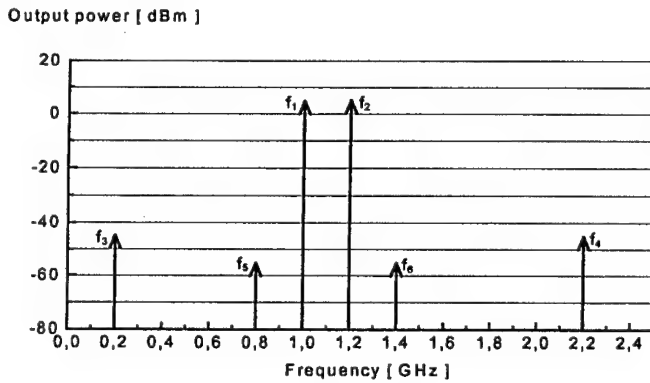


Fig. 4
Spectrum of the two
fundamental signals f_1 and
 f_2 , 2nd order IMD products
 f_3 and f_4 and 3rd order IMD
products f_5 and f_6

For a multi-channel transmission a large number of frequencies corresponding to each channel are present at the input of transmission chain. Due to the non-linearity of devices great number of spurious products is created, therefore the exact analysis is too difficult. However, simulation tools could help us significantly to overcome this problem. In our case we have investigated multi-channel high-speed optical receiver with TWA and MSM photodetector using the 32-carrier phase-aligned matrix generator. The frequency range of generator is from 0.825 GHz to 5.885 GHz with 140 MHz spacing between channels, except channels that are switched off from this interval. The current amplitude is $31.25 \mu\text{A}$ per channel. This corresponds to 5 mW of input optical power incident to MSM photodetector with sensitivity 0.2 AW^{-1} at 5 V bias. An investigation of spurious products has been made using HSPICE. Input and output signal time response was transformed by fast Fourier transformation to frequency response. The spectrum of 32-carrier phase-aligned matrix generator (Vsource) is displayed in the bottom part of Fig. 5. The simulated spectrum of input (Vin) and output (Vout) signal of optical receiver is shown in the top part of Fig. 5. The detail of these spectrums is shown in Fig. 6.

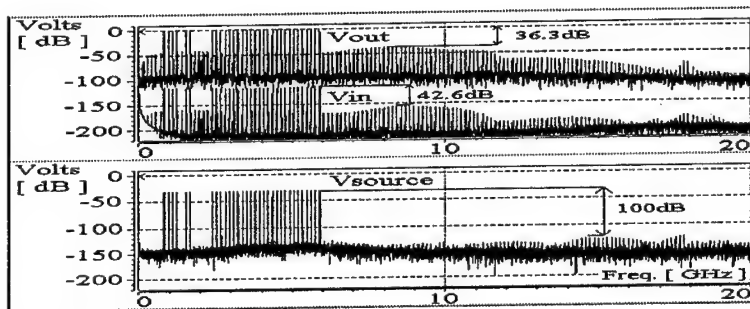


Fig. 5
Spectrum of input (Vin) and output (Vout) signal and spectrum of the 32 carriers phase-aligned matrix generator (Vsource)

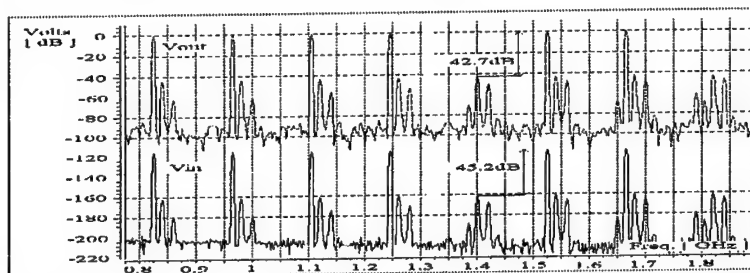


Fig. 6
Detail of spectrum of input (Vin) and output (Vout) signal

Rejection of the harmonics, 2nd and 3rd order IMD products are illustrated in Fig. 5 and detailed spectrum in the range of 2 GHz in Fig. 6. Contribution of amplifier transfer function nonlinearity on IMD is 2.5 dB and it's shown in Fig. 6 and the rejection of IMD is clearly seen to be near 40 dB. They are generated on non-linear input of MESFET's.

Conclusion

High-speed optical receiver employing travelling wave amplifier has been simulated and investigated in the frequency band 0.1-20 GHz to find intermodulation distortion (IMD) as a very important parameter for multichannel transmission systems. The 1 dB gain compression point was found equal to 9.7 dBm of output power near 5 GHz. From analyze simulated spectrum we found that spurious products originate mainly from input non-linearity of transistors and their suppression was found to be near 40 dB in full frequency band.

Acknowledgement:

This work was accomplished in the frame of the project No. 1/4219/97 of the SGA.

References

- [1] Krnáč Martin "Travelling wave amplifier for optical receiver", Diploma thesis, December 1998
- [2] HSPICE user's manual, software for IC design version 98.2
- [3] Martin Tomáška "MMIC Simulation and Optimization using HSPICE," internal report, 1999, FEI STU Bratislava, Slovakia
- [4] Tomáška M., Marso M., Fox A., Kordoš P "Microwave Properties of the MSM Photodetectors with 2-DEG," Conf. proc. ASDAM'98, 5-7 oct. 1998, Smolenice, Slovakia, pp. 295-298
- [5] GEC-Marconi Foundry Process F20 Design Guide
- [6] John J. Jacobi "IMD: Still unclear after 20 years," *Microwaves & RF*, pp. 119-126, November 1986

Computer-aided Design of Application Microcontrollers

D. Cherniakovski, K. Kazakevich, I. Kazimirovski, V. Stepanets,
S. Trofimov

*Dept. of Mechanics and Mathematics, Byelorussian State University,
pr.F.Skoriny 4, Minsk
Stepanets@mmf.bsu.unibel.by*

Abstract A customisable nodes' library, a special VHDL-model, programmed electronic mock-up, modern universal and original software-hardware means are necessary components of instrumental tools for their computer-aided designing. In the paper the computer-aided design tools and main characteristics of single-purpose microcontrollers NT80XX family have been given. Described tools have been used during the design of the large number of different microsystems.

I. Introduction

Microcontrollers' integrated circuits got broad spreading at the end 70-th years [1]. Originally, these chips had universal nature. Other components of different microprocessors' systems determined a specific character of their using. However, on the measure of their complication they transformed in typical example of the programming application specific integrated circuits (ASIC).

At present it is observed generalisation of experience of their development and using. On this base microcontrollers' families are formed, and also efficient computer-aided design tools are created. Such families are oriented on the building of single-purpose systems of determined class. A customisable nodes' library, a special VHDL-model, a programmed electronic mock-up, a modern universal and original software-hardware means are necessary components of instrumental tools for their computer-aided designing.

Below the main characteristics' features of NT80XX microcontrollers' family, the composition of customisable cells' library, the using VHDL and PLIC models, the employing software has been described.

II. Instrumental tools for microcontrollers and microsystems design

We will introduce the instrumental tools on example of microcontroller of NT80XX family.

The existing tools of CAD allow executing following types of customs:

- design and delivery of microsystems with using the having or a new variant of microcontroller of NT80XX family;

- programming and foundry the finished microcontroller of NT80XX family with primary delivery of VHDL- and/or PLIC- model;
- design, programming and foundry a new microcontroller of NT80XX family with primary delivery of VHDL- and/or PLIC- model;
- delivery of VHDL- and/or PLIC- model of having microcontroller of NT80XX family.

The MENTOR GRAPHICS(Design Architect, AccuSim, QuickSim II, IC Station), XILINX(Foundation), ACCEL(PCAD) companies and original software [3] are used during design of microcontrollers and microsystems.

Design process flow of these microcontrollers is typical route of CAD of Application Specific Integrated Circuits (ASIC) [4]. It contains following design stages:

- design capture;
- VHDL description;
- behavioural simulation;
- logic synthesis;
- gate-level simulation;
- PLIC-model synthesis;
- layout synthesis;
- foundry and delivery.

High speed and quality of design are secured by using of special microcontrollers' model. In first order it contains VHDL-description.

The using VHDL-model is universal description, adjusted to architecture of any single-purpose microcontroller of NT80XX family. The chip-level description [5] was chosen during its writing. The model has following distinctive features.

Description of microcontroller behaviour is "architectural body". Corresponding «processes» included in model reflect behaviour of each of general hardware blocks. The NT-model processes graph is shown on fig.1.

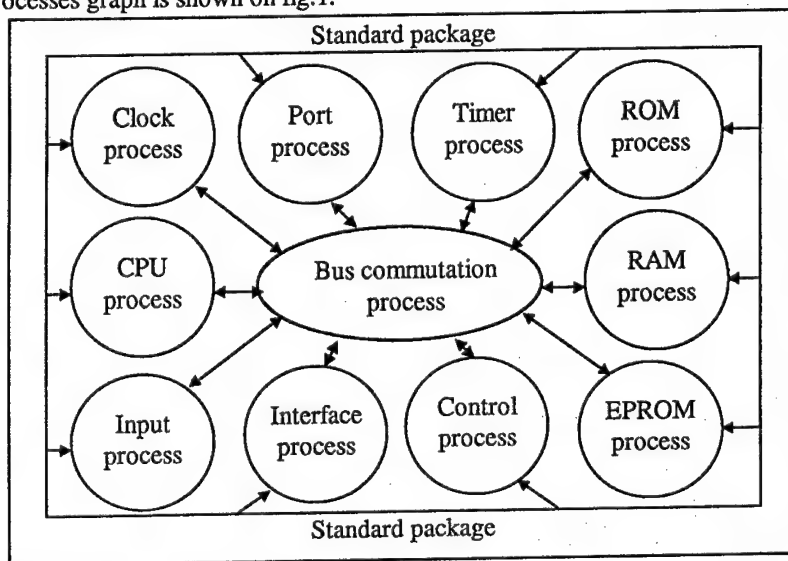


Fig.1. Graph of NT-model processes

A description of transformation algorithm has an abstract nature. For account of delay the result is transported by final operator (operators) to output signal (signals). Adequacy of blocks' interaction is ensured by "bus commutation process". The model "standard package" contains the type descriptions, parameters' values, subroutines and etc. Change of descriptions of "standard package" and "bus commutation process" allows tuning of the VHDL-model for necessary microcontroller architecture. Debugging microsystems program can be introduced into VHDL-model in bit or assembler form (fig.2.). Therefore, the use described VHDL-model ensures required any creating specialised microsystems accuracy and high velocity of modelling.

```

CalcCRC: [--rp]          /* store return address
        b = [sp++]       /* bh=[sp++], bl=[sp++]
        t = b            /* T buffer address
        b = 0            /* bh=0, bl=0
        [--sp] = b       /* CRC beginnig value
BuffCycle: [--rp]       /* byte cycle
        al = [t++]
        work = al        /* next byte

```

Fig.2. Example of assembler form program

Concrete technological and circuit's realisation of blocks (processes) is generated on the next stages of design flow. Under it the layout of blocks and whole source symbolic plan-model of chip are tuned. In the course of designing one-to-one correspondence between described the VHDL-model and microcontroller PLIC-model is ensured too.

III. Main characteristics of NT80XX family

NT80XX family is set of application specific CMOS microcontrollers. These chips are oriented to the solution of control and data acquisition tasks in independent from the AC/DC sources' systems with low level of power consumption. Now the family contains few finished chips programming by customer [2]. They are broadly using in different microsystems. This set may be quickly completed according to customer wishes too.

Architecture of new microcontroller of this series can include the following kit of tuning blocks:

1. Dual stack RISC microprocessor core includes ALU, set of basic registers and command decoder. It allows performance of main commands for one processor clock. Five addressing modes can be used to memory reference. The set of commands includes following groups: data transfer instruction; arithmetic and logical operations; branch instruction; group of special instruction. This block contains two stacks for realisation of subroutine call mechanism: a data stack and return stack.
2. Serial interface is a half-duplex asynchronous.
3. Kit of operating timers ensures a possibility of automatically rebooting.
4. The watchdog timer checks the program performing.
5. The input/output ports are programming.
6. The internal ROM is programming by mask.

7. The internal RAM is static.

8. The electrically erasable reprogrammable ROM (EEPROM) allows to store most important data during power off.

Architecture of any microcontroller allows programming the character of using (internal/external) of memory area. Customer may elaborate the range and space of the each of described blocks.

The microcontroller NT8020 has the following characteristics:

- Supply voltage..... 2.7 ÷ 3.9 V
- Supply current at stop mode 1.5 μ A @ 3 V
- Supply current at low-speed operation 10 μ A @ 3 V
- Supply current at high-speed operation 1 mA @ 3 V
- Internal clock frequency at $X_{IN} = 4$ MHz 2 MHz
- Internal clock frequency at $X_{CIN} = 32$ kHz 16 kHz
- Internal ROM size ... 16K bytes.

The kit of accessible hardware blocks is extended constantly.

IV. Final Remarks

The using of the described tools gives possibilities for high speed design of the ASICs in a short time. Orders are executed together with "High Technology - Scientific Centre" of Byelorussian State University and "NT-Laboratory" enterprises. They had used for design of several tens of domestic and foreign microsystems [6]. At present the design of new NT8030 microcontroller is completed. Improvement of computer-aided design tools is be realised constantly.

References

- [1] A. A. Vasenkov, V. A. Shagnov. *Microprocessor kits of integrated circuits*, Radio and communication, 1981.
- [2] *One-chip NT8020 microcontroller user's manual*, NT-Laboratory, 1997.
- [3] V. Stepanets. "The Mathematical Model for Computer-Aided Design of Integrated Circuit Layout", *Proceeding of 5-th International Conference Mixed Design of Integrated Circuits and Systems (MIXDES'98)*, Lodz, Poland, 1998, pp. 163-166.
- [4] J. R. Armstrong. *Chip-Level Modelling with VHDL*, Prentice-Hall, 1989.
- [5] J. P. Huber, M. W. Rosneck. *Successful ASIC Design the First Time Thorough*, Van Nostrand Reinhold, 1991.
- [6] V. Kuchko, V. Ravko "NT8020 microcontroller", *Radiolubitel*, N 12, pp. 42-44, 1996.

Design and Implementation of Error-Control Coding: Cyclic Code Architectures

K. Vlček

Dept. of Measurement and Control, Technical University of Ostrava,
17. listopadu 15, 708 33 Ostrava-Poruba, Czech Republic

E-mail: karel.vlcek@vsb.cz

Abstract: The specific design language properties of VHDL allow the designer to use the routines results in average two times improvement in the logic capacity of the programmable devices. The CPLDs and FPGAs architectures assume the technology specific optimisation techniques, including algorithms for state machine and glue logic, and module generation for data path and arithmetic logic, to take maximum advantage of unique architectures for significant speed and area reductions.

I. Introduction

The paper is dedicated to description of circuit implementations of encoders and decoders of error-control codes. To be technology independent, the descriptions are done in VHSIC Hardware Description Language (VHDL), which becomes the universal description mean of digital circuits. The hierarchical structure of VHDL is ideally suited for description of extensive electronic circuits and systems, which are needed with the requirement of high speed of communication. Other aspects of applications, which are not visible: the support of testing of circuits and systems.

The design methods must be versatile and technology independent for of CPLDs (Complex Programmable Logic Devices), FPGAs (Field Programmable Gate Arrays), and CMOS ASIC design. Students and designers can quickly efficiency, and economically consolidate multiple designs into one larger design, retarget a design, and use VHDL to accomplish their designs. The programme packages can optimise the designs for area and/or speed. The VHDL accepts designs described as equations, truth table descriptions or interconnection descriptions.

II. Example of Error-Control Architecture Design

It is introduced an example of VHDL models of the both encoder of Systematic Cyclic Hamming (15,11)-code with generating polynomial $g(x) = x^4 + x + 1$ and Meggit decoder of this code. It is used a permitted error vector to try the error correction of Meggit decoder model. The basic part of systematic (15,11)-code encoder uses the circuit for dividing by generating polynomial $g(x) = x^4 + x + 1$. The block diagram of this circuit is as follows:

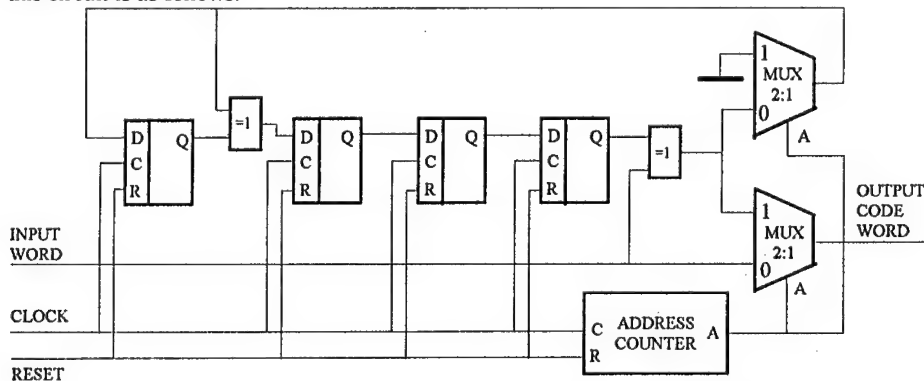


Figure 1: Block diagram of (15,11)-code encoder circuit

The circuit on the *Figure 1* consist of the Linear Feedback Shift Register (LSFR), which is in function for the first eleven steps of clock. To complete the output code word the remainder is affixed to the information bits. Due to it is for the last four steps changed address of multiplexers. It causes, that the remainder is shifted through the "lower" multiplexer to the output. During next four steps it is completed the output code word. The block of address counter must be configured to be possible use the address output "A" for addressing the both "lower" and "upper" multiplexers.

After finishing the code word, the encoder is prepared to generate another output code word, if the address counter is initialised. That is, it must do the multiplexers to address the first eleven steps of next fifteen cycle code word generating. The reset signal can be used for this initialisation. The initialisation of the LSFR is not necessary, because it was feed the value "0" through the "upper" multiplexer. The value "0" in the feedback wire is necessary to change the LSFR into usual shift register. The block diagram of (15,11)-code encoder circuit is described to do the encoder circuit model easier.

III. Encoder Circuit Model Composition

The first step of modelling is description of behavioural models of elementary parts of circuit. There are defined entities of flip-flop, EX-OR gate, multiplexer and counter:

```
-- description of overall structural model

entity encoder is
port ( input_word, clock, reset : in bit;
      output_code_word : out bit);
end encoder;

architecture encod_11_15 of encoder is
  const ground := '0';
  component ff_f
    port (d,c,r : in bit ;
          q : out bit);
  end component;

  component Ex_or
    port ( In1,In2 : in bit;
          Out1 : out bit);
  end component;

  component mux_2_1
    port ( I0, I1, a : in bit;
          y : out bit);
  end component;

  component counter
    port ( cl, res : in bit;
          out_a : out );
  end component;

begin
  p1: mux_2_1 port map (input_word, oxor2, count_out,
    output_code_word);
  p2: mux_2_1 port map (oxor2, ground, count_out, fb);
  p3: Ex_or port map (fb, q1, oxor1);
  p4: Ex_or port map (q4, input_word, d2);
```



```

p5: ff_f      port map (fb, clock, reset, q1);
p6: ff_f      port map (d2, clock, reset, q2);
p7: ff_f      port map (q2, clock, reset, q3);
p8: ff_f      port map (q3, clock, reset, q4);
p9: counter   port map (clock, reset, count_out);
end encod_11_15;

```

The model of cyclic Hamming (15,11)-code with generating polynomial $g(x) = x^4 + x + 1$ is written in VHDL language. The overall circuit is modelled by structural model. It is possible to add some delays in the model description to enhance the readability of output signal waves during the simulation.

IV. Decoder Circuit Description

The construction of Meggit decoder is based on the property of the cyclic codes: We can concentrate on the last position of each received word w , which we correct or not, according this syndrome. Then we make a cyclic shift of code word w , and again study the last position, etc. After n cyclic shifts, all positions will have been corrected. For the generating polynomial $g(x) = x^4 + x + 1$ we can compose syndrome computing circuit for the systematic cyclic Hamming (15,11)-code.

To correct an error we will use the syndromic value 0001. To be the received word corrected it must be delayed 15 steps. This delay is realised by the shift register with 15 flip-flops. For generating an correcting bit it is used the circuit completed by two inverters and one four input gate with AND function and concatenated gate with EX-OR function.

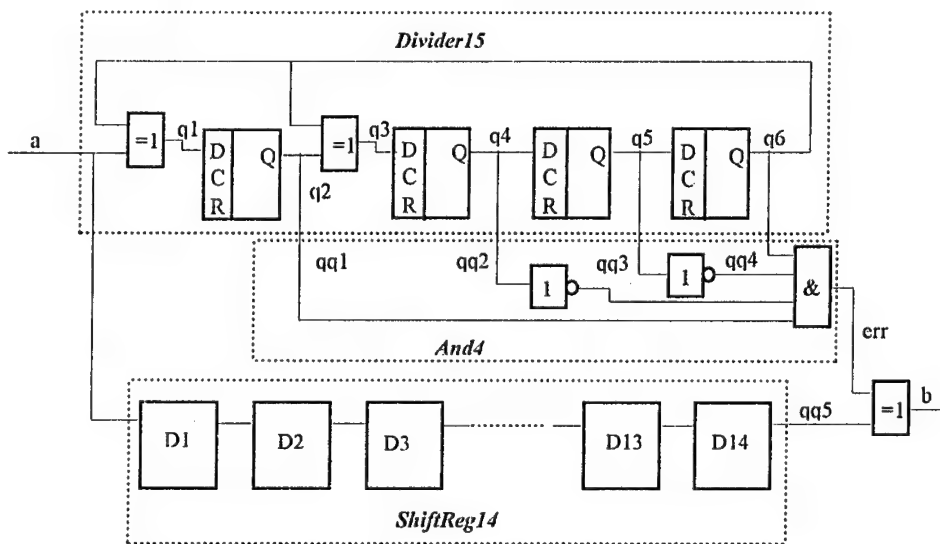


Figure 2: Block diagram of (15,11)-code decoder circuit

V. The Overall Model of Decoder Circuit

The modelling is defined by description of behavioural models of elementary parts of circuit. There are defined entities of flip-flop, EX-OR gate, inverter, and AND-gate:

```

entity hamdec15o1 is
  port (a, cl, rr: in bit;
        b : out bit);
end hamdec15o1;

architecture hdl15a of hamdec15o1 is
  component Ex_or
    port ( In1, In2 : in bit;
          Out1 : out bit);
  end component;
  component ShiftReg14
    port (in1 : in bit;
          cl,r: in bit;
          out1: out bit);
  end component;
  component And4
    port ( in1, in2, in3, in4: in bit;
          out1 : out bit);
  end component;
  component Divider15
    port (a, cl, rr: in bit;
          m1,m2,m3,m4: out bit);
  end component;
  signal qq1,qq2,qq3,qq4,qq5 : bit;
  signal err: bit;

begin
  n2: Divider15    port map (a,cl,rr,qq1,qq2,qq3,qq4);
  n5: And4         port map (qq1,qq2,qq3,qq4,err);
  n6: ShiftReg14   port map (a,cl,rr,qq5);
  n7: Ex_or        port map (err,qq5,b);
end hdl15a;
-----

```

VI. Conclusion

The Meggit decoder is realised as an structural model composed from behavioural models of components. Some components "Divider15", "And4" and "ShiftReg14" are modelled by structural models too. The model was verified by functional simulation using the software suite V-System. Decoder corrects one error when two errors occurs decoder detect error but it cannot be corrected.

Support for GACR project "Research and Development of Built-in Diagnostics Means of Integrated Circuits" (No. 102/98/1003) is gratefully acknowledged.

References

- [1] Adámek, J.: Kódování. SNTL Praha (1989)
- [2] Adámek, J.: Kódování a teorie informace. ČVUT Praha (1991), ISBN 80-01-00661-1
- [3] Blahut, R.E.: Theory and Practice of Error Control Codes. Addison-Wesley (1983)
- [4] Vlček, K., Miklík, D.: The VHDL Model of DEC-TED Memory Checker. Proc. of Ninth Europ. Workshop on Dependable Computing. (May 14-16, 1998, Gdansk, Poland), pp. 54-58.
- [5] Vlček, K.: The VHDL Model of Wzner-Ash Channel Coding for Medical Applications. Proc. of DECS, Szczyrk, (2-4 Sept., 1998), pp. 145-151, ISBN 83-908409-6-0

Electrodynamics Analysis of Shielded Microstrip Lines by Partial Domain Method

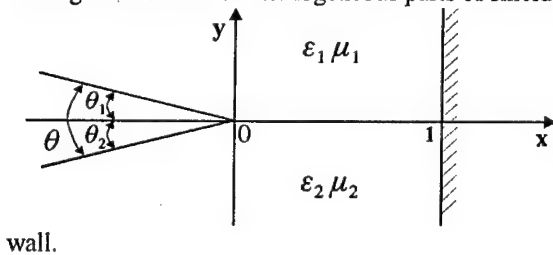
Ştefan Cantaragiu¹, PhD Eng.

¹Ministry of National Defence, Procurement Department, 9-11,
Drumul Taberei Street Sector 6, Bucharest, Romania,
Email: scantaragiu@hotmail.com

Abstract. In this paper partial domain method for the analysis of various homogeneous and non-homogeneous shielded microstrip lines is presented. This method determinate electromagnetic field configuration taking into account interface between two media and frontier conditions.

I. Introduction

The formulation for this problem has two parts: first of all it has to pass from the real object to the physical model and then it has to make the mathematical modelling of the adopted physical model. This method affords achievement of some efficiently computing algorithms for electromagnetic field, that take into account of various geometrical homogeneous and non-homogeneous parts of shielded lines (figure 1).



Having into account the transversal section of the shielded microstrip line it was created a model (figure 1), where interface between 1 and 2 domains coincide with 0x axis, the origin of the axis is next to the strip edge and for x=1, we have a electric

wall.

Figure 1. Model for the shielded microstrip line

II. Partial Domain Method

In order to determine the propagation parameters in this guiding structure, one must solve some partial differential equations, like the Helmholtz equation:

$$\Delta\Phi + k^2\Phi = 0, \quad (1)$$

which is the general equation for the longitudinal field components (E_z and H_z). Solving in the domain represented by the transverse section through the waveguide these equations, with consideration of the appropriate bordering conditions, one gets the field structures inside the waveguide and hence the desired propagation parameters.

Proceeding from the Meixner model [2], we have the condition in point x=0:

$$\{\varphi_n\}, \{\psi_n\} = O(x^{\alpha_0}), \text{ for } x \rightarrow 0,$$

where: $\alpha_0 = -1 + \tau_0$, for the tangential electromagnetic field components at the interface between media (E_x, E_y, H_x , și H_y);

$\alpha_0 = \tau_0$, for the longitudinal electromagnetic field components;

τ_0 is the minimum positive solution of the characteristics equation that is born after the introduction of the proposal solution in the Maxwell equations [2].

After the checking of the chosen function system orthogonality, we might use the following expressions for the approximation of the electromagnetic field components E_x, E_z, H_x and H_z at the strip edge and at the interface between two media:

$$\varphi_{en}(x) = \frac{1}{\sqrt{1-u^2(x)}} T_{2n}(u(x)); \quad (2)$$

$$\psi_{en}(x) = U_{2n}(u(x)); \quad (3)$$

$$\varphi_{hn}(x) = \frac{1}{\sqrt{1-u^2(x)}} T_{2n+1}(u(x)) \quad (4)$$

$$\psi_{hn}(x) = U_{2n+1}(u(x)); \quad (5)$$

where T_{2n} and T_{2n+1} are first rang and two order Chebyshev polynoms;

U_{2n} and U_{2n+1} are two rang and two order Chebyshev functions;

$$u(x) = 1 + \frac{2x-w}{w-a}, \quad u: \left[\frac{w}{2}, \frac{a}{2} \right] \rightarrow [1, 0].$$

Then the continuity relations are written for the determination of the unknown coefficients from the Fourier approximation. Having into account the Helmholtz solution equations and orthogonal function properties we obtain linear algebraic equation system [8].

$$\sum_{n=0}^{\infty} c_{kn} \bar{C}_n + \sum_{n=0}^{\infty} d_{kn} D_n = 0, \quad (7)$$

$$\sum_{n=0}^{\infty} c'_{kn} \bar{C}_n + \sum_{n=0}^{\infty} d'_{kn} D_n = 0 \quad (8)$$

$$\text{where: } c_{kn} = \frac{1}{k_0} \sum_m \xi_{mn} b_{km} \sum_{\delta=1}^2 \frac{(-1)^{\delta} k_{\delta}^2 Y h_{\delta m}(y_1)}{\mu_{r\delta} Y h_{\delta m}(y_1)},$$

$$d_{kn} = \frac{\beta}{k_0} \sum_m h_m \alpha_{mn} b_{km} \sum_{\delta=1}^2 \frac{(-1)^{\delta} Y h_{\delta m}(y_1)}{\mu_{r\delta} Y h_{\delta m}(y_1)},$$

$$c'_{kn} = \frac{\beta}{k_0} \sum_m e_m \xi_{mn} a_{km} \sum_{\delta=1}^2 \frac{(-1)^{\delta} Y h_{\delta m}(y_1)}{\mu_{r\delta} Y h_{\delta m}(y_1)},$$

$$d'_{kn} = \frac{1}{k_0} \sum_m \alpha_{mn} a_{km} \sum_{\delta=1}^2 \frac{(-1)^{\delta} \chi_{\delta m}^2 Y e_{\delta m}(y_1)}{k_{\delta m}^2 \mu_{r\delta} Y e_{\delta m}(y_1)},$$

$e_m = -h_m = \frac{X e'_m(x)}{X h_m(x)} = -k_{xm}$; $\chi_{\delta m}^2 = k_0^2 \epsilon_{r\delta} \mu_{r\delta} - k_{xm}^2$; a_{km} , α_{mn} , b_{km} and ξ_{mn} are the Fourier coefficients.

For having the solutions for the algebraic system it is necessary to determinate the propagation coefficients value, β that check the "dispersive equation" [8]:

$$\det \begin{bmatrix} c_{kn} & d_{kn} \\ c'_{kn} & d'_{kn} \end{bmatrix} = 0. \quad (9)$$

Fourier series from the infinite equation system are replaced after the analysis of them convergence with finite partial sums. The propagation coefficient values that check the equation (9) will decided the configuration of the hybrid propagation modes from the shielded microstrip line.

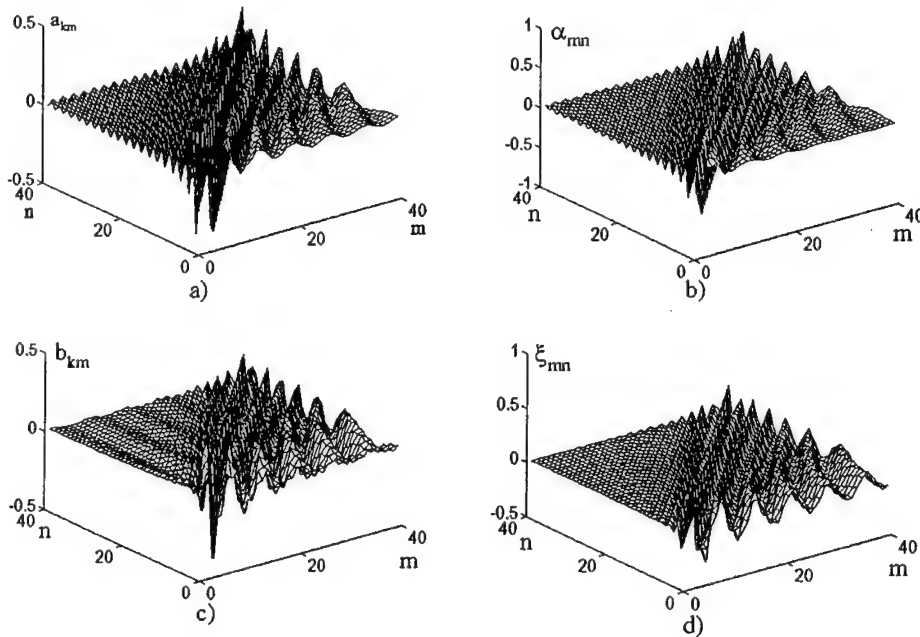


Figure 2. The variation of the Fourier coefficient values for $n=k=1 \div 40$ and $m=1 \div 40$

For the facility of the equation (9) solving it will be considerate $n=k$. The variation of the Fourier coefficient values a_{kn} , α_{mn} , b_{kn} and ξ_{mn} , obtained with Matlab program, are presented in figure 2 for $n=k=1 \div 40$ and $m=1 \div 40$.

III. Results. Final remarks

It will de considerate a real structure of the shielded microstrip line ($w=1 \times 10^{-3}$ [m], $a=3,5 \times 10^{-3}$ [m], $y_1=0,5 \times 10^{-3}$ [m], $y_2=2 \times 10^{-3}$ [m] and $\epsilon_{r2}=9$).

The propagation coefficient values that decide the configuration of the hybrid propagation modes are also computed with Matlab program. The minimum frequency where the propagation is made without loss is equal with 38.188 GHz.

The longitudinal component configurations of the electric and magnetic field at the 38.188 GHz are presented in the figure 3. The transversal components determination will be made with longitudinal components derivation expressions.

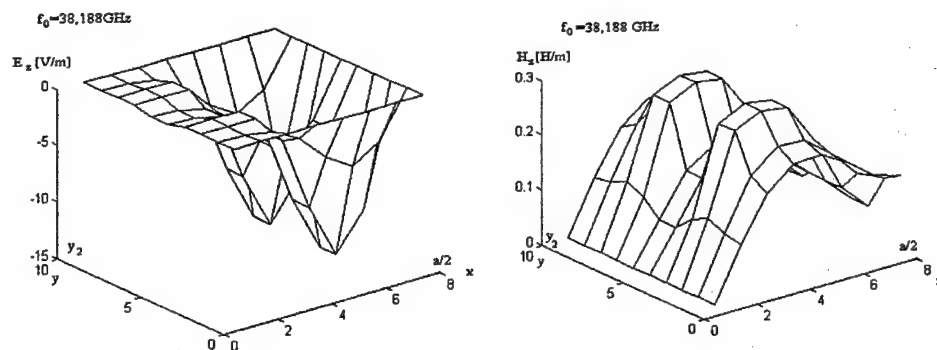


Figure 3. The variation of the longitudinal components of the electric and magnetic field in network points

References

- [1] E. YAMASHITA & R. MITRA Variational method for the analysis of microstrip lines, *IEEE Trans. Microwave Theory Tech.*, vol. MTT-16, pages 251÷256, Apr. 1968.
- [2] J. MEIXNER The Behaviour of Electromagnetic Fields at Edges, *IEEE Trans. A. P.* 20, 1972.
- [3] S. PATRICK & K. WEBB, A Variational Vector Finite Difference Analysis for Dielectric Waveguides", *IEEE Trans. Microwave Theory Tech.*, vol. 40, pages 692÷698, Apr. 1992.
- [4] G. I. VESELOV, *Microwave Device*, Moscow, 1989.
- [5] G. RULEA, *Theoretical and Experimental Bases of the Microwave Technique*, Bucharest, 1989.
- [6] G. E. LOJEVSCHI, *Transmission Lines for Microwave*, Bucharest, Technical Ed., 1996.
- [7] ȘT. CANTARAGIU Electromagnetic Field Calculations of Microstrip Lines using Finite Difference Method, *Technische Mitteilung TM-S-EA 94.08.02-2*, Oerlikon Contraves, Zurich, 1994.
- [8] ȘT. CANTARAGIU *Electromagnetic Field Shielded Microstrip Line Study by Means of the Analytical and Numerical Methods*, doctoral degree work, Military Technical Academy, Bucharest, 1997.

The Possibilities to Prepare Chemosensors by Thick Film Technology - The Market Implementation for the Future

Miroslav Pradka

Ivan Szendiuch

*Department of Microelectronics, Technical University of Brno, Udolní 53, Brno 602 00,
Czech Republic
pradka@umel.fee.vutbr.cz, szend@umel.fee.vutbr.cz, fax: +420-5-43167-298*

Abstract. The chemical sensors are recently designed also by Thick Film Technology (TFT). The experience with preparation of novel chemical sensors based on conductivity and biosensor principle are described.

The special emphasize has been put to the design of gas sensors with respect to production of suitable sensing parts for automotive industry.

The sensors for special high-precise analyses could be prepared also by TFT, the main results obtained at detection of drugs, poisoning substances and enzymes inhibitors by advanced chamber thick-film substrate RING 4 are mentioned. The testing of presence of drugs used in medicine can be seen as a new area of the usage of thick film chemical sensors. The implementation of such sensors to the market cannot be expected in the very near future and the possibilities of their usage and the market estimation will be discussed.

Keywords: thick film technology, electrochemical sensor, thick film sensor, gas sensing, chamber thick-film substrate

I. Introduction

The detection of dissolved species presents an important analytical measurement in a wide variety of industries. For example, the food and chemical industries require electrochemical sensors for dissolved species to control reaction rates occurring within process tanks through of monitoring of reactants and products, the medicine requires the frequent analysis of body fluids, environmental engineering and military provide routine analyses of poisoning substances and pollutants. The estimation of composition of various gases is valuable for many industrial branches, environment monitoring, medicine and military.

Recently, the Thick Film Technology (TFT) has been used also to design electrochemical sensors, chemical sensors and biosensors. Advantages of TFT can be seen especially in low cost production of small/middle amount of sensors sufficiently adapted to market requirements at acceptable design loop duration.

Nowadays one can distinguish two principal groups between chemical and electrochemical Thick Film Sensors (TFS). The first one is presented by sensors based on the measurement of conductivity among usually interdigitated electrodes and the second one based on another (amperometric, potentiometric, ..) measuring principle realized in elective electrode system (two-, three-electrode systems, various reference electrodes, enzymatic electrodes, etc.) Consequently the TFT enables to prepare integrated sensors, arrays of sensors and sensors equipped by electronic components.

The estimations for sensors market presume the remarkable increase of demand in so called typical applications: industrial machines, process control, automotive, security, communication and telemetry. The possibilities to place well the electrochemical TFS in the market are very uncertain to predict in global scale but last results in the research already show the good chance to start industrial production in sufficiently short time horizon.

II. Theory

The sensors are transducers converting measured quantity into a signal. When designed like TFS, the procedures of screen printing and firing are employed. The overview of possible TFS' types has been summarized i.e. in [1], [2].

In most cases the conductometric gas chemosensors make use of the chemiresistor fixed on interdigitated electrodes. The chemiresistor, most frequently made from organic material, changes its conductivity in the presence of suitable chemical compounds, i.e. reducing/oxidising gas. Gas chemisensor operate in elevated temperatures, up to 600K. The poor selectivity of the response to given gas in gas mixture belongs usually to principal problems of chemisensors. The metal-phtalocyanines (CuPC, FePC, CoPC, ZnPC, GaPC, ..) present a kind of chemical compounds frequently used like chemiresistors.

The problem with insufficient selectivity, as in gas chemical sensors, can be treated by the use of more selective sensing principle, as shown in biosensors [2], [3]. The biosensor is the type of chemisensor which uses biologically sensitive material to detect chemical species; enzymes, tissue patterns and microbial cells can be used like sensitive part of biosensor. Also biosensors as very specific type of chemosensors are designed like TFS. Main disadvantage of biosensors can be seen in easy vulnerability of layers made from biological material.

III. Conductometric Gas Sensor for Automotive Industry

The detection of pollutants contained in exhaust gases is expected to be required in the near future and in fact this means the design of reliable sensors for analyses of nitrogen oxides (NO_x), methane (CH_4), carbon oxide (CO) and carbon dioxide (CO_2). At the use of metal-phtalocyanines as chemiresistor, the significant aspect of phtalocyanine response which affects the functionality of sensors, is the change of central atom of the material and the operating temperature. We have put an emphasis to obtain the good reproducibility of the response of sensors to one selected gas - NO_2 . The best results have been reached with copper-phtalocyanine (CuPC) like a chemiresistor. The layout of the used chemisensor (interdigitated electrodes, temperature sensing element and heater) on alumina substrate (96 per cent) and the molecule of copper-phtalocyanine (chemiresistor) are described in figure 1. When printed copper-phtalocyanine containing paste the experience shows to the best stability of changes of conductivity for the squeegee pressure of 22,5PSI ($1,5\text{kg/cm}^2$) and squeegee speed of 10mm/sec. Tested sensors have been operated at the temperature of 433K and the evaluation of response dispersion has been provided for the serie of 20 pieces of sensors, see figure 2.

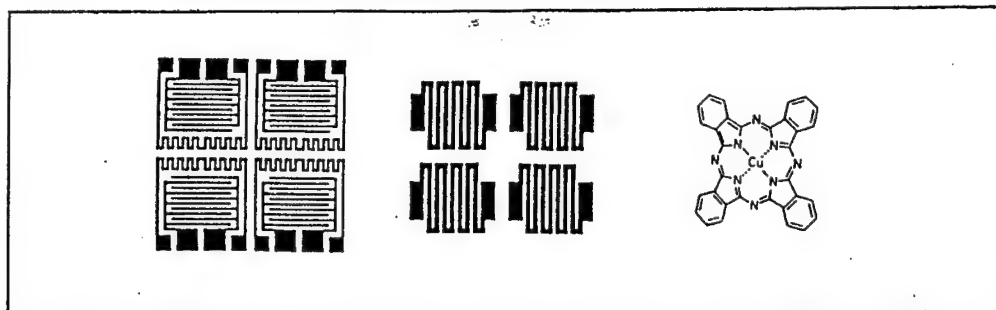


Fig. 1. a) Platinum interdigitated electrodes (Heraeus C3657) and temperature sensing element (Heraeus LPA 88-11), b) heater (Heraeus C3657) on alumina substrate (96 per cent); c) molecule of CuPC

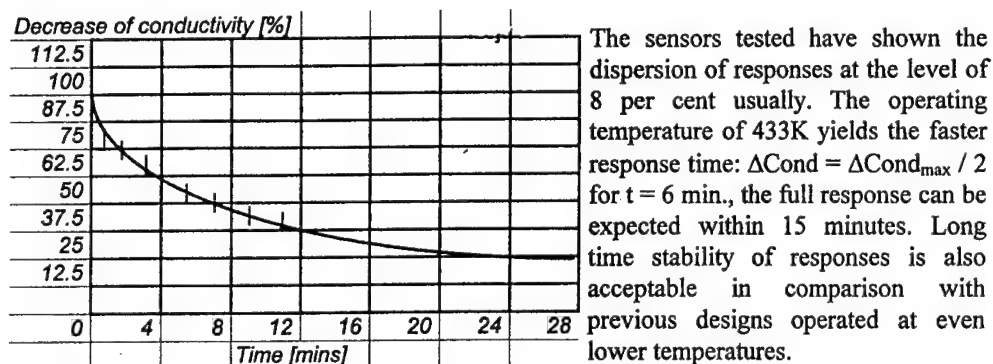


Fig.2. Time response of CuPC chemosensor to NO_2 , $T=433\text{K}$

IV. Drug Evaluation by Thick Film Chemosensor Based on Biosensing Principle

The thick film substrate RING4 (Fig.3.) has been used for preparation three-electrode biosensor to detect pattern drug - demecarium. Three-electrode system (working, reference and auxiliary electrode) placed on two alumina substrates (96%) borders the flow reaction cell. The working electrode made from platinum paste (Heraeus C3657) is polarized vs. reference Ag/AgCl electrode $+365\text{mV}$, the output signal has been processed by the usual potentiostat. Biosensing membrane contains AChE (acetylcholine esterase) from *Electrophorus electricus* (EC 3.1.1.7), $A \approx 450\text{IU/mg}$; total activity of the enzyme membrane is approx. 20IU . Electron transfer to Pt electrode is realized by CuPC-containing composite layer; its composition: 6 (CuPC): 89 (graphite): 5 (acetylcellulose), modification of [4] - carefully screen printed. Reference electrode Ag/AgCl has been prepared by electrochemical chloridization of silver layer, finally both layers are protected by KCl deposition. Lifetime of reference electrode has been estimated to 6 weeks. AChE inhibitor and drug demecarium has been evaluated at following conditions: $T=298\text{K}$, cell flow $125\mu\text{l/min}$, $0,4\text{ mmol/l}$ of acetylcholine chloride as reaction substrate (Aldrich, $M_r=226.12$, pur. 99%) in 50mmol/l phosphate buffer, time to reach the steady-state response for substrate is about 20 minutes, output current approx. 270nA , output current decrease 4nA/hour , output signal stability in steady-state at least for 48 hours, the average time of inhibition effect of demecarium was 10 hours.

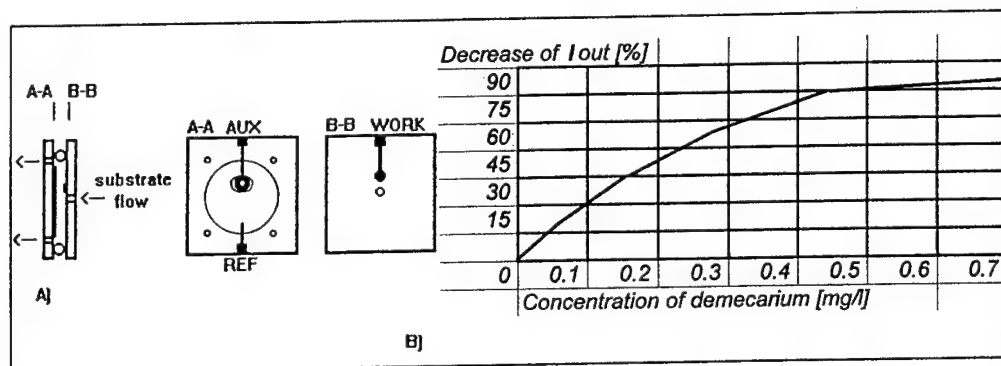


Fig. 3. a) biosensor substrate RING4, b) decrease of I_{out} with respect to concentration of demecarium

V. The Market Implementation for the Future

The recent prognoses of total sensor market estimate the growth up to 65 bil DM in 2001 from 49.7bil DM in 1996; the massive increase expects the automotive industry, about 90 per cent. The expected distribution of market around the world in 2001 is mentioned in fig.4. Nowadays the situation in novel thick film designs gives a good chance to expect the massive increase also here but there is problem of research phase duration, i.e. the development of thick film sensor for glucose diagnosis has lasted about 14 years but then the production and improvements of sensor went very fast. So that we have to distinguish 1) the TFS almost suitable for mass production (gas sensors for automotive industry) and 2) the other designs like biosensors that will be introduced to market after several years of improvements. But in spite of this fact, these designs are very prospective and the demands of low cost disposable diagnostic stripes (i.e. TFS) in various branches will rapidly grow.

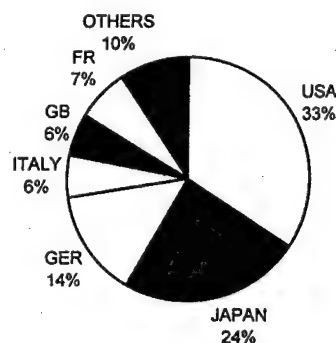


Fig.4. World Sensor Market in 2001

VI. Conclusion

The brief description of two prospective designs of TFS has been shown for gas sensor for NO_2 and chamber two-substrate chemosensor based on biosensing principle for the determination of concentration of drug demecarium (AChE inhibitor). The prospective market implementation of such designs can be documented by expectations in global sensor market predicted for 2001, specific limitations valid for TFS have been briefly mentioned.

VII. Literature

- [1] Harsanyi G., "Sensor Tec. and Applications," Dept. Elect. Tec., TU Budapest, Hungary.
- [2] Krejci J., Primovich M., Szendiuch I., Pradka M., "Thick Film Sensors - New Trend in Hybrid Technology," *Proceedings of IMAPS 98 Conference*, 1998, San Diego, USA.
- [3] Kulys J., D'Costa E J, Biosens. Bioelectron., 6 (1991) 109.
- [4] Skládal, P.: Determination of organophosphate and carbamate pesticides using a cobalt phtalocyanine-modified carbon paste electrode and a cholinesterase enzyme membrane, *Anal.Chim.Acta*, 252(1991) 11-15

Synthesis and Simulation of HW/SW Systems with Performance Estimation

Gregor Polanšek¹ Andrej Žemva² Andrej Trost² Baldomir Zajc²

¹IskraTEL, Ljubljanska 24a, 4000 Kranj, Slovenia

²University of Ljubljana, Faculty of Electrical Engineering
Tržaška 25, 1000 Ljubljana, Slovenia

Abstract. In this paper, we present an environment for synthesis and simulation of the industrial digital system composed of the target microprocessor, memory and hardware devices. We use C++ for coding the program for the target microprocessor and VHDL for describing the operations in hardware. The presented system combines C++ compiler and VHDL tools for simulating the design. The applicability of the environment for performance estimation of the designed digital system is demonstrated.

I. Introduction

Today, typical digital system is composed of the specific microprocessor, memory and hardware environment implemented either as full custom ASICs or programmable devices [1]. Traditional design flowchart of these systems starts with the high level system description, hardware/software partitioning, hardware and software implementation and system integration into the target environment. Since the errors in software and hardware are commonplace and in most cases encountered only once the system is integrated into the target environment, software program and hardware devices are likely to be modified. This is a difficult and time consuming step which may lead even to the modification of the printed circuit board.

In contrast to the traditional system flowchart, HW/SW co-design enables simultaneous design of hardware devices and software program at the earliest stages of the design which reduces and minimizes any design errors [2,3,4].

In this paper, we will present our approach for the HW/SW co-simulation of the telephone exchange boards developed and used in telecommunication industry. We use C++ for coding the program for the target microprocessor and VHDL for defining the operation of hardware devices. For the given HW/SW partitioning, the presented system combines C++ and VHDL tools for simulating the designed system. We demonstrate the applicability of the environment for estimating the timing performances of the designed digital system.

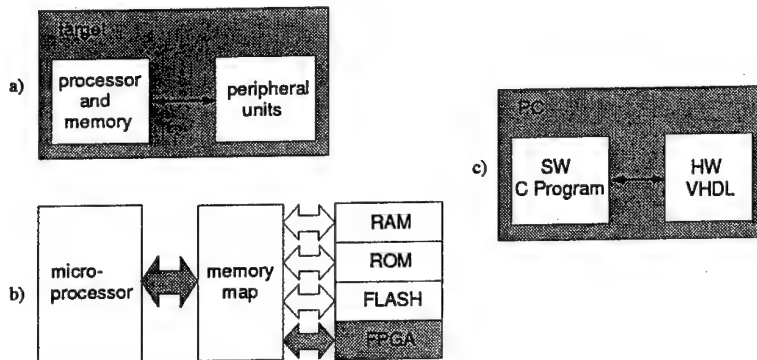


Figure 1: Digital system simulated.

II. Co-simulation of C++ program and VHDL code

The main idea is to simulate the digital system composed of the processor, memory and peripheral units (Figure 1a) on the PC. The microprocessor memory address map consists of RAM, ROM, FLASH and registers of the peripheral units implemented in FPGA devices (Figure 1b). The simulation model of the digital system from Figure 1b is presented in Figure 1c. The behaviour of the microprocessor and the memory is described with the C++ program while the operations in hardware (FPGAs) are defined in VHDL. The primary goal of our work is to automatically generate an interface between C++ program and VHDL simulator [5] by modifying the C++ program as described next.

Modifications of the C++ Program

There are two reasons for modifications of the C++ program. Since we replace the target microprocessor with the PC, the first modifications require:

- replacing functions and libraries of the target operation system (pSOS [6]) with the standard C++ functions and libraries (stdlib.h, string.h, time.h, etc),
- replacing functions for terminal communication with standard functions for reading and writing from the standard input/output devices.

The second modifications are due to the communication with the VHDL simulator. These modifications include:

- including functions `ReadAccess()` and `WriteAccess()` for communication with the VHDL simulator. These functions read data from the output file or write data to the input file of the VHDL simulator.
- replacing program lines with `*Point_HW`, where `Point_HW` is a pointer to the location in hardware devices, with the functions `ReadAccess()` and `WriteAccess()`.

The approach is illustrated with a sample C++ program shown in Figure 2.a. A value of 0XFF is written to the memory location 0X3000 in the hardware device and the contents

<code>#define REGISTER 0X3000;</code>	<code>#define REGISTER 0X3000;</code>
<code>main()</code>	<code>main()</code>
<code>int *Point_HW, a;</code>	<code>int a;</code>
<code>Point_HW = REGISTER;</code>	
<code>*Point_HW = 0XFF;</code>	<code>WriteAccess(REGISTER, 0XFF);</code>
<code>a = *Point_HW;</code>	<code>a = ReadAccess(REGISTER);</code>
a.)	b.)

Figure 2: Sample C++ program.

of this location is then assigned to the variable *a*. The modified code is illustrated in Figure 2.b. Modifications of the code are done automatically in the preprocessing step. In the next subsection, the communication between the C++ program and the VHDL simulator is described.

Communication Between the C++ Program and VHDL Simulator

When in the C++ program an access to the location in hardware devices is detected, data for the VHDL simulation are automatically written in the command file and the simulator is invoked. Simulator may return the processed data in the output file, C++ program reads the obtained results and continues with the execution. It must be noted that the C++ program communicates with the VHDL simulator only if the access to the registers in hardware is detected. Accesses to the other memory addresses do not affect the flow of the C++ program.

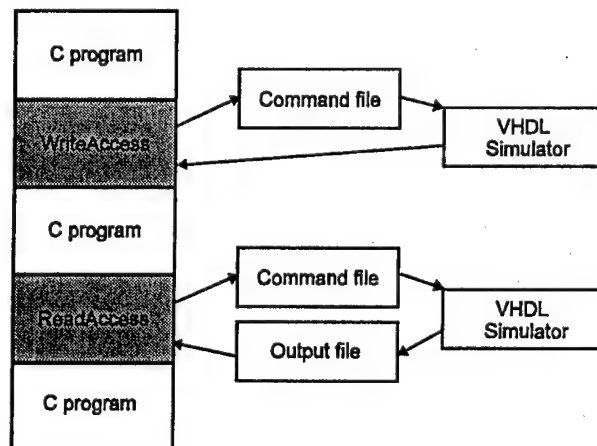


Figure 3: Communication between C++ program and VHDL simulator.

However, the co-simulation can be accelerated by decreasing the number of communications between the C++ program and the simulator. The sequence of write accesses is performed then with a single run of the simulator once a read access is detected.

III. Performance Estimation of the System

One of the main issues of the HW/SW co-design is to optimize the design considering either timing performances or cost of the system or power consumption etc. Here, we will describe the method for estimating timing performances of the system. Since the timing performances of the hardware devices can be accurately determined with the VHDL simulator, the basic idea is to estimate the execution time of the C++ program on the PC.

Timing performances of the software are estimated with the C++ function *clock* which returns the number of ticks corresponding to the processor execution time. Since functions *WriteAccess()* and *ReadAccess()* are due to the communication between C++ program and VHDL simulator, they are both excluded from this calculation. The approach is illustrated in Figure 4.

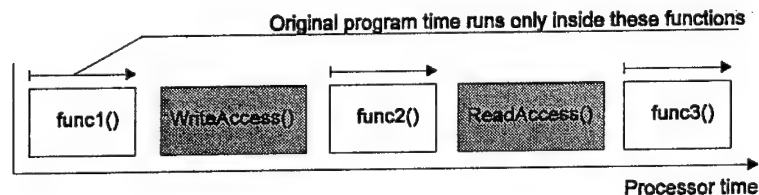


Figure 4: Estimating the timing performance of the system.

IV. Conclusions

In this paper, an open environment for HW/SW co-simulation is presented. The presented environment is opened in terms of the target system and different programming tools for simulation. The future work will be based on accelerating the HW/SW co-simulation.

References

- [1] R. Ernst, Codesign of Embedded Systems: Status and Trends, *Design and Test of Computers*, 45:45-54, April-June 1998.
- [2] G. de Micheli and R.K. Gupta, Hardware/Software Co-Design. *Proceedings of IEEE*, 82:349-365, March 1997.
- [3] A. Sedelmeier, K. Buchenrieder and C. Veith, Industrial HW/SW Co-Design, *Hardware/Software Co-Design*, pp. 453-466, 1996.
- [4] S. Kumar and F. Rose, A Codesign Environment Supporting Hardware/Software Modeling at Different Levels of Detail, *Fifth International Workshop on Hardware/Software Co-Design*, 1998.
- [5] Model Technology, V-System/Plus, PC User's Manual, 1997.
- [6] pSOS User's Manual, Integrated Systems, Inc., 1995.

Single-Input Rail-to-Rail Voltage-to-Current Converter Consisting of Three Complementary MOS Transistor Pairs

Richard Izák

*Dept. of Microelectronic Circuits & Systems, Technical University of Ilmenau,
P.O.Box 10 05 65, D-98684 Ilmenau, Germany
izak_dfw@inf-technik.tu-ilmenau.de, izak@ieee.org*

Abstract. We discuss an simple approach of voltage-to-current conversion intended to provide a front-end interface for current-mode processing systems. The circuit principle is based on a high-resistive CMOS inverter followed by current-mirrors. Over the entire rail-to-rail input range an output linearity error less than 4.37% and THD of 2.253% are achieved. The six-transistor circuit does not require any bias voltage and operates for power supply down to 3.3V, with a PSRR of 30dB and 1.6mW power dissipation.

I. Introduction

One of the main drawbacks of existing MOS technologies are the low-value ($2.5\text{k}\Omega/\square$), but inaccurate resistors (20% mismatching). However, many IC applications require linear transconductors (voltage-to-current converters), e.g. for implementing continuous-time active filters [7, 8], and interfacing the current-mode on-chip processing [9]. By using the operational transconductance amplifier (OTA) the input voltage range is limited to a fraction of the supply range [1, 7, 8], otherwise, extensive circuit techniques are used to obtain a true input rail-to-rail operation [2, 3]. We propose a CMOS transconductor circuit which consists of six transistors and operates in a rail-to-rail voltage input range. The high-ohmic input is suitable for decoupling the input node from the previous output, as used for current generation of a sensitive voltage node, where the value was stored on a capacitor [4]. Providing a voltage-current interface, another application of this circuit is the analog high-level synthesis [5], on the level transition from information flow graph (i.e. without signal denotation values) to a signal flow graph, called as electrical conditioning synthesis [5].

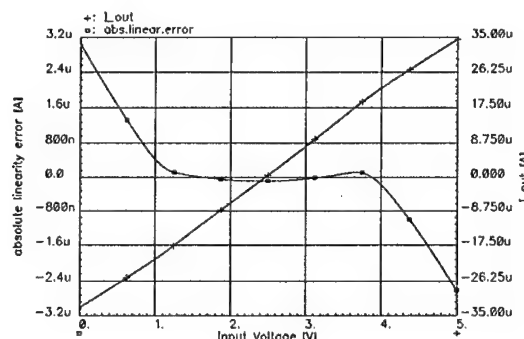
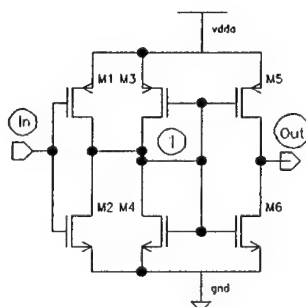


Figure 1: Single-input CMOS V-I converter and its DC-transfer curve, including the absolute linearity error referred to a linear regression ($L_{1,2}=30\mu\text{m}$).

II. Circuit description and analysis

The discussed circuit is a modification of the voltage-to-current converter introduced by Wang [10]. Wang's proposal of a CMOS transconductor included the circuit consisting of transistors M3–M6 from Fig.1-left. We extended this circuit by an inverter M1–M2 at its input. Using long-channel transistors M1, M2 ($L > 20\mu\text{m}$) the inverter stage becomes high-resistively compared to the succeeding minimally sized transistors in the current-mirrors, thus the transfer curve of the inverter is linearized, as shown in Fig.2-left. The inverter stage can be considered operating as a high-impedance current source, providing input current to the mirror M3–M6. The current magnitude and flow direction are determined by the operating regions of the inverter transistors, these again depend on the input voltage V_{in} (see Fig.2-middle). The DC-voltage at node 1 is fixed nearby to $V_{dd}/2$ potential (if $K_p \frac{W_3}{L_3} = K_n \frac{W_4}{L_4} = \beta_{3,4}$), and the rail-to-rail amplitude of input signal V_{in} causes only a small deflection in a range of hundred mV around this potential. The transistors M3 through M6 operate in saturation, whereas M1 and M2 change from turned-off through saturation to linear region, and vice versa. Using the current-mirror M3–M6, an output impedance transformation from high- to a low-resistive circuitry ($g_{DS5} + g_{DS6} \gg g_{DS1} + g_{DS2}$) on condition of retaining the current magnitude at nodes *Out* and *1* is achieved.

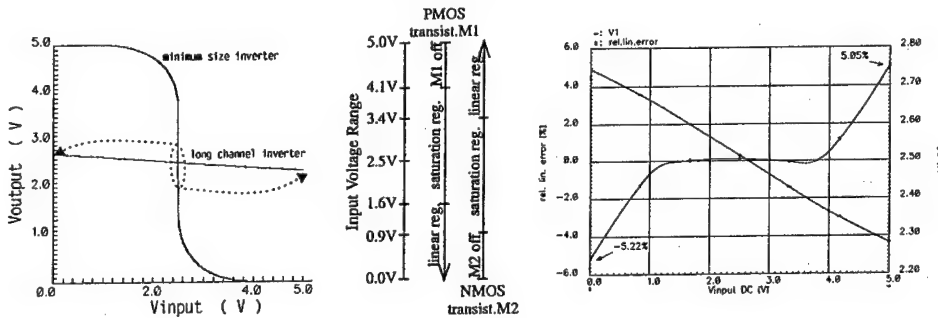


Figure 2: Left: Linearizing the inverter characteristic by stretching the region around the midpoint [2.5;2.5] (principle diagram for a single power supply of $V_{dd}=5V$). Middle: Operating regions of transistors M1, M2 depending on the input voltage V_{in} . Right: V_1 vs. V_{in} and corresponding relative linearity error referenced to V_1 -dynamic range.

A. Circuit analysis

Since the transistors in the inverter stage must be considered as changing their operating region while varying V_{in} within the range gnd – V_{dd} , we cannot apply the small-signal transistor models to calculate the transfer characteristic. By drawing the current balance equation (1) at node 1 for an input voltage $V_{in}=V_{dd}/2$, when all transistors M1 through M4 are in saturation, we can ascertain the midpoint potential, the nearby $V_{dd}/2$ operating point in the circuit.

$$I_{D1} + I_{D3} = I_{D2} + I_{D4} \quad (1)$$

$$\begin{aligned} & \frac{K_p}{2} \frac{W_1}{L_1} (V_{SG1} - V_{thP})^2 \cdot (1 + \lambda_1 V_{SD1}) + \frac{K_p}{2} \frac{W_3}{L_3} (V_{SG3} - V_{thP})^2 \cdot (1 + \lambda_3 V_{SD3}) = \\ & = \frac{K_n}{2} \frac{W_2}{L_2} (V_{GS2} - V_{thN})^2 \cdot (1 + \lambda_2 V_{DS2}) + \frac{K_n}{2} \frac{W_4}{L_4} (V_{GS4} - V_{thN})^2 \cdot (1 + \lambda_4 V_{DS4}) \end{aligned} \quad (2)$$

Neglecting the channel-length modulation effect λ in (2) the DC-voltage V_1 results from solving an quadratic equation. For a $2.4\mu\text{m}$ CMOS technology with symmetrical thresholds $V_{thN}=V_{thP}=0.9\text{V}$, and transconductances $K_{p,n}$ of 57 and $17\mu\text{A}/\text{V}^2$ for NMOS and PMOS, respectively, we can calculate a DC-voltage of $V_1=2.513\text{V}$, whereas Spectre simulator yields an operating point of 2.516V . When $V_1 \approx V_{dd}/2$ only a quiescent current flows through the current-mirror, thus $I_{out}=0$, except a small offset due to not exactly $\beta_3=\beta_4$. Applying equation (2) for a general input voltage V_{in} yields:

$$K_p \frac{W_1}{L_1} (V_{dd} - V_{in} - V_{thP})^2 + K_p \frac{W_3}{L_3} (V_{dd} - V_1 - V_{thP})^2 = K_n \frac{W_2}{L_2} (V_{in} - V_{thN})^2 + K_n \frac{W_4}{L_4} (V_1 - V_{thN})^2 \quad (3)$$

This can be converted into a linear equation of a type $ax + b = cy + d$, which results in:

$$V_1 = -\frac{\beta_{1,2}}{\beta_{3,4}} V_{in} + \frac{(\beta_{1,2} + \beta_{3,4})(V_{dd}^2 + V_{thP}^2 - V_{thN}^2 - 2V_{dd}V_{thP})}{2\beta_{3,4} \cdot (V_{dd} - V_{thP} - V_{thN})} \quad (4)$$

However, this linear dependence is only valid if both transistors, M1 and M2 stay in saturation. When $(\frac{V_{dd}}{2} + V_{thN}) < V_{in} < (\frac{V_{dd}}{2} - V_{thP})$ equat. (2) changes, e.g. for $V_{in}=0\text{V}$, into:

$$K_p \frac{W_1}{L_1} (V_{dd} - V_{in} - V_{thP} - \frac{V_{dd} - V_1}{2}) \cdot (V_{dd} - V_1) + \frac{K_p}{2} \frac{W_3}{L_3} (V_{dd} - V_1 - V_{thP})^2 = \frac{K_n}{2} \frac{W_4}{L_4} (V_1 - V_{thN})^2 \quad (5)$$

Hence the solution for V_1 becomes nontrivial, consisting of a linear term of V_{in} plus an additional square-root term proportional to V_{in}^2 . Accordingly to Fig.2-right, the mismatch between the linear dependence of (4), and equation (5) amounts less than 5.214% on the margin of the input range.

Transistor size	$L_{1,2} = 20\mu\text{m}$	$L_{1,2} = 30\mu\text{m}$	$L_{1,2} = 60\mu\text{m}$
circuit analysis for v_1	$\pm 233\text{mV}$	$\pm 171\text{mV}$	$\pm 91\text{mV}$
Spectre simulation	-233mV $+230\text{mV}$	-156mV $+154\text{mV}$	-78mV $+76\text{mV}$
rel. linear. error of v_1	5.214%	4.335%	3.58%
circuit analysis for i_{out}	$\pm 48.39\mu\text{A}$	$\pm 31.68\mu\text{A}$	$\pm 15.565\mu\text{A}$
Spectre simulation	$-49.32\mu\text{A}$ $+51.55\mu\text{A}$	$-32.83\mu\text{A}$ $+34.53\mu\text{A}$	$-16.31\mu\text{A}$ $+17.37\mu\text{A}$
rel. linear. error of i_{out}	4.37%	3.42%	2.63%

Table 1: Comparison of circuit analysis and simulation results for v_1 and i_{out} signals

Due to a fixed operating point at node 1 the transfer characteristic of the current-mirror can be determined applying small-signal models. Regarding the voltage v_1 as its input signal, the output current is given by

$$i_{out} = \frac{-(g_{m5} + g_{m6})}{(g_{DS5} + g_{DS6})R_x + 1} \cdot v_1 \quad (6)$$

with the transistor parameters calculated in saturation, by $g_m = K_p \frac{W}{L} (V_{GS} - V_{th})(1 + \lambda V_{DS})$ and $g_{DS} = K_p \frac{W}{L} \frac{(V_{GS} - V_{th})^2}{2}$, with both V_{DS} and $V_{GS} \approx 2.5V$. For ideal performance the output operating point at node *Out* also has to be set near $V_{dd}/2$. Equation (6) is valid only as long as M5, M6 remain in saturation, i.e. $V_{GS} - V_{th} = 1.6V < V_{DS} = |\frac{V_{dd}}{2} - I_{out}R_x|$. This condition limits the maximal impedance value R_x of the succeeding stage.

The AC-behaviour of the transconductor is determined by the pole at the output node of the circuit, given by

$$\omega_{p1} = \frac{g_{DS}}{C_{out}} \quad (7)$$

whereas in expression $g_{DS} = (g_{DS5} + g_{DS6} + \frac{1}{R_x})$ and $C_{out} = (C_{dg5,6} + C_{db5,6} + C_x)$ the load $R_x \parallel C_x$ is dominating. For current-mode applications, e.g. a following current comparator or conveyor, the bandwidth can be increased up to hundred-MHz range, due to decreased capacitance C_{out} and small R_x . Since the AC-analysis uses small-signal transistor parameters, a certain statement concerning the frequency behaviour of a rail-to-rail transconductor can be performed only by harmonic distortion obtained from a transient analysis. The Spectre simulation results have shown a THD less than 5% up to 18.1MHz.

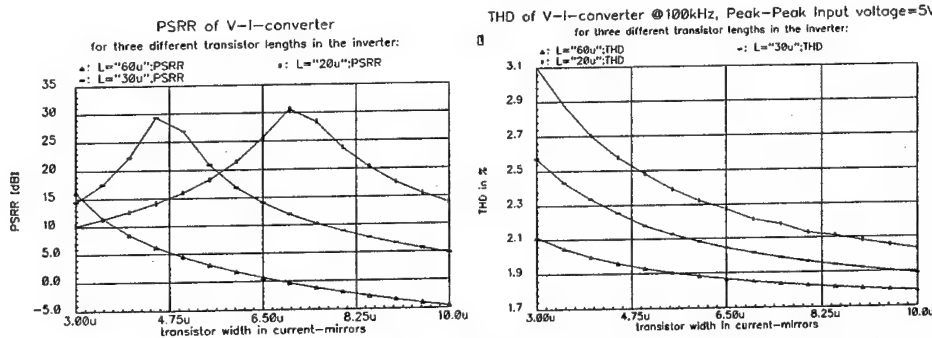


Figure 3: Power supply rejection ratio (PSRR) and Total harmonic distortion (THD) depending on transistor width in current-mirrors, for 3 different inverter, both at 100kHz.

B. Design considerations

Although, the circuit analysis has been exercised for minimal-sized transistors, except the long-channel inverter, transistor dimensions of $>5\mu m$ for good mirror-matching are recommended. Fig.5 shows the mask layout of the proposed voltage-to-current converter with $60\mu m$ -long transistor in the inverter stage and cascode current-mirror. The chip area is small ($180\mu m \times 110\mu m$) compared to some other OTA implementations [2]. Another advantage of this circuit is, that it does not require any bias voltage. Using this advantage, the circuit suffers of the drawback of increased power consumption. Caused by a quiescent current of $225\mu A/143\mu A$ through the current-mirrors, and up to $60\mu A/40\mu A$ in the inverter stage, the total power consumption at maximum PSRR of 30dB, is approximately $2.5mW/1.6mW$ for an $20\mu m$ -/ $30\mu m$ -long inverter, respectively. Fig.3-left shows

that the maximally achievable PSRR is nearby 30dB, when the current-mirror is properly dimensioned. The PSRR is symmetrically regarding to positive and negative power supply rails. The circuit operates for single supply V_{dd} of 5V, as well as 3.3V without any reduction in PSRR. Running with a 3.3V voltage supply, the transconductor can also provide an simple input interface to systems with higher power supply. For the reason of current symmetry with regard to V_{in} -range, the g_{nda} -potential ($V_{dd}/2$) has to be set equal for both, the lower (3.3V) and the higher (5V) powered systems. Another approach for a 3.3V supply system to achieve symmetrical current range opposite to 5V-system, is moving the transconductor characteristic accordingly to Fig.4-left.

As a simple approach for designing the proper V-I converter the following scheme can be considered:

- estimate $L_{5,6}$ by the required output g_{DS} for a given R_x of the following stage
- adjust the $W_{5,6}$ from equation (6) for the desired output current range
- optimize transistors in the current-mirror for the lowest THD and the largest PSRR
- from equation (4) ascertain the needed inverter length $L_{1,2}$, accordingly to v_{in}
- check the required performance and redesign once more.

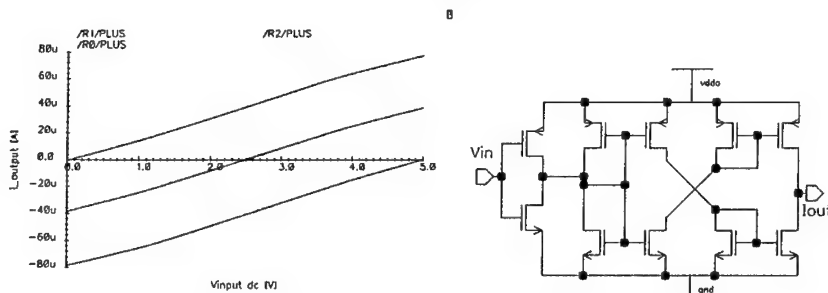


Figure 4: Left: *Movable DC-transfer curve of the V-I converter of Fig.1.* Right: *Schematic of a transconductor with cross-coupled mirrors.*

III. Circuit modification

By changing the dimensions of the current-mirror transistors different output current offsets are adjusted, see equation (4). This way the transfer curve can be moved to achieve either positive or negative currents as shown in Fig.4-left. Applying the additional cross-coupled current-mirrors an 180°-phase shifting, and thus inverted transconductance curves in compare to Fig.4-left can be attained. Making the circuit more insensitive to output voltage deviation caused by the voltage drop over R_x , the cascode mirror version of Fig.5 can be employed. The output impedance increases by $\frac{g_m}{g_{DS}}$ of the additionally inserted transistors, however, also larger channel length for M1,M2 is required to maintain the same linearity. However, the THD increases up to 4%, and the PSRR is reduced noticeable.

IV. Final Remarks

A very simple circuit approach for voltage-to-current conversion has been presented. The linear characteristic is a result of stretching the CMOS inverter curve with high-ohmic transistors. It has been shown that the circuit can be optimized for best linearity, lowest harmonic distortion, and largest PSRR by appropriate dimensions of the two types of

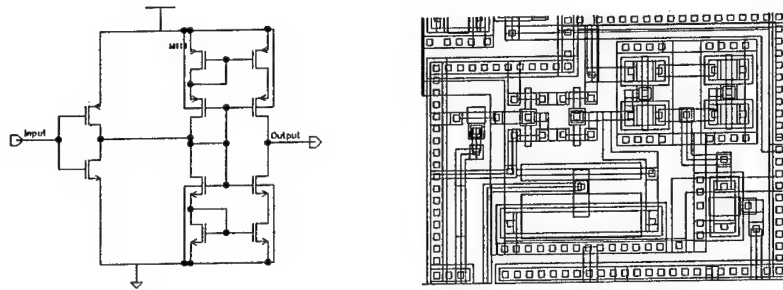


Figure 5: Cascode version of the voltage-to-current converter and corresponding layout in a $2.4\mu\text{m}$ CMOS technology ($L_{inv}=60\mu\text{m}$).

transistor pairs used in the inverter and in the current-mirrors. The proposed circuit attains, even for a true rail-to-rail operation range of 5V, a THD of 2.253% and linearity error of 3.42% in compare to those reported in [2, 3]. The linearity and THD in these references are given only for approximately 60 percent of the rail-to-rail dynamic range. For comparison, in our circuit for a 3V peak-peak input (60 percent of the rail-to-rail dynamic range) the achieved linearity error of 0.9% is better than in [1, 2, 3, 8], as well as the THD of 0.75% is similar to those reported in [2, 3, 6, 8].

Acknowledgments

The author would like to thank the German Research Community (DFG) for granting this research as GRK-164 and to Jan Strömer for useful comments on the manuscript.

References

- [1] A. Durham and W. Redman-White. Very high linearity tunable OTA in 5V CMOS. *IEE Proceedings, Part G*, 140(3):207–210, June 1993.
- [2] G. Ferri and W. Sansen. A rail-to-rail constant- g_m low-voltage CMOS operational transconductance amplifier. *IEEE Journal of Solid-State Circuits*, 32(10):1563–1567, Oct. 1997.
- [3] C. Hung, C. Hwang, M. Ismail, K. Halonen, and V. Porra. Low-voltage CMOS rail-to-rail V-I converters. *Analog Integrated Circuits and Signal Processing*, 13(3):261–274, July 1997.
- [4] R. Izák. VLSI implementation of a Neural Network for Acoustical Processing. In *Proceedings of the 1st ECS'97*, pages 307–310, Bratislava, Slovakia, 4–5 Sept. 1997.
- [5] J. Kampe and G. Scarbata. Automatisierbare Synthesemethode für analoge Systemkomponenten. In *Proc. of the 6th E.I.S. Workshop*, Tübingen, Germany, Nov. 25–26, 1993. available at: www.inf-technik.tu-ilmenau.de/~jk.
- [6] C.-S. Park and R. Schaumann. A high-frequency CMOS linear transconductance element. *IEEE Transactions on Circuits and System*, 33(11):1132–1138, Nov. 1986.
- [7] J. Silva-Martinez, M. Steyart, and W. Sansen. A large-signal very low-distortion transconductor for high-frequency continuous-time filters. *IEEE Journal of Solid-State Circuits*, 26(7):946–955, July 1991.
- [8] R. R. Torrance, T. R. Viswanathan, and J. V. Hanson. CMOS voltage to current transducers. *IEEE Trans. Circuits and Systems*, 32(11):1097–1104, Nov. 1985.
- [9] C. Toumazou, F. J. Lidgey, and D. Haigh. *Analogue IC design: the current-mode approach*. Peregrinus Press (on behalf of IEE), Stevenage, U.K., 1990. ISBN 0-86341-297-1.
- [10] Z. Wang. *Current Mode Analogue Integrated Circuits and Linearization Technique in CMOS-Technology*. Hartung-Gorre-Verlag, Konstanz, 1990. chapter 6.

A low-pass 1-Hz 2V-supply current conveyor-based filter

Pierpaolo De Laurentiis - Giuseppe Ferri

*Dipartimento Ingegneria Elettrica, Università di L'Aquila
Localita' Monteluco di Roio 67040 L'Aquila, Italia*

Gaetano Palumbo - Salvatore Pennisi

*DEES, Università di Catania,
Viale A.Doria, 95125 Catania, Italia*

Abstract. In this work, we present a novel low-voltage low-power current conveyor designed and optimized to be used in capacitive multiplier topologies. The proposed circuit allows to obtain very high capacitive gain factors (up to 50000), with a high degree of accuracy. In order to investigate the effectiveness of this topology, we have implemented a low cut-off frequency filter with a standard 0.5μ CMOS technology. The supply voltage is 2 V and the quiescent power consumption is 110μ W. SPICE simulations confirm that the described multiplication technique is sufficiently accurate for capacitances higher than 2pF.

I. Introduction

Research activity in analog circuit design has gone towards the realization of low-voltage low-power circuits [1,2]. As more and more complex systems are being integrated on chip, area reduction is of a fundamental importance. It is well known how a limiting problem in integrated circuits is the realization of capacitance values higher than 100 pF, because of their large occupied area.

In this paper, we intend to give an original contribution to the solution of the realization of on-chip capacitance values higher than the integratable ones. This is done by performing a capacitance multiplication, so high equivalent RC products, which cannot be directly implemented in integrated version, have been realized. With respect to other topologies proposed by the same authors of this paper [3,4], this circuit contains a current divider which allows to save power consumption. It can be also utilized in the design of very low cut-off frequency filters, which are needed in a wide range of applications as, for example, in biopotential amplifiers and in the control of slowly-varying geological variables [5,6].

II . The proposed topology

The proposed topology of the low voltage low power current conveyor, performing the capacitance multiplication, is shown in Fig. 1.

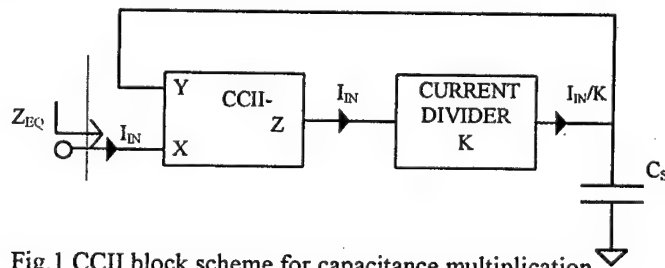


Fig.1 CCII block scheme for capacitance multiplication

From the circuit shown in Fig.1, assuming ideal components, a straightforward analysis shows that

$$Z_{EQ} = \frac{1}{sKC_s} \quad (1)$$

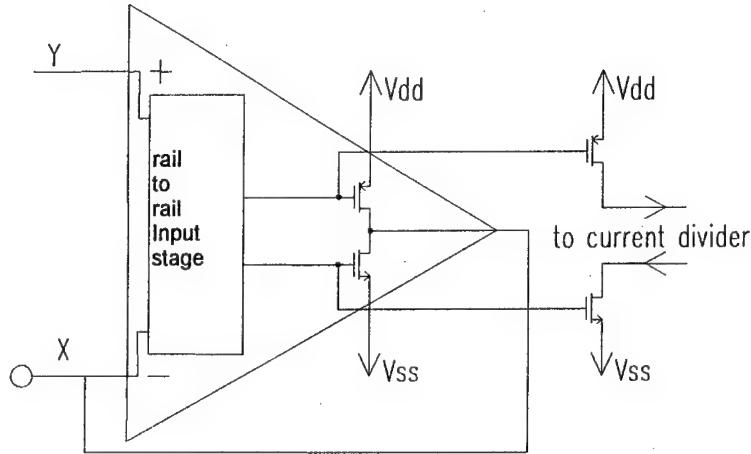


Fig.2 Simplified schematic of low-voltage CCII

In fig.2 the simplified schematic of the CCII is shown. A low voltage op-amp performs the voltage following action between Y and X with good accuracy, while the output current (high impedance node) is drawn by copying the current of the output stage of the op-amp. The op-amp has a complete rail-to-rail dynamic range, ensured by a traditional constant-gm input stage working in weak-inversion (one-to-one current mirror switch), followed by a typical low-voltage AB biased output stage.

The impedance on the input node X is kept sufficiently low by the feedback of the op-amp (open-loop-gain ≈ 80 dB). Unfortunately, this impedance reduction takes place as long as the feedback is effective, that is in low frequency range, so this technique is truly appropriate for not very high frequency operation.

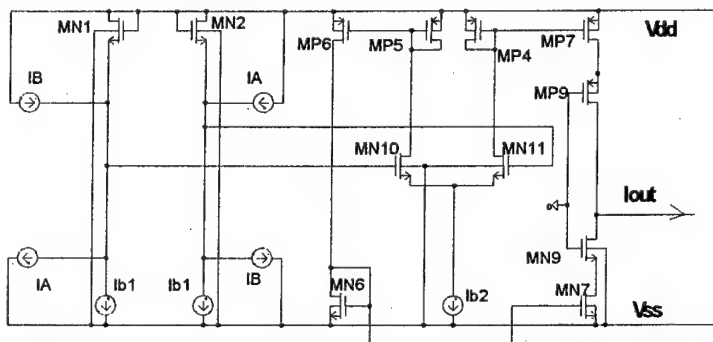


Fig.3 Schematic of the current divider. $K=A \cdot (I_{b1}/I_{b2})$

In the circuit depicted in fig.3, I_A and I_B represent, respectively, the pull-down and pull-up currents of the output stage of the current conveyor. The principle of the current division is based on the translinear loop, composed by transistors MN1-MN2 and MN10-MN11 and the proper operation of the circuit is ensured by biasing all the transistors in weak inversion, where the drain current shows an exponential dependence on gate-source voltage, as follows

$$I_D = I_{D0} \frac{W}{L} e^{\frac{V_{GS}}{nU_T}} \quad (2)$$

From the fig.3, we have also

$$V_{GS}(MN1) - V_{GS}(MN2) = V_{GS}(MN11) - V_{GS}(MN10) \quad (3)$$

From (2) and (3) we obtain

$$\frac{I_D(MN1)}{I_D(MN2)} = \frac{I_D(MN11)}{I_D(MN10)}, \quad (4)$$

from which

$$\frac{I_D(MN1) - I_D(MN2)}{I_D(MN1) + I_D(MN2)} = \frac{I_D(MN11) - I_D(MN10)}{I_D(MN10) + I_D(MN11)} \quad (5)$$

Being the differential current of MN10 and MN11 mirrored and single-ended converted we obtain, after proper replacements

$$I_{OUT} = \frac{1}{A} \frac{I_{b2}}{I_{b1}} (I_A - I_B) = \frac{1}{K} (I_A - I_B) \quad (6)$$

where A is a further division factor, performed by transistors MN7 and MP7, which has been fixed to 10. Fig.4 shows the THD of the current divider vs. input current amplitude for different I_{b2} values and $A=10$. From this figure, it is possible to deduce that the body effect of transistors MN1 and MN2 does not affect the circuit linearity performance. The only consequence is a light increase of the K value.

In fig.5, the module of the equivalent input impedance, Z_{EQ} , versus frequency is plotted, for a 20 pF starting capacitance and a current division of $5 \cdot 10^4$, having imposed that $I_{b1}=10 \mu A$, $I_{b2}=2 \text{ nA}$ and $A=10$.

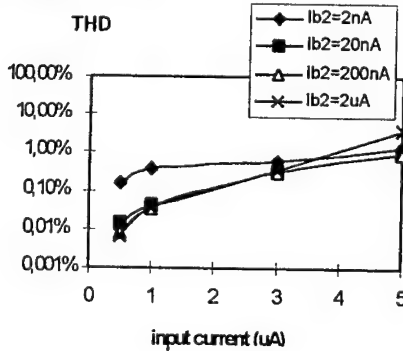


Fig.4. Current divider THD vs. input current amplitude

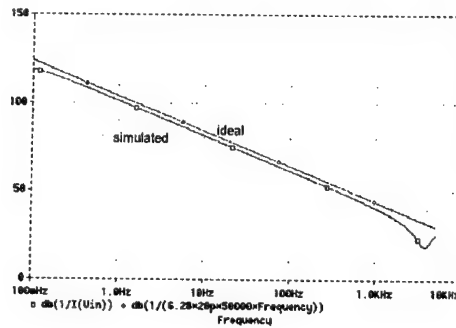


Fig.5. Module of Z_{EQ} for $C_s=20\text{pF}$ and a current division of $5 \cdot 10^4$

Fig.6 shows the schematic of the low-pass filter, while in fig.7 the magnitude response of the proposed filter is reported. The resistance R has been fixed to a $159\text{ K}\Omega$ value.

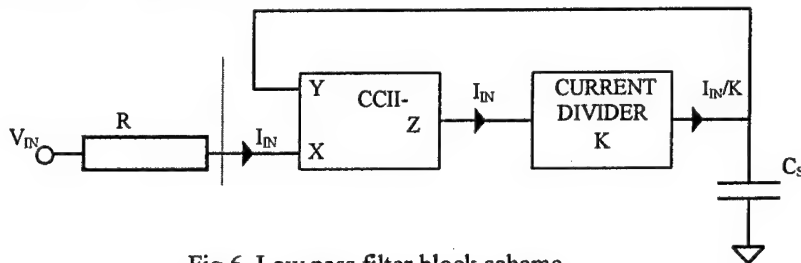


Fig.6 Low pass filter block scheme

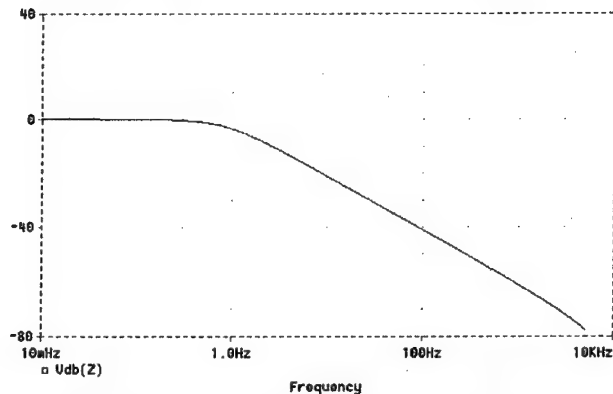


Fig.7. Magnitude response of the proposed filter.

III. Final remarks

A novel solution for the implementation of a capacitive multiplier has been here presented. The proposed circuit shows low supply voltage low power characteristics and good multiplication accuracy in a sufficiently high bandwidth. An example of the circuit application in the design of a low cut-off (1 Hz) low pass filter is also presented.

References

- [1] E.Vittoz : "Limits to LV/LP analog circuit design" - *Advance Course on LV LP analog CMOS IC design*, Lausanne, June 1998
- [2] R.Hogervorst, J.H.Hujsing : *Design of low voltage low power operational amplifier cells*, Kluwer, 1996
- [3] G.Di Cataldo, G.Ferri, S.Pennisi: "Active capacitance multiplication by current conveyors" - *ISCAS '98*, Monterey, May 31- July 3, 1998
- [4] G.Ferri, S.Pennisi: "A 1.5 V Current-Mode Capacitance Multiplier", *ICM'98-International Conference on Microelectronics*, Monastir (Tunisia), 14-16 December 1998
- [5] W.H.G. Deguelle : "Limitations on the integration of analog filter for frequencies below 10 Hz" - *Proc.ESSCIRC 1988*, pp.131.134.
- [6] S.Solis-Bustos, J.Silva-Martinez : " A 4 Hz low-pass continuous time filter" - *Proc.ICECS 1998- Lisbon*, pp.169-172.

Neural Network Control Using Sliding Mode Technique

Vardan Mkrttchian and Anri Lazaryan

*State Engineering University of Armenia
Armenian Automatic Control Council
105 Terian Str., Yerevan 375009, Armenia
e-mail: aacc@seua.am, anri@arm.hpl.com*

Abstract. The new approach of single neuron and neural network control problems with the sliding mode application is considered in this article. Sliding mode examination provides some advantages of stability etc. The region of the neuron and neural network stable operation is estimated and some conclusions are made on the basis of this research.

I. Introduction

Information and neural science as a result of the study of the mechanism and structures of the brain have proposed artificial neural networks (ANN). This has led to the development of new computational models, based on this biological background, for solving complex problems like pattern recognition, fast information processing, learning and adaptation.

Single neuron and neural network control is connected with discontinuities. These discontinuities cause the stability problems on the surface. As it is shown in the works of V. Utkin [1] and V. Mkrttchian [2] in discontinuous control the sliding mode is arising.

The sliding mode gives the following advantages:

- The trajectories the state vector belong to manifolds of lower dimension than that of the whole state space, therefore the order of differential equations describing sliding motions is also reduced.
- In most of practical systems the sliding motion is control-independent and determined merely by the properties of the control plant and the position (or equations) of the discontinuity surfaces.
- Under certain conditions sliding mode may become invariant to variations of dynamic characteristics of the control plant which poses a central problem death with in the theory of automatic control.

Even, if we employ continuous control algorithm the control itself is shaped as a high frequency discontinuous signal whose mean value is equal to the desired continuous control.

II. Dynamic Neuron and Neural Network

The network architecture is defined by the basic processing elements and the way in which they are interconnected. The basic processing element of the connectionist architecture is often called a neuron by analogy with neurophysiology, but other names as perception or adaline are also used. The basic model of a neuron is illustrated in [3, 4]. The neuron is composed of three components: a weighted summer; a linear dynamical single-input, single-output (SISO) system; a non-dynamical, non-linear function, which is also, called the activa-

tion function.

The weighted summer is described by

$$s_i(t) = \sum_{j=1}^{N_i} w_{ij} x_j(t) + \sum_{k=1}^{M_i} b_{ik} u_k(t) + z_i \quad (1)$$

giving a weighted sum s_i in terms of the internal inputs x_i , external (control) inputs u_k and corresponding weights w_{ij} and b_{ik} together with constants z_i which play a role of standard bias; t denotes a time variable, which can be either continuous or discrete.

Equation (1) can be written in the matrix form as

$$s_i(t) = W_i x(t) + B_i u(t) + z_i. \quad (2)$$

The linear dynamical system has input v_i and output y_i . The variable y_i is the i th neuron output. Its mathematical model can be written for continuous systems as

$$T_i y_i(t) + y_i(t) = v_i(t). \quad (3)$$

The discrete time model can be represented as

$$T_i y_i(t+1) + (1 - T_i) y_i(t) = v_i(t). \quad (4)$$

The non-dynamical non-linear function $f_i(\bullet)$ (activation function) gives the signal $v_i(t)$ in terms of the summer output $s_i(t)$: $v_i = f_i(s_i)$. (5)

III. Sliding Mode Technique

A distinguished feature of differential equations describing any control system is known to be the presence of a scalar or vector parameter u referred to as *control*:

$$\dot{x} = f(x, t, u), \quad u \in R^m. \quad (6)$$

In early regulators, the controls have mostly been of relay type. As a result, the right-hand part of the differential equation of the system motion proved to be a discontinuous function of the system state vector. For systems with isolated discontinuity points, some analysis and synthesis methods have been designed based on the classical theory of differential equations with the use of point-to-point transformations and averaging at the occurrence of high frequency switching.

However, in attempts to mathematically describe certain application problems the same case as in the Coulomb friction mechanical system were often faced when the totality of discontinuity points proved to be a nonzero measure set in time. This fact is easily revealed for a sufficiently general class of discontinuous controls defined by the relationships

$$u_i(x, t) = \begin{cases} u_i^+(x, t) & \text{with } s_i(x) > 0 \\ u_i^-(x, t) & \text{with } s_i(x) < 0 \end{cases} \quad (7)$$

where $u^T = (u_1, \dots, u_m)$ and all functions $u_i^+(x, t)$ and $u_i^-(x, t)$ are continuous. The state vector of such systems may stay on one of the discontinuity surfaces or their intersection within a finite time. For example, the system state vector trajectories belong to some discontinuity surface $s_i(x) = 0$ if in the vicinity of this surface the velocity vectors $f(x, t, u)$ are directed toward each other.

As evidenced by these examples, the motion trajectories which belong to the set of discontinuity points are singular since in any combination of continuous controls $u_i^+(x, t)$ and $u_i^-(x, t)$ they differ from the system trajectories. An accepted term for the motion on discontinuity surfaces is *sliding mode*. Incidentally, the motion along the segment $|x| \leq P_0/k$ in the

Coulomb friction mechanical system is also a sliding mode motion.

Here it will be apt to note that a sliding mode does exist on a discontinuity surface! whenever the distances to this surface and the velocity of its change \dot{s} are of opposite signs, i.e. when

$$\lim_{s \rightarrow 0} \dot{s} > 0 \text{ and } \lim_{s \rightarrow 0} \dot{s} < 0 \quad (8)$$

The mathematical description of sliding modes is quite a challenge. It requires the design of special techniques. The solution of $x=f(x,t)$ equation is known to exist and be unique if a Lipschitz constant L may be found such that for any two vectors x_1 and x_2

$$\|f(x_1, t) - f(x_2, t)\| \leq L \|x_1 - x_2\| \quad (9)$$

It is evident that in the dynamic system with the discontinuous control, condition (9) is violated in the vicinity of discontinuity surfaces. Indeed, if points x_1 and x_2 are on different sides of the discontinuity surface and $\|x_1 - x_2\| \rightarrow 0$, inequality (9) is not true for any fixed value of L . Therefore, at least formally, some additional effort is needed to find a solution to systems at an occurrence of a sliding mode. Moreover, Iota function $x(t)$ pretend to be a solution lying on the set of discontinuity points. Even in this case the way this function may turn Eq.9 into identity is not clear since control is not defined on the surface $s_i(x) = 0$.

Let us give a closer look to the physical approach to obtaining the sliding mode motion equations. Uncertainty in the system behaviour on a discontinuity surface has appeared as a result of the imperfection of a model of the type [1] which was supposed to idealise the real life system. This model fails to recognise such factors as imperfections of the switching device (time delay, dead zones, hysteresis loops, infertility of elements, etc.). Besides, the equations of an actual control plant may be of an order higher than those of a model. And, finally, the instruments used to obtain the information on the state vector, which is necessary to realise controls [2] may also prove inertial. Recognition of all these factors makes all discontinuity points isolated thus removing mathematical (but not analytical) difficulties in describing the system behaviour. The physical approach implies introduction of such imperfections, which subsequently tend to zero. A result obtained in such limit transitions was chosen as an appropriate mathematical description of a sliding mode.

The system considered was a second order relay control system whose discontinuity surface was actually a straight line on the plane of co-ordinates of error x and its derivatives \dot{x} :

$$cx + \dot{x} = 0, \quad c - \text{const} \quad (10)$$

The behaviour of the system was studied under the assumption that a time delay was inherent in the switching device and, consequently, the discontinuity points were isolated. It was found that irrespective of the control plant parameters and disturbances affecting it, the solution of the second order equation in sliding mode always tends to the solution of the first order linear differential Eq.10 which depends only on the angle factor c of the switching straight line.

In all of the above cases, the sliding equations are not postulated, their validity being proved with the help of limiting procedures. However, a special form of the switching device model restricts the scope of applications of these results. Therefore the question of their applicability to models of other types remains unanswered (for intense, piecewise linear approximation of the discontinuous characteristic). Besides, the limiting procedures treated in the above papers have been designed exclusively around the point-to-point transformation technique, too analytically difficult to be applied to the study of any systems but those with a single discontinuity surface.

Assume that a sliding mode exists on manifold $s(x)=0$, $s^T(x)=[s_1(x), \dots, s_m(x)]$. Let us find a continuous control such that under the initial position of the state vector on this manifold, it yields identical equality to zero of the time derivative of vector $s(x)$ along system [1] trajectories:

$$\dot{s} = Gf(x, t, u) = 0, \quad (11)$$

where the rows of the $(m \times n)$ matrix $G=\{\partial s/\partial x\}$ are the gradients of the functions $s_i(x)$.

Assume that a solution (or a number of solutions) of the system of algebraic Eq. (11) with respect to m -dimensional control does (or do) exist. Use this solution, hereinafter referred to as *equivalent control* $u_{eq}(x, t)$, in system (12) in place in u :

$$\dot{x} = f[x, t, u_{eq}(x, t)]. \quad (12)$$

It is quite obvious that, by virtue of condition (11), a motion starting in $s[x(t_0)] = 0$ will proceed along the trajectories which lie on the manifold $s(x) = 0$.

The above procedure will be called the *equivalent control method* and Eq. 12 obtained as a result of applying this method will be regarded as the sliding mode equation describing the motion on the intersection of discontinuity surfaces $s_i(x) = 0$, $i = 1, \dots, m$.

From the geometric viewpoint, the equivalent control method implies a replacement of the undefined discontinued control on the discontinuity boundary with a continuous control which directs the velocity vector in the system state space along the discontinuity surfaces intersection.

For example, in order to find this vector in a system with a single discontinuity surface $s(x) = 0$ at some point (x, t) [1] one should vary the scalar control from u^- to u^+ , plot the locus of $f(x, t, u)$ and find the point where it intersects the tangential plane. The point of intersection determines the equivalent control $u_{eq}(x, t)$ and the right-hand part $f(x, t, u_{eq})$ of the sliding mode differential Eq. 12.

IV. Conclusion

1. Artificial Neural Networks (ANN) is a new method of developing high-efficiency computational models.
2. Discontinuities of ANN control circuits can be eliminated using the sliding mode characterized by reduced order of mathematical support, automatic adjustment through feedback from discontinuities, interference-free operation.

A basic element of ANN architecture is a neuron model structure described by substantiated formulae containing continuous and discrete variables and a scalar parameter formulated as a characteristic of any control system.

References

- [1] Vadim I. Utkin, *Sliding Modes in Control and Optimisation*, Springer-Ver., Berlin, 1992.
- [2] Vardan Mkrtchyan, Anri F. Lazaryan, Suren Mkrtchyan, "Sliding Mode in Neural Network Control," *Proceedings of The Third Asia-Pacific Conference on Communication (APCC'97)*, 1997, Sydney, Australia.
- [3] Senik H. Mkrtchyan, Anri F. Lazaryan, "Learning Algorithm of Neuron and Its Hardware Implementation," *Proceedings of 4th Seminar on Neural Network Application in Electrical Engineering (NEUREL'97)*, 1997, Belgrade, Yugoslavia.
- [4] Senik H. Mkrtchyan, etc., *Adaptive Threshold Element*. Patent 96065, Republic of Armenia, Yerevan, 1996.

Pattern Classification with the BCM Neural Network

Stanislav Poljovka and Ľubica Beňušková

*Department of Computer Science and Engineering, Slovak Technical University,
Ilkovičova 3, 812 19 Bratislava, Slovakia*

E-mail: poljovka@decef.elf.stuba.sk, benus@elf.stuba.sk

Abstract. Synaptic weights of the model neurons in our selforganizing artificial neural network (ANN) modify according to the Bienenstock, Cooper and Munro (BCM) unsupervised learning algorithm. What makes the BCM rules different from any other learning procedure is the dynamic synaptic modification threshold θ_M , which determines whether a neuron's activity at any moment will lead to strengthening or weakening of its synaptic weights. We design, perform and discuss several pilot experiments with the 2D alphanumeric pattern classification in order to investigate the computational properties of the BCM neural network with the so called feedforward inhibition.

1 Introduction

The BCM theory was introduced in order to explain selforganization in the developing visual cortex [1]. Later it was used for explanation of the experience-dependent plasticity in the mature somatosensory cortex [2]. It was shown theoretically [3] and in simulations [4], that the BCM neural network with the so called feedforward inhibition can perform projection pursuit, i.e., it can find projections in which the departures from normality in the statistical distribution of input data are the most prominent. This is an important property implying the feature detecting abilities of this neural model. Thus, the BCM neural network was successfully applied to the pattern recognition tasks [5-7]. Since, to our knowledge, this model has not been yet applied to the 2D alphanumeric pattern classification, we decided to explore this field of its application. We constructed our own database of letters and performed several experiments exploring the architecture and training parameters of the BCM neural network.

2 Description of the BCM Neural Network

We now define a network of n neurons with feedforward inhibition which we use in our computer simulations of pattern classification. The input vector x is fed into a one layer ANN in which each neuron is inhibited proportionally to activities of other neurons. The inhibited activity of the k^{th} neuron reads [3]

$$\bar{c}_k = \sigma(c_k - \mu \sum_{j \neq k} c_j) \quad (1)$$

where $c_k = x \cdot m_k$, m_k is the synaptic weight vector, and σ is the sigmoidal nonlinearity. It was shown that the BCM feedforward inhibition network is the first-order approximation

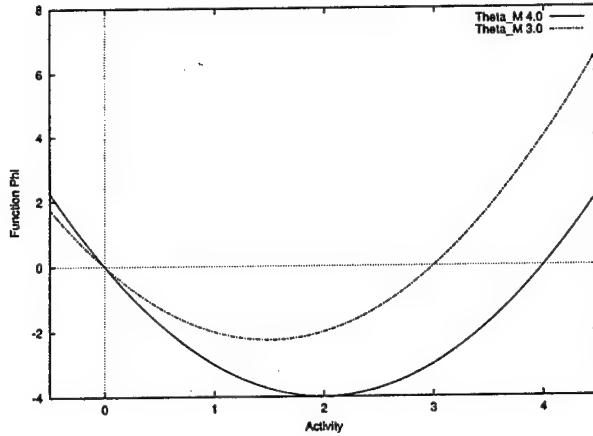


Figure 1: The modification function ϕ for two different values of θ_M

of the BCM lateral inhibition network [3]. The BCM learning rule is found through the gradient minimization of the objective function $R = \sum_k R_k$, where [3]

$$R_k = -\eta \left\{ \frac{1}{3} E[\tilde{c}_k^3] - \frac{1}{4} E^2[\tilde{c}_k^2] \right\} \quad (2)$$

where E means the expected value. After writing down the corresponding derivatives we arrive at the learning rule [3]

$$\dot{m}_k = -\frac{\partial R}{\partial m_k} = \eta \left\{ E[\phi(\tilde{c}_k, \theta_M^k) \sigma'(\tilde{c}_k) x] - \mu \sum_{j \neq k} E[\phi(\tilde{c}_j, \theta_M^j) \sigma'(\tilde{c}_j) x] \right\} \quad (3)$$

where the modification threshold $\theta_M = E[\tilde{c}_k^2]$ is the point where the modification function $\phi = \tilde{c}_k(\tilde{c}_k - \theta_M^k)$ changes sign from minus to plus (Fig. 1). We calculate θ_M as a moving average of the past squared activity of a neuron, such that [2]

$$\theta_M(t) = \langle c^2(t) \rangle_\tau = \frac{1}{\tau} \int_{-\infty}^t c^2(t') e^{-\left[\frac{t-t'}{\tau}\right]} dt' \quad (4)$$

The parameter τ determines the length of the recent past over which the squared neuron's response is averaged. We call it a neuron's memory of its past activity. The smaller (larger) τ , the shorter (longer) memory. The whole notion of the dynamic modification threshold θ_M was biologically inspired [1]. From the above relations it follows that when $0 < \tilde{c}_k < \theta_M$ all active synaptic weights weaken. When $\tilde{c}_k > \theta_M$, all active synaptic weights potentiate.

3 Results

The network input x was the binary $\{1, 0\}$ bitmap with 10×13 pixels. During training and testing, noisy representatives of $m = 8$ artificially created letters (classes) were presented in random order. The noise was introduced by randomly switching 5% of bits. We

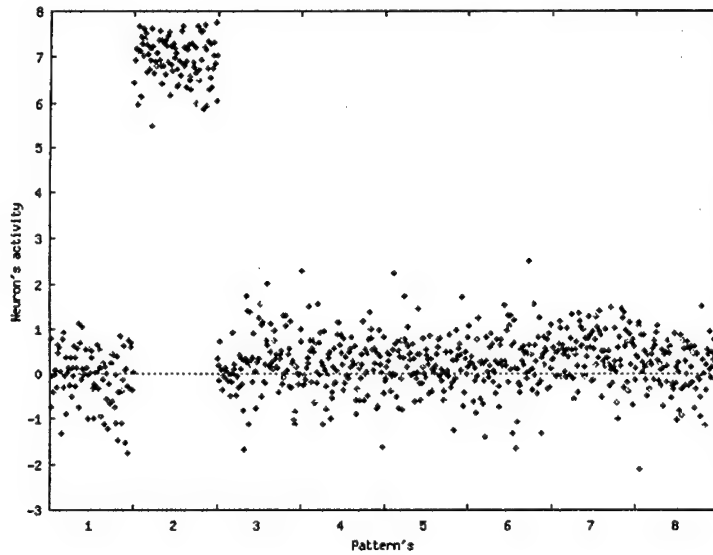


Figure 2: Responses of one randomly chosen neuron out of $n = 8$ after it became selective to one pattern (letter) out of $m = 8$. Each point represents a neuron's response to one noisy test pattern. There were 100 test patterns for each letter. We can see that the neuron became selective for one letter.

chose these values of parameters: $\sigma(z) \in (-20, 20)$ with the slope equal to 1, $\eta = 10^{-4}$, and $\tau = 200$ iterations. Training was stopped after 1.5×10^6 iterations, while convergence happened roughly after 0.8×10^6 iterations as judged according to the stabilization of the total sum of individual weights of all neurons. In our simulations, we investigated the effect of different number of neurons n and different strengths of inhibition μ . For all examined n we arrived at the optimal value of $\mu = 1/n$.

With $n = 8 = m$ neurons and no inhibition, the ANN did not classify at all. With $n = 8$ neurons and $\mu = 1/n$, after 8 trainings out of 10, each neuron became selective to one letter. The ANN classified all test patterns 100% correctly (because the noise was very low) (Fig. 2). After remaining 2 trainings, some 2 neurons became selective to the same letter, thus one class remained unrepresented.

With $n = 4 = m/2$ neurons and $\mu = 1/n$, after all 10 trainings, each neuron became selective to one letter at random. Thus, since there is 8 classes (letters), the ANN classified correctly only 1/2 of the test patterns. This result is not surprising since one BCM neuron can find only one projection for the input data which cannot be the same for two different classes.

With $n = 16 = 2m$ neurons and $\mu = 1/n$, after 8 trainings out of 10, pairs of neurons became selective to one letter. This means that 2 neurons would give the responses as in Fig. 2 to the same class. After remaining 2 trainings, some 3 neurons became selective to the same letter, but it never happened that some letter remained unclassified.

4 Conclusion

We have investigated the BCM neural network with feedforward inhibition in computer experiments with classification of letters. When the number of neurons was the same as the number of classes, i.e. $n = m$, each neuron became selective to a different letter. When $n = 2m$, and the number of training patterns was the same for each letter, we found a typical but still interesting selforganizing tendency towards a uniform and even representation of the input data. These results suggest that the BCM ANN can have similar properties as for instance the Kohonen ANN [8]. This requires more investigation. It is also desirable to experiment with a more sophisticated database of scanned hand written characters and to compare the performance with, for instance, the standard back-propagation ANN. At last, it could be interesting to program and run the BCM classifier on a transputer system [9].

Acknowledgements

Supported by the U.S.-Slovak Science and Technology Joint Fund in cooperation with the Dept. of Health and Human Services in USA and the Ministry of Education in Slovakia, grant 015-95, and by the VEGA of MŠ SR and SAV, grants 2/6018/99 and 1/4289/97.

References

- [1] Bienenstock E.L., Cooper L.N., Munro P.W. "Theory for the Development of Neuron Selectivity: Orientation Specificity and Binocular Interaction in Visual Cortex," *J. Neuroscience*, Vol. 2, pp. 32-48, 1982.
- [2] Beňušková L., Diamond M.E., Ebner F.F. "Dynamic Synaptic Modification Threshold: Computational Model of Experience-Dependent Plasticity in Adult Rat Barrel Cortex," *Proc. Natl. Acad. Sci. USA*, Vol. 91, pp. 4791-4795, 1994.
- [3] Intrator N., Cooper L.N. "Objective Function Formulation of the BCM Theory of Visual Cortical Plasticity: Statistical Connections, Stability Conditions," *Neural Networks*, Vol. 5, pp. 3-17, 1992.
- [4] Dotan Y., Intrator N. "Multimodality Exploration by an Unsupervised Projection Pursuit Neural Network," *IEEE Trans. Neural Net.*, Vol. 9, pp. 464-472, 1998.
- [5] Intrator N. "Feature Extraction Using an Unsupervised Neural Network," *Neural Computation*, Vol. 4, pp. 98-107, 1992.
- [6] Intrator N., Gold J.I. "Three-Dimensional Object Recognition of Gray Level Images: the Usefulness of Distinguishing Features," *Neural Computation*, Vol. 5, pp. 61-74, 1993.
- [7] Bachman C.M., Musman S.A., Luong D., Shultz A. "Unsupervised BCM Projection Pursuit Algorithms for Classification of Simulated Radar Presentations," *Neural Networks*, Vol. 7, pp. 709-728, 1994.
- [8] Kohonen T. *Self-Organizing Maps*. Springer, 1995.
- [9] Krajčovič T. "Debugging Tool for the Transputer Based Embedded Systems," In: *Embedded Microprocessor Systems*, C. Müller-Schloer et al. (Eds.), IOS Press, 1996.

Use of Information Technology Implementation Methods in Microelectronic Systems Design

Peter Áč¹, Vladimír Áč²

¹Spartan a.s., Trnava, Slovakia, pac@spartan.sk

²Derby s.r.o., Piešťany, vladimir.ac@derby.sk

Abstract. In this paper, we briefly analyze methods used at implementation of complex information systems in real applications and try to point out similarity to the methods used for a functional specification and design of complex microelectronics systems. Methods currently used in both cases are empirical. These lead to acceptable but not optimal results. We would like to show in this paper the possibilities to improve the microelectronic system functional specification, especially from optimal functional coverage of the application field point of view and with regard to its interaction to the application environment.

I. Introduction

In recent time, we may see rapid development of information systems and their implementation into nearly all human environments. Their use in industry helps to save cost as well as improve quality of production process and decrease dependency of production process on a human factor. A good information system is well integrated complex of hardware and software parts implemented into the specific production-administrative environment. A conformity with environment and adaptability to specific demands are key factors to success of such a system. Methods used in implementation process of information systems into real environments might be a good example for definition of general aspects of the functional specification and design of complex microelectronics systems. We briefly analyze the implementation aspects of information systems into an extensive production environment with pointing to the vertical and horizontal application structure. The important aspect is the optimal definition of data flow and its transformation into clear and easily used structure. Another important aspect is the resistance of the data structure to any kind of distortions and to errors in hardware structure of the system.

II. Information system and real environment

Positioning of an information system (IS) in real environment (production company) is shown on Fig. 1. The area 1 covers the whole application environment from which the area 2 shows the functional part covered by the IS and the area 3 is the part functionally not covered by the IS. Vertical lines 4 show a hierarchical structure of the environment (organizational structure, internal processing and management decision rules). The data flow through the IS is shown by the trajectory 5. The hierarchical environment structure with its own characteristics means a kind of a barrier 6 to the data flow. Another barrier 7 is a border between IS and the functionally not covered area. Similar influence (8) means to the data

flow an interface to environment 9 around the implementation environment 1. Non linear borders between different areas show incompatibilities, these may lead to the data flow distortion (fluentness or contents) and in worst case even to data loss. Overall success of the IS implementation does not depend just on quality of IS or characteristics of non-covered functional part alone. Even with the best quality IS available the overall functionality might be insufficient due to an improper interface between IS and environment or an improper hierarchical structure of the environment. Improvement of the interface may be done in narrowing and smoothing borders:

- From the IS side (2) – by parametrizing (i.e. functional change made by change of set of standard parameters) or by the modification of the standard functionality (algorithm modifications and data conversions)
- From the environment side (3) – by process improvement (reengineering).

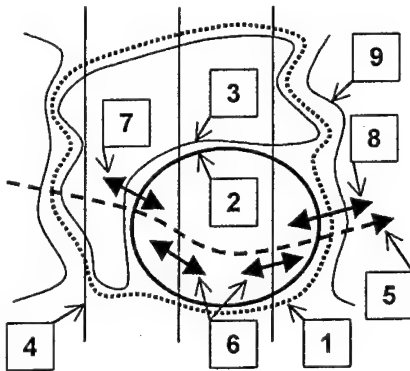


Fig.1. The information system in real environment.

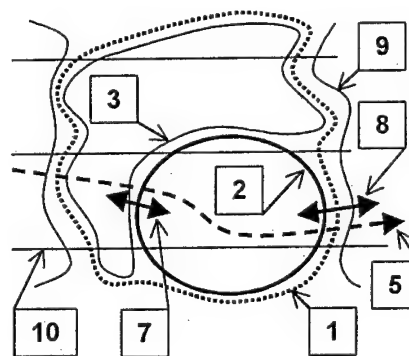


Fig.2. Modified environment for IS implementation.

From experiences made at various implementations we can say, the best result is obtained, if there is implemented standard IS with as few modifications as possible. The internal flexibility of IS is used against environment influences. Another possibility to avoid environment influences is to change the hierarchical structure. This leads to more clear and simple information process flow. This is shown on Fig. 2. The vertical borders 4 are replaced by the horizontal borders 10, which direction is similar to the data flow trajectory 5. The horizontal lines show split of the whole environment to fully or partly independent processes. In this case is an internal functionality of the IS influenced only by the borders to surroundings. These principles are in practice used for instance in quality management of the production processes.

The quality verification of the IS implementation is usually made in at least two steps:

- Functional verification with a sample data load – functional connections among all parts are tested in this step
- Functional verification with regard to full data load and real environment – process throughput capacity is tested.

Results from the verification processes are usually used for making corrections in IS internal structure or modification of interfaces.

III. Functional specification of the microelectronic system

The design of microelectronic system (MS) is a multi-stage process. Highest level is the system functional specification (behavior of the system) which is often simplified as a "customer-supplied specification". Then the MS is described at a behavioral level. In the successive design steps, the description is refined to impose more structure into the design with the filling in of the implementation details. At each step of the refinement process the behavior of the refined design is verified against the preceding design.

A typical top down design methodology would start with the design description in a hardware description language (HDL). The principal feature of HDL is the capability to describe the function of a piece of hardware independently of the implementation. The great advance with modern HDLs was the recognition that a single language could be used to describe the function of the design and also to describe the implementation. This allows the entire design process to take place in a single language and a single representation of the design. The description in HDL is compiled into a gate level implementation by a hardware compiler. The gate level design is optimized using combinational and sequential optimizers. The functionality of the implementation is checked by some verification or simulation tools. The gate level design is mapped into transistors using technology mapping. The transistor level design is further simulated to check for critical path analysis. And finally transistors are mapped into rectangles using placement and route tools.

All above mentioned steps are currently supported by various CAD systems. For most complex MS is only open the question coverage of the required functionality. This is the highest level above the behavioral level. Let us look closer to this problem. If the system is described by a descriptive tool, for instance VHDL, there exists number of exact tools to transform it down (to lower levels). To obtain the descriptive form means to include all application requirements (including all not exact defined) and specify them. Expected is the full functional coverage, i.e. the functional specification may include over-covering which may be used as spare for non-specified application requirements. In recent MS are these self-test, self-calibration, error detection and internal compensations. Important step to confirm the functional coverage is the functional verification from the description level, i.e. the functional simulation at highest level. In complex systems with huge input data combinations, formal verification methods are used by which is tested validity of the systems functional specification, not functionality of the system itself. The direct functional simulation of complex systems is usually not possible due to very long simulation time.

Let us try to validate the knowledge from previous chapter toward the methodology of the MS functional specification. The basic parts of the MS functional specification are:

- Making clear borders of the MS functional area (extracting the MS functionality from the whole application)
- Definition of an interface to the environment (communication resources and communication methods)
- Definition of an input and output data flow (communication protocols and data structure)

The structure of these parts is basically similar to those at the IS. In practical reality, often appears the question of completeness of the MS functional specification caused by not sufficient analyze of all important influences from area of the application. The functional

specification should cover for instance the human environment influences to the MS. From this point of view we may see two groups of MS:

- Systems cooperating only with other MS
- Systems with interface to human operator.

If in the first case the specification of the interface and data flows is usually clear (in case of too complex systems even this might not be true), then in the second case, we must consider the factor of instability caused by the human operator characteristics. At this point is often considered user friendliness (simplicity, clearness) to the operator and resistance of the system to mistakes at controlling and using it.

Solution methods to above mentioned problems are today mostly empirical and there does not exist any formal theory. The formal specification methods has been developed only for some specific types of MS (computers, communication systems, etc.) with mostly consist of relatively simple and clear internal structure.

From positioning of IS point of view is possible to use for design of MS data flow analysis and its distortion by various factors. If MS should be conform with application environment, it is necessary define the interface to this environment unambiguously. Internal functionality of the system should over-cover required functionality. It is necessary to count with some extra functionality as a foresight for future needs, for example by mean of parametrizing not exactly described functionality. The definition should be flexible and open to future extensions from this point of view. We may learn from useful reorganization of hierarchical structure at IS implementation and try to apply it to optimizing the internal structure of MS. It may be used in:

- split MS to independent and partly independent processes.
- simplification of internal structure of MS.
- simplification of interface between MS and environment by moving it to more advantageous position.

Split of MS to more simple parts lead to more efficient design process, more clear functional coverage and better conditions for verification processes.

IV. Conclusion

We presented possibility to share knowledge from two similar areas. At certain conditions, for the functional description of microelectronic systems are used the same rules and methods as for functional definition of the information systems. As complexity of both systems grows, the methodology of their functional specification becomes similar.

References

- [1] T. Schlipf, T. Buechner, R. Fritz, M. Helms and J. Koehl, "Formal Verification made easy", IBM Journal of R&D, No.4/5, July 1997
- [2] G. Wachutka, P. Voigt, G. Schrag, "CAD Tools for Microdevices and Microsystems: Today's Demands, Potentials and Visions, Proc. of ASDAM '98, October 1998, Smolenice Castle, Slovakia, pp.299

Validation of Behavioral VHDL Descriptions Using Software Engineering Concepts

Christophe Paoli - Jean-François Santucci

*SDEM – Systèmes Dynamiques, Energétiques et Mécaniques, URA CNRS
2053, Université de Corse, BP 52 Quartier Grossetti ; 20250 Corté France
{cpaoli, santucci}@univ-corse.fr*

Abstract. This paper deals with validation of VHDL descriptions at the early phase of the design of a digital system. Our approach consists in generating test data from a given VHDL behavioral description. The validation is achieved by comparing the results obtained using the simulation of the VHDL description within the test data and the results which should have been obtained from the specification of the system to be designed. In this paper we propose an original approach based on software testing concepts.

I. Introduction

We propose in this paper an original approach based on software testing concepts[1] in order to validate behavioral VHDL[2] descriptions. We choose such an approach because a VHDL description is a software program describing the behavior of a digital system. The problem is to generate test data using software engineering concepts. Generating test data points out the resolution of three basic problems : (i) it is necessary to define the number of test data to be considered (this number is called the length of the test data in the following) ; (ii) it is necessary to define criteria which express the "quality" requirements that the test data have to fulfill ; (iii) it is necessary to define an algorithm allowing to generate test data. To solve these problems we are concerned with testing techniques developed in the field of software engineering[1]. This interest is motivated by the fact that behavioral hardware languages such as VHDL and conventional languages such as C or ADA[3,4] are supported by common concepts. Having selected criteria from the field of software testing allowing the three aforementioned problems to be solved, we are in the phase of studying how such criteria could be measured and applied to VHDL behavioral descriptions. In order to find criteria which could estimate the length of test data and express the quality of test data, we have been concerned with two kinds of techniques: (i) the computation of cyclomatic complexity metric (McCabe metrics[4]) and (ii) the application of coverage-based metrics[1]. The generation of test data is based on a powerful algorithm[5] issued from software testing methods : this algorithm allows to calculate the minimum number of control flow paths which are sufficient for the generation of all possible execution paths involved in a VHDL description. The McCabe metric and the previous algorithm are based on a graphical representation of the control part of the software being tested. McCabe defined a cyclomatic number of a graph associated with the control part of software. This number represents the number of linearly independent paths of the graph. He proved that the cyclomatic number represents the minimum number of test data to be generated in order to test the control part of software. In order to evaluate the quality of test data, conventional software testing criteria are used. These criteria correspond to coverage based metrics[6].

The first part of the paper will deal with the graphical representation of the control flow graph (CFG) of a VHDL description we have chosen. We will present in detail in a second part the cyclomatic complexity concept and the coverage based criteria. This part will be illustrated by pedagogical examples. In the third part we will present the algorithm we select for generating the test data from a set of independent paths. In the last part we will present how these previous concepts are used in the case of VHDL descriptions. Furthermore we will give a brief overview of future work we envision to perform.

II. Graphical Representation of Control Flows

In this part we briefly present how the control flow part of a VHDL description is modeled using graph concepts. These concepts are used : (i) to represent the sequencing of operations involved in a VHDL description and (ii) to point out the different execution paths. CFGs describe the structure of software modules. The definition of a module is language dependent. In general, it is a unit of code with an entry point and an exit point. Each CFG consists of nodes and edges. The nodes represent computational statements. Edges represent transfer of control between nodes. This graphical description helps to understand complex algorithms. The general structure and the CFG of a VHDL module is given in figure 1.

```

ARCHITECTURE BEHAVIOR OF circuit_name IS
A(SOURCE), B, C, Y: BEGIN
PROCESS 1: PROCESS WAIT ON (signal, ..)
  "Instructions describing the behavior"
END PROCESS
PROCESS 2: PROCESS WAIT ON (signal, ..)
  "Instructions describing the behavior"
END PROCESS
PROCESS 3: ...
T(sink): END BEHAVIOR
  
```

} Declarations of processes

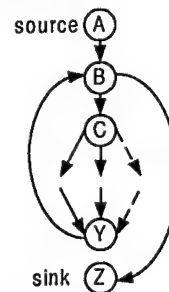


Fig 1 General structure and CFG of a module in VHDL code

A module is declared with the key word *ARCHITECTURE BEHAVIOR*. The processes involved in the behavioral description are executed in a concurrent way. The execution involves three kind of phases : (i) the scanning phase allowing to detect which processes are going to be activated ; (ii) the process activation allowing the execution of the statements belonging to the active processes ; (iii) the execution of the control structure (assignment, repetitive or selective) involved in the VHDL description of a given process. The key words *BEGIN* (A, B, C and Y nodes) and *END BEHAVIOR* (Z node) define the beginning and the end of a behavioral VHDL description. The A node is called the source node of the description. It has no incoming edge and only one outgoing edge which leads to the B node. The B node is used to model the scanning phase : (i) if at least one of the processes involved in the description is active then the following node in the execution path will be the C node ; (ii) in the contrary, the node which follows node B in the execution path is the Z node (see figure 1). The C node is the process distributor node. It allows to point out all the active processes. The number of outgoing edges of the C node is equal to the number of the processes in the description. The Y node is the process junction node. It represents the end of the execution of the active processes of the description. The number of incoming edges of the Y node is equal to the number of the processes in the description. The outgoing edge of this node always leads back to the B node. This outgoing edge allows to model the

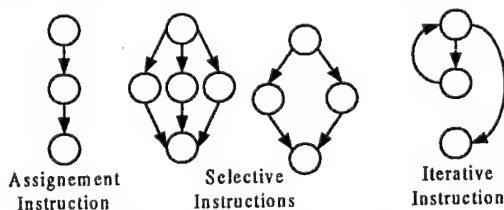


Fig 2 Control flow sub-graphs

fact that the scanning phase is going to happen once again. Between the C and Y nodes, we find the nodes that correspond to the description of each individual process and that allow the modeling of the execution of the control structures (assignment, repetitive or selective) involved in the VHDL description of a given process. The figure 2 shows the control flow sub-graph of such control structures.

III. Cyclomatic Complexity and Structured Testing

Cyclomatic complexity[7] measures the amount of decisions in a single software module. It is also known as $v(G)$, where v refers to the cyclomatic number in graph theory and

G indicates that the complexity is a function of the graph. Given a module, whose CFG has e edges and n nodes, its $v(G)$ is : $v(G) = e - n + 2$. Considering a set of several paths gives a matrix in which columns corresponds to edges and rows correspond to paths. From linear algebra, it is known that each matrix has a unique rank (number of linearly independent rows) that is less than or equal to the number of columns. This means that no matter how many number of possible paths are added to the matrix, the rank can never exceed the number of edges in the graph. In fact the maximum value of a rank is exactly $v(G)$. A minimal set of vectors (paths) with maximum rank is known as a basis. A basis can also be described as a linearly independent set of vectors that generate all vectors in the space by linear combination. So a basis is the minimum number of paths that should be tested. Therefore $v(G)$ is the number of paths in any independent set of paths that generate all possible paths by linear combination. Structured testing as presented in this sub-section applies to individual software modules. It is simply stated: "Test a basis set of paths through the CFG of each module". This means that any additional path can be expressed as a linear combination of paths that have been tested. This criterion establishes a complexity number, $v(G)$, of test paths that have two critical properties : (i) a test set of $v(G)$ paths can be realized ; (ii) testing beyond $v(G)$ independent paths is redundantly exercising linear combinations of basis paths. Therefore the minimum number of tests required to satisfy the structured testing is exactly $v(G)$. Note that structured testing criterion measures the quality of testing, providing a way to determine whether testing is complete. Structured testing is more theoretically rigorous and more effective at detecting errors in practice than other common test coverage criteria such as statement coverage and branch coverage[8]. It is not a procedure to identify and generate test data inputs. The independent test paths can be identified by the Poole's algorithm described below.

IV. The Poole's Algorithm : A Method to Determine a Basis Set of Paths

A major problem in unit testing of programs is to determine which test data are to be applied. One technique that is in widespread use is to take the CFG from each of the program functions and calculate a basis set of test paths. Path construction is defined as adding or subtracting the number of times each edge is traversed. While this is not a total solution for test data generation, it does provide a good starting set of test data. Poole[5] gives an algorithm for taking a function's CFG and determining a basis set of paths. Two nodes can be either unconnected, connected by an edge in either direction or connected by an edge in each direction. When tracing a path from the source to the sink, a back edge is a edge that leads back to a node that has already been visited. For example, in the figure 1, it is the edge that outgoes of the Y node and incomes in the B node. A CFG contains one source node and one sink. For example, consider a graph with 4 edges: a, b, c and d. The path ac can be represented by the vector [1 0 1 0]. Paths are combined by adding or subtracting the paths' vector representations. Each path in the basis set can not be formed as a combination of other paths in the basis set. Also, any path through the CFG can be formed as a combination of paths in the basis set. Figure 3 shows a simplified CFG. While a complete CFG would not have two edges going to the same destination, this requirement has been relaxed to keep the number of paths to a manageable size for this example. A basis set for this graph is {ac, ad, bc}. The path bd can be constructed by the combination $bc+ad-ac$ as shown in figure 3. The set {ac,bd} is not a basis set, because there is no way to construct the path ad. The set {ac,ad,bd} is also a basis set. Basis sets are not unique; thus a flow graph can have more than one basis set.

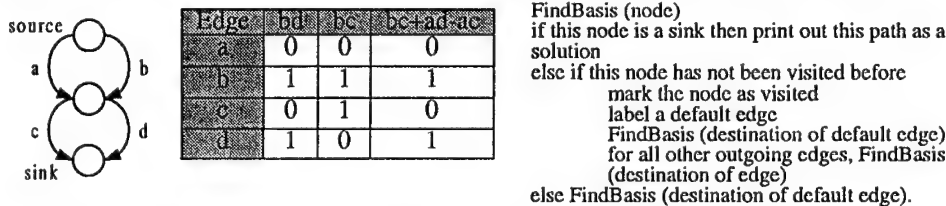


Fig 3 Simplified CFG and Demonstration of Path Construction and Poole's Algorithm

The algorithm for this basis set method is a modified depth-first search algorithm. The search starts at the source node and recursively descends down all possible outgoing paths. If the node visited has never been visited before, a default outgoing edge is picked, then the current path is split into new paths that traverse each outgoing edge, going down the default edge first. The default edge is any edge which is not a back edge or which later causes a node to have two incoming edges. For example, in the test condition of a pre-test loop, the default edge would be the edge which exits from the loop. If the edge that traversed the body of the loop was chosen, then a back edge from the last node in the body to the test condition node would have to be traversed later. If the node visited is a sink (no exit edges), then a path in the basis set has been found. Otherwise, the path traverses the default edge. A pseudo-code outline of this method is shown in right side of the figure 3. If we apply this algorithm to a VHDL description, our result will be a set of independent paths. In fact we obtain a number of paths equal to the cyclomatic complexity (see section 2 and 3) with the correspondent edges that are traversed for each path.

V. First Results and Future Work

Using the concepts issued from software engineering and presented in section 3 and 4, it is obvious that these concepts are easily used on the control flow representation of VHDL descriptions presented in section 2. We propose in figure 4 a framework for deriving test benches for VHDL descriptions. The proposed approach is based on McCabe cyclomatic complexity, the structured testing method and the definition of the specification of a test benches generator using the Poole's algorithm. We are in the phase of defining the specification of a software allowing to automatically generate test data for VHDL descriptions from the previous concepts. For the moment we have generated by hand input data from paths of a simple

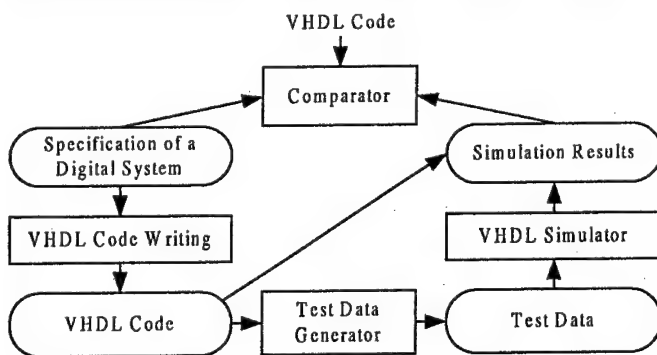


Fig 4 VHDL behavioral description validation scheme

VHDL description CFG in order to execute each path. Furthermore we have generated their corresponding output data. The result has been expressed through the compilation of a test bench. Its simulation allowed us to validate a simple VHDL behavioral description[9].

References

- [1] E. Miller, W.E. Howden, Software Testing & Validation Techniques, IEEE Computer Society Press, pp 4-16, pp 209-231.
- [2] VHDL, Language reference Manual, IEEE Standard 1076, 1987.
- [3] Manuel de reference du langage de programmation ADA, US Defense; 1982.
- [4] ADA and C language supplement, McCabe.
- [5] J. Poole, A Method to Determine a Basis Set of Paths to Perform Program Testing, NISTIR 5737.
- [6] A.H. Watson, T; J McCabe, Structured Testing: A testing Methodology using the cyclomatic Complexity Metric, NIST Special Publication 500-235, August 1996.
- [7] T.J. McCabe, A Complexity Measure, IEEE trans. Software Testing Engineering, N°2, pp 308-320, 1976.
- [8] A. Watson, Structured Testing: Analysis and extensions, Ph.D. dissertation.
- [9] C. Paoli, J. F. Santucci, Data generation from CFG of VHDL descriptions, to be published at the ATW'99, 1999, Ajaccio, France.

Real Implementation of Artificial Neural Networks

J. Cabestany

*Department of Electronic Engineering
Universitat Politecnica de Catalunya-UPC, Gran Capita,s/n Building C4
E-08034 BARCELONA, Spain
cabestan@eel.upc.es*

Abstract. Artificial Neural Networks (ANN) have become an interesting solution for many real life applications. The problems related with pattern recognition, data clustering, classification, identification,... are all suitable to be solved using neural networks methods. Usually, neural methodology is based on specific models and algorithms. Depending only on the application constraints, it is possible to decide how to implement them.

Along this work, we will try to make clear the different alternatives for the implementation of ANN, going from the use of commercial software simulators running on conventional computing platforms, to more specific and sophisticated VLSI electronic implementations.

I. Introduction.

Artificial Neural Networks (ANN) belong to the category of intelligent systems able to manage information in a way resembling more or less the nervous system. The main properties of a neural computing system are the following:

- Ability to learn from examples (no prior knowledge about the problem is required).
- Ability to generalise from learnt examples.
- Ability to predict with new data.
- Possibility to deal with missing information or noisy environments.

ANN process data in a massively parallel way, involving many elementary processors interconnected through different paths. The high intrinsic parallelism of these systems is remotely inspired in biology, and its ability to process information is done using specific algorithms. These algorithms implement learning and processing phases on particular architectures, each of them composed of several layers of processing elements with interconnection paths between them.

Figure 1 shows such a structure for the particular case of the Multilayer Perceptron (MLP) network. In this ANN, learning procedure is done by using the Backpropagation or a

similar algorithm. The process consists on the presentation of the input data to the neural structure followed by the comparison of the actual known answer together with the predicted one. If there is a difference between the two, the weights are adjusted to reduce the error. This process is repeated for all examples until the best solution is found.

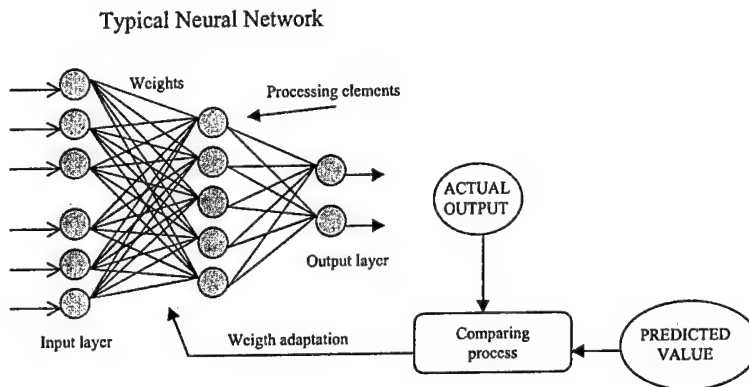


Fig 1. MLP structure with supervised learning scheme.

The above learning algorithm is a good example of the so called *Supervised Learning*, as opposed to the *Unsupervised Learning* one, specially employed with SOM (Self-Organised Maps) ANN.

SOM structure is mainly composed of one input and one output layers with a two-dimensional cluster layer of interconnected elements between them. The learning process is performed by the presentation of data to the input layer and the identification of the elements in the cluster layer with the most similar profile. Weights are adapted with a re-enforce technique.

After many iterations of the presented data, the structure is self-organised in such a way that similar inputs force similar outputs after processing. In fact, the obtained effect is a clustering process in the two-dimensional layer. To use the SOM network, inputs are presented to the trained ANN and the resultant location on the cluster layer indicates the input group.

Another very useful ANN model is the RBF (Radial Basis Function) one. It consists of two layers. The first one (hidden layer) is constructed using a set of basis functions whose centres correspond to the prototype vectors in input space. The basis functions are usually chosen to be un-normalized Gaussians. The output units (second layer) form a linear combination of the basis functions computed by the hidden units.

The learning process in RBF ANN is not completely fixed, and takes place in two main phases. First of all, it is necessary to determine the position of Gaussian functions along with their shape and characteristics. This is done by means of a clustering method, together with a proper parameter value selection in accordance with the internal organisation of the data representing the problem. These parameters will vary depending on the data density in different regions of the input space. Setting the weights in the second layer is a linear optimisation task, and can be done using conventional matrix methods or iteratively using the Least Mean Square (LMS) algorithm.

II. Models and identification of operators.

In the above section we introduced the basic models for ANN. Usually the ANN application is limited to a small number of structures and associated learning algorithms. By expanding this set of ANN, it is possible to obtain a great variety of solutions with the resulting combination of the particular properties.

The set of ANN structures most used in practice is the following [1]:

- Perceptron (Single Layer Perceptron).
- Multilayer Perceptron (MLP).
- SOM (Self-Organised Maps).
- RBF (Radial Basis Functions).

The associated basic strategies for training and execution phases are listed in Table I:

ANN	Learning	Algorithm	Operations (learning and execution)
Single Layer Perceptron	Supervised	Perceptron learning rule	<ul style="list-style-type: none"> • Product and Addition • Non-linearity
MLP	Supervised	Backpropagation	<ul style="list-style-type: none"> • Product and Addition • Non-linearity
SOM	Unsupervised	Re-enforcement	<ul style="list-style-type: none"> • Distance calculation • Product and Addition
RBF	Mixed	Clustering LMS	<ul style="list-style-type: none"> • Distance calculation • Exponentiation • Product and Addition

Table I. Basic ANN structure and characteristics.

Taking a look on the table, we can observe that only a few operations are identified, and depending on the phase (learning or execution) the required precision could be very different. Usually, a precision equivalent to 8 digital bits is enough for the execution phase, and 16 bits may be necessary for training process when an error function optimisation procedure is used (backpropagation algorithm for example). Summarising, the computational requirements for a platform implementing an ANN are: addition, product, non-linearity computation, distance calculation and exponentiation. All of them executed in a collective way, and within the frame of a given structure with specific data paths.

III. Technological solution for ANN implementation.

In 1987, Lippman published a fundamental review article on the field [2]. He wrote: *"the greatest potential of neural nets remains in the high-speed processing that could be provided through massively parallel VLSI implementations"*. Nowadays, this is no longer prevalent because most neural networks applications are developed, tested and run on PCs or standard workstations (in fact, serial-processing machines). This is possible because of the present microprocessor possibilities and working frequencies.

From a general point of view, and taking into account the electronic technology state-of-the-art, we can summarise that there exist many ways for real ANN implementation:

- Analogue implementations
- Digital implementations
 - Stand-alone neurocomputers (with custom or commercial processors)
 - Accelerator boards (with custom or commercial processors)
 - Chips with on-chip controllers.
 - Microprocessor peripherals
 - Stand-alone on-board applications.

In the literature we can find many excellent works with accurate reviews on hardware for ANN, especially for the digital alternative [3,4,5]. The analogue implementations are reviewed in [6], with an extension to mixed (analogue/digital) solutions. Table II, taken from [6] shows the digital vs. analogue comparison in terms of main merit factors.

Merit factor	Digital	Analogue
Area		*
Power		*
Speed		*
Memory	*	Difficult
Noise	Quantisation	Random
Technology independence	*	
Repeatability	*	
Scalability/Modularity	*	
Precision/Dynamic range	Limited by area	Tech. and design
External interface	Numerical data	Physical signals

Table II. Digital vs. Analogue neural processing comparison.

Analogue is very attractive in terms of area, speed and power consumption. Because of these conditions, analogue can be considered a suitable candidate for high-speed and low-power applications. On the other side, digital solutions benefit from reliable and well-established memory cells, good technology independence, repeatability of the operations, and easy scalability and modularity.

External real world physical signals interfacing is easier in analogue domain, but synchronism, control and communication processes are more straightforward for digital processors. The most suitable real world implementation or realisation of an ANN application will depend on many conditions. Figure 2 summarises this concept.

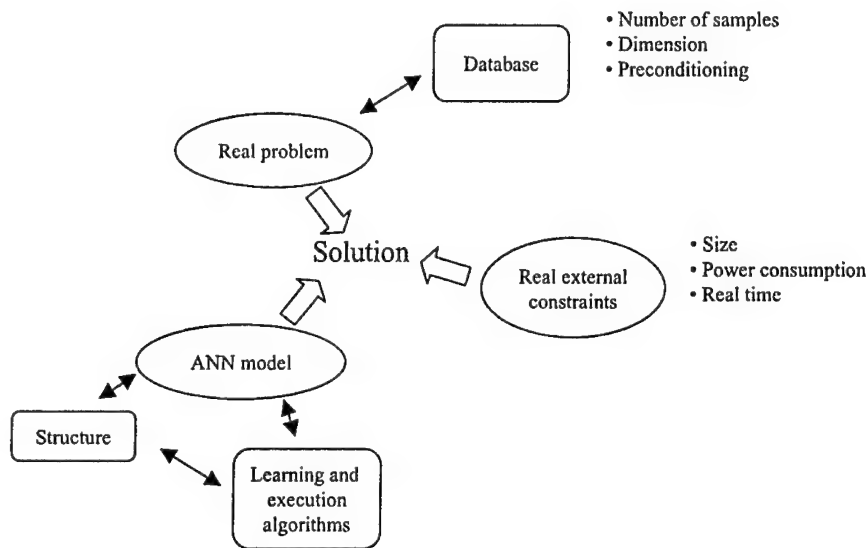


Fig 2. Map for real ANN implementation.

When considering a real world problem, described using a database, and after a proper selection of the most suitable ANN model, it is possible to take into account the real external constraints for the application, and decide the best solution.

In our opinion, the most restrictive conditions are:

- *Size and power consumption.* When these conditions are dominant, it will be necessary to consider analogue or mixed solutions. The only problem could be here the learning process and the information storage strategies.
- *Real-time.* In real world problems, this condition could be very important, and it is possible to satisfy it in a great variety of ways. In fact, "real-time" meaning is application dependant, and it can range from nanoseconds to seconds or minutes. The concept can be very different from one application to another.

Nowadays it is possible to obtain real time characteristics with general-purpose microprocessors (like Intel, SUN or Motorola) because their working frequency, managing memory possibilities and input/output interface properties [7].

Platforms based on these processors are very good solutions for ANN implementation. Additionally, we will need a software package for the proper emulation of our ANN model. Software must have the right data managing possibilities.

The criteria for selection of the platform [1] will be price, availability, ability to run the chosen software, and computing power required for training process. We must ensure that:

- It has sufficient processing power to cope with the computations required during ANN training.
- It has the disk capacity to hold the expected volumes of data, including both the training data and the network parameters (weights and/or centre positions and widths).
- It has any special interface hardware required during the data collection phase.

For the software packages themselves, it is possible to consider the use of a commercial or public domain solution [8], or alternatively, to write one's own software according with specific needs.

If the requirements match with the use of development software on a general purpose processing platform, this can be the best solution for implementation. The main reasons are:

- It is an open solution.
- The time required until the solution is low.
- It is flexible.
- It accepts a continuous updating.
- The user interface is optimal.

IV. Specific approaches and new possibilities.

When the requirements of a specific problem overcome the global possibilities of general-purpose platforms in terms of speed and adaptation to a specific ANN structure, it could be necessary to think on *Special-purpose hardware* solutions. As it was stated in above section, we have two main families of solutions:

- *Accelerator systems*, available for standard PCs and workstations and based on general purpose microprocessors or, alternatively, on special VLSI custom processors well adapted for the execution phase of some ANN algorithms. In the literature [3] we can find examples of such a realisations: ANZA plus from Hecht-Nielsen Co., board based on Lneuro chip from Philips, accelerators around MA16 chip from Siemens, ZISC board from IBM-France, ...
- *Special-purpose systems*, generally based on specific VLSI designed neurochips. Some well known examples are [3,4]: the SYNAPSE-1 machine from Siemens, the CNAPS engine from Adaptive Solutions Inc., MANTRA from EPFL in Switzerland,...

Special purpose systems are very expensive, and, generally, they present some problem with the user-interface. In conclusion, we have serious doubts about their usefulness except in very specific cases with very strong boundary conditions.

Looking at new possibilities based on actual electronic technology progress, a new and promising scenario is offered by electronic reconfigurable systems around FPGAs (Field Programmable Gate Arrays) devices. The capabilities of the coming devices from many manufacturers, like Xilinx and Altera, allow the realisation of systems equivalent to thousands of logical gates. It is easy and relatively fast to implement operations related with ANN computation on a chip, giving the additional opportunity to implement different ANN structures on the same basic hardware (reconfigurability properties).

One recent example of these possibilities is the solution proposed by M. Chiaberge [9] from Politecnico di Torino. The OpenDSP system is able to implement several ANN models, and it is based on a Texas DSP processor together with a FPGA device from Altera. The complete system is composed of several boards connected by means of a proprietary bus.

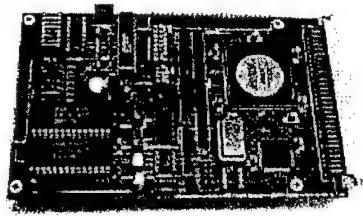


Fig 3. Overview of OpenDSP board (Politecnico Torino)

The internal configuration of FPGAs devices with limited routing resources forces the consideration of special solutions for implementing arithmetic operators, like On-line arithmetic [10]. These specific design techniques together with the possibilities offered by the very new dynamically reconfigurable devices, integrating the FIPSOC family (Field Programmable System on a Chip) [11,12], give us the opportunity for compact solutions in the field of ANN models realisation. FIPSOC is a special system-on-a-chip composed of one digital FPGA part (equivalent to 5000 gates), a microcontroller core (standard 8051) and an analogue part (fully differential amplifiers, comparators, 8 bit A/D – D/A converters). Figure 4 shows the organisation of the device.

V. Conclusion.

This paper has discussed different current ways for the implementation of ANN structures for real world applications domain. Special attention must be paid to the characteristics of present commercial platforms based on novel microprocessor devices.

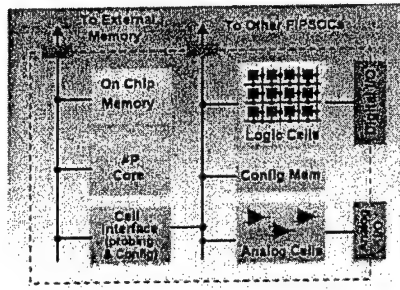


Fig 4. Bloc diagram of FIPSOC device.

References

- 1 L.Tarassenko *A guide to Neural Computing Applications*. Arnold Publ. 1998
- 2 R.P.Lippmann. "An introduction to computing with neuralnets". *IEEE ASSP Magazine*. April 1987
- 3 J.N.Heewskerk. *Neurocomputers for Brain-Style Processing. Design Implementation and Applications*. PhD Thesis. 1995
- 4 P.Ienne, T.Cornu, G.Kuhn. "Special-purpose Digital Hardware for Neural Networks: An Architectural Survey". *Journal VLSI Signal Processing Systems* 13, 1996.
- 5 A.Köning. "Survey and current Status of Neural Network Hardware". *Proc. ICANN. Paris*. 1995
- 6 J.Madrenas, J.M.Moreno, J.Cabestany. "Analog and mixed-signal neural VLSI processors: taxonomy, comparison and performance evaluation". *Proc. MIXDES96. Poland*, 1996
- 7 B.Granado, L.Lacassagne, P.Garda. "Can General Purpose Micro-processors Simulate Neural Networks in Real Time?" *Proc. IWANN'99. Alicante (Spain)*. 1999
- 8 Overview can be find at: <ftp://ftp.sas.com/pub/neural>
- 9 M.Chiaberge, E.Miranda, L.Reyneri "An HW/SW Co.design Approach for Neuro-Fuzzy Hardware Design". *Proc. Micro-Neuro '99. Granada*. 1999.
- 10 J.L.Beuchat, E.Sanchez "Using On-line Arithmetic and Reconfiguration for Neuroprocessor Implementation". *Proc. IWANN'99. Alicante (Spain)*. 1999
- 11 Technical information from SIDA (Madrid - Spain) <http://www.sidsa.com/fipsoc.htm>
- 12 J.M.Moreno, J.Cabestany, E.Canto, J.Faura, J.M.Insenser "The Role of Dynamic Reconfiguration for Implementing ANN Models in Programmable Hardware". *Proc. IWANN'99. Alicante (Spain)*. 1999

Mixed-Signal VLSI for Skeletonization by Grassfire Transformation - Design and Evaluation

M. Oláh¹, S. Török², A. Poppe³, P. Masa⁴ and A. Lőrincz⁵

^{1,2,3} *Department of Electron Devices, Technical University of Budapest, H-1521
Budapest, Hungary, e-mail: olah@mozart.eet.bme.hu*

⁴ *Swiss Center for Electronics and Microtechnology, Neuchatel*

⁵ *Department of Information Systems, ELTE University, Budapest*

Abstract. This paper presents a novel mixed-signal VLSI focal-plane array processor performing the morphological operation of skeletonization of binary images in real time. The chip exploits the inherent parallelism of the grassfire algorithm by using a massively parallel mixed-mode array achieving high computational speed and relatively low power consumption. The system is a two-dimensional array of identical processing elements (PEs) with integrated photodetectors allowing parallel optical input. The skeleton computation is performed in a fully parallel, asynchronous manner by local interactions between PEs, the transformed image is represented by analog values. The output of the transformation can be serially accessed with an on-chip raster-scan circuit generating multiscanning-compatible video signal. The system was physically designed and prototypes of 22x26 array were fabricated in a standard 0.7 μm CMOS process. System and layout design considerations as well as output data sample of the fully functional fabricated chip are presented.

I. Introduction

Our efforts on the VLSI implementation of a skeletonization system are motivated by the demand for high computational throughput at low-power and small dimensions [1]. The skeletal representation compresses topological information of shapes, and has been recognized as a useful pre-processing step in image recognition tasks [2]. Results based on psychophysical measurements suggest that the human visual system extracts 'skeletons' as descriptor of planar objects [3]. We have chosen a low-cost standard digital CMOS process to implement a skeletonization chip.

The skeletonization algorithm developed by us is based on the grassfire method proposed by Blum aimed at eliciting the Symmetric Axis Transform (SAT) of planar shapes [4]. Our method produces a greyscale skeleton which is a generalization of the traditional binary one. This 'generalized skeleton' can be extracted by monitoring an activation spreading process - the 'grassfire' - implemented on a multilayer network. The inherent parallelism of skeletonization by the grassfire method can be exploited by building a VLSI system consisting of a 2D array of identical processing elements collectively processing the input data. A dedicated parallel VLSI chip can solve the generalized skeleton computation in a few microseconds at low power consumption, in a small volume. Analogue processor arrays for basic morphological operations have been already presented by others [5].

II. A Neural Model of the Grassfire Transformation

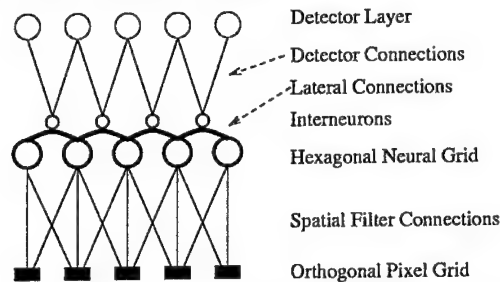


Fig 1 Architecture of the grassfire transformation

The architecture of our grassfire transformation model is a multilayer network (Fig. 1). The algorithm of the transformation consists of three main steps: (i) set the initial grassfire activation on the neural grid according to the figure-ground separated input image, (ii) let the grassfire activity propagate from the boundary points of the shape along the lateral connections between adjacent neurons, (iii) detect the incoming and outgoing activity to/from each neuron. Constant propagation speed of grassfire wavefront can be achieved by the self-excitatory behaviour of the neurons. To monitor the propagation process to each lateral connection a processing unit (or *interneuron*) is assigned. The interneural activations are summed up and time-integrated on the output detectors. Those points where at least two firefronts collided are skeleton (symmetry) points, since they are equidistant from two boundary points. Skeleton points are marked by positive detector values, because the sum of activity inflow is greater than the outflow. A single passing firefront results in zero detector value, since activity in- and outflow cancel each other.

After saturation of the grassfire activity over the neural grid, the activity distribution over the detector layer carries the output of the transformation (i.e., the generalized skeleton).

III. System Architecture

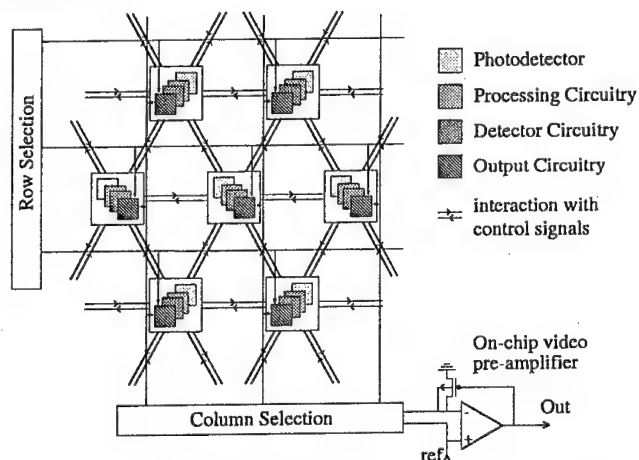


Fig 2 Architecture of the Grassfire Skeletonization Chip

The implemented VLSI system is an array of identical PEs consisting of four functional layers of circuitry (see Fig 2). The PEs are arranged on a hexagonal grid with local non-linear type connections. Replacement the linear lateral connections with hard limiting ones causes rotational dependence of the computed skeleton, but it does not influence system level functionality and allows much more efficient VLSI implementation. The photodetector circuitry senses and binarizes the image focused onto the chip to figure and ground points via a single thresholding. The initial grassfire activation distribution is set as high and low voltages on a capacitor array integrated in the processing circuitry according to the thresholded image. The processing circuitry propagates the 'grassfire', the detector circuitry monitors the propagation process and encodes the resulted skeletonized image as voltage distribution over a capacitor array. The output of the transformation can be serially accessed by an on-chip scanner circuitry [6] enabling real-time visualization on a commercial VGA-compatible computer display.

IV. Physical Design

The PE cell as well as the necessary input/output interfaces to the processing array were physically designed using a standard digital 0.7 μm dual metal CMOS process (ES2 ecpd07). The PE cell is layed out in a rectangular area (approx. $120 \times 140 \mu\text{m}$) with an aspect ratio of approximately $\sqrt{3}/2$ to build up the required hexagonal tessellation of the plane. The entire surface except over the photosensing device is covered with the second metal layer (see Fig 3) in order to protect the circuit parts susceptible to light induced currents (e.g. MOS transistors operated in subthreshold mode). This shielding also serves as power routing.

V. Evaluation

A 22 by 26 test array was fabricated using Europractice low-cost Multi-Project-Wafer prototyping service consuming approximately 20 mm^2 silicon area. The chip package is closed with a transparent lid for the optical image projection. The original binarized input image and its grey-scale skeletonized transform is serially read out by means of a minimum number of off-chip components. The test setup is shown on Fig 3. Fig 4 shows the image of a rectangle and its skeleton as computed by the chip.

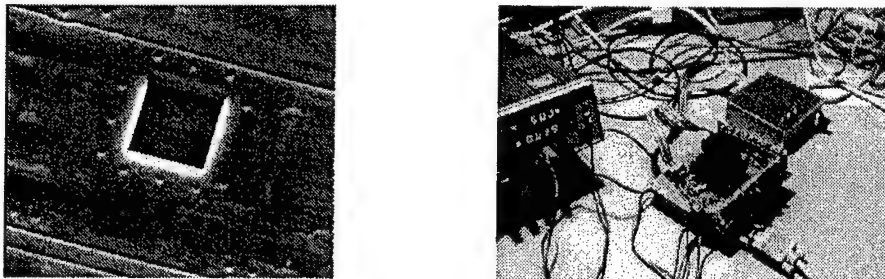


Fig 3 (left) Scanning electron microscope photograph of the PE on the fabricated chip around the photodiode. (right) Test panel for chip testing. The chip is surrounded by biasing potentiometers and a video buffer (front panel). Image is projected onto the chip with a camera lens (black object in the middle).

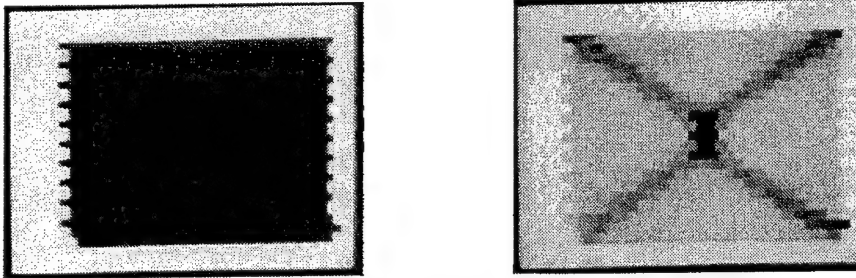


Fig 4 Image of a rectangle optically projected onto the chip (left) and its skeleton as computed by the same VLSI (right). Visualization on a standard VGA monitor, snapshot taken with a conventional camera.

The chip consumes 100mW and its computational power efficiency (excluding input/output) is 0.25×10^{12} Op/J.

The measurements confirmed that the chip is fully operational capable of computing the generalized skeleton of binary images. By exploiting the inherent parallelism of the algorithm in an asynchronous mixed-mode implementation an estimated processing speed of 10Kframes/second can be achieved. The combined use of analog and digital computation at the pixel level offers compact design compared to pure digital or analog implementations.

The development of the photoreceptor circuit is now under consideration in order to solve the figure-ground segregation problem under inhomogeneous illumination conditions. We also plan to investigate the possibilities of the integration of a skeletonization array with further on-chip processing for optical character recognition.

References

- [1] E.A.Vittoz, "Analog VLSI signal processing: why where and how?", *Journal of VLSI signal processing*, Vol. 8, 8 1994, pp. 27-44
- [2] L. Lam and C.Y. Suen, "An evaluation of parallel thinning algorithms for character recognition", *IEEE Trans. On Pattern Analysis and Machine Intelligence*, Vol. 17(9), September 1995,
- [3] I.Kovács and B.Julesz, "Perceptual sensitivity maps within globally defined visual shapes", *Nature*, Vol. 370, 25 August 1994, pp. 644-646
- [4] H. Blum, "Biological shape and visual science (part i)", *Journ. of Theoretical Biology*, Vol. 38, 1973, pp. 205-287
- [5] T.G. Morris and S.P. DeWeerth, "Analog VLSI arrays for morphological image processing", *Proc. of the Int. Conf. On Application Specific Array Processors*, IEEE Computer Society Press: Los Alamitos, CA, 1994, pp. 132-142
- [6] T. Delbrück and C. Mead, "Scanners for visualizing activity of analog VLSI circuits", *Technical Report, CNS memo 11*, Caltech, 1991,

A New Refresh Circuit for Analogue Artificial Neural Networks

Molnár Jozef V. ⁽¹⁾ and Daniela Ďuračková ⁽²⁾

⁽¹⁾ *Infineon Technologies, Villach, Austria*

⁽²⁾ *Department of Microelectronics,
FEI STU, Bratislava, Slovakia*

Abstract

Although we live surrounded by computers and other digital circuits, there are still applications that require some analogue parts. And here belongs also the neural networks domain. One of the biggest problems is to store the weight voltage in analogue form with a desired accuracy and without time degradation. This article introduces a method to solve this problem.

1. Introduction

As follows of the nature of Analogue artificial neural networks, they work on analogue signals, amplifying, adding them to get the desired output. They have to memorize the weight of each synapse in some way. Depending on the physical quantity they use different methods. A very efficient way is to use digital circuits. The weight can be stored in a digital memory and reproduced with a DAC. The accuracy of this solution is dependent on the resolution of the used DAC, which can be up to 24 bits, but this solution would need a DAC in every synapse. A very efficient and precise method is to use a sample and hold circuit in every synapse and an analogue demultiplexer at the DAC output. This article explains, how to apply such a weight storage in the analogue neural networks.

2. The digital refresh

Fact, on that this circuit is based is the long developed method of storing digital information. The time degradation is negligible in this type of memories, because the read voltage, stored in a memory cell is "compared to a reference value" and the result is then one bit of digital voltage of log.L or log.H level. Several bits are then applied to a digital to analogue converter, which generates analogue value of voltage. The DAC with a latch at the input holds the corresponding voltage at its analogue output. To use only one DAC for several synapses it is necessary to add an analogue demultiplexer to the output of the DAC and a sample and hold circuit to each synapse. Fig.1 shows the block schematic of the refresh circuit. The system consists of a clock generator, an address generator, binary to decimal decoder, memory, digital to analogue converter and an analogue demultiplexer.

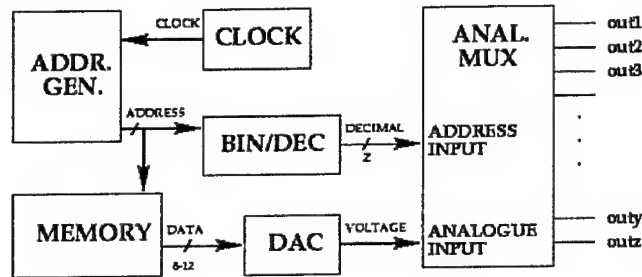


Fig.1: Block diagram of the refresh circuit

3. The digital subsystem

The main part of the digital subsystem is the memory. The number of bits in a word depends on the accuracy of the digital to analogue converter and the sample and hold circuits. It can be 8 to 24 bits depending on the used technology and desired accuracy. The number of words is dependent on the size of the network and the number of synapses respectively, and it should not be too high due to the refresh rate, which depends on the used sample and hold circuits (quality of capacitors, leakage) and the technology. If the sample rate is too low, the voltage at the output of the S&H circuit is not stable enough and the precision of the neural network is then decreased. It happens also in case, when there is a high bit resolution DAC used, the height of the refresh rate is already limited by the technology and there is a lot of synapses, connected to the circuit. The quantity level of the DAC is then very small and the voltage on the S&H capacitor, decreasing by time reaches the lower weight values.

The refresh circuit has an input bus for programming the memory and connecting more circuits to the programmer, so there can be used more refresh circuits on one neural network. The advantage is a higher refresh rate, more stable weight voltage and more accurate response of the neural network.

The main advantage of this solution of the refresh is that the digital subsystem is completely independent of the neural network, so it can operate at the highest possible frequency and the system is very easily programmable.

Another important part of this subsystem is the address generator. This circuit generates the address for the memory, from which the output data are provided to the DAC. This generator is an n-bit continuous counter. The number of bits of the counter and the width of the address bus depends on the number of the synapses.

3. The analogue subsystem

The analogue subsystem consists of the digital to analogue converter and the analogue multiplexer, which is actually the input part of the S&H circuit.

The multiplexer has two inputs: the analogue input and the digital address bus. The analogue input is connected to the DAC and provides the output voltage to the capacitors. The digital address bus is a decimal input bus that handles the switching of the analogue switches. The system charges the capacitors with a voltage pulse from the analogue input. The

refresh rate (see equation (1) for f_{Rmin}) should be equal or less than the time, during that the voltage of the capacitors decreases one quantity level of the DAC.

$$t_{MAX} = -\frac{1}{n} \tau \cdot \ln \left(\frac{\Delta u}{u_0} + 1 \right) \quad (1)$$

where Δu is the elementary step of the DAC,
 τ is the time constant of the capacitor,
 n is the number of the synapses
 and u_0 is the weight voltage.

The multiplexer does not have any built-in intelligence thus the binary-to-decimal decoder should care about to provide log.H level only on one output at the same time. The simulation results of a 4 bit decoder are shown in fig.2.

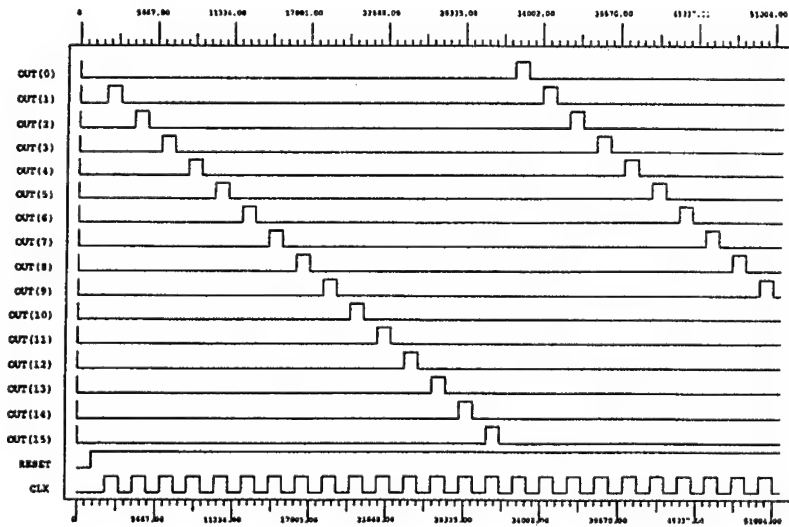


Fig.2.: The output of the decoder

An example of the S&H circuit simulation is shown in fig.3. A small number of synapses were used just to demonstrate the functionality of the system. The quantity level of the 8 bit DAC with 3.3V voltage reference was approximately 0.0129V. The next refresh pulse must come before the voltage of the capacitor decreases below 1.487V (by 1.5V weight), see fig.3. Unfortunately the parasitic resistance of such a structure was not known to us, so in the simulation we first used a dummy NMOS transistor and than a 5GΩ resistor. The result is satisfying, the voltage difference was 0.004V, three times smaller, than the quantity level of the DAC by 300μs (3.34 kHz) refresh rate.

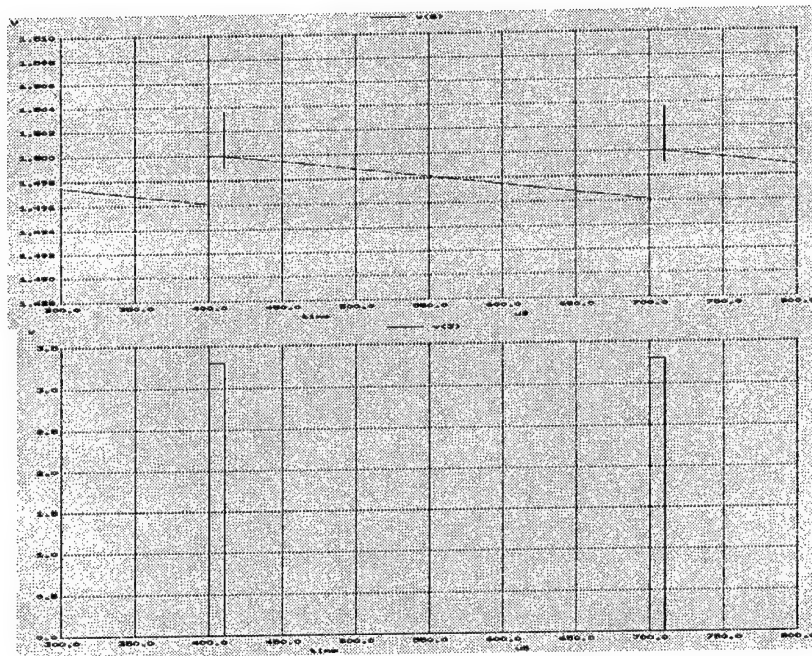


Fig.3.: Simulation results of the S&H circuit

Conclusions

The presented circuit can be used to keep the weight values also by existing analogue neural networks. The advantage is that the system is continuously programmable, allowing self-learning capabilities of the applications with e.g. a microcontroller. The clock and the programming of the memory do not affect the networks, so they can operate without interrupts. The circuit is also applicable in a mixed design reducing the number of external parts. The experimental circuit is designed in Solo1400's 1.0 μ m technology, the chip area is approximately 4mm². This work has been supported by the Ministry of Education of the Slovak Republic under Grant No.: 1/6096/99.

References

- [1] Shibata T., Kosaka H., Ohmi T.: "A Neuron-MOS Neural Network Using Self-Learning-Compatible Synapse Circuits," *IEEE Journal of Solid-State Circuits*, Vol.30, No.8, August 1995.
- [2] Atkin T., Najfi K., Bradley R.M.: "A Wireless Implantable Multichannel Digital Neural Recording System for a Micromachined Sieve Electrode," *IEEE Journal of Solid-State Circuits*, Vol.33, No.1, August 1998.
- [3] Piovaccari A.: "CMOS Integrated Third Generation Current Conveyor", *Electronics Letters*, Vol.31, No.15, July 1995.

RBF neural network models for estimating human signal detection performance

Martina Rohál'ová

*Institute of Informatics, Faculty of Mathematics and Physics,
Comenius University, Mlynská dolina, 84215 Bratislava
rohalova@fmph.uniba.sk*

Miloš Koska

*Institute of Measurement, Slovak Academy of Sciences,
Dúbravská cesta 9, 842 19, Bratislava
umerkosk@savba.sk*

Abstract. In this paper, we compare two radial basis function neural network (RBF NN) models for estimating human signal detection performance from brain event-related potentials (ERP) elicited by task relevant signals. Data consist of ERPs and performance measures (PF1) from five human operators. Individual RBF NN models are built of PF1 using modified Minimum Description Length (mMDL) method. The results (the number of hidden units and the quality of approximation) are compared with the ones achieved with RBF NN models which were designed using orthogonal least squares (OLS) method. We arrived at a conclusion, that using the mMDL method it is possible to build the RBF NN with substantially lower number of hidden units but at the expenses of slightly worse quality of approximation as with the OLS method.

1 Introduction

In many important tasks (e.g. air traffic control, piloting of vehicles) the control is based on ability of operator to detect and evaluate task relevant signals in presented visual data. Performance quality of the operator varies over time, often falling below acceptable limits. Such performance variability may have serious consequences. In many of these tasks, the likelihood of such errors could be reduced if objective methods for assessment of human performance were available. We have utilised ERP data to build the RBF NN model for estimating human signal detection performance. The ERPs reflect mental processes and are known to be related to human performance, including signal detection, target identification and recognition, memory and mental computation [6].

2 Data set

The ERP data (which were recorded from 3 electrodes) were acquired in earlier study ([6]) during a signal detection task from 5 human operators.

Within each blok of trials a running mean ERP was computed for each operator using 10-trials moving window ([2]). As we were confronted with the curse of dimesionality, the principal component analysis (PCA) was applied on the running mean ERPs. The ERP

data preprocessed in this way form the input data for the RBF NN models for estimating human signal detection performance. The dimension of the input vector for individual operator is 30 and their number gets values between 400 and 900.

The performance of each operator was measured by monitoring three parameters: speed, accuracy and confidence. The performance measure, PF1 was derived using factor analysis of the performance data ([2]):

$$PF1 = 0.33 * Accuracy + 0.53 * Confidence - 0.51 * Reaction Time \quad (1)$$

Running mean PF1s (computed in the same way as running mean ERPs) form the output scalar for the RBF NN models.

3 RBF neural network model

An RBF NN with n inputs and scalar output is given by

$$\mathcal{F}(\mathbf{x}) = w_0 + \sum_{j=1}^m w_j h(\|\mathbf{x} - \mathbf{c}_j\|) = w_0 + \sum_{j=1}^m w_j e^{-\frac{\|\mathbf{x} - \mathbf{c}_j\|^2}{r_j^2}} \quad (2)$$

where $\mathbf{x} \in \mathcal{R}^n$ is the input vector, $\mathcal{F}(\mathbf{x})$ is the output of the RBF network, w_j ($0 \leq j \leq m$) are the weights, $h(\cdot)$ is given radial basis function (RB-function) from \mathcal{R}^+ to \mathcal{R} (we have used Gaussian RB-function), $\|\cdot\|$ denotes the Euclidean norm, $\mathbf{c}_j \in \mathcal{R}^n$ ($1 \leq j \leq m$) are the centers and $r_j \in \mathcal{R}^n$ are the widths of RB-functions and m is the number of centers, and thus the number of RB-functions (number of the hidden units).

The design and training of RBF NNs consist of 5 tasks: the choice of RB-function; determining the number of RB-functions; finding their centers and widths and adapting the weights([4]). The choice of RB-function is not so critical for performance of the RBF NN as the process of finding their centers [1]. Thus, the main question is, how to select appropriate centers from the training set.

4 Methods

In earlier study [2] the OLS method was used to design the RBF NN models for estimating human signal detection performance. The OLS method ([1]) is an algorithm for selecting a suitable subset of input vectors as the centers. The center selected in each step reduces the error of the network at most. The centers are selected until an adequate RBF NN is constructed. There is no guarantee that this method produces the smallest RBF NN for a given quality of approximation ([5]). Encouraged by preliminary results [3] we decided to use the MDL method which seems to produce smaller networks and preserve approximation quality.

The mMDL method ([3]) involves two procedures: adaptation (training) and selection. The adaptation procedure changes the locations and widths of the RB-function centers and adjusts the weights. The selection procedure, according to the Minimum Description Length (MDL) principle, selects those RB-functions from the set of all RB-functions, that describe the training data with the shortest possible encoding. In other words, if there are more RB-functions that cover the same space, those RB-functions should be selected that describe a larger portion of the data and which contribute less to the overall error of the network. More specifically, at the beginning all samples from the training set are used

Oper.	ERPs	<i>RBF NNs + OLS</i>				<i>RBF NNs + mMDL</i>			
		NC		Test set NMSE		NC		Test set NMSE	
		mean	(std)	mean	(std)	mean	(std)	mean	(std)
A	891	387	(56)	0.163	(0.030)	61	(3)	0.306	(0.081)
B	592	171	(42)	0.119	(0.028)	74	(1)	0.139	(0.040)
C	417	175	(26)	0.231	(0.050)	44	(3)	0.316	(0.094)
D	734	249	(109)	0.080	(0.020)	82	(7)	0.107	(0.030)
E	776	249	(60)	0.175	(0.025)	76	(4)	0.240	(0.059)

Table 1: The comparison of the approximation errors (NMSE) achieved at the test set and the number of hidden units (NC) between RBF NNs using OLS and mMDL methods. The values represent an average of 10 simulations with standard deviation in parentheses.

as centers for the RB-functions. Such a network behaves like a look up table. In order to achieve the generalization it is allowed the network to adapt. Since the consequence of this adaptation is usually the overlap among the RB-functions, it is necessary to eliminate redundant ones from the whole set, which is done by the selection procedure. These two procedures are repeated until no more RB-functions are removed as redundant ones.

5 Results

Both models of RBF NNs were validated using 10-fold cross validation ([4]). The simulations (using the mMDL method) were implemented in Matlab using the package of routines provided by H. Bishof. The quality of approximation was measured in terms of number of centers (NC) of RB-functions and normalized mean square error (NMSE) defined as

$$NMSE = \frac{\sum_{p=1}^P (t^p - \mathcal{F}(\mathbf{x}^p))^2}{\sum_{p=1}^P (t^p - \bar{t}^p)^2} \quad \text{where} \quad \bar{t}^p = \frac{1}{P} \sum_{p=1}^P t^p \quad (3)$$

and P is the number of ERPs (gathered for one operator), t^p is the target output value and $\mathcal{F}(\mathbf{x}^p)$ is the output value of the network for the p -th input vector from the training set.

First, let us look at the number of hidden units (NC) of the RBF NN models which were constructed by both methods. As we can see in the Table 1 better results are achieved using the mMDL method (NC is on average 3.8 times lower than NC achieved using the OLS method). Across operators the average NC for the RBF networks + mMDL is 67 which is less than 246 for the RBF NNs + OLS. Also the standard deviation for the RBF NNs + mMDL method (on average 5.4% from the NC) is less than for the RBF NNs + OLS method (on average 24.4% from the NC).

Now, let us look at the quality of approximation in terms of NMSE. NMSE achieved at the test set with the RBF NNs + OLS is lower than with the RBF NNs + mMDL (on average 1.424 times). Across operators the average NMSE for the RBF NNs + OLS is 0.1536 and for the RBF NNs + mMDL is 0.2216. And also the standard deviation for the RBF NNs + OLS (on average 20.6% from MNSE) is lower than for the RBF NNs + mMDL (on average 27.5% from NMSE).

From the comparison above we can conclude that using the mMDL method it is possible to construct the RBF NN with lower number of hidden units but at the expenses of a little worse quality of approximation as with the OLS method.

6 Conclusions

In this paper we have compared the RBF NNs models for estimating human signal detection performance. The results achieved using the mMDL methods were better as ones using the OLS method with respect to NC.

Our preliminary simulations show that for achieving better results in terms of NMSE it would be desirable to use more powerful training algorithm (e.g. Levenberg-Marquardt algorithm) in the adaptation procedure of the mMDL method as the backpropagation (BP) with momentum and adaptable learning rate. The BP algorithm was used because of the computer capacity limitations.

When we look more closely at the NC achieved with the RBF NNs based on the mMDL method they seems to be comparable for all operators. This fact indicates the existence of general model for estimating performance of human operator. It would then remain only to adjust this model for individual operator. However verification of this hypothesis would require more data (not only from 5 operators).

Acknowledgments: M.K. was partially supported by Slovak Grant Agency for Science (grants No.2/5088/98 and No. 98/5305/468). We thank the Director of Training Dept. at the Navy Personnel Research and Development Centre, San Diego for providing us with data. We also thank H. Bishof for providing a Matlab source for mMDL method. We thank Dr. L. Beňušková for useful comments on the manuscript.

References

- [1] S. Chen, C.F. Cowan, and P.M. Grant. "Orthogonal Least Squares Learning Algorithm for Radial Basis Function Networks," *IEEE Transactions on Neural Networks*, Vol. 2, No. 2, pp. 302-309, 1991.
- [2] M. Koska, R. Rosipal, A. König, L.J. Trejo. "Estimation of Human Signal Detection Performance from Event-related Potentials Using Feed-forward Neural Network Model," *CMP'96*, 1996, Praha, Czech republic, pp. 271-281.
- [3] A. Leonardis, H. Bishof. "Complexity Optimization of Adaptive RBF Networks," *Proceedings of 13th International Conference of Pattern Recognition*, 1996, pp. 645-658.
- [4] M. Rohál'ová. *Návrh modelu výkonnosti operátora pomocou modifikovanej MDL metódy*, Master Thesis, Comenius University, 1998.
- [5] A. Shertinsky, R.W. Picard. "On the Efficiency of the Orthogonal Least Squares Training Method for Radial Basis Function Networks," *IEEE Transactions on Neural Networks*, Vol. 7, No. 1, pp. 195-200, 1996.
- [6] L.J. Trejo, A.F. Kramer, J.A. Arnold. "Event-related Potentials as Indices of Display-monitoring Performance," *Biological Psychology*, Vol. 40, pp. 33-71, 1995.

Switched Capacitor-Based Learning Synapse For Integrate-And-Fire Neural Networks

Daniel Hajtáš, Daniela Ďuračková and Fedor Mika

*Department of Microelectronics
Slovak University of Technology
Ilkovičova 3, 812 19 Bratislava, Slovakia
hajtas@elf.stuba.sk*

Abstract This paper is dealing with an analog implementation of a learning synapse, which is a vital part of a neural network. The proposed synapse includes a postsynaptical potential forming block which makes it possible to uniquely characterise each synapse output in a complete neural network. This approach is conceptually closer to its biological counterpart. The design uses switched capacitor technique in order to minimise the design area to make the above described modification realisable.

1 Introduction

In many neural network applications an implementation of a learning synapse is required. Such synapses provide interconnections of all neurons in the network. In order to create the matrix of synapses, following synapse parameters should be taken in account: time constant of exponential decrease of postsynaptical potential (PSP), learning rate for up and down learning and external threshold NMDA potential. It is important for each synapse to have a specific output signal characteristic (time constant of PSP discharge is assumed in our case) [1]. Therefore, it is not possible to use a circuit with *soma potential capacitor* (SPC) at the input of the neuron and charge it only by a current pulse from the output of a synapse, as it was proposed in [2]. Rather some mechanism for controlling of the synapse output characteristic has to be introduced.

In this paper, a design of SPC based circuit for realisation of learning synapse is presented. In order to achieve an efficient implementation of the synapse from the area point of view switched capacitor technique was employed for the design. Moreover, in SC circuit the unique output characteristic of each synapse can be easily tuned by capacitance ratio. Finally, the synapse output characteristic (i.e. the time constant of SPC defined in a number of clock cycles) does not depend on the clock signal frequency that offers the possibility to use this solution in a wide frequency range.

2 SC Synapse Realisation

The goal of a synapse in a neural network is to provide a transformation of a neuron output signal. The possible transformations include voltage to current conversion, pulse shaping and signal weighting. The general scheme of a learning synapse is depicted in Fig. 1. The functionality of the building blocks can be described as follows:

- A circuit for shaping the postsynaptic potential (PSP), which causes exponential decay of the PSP upon the arrival of signal ACTIVITY from transmitting neuron.
- A voltage adder, producing a new initial voltage, up to which SPC must be charged
- A weight adjustment circuit, causing changes of the weight stored on the memory capacitor
- A weight refresh circuit dynamically refreshing the weight value on the memory capacitor
- A V/I converter converting the PSP to output current from the synapse

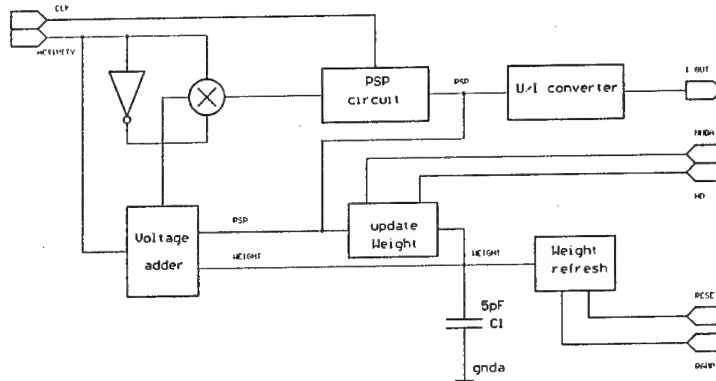


Fig. 1 Block diagram of learning synapse

Learning is based on Hebb's learning rule where the value and direction of weight changes is directly proportional to time between the transmitting and the receiving neuron activity.

2.1 Circuit for exponential decay of PSP

The proposed PSP circuit employs two capacitors and two switches controlled by main clock signal with complementary phases, as shown in Fig. 2. Total time constant of the circuit is given by $C1/C2$ ratio and clock signal frequency (where $C1$ and $C2$ represents SPC and an auxiliary capacitor, respectively). The whole circuit acts in fact as a classical RC low-pass filter. The SPC could be charged by a current source.

However, due to a small capacitance value of SPC very low currents have to be used to charge it what makes the design difficult. Alternatively, a voltage source can be used to charge SPC as well. Nevertheless, the value of new voltage across SPC has to be provided by summing of weight value and old voltage across SPC. This sum is calculated in the voltage adder block described in the next section.

Voltage adder

This circuit is controlled directly by Activity signal from the transmitting neuron. Thus the new voltage for charging SPC is available only during the active state of this signal. The scheme of the voltage adder block is shown in Fig. 3.

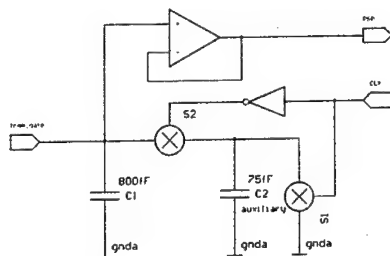


Fig. 2 PSP circuit as SC equivalent of RC LPF

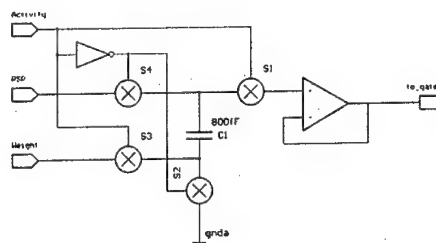


Fig. 3: SC Voltage adder block

Weight adjustment circuit

In the simplest case the designed synapse contains a dynamic up and down learning circuit (down learning is also called forgetting), where the value of the weight is adjusted (see Fig. 4). The change itself depends on instantaneous PSP value in time of Activity of receiving neuron signal (Hd), constant α given during by ratio of weight memory capacitor and auxiliary capacitor C_1 and NMDA value determining the learning direction over the time.

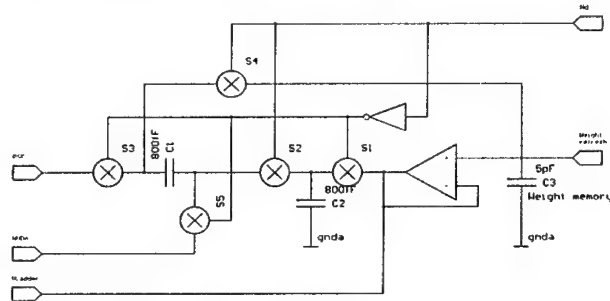


Fig. 4: Weight adjustment block

Weight refresh

The weight memory capacitor is self-discharging by surface currents caused by various side effects like SiO_2 impurities etc. Due to that the value stored in weight memory capacitor has to be regularly refreshed. The designed circuit was derived from the refresh scheme proposed in [3] only a simple sawtooth signal can be used in our case. The dynamic range of the stored weight memory value is divided into 255 intervals which is equivalent to the 8 bit weight. The whole block is controlled by Reset, Reset2 and Ramp signals. The Reset and Reset2 are derived from main clock signal (with $\text{Treset} = \text{Tclk}$, $\text{Treset2} = 256 \cdot \text{Treset}$). The Ramp signal has a period equal to the Treset2 and its value corresponding to the dynamic range of the stored memory value.

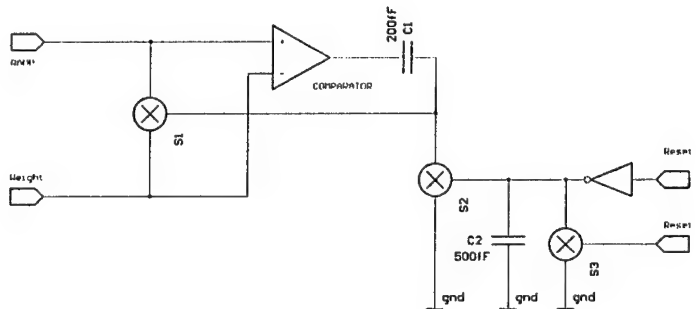


Fig. 5: Weight refresh block

3 Experimental Results

The circuit was designed in CADENCE DF II ver 4.4.1 in MIETEC $2.4\mu\text{m}$ technology. Results were obtained by means of CADENCE Analog Artist and Hspice ver. 8.2 simulators. In Fig.6 the simulations of PSP block, Weight update block and Voltage adder block which are essential for the functionality of the synapse. The Fig. 6(a) shows the exponential decline of the

postsynaptic potential with respect to the Activity input and the proper functioning of the voltage adder block afterwards. The process of weight update with respect to the transmitting and receiving neuron activities and PSP value is depicted in Fig. 6(b).

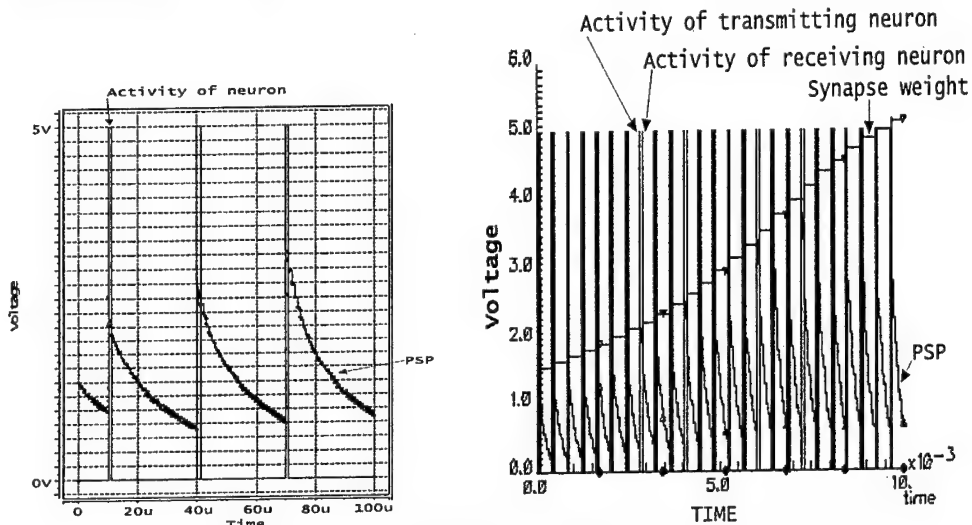


Fig. 6: a) Simulation of PSP and voltage adder circuit, b) Simulation of learning circuit

4 Conclusion

In this paper an analogue design of the complete learning synapse except V/I conversion block is presented. The total design area was $260 \times 110 \mu\text{m}^2$. The synapse was realised using switched capacitor technique which has a deep impact on the design. For example the realised SPC using the above mentioned technique has a value of 800 fF (compared to 20pF in non-SC design) what makes it feasible to include a postsynaptic potential block in each synapse. Therefore, it is possible to define unique output characteristic (time constant) for each synapse which is closer to a biological neural network.

Acknowledgement

This work was supported by the Ministry of Education of the Slovak Republic under Grant No: 1 / 6096 / 99 and No: 1 / 4294 / 97

References

- [1] Thomas Zahn, Richard Izak, Karsten Trott – Mixed analog-digital neurochip for acoustical attention. European workshop on neuromorphic systems, Stirling U.K., 1997
- [2] Mark A. Glover, Alister Hamilton, Leslie S. Smith – Analogue VLSI Integrate and Fire Neural Network for Clustering Onset and Offset Signals in Sound Segmentation System
- [3] E. Vittoz, H. Oguey, M. A. Maher, O. Nys, E. Dijkstra, M. Chevroulet – Analog storage of adjustable synaptic weights. In *VLSI Design of Neural Networks*, pages 47 – 63, Kluwer Acad. Publ. 1991

A 32-bit RISC Microprocessor with DSP Functionality

Byung In Moon¹, Dong Ryul Ryu¹, Jong Wook Hong¹,
Sangook Moon¹, Yong Hwan Lee², and Yong Surk Lee¹

¹ Dept. of Electronic Engineering, Yonsei University, Seoul, Korea

² Memory Design Team #2, LG Semicon, Seoul, Korea

E-mail contact: blue@dubiki.yonsei.ac.kr

Abstract. We have designed a 32-b RISC microprocessor with 16-/32-b fixed-point DSP functionality. This processor, called YD-RISC, has functional units for arithmetic operation, DSP and memory accesses. They operate in parallel in order to remove stall cycles after DSP or load/store instructions with one or more latency cycles. High performance is achieved with the parallel functional units while adopting a sophisticated five-stage pipeline structure. The DSP unit can execute one 32-b multiply-accumulate or 16-b complex multiply instruction every one or two cycles through two 17-b \times 17-b multipliers and operand examination logic circuits. Power-saving circuits allow low power consumption.

I. Introduction

Embedded microcontrollers are used to execute general-purpose programs [1], [2]. DSPs are used for specialized applications such as image and voice processing [3]. Recently low-cost embedded processors with both microcontroller and DSP functionality have become necessary in the advanced consumer electronics applications. Simply combining both functions using two separate cores in a single chip is not cost-effective and not appropriate for embedded systems considering the low-cost need in consumer electronics [4]. Therefore, we designed a processor that combines both microcontroller and DSP functions into one processor without doubling resources, while providing the main features of RISC architectures for flexibility in programming, also achieving high DSP performance.

Design methodology, which is mainly classified into full-custom design and logic synthesis using gate-level cell libraries, is a very important point for successful processor designs. The full-custom method is suitable for high performance, small area and low power consumption, but it is time-consuming and labor-intensive. The method through synthesis is time and labor-saving, thus making short time-to-market possible which is an important requirement for successful marketing. Moreover, synthesis makes it easy to improve designs, because updating designs is simply re-synthesizing using improved libraries and process technology. We designed the YD-RISC through logic synthesis and automatic place-and-route and achieved a high clock frequency by refining the architecture with the five-stage pipeline.

II. Design Points

In the design of the YD-RISC, various new concepts are used to optimize performance, area and power consumption. These concepts are described in detail below.

A. Pipeline and Parallelism

Instructions are divided into ALU, DSP and load/store instructions. As shown in Fig. 1, the ALU pipeline consists of five stages in accordance with the basic RISC pipeline structure, and DSP and load/store pipelines have separate and parallel execution stages independent of ALU execution and write-back stages. This enables the instructions to be executed continuously after the DSP or load/store instructions with one or more latency cycles regardless of the completion of these instructions as shown in Fig. 2, thus improving performance dramatically.

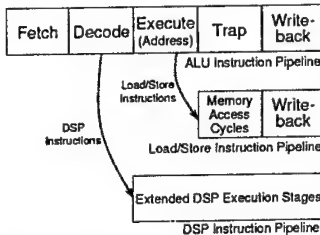


Fig. 1. Basic pipeline structure.

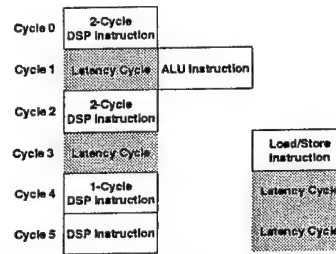


Fig. 2. Parallelism between functional units.

B. DSP Unit

The DSP unit can do both $16\text{-b} \times 16\text{-b}$ and $32\text{-b} \times 32\text{-b}$ multiplications. A $32\text{-b} \times 32\text{-b}$ multiplier occupies too large area and can perform only one 16-bit multiplication at one time. In contrast, two $16\text{-b} \times 16\text{-b}$ multipliers occupy about half the area of one $32\text{-b} \times 32\text{-b}$ multiplier and can perform two $16\text{-b} \times 16\text{-b}$ multiplications simultaneously. The DSP unit of the YD-RISC can execute two independent $16\text{-b} \times 16\text{-b}$ multiplications in one cycle and one $32\text{-b} \times 32\text{-b}$ multiplication in two cycles using the two $17\text{-b} \times 17\text{-b}$ multipliers. In addition, the number of cycles in $32\text{-b} \times 32\text{-b}$ multiplication is further reduced to only one through the operand examination scheme as shown in Tab. I.

Tab. I. Operand examination scheme for 1-cycle 32-bit multiplication

Operation	Operand condition for 1-cycle 32-bit multiplication
32-bit signed multiply	Operand[31:16] is equal to $0000_{(16)}$ or $FFFF_{(16)}$ or Operand[15:0] is equal to $0000_{(16)}$.
32-bit unsigned multiply	Operand[31:16] is equal to $0000_{(16)}$ or Operand[15:0] is equal to $0000_{(16)}$.

Tab. II. Average instruction length

Program	No. of executed instructions	Average instr. length
hello	1096	24.44
hanoi4	3021	25.41
bsort10	28160	26.64
ssort10	20455	23.27
qsort10	15425	24.35
siv1024	22044	21.84
dct22f	173583	21.20
fft8f	15389	21.41
dct22d	2381	22.28
fft8d	508965	22.98
fir	40653	24.74
iir	49362	22.37

C. Instruction Prefetch

This architecture has no instruction or data cache, and thus can be vulnerable to execution stall due to long memory access time and insufficient instruction availability. In order to overcome this drawback, the processor adopts an internal 4-Kbyte SRAM and a prefetch buffer, which is implemented as a circular buffer with a head pointer and a tail pointer. The loop control of the prefetch buffer reduces the bus utilization of this processor, and thus improves performance when the program consists of small loops to be processed repeatedly. Moreover, this architecture adopts a variable-length instruction format of 16 bits, 32 bits, or 48 bits, which reduces the average instruction length below 25 bits in most programs as shown in Tab. II. Improved code density due to this variable-length instruction format not only saves memories, but also improves instruction supply and performance. Also, bus arbitration between instruction memory access and data memory access is optimized using the results through various simulations.

D. Power Consumption

Low power nature is essential in embedded processors. In power-down mode provided in our processor, only the clocks for the logic related to the refresh, interrupt, timer and reset are enabled, while all other clocks are disabled, using the circuit shown in Fig. 3. Also, power consumption by unnecessary switching in execution blocks is avoided through the circuit in Fig. 4, which permits only enabled execution blocks to receive new input operands. Power consumption is noticeably reduced by these power-saving techniques.

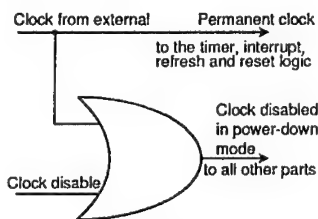


Fig. 3. Clock disable circuit.

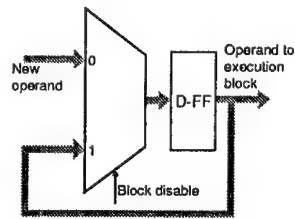


Fig. 4. Execution block disable.

III. Implementation and Performance

The block diagram in Fig. 5 shows the main architecture of the entire microprocessor. The logical model of this processor is described by using an industry-standard HDL and is verified with a HDL software simulator. The register file, prefetch buffer and internal SRAM are designed with established macro cell libraries, while the others are logic-synthesized with gate-level cell libraries. The layout of the processor is shown in Fig. 6 and measures about $8\text{mm} \times 8\text{mm}$. The processor designed in 3.3V 0.6- μm triple metal technology shows the clock frequency of 50 MHz. This frequency is high considering that the frequency of LG Semicon's custom-designed GMS30C32132 adopting the similar architecture and the same technology is 30MHz [5]. Moreover, the frequency of this processor can be almost doubled by redesign using current available 0.35- μm technology. The YD-RISC shows slightly better performance than GMS30C32132 in integer applications and twice as high performance as GMS30C32132 in DSP applications. Table III shows the complex FFT performance comparison of the YD-RISC with different DSP processors, assuming that the performance of the YD-RISC is one.

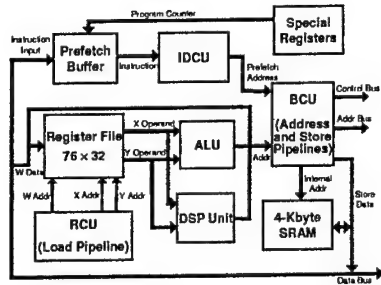


Fig. 5. Architecture of the YD-RISC.

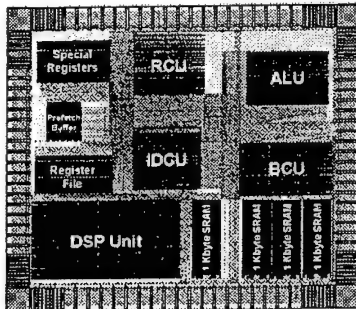


Fig. 6. Layout of the YD-RISC.

Tab. III. 1K 16-bit complex FFT performance comparison of the YD-RISC with different processors

DSP processor	Relative performance
YD-RISC	1.00
LGS GMS30C32132	0.54
TI TMS320C50	0.31
ADSP 2175	0.68
Motorola 56002	0.78
AT&T DSP1617	0.30
NEC uP77016	0.74

IV. Conclusions

In this microprocessor, RISC and DSP functionality are combined cost-effectively, while high performance is achieved. Excellent performance on 32-b \times 32-b multiplication and simultaneous 16-b \times 16-b multiplications is achieved through two 17-b \times 17-b multipliers and operand examination logic circuits. Power-down mode and disabling execution blocks reduce the power consumption. By designing with logic synthesis and established libraries, we reduced design time as well as achieved a high clock frequency by refining the processor architecture.

References

- [1] Manolis G. H. Katevenis, *Reduced Instruction Set Computer Architectures for VLSI*, MIT Press, 1985.
- [2] David A. Patterson, "Reduced Instruction Set Computers," *Commun. ACM*, Vol. 28, No.1, pp. 8-21, 1985.
- [3] Richard J. Higgins, *Digital Signal Processing in VLSI*, Prentice-Hall, 1990.
- [4] M. Dolle, S. Jhand, W. Lehner, O. Müller, and M. Schlett, "A 32-b RISC/DSP Microprocessor with Reduced Complexity," *IEEE Journal of Solid-State Circuits*, Vol. 30, No. 7, pp. 1056-1066, 1997.
- [5] *GMS30C32132, GMS30C32116 User's Manual*, MCU Application Team in LG Semicon Co., Ltd., 1996.

A Better Hearing for Cochlear Implant Subjects with an Improved CIS-Like Speech-Coding Strategy

M. Polák and O. Ondráček

*Department of Radioelectronics, Slovak Technical University,
Ilkovičova 3, 812 19 Bratislava, marek.polak@elf.stuba.sk*

Abstract. Coding CIS-like strategies for cochlear implants are discussed with respect to their ability to extract a speech signal envelope. This paper describes the new approach of the new HT CIS speech-coding strategy to obtain envelope of the speech signal by using Hilbert transformer.

I. Introduction

Cochlear prostheses are used for patients who have a mechanical defect in the inner ear. Although their nervous system may be completely intact, if the hair cells cannot be stimulated, acoustic sensation cannot be obtained. In such cases electrical stimulation can be used to overcome the defect of mechanical transmission.

Nowadays, the most commercially used speech-coding strategies for cochlear implant users are CIS strategies [2]. One of the main task of CIS strategy is to divide an input signal into a few frequency bands with the aim to obtain the signal envelope and to generate non-simultaneous biphasic current stimulation pulses. This signal envelope is usually captured by using a full wave rectifier and low pass filtering or by using a half wave rectifier. These solutions bring some distortions. However, the half wave rectifier in the lowest frequency bands preserves better temporal information. Due to frequency doubling by means of the full wave rectifier the temporal information may be lost. The recent results, e.g. [1], showed that the firing possibility of nerve fibres with high characteristic frequency is correlated with the envelope of the amplitude modulated (AM) stimulus. Joris and Yin also showed that the phase of low frequency AM signals clearly is present in the nerve fiber activity. The effect is referred to as 'phase locking'.

These problems may be solved by using Hilbert transformer in the new HT CIS speech-coding strategy so that we can capture an envelope with a minimal distortion.

II. Design of Hilbert transformer

Let us imagine a complex linear filter $H(e^{j\theta})$ with the frequency response

$$H(e^{j\theta}) = \begin{cases} 2 & 0 < \theta < \pi \\ 0 & -\pi < \theta < 0 \end{cases} \quad (1)$$

to obtain an output signal, for which spectrum vanishes for negative frequencies. Provided $x[n]$ is a real input sequence, the complex output sequence $y[n]$ of such a filter is

$$y[n] = x[n] \otimes h[n] = x[n] + j(x[n] \otimes h_i[n]) \quad (2)$$

where $h_i[n]$ is the imaginary part of the impulse response $h[n]$, as given by

$$h_i[n] = \begin{cases} \frac{2}{n\pi} & \text{for } n \text{ odd} \\ 0 & \text{for } n \text{ even} \end{cases} \quad (3)$$

It can be seen from (3) that the real part of the complex sequence $y[n]$ is just the original sequence $x[n]$ and the imaginary part of $y[n]$ is obtained by passing $x[n]$ through a linear filter with the impulse response stated in (3). The filter of equation (3) is called the ideal discrete time *Hilbert transformer*. The frequency response of the ideal discrete-time Hilbert transformer is

$$\mathcal{F}\{h_i[n]\} = \begin{cases} -j & 0 < \theta < \pi \\ j & -\pi < \theta < 0 \end{cases} \quad (4)$$

As in the continuous time case, the discrete time Hilbert transformer can be regarded as an allpass filter providing a phase shift of $\pi/2$ radians at all frequencies.

Assuming that an AM-input signal $x[n] = 2e[n]\cos\theta_0 n$, where θ_0 is a carrier frequency of the input signal and $2e[n]$ is the input-signal envelope. If the frequency response of the input signal can be written as $X(e^{j\theta}) = E(e^{j(\theta-\theta_0)}) + E(e^{j(\theta+\theta_0)})$, the analytic signal $y[n]$ can be written as

$$y[n] = \frac{1}{\pi} \int_0^\pi E(e^{j(\theta-\theta_0)}) e^{j\theta n} d\theta = 2e[n]e^{j\theta_0 n} = 2e[n]\cos\theta_0 n + j2e[n]\sin\theta_0 n \quad (5)$$

From (5) we can see that if the input signal $x[n]$ is real valued, the output sequence $y[n]$ has an equal envelope when compared to the input sequence $x[n]$.

III. FIR Linear-Phase Design

Specifically, suppose we shift the frequency response $H_i(e^{j\theta})$ of equation (4) by $\pi/2$ radians to obtain a new filter $G(e^{j\theta})$ with its frequency response

$$G(e^{j\theta}) = H_i(e^{j(\theta+\pi/2)}) = \begin{cases} -j & |\theta| < \pi/2 \\ j & \pi/2 \leq |\theta| < \pi \end{cases} \quad (6)$$

Note that this is simply the ideal half-band lowpass filter with passband magnitude scaled to the value 1. A complex half-band filter $H(e^{j\theta})$ can be realised by using a Hilbert transform as the imaginary part of a complex filter. Supposing that the order of the filter $G(e^{j\theta})$ is $2N$, where

N is odd. Furthermore, for impulse response $g[2N - n] = g[n]$ and every odd sample of $g[n]$ is set to zero. Consequently, by "decimation" of the filter $G(e^{j\omega})$ we may get the filter $E(e^{j2\omega})$

$$E(e^{j2\omega}) = G(e^{j\omega}). \quad (7)$$

The frequency response of the complex filter $H(e^{j\omega})$ may be written as follows

$$H(e^{j\omega}) = e^{-jN\omega} (1 + jH_i(\omega)) = e^{-jN\omega} (1 + jG(\omega - \frac{\pi}{2})) = e^{-jN\omega} (1 + jE(2(\omega - \frac{\pi}{2}))) \quad (8)$$

where $H_i(\omega)$, $G(\omega)$ and $E(\omega)$ are zero-phase responses of the mentioned filters. The term $E(2(\omega - \pi/2))$ describes a linear-phase filter with a group delay of N samples. The linear-phase FIR filter with an N -degree zero-phase response $E(\omega)$ and N odd and with a symmetrical impulse response, can be designed, e.g., by using the program of McClellan et al.

By using the starter-kit with a fixed-point 16-bit ADSP 2181 signal processor the envelope detection has been implemented to the CIS speech-coding strategy. All the software has been programmed in the assembler for ADSP-2100 family.

The sampling frequency is set to 16 kHz. The utilized stereo codec AD 1847 has linear-coded 16 bit A/D converter and on-chip antialiasing filter. The dynamic range of the A/D converter is 84 dB so it is not necessary to compress an input signal. After the signal is sampled the preemphasic filter is used. It is an FIR filter of the 6th order designed by rectangular-window method. Digital Gain Control (DGC) is used as a limiter to overcome the distortion or loud perception caused by very loud signals. When the input signal reaches very high value (usually the highest decibel level of used dynamic range), the output signal will be decreased by rate of programmable time constant and afterwards when the input decreases below a certain value (usually -3 dB from the maximum reachable value of the input), the output signal will be slowly increased. The attack and release time constants may be changed programmable. The signal is split into the 8 band-pass filters in the frequency range from 300 to 5500 Hz logarithmically. It is very important how the filter bank is designed. The frequency of the input signal can be assigned by means of a proper steepness of the filters. Theoretically, the steepness of the filters should not be higher than the steepness acquired from measurements of the masking effect on normally hearing subjects, e.g. [3]. Using the sensitivity control circuit we may adjust a gain for each channel separately. The following stage - rectifier is different for each designed strategy.

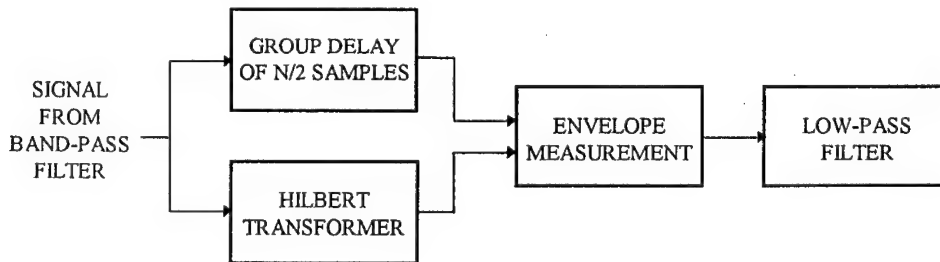


Fig. 1 A block diagram of the envelope detection for the programmed HT CIS speech-coding strategy

Figure 1 depicts a block diagram of the envelope detection for the proposed HT CIS speech-coding strategy. The output of the band-pass filter is split into two lines. In the first line the signal is delayed by $N/2$ samples where $N = 98$ is the order of the designed Hilbert transformer. In the second one the signal is filtered by the Hilbert transformer. The Hilbert transformer was designed for the frequency range from 20 to 6500 Hz. Furthermore, the values in both lines are squared, summed and evolved. After the exact envelope is detected, the signal is low-pass filtered with the cut-off frequency of 370 Hz. Especially, because of the 8 kHz sampling frequency for the first four channels in the HT CIS strategy a different low-pass filter had to be designed for these channels. The low-pass filters are FIR filters of 61 and 100 coefficients, respectively. The low-pass filter is at the output of the envelope detection not due to the distortion as it was when using a FWR, but only for the necessity the exact perception of modulation signal to have at least four stimuli samples per one period of modulation signal. Moreover, a loudness transformation compresses the signal into the range of current stimulation. Finally, after the loudness transformation is performed, a volume control and subjective adjustment is made use of. Volume control may change the volume in percentile range from 0 to 100% in two modes, RTI and IBK. The subjective adjustment is set for each channel separately and transforms the output signal into the dynamic range given by the electrically evoked hearing threshold T and the most comfortable level C .

IV. Discussion

Using Hilbert transformer to extract an envelope signal, the input pure tone is transformed into the direct signal with the amplitude proportional to the amplitude of the input signal. The input AM signal is transformed into the modulation signal so that at the output there are only the information or most of them that are important for stimulation of the auditory nerve fibers [1].

However, using the AM signal with carrier frequency lower than modulation frequency multiplied by 1.8, the output signal is different from those that are achieved with the half-wave rectifier especially for the two lowest channels. The differences among voiced phones are higher than by using the half-wave rectifier or "conventional" full-wave rectifier with 400Hz-smoothing low-pass filter so that the wider dynamic range of audible frequencies for an active channel is used. For this reason the voiced phones may be better understood by using the HT CIS strategy than the PL CIS and CIS strategy.

At the department ORL, University Faculty Hospital in Bratislava the new speech-coding method for cochlear implant subjects is under investigation and has been successfully used on three postlingually deaf subjects with cochlear implant Combi 40. More information may be seen in [2].

This work was supported by the Ministry of Education of the Slovak Republic under Grant VP 1/9097/99.

References

- [1] Joris, Ph., Yin, T.C.T.: Response to Amplitude-Modulated Tones in the Auditory Nerve of the Cat. *J Acoustic Soc Am*, Vol. 91, pp. 215-232, 1992.
- [2] Polák, M.: The New Method of Speech Signal Processing for Cochlear Implants. PhD. Thesis, Slovak Technical University, Bratislava, 1999.
- [3] Polák, M., Ondráček, O.: The Speech Processing for Cochlear Implants. *Proceedings Radioelectronics '97*, Brno, pp. 204-208, 1998.
- [4] Moore, B.C.J.: *An Introduction to the Psychology of Hearing*. St Edmundsbury Press Limited, Great Britain, 1994.

A Signal Processing Algorithm of the Digital Filter for the Improvement of the Signal to Noise Ratio of Magnetic Anomaly Detection System

Won-Ho Kim¹, Ki-Hong Song², Jong-Sik Park³

¹*Dept. of Electronics Engineering, Dongeui Institute of Technology, Korea
whkim@dit.ac.kr*

²*Dept. of Electronic Communications, Dongeui Institute of Technology, Korea*

³*Dept. of Electronics and Electrical Engineering, KyungPook Nat'l Univ., Korea*

Abstract. In this paper, we developed a signal processing algorithm of digital filter to improve the signal to noise ratio in magnetic anomaly detection system. Using this filter, we can remove the coherent noises in the time domain and improve the signal to noise ratio of the magnetic anomaly detecting system. We show the ability of the geological magnetic filter under various circumstances through computer simulations. Numerical simulation results show that proposed digital filter can excellently remove the sensor misalignment effects and the regular short range local noise as well as it delete the coherent noises.

I. Introduction

Magnetic anomaly detection system detects the change of the short range magnetic fields generated by magnetic materials and identifies the existence of magnetic anomalies. The detecting ability of magnetic anomaly detection system is mainly determined by the sensitivity of the magnetic sensor. Recently, the development of the high TC superconductor enables the implementation of very sensitive magnetic detection system at the fair expense. With the increase of the sensitivity of the magnetic detection system, the DSP algorithms to increase the signal to noise ratio become more important. Fowler[1] suggested that the change of measured magnetic fields at different locations can be modeled as a filter and concluded that the coherent magnetic filed noises are dominant over the incoherent terms based on the experimental results.

In this paper, we developed digital signal processing algorithms of the digital filter to improve the signal to noise ratio of the magnetic detection system using the spatial coherency of the magnetic noises. In the proposed algorithm, two sensors, detector sensor and reference sensor located at a distance, measure the magnetic fields concurrently at the absence of the magnetic sources. After that, the correlations between the two fields are calculated in the frequency domain and the digital filter coefficients are calculated. The coefficients reflect the environments where the sensors are located. From the coefficients in the frequency domain, the FIR filter coefficients are calculated. Using this digital filter, we can remove the coherent magnetic noises

II. Geological Magnetic Filter Theory.

Magnetic fields are generated by the magnetic moments which are originally due to the movements of the charged particles. The intensity of the magnetic fields drops rapidly as the distance from the source increase. We can separate the measured magnetic fields into two components, long range field and the short range field according to the distance from the magnetic source. If the distance between the detector and reference sensor is very short compared with the distance from the source, the difference of the measured magnetic fields between the two sensors is very small. But if the distance from the source is comparable to the sensor separations, the difference of the measured field is very large. The change of the measured long range magnetic fields between the detector and reference sensor is influenced by the environments where the sensors are located. The influence of the magnetic environments on the micropulsation fields can be modeled as follows. We can model the magnetic environments where the reference sensor is located as a linear filter[2]. The input of the filter is the micropulsation field with the orthogonal independent components, B_x^s and B_y^s . The characteristics of the filter is determined by the environments. The output of the filter is the reflected wave (B_x^r, B_y^r, B_z^r). And the measured micropulsation fields can be expressed as a sum of the input and reflected wave.

$$\begin{aligned} B_{R,x}(f) &= B_x^s(f) + B_x^r(f) \\ B_{R,y}(f) &= B_y^s(f) + B_y^r(f) \end{aligned} \quad (1)$$

The measured z direction field is the reflected wave.

$$B_{R,z}(f) = B_z^r(f) \quad (2)$$

From (1) and (2) the relation between the micropulsation input field and the measured magnetic field can be expressed as,

$$\begin{bmatrix} B_{R,x}(f) \\ B_{R,y}(f) \\ B_{R,z}(f) \end{bmatrix} = \begin{bmatrix} A_{11}(f) & A_{12}(f) \\ A_{21}(f) & A_{22}(f) \\ A_{31}(f) & A_{32}(f) \end{bmatrix} \begin{bmatrix} B_x^s(f) \\ B_y^s(f) \end{bmatrix} + \begin{bmatrix} B_x^r(f) \\ B_y^r(f) \\ 0 \end{bmatrix} \quad (3)$$

,where $A_{ij}(f)$ is the filter coefficient. (3) can be simplified as follows.

$$\begin{bmatrix} B_{R,x}(f) \\ B_{R,y}(f) \\ B_{R,z}(f) \end{bmatrix} = \begin{bmatrix} (1 + A_{11}(f)) & A_{12}(f) \\ A_{21}(f) & (1 + A_{22}(f)) \\ A_{31}(f) & A_{32}(f) \end{bmatrix} \begin{bmatrix} B_x^s(f) \\ B_y^s(f) \end{bmatrix} \quad (4)$$

The environments where the detector sensor is located are different from that around the reference sensor and expressed as another filter with different coefficients and the measured magnetic field at that point can be expressed as follows.

$$\begin{bmatrix} B_{D,x}(f) \\ B_{D,y}(f) \\ B_{D,z}(f) \end{bmatrix} = \begin{bmatrix} (1 + B_{11}(f)) & B_{12}(f) \\ B_{21}(f) & (1 + B_{22}(f)) \\ B_{31}(f) & B_{32}(f) \end{bmatrix} \begin{bmatrix} B_{D,x}^s(f) \\ B_{D,y}^s(f) \end{bmatrix} \quad (5)$$

The difference of input micropulsation fields at the two places can be expressed as,

$$\begin{aligned} B_{D,x}^s(f) &= B_x^s(f) + B_{N,x}^s(f) \\ B_{D,y}^s(f) &= B_y^s(f) + B_{N,y}^s(f) \end{aligned} \quad (6)$$

In (6), $B_{N,x}(f)$ and $B_{N,y}(f)$ are noise terms due to the spatial incoherency or gradient of the micropulsation field. Let's define the filter transformation operator C which reflects the difference of the environments around the two sensors.

$$\begin{bmatrix} C_{xx} & C_{xy} & C_{xz} \\ C_{yx} & C_{yy} & C_{yz} \\ C_{zx} & C_{zy} & C_{zz} \end{bmatrix} \begin{bmatrix} (1+A_{11}) & A_{12} \\ A_{21} & (1+A_{22}) \\ A_{31} & A_{32} \end{bmatrix} = \begin{bmatrix} (1+B_{11}) & B_{12} \\ B_{21} & (1+B_{22}) \\ B_{31} & B_{32} \end{bmatrix} \quad (7)$$

Then, we can obtain equation (8).

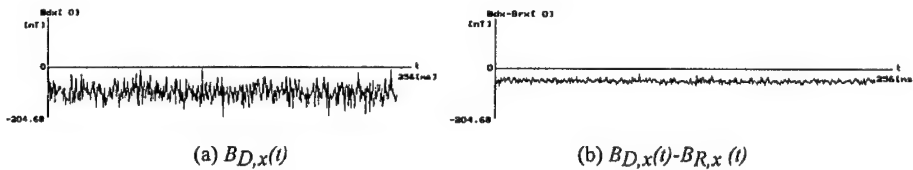
$$\begin{bmatrix} C_{xx} & C_{xy} & C_{xz} \\ C_{yx} & C_{yy} & C_{yz} \\ C_{zx} & C_{zy} & C_{zz} \end{bmatrix} \begin{bmatrix} B_{R,x}(f) \\ B_{R,y}(f) \\ B_{R,z}(f) \end{bmatrix} - \begin{bmatrix} B_{D,x}(f) \\ B_{D,y}(f) \\ B_{D,z}(f) \end{bmatrix} = - \begin{bmatrix} (1+B_{11}(f)) & B_{12}(f) \\ B_{21}(f) & (1+B_{22}(f)) \\ B_{31}(f) & B_{32}(f) \end{bmatrix} \begin{bmatrix} B_{N,x}(f) \\ B_{N,y}(f) \end{bmatrix} \quad (8)$$

In (8), the right terms are due to the incoherency of the source waves. Practically, it can be generated due to the short range magnetic fields which strongly affect only one sensor. In realization of the digital magnetic filter, we obtain the filter coefficients C_{ij} which minimize the magnitude of right term in (8). When the filter coefficients C_{ij} are determined in the frequency domain, we can obtain the FIR filter coefficients in the time domain and the real time digital filter outputs can be calculated in the time domain.

III. Computer Simulation Results

To test the performance of the proposed signal processing algorithm, we simulated the digital filter outputs under various conditions. We can input the magnitude of the earth magnetic field, misalignments of two sensors, coherent and incoherent components of the noise, and the parameters for the construction of the digital filter such as the number of samples per data acquisition window, the number of data acquisition windows, and the number of FIR filter tabs.

We can see from Fig. 1 that proposed the geological magnetic filter compensate mean value of the misalignments of sensor orientation.

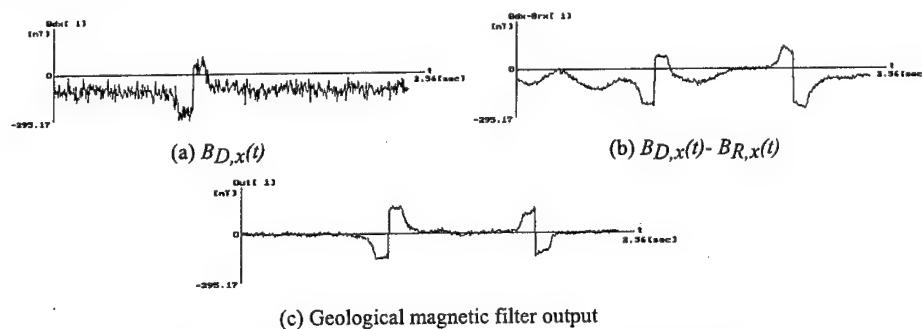




(c) Geological magnetic filter output

Fig.1. Misalignment compensation result using the geological magnetic filter

We performed simulations when the magnetic source appears. It is assumed that the detector, reference sensors and the source are aligned along the x axis. The distance between detector and reference sensors is 10 m. At $t=0$, magnetic sensor is at $x = 10$ m and moves at the constant speed of 10 m/s. Fig. 2 shows the results for $B_{D,x}(t)$, $B_{D,x}(t) - B_{R,x}(t)$ and the geological magnetic filter output. The calculated variance of $B_{D,x}(t) - B_{R,x}(t)$ is 50 nT^2 , nearly three times less than that of the geological magnetic filter output. This is the expected result because we assumed no frequency dependence of the environments around the detector and reference sensors.

**Fig. 2.** Simulation results when magnetic source appears

IV. Conclusion

A signal processing algorithm of the digital filter that can improve the signal to noise ratio of the magnetic detection system has been presented and the numerical simulation results have been shown in this paper. Digital filter is constructed using two 3-axis magnetic sensors, detector sensor and reference sensor. The main object of digital filter proposed is to cancel out the coherent magnetic noises using two sensors. From the simulation results we could also observe that proposed digital filter can effectively remove the sensor misalignment effects and the localized noises due to short range magnetic sources.

References

- [1] B. Fowler, "A Study of the Geomagnetic Micropulsations Using Gradiomagnetic Techniques," Ph. D. dissertation, The University of Texas at Austin, 1973.
- [2] W.H Kim and J.S. Park et.al., "A Theory of the Geological Magnetic Filter for the Improvement of the Signal to Noise Ratio of the Magnetic Detection System," *Journal of the Korean Sensors Society*, Vol.6., Nov. 1997.

Modified 4-IF Downconversion Technique with Flexible IF Settings

R. Paško¹, S. Vernalde², and D. Ďuračková¹

¹Dept. of Microelectronics, STU, Ilkovičova 3, Bratislava, Slovakia,

²IMEC v.z.w., Kapeldreef 75, Leuven, Belgium

Abstract³. In this paper, we present a modified 4-IF all-digital downconversion/decimation technique. The original 4-IF method provides an alternate way to perform downconversion from an intermediate frequency (IF) placed at $f_s/4$ into the baseband by purely digital means. It results in a very simple and power efficient architecture. We show that some flexibility in IF settings can be achieved by a scheme very similar to the 4-IF technique. In this modified 4-IF scheme, the IF is not fixed at $f_s/4$ but rather can be selected from a limited set of possible frequencies. We also show, that this modification causes only a small increase of the design area and estimated power consumption.

I. Introduction

In current telecommunication applications the straight line between the analog and digital circuitry (conventionally implementing IF and baseband parts) does not exist anymore. Rather some combinations of analog and digital implementation with emphasis on a low power consumption are investigated and used. The key is a trade-off between programmability (or flexibility) and performance. In this paper we will discuss a digital scheme for downconversion of a QAM signal from IF to the baseband. A conventional downconversion approach with mixer and sine wave generator is difficult to realize by digital means outside baseband or very low IF since it uses a mixer (multiplier) working on the highest frequency. On the other hand, a digital implementation usually requires the use of decimation in order to obtain a power efficient solution. If this is the case, an alternate approach utilizing properties of decimation can be exploited to accomplish the downconversion simultaneously at practically no costs. The basic idea is indicated in Fig. 1. Both schemes in Fig. 1 are functionally equivalent, only a frequency

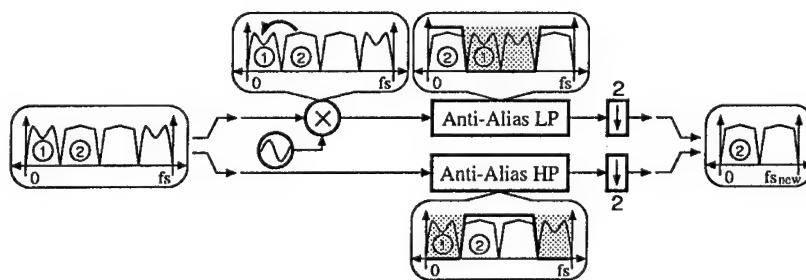


Figure 1: Decimation and downconversion

shift of the signal (i.e. downconversion) in the first case is replaced by a frequency shift of the anti-alias filter (i.e. using HP filter instead of LP prototype). This transformation is well known from the filter bank theory. The whole system as shown in Fig. 1 can be considered to be a part of a filter bank tuned to a selected frequency band. However, compared to the ordinary filter banks, the goal in this case is not to obtain a perfect reconstruction, but rather to downconvert one selected band into the baseband with specified requirements. This often results in a simpler design process and cheaper implementation. The obvious disadvantage of this approach lays in the fact that the actual frequency to downconvert is transformed into the modified filter

³This research was supported by the Copernicus project SISPAS CP94-0223.

coefficients which makes an eventual change of IF more difficult. In this paper, we propose a modified 4-IF downconversion scheme which grants a limited freedom in IF settings at cost of a small hardware overhead. The rest of the paper is divided as follows: in the next section, the 4-IF sampling scheme is described more in detail. In section 3, the downconversion from IF different from $f_s/4$ is discussed followed by the description of the modified 4-IF scheme. The experimental results are given in section 5 and conclusions are drawn in section 6.

II. 4-IF Digital Downconversion

The 4-IF downsampling technique is used for downconversion of a signal centered around $f_s/4$ into the baseband with simultaneous decimation by factor $R = 4$. It takes advantage of the fact, that the mixer values for this IF position can only be 1, -1 and 0 (i.e. the values of $\sin(2\pi n/4)$ and $\cos(2\pi n/4)$). Mixing of the input signal with these numbers combined with polyphase decomposition of the anti-alias filter during downconversion by 4 results in a very efficient hardware implementation since one filter is necessary for both I and Q components as shown in Fig. 2. This idea was first introduced in [1] in a QAM modulator/demodulator design working

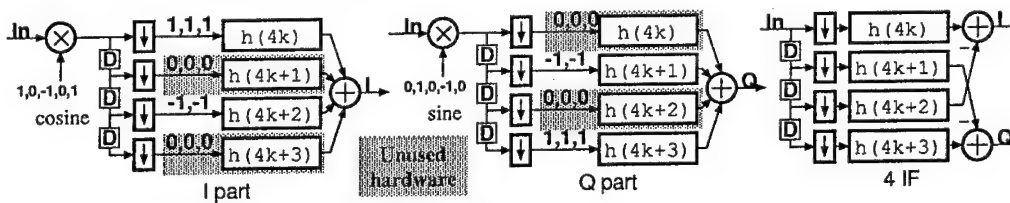


Figure 2: 4-IF sampling method

at high frequency ($f_s = 200\text{MHz}$). It was further extended in [2], where various multistage configurations derived from the basic 4-IF scheme were tested and compared with respect to their area/power figures. For a design of multiple filter stages the *Interpolated FIR Method* was used. As an example a CDMA cellular proposed by Qualcomm (originally an analog circuit) was analyzed. The final 4-IF downconversion scheme from [2] is shown in Fig. 3

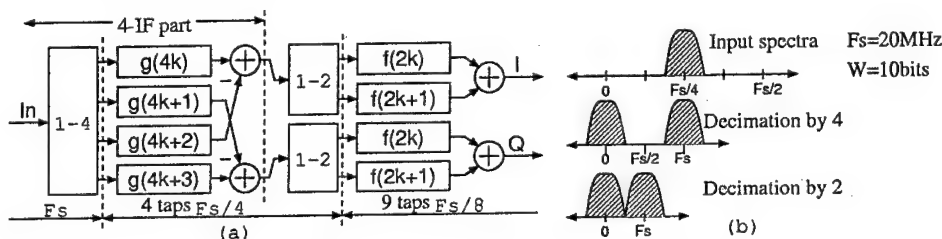


Figure 3: 4-IF downconversion system proposed in [2]

III. Downconversion from arbitrary IF

A possibility to use a frequency shifted anti-alias filter coupled with a decimator as downconverter for IF different from $f_s/4$ was investigated in [3]. This approach was proven to be directly applicable for IF satisfying Eq. 1, where R is the decimation ratio and N is a whole number.

$$IF = f_s N / R \quad (1)$$

In that case there is no need for an additional mixer at any stage during the downconversion, since for these frequencies the IF is translated directly into the baseband. There was further shown in [3], that the frequency shifted anti-alias filter coefficients can be calculated from their LP prototypes by a complex rotation (see Fig. 4).

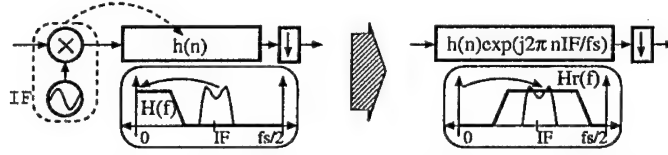
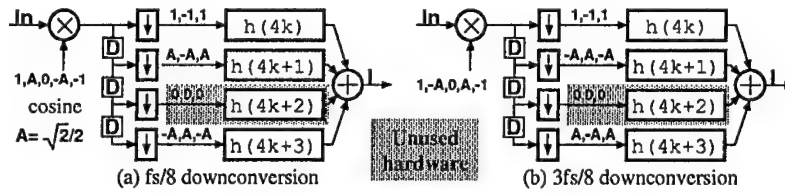


Figure 4: Calculation of frequency shifted filter coefficients

IV. Modified 4-IF Downconversion Scheme

We start from the original 4-IF scheme in Fig. 3. The set of possible IF's fulfilling Eq. 1 in this case is $IF \in \{0, f_s/8, f_s/4, 3f_s/8\}$. This implies the integration of four different anti-alias filters (i.e. one for each IF). Since these filters do not have to work simultaneously (only one band is downconverted at any time) a single filter with 4 selectable sets of coefficients can be used. The issue of multiple shape FIR filter design was discussed in [4]. The obvious problem is an integration of the anti-alias filters for $IF = f_s/8$ and $IF = 3f_s/8$. The downconversion from $f_s/8$ and $3f_s/8$ for the I branch of the downconverter with indicated distribution of mixer multiplicants through the polyphase structure is shown in Fig. 5. This indicates the necessary

Figure 5: Downconversion from $f_s/8$ and $3f_s/8$

modifications of the filters for $f_s/8$ and $3f_s/8$ cases. From comparison of Fig. 2 and Fig. 5 we can see that the filters $h(4k)$ and $h(4k+2)$ can be implemented as shown in Fig. 6(a) since the multiplicands differ only in signs. The branches $h(4k+1)$ and $h(4k+3)$ must integrate two

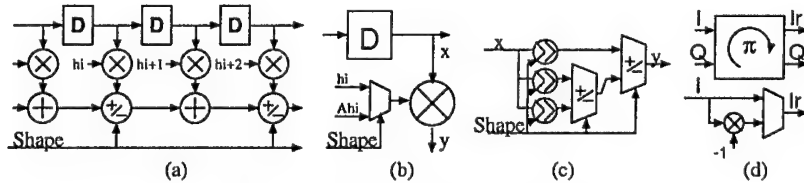


Figure 6: Implementation of the filters

different shapes: the "original" 4-IF shape and the scaled one (with scaling factor $A = \sqrt{2}/2$). We have found that the scaling of the filter coefficient results in a cheaper implementation compared to the additional scaling of the filter outputs. The multishape filters are implemented as in Fig. 6(b) (where realization of a single tap is shown). The filter coefficients were encoded in CSD format and the different coefficients were implemented by programmable shifts in the CSD add-shift structure as in Fig. 6(c) (for more details see [4]). In the decoder unit, the four filter outputs are added according to Eq. 2 to produce the correct I and Q components for each IF.

$$\begin{aligned}
 I_d &= Q_d = y_0 + y_1 + y_2 + y_3 & \text{for } IF = 0 \\
 I_d &= y_0 + y_1 + y_3; Q_d = y_1 + y_2 - y_3 & \text{for } IF = f_s/8 \\
 I_d &= y_0 - y_2; Q_d = y_3 - y_1 & \text{for } IF = f_s/4 \\
 I_d &= y_0 - y_1 - y_3; Q_d = y_1 - y_2 + y_3 & \text{for } IF = 3f_s/8
 \end{aligned} \quad (2)$$

Finally, since the signals at $f_s/8$ and $3f_s/8$ are centered around $f_s/2$ after the decimation by 4, the signal must be frequency shifted by π before the decimation by 2 can take place. The shift by π can be realized very efficiently in hardware since it requires only multiplications by 1 and -1 (see Fig. 6(d)). The complete scheme of the downconversion unit with selectable IF is shown in Fig. 7.

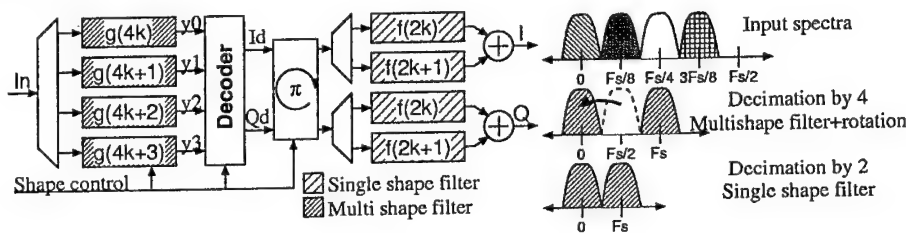


Figure 7: Modified 4-IF downconversion system with selectable frequency

V. Experimental Results

We have synthesized the original 4-IF system proposed in [2] and our modified circuit by means of Synopsys Synthesis Tools into 0.7μ CMOS Alcatel-Mietec library. The power estimates have been performed by Synopsys Design Power Tools. The results are shown in Table 1. The area

Table 1: Synthesis Results

Part	4-IF				Modified IF			
	Area [IVA]			P[mW]	Area [IVA]			P[mW]
	Comb	Seq	Tot		Comb	Seq	Tot	
20MHz	8.7	816.0	824.7	4.11	8.7	816.0	824.7	4.11
5MHz	1816.0	1725.4	3541.4	5.02	2860.5	1733.7	4594.2	7.22
1.25MHz	2513.8	1782.0	4385.8	1.42	2513.8	1782.0	4385.8	1.42
Σ	4338.5	4323.4	8751.9	10.55	5383.0	4331.7	9803.7	12.75

is given in equivalent number of IVA gates. The stages were synthesized with clock frequencies 20, 5 and 1.25 MHz, but the critical path of the 4-IF part was only 13.54 ns which indicates the possibility to use it on much higher frequencies.

VI. Conclusions

The presented technique shows the trade-off between flexibility and area/power consumption parameters in the digital downconverter. In our example, the limited programmability of IF settings results in an increase of the design area of the 4-IF block by factor 1.3 and estimated power consumption by 1.44 (respectively 1.12 and 1.2 if the whole circuit is considered), compared to the original 4-IF technique. It demonstrates the possibility to process an IF signal by digital means effectively also at higher frequencies which can simplify the design of analog circuitry.

References

- [1] B.C. Wong and H. Samuelli, "A 200 MHz all digital modulator and demodulator in 1.2- μ m CMOS for digital radio application", IEEE J. SSC, vol. 26, pp. 1970-1980, Dec. 1991.
- [2] S. Jou, S. Wu, and CH. Wang, "Low-Power Multirate Architecture for IF Digital Frequency Down Converter", IEEE Trans. Circuits and Systems II, vol. 45, pp. 1487-1494, Nov. 1998.
- [3] P. Schaumont, S. Vernalde, M. Engels, and I. Bolsens, "Low Power Digital Frequency Conversion Architectures", Kluwer J. VLSI Signal Proc., vol. 18, pp. 187-197, 1998.
- [4] R. Paško, P. Schaumont, and S. Vernalde, D. Ďuračková, "Efficient Implementation of Multiple Shape FIR filters", Proc. of EDS conf., pp. 197-200, Brno Jul. 1998.

Feasibility of a Fully Digital Radio-Frequency Stage for a DAVIC Compliant Modem Application.

J.Ph. Lambert, A. Dandache, F. Monteiro, B. Lepley.

*LICM / CLOES / SUPELEC, University of Metz
2 rue E. Belin, 57078 METZ Cedex 03, FRANCE
Tel: +33.(0)3.87.74.61.00, Fax: +33.(0)3.87.20.33.87,
Email: lambert@ese-metz.fr*

Abstract: In this paper, we study the feasibility of a fully digital radio-frequency stage dedicated to multimedia applications compliant to the DAVIC recommendation. We particularly focused on the 1.544 Mbits/s rate using the DQPSK modulation. After choosing an adequate block diagram of the architecture, these blocks have been described using VHDL for synthesis. The functional simulation of the complete system was performed on the Ptolemy software.

I. Introduction.

Designing modem application compliant to the DAVIC [1] recommendation using analogue techniques is a quite complex operation [2]. Recent realisations [3-5] clearly show that the current tendency is to design systems using digital techniques, especially in the telecommunication area, in order to remove most of the analogue design problems. The digital architecture of our design has been defined from the specification of the DAVIC recommendation. Each block of the radio-frequency stage has been described in VHDL, synthesised and simulated on the MaxPlusII software from ALTERA. The functional verification of the full system has been performed using the Ptolemy software from Berkeley University.

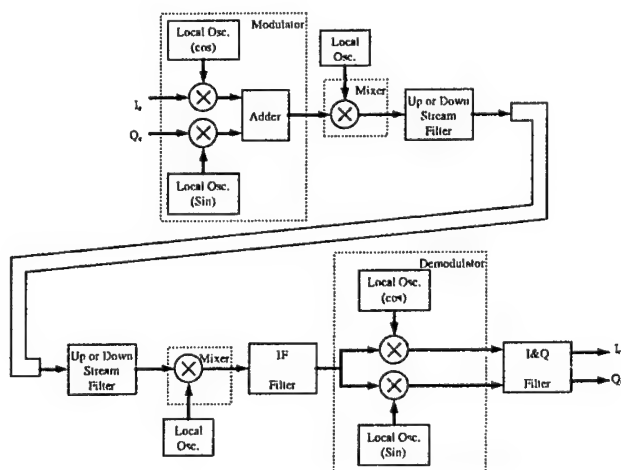


Fig. 1: DAVIC recommendation radio-frequency transmission line.

II. DAVIC Recommendation constraints.

The figure 1 shows the global architecture of the digital radio-frequency stage for a modem compliant to DAVIC recommendation [1]. This recommendation defines two transmission bands: the upstream band from 10 MHz up to 30 MHz, and the downstream band from 50 MHz up to 87 MHz. In each one, the frequency agility must be ensured. Furthermore, the characteristics of the intermediate frequency filter are fixed (10th order, 772 kHz bandwidth, and a rejection level of 30 dB between the modulated signal and the demodulation carrier). The use of in-phase and quadrature modulation (demodulation) is recommended.

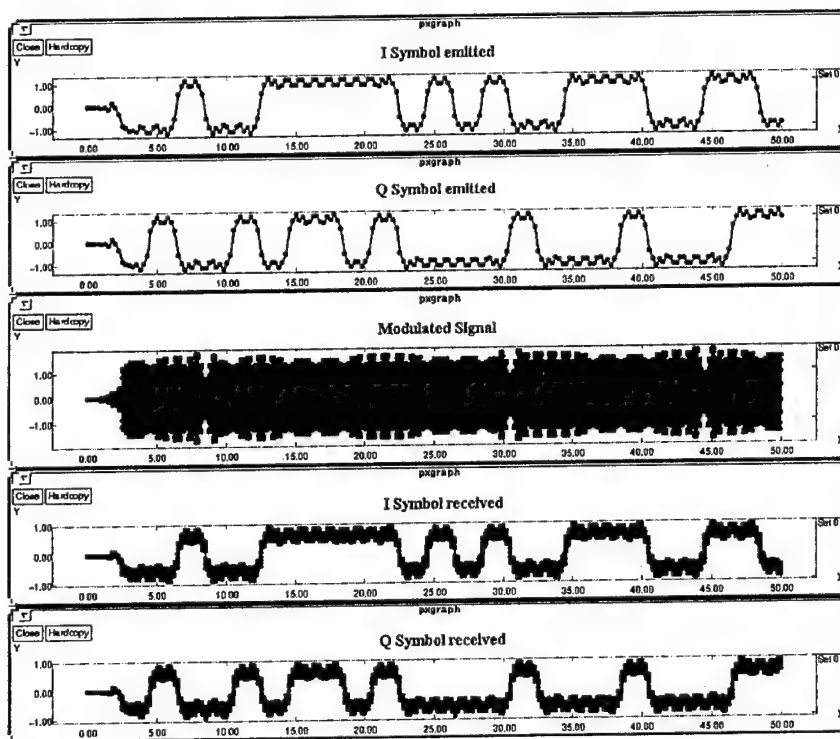


Fig. 2: Overview of the signals performed by the digital radio-frequency stage.

III. Architecture and VHDL modelisation.

The modulation, demodulation, mixer, and filter blocks make large use of multiplication, summation and multiplexing. As most of these functions are time-consuming, the overall structure has to be changed in order to accelerate the clock rate. The pipeline approach allows, thanks to the internal latches, a substantial increase of the data flow throughput. Simulations have been performed for several architectures including an array multiplier [6], a ripple-carry adder [7], a Wallace-tree adder [7], and a decimation-FIR filter [5]. The maximal clock frequency is the same for all of them and equates 116.27 MHz on the FPGA FLEX10K family of ALTERA.

IV. Simulation results on the Ptolemy software.

The simulation on the Ptolemy software allows to validate the complete functional operation of the architecture. The choice for the intermediate frequency value was done taking into account a previous study on analogue radio-frequency stages [2]: this frequency was set to 20 MHz. In order to simplify the functional block implementation, 16 sample values per period were used to describe the digital signals. Thus, to perform spectral shifting in each transmission band, three clock rate must be used. The first one equates 320 MHz and is used to generate the sine and the cosine waves in the modulator and the demodulator, which both work at the 20 MHz intermediate frequency. The two other can vary from 480 MHz to 1.072 GHz, and are used to generate the sine carrier needed to perform frequency transposition (30-67 MHz). The figure 2 shows signals obtained in a noise free transmission. Simulations using additional white Gaussian noise prove that the digital radio-frequency stage performs a higher transmission quality than usual analogue equivalents [2]. On the digital design, the first transmission errors appears with a signal to noise ratio close to 12.5 dB, while an efficient analogue design requires a signal to noise ratio of 17 dB. The figure 3 shows the bit error rate according to the signal to noise ratio variations the 10 MHz and the 87 MHz channels.

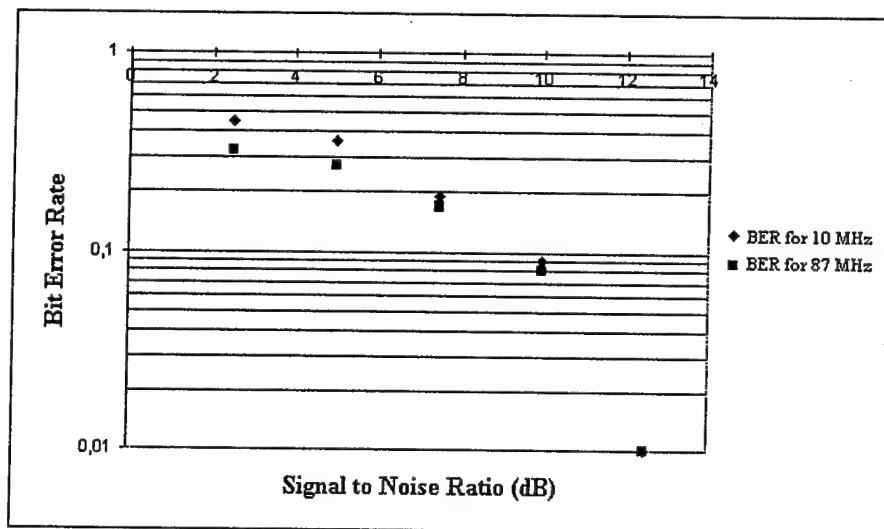


Fig. 3: Bit Error Rate as a function of Signal to Noise Ratio.

V. Conclusion.

The simulation of a digital radio-frequency stage dedicated to a DAVIC compliant modem has been done. This study, focusing on the 1.544 Mbits/s transmission rate on DQPSK modulation, points out the main problems to design such an architecture. Our approach showed, using functional simulation on the Ptolemy software, that our architecture performs a better quality of transmission than an analogue radio-frequency stage does. The high clock rate required are obtained using pipeline techniques. According the state of the art, the implementation of the design cannot be done using only CMOS technology. A faster technology (such as AsGa, ECL, or BiCMOS) is needed to perform the high clock rates required. In the close future, an implementation of the complete system should be done to

validate the architectural design.

References:

- [1]: DAVIC. « The specification DAVIC 1.0, rev 4 » *Digital Audio Visual Council*; Berlin, 11-15 December 1995.
- [2]: LAMBERT; DANDACHE; MONTEIRO; LEPLEY. « Design of Radio-Frequency Stages for a High Rate Digital Modem » ICECS'98; *IEEE International Conference on Electronic Circuit and System*. Vol 2; pp 319-322; 7-10 Septembre 1998; Lisbon, Portugal; (IEEE1998).
- [3]: GYSELINCKX; RYNDERS; ENGELS, BOLSENS « A 4*2.5 Mchip/s Direct Sequence Spread Spectrum Receiver with Digital IF and Integrated ARM6 Core. » *IEEE Custom Integrated Circuits Conference*, May 1997.
- [4]: SCHAU MONT; VERNALDE; ENGELS; BOLSENS. « Digital Up-Conversion Architecture for Quadrature Modulators. » *EDTC'97; European Design & Test Conference*; pp 542-546; March 1997; Paris, France.
- [5]: BARRET. « Low-Power Decimation Filter for Multi-Standard Transceiver Applications. » *Master Thesis*; University of California, Berkeley, USA. 1997.
- [6]: GHOSH; NANDY. « Design and realization of high performance wave-pipelined 8*8 bit multiplier in CMOS technology. » *IEEE Transactions on VLSI Systems*. Vol 3; N°1; 1995.
- [7]: ZIMMERMANN. « Binary Adder Architectures for Cell-Based VLSI and their Synthesis. » *PhD Thesis*. Swiss Federal Institute of Technology; Zürich 1998.

A Novel ATM System over PON Access Network Using Fuzzy Logic Sets

M. M. Jahromi, Student Member, IEEE and H. S. Al-Raweshidy, Senior Member, IEEE

Communication Systems Division,
Electronic Engineering Laboratory,
University of Kent at Canterbury,
Canterbury, Kent, CT2 7NT, UK

Tel: (+44 1227) 764000

Fax: (+44 1227) 456084

mj8@ukc.ac.uk

Abstract

For next generation services, telecommunication systems require maximum possible bandwidth efficiency with guaranteed QoS at optimum transmission bit rate. A system can gain these three characters only when the queuing traffic and delay set to the minimum. For this purpose, a novel ATM system over PON access network using Fuzzy Logic sets is designed and simulated. In this system, to avoid over saturated queuing problem due to cell multicasting, the Lock and Key multicasting-multiplexing approach is modelled. This leads to the minimum queuing delay and increases the number of cells transmitted to end-subscribers to be 2.75 times higher than normal system. Furthermore, an implementation of a dynamic time division multiplexing adapter over upstream transmission links that distributes the available bit rate over active subscribers is achieved. Over a system with 12.63% ABR, this adapter improves the number of cells transmitted during the upstream transmission by 14.5% with an average delay reduction up to 40%.

1. Introduction:

According to future telecommunication demands and services, ATM considered being the ground on which the future telecommunication systems built on. From this point of view, ATM systems should be upgraded to meet the requirement of both near and long term future telecommunication services. This upgrade should provide maximum possible bandwidth efficiency with guaranteed Quality of Service (QoS) at optimum transmission bit rate. These three characters can be achieved only when the queuing traffic and delay set to the minimum [1-4].

In this paper we present an advanced ATM switch with multicasting-multiplexing function that avoid loosing bandwidth by minimising the use of bandwidth via repeated common signals and supporting the ABR services [1-8]. This will lead to a reduction in cell queuing traffic that guaranteed better QoS. It also affects the transmission bit rate and enables the increment to be proportional directly with the amount of decrement in the cell queuing traffic. Therefore, the overall network capacity will be improved [3-7].

Considering ATM ability to provide central office broadband switching capability and deliver multiple services over cell based transport technology, it can be used to transport the information stream from the source up to the access node over a backbone network. This network connects several access networks to the source server or the core which means more services can be provided as the network capacity improves by sharing the common capacity and reducing the number of repeated signals to a single copy specially in point-to-multipoints (P-M) services. The transport network can be spread over several locations, areas, cities or districts and connect multi-access networks. Therefore, it is known as the regional transport network [3-5] and [8-12].

To complete end-to-end transportation links, signals transport from each access node to end-subscribers through access networks. The access network that connects the access node or the central office, where ATM switch are placed, to end-subscribers multicast and multiplex the ATM cells of the services signals to their specific end-subscribers according to cells header information. For this purpose and to take full advantage of ATM's capability, several access networks with different service coverage limitation over different topologies

are possible. Taking into account future telecommunication demands and services, the most suitable access networks are active double or single star and ATM-PON networks [8-9].

In active double or single star access network the central office connected to each subscriber through individual fibre link. Therefore, it provides each user with 155 Mb/s bi-directional transmission links which means it can cover all the telecommunication services described previously. However, it is the most costly access network and its bandwidth efficiency during the upstream transmission is low as the available bit rate for each subscriber during the upstream transmission is not being used most of the time [8].

The other suitable access network, which is recommended for next generation is ATM-PON access network. It has the advantage of low cost and high bandwidth efficiency comparing to active double or single star network. Although, this access network provides each user with 155 Mb/s downstream transmission links, the upstream transmission links is limited to $155/n$ Mb/s where n is the number of the access network subscribers [8].

2. Fuzzy Logic Sets:

As an outcome of merging the techniques of traditional rule-based expert systems, fuzzy set theory and control theory, fuzzy control departs significantly from traditional control theory which is essentially based on mathematical models of the controlled process. Instead of deriving a controller via modelling the controlled process quantitatively and mathematically, the fuzzy control methodology tries to establish the controller directly from domain experts or operators who are controlling the process manually and successfully. Clearly, this is a typical characteristic of an expert system where primary attention is paid to the human's behaviour and experience, rather than to the process being controlled [13-14].

Normally, applying fuzzy control over numerical environments employs two procedures: fuzzification and defuzzification. Fuzzification procedure converts numerical values (x) into fuzzy values (X) and the inferred values (Y) are converted into crisp values (y) which are compatible with the numerical environment form via defuzzification procedure [13-14].

In our case, three numerical inputs that are routing information categories elements for received cells (x_1, x_2, x_3) are entered the fuzzification procedure. The results will be as follow:

X_1 -Cell's signal information and details, X_2 -Signal's end-subscribers number and the required number of copies from each cell, X_3 -Signal's end-subscribers addresses.

According to fuzzy values X_2 and X_3 , the fuzzy sets within the inference engine controls the cell's multicasting-multiplexing rout. For this aim the fuzzy sets are in the following form:

$$\text{If } X_2 = \text{"Situation"} \text{ and } X_3 = \text{"Situation"} \text{ Then } R = \text{"Action"} \quad (1)$$

The action will depend on the multicasting-multiplexing approach. Finally, the inference engine's outputs which are the action's results defuzzicated into numerical environment.

3. Lock and Key Multicasting-Multiplexing Approach:

This approach is designed to avoid over saturated queuing problem due to cell multicasting within the access node. In this approach, specific decoder called the lock identifies each subscriber. Each cell, according to the signal that it belongs to and its multicasting-multiplexing information, addresses with specific code called the key. The key depends on the signal's end-subscribers in other word each code is a master key that opens all the signal's end-subscribers locks.

In our simulation, we have designed digital binary locks and keys with n digits where n is the total number of the access network subscribers. Each digit represents a specific subscriber. Each subscriber's lock has been identified by setting the digit that represents it to

one and the rest of the digits are blanked. While in each key, the digits which represents cell's end-subscribers are setting to ones and the rest to zeroes.

However, fuzzy logic sets and their actions are used in designing and modelling the required key for each cell. The multicasting-multiplexing routes consist of a key maker and addresser. The key maker according to the fuzzy sets action and fuzzy values X_2 and X_3 designs and models the required key and passes it to the addresser where it will be placed on the cell. Through the defuzzification procedure the key converts to the numerical corresponding and passes to all the subscribers via the transmitter. The end-subscribers whose lock will be opened with the key, as a function of an AND get, can get access to the cell otherwise the access will be prohibited.

Furthermore, to insure the network security and its privately fuzzy sets are arranged to control the filled digits in each subscriber's lock. The owner of any lock that has more than one filled digit will be shutoff from the network.

4. Dynamic Time Division Multiplexing Adapter:

In addition to the lock and key approach achievements over ATM-PON access network, the ATM-PON limitation during upstream transmission should be improved to cover almost all the telecommunication services. This is applicable by implementing a dynamic time division multiplexing adapter over the upstream transmission links. This adapter will provide each active subscriber with 155 Mb/s transmission links at specific time slots.

The dynamic adaptation that is employed in this adapter, controls the time slots length and distributes the available bit rate over active subscribers. The fuzzy sets involved in this adapter are in the following form:

$$\text{If } S_m = \text{"Situation"} \text{ Then } T_a = \text{"Action"} \quad (2)$$

The situation of S_m represents the subscriber "m" request to be active or not and then the action is to assign a specific time slot to the subscriber m or not. The assigned time slots to any active subscriber will be cancelled and assigned to other active subscribers as the subscriber's data transmission is finished.

5. Simulation Results:

Figure 1 shows the queuing delay at the core's transmitter buffer and an access network multiplexer's transmitter buffer for two simulated systems: a normal system and a system with Lock and Key approach. From figure 1 it is clear that by implementing the Lock and Key multicasting-multiplexing approach the queuing delay reduces to the minimum and the number of cells passed the multiplexer's transmitter is 2.75 times higher than the normal system.

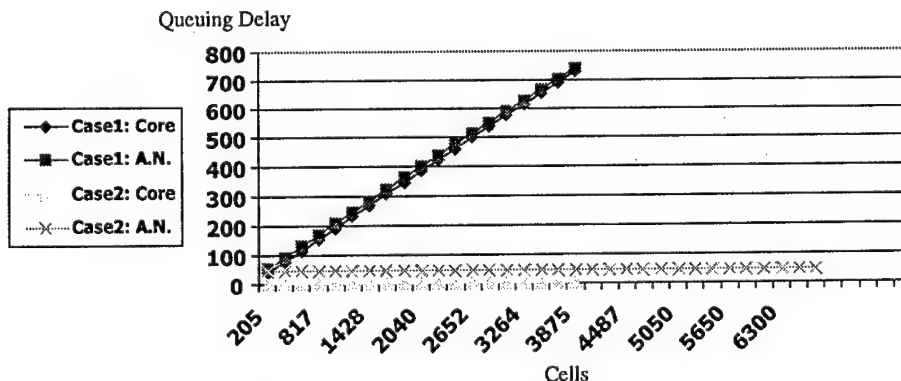


Figure 1: Queuing Delay against Cells Passed the Transmitters

The result of implementing the dynamic time division multiplexing adapter during the upstream transmission is shown in figure 2. For a system with 12.63% ABR, this adapter improves the number of cells transmitted during the upstream transmission by 14.5% with an average delay reduction up to 40%.

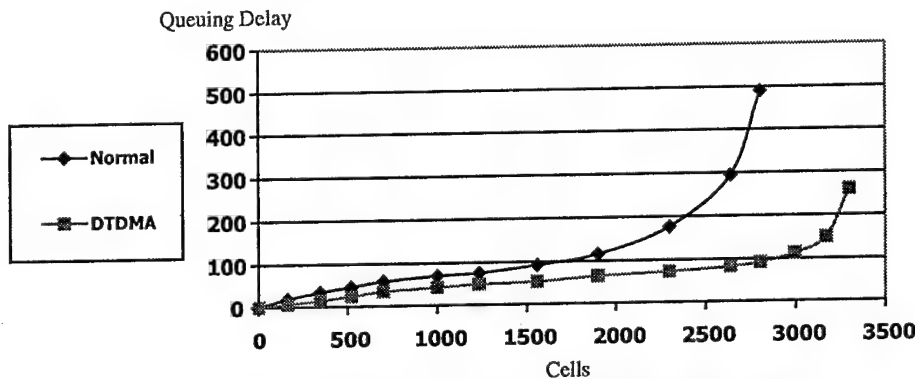


Figure 2: Dynamic Time Division Multiplexing Adapter Result

9. Conclusions:

From this paper it can be concluded that by implementing the lock and key multicasting-multiplexing approach, the over saturated queuing problem due to cell multicasting is avoided. Furthermore, it reduces the queuing delay to the minimum and improves the number of cells passed the multiplexer's transmitter by factor of 2.75. Finally, the dynamic time division multiplexing adapter over a system with 12.63% ABR, improves the number of cells transmitted during the upstream transmission by 14.5% with an average delay reduction up to 40%.

References:

- [1] Dong Lin, "Constant-time dynamic ATM bandwidth scheduling for guaranteed and best effort services with over booking", IEEE Globecom 97, pp. 398-405, Dec. 1997.
- [2] Tai H. Noh, "End-to-End self healing SDH/ATM networks", IEEE Globecom 96, CD-Rom, Dec 1996.
- [3] Kai Y. Eng and Mark A. Pashan, "Advances in shared-memory designs for Gigabit ATM switching", Bell Labs Tech. Journal, pp. 175-187, spring 1997.
- [4] Humberto J. La Roche, Stephen L. Myers, James P. Runyon, Gerald S. Soloway and David W. Spears; "High-speed data services using the switched digital broadband access system", Bell Labs Tech. Journal, pp. 187-201, spring 1997.
- [5] Paul A. Veitch, Dave Johnson and Ian Hawker; "Design of resilient core ATM network", IEEE Globecom 97, pp. 1450-1454, Dec. 1997.
- [6] Tai H. Noh, "ATM scenarios for SDH/SONET networks", Bell Labs Tech. Journal, pp. 81-93, Jan.-Mar. 1998.
- [7] Teruyuk Kubo, "Traffic Issues in ATM LAN-principle and practice", IEICE Transaction communication, Vol E81-B, No. 5, pp. 840-848, May 1998.
- [8] T. Ishihara, J. Tanaka, I. Nakajima, M. Okuda and H. Yamashita; "ATM-based networking concept and hardware architecture providing broadband multimedia services", ISSLS 96, pp. 257-262, 1996.
- [9] Ingrid Van de Voorde and Gert Van der Plas, "Full service optical access networks: ATM transport on passive optical networks", IEEE Communication Magazine, pp. 70-75, April 1997.
- [10] Mario Gerla, Prasath Palnati, Simon Walton, Emilio Leonardi and Fabio Neri; "Multicasting in Myrinet-a high-speed, wormhole-routing network", IEEE Globecom 96, pp. 1064-1068, Dec. 1996.
- [11] Mario Gerla, Milan Kovacevic and Joseph Bannister; "Optical tree topologies: Access control and wavelength assignment", Computer Networks and ISDN systems, Vol 26, pp. 965-983, 1994.
- [12] M. M. Jahromi, H. S. Al-Raweshidy and J. M. Senior; "An ATM Interface for connecting the core to access networks", NOC 98, Vol 2, pp. 134-140, 1998.
- [13] Junhong Nie and Derek Linkens, "Fuzzy-Neural Control: principles, algorithms and applications", first edition, Prentice Hall, 1995.
- [14] Dimiter Driankov, Hans Hellendoorn and Michael Reinfrank; "An Introduction to Fuzzy Control", second edition, Springer, 1996.

Empirical Formula of Diffracted Field from Corners for Urban Micro-cellular Communications

Ki-Hong Song¹, Won-Ho Kim², Che-young Kim³

¹*Dept. of Electronic Communications, Dongeui Institute of Technology, Korea
skh@dit.ac.kr*

²*Dept. of Electronics Engineering, Dongeui Institute of Technology, Korea*

³*Dept. of Electronics and Electrical Engineering, KyungPook Nat'l Univ., Korea*

Abstract. This paper proposes an empirical formula based on uniform geometrical theory of diffraction (UTD) model to predict the diffracted fields from corners of buildings. An empirical formula is derived from the statistical results for the characteristic parameters such as frequency, distance parameter, incident and observation angles, etc. The introduced formula is possible to calculate the diffracted fields effectively with a small difference compared to the fields by using UTD method.

I. Introduction

In system planning for land mobile radio service or service quality evaluation, it is important to predict the propagation characteristics such as direct, reflected, and diffracted fields around corners. Several prediction models to predict the propagation characteristics have recently been reported for micro-cellular communications [1,2]. Most empirical prediction models developed previously have been used to obtain the signal strength including diffracted fields over rooftops of surrounding buildings. However since base station for micro-cellular systems is located below the rooftops of buildings, the diffracted fields from corners of buildings are greater than the field over rooftops.

In this study, we propose an empirical formula to predict the diffracted fields from corners by using the statistical results obtained by UTD formulation. From many literatures, the UTD model is seen to give good general agreement with the available measurements.

Diffracted field is mainly affected by the incidence and observation angles on scattering body, frequency, distance parameters such as the distance from diffraction point to source and distance from diffraction point and observation point. Therefore the proposed formula is constituted with a function of above parameters. We show that the theoretical and empirical results were in good agreement.

II. Empirical Modelling of Diffracted Fields

The magnitude of diffraction coefficient is affected by the frequency, distance parameters, and incidence and observation angles, etc.

A. Analysis of Diffraction Coefficient

Diffraction coefficients are constituted with the sum of incident diffraction coefficients, reflection diffraction coefficients, and reflection coefficients on scattering body. The incident diffraction coefficient possess singularities at incident shadow boundary (ISB) which occur when $\phi = \pi + \phi'$ and $\phi - \phi' = -\pi$ and the reflection diffraction coefficient possess singularities at reflection shadow boundary (RSB) which occur $\phi = \pi + \phi'$ and $\phi + \phi' = (2n-1)\pi$ in figure 1 and 2. Figure 1 and 2 show the incident and reflection diffraction coefficients according to observation angles the when incidence angles are 10° and 110° , respectively.

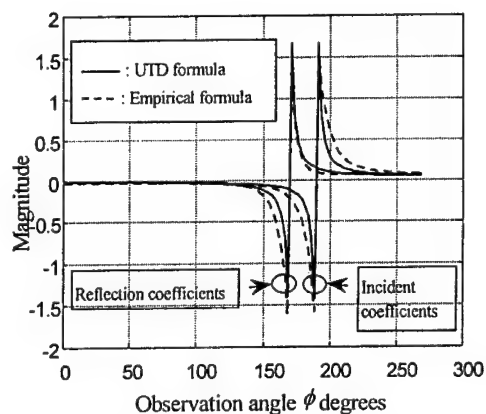


Fig.1. Field distribution of various components of diffraction coefficients. (Incidence angle (ϕ') is 10° degree)

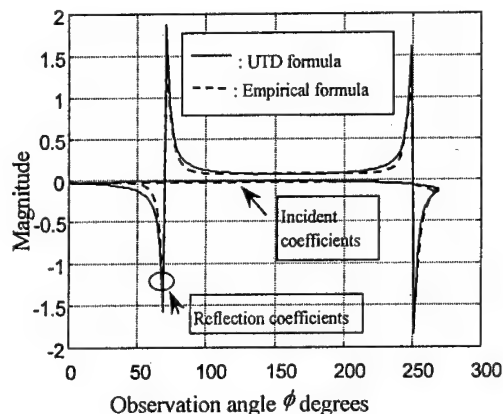


Fig. 2. Field distribution of various components of diffraction coefficients. (Incidence angle (ϕ') is 110° degree)

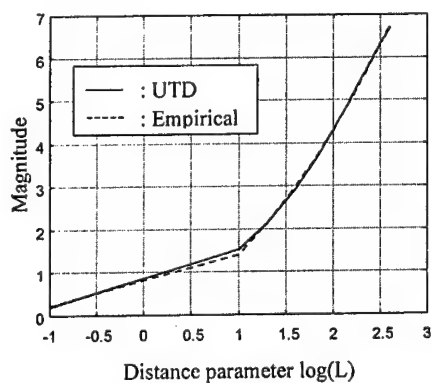


Fig.3. Diffracted field distribution versus the distance parameters

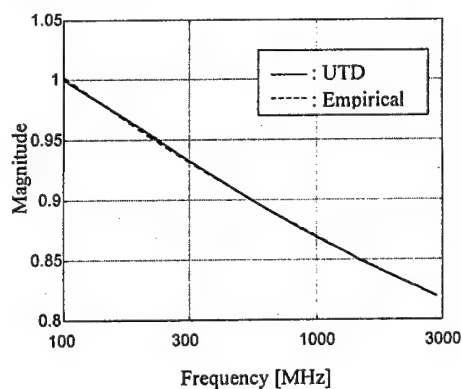


Fig.4. Diffracted field distribution versus the various frequencies

Figure 3 shows the magnitudes of positive maximum diffraction coefficients according to the observation distances at 1800MHz. In figure 3, incidence distance is set to be 400m, and incidence angle is 1.25° . Figure 4 represents the magnitude of positive maximum diffraction coefficients for the various frequencies at distance parameter $L = -1$.

The solid curves are represented the theoretical results, and dotted curves are represented the empirical results. It can be seen that the magnitudes of incident and reflection diffraction coefficients vary with the frequencies and distance parameters as well as the incidence and observation angles in figure 1 to 4.

B. Empirical Formula of Diffraction Coefficient

In previous session, we investigated the various parameters that affect to the diffraction coefficient. By using fig. 3 and 4, we derived the empirical formula for distance parameters and frequencies as follows.

$$F_{pos} = 0.0183(\log f)^2 - 0.2241 \log f + 1.3770 \quad (1)$$

$$L_{pos} = -0.0174(\log L)^3 + 0.8070(\log L)^2 + 0.6150 \log L - 0.0128 \quad (2)$$

$$B_{pos} = 0.0151(\log f)^2 - 0.1724 \log f + 0.4592 \quad (3)$$

$$F_{neg} = -0.0981(\log f)^2 + 0.3990 \log f + 0.7352 \quad (4)$$

$$L_{neg} = 0.4929(\log L)^3 - 3.1451(\log L)^2 + 3.5616 \log L - 2.4067 \quad (5)$$

$$B_{neg} = -0.0301(\log f)^2 + 0.2215 \log f - 0.4269 \quad (6)$$

where f is the frequency (in MHz) from 500MHz to 3000MHz, L is the distance parameter[3].

By using equation (1) to (6), the empirical formula for the diffraction coefficient can be written as equation (7) to (13). The empirical formula can be classified by two part such as incident coefficient((7) to (9)) and reflection coefficient((10) to (13)). Each coefficient is also divided according to the various shadow boundaries.

$$D_{ref} = P_{coef} \cdot \exp \left[-2\pi \left(1 - \left(\frac{\phi - CT}{C_{RSB}} \right)^4 \right) \right] + B_{pos} \quad \text{for } RSB1 \leq \phi \leq RSB2 \quad (7)$$

$$D_{ref} = N_{coef} \cdot \exp \left[-2\pi \left(1 - \left(\frac{\phi}{RSB1} \right)^4 \right) \right] + B_{neg} \quad \text{for } \phi < RSB1 \quad (8)$$

$$D_{ref} = N_{coef} \cdot \exp \left[-2\pi \left(1 - \left(\frac{2\pi - \phi}{E_{RSB}} \right)^4 \right) \right] + B_{neg} \quad \text{for } \phi > RSB2 \quad (9)$$

Where $P_{coef} = L_{pos} \cdot F_{pos} - B_{pos}$ and $N_{coef} = L_{neg} \cdot F_{neg} - B_{neg}$. $RSB1$ and $RSB2$ are incidence shadow boundaries, $RSB1 = \pi - \phi'$ for $\phi' < 90$, $RSB2 = 2\pi - \phi'$ for $\phi' \geq 90$. In addition, $C_{RSB} = (RSB2 - RSB1)/2$ and $CT = RSB1 + C_{RSB}$, $E_{RSB} = 2\pi - RSB2$. The incident coefficients are affected by the $ISB(\pi + \phi')$. In case of $ISB \leq (2\pi - \text{wedge angle})$,

$$D_{inc} = N_{coef} \cdot \exp \left[-2\pi \left(1 - \left(\frac{2\pi - ISB}{2\pi - \phi} \right)^4 \right) \right] + B_{neg} \quad \text{for } \phi < ISB \quad (10)$$

$$D_{inc} = P_{coef} \cdot \exp \left[-2\pi \left(1 - \left(\frac{ISB}{\phi} \right)^4 \right) \right] + B_{pos} \quad \text{for } \phi \geq ISB \quad (11)$$

In case of $ISB > (2\pi - \text{wedge angle})$,

$$D_{inc} = N_{coef} \cdot \exp \left[-2\pi \left(1 - \left(\frac{\phi' - \phi}{\pi} \right)^4 \right) \right] + B_{neg} \quad \text{for } \phi < \phi' \quad (12)$$

$$D_{inc} = N_{coef} \cdot \exp \left[-2\pi \left(1 - \left(\frac{\phi - \phi'}{\pi} \right)^4 \right) \right] + B_{neg} \quad \text{for } \phi \geq \phi' \quad (13)$$

III. The Empirical Results of Diffracted Fields

By using the empirical results derived by the proposed formula, we compared the empirical results with the theoretical results for the various frequencies, and number of diffraction points. Figure 5 shows the diffracted fields according to the distances at 900MHz and 1900MHz. Figure 6 shows the diffracted fields for the different number ($D=1$ and 3) of diffraction points located at 160m from transmitter. From figure 5 and 6, it can be seen that the empirical and theoretical results are in good agreement within 5 dB difference.

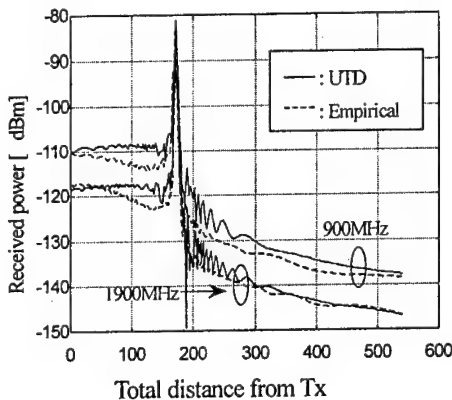


Fig.5. Diffracted field distribution according to the various frequencies

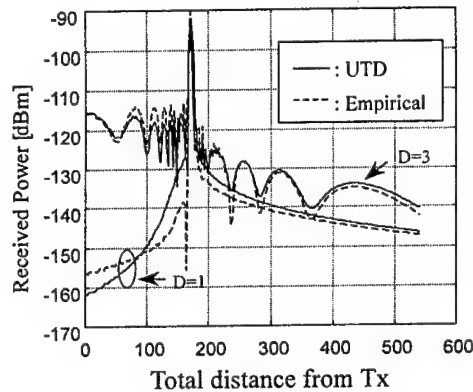


Fig.6. Diffracted field distribution according to the different number of diffraction points

IV. Conclusion

In this paper, we have developed the empirical formula available for calculating the diffracted fields on the basis of the UTD model described by [3]. In order to derive the introduced formula, we analyzed the statistical properties of the incidence and observation angles, frequency, distance parameters.

The introduced formula is applicable to system design effectively, because it improves the computational efficiency, the results are in good agreement with the theoretical results.

References

- [1] COST 231, "Urban Transmission Loss Models for Mobile Radio in the 900- and 1,800 MHz bands (Revision 2)," *COST 231 TD(90)119 Rev. 2*, The Hague, The Netherlands.
- [2] JTC Ad hoc Group, Technical Report on RF Channel Characterization and System Deployment Modelling, *JTC(AIR)*, 1994.
- [3] Constantine A. Balanis, *Advanced Engineering Electromagnetics*, John Wiley & Sons, 1989.

Simulated Annealing for Optimisation Multipoint Routing in Broadband Telecommunication Networks

R. VRBA¹, V. OLEJ² and K. BLUNÁR¹

Department of Telecommunication, Faculty of Electrical Engineering, University of Žilina,
Veľký diel, 01026 Žilina, vrba@fel.utc.sk, blunar@fel.utc.sk

Department of Information Systems, Faculty of Finance, Matej Bel University,
Tajovského 10, 97401 Banská Bystrica, olej@financ.umb.sk

Abstract:

The paper presents design and analysis of exploitation of algorithm Simulated Annealing to look for optimal multicast routing in broadband telecommunication networks. Routing in broadband telecommunication networks is procedure for serve of demand for creating of connection, which arrived to the network. For to create of multipoint connection in broadband telecommunication network, is needed to connect the nodes, which demand connection, with a minimal cost of connection. From results result, that computing resources, computing time and cost of design connection in broadband telecommunication networks depend on the parameters of algorithm. For good result of design of the network is needed a compromise between cost of connection and computing time of designed connection

1. Introduction

Evolution optimisation algorithms [2,6,7,8] present a set of algorithms, which use evolution processes for solving problems, search and optimisation in complicated systems. In precise mathematical formulations of some solving problems, e.g. searching of multicast routing scheme in broadband telecommunication network [9,11], number of mathematical operations is increased with second power of number of nodes in the network. During scanning of multidimensional space, calculation was often stopped in a local extreme and did not achieve required global extreme. Search of solutions of these problems initiates usage of evolution optimisation algorithms, which look for optimal solution by stochastic scanning of solution space.

2. Routing in Broadband Telecommunication Networks

Routing in broadband telecommunication network is an important part of control of the broadband telecommunication network. It is a procedure for serve of demand for creating of connection, which arrived to the network. The aim of routing in the broadband telecommunication network [5,9,11,14,15] is to find optimal connection between two or more nodes in the network, which demand connection. This connection is optimal, when a cost of this connection is from a set of all possible connections minimal, or when a distinction between the cost of this connection and minimal cost can be omitted, considering size and state of the network and time of design of routing with appropriate algorithm.

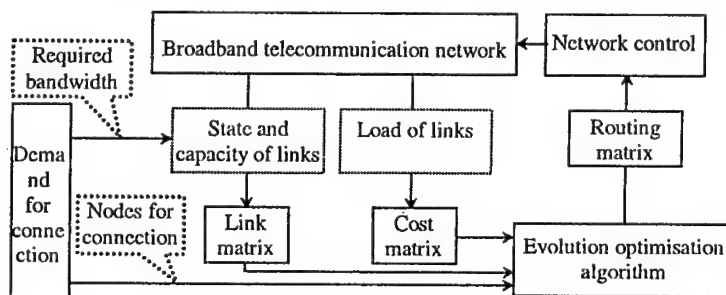


Fig.1 Routing of connection in a broadband telecommunication network

The cost of connection is a value incident a distance between nodes of connection d_{ij} , bandwidth of connection b_{ij} and actual load in individual links in the connection. In routing in telecommunication networks is tendency to route load through links with minimal load. Accordingly, when in some link load is increase, cost of this link is increase too. So, on the cost has effect total length of connections between all nodes in the connection, number of the nodes in the connection, actual load in the network and propagation delay in transmission mediums. Objective of routing in broadband telecommunication network is effective use of network resources.

Fig.1 described routing of a connection in the broadband telecommunication network. Demand for creating of connection arrived to the broadband telecommunication network. This demand contains set of nodes, which demand connection and required bandwidth for this connection. According to actual state of network are created input parameters for evolution optimisation algorithm - link matrix and cost matrix. From this input parameters evolution optimisation algorithm computes a routing matrix. This matrix defines, which links in the network will be used for the connection. According to this matrix will be reserved network resources for the designed connection.

3. Evolution optimisation algorithms

Evolution optimisation algorithms (EOA) are stochastic algorithms during whole behaviour of computation, every time find global extreme, but in independence time. During computation using EOA is important to set conditions, when actual result from algorithm is a global result of solve problem. Therefore to each partial result is compute fitness of this result. If fitness satisfy defined conditions, the algorithm is stopped and result from the algorithm is a solution of defined problem.

Algorithm Simulated Annealing

Algorithm Simulated Annealing (SA) [2,3] is deducted from an idea, that searching of global extreme is analogous to annealing of a solid body. Hence, simulate physical process, when the solid body is heated on the some temperature and after this is cooled slowly. With this process are eliminated some defects in a crystal grid. In this case is solid body represents by genotype, represents by array x . To this array x can be assign some energy of solid body $f(x)$. In case of annealing of solid body energy of solid body is minimised, in case of SA function value $f(x)$ is minimised. An array x is changed to a new array x' , which replaced array x with probability set by the Metropolis relation [2]:

$$P(x \rightarrow x') = \begin{cases} 1 & , \text{ak } f(x') \leq f(x) \\ e^{-\frac{f(x') - f(x)}{\tau}} & , \text{ak } f(x') > f(x) \end{cases} \quad (1)$$

where $\tau_{\min} \leq \tau \leq \tau_{\max}$ is an analogy of temperature. Temperature τ is limited by its maximal τ_{\max} and minimal τ_{\min} value, temperature is decreased by its multiply with a constant $\gamma=0$. Variable h is number of trials for given temperature τ and variable k is number of successful trials. Maximal value k_{\max} can be select from several hundred to several thousand, for its don't exist exact rule, $h_{\max} = 10 * k_{\max}$. Using function Rnd are generated numbers from interval $(0,1)$. In the array \hat{x} is stored the best result within the run of.

Algorithm SA can be expressed follow:

1. Create initial array x randomly
2. $\tau = \tau_{\max}$; $\hat{x} = x$; $k = 1$
3. $h = 0$; $k = 0$
4. $h = h + 1$
5. $x = t \cdot x$
6. if $f(x) \leq f(\hat{x})$, then $P = 1$, else $P = e^{-\frac{f(x) - f(\hat{x})}{\tau}}$
7. if Rnd $< P$, then $x = x$; $k = k + 1$
if $f(x) < f(\hat{x})$, then $\hat{x} = x$
8. if $h < h_{\max} \wedge k < k_{\max}$ then go to step 4
9. $\tau = \gamma \cdot \tau$
10. if $\tau > \tau_{\min} \wedge k > 0$ then go to step 3
11. End

4. Routing in broadband telecommunication network

For to create multipoint connection in broadband telecommunication network [5,9,11,14,15] is needed to connect nodes of network, which demand connection, with a minimal cost of connection. Algorithm is applied to the network on Fig.2, selected randomly. Table 1 describes cost matrix of this network according to actual state of the network. Marked links enabled transmission in the brier direction only. Bandwidth of all links is sufficient for to create of connection.

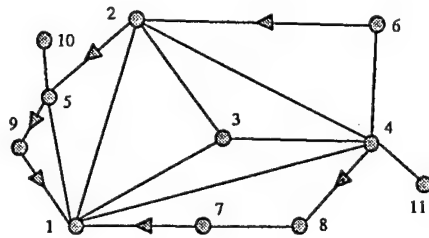


Fig.2 Broadband telecommunication network

	1	2	3	4	5	6	7	8	9	10	11
1		80	80	12	30						
2	10		90	12	20						
3	10	90		60							
4	14	12	70			40		30			20
5	30								20	20	
6		80		40							
7	30							20			
8								20			
9	30										
10					20						
11				20							

Tab.1 Cost matrix

In the next part is described an example of routing in broadband telecommunication network using algorithm Simulated Annealing. Connection is designed in the network on the Fig.3 between nodes 7, 10, 11. Costs of connection using individual links are described in the table 1.

Dependency of cost of connection on the parameters of algorithm SA τ_{min} , τ_{max} , k_{max} is presents in the Table 3. Parameters of algorithm must be set thus, that an optimal or a near to optimal solve will be found the most quickly. In each designed connection are two times of computing. The first one is time, when optimal solution was found. The second one is the time, when algorithm was stopped. The aim is to stop algorithm, when optimal solution is find. This limit satisfies values, marked by grey colour. From Table 4 result, when limit values of parameters of algorithm are set, algorithm doesn't achieved optimal solution always. If optimal solutions are needed, parameters of algorithm must be to move to the optimal area. In the Fig.3 is design of optimal connection with cost = 340. Optimal matrix of designed connection for multipoint routing between nodes 7,10,11 with cost of connection 340 is in Tab.6.

k_{max}		50	100	200	400	600	800	1000
τ_{min}	τ_{max}	Cost of connection						
10	1000	340	340	340	340	340	340	340
Time of opt. solution		17	29	86	74	97	136	228
Time of computing		47	94	192	226	337	452	692
50	1000	360	340	340	340	340	340	340
Time of opt. solution		x	28	53	44	120	161	283
Time of computing		17	33	66	132	199	276	327
50	500	360	340	340	340	340	340	340
Time of opt. solution		x	16	47	39	90	189	255
Time of computing		10	18	49	77	158	209	181
100	500	460	440	380	340	360	360	360
Time of opt. solution		x	x	x	47	x	x	x
Time of computing		9	17	35	66	115	124	127

Tab.3 Parameters of Simulated Annealing and cost of connection

	$\tau_{min}=50$		$\tau_{max}=500$		$k_{max}=100$					
Time of computing	23	16	16	17	17	17	17	16	16	17
Cost of connection	340	360	340	360	410	360	340	340	360	340
	$\tau_{min}=50$		$\tau_{max}=500$		$k_{max}=200$					
Time of computing	33	32	32	33	32	32	33	33	31	33
Cost of connection	360	340	340	380	340	340	340	340	340	340
	$\tau_{min}=50$		$\tau_{max}=1000$		$k_{max}=100$					
Time of computing	21	21	20	21	21	21	21	21	21	21
Cost of connection	340	360	360	360	360	340	360	340	340	340

Tab.4 Limit values of parameters of Simulated Annealing

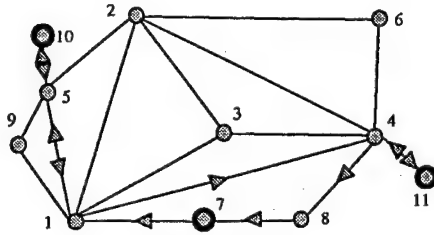


Fig.3 Optimal connection - cost 340

	1	2	3	4	5	6	7	8	9	10	11
1	0	0	0	1	1	0	0	0	0	0	0
2	0	0	0	0	0	0	0	0	0	0	0
3	0	0	0	0	0	0	0	0	0	0	0
4	0	0	0	0	0	0	0	1	0	0	1
5	1	0	0	0	0	0	0	0	0	1	0
6	0	0	0	0	0	0	0	0	0	0	0
7	1	0	0	0	0	0	0	0	0	0	0
8	0	0	0	0	0	0	1	0	0	0	0
9	0	0	0	0	0	0	0	0	0	0	0
10	0	0	0	0	1	0	0	0	0	0	0
11	0	0	0	1	0	0	0	0	0	0	0

Tab. 6 Connection matrix

5. Conclusion

From results result, that effect of individual evolution optimisation algorithms at design of connection in broadband telecommunication network depends on the size and structure of the broadband telecommunication network. For a small network can be sufficiency algorithm Hill Climbing, for a large network Simulated annealing or Evolution strategy, it depends on computation capacity, which is available. Time of computing of algorithms cannot be compared objectively, because it depends on the implementation of algorithm using software and hardware. Algorithm Simulated annealing can be accelerated using more quickly hardware, Evolution strategy can be distributed on the multiprocessor system, where each individual in the population is computed by own processor. Time of computing can be reduced too with a combination of individual algorithms.

For good result of design of the network is needed a compromise between kind of algorithm cost of connection and computing time of designed connection. This is, design of the connection will be approached to the optimal connection an computing time will be guaranteed desired criteria for routing in broadband telecommunication network.

References

- [1] KAPSALIS, A. - RAYWARD - SMITH, V. J. - SMITH, G. D.: Solving the Graphical Steiner Tree Problem Using Genetic Algorithms. *Journal of the Operational Research Society*, Vol.44, No.4, 1993, pp.397 - 406.
- [2] KVASNIČKA, V. a kol.: Introduction to Theory of Neural Networks. Iris, Bratislava, Slovak Republic, 1997.
- [3] KVASNIČKA, V. - POSPÍCHAL, J. - HESEK, D.: Augmented Simulated Annealing Algorithm for the TSP. *Central European Journal for Operations Research and Economics*, Vol.2, No.4, 1993, pp. 307 - 317.
- [4] Vrba, R. - Olej, V. - Blunár, K.: Multipoint Routing in Broadband Telecommunication Networks Using Evolution Optimisation Algorithms. *Mendel 98, 4th International Mendel Conference on Genetic Algorithms, Optimization Problems, Fuzzy Logic, Neural Networks, Rough Sets*, Brno, 1998, Czech Republic, pp. 145 - 151.
- [5] MARTINEC, L. - BLUNÁR, K. - KEVICKÝ, F.: A Multipoint Connections Routing in B - ISDN by Means of Neural Networks. *Proc. of 3rd International Conference on Genetic Algorithms, Optimization Problems, Fuzzy Logic, Neural Networks, Rough Sets*, Mendel '97, Brno, Czech Republic, 1997, pp.348-351.
- [6] OLEJ, V.: Comparison of Distributed Genetic Algorithms and Evolution Strategies. *Proc. of 3rd International Conference on Genetic Algorithms, Optimization Problems, Fuzzy Logic, Neural Networks, Rough Sets*, Mendel '97, Brno, Czech Republic, 1997, pp.99 - 104.
- [7] OLEJ, V.: Realization of Distributed Genetic Algorithms and Evolution Strategies. *Proc. of 17th International Conference on Artificial Intelligence and Information Control Systems of Robots*, World Scientific, Printed in Singapore by Uto-Print, Smolenice, Slovak Republic, 1997, pp.277 - 285.
- [8] OLEJ, V. - UNGER, M. - KRUTÝ, T.: Analysis of Distributed Genetic Algorithms and Evolution Strategies. *Proc. of International Symposium on New Trends in Control of Large Scale Systems, Intelligent Technologies*, Vol.1, Herľany, Slovak Republic, 1996, pp.51 - 65.
- [9] ONVURAL, R. O.: Asynchronous Transfer Mode Networks Performance Issues. Norwood, Artech House, 1994.
- [10] PALMER, Ch. C. - KERSHENBAUM, A.: An Approach to a Problem in Network Design Using Genetic Algorithms. Brooklyn, New York, Polytechnic University, and Yorktown Heights, John Wiley and Sons, 1995, pp.151 - 163.
- [11] SATTO, H.: Teletraffic Technologies in ATM Networks. Norwood, Artech House, 1994.
- [12] TANAKA, Y. - BERLAGE, O.: Application of Genetic Algorithms to VOD Network Topology Optimization. *IEICE Trans. Commun.*, Vol.E79-B, No.8, 1996, pp. 1046 - 1053.
- [13] TANAKA, Y. - HUANG, C.: Multiple Destination Routing Algorithms. *IEICE Trans. Commun.*, Vol.E76-B, No.5, 1993, pp.544 - 552.
- [14] TU, S.C. - LEUNG, W. H.: Multicast Connection - Oriented Packet Switching Networks. *IEICE Trans. Commun.*, Vol.E78-B, No.9, 1995, pp.495 - 501.
- [15] WAXMAN, B. M.: Routing of Multipoint Connections. *IEEE Journal on Selected Areas in Communications*, Vol.6, No.9, 1988, pp.1617 - 1622.

Radio Over Fibre for the Third Generation Microcellular Networks

H. S. Al-Raweshidy

*Communication Systems Division
Electronic Engineering Laboratory
University of Kent
Canterbury, Kent CT2 7NT, United Kingdom
Tel: 0044-1227-823396
Fax: 0044-1227-456084
Email: h.al-raweshidy@ukc.ac.uk*

Abstract. This paper presents an assessment of the performance of a radio over fibre link between a remote antenna unit and a base station. A novel technique using direct sequence spread spectrum is proposed to minimise the IMD by decreasing the signal amplitude prior to a direct modulation of a laser diode. The results show that the optical fibre microcellular system is outperforming the full wireless system.

1. INTRODUCTION

The transmission system that uses both radio and optical fibre elements, so-called radio over fibre, has been a subject of many investigations [1-4]. In mobile communication system, microcellular system, whose cell size is reduced to several 100 meters [5-11], has been proposed in order to face a rapid increase in the number of subcarriers. The requirement for both the huge capacity and the multimedia applications (broadband) will lead to the minimisation of the cell size. The reduction in cell size improves the frequency utilisation efficiency, reduces the power consumption of radio equipment and makes portable sets smaller. But this implementation needs the placement of many radio base stations (RBS) collecting and delivering RF signals and the effective connection among so many RBSs. To solve these technical problems, it is proposed that microcells in wide area are connected via optical fibres, and radio signals are transmitted over optical fibre link among RBSs and control station (CS). By employing this system, analogue optical links are ideal for this application because of fibre's exceptionally low loss, high bandwidth, and low distortion in the 1.3 and 1.55 μm bands. By modulating the received RF signal on a lightwave, high fidelity transport of these signals without repeaters or optical amplifiers can be achieved over many tens of kilometres. Furthermore, RBS is equipped only with an electric-to-optic converter (E/O) and an optic-to-electric converter (O/E), and all of the complicated function such as RF modulation and demodulation, frequency assignment, spectrum delivery switching and so on, are performed at the CS as shown in figure 1.

Subcarrier multiplexing (SCM) allows the radio frequency carriers to modulate directly a laser diode and be transported over the optical fibre without the need for frequency conversion and multiplexing/demultiplexing functions. The presence of non-linear device,

such as a laser diode (LD), causes mixing of the frequency-division multiplexed (FDM) subcarriers and creates new frequencies [10-18], some of that may coincide with the subcarrier of interest. These frequencies are an additional source noise, commonly referred to as the intermodulation distortion (IMD) noise. Several techniques have been proposed to reduce the impact of harmonic and intermodulation in modulated semiconductor LD such as pre-distortion and FM modulation techniques [5,6].

The proposed distributed antenna (DA) system is also compatible with existing analogue and digital cellular systems and upgradable to future standards. It can increase the user capacity without adding expensive base stations. A low cost, simple, and compact optical transceiver with a simple omnidirectional antenna can be located anywhere within a normal macrocell, where the traffic demand is high or the proper signal reception is difficult due to shadowing. Thus, DA systems can be extended to cover the indoor PCS as well.

The analogue optical fibre link benefits as a subsystem in microcell designs, as well as an antenna-remoting applications in general, are:

- High bandwidth
- Low loss
- Ease of installation compared with copper cables
- Insensitivity to EMI
- Simplicity of design
- Reliability

In considering a suitable method of analysing the intermodulation distortion in a GSM radio-over-fibre system, a number of factors must be considered. Firstly, the number of subcarriers in the system is important. In a picocellular system there may be only a single frequency, in which case there may be no IMD to consider (neglecting interference from distant base-stations). However, any base station that is required to process more than one frequency may or may not, depending on the frequency allocation, suffer from IMD all relate to two tone analysis, and although consider the effects of more than two carriers, the work is based upon the assumption that triple beat distortion will be 6 dB higher than two tone. The analysis allowed for an unlimited number of subcarriers, but assumed equal amplitude. However, the relative amplitude of the subcarriers will have a bearing on the intermodulation effects, and uplink carrier amplitudes will not be equal. A second consideration is the bandwidth, frequency spacing and modulation methods of the carriers which are multiplexed. The GSMK carrier modulation that is used in the GSM system can be considered to be a Gaussian-filtered FM signal. Hence, the frequency modulated, (electrically) frequency-division multiplexed carrier (FM/FDM), could be applicable as a simple approximation.

This paper presents a GSM-specific assessment of the performance of a radio over fibre link between a remote antenna unit and GSM base station. The combination of GSM physical layer model and optical environment model within the same simulation package allows a comprehensive evaluation of performance of the fibre-link under specific signalling conditions. A novel strategy using spread spectrum has been proposed to decrease the IMD parameters, which consequently improves the carrier to noise ratio of the system.

II. RADIO OVER FIBRE PHYSICAL LAYER MODEL

A. GSM Physical Layer Model

A comprehensive model of the GSM physical layer is simulated from the Speech and Channel Coder, through interleaving, modulation, filtering and transmission into the air. A radio environment model includes multipath fading as a function of operating frequency and mobile speed. In addition, co-, adjacent-, and alternate channel interference and thermal noise are simulated. Reception includes a Viterbi equaliser followed by a channel and bit-accurate speech decoder. Many performance measures are available including bit-error rate (BER) and frame erasure rate (FER). The layer is implemented in block form under the discrete-time simulation software Signal Processing WorkSystem[®] (SPW[®]), as shown in figure 2 [19].

B. Optical Fibre Link Model

A model of a single mode Fabry-Perot semiconductor laser that predicts laser performance in analog transmission has been developed as shown in figure 3. The non linearity model of a semiconductor laser diode is based on the simulation of the memoryless methode using Taylor's Series. The model can therefore be used to simulate amplitude and frequency modulation of the laser to allow investigation of characteristics such as light versus current, step response, harmonic and intermodulation distortion. The use of discrete time simulation software, in this case Signal Processing WorkSystem[®], allows easy simultaneous solution of the nonlinear equations in a block oriented manner shows the constituent blocks of the optical environment. The laser driver block in figure 3 allows the provision of a signal pre-processing scheme such as some form of predistortion, secondary modulation or signal spreading [5,6].

III. CARRIER-TO-NOISE RATIO (CNR)

A. Principles of Radio over Fibre

The goals of analogue system designers are large bandwidth, low distortions, large signal-to- noise ratio (SNR), and large spurious free dynamic range (SFDR). The SFDR of an analogue optical link is the range of radio frequency (RF) input powers for which a two-tone RF input signal could be clearly distinguished from noise and nonlinearities at the link output.

The most important characteristics of the analogue optical link is the carrier-to- noise ratio (CNR), defined as the ratio of rms carrier power to rms noise power at the output of the optical receiver, and is given by

$$\text{CNR} = \frac{\text{Carrier power}}{\langle I_{\text{source}}^2 \rangle + \langle I_{\text{shot}}^2 \rangle + \langle I_{\text{thermal}}^2 \rangle + \langle I_{\text{ind}}^2 \rangle} \quad (1)$$

Where

$\langle I_{\text{source}}^2 \rangle$ – source noise, given by

$$\langle I_{\text{source}}^2 \rangle = \text{RIN}(\mathcal{R}P_c)^2 B$$

P_r average received optical power;
 \mathcal{R} photodiode responsivity;
 B noise bandwidth of receiver;
 RIN laser diode relative intensity noise is defined by

$$RIN = \frac{\langle (\Delta P_L)^2 \rangle}{P_L^2}$$

$\langle (\Delta P_L)^2 \rangle$ - the mean square intensity fluctuation of the laser output;
 P_L average laser output intensity.

$\langle I_{shot}^2 \rangle$ - photodiode noise known as shot noise,

$\langle I_{thermal}^2 \rangle$ - the preamplifier noise (thermal noise).

The intermodulation distortion (IMD) term, $\langle I_{imd}^2 \rangle$ in (1) is additional source of noise that arises when multiple message channels operating at different carrier frequencies, particularly in FDMA systems, are sent simultaneously over the same fibre.

B. Intermodulation Distortion

The IMD occurs mainly in laser diode modulation process as a result of its nonlinear behaviour, which has its origin from

1. Injection current versus output light (I-P) curve nonlinearity;
2. Dynamic nonlinearity due to intrinsic photon-electron nonlinear interaction;
3. Nonsymmetric threshold clipping (overmodulation distortion).

The dynamic nonlinearity effect is frequency dependent and increases with modulation frequency. If the operating frequency band of the channel is less than one octave, all the harmonic distortions and even order IMD products will fall outside the passband. Thus third order types at frequencies $f_1 + f_j - f_k$ (triple-beat IMD products) and $2f_1 - f_j$ (two-tone third-order IM products) are the most dominant, higher order products tend to be significantly smaller. IMD increases with increasing modulation index and signal power (i.e. increasing number of users in CDMA systems) as well as increasing number of channels in FDMA systems. Hence IMD places restrictions on maximum average signal-to-noise ratio of a system.

A new method is proposed to improve the CNR and increase the dynamic range of the system as shown in figure 4. The direct sequence spread spectrum (DS-SS) is used to spread the output signals from the combiner which will be used as a modulating input signal to the laser diode. Therefore, the amplitude of the input signal to the laser diode after spreading is lower than the signal before spreading as shown in figure 5. This will lead to a reduction in the relative intensity noise, shot noise and intermodulation noise while the thermal noise will not be effected. The amount of the reduction in the noise will depend on the processing gain (G_p) of the spread spectrum. For example both the relative intensity noise and intermodulation noise will be reduced by a factor of G_p^2 while the shot noise will be reduced by a factor of G_p .

In this paper, the radio channel is assumed to be Rayleigh fading channel corrupted by additive white Gaussian noise (AWGN) and the optical fibre behaves as a non-dispersive channel for the distance involved. The average carrier to noise ratio for the wireless system (in the absence of optical fibre link) is

$$CNR_{WL} = K_{mw} \frac{\sigma_c^2}{\sigma_{awgn}^2} \quad (2)$$

where σ_{awgn}^2 is additive white Gaussian noise (AWGN), σ_c^2 is the carrier signal and K_{mw} is the average microwave attenuation factor from the RBS to the CS. While the total noise power σ_n^2 at the output of the IF filter in the GMSK receiver is the sum of the optical fibre system noise and the AWGN from the radio channel [3], and is expressed as

$$\sigma_n^2 = \sigma_{of}^2 + \sigma_{awgn}^2 \quad (3)$$

where σ_{of}^2 is the noise power for the optical fibre system. The average carrier to noise ratio for the optical fibre microcellular system is

$$CNR_{OF} = K_{OF} \frac{\sigma_c^2}{\sigma_n^2} \quad (4)$$

where K_{OF} is the total optical fibre attenuation factor.

Figure 5 shows the performance of the full wireless system and optical fibre microcellular system with and without CDMA. The actual performance of the non-optical fibre system will be worst than that depicted in figure 5. Because, for the simulation, the link in the non-optical fibre system between the base station and the central station is assumed to be lossless, which is not the case when the actual microwave/coaxial cable link is taken into account. This would mean that with optimum design such that $SNR_{of} \sim SNR$, the optical fibre system may outperform the non-optical fibre system as seen in figure 5, where the exact BER of the former is less than the BER of the latter. This allows lower launch power requirements, making the handheld sets more compact (or conversely, yields longer uninterrupted service time). The lower exact BER performance of the optical fibre system is a consequence of the randomness in the noise power due to its dependence on the fluctuating subcarrier envelopes.

V. CONCLUSION

The integration of an optical fibre link within a GSM physical layer verification environment has allowed evaluation of microcellular-based radio over fibre. The paper shows that by using spread spectrum technique, the intermodulation distortion is decreased. Therefore, the optical fibre microcellular system has a potential to be one of the most successful candidates for the future third generation mobile communications especially with the advancement of the software radio networks. The improvement of the CNR in this technique is due to the inherited properties of the spread spectrum, where the power of the signal, just after spreading at the transmitter, is compressed (reduced). The power compression has a positive affect on the reduction of the RIN, phase noise and IMD. The despreading process, at the receiver,

has a positive affect on the signal by increasing its level by a value of G_p . This radio over fibre modelling is currently support the 900MHz GSM standard and further studies are in progress to cover the 1800MHz GSM.

REFERENCES

- [1] H. Harada, S. Kajiya, K. Tsukamoto, S. Komaki, and N. Morinaga, "TDM Inter-cell Connection Fiber-Optic Bus Link for Personal Radio Communication Systems." *IEICE trans. commun.*, vol. E78-B, NO. 9, pp. 1287-1294. September 1995.
- [2] H. Harada, H.J. Lee, S. Komaki and N. Morinaga, "Performance Analysis of Fiber-Optic Millimeter-Wave Band Radio Subcarrier Loop." *IEICE TRANS. COMMUN.*, vol. E76-B, No. 9, pp. 1128-1135. September 1993.
- [3] B.J. Koshy and P.M. Sankar, "Efficient Modeling and Evaluation of Fiber-Fed Microcellular Networks in a Land Mobile Channel Using a GMSK Modem Scheme." *IEEE J. on selected areas on Com.*, vol.15, No. 4, pp. 694-705. May 1997.
- [4] R. Ohmoto, H. Ohtsuka, and H. Ichikawa, "Fiber-Optic Microcell Radio Systems with a Spectrum Delivery Scheme." *IEEE Journal on Selected Area in Com.*, vol.11, No. 7, pp. 1108-1116. September 1993.
- [5] N. Tayebi and M. Kavehrad, "Laser Nonlinearity Compensation for Radio Subcarrier Multiplexed Fiber Optic Transmission Systems." *IEICE TRANS. COMMUN.*, vol. E76-B, No. 9, pp. 1103-1114. September 1993.
- [6] R. Ohmoto and H. Ohtsuka, "Performance of FM Double Modulation for Subcarrier Optical Transmission." *IEICE TRANS. COMMUN.*, vol. E76-B, No. 9, pp. 1103-1114. September 1993.
- [6] S. Komaki, K. Tsukamoto and M. Okada, "Requirements for Radio-Wave Photonic Devices from the Viewpoint of Future Mobile Radio Systems." *IEEE Transaction on Microwave Theory and Techniques*, vol.43, No. 9, pp. 2222-2228. September 1995.
- [7] H.M. Salgado and J.J. O'Reilly, "Accurate Performance Modeling of Subcarrier Multiplexed Fiber/Radio Systems: Implications of Laser Nonlinear Distortion and Wide Dynamic Range." *IEEE Transaction on Communications*, vol.44, No. 8, pp. 988-994. August 1996.
- [8] M. Shibutani, W. Domon and K. Emura, "Performance Improvement in Optical Fiber Feeders for Microcellular Mobile Radio Systems." *IEICE TRANS. COMMUN.*, vol. E76-B, No. 9, pp. 1145-1151. September 1993.
- [9] S. Kajiya, K. Tsukamoto, and S. Komaki, "Proposal of Fiber-Optic Radio High Networks Using CDMA Method." *IEICE TRANS. ELECTRON.*, vol. E79-C, 1, pp. 111-116. January 1996.
- [10] O.K. Tongus, and H. Jung, "Personal Communications Access Networks Using Subcarrier Multiplexed Optical Links." *JOURNAL OF LIGHTWAVE TECHNOLOGY*, vol.14, NO.6, pp. 1400-1409. June 1996.
- [11] Y. Matsunaga and M. Shibutani, "A Short-Span Optical Feeder for Wireless Personal Communication Systems Using Multimode Fibers." *IEICE TRANS. ELECTRON.*, vol. 79-C, NO.1, pp. 118-123. January 1996.
- [12] H. Junga and O. K. Tongus, "Coax/Fiber Hybrid Access Network for Microcellular Personal Communication Systems." *IEICE TRANS. COMMUN.*, vol.9-B, NO.7, pp. 932-938. July 1996.
- [13] J. Namiki, et al., "Optical Feeder Basic System Design for Microcellular Mobile Radio." *IEICE TRANS. COMMUN.*, vol. E76-B, No. 9, pp. 1069-1077. September 1993.

- [14] W. I. Way, "Optical Fiber-Based Microcellular Systems: An Overview." IEICE TRANS. COMMUN., vol. E76-B, No. 9, pp. 1091-1101. September 1993.
- [15] J. Namiki, et al., "Optical Feeder Basic System Design for Microcellular Mobile Radio." IEICE TRANS. COMMUN., vol. E76-B, No9, pp.1069-1077, September 1993.
- [16] A. M. Daher and H. S. Al-Raweshidy, "Design considerations of Radio on Fibre for Microcellular CDMA systems," *Third Communication Networks Symposium*, pp. 94-97, 8 - 9 July 1996.
- [17] H.S. Al-Raweshidy, F. A. Muhammađ and J.M. Senior, " D-fibre antenna for microcellular mobile communication systems", IEE Proceedings Optoelectronics, vol.143. no. 6. pp. 370-374, December1996.
- [18] J.C. Fan, C.I. Lu, and L.G. Kazovsky, "Dynamic Range Requirements for Microcellular Personal Communication Systems Using Analog Fibre-Optic Links," *IEEE Trans. On Microwave Theory and Techniques*, vol. 45, no. 8, pp.1390-1397, August 1997.
- [19] ALTA Group at Cadence Design System Inc., Signal Processing Work System Manual, March 1995.

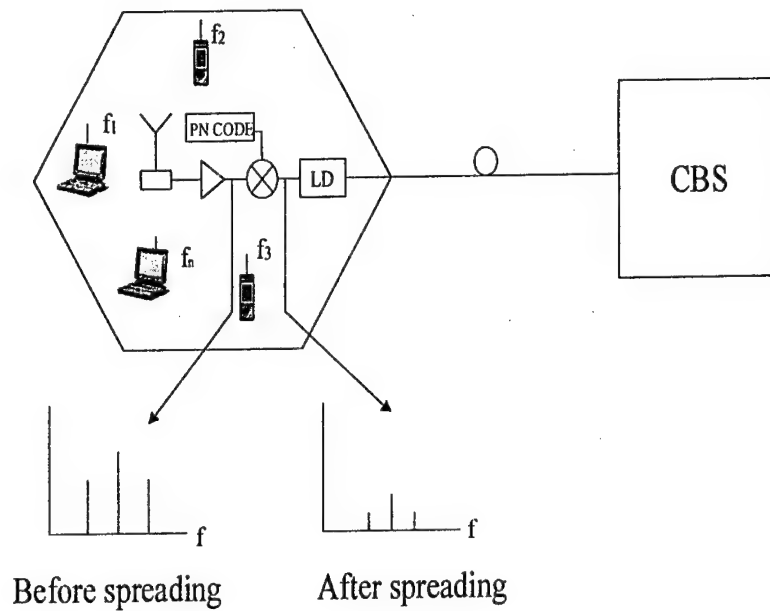


Figure 1. The optical connection between a radio base station and the central base station.

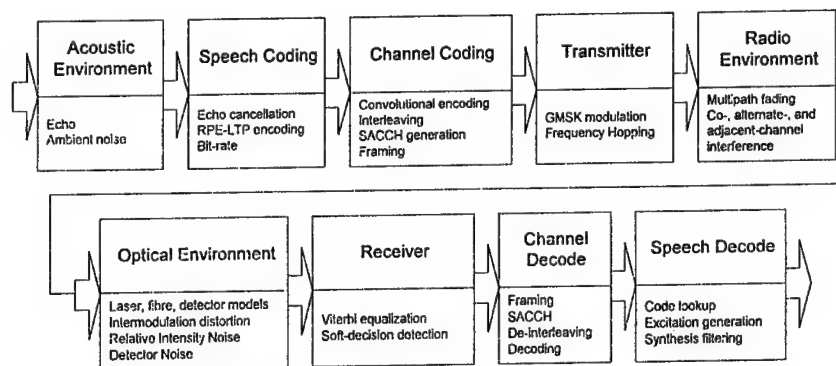


Figure 2. GSM digital speech channel simulation block diagram including the additional optical fibre link model.

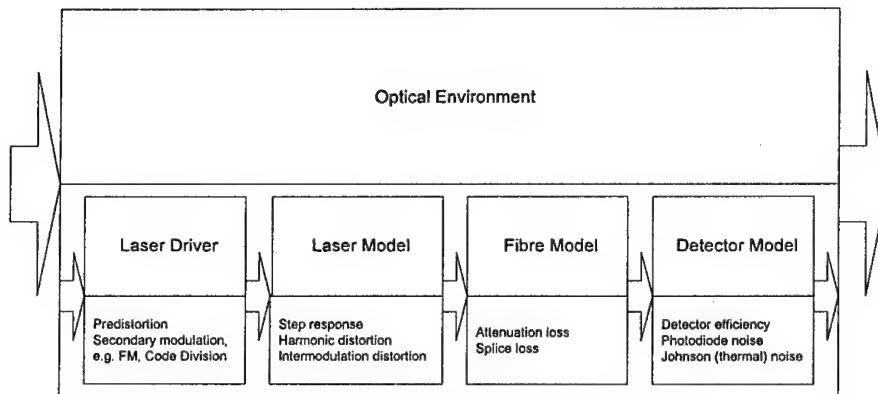


Figure 3. Block diagram of optical environment.

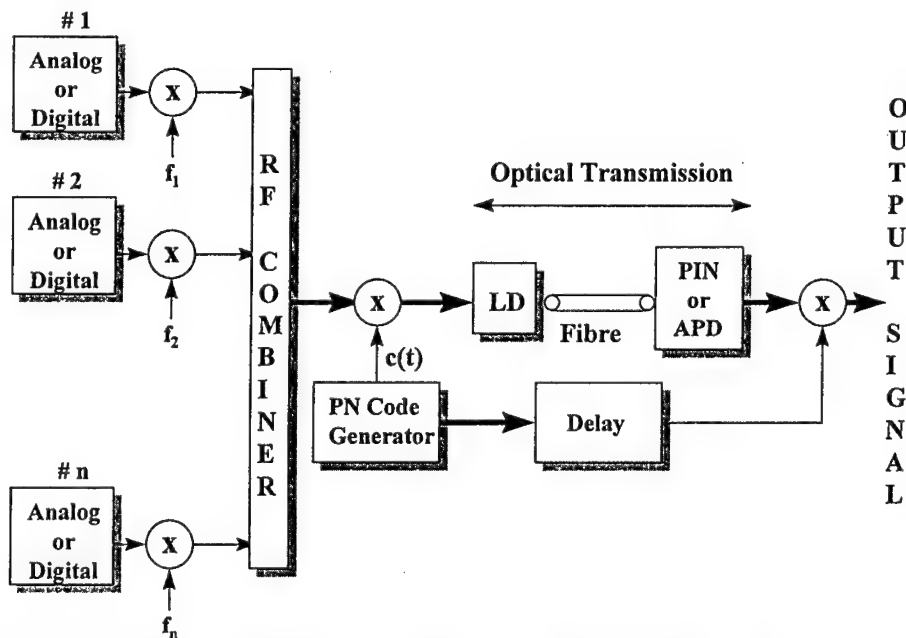


Figure 4. Block diagram of subcarrier multiplexing system using the direct sequence spread spectrum DSSS

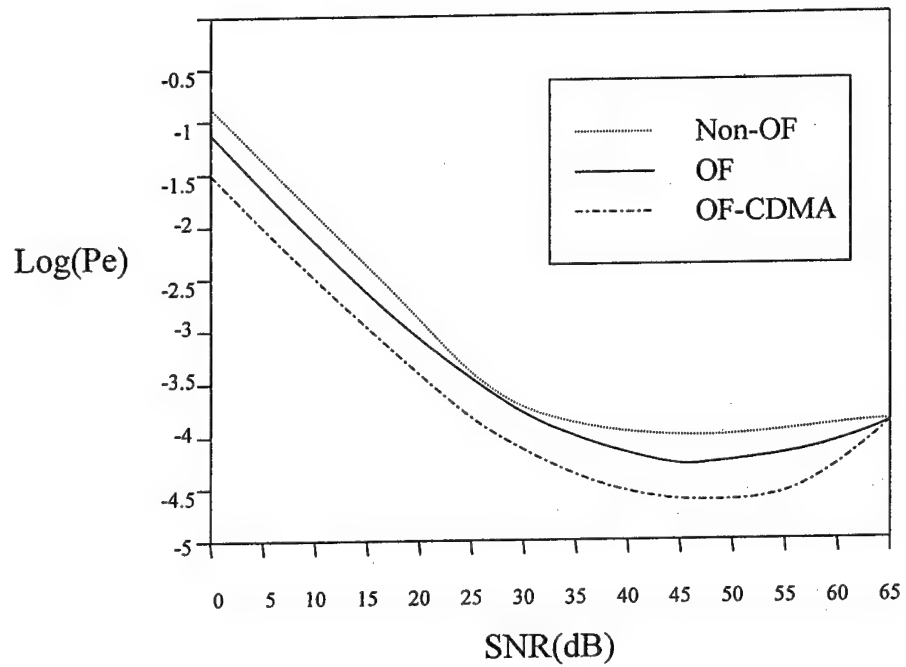


Figure 5. Probability of error versus SNR for non-optical fibre, optical fibre and optical fibre with CDMA.

Analog V-Series Modems for Embedded Internet Products

A. Miller¹
A. Moskowitz²

¹ Motorola, Inc., 6501 William Cannon Dr. W., OE10, Austin, TX 78735
rmtn10@email.sps.mot.com

² Motorola Semiconductors Israel, Ltd 1 Shenkar Street, Herzlia Industrial Zone,
Herzlia 46120 Israel, *r52711@email.sps.mot.com*

Abstract: This paper describes current implementations of wireline V-Series modems, (V.34 and V.90), by contrasting them with fixed DSP and desktop modem implementations, including Host Signal Processing (HSP) variants.

I. Introduction

The rapidly expanding infrastructure of the Internet and intranets is creating rapid development of various web appliances beyond the personal computer (PC). These appliances require wireline or wireless connectivity. For wireline connectivity there are various new possibilities through Asynchronous Digital Subscriber Lines (ADSL), cable modems, or company local area networks (LAN's). However, for the majority of subscribers in the next 5-10 years, the most common connection will be through V.34 or V.90 analog modems. With increases in processing power available from both microprocessors and digital signal processors (DSP's), various implementations of such modems are possible. This paper describes typical modem implementations, and then the structure and benefits used in porting the modem to a specific communications microprocessor that yielded a full-featured, low cost port for embedded systems.

II. Typical Modems

In the "early days of electronics history," 7-8 years ago, when the V.32 (9600 bps) analog modem was being introduced, typical modem architectures consisted of:

- A DSP and memory,
- A microprocessor and memory,
- A coder / decoder (CODEC) converting signals between digital and analog, and
- A lot of analog circuitry comprising a data access arrangement (DAA), which handled the conversions in voltage between the telephone line and the CODEC, as well as isolating various noise events that could happen on the telephone line.

A block diagram of such a modem is shown in the following figure:

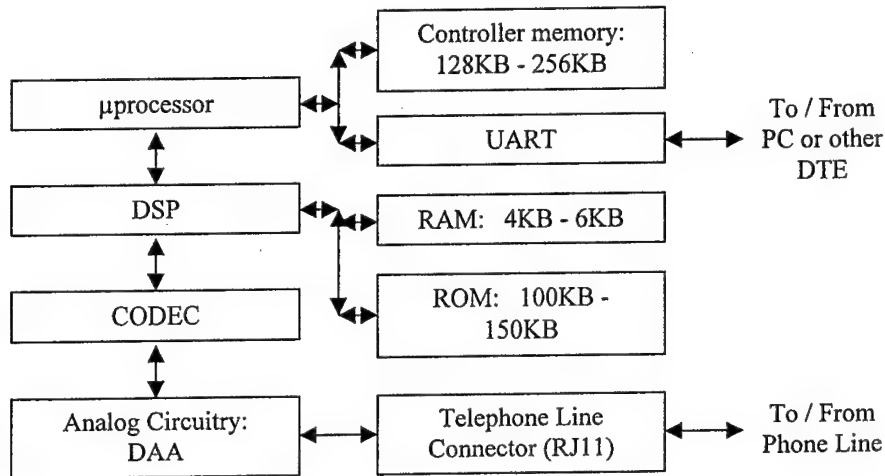


Figure 1: Typical Modem Architecture, mid-1990's

The connection from the modem to the device using the modem was typically through a universal asynchronous receiver transmitter (UART), such as the UART port on PC's. The PC did, and still does, make requests for services from the modem through a command protocol referred to as the "AT Command Set," developed by Dennis Hayes of Hayes modem fame.

The progression of events as modem speeds increased over the years led to a few fundamental changes in modem implementation:

1. CODEC's were improved with better linearity and clocking mechanisms.
2. DAA's were integrated and made programmable for worldwide capability. In some cases, the DAA has been integrated in new structures with the CODEC function. This allowed miniaturization since the circuit board area required for the analog CODEC / DAA functionality has shrunk from several 10's of square centimeters to approximately 10 square centimeters. Performance of such integrated components has also improved, and cost has decreased from 10's of U.S. dollars to less than 5 U.S. dollars.
3. The algorithms used for the modem function itself became much more intensive in the requirements for digital signal processing. A good description of the types of algorithms used along with their effects and general processing requirements, is available on the worldwide web (WWW) from Texas Instruments (www.ti.com).¹ Although this application note is too old to be of much use in current applications, it does clearly describe many issues in wireline modem design.
4. More and more implementations of modems were for PC's or the corresponding infrastructure. As PC processors became more and more powerful, it became possible to provide the signal processing on the PC host processor - usually an Intel

x86 or IBM / Motorola PowerPC™ microprocessor. On the other end of the wire, at the network interface, more powerful DSP processors have lowered the cost of infrastructure modems by providing several modem channels on a single DSP or multiple DSP's on a monolithic die.

5. V.34 (28.8 - 33.6 Kbps) / V.90 (56 Kbps) DSP implementations of modems require approximately 40 MHz processing speed for a single clock multiply-accumulate (MAC) DSP chip, while advanced Pentium or PowerPC will use approximately 60 MHz of its available bandwidth to run the modem function. In order to be able to run browsers or other applications programs, it is usually not advisable to run the modem in a host signal processing (HSP) implementation unless the host processor is running at 200 MHz or faster. Many customers still feel comfortable with a hybrid approach where the high MIPS DSP functions are still done on a DSP / CODEC / DAA board attached to the PC through an ISA or PCI interface. In this environment, the bulk of the modem code exists in the PC memory space and is run on the host computer versus a dedicated modem controller.
6. The memory requirements for modem implementations increased, both for the baseline modem function and for typical features like speakerphone, voicemail, caller identification, ... Memory requirements for a V.34 modem were on the order of 500 KB while a V.90 modem will typically use close to 1MB. It is worthwhile to note that the signal processing portion of the code, the data pump, only requires a few 10's of KB of scratchpad and code space.
7. Many modems, including of course HSP modems, have become programmable. Much of this is for features, like answering machine functionality, but in the transition from V.34 to V.90 it also became a big selling point. The main reason that this happened was because there were two competing proposals for the V.90 standard, and suppliers wanted to deliver the modems but had to promise upgrades to conform to the standard. This means that the memory used for the DSP's is now usually RAM or non-volatile memory versus the typically ROM-based modems of the early 1990's.

III. Implementing Infrastructure DSP Modems

Infrastructure modems try to put as many modems into as small a space as possible. Usually the various phone lines are switched to the DSP "channel bank" through a serial structure like a PCM-30 interface. (PCM stands for pulse-code modulation, and here the channels are usually 64 Kbps channels formed by sampling the phone line at the switch at 8K samples per second with 8-bit resolution. This is the standard method for converting an analog voice line into a digital signal for call routing through the switching network.)

The PCM interface is interconnected to multiple DSPs and control software tells each DSP what time slot(s) it is supposed to function as a modem for.

The major difference between infrastructure modem requirements relates to the implementation of the modem control code and making the modem code efficient.

As previously mentioned, modem control code is quite a large body of code and, for a normal microprocessor doing V.90, for example, can typically be done in a 10 MIPS machine. If the control software is done on a DSP, the architecture is usually not well suited to dealing with lots of off-chip code. This typically leads to one of several implementations:

1. An implementation where the DSP does the data pump and control code with lots of on-chip memory increasing the cost of the DSP significantly,
2. An implementation where there is a control processor handling modem control code for a large number of DSP's, each one running one or more data pumps.

The second implementation is the most frequently applied. New infrastructure channel banks might have 32 - 64 channels handled by 8 - 16 DSP's and a single control processor.

IV. Implementing HSP Modems

HSP modems are typically for one of two markets: applications for embedded or desktop.

In the desktop market, the biggest issue with an HSP modem is to get it to perform correctly with the desktop operating systems, such as Windows or MacOS. These operating systems are not real-time operating systems with guaranteed performance at the sample rate of modem CODECs in the thousands of interrupts per second. There are also a wide range of software applications which could be operating in the desktop environment and which could interfere with the required performance.

Nevertheless, several manufacturers, including Motorola, have successfully released HSP modems for the PC. The only concession that is required is a small integrated circuit that maps the CODEC / DAA to the PC input bus, typically ISA or PCI, and which provides a hardware first-in first-out (FIFO) buffer to lower the required interrupt rate for HSP processing into an acceptable range. These implementations also rely on the fact that the newer, faster desktop processors also provide enhanced mathematics processing capability to perform the DSP functions.

For the embedded market, HSP processing is only done on the newer, faster RISC embedded processors. These processors typically have much smaller on-chip caches and much smaller associated system memories than desktop processors. Embedded processors do use real-time operating systems (RTOS), so they are typically able to balance the embedded nature of the operating system to achieve similar results to a desktop processor for modem operation; HSP can be done with approximately 60 MHz of embedded processor bandwidth. However, the smaller caches and overall slower memory of the system also usually mean that running applications on top of the modem function is much slower than such additions would be on a desktop machine.

The remainder of this paper points out how these limitations were overcome with a specific embedded microprocessor architecture.

V. An Embedded Internet Appliance Modem Implementation

A target internet appliance microprocessor architecture is shown in Figure 3 and is implemented in the Motorola MPC8XX microprocessor family.

Internet appliances can include PC's, but also screen phones and voice-over-IP phones, beverage machines, television browser boxes, automobiles, planes, cellular phones, aircraft carriers, and refrigerators. An integrated device, such as this, is typically used where a user interface (display) and communications are required.

Systems may have a requirement to function as a bridge between one communications channel and another. For example, you might have an internet phone that can act as a wireline modem for a PC connected to the internet phone by the PC's ethernet channel. There could also include a USB connection to a local printer, or an ATM connection to a digital set top box.

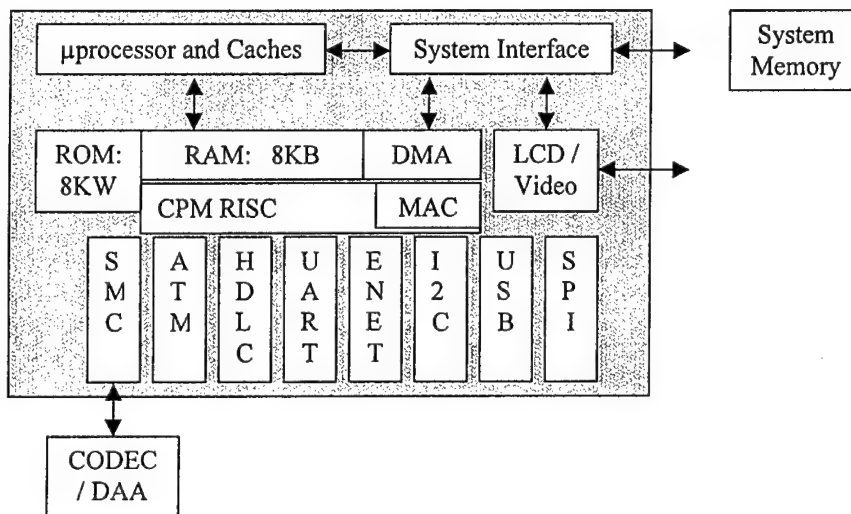


Figure 2: MPC8XX Embedded PowerPC™ Microprocessor Architecture

Implementing a modem on such a device was a challenge, because one of the targets was to have a system which can be running an analog modem and a browser written in Java.

Java is well known for its requirement to have lots of processing capacity available to it to operate well. Also, the on-chip RAM availability in the communications block is very small, with only 8KB of dual port memory shared between the processor and the communications processor module (CPM) RISC. Further, the on-chip ROM (microROM) in the communications block could not all be dedicated to the modem as it holds lots of routines for the various communications channels.

The initial path in a solution was to add a multiply-accumulate block into the arithmetic logic unit (ALU) of the RISC microcontroller in the CPM block. This MAC

was to be used in conjunction with special routines in the microROM to implement the modem in a balance between the main microprocessor and the CPM microcontroller with DSP intensive algorithms performed on the MAC in the CPM.

The method for specifying the interface to DSP routines in the microROM was to copy the method for interfacing to the communications channels. In specific, the communications software running on the microprocessor deals with the communications channels through buffer descriptor rings. These buffer descriptor rings point to data buffers that are located in system memory. Buffer descriptors contain:

- Control bits,
- Buffer pointers, and
- Length information and are 8 bytes in length.

Function descriptors, as they are called when they are in the DSP rings, are also 8 bytes in length and contain:

- Control bits,
- An op-code for the DSP function requested,
- Modulo information where needed,
- The number of times the function is to be run, and
- Pointers for input data, output data, and coefficients for the routine.

In the case of communications functions, data buffers can typically be very large and are usually located in system memory while buffer descriptors, which need to be accessed quickly when servicing a channel, are located in on-chip RAM.

For DSP functions the order is reversed: function descriptors are infrequently accessed. Data and coefficients are relatively small and are accessed at high speed in the inner loops of DSP processing. Therefore it was decided that the DSP data and coefficients would be in on-chip RAM while the function descriptors would be in off-chip RAM.

The time for getting the next function descriptor is hidden from the system by using the DMA to fetch the next descriptor in the middle of processing the present descriptor.

Since it is expected that the CPM will be concurrently handling other channels, like ethernet and USB, while taking care of modem tasks, it was decided to write the DSP routines as standalone blocks. Thus each DSP routine goes through a setup procedure initializing the CPM pointers and counters and then processes the inner loop of the algorithm. When the inner loop is done, the routine is "put away," much like calling an object in Java or C++ and the CPM interrupt controller is checked for pending tasks. FIFO's in the communications channels and the operating speed of the CPM are balanced to make sure that the channels operate correctly in this environment.

In many respects this worked very well. A typical CPM DSP routine was on the order of 50 instructions so a small amount of on-chip ROM could hold many DSP routines. Also, a single routine could be re-used multiple times on different data. The MAC is also well tuned and, in complex routines, averages very close to one MAC per clock.

One cloud early on in the project, which ended up having a silver lining, was that the interrupt load and synchronization requirements to have the microprocessor and CPM microcontroller share tasks back and forth in the data pump was too high. But a quick analysis showed that was possible to use the microprocessor to do the state transitions for the data pump during training. This kept the size of the routines required to be in memory on-chip at any given time small. There was also sufficient time for the microprocessor to re-load the CPM memory with the next state and to assist in training.

Finally, since this work was being done while the V.34 and V.90 standards were in progress, it was also necessary to be flexible in some DSP routines; they couldn't all be put into microROM.

This requirement was handled by the capability of the device to have "microROM routines" actually function from the on-chip RAM. This is called "download ROM."

The end results show the effectiveness of this approach with the following statistics:

- Microprocessor MIPS required in data mode: less than 10
- Microprocessor MIPS required during training: less than 35
- Microcontroller peak MIPS, V.34 or V.90: less than 22
- Interrupts to microprocessor during data mode: 0
- Peak on-chip RAM requirements including download RAM, Coefficients, inputs, outputs: less than 5KB
- Total MicroROM DSP codes space: Less than 2K words
- Total function code list, combined transmit and receive chain: Less than 1KB

VI. Summary

This paper has described typical DSP and microprocessor implementations of modems, and has then described a unique implementation of wireline modems on a communications microprocessor. Contrasted to HSP implementations, this implementation leaves the embedded microprocessor virtually free to handle user tasks while the communications channel is kept open by a flexible communications processor. When compared to a pure DSP implementation, the cost is kept low by keeping on-chip memory requirements low through a set of unique implementation characteristics.

References

- [1] V.34 Transmitter and Receiver Implementation on the TMS320C50 DSP, spra159.pdf – www.ti.com, June 1997.

Implementation of Telecommunications Department of FEI STU into the ATM Network in the Slovak Republic – The Pilot Project

I. Baroňák

*Dept. of Telecommunications, Slovak Technical University, Ilkovičova 3,
81219 Bratislava
baronak@guy.stl.elf.stuba.sk*

Abstract. At Department of telecommunications Faculty of Electrical Engineering and Information Technology at the Slovak Technical University in Bratislava within the years 1995-98 there were realized activities to solve the tasks of private telecommunications networks and services as a part of the branch project 101/240/1995.

There was followed Department of telecommunications endeavour in the conditions of Faculty of Electrical Engineering and Information Technology at the Slovak Technical University in Bratislava to build up the modern, technological workplace oriented to support particularly the scientific-technological and educational activities of the university, workplaces of the Slovak Telecom, the Research Institute of Telecommunications and also companies which are concerned with implementation of the telecommunications technology into PSTN in the Slovak Republic.

1 The Pilot Project of Department of Telecommunications implementation at Faculty of Electrical Engineering and Information Technology into the ATM network

The natural resumption of the project is the effort to utilize the results of the project successfully in the activities which are oriented to the area of the broadband telecommunications. In the present area also our workplace is obliged to fill important functions for the future (science, research and education), and therefore the pilot project of building up the ATM (Asynchronous Transfer Mode) node at the Department of Telecommunications Faculty of Electrical Engineering and Information Technology in Bratislava does not have other choice and it is need and right step.

The single project Private telecommunications networks and services, as it was drafted and solved at the Department of telecommunications Faculty of Electrical Engineering and Information Technology in Bratislava, has created the favourable conditions to continue in solving of other tasks of scientific-technological character- especially oriented on the broadband telecommunications systems, networks and services.

The content of the solving task was following :

1. Building up the ATM node (switch) in the area of the experimental and educational laboratory at the Department of telecommunications Faculty of Electrical Engineering and Information Technology in Bratislava and realization of its implementation into the lap ATM network in the Slovak Republic.
2. Realisation of completion of the existing ISDN technology (PABX A4300L) and technology of LAN network with technical and programming moduls for the performance of broadband communications in the connection to the ATM node.
3. Extension of the existing opportunities of videoconference (N-ISDN) in the experimental and educational laboratory of the Department of telecommunications Faculty of Electrical Engineering and Information Technology in Bratislava, with the following building of video-conference workplace up.
4. Along with point 2 realization of interconnection into the ATM network of the Slovak Republic. The present activities should be oriented the way to create the functional interconnection to the Technical University in Košice and the Research Institute of Telecommunications in Banská Bystrica and to create conditions for experimental verification of long distance broadband video-conference transmission and fast data transmission (for optional applications including of tele-education). Using of such transmission speed for the mentioned versions, that enable to realise test activities to verify application services.
5. In the connection to the established ATM node to realise and laboratory verify technologies for Wireless access network in the application connection to, the Research Institute of Telecommunications (Banská Bystrica). Orientation of experimental activities to opportunities to apply the mentioned technologies for the purpose of flexible realization of broadband video-conference and fast data transmission (for example in the health service).
6. Intro the project to solve the procedure of transmission of other protocols trough the ATM (Frame Relay-voice and data, IP protocol-Internet and Internet atc). To verify mentioned activities in accordance with the needs and requests at the Department of telecommunications Faculty of Electrical Engineering and Information Technology in Bratislava in Bratislava.

In the connection with the project Private telecommunications network and services the aim of the planning task was building up the technological and functional infrastructure at the Department of telecommunications Faculty of Electrical Engineering and Information Technology in Bratislava covering the problems of broadband networks and services in link to the B-ISDN process.

Results of such drafted aim create the real assumes for the developing of cooperation with the Slovak Telecom, state enterprise for next years, and present technical basis for fulfilling of the most difficult tasks.

Considering of the fact that task was formulated in the 4th quarter of the year 1998 - content and organisation aims of the task were subordinated to the shortage of time and real opportunities to build up the technological ATM node at the Department of telecommunications in Bratislava with the cooperation with the Slovak Telecom and implementation of this node into the ATM network in the Slovak Republic. Listed task presented the centre of the Pilot Project.

2 Conditions of realization of the Pilot Project

The group of solvers followed the tendency of tasks solving, so that their realization and verification were bound to the real technical environment- to the broadband ATM network, activated since September 1998 in conditions of the Slovak Telecom and whole area of the Slovak Republic.

It meant to realise the interconnection of telecommunication and computer technologies of the Department of telecommunications Faculty of Electrical Engineering and Information Technology in Bratislava on the technological ATM system of network of the Slovak Republic (Metropolitan network Bratislava).

The main tasks of the whole Pilot Project were divided into three parts:

1. Building up the ATM junction (switch) and realization its implementation to the lap ATM network in the Slovak Republic in the workplace of experimental and educational laboratory of the Department of telecommunications Faculty of Electrical Engineering and Information Technology in Bratislava.
2. Realization of completion of the existing ISDN technology (PABX A4300L) and technology of LAN network with technical and code modules for performance of broadband communication in connection to the ATM node.
3. Extension of the existing possibilities of video - conference (N-ISDN) in experimental and educational laboratory of the Department of telecommunications Faculty of Electrical Engineering and Information Technology in Bratislava, with the followed establishment of the video - conference workplace.

To realise the needs of the Pilot Project there was necessary to secure:

1. ATM technology (switch)-type APEX MAC 1 (2x155 Mbit/s) from the GDS company.
2. Creation of the necessary project documentation to install technology in the field of the Department of telecommunications Faculty of Electrical Engineering and Information Technology in Bratislava.
3. Realization of connection and implementation of the ATM node into ATM lap network (MAN Bratislava) through the optical fibre with the transmission speed 155 Mbit/s.
4. Available/needed modules-interface for possible interconnections of infrastructure of the Department of telecommunications Faculty of Electrical Engineering and Information Technology in Bratislava into the ATM network. The result is the technical support of modules-interfaces and there are: 4xE1, 4xCe, 4xEthernet and 1x 155 Mbit/s.

Detachable architecture of the technical means for the Pilot Project presents the integration of LAN network and branch exchange of ISDN rank into the ATM node with the following connection to the ATM metropolitan network of Bratislava.

In the case of LAN network there is connection of Ethernet at the level of 10 Mbit/s. Previous intention was to connect LAN into the ATM node through the module 100 Mbit/s. The mentioned module is not available at this time.

In the case of ISDN private telecommunications network on the base of PABX of Alcatel A 4300L system there is connection into the ATM node through the E1 module with transmission speed 2,048 Mbit/s which is supported by the manufacturer Alcatel company.

According to the consultation with the representants of the company ensued that Alcatel disposes modul for PABX A4300L for connection on the base 155 Mbit/s direct through the optical fibre (UNI 3.2), there was offered the cooperation to verify the mentioned type of connection in the conditions of the Slovak Republic at the Dapartment of telecommunications Faculty of Electrical Engineering and Information Technology in Bratislava.

3 Architecture for the broadband infrastructure

To solve the tasks of the Pilot Project there were some possibilities how to built up the broadband infrastructure.

The group of solvers have not supported the tendency to solve the isolated broadband structure, but have oriented the project to implementation already existing computer and ISDN private telecommunication network into the ATM enviroment.

The chosen architecture answers a purpose for more reasons:

1. Relatively cheap and lap functional integration of LAN network and ISDN private telecommunications network into the ATM enviroment.
2. Open for implementation of farther technologies.
3. From the view of broadband applications presents the multi-purpose enviroment.
4. Mainly covers conditions for the solving of the tasks from the view of coexistence and migration of the technological means into the broadband applications (ATM enviroment).

3.1 Description of architecture of network at the Department of telecommunications

Architecture of the technical means is at the picture 1.

As it is clear from the picture, it is joined from the ATM node (Apex MAC1) which is connected through the optical fibre to the node of the metropolitan ATM network Bratislava (Nábělkova ulica) and there is used up the accessing optical port 155 Mbit/s.

The present optical connection was enabled by connecting to already built optical contact (20 fibres connection) of the Department of telecommunications Faculty of Electrical Engineering and Information Technology in Bratislava that is a part of urban optical SDH network (circuit 2-level STM1). There is necessary to emphasize that the connection to the PSTN through optical network SDH at present is used by the ISDN private telecommunication network - A4300L (2x PRI ISDN), and the interconnection is directed to the connecting system EWSD in Petržalka and S12 on the SNP square.

The ATM unit MAC1 provides for the internal connection opticalport with the accessing speed 155 Mbit/s. For solution of the Pilot Project we do not count with its utilization in the first phase.

The ATM node was mounted by followed modules-interfaces to connect the internal infrastructure of the Department of telecommunications :

1. Module 4 x port Ce (n x 64 kbit/s),
2. Module 4 x port E1 (G.703),
3. Module 4 x Ethernet (10 Mbit/s).

For the purposes of the project there was realised the connection of LAN network into the place of dislocation of the ATM node with metallic technic (termination RJ 45). Connection was realised to the ATM node from port Ethernet (10 Mbit/s).

Farthermore there was realised the connection ISDN branch exchange Alcatel A4300L into the place of dislocation of the ATM node by the metallic technic (termination BNC). Connection was realised on ATM node to E1 port (G.703-2,048 Mbit/s). On this purpose was PABX supplemented by the module for communication through E1 port (G.703-2,048 Mbit/s). There is a need to emphasize and the picture 1 documents that the ISDN connections on the level PRI (2 x 2,048 Mbit/s) between A4300L and PSTN stay farther functional and this will be used up in the future to solve tasks of cooperation N and B ISDN environment (technical and functional).

For the purposes of the project were verified by experiments the facilities for realization of ISDN teleservice Videotelephones and on the interface S0 (BA ISDN) in the experimental and research laboratory. Equipment for experiment we have received from Alcatel company (2x PictureTel) and Siemens (2x IVIEW).

In both cases the equipments realise the service to support signalling DSS1(Euro ISDN) and according to experiments carried out on PABX ISDN Alcatel 4300L can work with the utilization of digital channel 64 kbit/s or 2 x 64 kbit/s, so with the utilization of the ISDN channel structure BA ISDN (2B+D).

Farther extension of possibilities of the existing videoconferences on the base N-ISDN in the experimental and educational laboratory of the Department of telecommunications Faculty of Electrical Engineering and Information Technology in Bratislava will be done by experimental loading of the videoconference systems VIDEO ALCATEL 3276 (3x BA ISDN).

Mentioned system presents relatively cheap solution for the creation of the videoconference workplace (place) without necessity to create the channel of H type in ISDN network.

3.2 Description of ATM node implementation into ATM network in the Slovak Republic

The effort of the Pilot Project was not to create the isolated ATM node. Creating of the node there are followed possibilities of connection into the whole slovak wideband network, which is serviced by the Slovak Telecommunications, state enterprise. Essentially there is the aim to create some assumptions for farther experimental and research projects and experiments for the technological, network and functional area. There is natural effort to realise and verify the assumptions of the projects presenting the possibilities for the application of broadband services into the society infrastructure.

In the mentioned aspects the Pilot Project fulfils these expectations because by optical connection to the node-Nábělkova ulica-with the accessing speed 155 Mbit/s there has been connected the ATM node at Department of telecommunications Faculty of Electrical Engineering and Information Technology in Bratislava into the metropolitan network MAN Bratislava.

At this place there is necessary, after considering of the situation of the Pilot project, to say that the aim is not only connection into ATM network of the Slovak Republic already in the first phase, but also the solving of wideband connection among:

1. Department of telecommunications Faculty of Electrical Engineering and Information Technology in Bratislava and the Technical University in Košice (purpose: fast data transmission, videoconference, cooperation on the verification of the broadband applications,...).
2. Department of telecommunications Faculty of Electrical Engineering and Information Technology in Bratislava and the Research Institute of Telecommunications in Banská Bystrica (purpose: fast data transmission, verification ISDN PABX connection from the view of transparency of ISDN services, verification of the possibilities of using up wireless broadband units and their connection through the ATM network on the purpose of videoconference in the health service facilities,...).

In the first phase there is functional connection of three nodes through the WAN network and verification of the possibility for broadband communication. Single picture 2 marks only interesting points and does not show complete topology of the ATM network in the Slovak Republic.

According to information from the Slovak Telecom, state enterprise there will be possible to assume the use of transmission speed to 20 Mbit/s for the purposes of the experimental work for the year 1999.

4 Perspective of utilization of the Pilot Project

There might be distinguished tasks of the nearest year 1999 but also tasks that continue the present year.

In the range of preparations of the Pilot Project there were realised many meetings and conferences not only with the representants of the Slovak Telecom, state enterprise, and the Research Institute of Telecommunications Banská Bystrica, but also with the representants of the foreign companies in our country (Alcatel, Siemens). Impulses from the meetings will be included in the formulating of the new tasks of scientific and technical trends for the next period.

On the other hand the realization of the mentioned three tasks we prepare for the first half of the year 1999. Their successful termination is for us significant. There are followed tasks:

1. Realization of the broadband transmission of data among the workplaces the Research Institute of Telecommunications Banská Bystrica, TU Košice and the Department of telecommunications Faculty of Electrical Engineering and Information Technology in Bratislava.
2. Realization of the videoconference transmission among the workplaces TU Košice, the Research Institute of Telecommunications Banská Bystrica and the Department of telecommunications Faculty of Electrical Engineering and Information Technology in Bratislava, with the verification of its possibilities.
3. Realization of the broadband videoconference transmission with the application into the health service system between the Roosevelt Hospital in Banská Bystrica and the Hospital on Kramáre in Bratislava. To solve the videoconference there should be used the wireless wide bound units. The base stations should be situated in the Research Institute of Telecommunications Banská Bystrica and at the Department of telecommunications Faculty of Electrical Engineering and Information Technology in Bratislava and the

remote transmission will be realised through the ATM network. The mentioned situation as it is drawn will be presented during the conference.

There is a high assumption that the conditions for the realization will be successfully verified in the short term and the following experiments can be realised.

The single task in the point 3 opens the opportunities for our workplaces to participate on the European projects of Information Society namely for the area of the Health Service system (TEMEP Telemedicine Services Delivered to the Point of Need). The project presents the extremely meaningful application of videoconference in the human area.

For the presented aim of the project there has been made an agreement between the Research Institute of Telecommunications Banská Bystrica and the Department of telecommunications about the common process of solving of conditions to achieve the experiment in the presented area. Among the chosen workplaces there belong Rooswelt Hospital in Banská Bystrica and the Cardiovascular Centre in the Hospital in Kramáre in Bratislava.

By itself realization of the videoconference in the represented application according to the last specifications there is needed the channel with the transmission speed 20 Mbit/s (Siemens + NewBridge...).

Conception of the prepared project-application, does not remain strictly on the solving of technical connection into the accessing network only through the metallic and optical sphere. Project goes on and has ambition to solve the interconnection between transport bands and application place with the help of broadband wireless units of accessing network.

Naturally the presented questions exceed the range of this project, therefore we will not specify the technical and functional conditions at this place. We can only remark that application of the broadband videoconference without the need of fixed broadband connection into the accessing network (metalics, optic), multiplies the opportunities for the various application and definitely we see great perspective in such oriented project.

5 Conclusions

The Department of telecommunications Faculty of Electrical Engineering and Information Technology in Bratislava as the educational institution understands the need and takes the initiative in some process that influences successful implementation of the modern telecommunication services into the life of society.

The workplace in the presented area has solved a lot of important research tasks and scientific projects in last period.

At the Department of telecommunications we have realised and installed in very short time the ISDN private telecommunication network and namely even in advance before the society practice and we have also realised from the view of telecommunication system unique hybrid system (cooperation of signal systems).

In the nearest future we want to orientate to the solving of already presented application of broadband services with our famous partners and also to work on the preparation and definitions of the tasks connected with the cooperation N and B ISDN means, solving of the migration of the telecommunication technologies into the broadband environment (technologies, compatibility and transparency of services, quality of provided services, supervision of broadband network and so on).

In spite of these tasks are waiting for solution, theoretical and practical preparation is the best way to manage them. Therefore we emphasize this Pilot Project so much as the mean to start theoretical and practical activities in the B-ISDN environment.

References :

- [1] ITU-T Recommendation I.363_1 : B I-SDN ATM Adaptation Layer specification : Type 1 AAL.
- [2] ITU-T Recommendation I.363_5 : B I-SDN ATM Adaptation Layer specification : Type 5 AAL.
- [3] ITU-T Recommendation Q.2660 : Interworking between Signalling System No.7 – Broadband ISDN User Part (B-ISUP) and N – ISDN User Part (N-ISUP).
- [4] ITU-T Recommendation Q.2931 : Digital Subscriber Signalling System No.2 (DSS2) – User Network Interface (UNI) Layer 3 Specification for Basic Call/Connection Control.
- [6] Medvecký, M.: ATM and IP Networks Internetworking. 3rd International Workshop of TEMPUS TELECOMNET Project. Košice, 2nd Sept.1997.

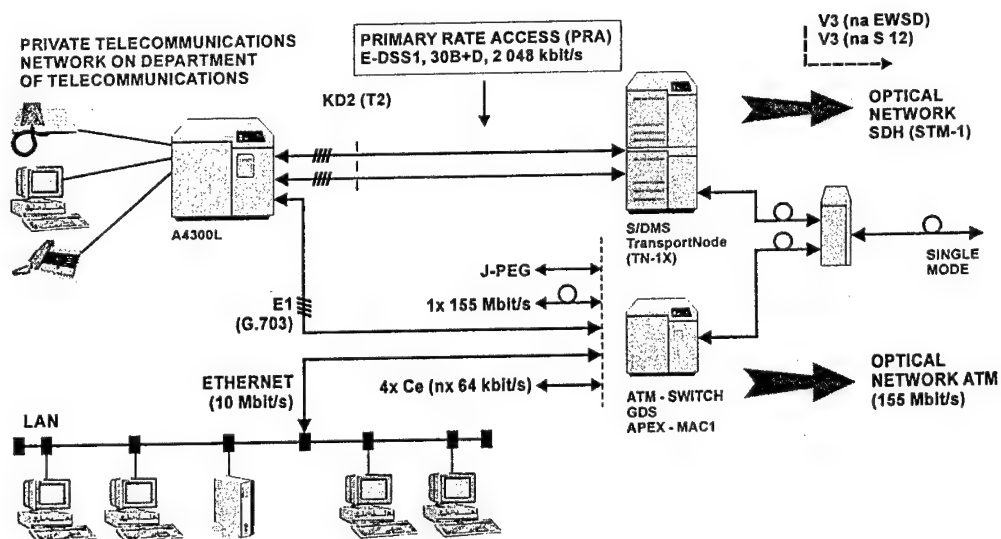


Figure 1.

Design and Test of Next Generation Integrated Systems Embedding MEMS

S. Mir

*TIMA Laboratory, 46 Av. Félix Viallet, 38031 Grenoble, France
salvador.mir@imag.fr*

Abstract. This paper presents an overview of microelectromechanical systems (MEMS) research topics. Manufacturing technologies, including bulk and surface micromachining, are illustrated using fabricated devices. Optimal exploitation of these technologies relies on the integration in a single chip of MEMS parts with their electronic interfaces. Current challenges for bringing the analysis, design and test of these new generation of devices in line with microelectronics are then discussed.

I. Introduction

Manufacturing batch processes initially developed for IC fabrication are at the heart of the rapidly growing MEMS technologies. This is because the principles governing the manufacturing of MEMS are an evolution of microelectronics. Superposition of different thin film layers is used for implementation. In addition to electrical phenomena, MEMS exploit other phenomena occurring in these layers in the mechanical, thermal, chemical, radiant or magnetic domains.

At the current stage of MEMS technology development, much work is still carried out within research laboratories. The two primary classes of MEMS devices are sensors and actuators, but a wide range of micromachines have already been demonstrated. Transfer to industry is increasingly taking place in applications such as accelerometers, pressure sensors, chemical and flow sensors, or microoptics. Optimal exploitation relies on the integration in a single chip of MEMS parts with their electronics interfaces, which provides scope for very low cost production and significant improvement in system reliability.

As technological hurdles are removed and stable fabrication processes emerge, research efforts shift towards the design of systems of increasing complexity where limitations are only those stemming from the imagination of researchers and engineers. Before this advanced stage can be reached, as for microelectronics, new CAD methodologies and tools need to be developed for MEMS. MEMS design is still a very complex process, which is not approached in the analytical hierarchical style of microelectronics. Computational methods at a very low level of abstraction are necessary, and the lack of adequate higher levels of abstraction makes very difficult a systematic approach to the design of larger systems. In addition, as these systems grow in size and the levels of integration increase, testing becomes a major barrier.

This paper provides an overview of MEMS research topics. After introducing the most basic technologies, current challenges for bringing the design and test of MEMS parts in line with microelectronics are discussed.

II. Fabrication methods

The most common processing techniques for microelectromechanical systems include bulk and surface micromachining.

CMOS-compatible bulk micromachining provides a low cost monolithic solution for the integration of MEMS [1]. A commercial CMOS process is followed by a selective anisotropic etching post-process. Silicon etching takes place over some preferential crystallographic planes, which have a much faster etching rate than other planes. The selective removal of silicon etches wells in the substrate, giving place to membranes, cavities, masses and bridges which are basic MEMS components for combination with microelectronics. For example, suspended parts such as bridges and membranes have a good thermal isolation from the bulk. This is typically exploited in devices such as infrared sensors, electrothermal converters and thermal pixels. Bulk micromachining can take place from the front side, back side or both.

Front-side bulk micromachining has often been used by CMP since allows low cost maskless silicon etching. A cross section of a bulk micromachined suspended structure is shown in Figure 1(a). During layout, areas of naked silicon exposed for micromachining are created by stacking a contact, a via and an open in the passivation. Suspended structures are made of a sandwich of oxides (LOCOS, gate and interlevel oxides), nitride passivation, polysilicon and metal levels. Anisotropic etching takes place in areas of exposed silicon, creating a cavity with the shape of an inverted pyramid. The etchants used include EDP, KOH and TMAH. EDP has the advantage that does not significantly attack aluminum, and it does not attack passivation layers, although is highly toxic. KOH allows very clean surfaces and etching plans, but has the disadvantage that it attacks aluminum. TMAH has the fastest etching rate, and does not attack aluminum pads when silicon or silicic acid are adequately dissolved in the solution, but pyramidal protuberances (hillocks) may appear at the bottom of the cavities created.

The Electro-Thermal Converter (ETC) shown in Figure 2(a) has been fabricated by means of this process. ETC devices are typically used as true rms converters, transferring the root-mean-square value of an AC voltage or current to its equivalent DC value. The schematic diagram of Figure 2(b) shows the ETC (without interface electronics) composed of a cantilever beam which supports a heating resistor at its end and a thermopile. The resistor transforms the electrical input into heat which flows by conduction through the beam, by convection into the air surrounding the beam, and by radiation. The fact that the beam is suspended leads to an increase in thermal resistance between the resistor

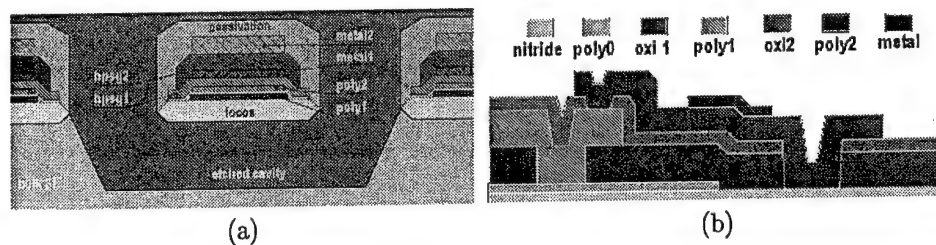


Fig. 1. MEMS technologies: (a) CMOS-compatible silicon-bulk micromachining, and (b) three-poly surface micromachining [1].

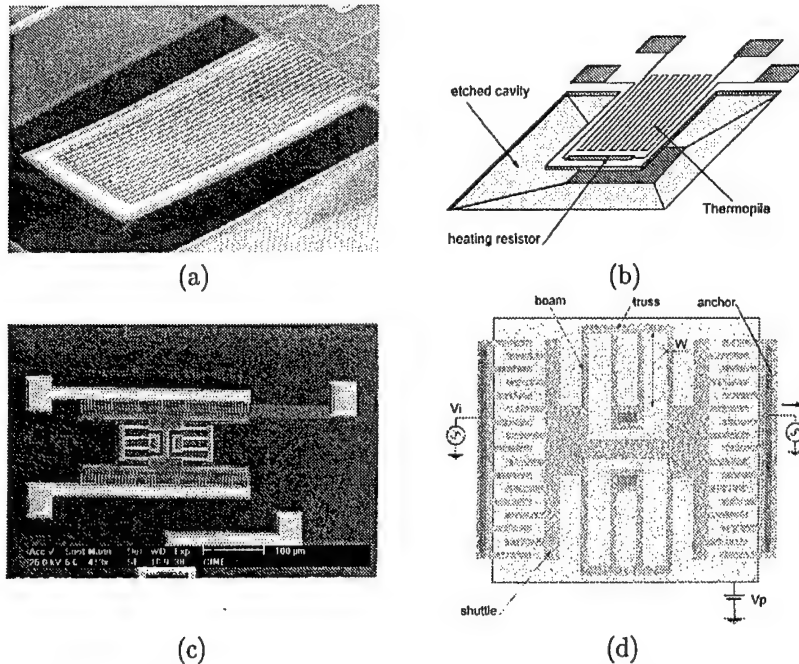


Fig. 2. MEMS examples: (a) SEM of CMOS-compatible silicon-bulk micromachined electro-thermal converter, (b) schematics of the ETC, (c) surface micromachined 300 kHz microresonator, and (d) schematics of the microresonator.

and the substrate (which acts as a heat sink and corresponds to thermal ground). This increase in thermal resistance results in higher beam temperatures. The thermopile, which senses the temperature gradient and produces an output voltage, is made of a set of thermocouples connected in series. Each thermocouple is made of a couple of n- and p-type polysilicon, which have different Seebeck coefficients α . One side of each thermocouple is at thermal ground (T_{cold}) and the other side is near the heating resistor (T_{hot}), so that an electrical voltage is generated between both ends of each thermocouple when a temperature gradient $\Delta T = (T_{\text{hot}} - T_{\text{cold}})$ exists. The total voltage at the thermopile output is the number of thermocouples times the voltage through one of them.

Surface micromachining technologies are having increasing success in the fabrication of complex MEMS. Typically, microaccelerometers based on sensing capacitance changes and microfilters can be produced. Devices including many suspended elements, such as electrostatic comb-drives and microgears for microengines, are also appearing together with libraries of suspended elements and adequate structured design methodologies [2]. Surface micromachining is based on the deposition of thin films on the surface of the wafer. The micromechanical layer is normally polysilicon or nitride. Polysilicon is a material frequently used for both electronics and sensors. Silicon nitride is the second main material used in mechanical layers since is mechanically strong with low optical absorption. The stress level in both materials is highly dependent upon both deposition

parameters and subsequent thermal processing. A sacrificial layer of a material such as silicon oxide, polysilicon, porous silicon or aluminum is also deposited. A postprocessing operation removes this sacrificial layer to suspend the micromechanical part. Various types of oxides including thermal oxide, LPCVD (LTO, PSG, BPSG) and PECVD can be used having each advantages and disadvantages in terms of quality, etch rate or thickness uniformity.

Figure 1(b) shows a cross section of a microstructure fabricated via the MCNC Multi-User MEMS Process (MUMPs) [3]. This is a MEMS specific technology, using three polysilicon levels: Poly 0 on nitride for electrodes and interconnections, and thick Poly 1 and Poly 2 for structural layers. A metal layer (on Poly 2) is used for optical and electrical purposes. Contact cuts in the phosphosilicate glass (PSG) layer allow for the formation of mechanical anchor points, which fix a microstructure to the silicon substrate. The microstructures are suspended by immersion of the chip in a bath of HF (hydrofluoric acid). This wet chemical etch removes the sacrificial PSG layers that encapsulate the movable parts. In Figure 1(b), the Poly 2 structural layer will be released after removing the sacrificial oxides underneath. This technology allows many applications such as accelerometers, micromechanical resonators or electrostatic micromotors.

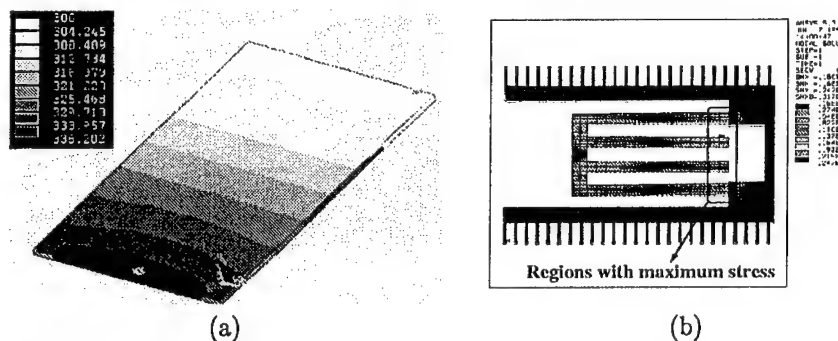
Figure 2(c) shows an example MEMS resonator. MEMS resonators are being proposed for highly selective micromechanical filtering for wireless communications and high-Q oscillators [4]. As shown in the schematics of Figure 2(d), the resonator is a mechanical mass-spring-damper system consisting of a central shuttle mass that is suspended by two folded-beam flexures. The topology of the suspension is designed to be compliant in the x direction (direction of motion), and to stiffen against y -direction and torsional movement to keep the fingers of the comb-drive transducers aligned. The comb-drive transducers (interdigitated finger structures) are used for exciting and sensing vibration parallel to the plane of the substrate [5]. They are DC biased with a voltage V_p applied to the shuttle mass via the anchor points of the suspension (three pads can be seen in the resonator of Figure 2(c) for input, output and DC bias). An electrostatic driving force is generated by the input voltage, which can make the resonator vibrate when the input frequency is close to the resonance frequency of the suspended microstructure. The vibrations of the central mass generate a current in the output comb-drive capacitive transducer.

III. Design methodology

In general, MEMS design is a complex process which is not approached in the traditional hierarchical and analytical style of microelectronics. It often requires solving for strongly coupled non-linear partial differential equations. Thus, MEMS devices are often designed at a low level of abstraction using exact computational methods or at a high level of abstraction using signal flow analysis. On one hand, signal flow analysis does not provide a direct linkage between physical layout and behavioral simulation due to the high level of abstraction. On the other hand, computational techniques such as FEM are very general but they are arduous and time consuming for system design, due to the low level of abstraction and the lack of design hierarchy.

FEM models are difficult to construct and simulation is very time consuming. In the case of the ETC converter, a coupled FEM electrothermal analysis gives back a temperature map of the cantilever as shown in Figure 3(a). The global geometry of the ETC is

represented by a set of nodes coupled with their neighbors, each node having in general several degrees of freedom. Values of thermal capacitance and thermal conductances are required for the beam material. Boundary conditions are imposed on substrate nodes which must be at thermal ground. The loads applied to the system include the voltage difference at the resistor inputs and heat convection on surfaces with air contact. For the microresonator, a coupled electromechanical FEM analysis is very difficult to perform. Mechanical FEM simulations can be performed to check for stress and deformations in the microstructure shuttle and the supporting folded beams. The beams must be sufficiently wide in order to support a maximum stress in the regions indicated in Figure 3(b), given that their thickness is fixed by the MUMPS fabrication process.



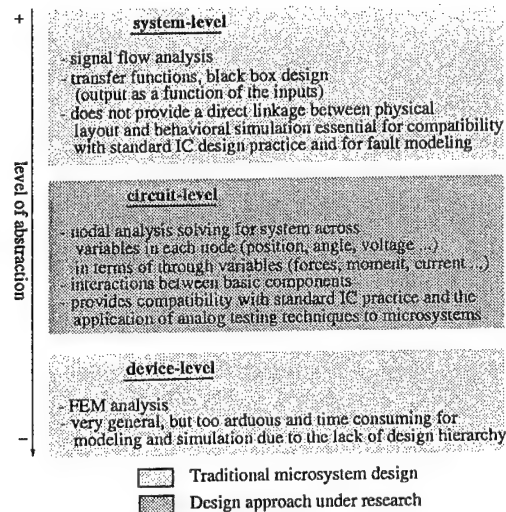


Fig. 4. Levels of abstraction in the microsystem design flow.

sistor and outputs of the thermopile. The heat transfer in the microstructure is modeled by means of an one-dimensional heat transmission line, as suggested by the FEM results of Figure 2(a). The heating power generated in the input resistor is modeled as a heat source coupled to the transmission line, where each thermal element models the thermal conductances and thermal capacitance of one beam portion. Thermal conduction, convection and radiation losses are modeled by means of equivalent thermal resistors. The substrate of the microstructure is treated as a heat sink at room temperature and corresponds to electrical ground. Figure 5(d) shows the simulation of the ETC when a pulse excitation of 1V of amplitude and 25 ms of width is applied as input. Each curve shows the evolution in time of the temperature ($^{\circ}\text{K}$) in different nodes of the beam, the higher the curve the closer the node to the input resistor.

Circuit-level simulation of the microresonator involves decomposing the device into components having electrical and mechanical interfaces. Each component contains nodes for coupling with other components. Circuit simulation solves for system across variables in each node (for example, position x, y , angle θ and voltage) by making the sum of through variables in each node (forces in x and y directions, moment about θ and current) equal to zero. Component models which relate multi-domain through variables in terms of across variables can be built with an A-HDL language, and structured design schematics can be captured. A first approach is shown in Figure 5(b). Components include two comb-drive transducers, one mass-spring-damper system, and a transimpedance amplifier for current-to-voltage conversion. A simple one-dimensional (x -translation) HDL-A model for the comb-drive component is used. The results of AC simulation for the mechanical displacement of the shuttle and the output voltage are shown in Figure 5(e) illustrating the band-pass filtering behavior. A more refined circuit-level approach requires the analysis of the interactions between basic components such as beam flexures, electrostatic gaps, plate masses and anchors. As an example, Figure 5(c) shows the schematic capture of a microresonator mass-spring-damper system for circuit-level analysis. A beam flexure, for example, is represented as an element having two nodes with three mechanical

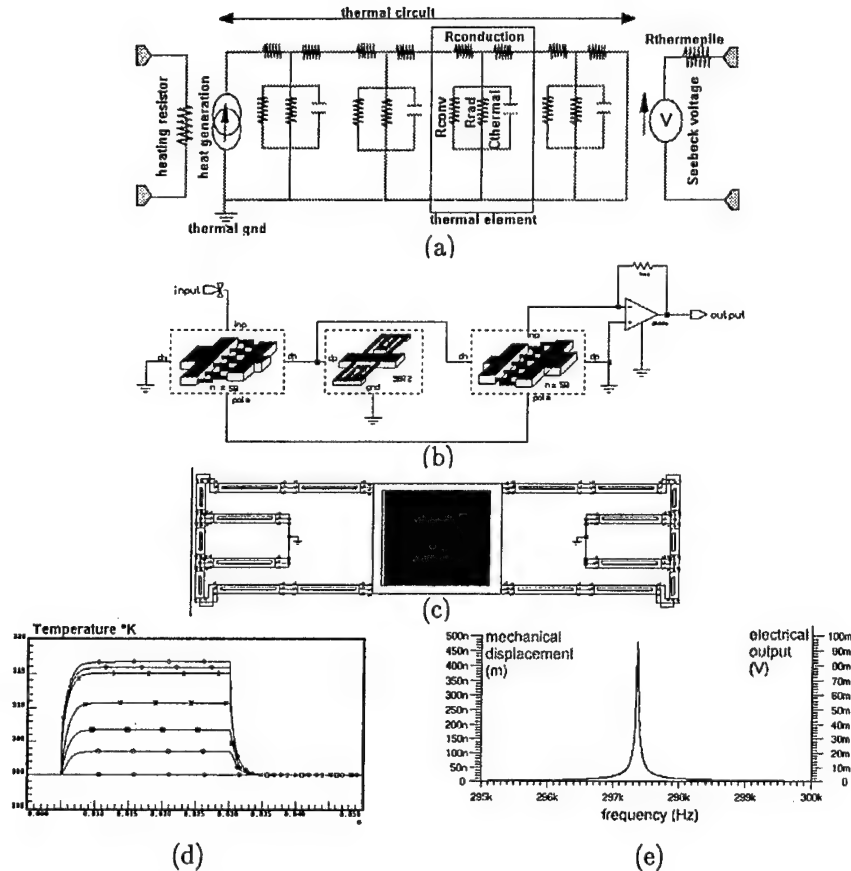


Fig. 5. MEMS HDL-based simulation: (a) thermal circuit for the ETC cantilever, (b) system-level description of the microresonator, (c) mass-spring-damper system for circuit-level mechanical analysis, (d) circuit-level simulation of the ETC with an input 1V 25ms pulse, and (e) system-level simulation of the μ resonator with 100 mV input.

across variables in each node (x , y and θ). Since elements directly linked to the layout are now available, the injection of the most realistic faults is possible. For example, faults resulting from the break of a beam or an anchor point or the stiction of a beam can be readily injected in such a circuit.

IV. MEMS Testing

MEMS devices fabricated today are tested functionally. Being essentially analog devices, their test is being approached by means of techniques from the analog test domain. In general, a MEMS device must be tested as an entity after manufacturing, with all modules in interaction and after packaging. For instance, additional stresses due to packaging can significantly impact device behavior. Since encapsulation of MEMS is often a very critical issue, accounting sometimes for even over 80% of the overall cost, testing a device should also be considered before packaging, screening out defective devices as early as

possible. Functional testing of large volume chips embedding MEMS risks to be extremely expensive. As for purely microelectronic chips, the development of cost-effective tests for large volume chips embedding MEMS may well require test stimuli targeting actual faults, developing fault lists and fault models for realistic defects, and using fault simulation as a major approach for assessing testability and dependability. This is illustrated in Table I.

Tab. I. Testing of integrated systems

Integrated Systems Testing	Digital Circuits 1980s-...	Analog and Mixed-Signal Circuits 1990s-...	Microsystems 2000s-...
failure mechanisms failure modes fabrication defects fault models	gate-oxide breakdown, electrical overstress, contaminants, latchup, and in addition : μ machining defects, fatigue, friction ...
	stuck-at, stuck-on, stuck-open, bridge ...	parametric faults catastrophic faults (electrical shorts & opens)	... and in addition : shorts & opens in the thermal, mechanical ... domains
test techniques	fault simulation (concurrent, VHDL, HSPICE), ATPG (PODEM, ...) diagnostic (fault, dictionary, boolean) BIST (scan path, LFSR, signature ...)	fault simulation (sequential, HSPICE, SABER, VHDL-AMS) ATPG (sensitivity ...) diagnostic (e.g. frequency signature) BIST (no general solution)	modeling of μ systems at circuit-level (HDLs) & transposition of techniques developed for microelectronics

The distinction between parametric and catastrophic faults typical of analog electronics testing appears again for MEMS. In MEMS parts, parametric faults due to deviations of electrical, mechanical or thermal parameters seem to dominate over catastrophic faults. For example, faults caused by defects originating from particulate contaminations, of much relevance in microelectronic parts are of lesser concern for micromechanical parts, at least in fabrication steps previous to dicing and packaging. On the other hand, new technological steps such as silicon micromachining introduce new types of defects and failure mechanisms specific to MEMS parts.

Figure 6 shows some example bulk and surface micromachining defects. Typical defects occurring during bulk micromachining include an inadequate release of a suspended microstructure. This can be due to the presence of oxide residuals which prevent etching, insufficient etching time, slow etching rate because of an inadequate solution (e.g. formation of hillocks), or re-depositions of etched material which may occur after micromachining [7]. Figure 6(a) shows an ETC cantilever which has not been fully suspended due to insufficient etching time. It is possible to see through the silicon dioxide beam, semi-transparent to the electronic microscope, the triangular shape of the silicon material under the beam which has not yet been removed. This defect results in an incorrect cantilever temperature map. Figure 6(b) shows the formation of hillocks (pyramidal protuberances) at the bottom of a microcavity. Hillocks reduce the etching rate, and the microbridge of Figure 6(b) is not fully freed in its central part.

The largest impact on the yield of surface micromachining technologies has by far been dominated by stiction. Stiction can mostly occur when the structure is released. Figure 6(c) illustrates the beams of a microresonator stuck down on the substrate. A

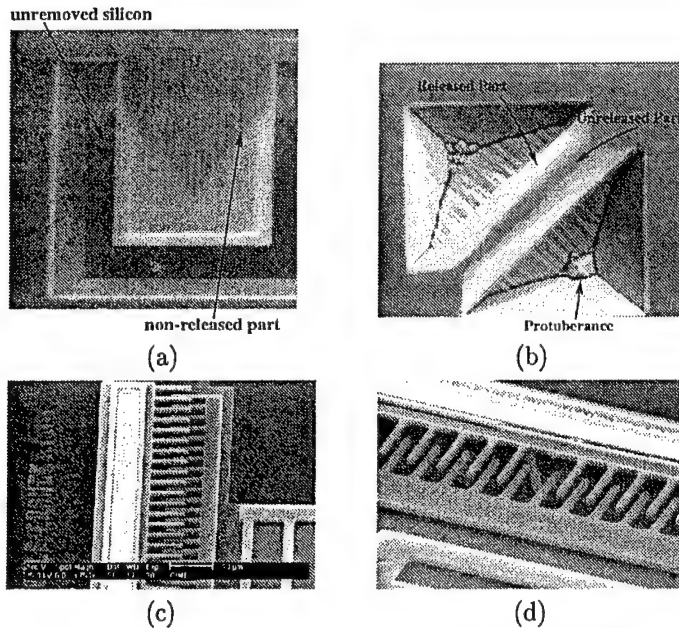


Fig. 6. Typical micromachining defects: (a) ETC with a cantilever only partially released, (b) pyramidal protuberances at the bottom of a microcavity etched with TMAH 25%, (c) stiction in a surface micromachined comb-drive, and (d) finger break.

broken finger in a comb-drive transducer as shown in Figure 6(d) may submit the shuttle to additional torques giving mechanical instability of the vibrating mass and unwanted lateral forces leading to impaired functionality or failure.

By adequately modeling fault effects for simulation, integration of design and test can be envisaged, selecting adequate test patterns which optimize defect and fault coverage and facilitate diagnosis. Deriving adequate fault models is obviously linked to the level of description and procedures used for their simulation. By modeling faults at the circuit-level, techniques already developed for the testing of analog microelectronic circuits can be transposed to MEMS. For example, Table II describes fault models which can be used for modeling the fault effects of the above defects.

For suspended thermal MEMS, faults can be modeled conveniently using fault models such as thermal shorts and thermal opens. For example, faults caused by the micromachining defects shown in Figure 6(a) are modeled using thermal shorts between the suspended cantilever and the substrate. For the microresonators, faults resulting from the break of a beam, the break of a joint or an anchor point, or the stiction of a beam can be readily injected in a mechanical circuit, such as that shown in Figure 5(c), using the fault models of Table II.

V. Conclusions

Current research efforts in MEMS development are trying to bring the analysis, design and test of microsystems in line with microelectronics. Higher levels of design abstrac-

Tab. II. Example fault models for modeling the effect of micromachining defects in suspended thermal MEMS and microresonators

Class of MEMS	Defects	Fault Model	Typical Example
Suspended thermal MEMS	inadequate release	thermal short	nodes of suspended part stuck-at ground temperature (body)
	break	thermal open	thermal path broken by break of suspended beam.
Micro-resonators	stiction	mechanical short	nodes stuck-at ground, movement impeded.
	break	mechanical open	joint or anchor break, floating nodes.

tion are searched, with a cleaner separation between technological processing and design effort. By relying on adequate design tools and methodologies, large and reliable MEMS systems can be envisaged. Clearly, this next generation of highly integrated systems pose important test challenges. Test technology already developed for microelectronics will need to tackle also the MEMS parts if the applications are to justify their cost. This paper has then tried to illustrate current steps towards the tuning of MEMS development with that of microelectronics.

References

- [1] Multi-Project Circuits (CMP) Service. *Reference Manual for ICs, MEMS and MCMs Manufacturing*. <http://tima-cmp.imag.fr/CMP/CMPMan.html>.
- [2] T. Mukherjee and G.K. Fedder. Structured design of microelectromechanical systems. In *34th Design Automation Conference*, pages 680–685, Anaheim, USA, June 1997.
- [3] D.A. Koester, R. Mahadevan, A. Shishkoff, and K.W. Markus. *SmartMUMPS Design Handbook*. MEMS Technology Applications Center MCNC, March 1996. Revision 4.0. <http://mems.mcnc.org>.
- [4] C.T.-C. Nguyen. Microelectromechanical devices for wireless communications. In *IEEE International Micro Electro Mechanical Systems Workshop*, pages 1–7, Heidelberg, Germany, January 1998.
- [5] W.C. Tang, T.-C.H. Nguyen, and R.T. Howe. Laterally driven polysilicon resonant microstructures. *Sensors and Actuators*, 20:25–32, 1989.
- [6] A. Dewey, H. Dussault, J. Hanna, E. Christen, G. Fedder, B. Romanowicz, and M. Maher. Energy-based characterization of microelectromechanical systems (MEMS) and component modeling using VHDL-AMS. In *Modeling and Simulation of Microsystems, Semiconductors, Sensor and Actuators (MSM'99)*, pages 359–362, Puerto Rico, 1999.
- [7] A. Castillejo, D. Veychard, S. Mir, J.M. Karam, and B. Courtois. Failure mechanisms and fault classes for CMOS-compatible microelectromechanical systems. In *IEEE International Test Conference*, pages 541–550, Washington DC, USA, October 1998.

An Object Oriented Methodology for Hardware Design

S. Vernalde, P. Schaumont, I. Bolsens

IMEC, Kapeldreef 75, B-3001 Leuven, Belgium

Abstract. Currently, no design environment exists that supports the design of a complex digital chip all the way from initial design exploration down to and including the detailed synthesis phase. In this paper, an object oriented programming approach for the design of complex systems in hardware is presented that covers the whole trajectory. It is shown how the usage of object oriented techniques resolves some major obstacles for system-on-chip design. The design of a 10 Mbit/s upstream cable modem is used as a driving example.

I. Introduction

The continuous evolution in ASIC technology allows the integration of complete telecom systems on silicon. This includes the complete information-processing path starting from physical transport of bits, over network layer processing down to user-level multimedia presentation.

Unfortunately not the same can be said from the tools that are needed to design these digital systems. In fact, the tools required to design for instance a mobile phone ASIC, are even far from fitting onto the hard disk of a single high-end Personal Computer.

For one thing, this is due to the fact that each design discipline (like DSP algorithm design, network performance simulation, hardware synthesis and embedded software design) has its own tool and/or favourite environment. As a result, a system level design flow is a patchwork of scripts, translators, and tools.

In addition, much tasks in the construction of an ASIC are still more of an art than a method. Think for instance of bringing a DSP algorithm designed in Matlab to a hardware implementation. There is a multitude of paths leading to a possible solution, and even more of them leading to a dead end.

We observe that there are some major obstacles today to do successful system-on-chip design.

- There is a lack of a single system-level environment that can be used throughout the design flow. While algorithms might be designed at high level in C, gates still have to be synthesised out of HDL. Each manual format translation, no matter how small, is a possible source of errors.
- The designer has insufficient control over the design process. He or she has to accept the result that (synthesis) tools produce. This is a result of those tools being sold as closed boxes. Assembling a system level design flow out of such tools however requires an open environment.
- There is lack of a systematic verification strategy. There are as many testbenches as there are tools used in the design flow. Especially at phases in this flow where drastic changes

are done to the design representation (e.g. during the transition from Matlab to Verilog), the development of corresponding or equivalent testbenches is extremely hard – if possible at all.

Being stuck with this situation in several recent demonstrator designs, we turned towards object-oriented C++ technology [6,7]. This allowed us to overcome all of the obstacles that were mentioned. The use of C++ has been demonstrated for the modeling and simulation of parallel hardware systems [1]. Our environment also provides VHDL code generation and HDL testbench generation.

In this paper, an overview of the resulting C++ design environment (called OCAP) will be given, in addition to the discussion of a concrete design experience. We start by giving a small example of C++ based design, and contrast it to traditional VHDL design. Next, the scope is broadened towards using C++ for a complete system level design flow. This is finally illustrated by the design of an upstream cable modem.

II. Hardware design with C++

When designing a system on chip in C++, we need to take care of both the hardware and software parts of this system. While C++ is a logical choice to devise the software parts, using it for hardware descriptions is less obvious. The match is however closer than one might think at first. The object-oriented capabilities of C++ allow us to write down a representation in terms of objects that closely resemble the actual intended circuit. To illustrate this point, consider the design of a simple incrementer circuit. It is desired to create a synchronous, digital machine, with one controller sending instructions to a datapath. The descriptions in table 1 show the result in both traditional VHDL coding and in our C++ design environment.

Incrementer in VHDL	Incrementer in C++
<pre> Architecture RTL of my_processor is Begin SYNC : process (clk) Begin If (clk'event and Clk = '1') then Current <= next_state; A_atl <= a; End if; end process; COMB : process (a, a_atl) Begin A <= a_atl; Case current is When state1 => a = 0; next_state <= state2; when state2 => a = a_atl + 1; end case; if (reset = '0') then a = 0; end if; end process; end RTL; </pre>	<pre> #include "ocapi.h" void main() { sig a(ck); // register sfg reset; // instruction a = 0; sfg inc; a = a + 1; fsm f(ck); // controller state statel; state state2; f << deflt(statel); f << state2; // state transitions statel << always << reset << state2; state2 << always << inc << state2; } </pre>

Table 1: Comparing equivalent VHDL and C++ descriptions

The circuit has a fairly standard description style in VHDL. We observe however that, by making this VHDL description, the distinction between the controller (finite state machine) and the data processing is lost. In addition, the constructs that are used to write VHDL (processes, variables, case statements, etc) bear little resemblance with the RT-level structure of the incrementer circuit. The C++ description, shown on the right, approaches the description from another side. It uses objects like *sfg*, *state* and *fsm* to reflect the exact design concept that was intended. In this case, *sfg* creates a datapath instruction, while *state* and *fsm* are parts of the controller. All these objects are related to each other through the use of C++ operators and expressions. As these operators execute, an object hierarchy is constructed that reflects the RT behaviour of the processor.

As will be discussed further, we can simulate this object hierarchy and generate VHDL code out of it. But it also allows us to design more effectively.

III. Design flow

In this section, the complete system level design flow is presented. To be able to construct systems on chip in an effective way, the following requirements must be met.

- A SoC design environment must be able to capture behaviour at high level. This is needed for doing algorithmic design and exploration. Therefore, OCAPI initially captures behaviour as a dataflow description, much in the same way as an environment like COSSAP [9] does. One difference is that our system description is a C++ program, where current environments are block-diagram based.
- A SoC design environment must offer the possibility to do detailed design description of hardware, similar to traditional HDL environments. OCAPI includes a set of objects that allow describing hardware at the RT level. In addition, these objects can be co-simulated with the high-level dataflow description.
- A SoC design environment should avoid making manual translations between equivalent design representations. For this purpose, a C++ description made in terms of OCAPI objects can be translated automatically to VHDL. In addition, VHDL testbenches and test vectors are generated which can be used to repeat simulations in correspondence with the C++ simulation.
- A SoC design environment must support incremental refinement which allows a smooth transition from pure behavioural descriptions down to architecture descriptions. In OCAPI, dataflow and architecture descriptions can be co-simulated. In addition, also floating point and fixed point datatypes can be freely mixed.

The design flow that we use is illustrated in Figure 1. The flow contains three major parts: a system level design part, a hardware synthesis part and a hardware verification part.

A. System design

The goal of the system design phase is to construct a functional RT-level model of the ASIC under construction. For verification and test purposes, a system level environment model is required. We will use a cable modem receiver example as we go through the entire design flow. For the design of this receiver, the environment model consists of a transmitter model and a channel model. This allows system level simulations and verification of the receiver algorithms. These simulations are collected in a set of C++ testvectors that will be reused in the hardware testbenches.

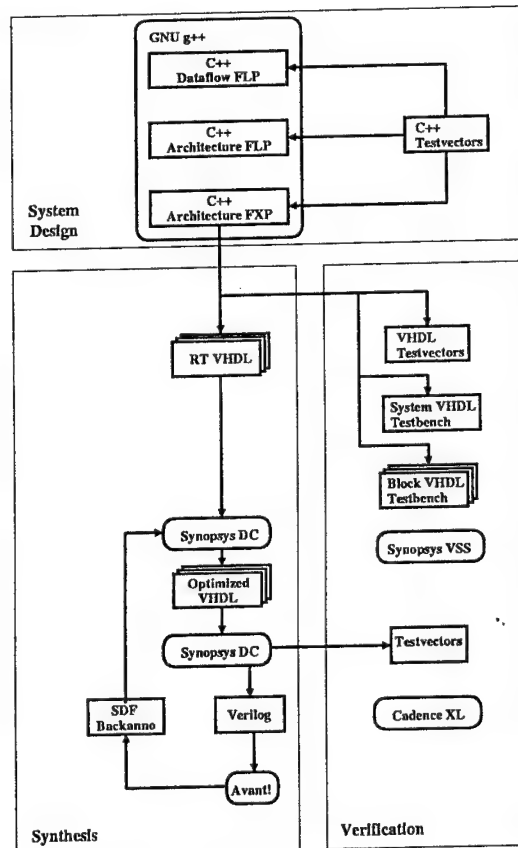


Figure 1: The C++ based system design flow

Initially, a floating-point data flow model of the complete system is constructed (transmitter, channel model, receiver). Next, the receiver is refined to a cycle true architecture model. Scheduling the operations of high level descriptions to clock cycles does this. In addition, bringing dataflow to hardware also requires the mapping of the dataflow system-level semantics to an implementation. This is a standard design task for which several solutions exist.

After the architecture has been obtained, the chip signal wordlengths are decided in order to yield a cycle true, bit-true architecture model. Fixed-point refinement is done by means of simulation. The required refinement strategy is dependent on the type of application. However, a good strategy for a digital receiver is the following one. First, a reception quality metric (e.g. constellation purity) is determined using only quantization at the A/D side. Next, the other wordlengths are decided such as to prevent overflow and to maintain the reception quality metric. After these steps, the C++ model is a bit-true clock-cycle true representation of the architecture.

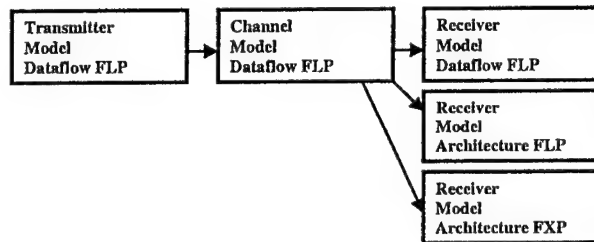


Figure 2: Three possible simulations during system level design of a cable modem

The advantage of using C++ during system design is clear by considering Figure 2. Since OCAPI allows to freely mix algorithmic and architecture descriptions, as well as floating and fixed point datatypes, the receiver description can be co-simulated with the transmitter and channel model at various level of receiver design detail.

The system level design phase concludes with the use of a code generator that creates, out of the C++ description, the input for subsequent hardware synthesis and verification.

- For each block (FSMD) of the receiver, a synthesizable RT-VHDL file is created.
- For the overall chip, a system netlist is generated to connect the various blocks in the design.
- The C++ test vectors are translated into block-level and system-level testbenches. In addition, appropriate testbench drivers are generated.

B. Synthesis

The generated VHDL code is directly fed into the Synopsys logic synthesis tools [8]. It is in essence a fully automated process that can be run in batch.

While this synthesis flow is industry standard, the C++ environment and verification that surrounds it is innovative.

C. Verification

During synthesis, simulation-based verification is used extensively to track the correctness of the synthesis results. All VHDL-level simulations are done using the generated testbenches with the Synopsys VSS simulator at block-level and system level. The final Verilog netlist is checked using generated production test vectors with the Cadence Verilog-XL simulator.

Verification is done by C++ simulation during the system design phase and by HDL simulation during the synthesis phase. There are 5 verification levels that correspond to the 5 description levels of the design. Three of them are in C++ (dataflow floating point, cycle-true floating-point and cycle-true fixed point). The remainder two are at VHDL (RT-VHDL and Synopsys-DC VHDL outputs) and Verilog (final netlist) level. The design of testbenches is done in C++, since corresponding HDL testbenches are obtained by code generation. As shown by Figure 3, the test simulations can be categorised in three areas: Performance tests, functional tests, and equivalence tests.





	Performance	Functional	Equivalence
C++ Dataflow FLP	X	X	
C++ Architecture FLP		X	
C++ Architecture FXP		X	
Block HDL		X	
System HDL		X	

Figure 3: Verification strategies at different levels

The performance tests are used to check the initial performance of the design. For a digital receiver, test scenarios include varying levels of channel noise, phase distortion, carrier frequency deviation, amplitude slope distortion, gain variation and burst spacing. These tests ensure that the initial algorithmic model has the desired performance.

The functional tests check the correct operation of a design within one verification level. Typical tests include for instance the reception of a known data sequence. The goal of these tests is to perform a simulation with maximal coverage of the design description.

Equivalence tests compare the operation of one level to the next. They are applied at either floating-point level or else fixed-point level. Equivalence tests do a one-to-one comparison of values on the system interconnect at corresponding time-points.

IV. An upstream cable modem

Using the OCAPI object library and the design flow discussed above, we have completed several demonstrator designs including an upstream cable modem, a DECT transceiver and a MPEG-4 image coder. Some details on the cable modem design are included here to illustrate the power of C++ based design.

This upstream cable modem was developed in a research project in co-operation with Siemens-Atea, Belgium [5]. An upstream cable modem receiver resides at the head-end of the HFC television access network. HFC is a network architecture that is built up of coax and fiber. In upstream HFC communications, modulated data is transmitted from the consumer side to the head-end. The single chip digital receiver that we have developed is embedded in the head-end and demodulates this data. It takes care of the physical layer signal processing required for QAM16 or QPSK modulation. Offering 10 Mbits/s data throughput in a 3.3 MHz upstream channel band, it is compliant with the main HFC communications standards (MCNS/DOCSIS [2], DAVIC/DVB [3] and IEEE 802.14 [4]). The chip relies extensively on digital signal processing to demodulate and decode upstream signal bursts. It also estimates and automatically corrects various transmission impairments occurring on the upstream HFC channel. Such impairments include varying signal levels, carrier frequency deviations, group delay distortion and amplitude variation. In addition, the chip provides an interface for an external Reed Solomon channel decoder that combats channel noise effects.

A. Development

The chip was developed from scratch with the C++ based design flow. Therefore we started by constructing a system level functional model in C++. This model includes a burst transmitter, a channel model, and a receiver functional dataflow model. Such a system model allows to explore various receiver algorithms and to construct system level testbenches that determine the overall system performance.

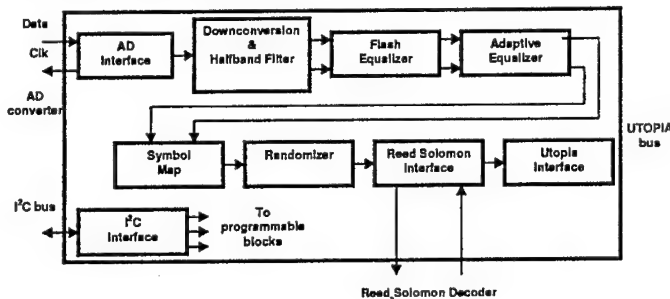


Figure 4: Upstream cable modem chip architecture

The resulting receiver, shown in Figure 4, has been optimised for minimal communication overhead. For this purpose, it contains an advanced flash equalisation algorithm that works with a short, fixed length preamble independent of the communication channel conditions. It also makes the core particularly suited for multimedia applications, in which wide ranges of bitrates need to be supported. All signal processing is done entirely digital, making the performance reliable, predictable and free of tuning. This signal processing is performed in a chain of independent blocks. This complex allows receiving QAM16/QPSK burst signals with an interburst spacing of only 4 symbols and a preamble of 17 symbols.

Care was taken to make the functionality programmable. An I2C programming interface allows in-the-field configuration and adjusting of demodulation parameters. The burst payload length is programmable. In addition, various parameters such as received signal power and equaliser coefficients can be extracted for signal quality estimation.

The complete development process starting at algorithm design and ending with a clock-cycle true, bittrue architecture was done in C++ with the OCAPI library. Once the architecture model was available, synthesisable RT-VHDL code was generated to bring the receiver circuit to a gate level implementation. The code size statistics of the chip in the subsequent design phases are shown in table 2. They illustrate the compactness that can be achieved by using object orientation.

Specification		
C++ Dataflow	922	Lines
C++ Architecture	4426	Lines
RT VHDL	21798	Lines
Gate Level VHDL	154952	Lines

Table 2: Cable modem code size

Using C++ based design we experienced tight control over the entire design flow. This is because there is only a single environment in which system level design was performed,

including the development of testbenches. We ensured that the C++ simulations were correct, after which only the equivalence between C++ and generated HDL had to be shown. This was straightforward since the testbenches are generated from the C++ design too.

V. Conclusions

A design methodology for systems on silicon was presented that is based on object oriented programming techniques. It was shown that the application of object oriented programming to hardware design allows to alleviate some of the major obstacles for efficient system level design:

- There is a single system-level design environment for both algorithm design and architecture design. The transitions between the two levels are done by incremental refinement of descriptions.
- By using a programming language, the designer has full control over the design process. This open environment provides a very effective way to deal with the diversity and heterogeneity of system-on-chip design.
- Because of the open design environment, verification is supported throughout the design process. Three types of verification were identified.

The design of an upstream cable modem using this methodology has resulted in a short design time and first time right silicon.

Acknowledgements

This work was carried out under the Flemish Impulse Program for Information Technology. For the realisation of the cable modem, we would explicitly like to thank Siemens Atea for their effort in the collaboration.

References

- [1] R. K. Gupta and S. Y. Liao, "Using a programming language for digital system design", *IEEE design and Test of Computers*, pp. 72-80, April-June 1997.
- [2] Data Over Cable Service Interface Specifications (DOCSIS) MCNS. <http://www.cablemodem.com>.
- [3] DAVIC 1.3 part 8 Digital Audio Visual Council. <http://www.davic.org>.
- [4] IEEE 802.14 Cable TV Protocol Working Group. <http://walkingdog.com/catv>.
- [5] Siemens Atea R&D Technology Homepage. http://www.siemens.be/atea/products_services/rd_technology/rd_frames.htm.
- [6] P. Schaumont, S. Vernalde, L. Rijnders, M. Engels and I. Bolsens, "A programming environment for the design of complex high speed asics", *In Proc. DAC*, 1998.
- [7] P. Schaumont, S. Vernalde, M. Engels and I. Bolsens, "Synthesis of multi-rate and variable rate digital circuits for high throughput applications", *In Proc. EDTC*, 1997.
- [8] Synopsys Inc., 700 E. Middlefield Rd, Mountain View, CA 94043. DC User's Manual.
- [9] Synopsys Inc., 700 E. Middlefield Rd, Mountain View, CA 94043. COSSAP User's Manual.

Author Index

A		E	
Aboulhamid E. M.	81	Eles P.	21
Áč P.	211	Eshraghian K.	37
Áč V.	211		
Al-Raweshidy H. S.	125, 157, 263, 275	F	
Ampem-Darko S. O.	125	Ferri G.	199
Azizi M.	81	Feske K.	45
		Foley J. B.	33
B		G	
Baraniecki R.	49	Gašpar J.	29
Barker P.	129	Giustolisi G.	143
Baroňák I.	293	Glesk I.	103
Becker J.	85	Glesner M.	85
Bečková J.	29	Gramatová E.	29
Bennetts R.G. Ben	55	Graupner A.	117
Beňušková L.	207		
Bhatti A.	157	H	
Blunár K.	271	Hábovčík P.	161
Bolsens I.	53, 311	Hajtáš D.	239
Boucoulalas A. C.	129	Haniotakis Th.	13
Brasching A.	33	Hollreiser M.	37
		Hollstein T.	85
C		Hong J-W.	243
Cabestany J.	219	Husák M.	77
Cantaragiu S.	181		
Catthoor F.	93	I	
Cherniakovski D.	173	Issa B.	161
Chovan J.	161	Ivanov K. P.	121
Comiskey P. A.	33	Ižák R.	193
Čupák M.	93		
		J	
D		Jahromi M. M.	263
Dandache A.	259	Janicki M.	73
De Laurentiis P.	199	Janiszewski I.	49
De Man H.	93	Jervan G.	21
Deng K-L.	103		
Đuračková D.	231, 239, 255		

K

Kazakevich K.	173
Kazimirovski I.	173
Kim C-Y.	267
Kim W-H.	251, 267
Koort M.	149
Koska M.	235
Krebs A.	45
Krnáč M.	169
Kukk V.	145

L

Lachowicz S.	37
Lambert J. Ph.	259
Langer M.	45
Larsson E.	25
Lazaryan A.	203
Lee Y-H.	243
Lee Y-S.	243
Lepley B.	259
Lőrincz A.	227

M

Manhaeve H.	65, 69
Markus A.	17
Masa P.	227
McCarthy O.	113
Mijat N.	153
Mika F.	239
Miller A.	285
Mir S.	301
Mkrttchian V.	203
Molnár J. V.	231
Monnier T.	89
Monteiro F.	259
Moon B-I.	243
Moon S.	243
Moon U-K.	97
Moskowiz A.	285
Murtaza G.	157

N

Napieralski A.	73
Neag M.	113
Nicolaidis M.	13
Nikolos D.	13

O

Oláh M.	227
Olej V.	271
Ondráček O.	247

P

Palán B.	77
Palmisano G.	143
Palumbo G.	143
Palumbo G.	199
Paoli Ch.	215
Park J-S.	251
Paško R.	255
Peng Z.	21, 25
Pennisi S.	109, 199
Perić I.	135
Pessolano F.	41
Pfleiderer H-J.	37
Pojlovka S.	207
Polák M.	247
Polanšek G.	189
Poľáško M.	139
Poppe A.	227
Pruncal P.R.	103
Přádka M.	185

R

Radev N. A.	121
Raik J.	17
Roháčková M.	235
Roche F. M.	89
Runsen R. J.	103
Ryan A.	113
Ryu D-R.	243

S

Santucci J-F.	215
Schaumont P.	311
Schüffny R.	117
Schwarzbacher A. Th.	33
Sidiropulos M.	69
Siekierska K.	49
Song K-H.	251, 267
Srdić I.	135
Steensgaard J.	97
Stepanets V.	173

Stojković N.	153
Stopjaková V.	65
Straka B.	65, 69
Szendiuch I.	185
Švajda M.	69

T

Tahar S.	81
Temes G.C.	97
Theisen M.	85
Tomáška M.	165, 169
Tommasino P.	109
Török S.	227
Trifiletti A.	109
Trofimov S.	173
Trost A.	189
Tsiatouhas Y.	13

U

Ubar R.	17
Uherek F.	161

V

Vanneuville J.	69
Vergos H. T.	13
Vernalde S.	255, 311
Vladov S. S.	121
Vlček K.	177
Vrba R.	271

W

Wahl Th. H.	33
Weber B.	65

Z

Zajc B.	189
Zorian Y.	1
Zovko-Cihlar B.	135
Žemva A.	189

IEEE Computer Society

TTTC: Test Technology Technical Council

PURPOSE: The Test Technology Technical Council (TTTC) is a volunteer professional organisation sponsored by the IEEE Computer Society. The goals of TTTC are to contribute to member's professional development and advancement and to help them solve engineering problems in electronic test, and help advance the state-of-the art. All activities are led by volunteer members.

MEMBERSHIP: TTTC membership is open to all individuals interested in test engineering at a professional level. In addition to the benefits of personal association with other test professionals and the opportunity to serve on a wide range of committees, members receive TTTC Newsletters and announcements.

DUES: There are NO dues for TTTC membership and no parent-organisation membership requirements; however there are substantial reductions in fees for TTTC-sponsored meetings and tutorials for members of IEEE and/or IEEE Computer Society (IEEE and IEEE/CS do have member fees).

NEWSLETTER: Every year TTTC publishes four issues of its newsletter embedded in the magazine IEEE Design & Test of Computers. In addition TTTC publishes several issues of a more comprehensive newsletter that is mailed to all members. The newsletter covers current issues in test, TTTC technical activities, standards, technical meetings, etc.

STANDARDS: TTTC initiates nurtures and encourages new test standards. TTTC-initiated Working Groups have produced numerous IEEE standards, including the 1149 series used throughout the industry.

TECHNICAL ACTIVITIES: TTTC sponsors a number of Technical Activity Committee (TACs) that address emerging test technology topics. TTTC TACs guide a wide range of activities in these topic areas.

TECHNICAL MEETINGS: TTTC sponsors several well-known conferences and symposia and holds numerous regional and topical workshops to spread technical knowledge and advance the state-of-the art.

TUTORIALS and EDUCATION: TTTC sponsors a comprehensive *Test Technology Educational Program (TTEP)*. This program provides opportunities for design and test professionals to update and expand their knowledge base in test technology, and earn official accreditation from IEEE TTTC, upon the completion of four full day tutorials offered by TTEP. TTEP tutorials are held in conjunction with ITC, VTS, ATS, ETW, and DFTS.

TTTC On-Line: The TTTC Web Site at <http://computer.org/tttc> offers samples of the TTTC Newsletter, information about technical activities, conferences, workshops and standards, and link to the Web pages of a number of TTTC-sponsored technical meetings.

TTTC Officers for 1999

TTTC Chair	Yervant ZORIAN	LogicVision, Inc	zorian@logicvision.com
Past Chair	Fred LIGUORI	ATE Consulting Services	fliguori@aol.com
Senior Past Chair	Ned KORNFIELD	Widener University	ned613@aol.com
TTTC Vice Chair	Michael NICOLAIDIS	TIMA	michael.nicolaidis@imag.fr
TTTC Vice Chair	Paolo PRINETTO	Politecnico di Torino	Paolo.Prinetto@polito.it
ITC General Chair	Mike TOPSAKAL		topsakal@jps.net
IEEE D&T Editor-in-Chief	Yervant ZORIAN	LogicVision, Inc.	zorian@logicvision.com
Secretary	Mouli CHANDRAMOULI	Synopsys, Inc.	mouli@synopsys.com
Finance	Fred LIGUORI	ATE Consulting Services	fliguori@aol.com

Group Chairs

Technical Meetings	Dimitris GIZOPOULOS	4Plus Technologies	dgizop@4plus.com
Standards	Patrick McHUGH	Lockheed Martin	P.McHugh@ieee.org
Tutorials & Education	Michael NICOLAIDIS	TIMA	michael.nicolaidis@imag.fr
Technical Activities	Anthony P. AMBLER	University of Texas at Austin	ambler@mail.utexas.edu
Asia & Pacific	Kozo KINOSHITA	Osaka University	kozo@ap.eng.osaka-u.ac.jp
Europe	Christian LANDRAULT	LIRMM	landrault@lirmm.fr
Latin America	Fabian VARGAS	Catholic University - PUCRS	vargas@ee.pucrs.br
North America	André IVANOV	University of British Columbia	ivanov@ee.ubc.ca

Technical Activity Committees

Bare Substrate/Board	Christophe VAUCHER	T4	Vaucher@bare-board-test.com
Defect Tolerance	Claude THIBEAULT	Ecole de Technologie Super.	thibeault@ele.etsmtl.ca
	Vincenzo PIURI	Politecnico di Milano	piuri@elet.polimi.it
Economics of Test	Anthony P. AMBLER	University of Texas at Austin	ambler@mail.utexas.edu
	Magdy S. ABADIR	Motorola, Inc.	abadir@ibmto.com
Embedded Core Test	Yervant ZORIAN	LogicVision, Inc.	zorian@logicvision.com
High Level Design & Test	Prab VARMA	Veritable	prab@veritable.com
Iddq Testing	Keith BAKER	Philips ED&T	Baker@natlab.research.philips.com
Manufacturing Test	David LEPEJIAN	Heuristic Physics Lab.	dyl@hpl.com
MCM Testing	Yervant ZORIAN	LogicVision, Inc.	zorian@logicvision.com
Memory Test	Rochit RAJSUMAN	Advantest America R&D Center	r.rajsuman@advantest.com
MEMS Testing	Bernard COURTOIS	TIMA	Bernard.Courtols@imag.fr
Mixed-Signal Testing	Bozena KAMINSKA	OPMAXX Inc.	bozena@opmaxx.com
On-Line Testing	Michael NICOLAIDIS	TIMA	michael.nicolaidis@imag.fr
Software Testing	Yashwant k. MALAIYA	Colorado State University	malaiya@cs.colostate.edu
System Test	John W. SHEPPARD	ARINC Incorporated	Jsheppar@arinc.com
	Randy William SIMPSON	IDA	rsimpson@ida.org
Test Education	Mani SOMA	University of Washington	soma@ee.washington.edu
Test Synthesis	Kwang-Ting CHENG	Univ. of California Santa Barbara	timcheng@ece.ucsb.edu
Thermal Test	Bernard COURTOIS	TIMA	Bernard.Courtols@imag.fr
Verification & Test	Jacob A. ABRAHAM	University of Texas at Austin	jaa@ccrc.utexas.edu

Standards Working Groups

IEEE 1149.1	Christopher J. CLARK	Intellitech Corporation	cjclark@intellitech.com
IEEE 1149.5	Harry HULVERSHORN	LogicVision, Inc.	harryh@logicvision.com
IEEE P1149.4	Adam CRON	Synopsys, Inc.	acron@synopsys.com
IEEE 1450 - (STIL)	Gregory MASTON	Fluence	gregm@fluence.com
	Tony TAYLOR	Fluence	tonyt@fluence.com
IEEE P1500	Yervant ZORIAN	LogicVision, Inc.	zorian@logicvision.com
IEEE P1532	Neil JACOBSON	Xilinx Corp.	neil.jacobson@xilinx.com

TTTC sponsored Technical Meetings in 1999

Feb 23-26	Pacific Northwest Test Workshop	Bottega Bay, CA - USA	E. J. McCLUSKEY
Feb 28 - Mar 02	TWS'99 German Workshop	Potsdam - Germany	H. T. VIERHAUS
Mar 9-12	D.A.TE'99	Munich - Germany	R. ERNST
Mar 22-24	Test Synthesis Workshop	Santa Barbara, CA - USA	R. C. AITKEN
Mar 30 - Apr 01	Design, Test of MEMSIMOEMS	Paris - France	B. COURTOIS
Apr 25	IDDQ Testing Mini-Workshop	Dana Point, CA - USA	Y. K. MALAIYA
Apr 25-29	VLSI Test Symposium	Dana Point, CA - USA	M. NICOLAIDIS
Apr 28-29	Testing Embedded Cores Workshop	Dana Point, CA - USA	Y. ZORIAN
May 19-21	Signal Propagation Workshop	Titisee-Neustadt - Germany	J. P. MUCHA
May 25-28	European Test Workshop	Constance - Germany	H.-J. WUNDERLICH
May 27-28	North Atlantic Test Workshop	West Greenwich, RI - USA	J.-C. LO
Jun 06-09	Southwest Test Workshop	San Diego, CA - USA	W. R. MANN
Jun 15-18	Mixed Signal Testing Workshop	British Columbia - Canada	A. IVANOV
Jun 16-18	Rapid System Prototyping	Clearwater, FL - USA	R. LAUWEREINS
Jul 05-07	On-Line Testing Workshop	Rhodes - Greece	M. NICOLAIDIS
Aug 05-06	VLSI Design & Test Workshops	New Delhi - India	C. P. RAVIKUMAR
Aug 09-10	Memory Test Workshop	San Jose, CA - USA	R. RAJSUMAN
Aug 17-22	Computer Science Conference	Yerevan - Armenia	Y. SHOUKOURIAN
Sep 06-08	Electronic Systems Conference	Bratislava - Slovakia	D. DONOVAL
Sep 12-15	High Density Module Test VI	Napa, CA - USA	R. J. WAGNER
Sep 15-17	Known Good Die Industry Workshop	Napa, CA - USA	L. GILG
Sep 28-30	International Test Conference	Atlantic City, NJ - USA	M. TOPSAKAL
Sep 30 - Oct 01	Production Test Automation Workshop	Atlantic City, NJ - USA	A. P. AMBLER
Sep 30 - Oct 01	Microprocessor Test Workshop	Atlantic City, NJ - USA	M. S. ABADIR
Sep 30 - Oct 01	System Test and Diagnosis Workshop	Atlantic City, NJ - USA	R. W. SIMPSON
Oct 04-06	Thermal Investigations of ICs Workshop	Rome - Italy	B. COURTOIS
Oct 25-27	1999 DAK Forum	Trondheim - Norway	E. J. AAS
Nov 01-03	Defect & Fault Tolerance Symposium	Albuquerque, NM - USA	C. METRA
Nov 04-06	High-Level Design Validation Test W.	San Diego, CA - USA	A. ORAILOGLU
Nov 16-18	Asian Test Symposium	Shanghai - China	B. M. Y. HSIAO

TTTC Office

1474 Freeman Drive
Amissville, VA 20106
USA

Phone: +1-540-937-8280
Fax: +1-540-937-7848
E-mail: tttc@computer.org

<http://computer.org/tttc>